



Physical Processes in Natural Waters

13th International Workshop - Palermo, Italy, from Sep 1-4 2009

Proceedings

Editors: G. Ciraolo, G.B. Ferreri, E. Napoli

ISBN 978-88-903895-0-4

SESSION 1:

1. Observation of a monimolimnetic overturn in the iron-meromictic lake Waldsee -- *B. Boehrer, S. Dietz, C. von Rohden, U. Kiwel, K. D. Jöhnk, S. Naujoks, J. Ilmberger, D. Lessmann*.
2. Double-diffusive convection in mid-latitude meromictic lakes -- *C. von Rohden, J. Ilmberger, B. Boehrer*.
3. Basic modelling of double diffusive processes in meromictic lakes -- *J. Ilmberger and C. von Rohden*.
4. Sediment methane emission: sources and fate in the water column -- *D.F. McGinnis, S. Sommer, L. Rovelli, P. Linke*.
5. Gas exchange and deep water renewal in Lake Van (Turkey) estimated by inverse modelling of transient tracers -- *H. Kaden, F. Peeters, R. Kipferf, Y. Tomonaga*.
6. Release and distribution of methane in lakes -- *H. Hofmann and F. Peeters*.

SESSION 2:

7. Exchange Flow between Open Water and an Aquatic Canopy -- *X. Zhang and H. M. Nepf*.
8. Particle tracking in a gap of aquatic vegetation meadow -- *G. Ciraolo, C. Costa, G. B. Ferreri, A. Folkard, A. Maltese*.
9. Hydrodynamics of heterogeneous mussel beds: laboratory flume experiments -- *A. Folkard*.
10. Partial depth exchange flow between canopy and open water -- *M. Jamali and S. Marvi*.
11. Wind and tide induced currents in the Stagnone Lagoon (Sicily) -- *G. Ciraolo, M. De Marchis, C. Nasello, E. Napoli*.

SESSION 3:

12. Modeling of the thermal pollution in the lakes-coolers as an example of the Shatura Lakes system (Russia) -- *E.I. Debolskaya, E.V. Yakushev, I.S. Kuznetsov*.
13. Spring thermal bar in fresh basin: laboratory experiments and numerical simulations -- *N.Yu. Demchenko*.
14. The dynamics of internal wave resonance in periodically forced lakes -- *L. Boegman and G.N. Ivey*.
15. Basin scale internal waves in the bottom boundary layer of an ice-covered lake -- *G. Kirillin, C. Engelhardt, S. Golosov*.
16. The physical control of the size structure of the phytoplankton community in a Mediterranean reservoir -- *A.B. Hoyer, P.I. León-Díaz, J.M. Blanco, J. Rodríguez, C. Escot, F.J. Rueda*.

SESSION 4:

17. Simulation of the effects of projected pumped-storage operations on temperature and turbidity in the two affected lakes -- *M. Schmid, D. F. McGinnis, U. Vogel, A. Wüest*.
18. Past and future lake ice covers of the Berlin-Brandenburg area -- *J. Bernhardt, G. Kirillin, C. Engelhardt, J. Matschullat*.
19. Fate of groundwater inflow in Lake Þingvallavatn during early spring icebreakup -- *H. Ó. Andradóttir, A. L. Forrest, B. E. Laval*.
20. Modeling climatological circulation in Lake Michigan -- *D. Beletsky and D. Schwab*.
21. Summertime Inter-hypolimnetic Thermal Differences in a Small Multi-basin Lake -- *Y. Imam, B. Laval, D. Lim, G. Slater*.

SESSION 5:

22. Turbulence measurements from a Glider -- *Fabian Wolk, Rolf Lueck, Lou St. Laurent*.
23. In situ measurements of turbulence in fish shoals -- *A. Lørke and W. N. Probst*.
24. Field observations of breaking high-frequency internal waves -- *M. Preusse, F. Peeters, A. Lørke*.
25. Hydrodynamics and Salinity of the Future Sacramento-San Joaquin Delta -- *W. E. Fleenor, E. Hanak, J. R. Lund, J. F. Mount*.
26. Shear-induced bottom boundary layer convection in stratified basins: a modeling study -- *J. Becherer and L. Umlauf*.

SESSION 6:

27. An improved numerical solver of the 2D diffusive shallow waters equations over unstructured triangular meshes -- *C. Aricò, C. Nasello, M. Sinagra, T. Tucciarelli*.
28. Hydrodynamic and Hydraulic Modeling of the Huron-Erie Corridor -- *D. J. Schwab, E. J. Anderson, G. A. Lang*.
29. Temporal evolution and spatial heterogeneity of ecosystem parameters in a subtropical lake -- *I. Ostrovsky and Y. Z. Yacobi*.
30. A Comparison of Parameterized, Simulated and Measured Turbulent Mixing in the Gulf of Finland, the Baltic Sea -- *M. J. Lilover and A. Stips*.
31. Scenarios of multi-annual simulations of the coupled North Sea – Baltic Sea system -- *A. Stips, K. Bolding, M. Lilover*.

POSTER SESSION:

32. Flow characteristics in a large amplitude meandering bend -- *D. Termini*.
33. Flow velocity and turbulence intensity distribution in a vegetated straight laboratory channel -- *F. G. Carollo, V. Ferro, D. Termini*.
34. The use of high-resolution sismo-acoustic echosounder imaging for Estimation carbon sink in P. oceanica dead matte -- *F. Luzzu, A. Tomasello, G. Di Maida, C. Orestano, M. Pirrotta, C. Bellavia, C. Costantini, A. Scannavino and S. Calvo*.
35. Application of the Princeton Ocean Model to simulate the fate and behaviour of pharmaceuticals in a shallow urban lake -- *S. Schimmelpfennig, C. Engelhardt, G. Nützmann, G. Kirillin*.

36. Seagrasses as biological barriers against anthropic input in coastal marine ecosystems -- *S. Vizzini, C. Tramati, V.A. Tumbarello, V. Costa and A. Mazzola*.
37. Optical properties of Sicilian lakes during a Cyanophyceae *Planktothrix rubescens* algal bloom -- *V. Pampalone, A. Maltese, G. Ciraolo, G. La Loggia*.
38. Study of the accuracy of the mean flow from ADCP -- *M. Gutierrez, J. Planella, E. Roget*.
39. ADCP velocity profiles analysis in the Castellammare gulf -- *C. Nasello, G. Ciraolo, G. La Loggia*.
40. Investigating marine shallow waters dynamics to explore the role of turbidity on ecological responses -- *S. Di Marca, M. Lo Martire, C. Nasello, G. Ciraolo, G. Sarà*.
41. Turbidity analysis in Sicilian coastal zones by means of remote sensing images and spectroradiometric measurements -- *M. Tulone, A. Maltese, G. Ciraolo, G. La Loggia*.

Observation of a monimolimnetic overturn in the iron-meromictic lake Waldsee

Bertram Boehrer¹, Severine Dietz², Christoph von Rohden³, Uwe Kiwel¹, Klaus D. Jöhnk⁴, Sandra Naujoks¹, Johann Ilmberger³ and Dieter Lessmann²

¹ Helmholtz-Centre for Environmental Research - UFZ, Magdeburg, Germany

² Department of Freshwater Conservation, Brandenburg University of Technology, Cottbus, Germany

³ Institute of Environmental Physics, University of Heidelberg, Heidelberg, Germany

⁴ Department of Limnology of Stratified Lakes, Leibniz-Institute of Freshwater Ecology and Inland Fisheries, Neuglobsow, Germany

*Corresponding author, e-mail Bertram.Boehrer@ufz.de

ABSTRACT

From a small iron-meromictic lake, we present observations of a circulation pattern that has not been documented in the limnological literature before: a monimolimnetic overturn. While surface cooling drives a vertical circulation of the upper water layer (mixolimnion), the deeper water layer is not included due to its higher concentration of dissolved substances. However, higher diffusivity of heat than of dissolved substances (double diffusion) facilitates the faster escape of heat from the monimolimnion (deep water layer) compared to dissolved substances during cold periods. As a consequence, interfacial cooling of the monimolimnion drives a vertical circulation within the monimolimnion without breaking the stratification towards the mixolimnion. In the presented case, the geochemical setting does not permit dissolved substances to enter the mixolimnion, as iron does not dissolve in oxic pH-neutral water. As a consequence, the system approaches the case of two immiscible layers in thermal contact. Below the chemocline, a convection layer is formed, that exceeds the staircase layer thickness of double diffusion when conservative salts are involved.

KEYWORDS

Double diffusion, meromixis, monimolimnetic overturn, surface cooling, iron meromixis, physical limnology

ACKNOWLEDGEMENTS

This work was funded by the Deutsche Forschungsgemeinschaft (DFG)

REFERENCES

- Boehrer, B., and M. Schultze (2008), Stratification of lakes, Rev. Geophys., **46**, RG2005, doi:10.1029/2006RG000210.
Boehrer, B., S. Dietz, C. von Rohden, U. Kiwel, K. D. Jöhnk, S. Naujoks, J. Ilmberger, and D. Lessmann (2009), Double-diffusive deep water circulation in an iron-meromictic lake, Geochem. Geophys. Geosyst., 10, Q06006, doi:10.1029/2009GC002389.

Double-diffusive convection in mid-latitude meromictic lakes

Christoph von Rohden^{1*}, Johann Ilmberger¹, and Bertram Boehrger²

¹ Institute of Environmental Physics, University of Heidelberg, Im Neuenheimer Feld 229,
D-69120 Heidelberg, Germany

² UFZ-Helmholtz Centre for Environmental Research, Brückstr. 3a, D-39114 Magdeburg,
Germany

*Corresponding author, e-mail Christoph.vonRohden@iup.uni-heidelberg.de

ABSTRACT

Meromictic lakes are characterised by strong stable density stratification in and below the chemocline, which separates the oxic mixolimnion from the anoxic monimolimnion. Stable density gradients involve slow vertical exchange, especially in the chemocline.

Vertical transport within the chemocline can be as low as molecular. Typically, destabilising temperature profiles establish in the monimolimnion as a consequence of the heat flux from the sediments and the lower mean temperature at the chemocline surface (close to the temperature of maximum density). However, gradients of solutes extending to the lake bottom stabilise stratification.

Double diffusive processes may create local instabilities and subsequently cause convective mixing when the destabilisation due to heat gradients approaches the stabilisation by solutes (diffusive regime). If the seasonal temperature cycle in the hypo- and mixolimnion ranges to the upper surface of the monimolimnion, convective mixing may be triggered seasonally, i.e., by cooling of the lower mixolimnion during the circulation period, and by the (slow) progression of this signal into the monimolimnion.

We show CTD-measurements from meromictic mining lakes in Germany, which document the seasonal occurrence of convective mixing in discrete layers and the characteristic step-like structure within the monimolimnion. In the deeper layers, the steps emerge with a time delay which is determined by the progression speed of the mixolimnetic temperature changes into the monimolimnion.

Interestingly, in the case of the investigated lakes, the chemocline interface is not degraded by these processes, rather it is sharpened. However, double diffusive convection is essential for the redistribution in the inner parts of the monimolimnion at time scales more than seasonal, which is crucial for the assessment of the ecologic development of such lakes.

KEYWORDS

Double-diffusive convection, meromictic lake, monimolimnion

INTRODUCTION

The phenomenon of double diffusive convection has widely been discussed in numerous observational, laboratory, and theoretical studies (e.g. Turner, 1973; Schmitt, 1994; Kelley et al., 2003). Research in this field at first focussed to the ocean at mid and low latitudes where the salt finger regime dominates, and to a lesser extend to the high latitudes where the diffusive regime occurs. Soon, double diffusion and the step-like structure of the associated salt and temperature profiles were described in lakes from different climate zones. Prominent examples are Lake Vanda in Antarctica (e.g. Hoare, 1966), Powell lake in British Columbia (Osborn, 1973), Lake Kivu (Newman, 1976) and Lake Nyos (Schmid et al. 2004) in Africa.

The occurrence of diffusive layering, which is the dominant double diffusive regime in lakes, requires a salt stratification geothermally heated from the sediments, where the salt gradient stabilises to a large extend the destabilising bottom heating. Many meromictic lakes are subject to establish these conditions.

Meromixis is also well known from lakes in temperate climates (Findenegg, 1933; Boehrer and Schultze, 2008). Many of these lakes are inversely temperature stratified within the monimolimnion. Although it was shown in a few studies that the configuration of the heat and salt stratification in the deep water should be at least sensitive to double diffusive processes, for example in Lake Lugano (Wüest et al., 1992) or in the strongly meromictic Brenda Mines pit lake (Stevens and Lawrence, 1998), the explicit appearance of (multiple) double-diffusive layers was — to our knowledge — not reported for lakes in temperate climates so far, especially in the monimolimnion of meromictic lakes.

In this study we report from observations in 2006-2008 in two meromictic mining lakes situated in the Lusatian lignite mining district in East Germany (Fig. 1), Lake Waldsee ($51^{\circ}37'14.1''$ N, $14^{\circ}34'16.7''$ E), and Lake Moritzteich ($51^{\circ}35'20''$ N, $14^{\circ}34'30''$ E). The lakes were created by inflowing groundwater after mining had ceased in the area. Surface areas, volumes and maximum depths are 2387 m^2 and 16.57 ha , 6542 m^3 and $1.26 \cdot 10^6 \text{ m}^3$, 4.7 m and 17.4 m , respectively. Both lakes show a strong meromixis, indicated by strong vertical gradients of electrical conductivity in a distinct depth region (Figs. 2 and 3). The chemoclines are mainly formed by gradients of dissolved iron. Ferrous iron (Fe^{II}) which diffuses slowly from the anoxic monimolimnia through the chemocline becomes oxidised in the oxic layers above. Emerging particular ferric iron (Fe^{III}) settles back to the monimolimnion as iron hydroxides, where it can be redissolved. This mechanism implies an evanescent effective transport of the density regulating iron, sustaining the chemical and therefore the density stratification within the chemocline (Boehrer et al., 2009).

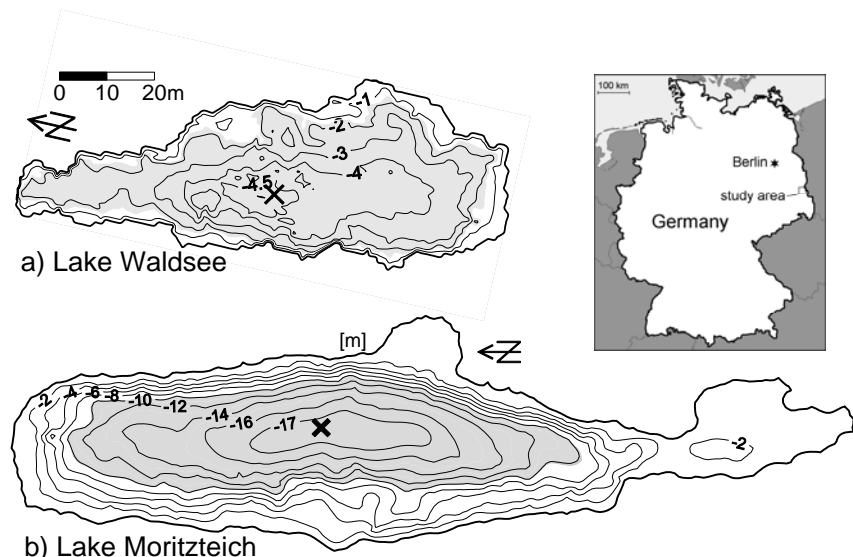


Figure 1. Bathymetric maps of Lake Waldsee and Lake Moritzteich. The grey shaded areas denote the surfaces of the monimolimnia. Measurements took place at the deepest sites, marked by crosses.

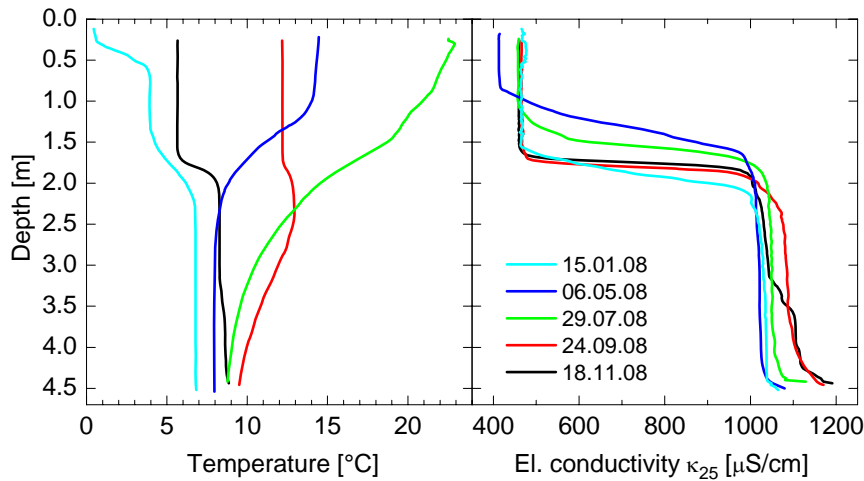


Figure 2. Temperature and electrical conductivity (corrected to 25 °C) of Lake Waldsee.

The seasonal cycle of temperature and electrical conductivity associated with the strong meromixis is shown for the shallow Lake Waldsee in Fig. 2: During the warm period the temperature stratification is stable throughout the water column. Heat proceeds slowly through the chemocline into the monimolimnion towards the lake bottom. During the autumnal cooling period, temperature inversions temporarily form within and below the chemocline while the deeper monimolimnion remains stably stratified. In winter we find comparatively strong inverse temperature stratification confined within the chemocline, which is stabilised by the conductivity step. This is the result of a low diffusive vertical heat flux into the mixolimnion. The depth of the chemocline in Lake Waldsee varies seasonally as the result of convective mixing in the mixolimnion causing an erosive descent of the chemocline and the interaction of the monimolimnion with groundwater (von Rohden et al. 2009).

The situation in Lake Moritzteich is illustrated in Fig. 3. Similar to Lake Waldsee, heat slowly enters the upper monimolimnion during the warm season starting in April. This heating even moves on while autumnal cooling already starts in the mixolimnion. After temporal forming of local temperature maxima (e.g., on 19 November at 12 m depth, see right panel of Fig. 3), strong inverse stratification establishes with gradients of 2-3 °C/m between the fully mixed

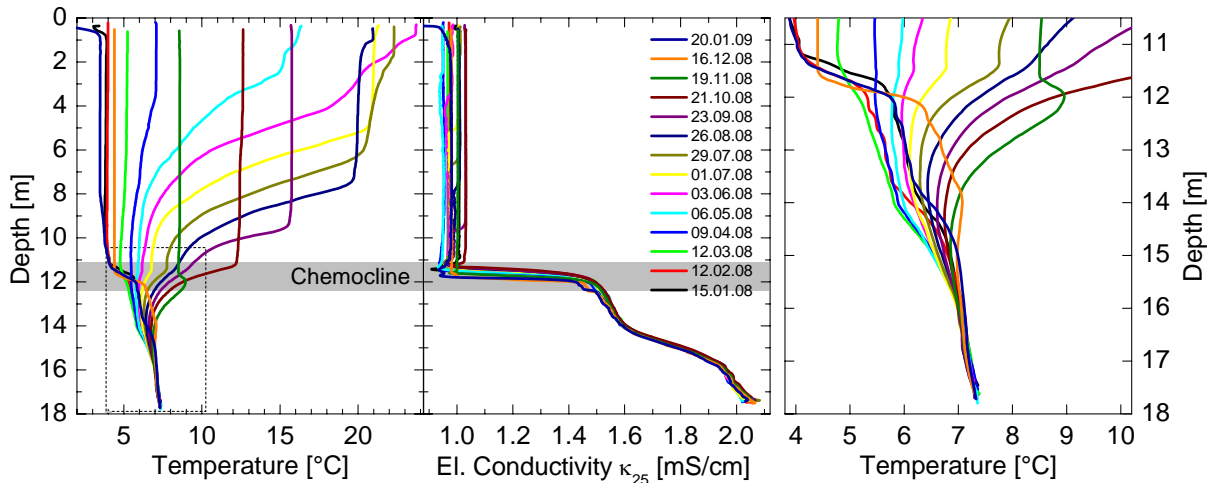


Figure 3. Temperature and electrical conductivity (corrected to 25 °C) of Lake Moritzteich. The right panel shows enlarged the temperatures in the monimolimnion (dashed box in the left panel).

~4 °C mixolimnion and the warmer monimolimnion. Heat then slowly diffuses out of the monimolimnion along these gradients. In general, the seasonal temperature signal at the top of the chemocline intrudes to a depth of about 16 m. The low vertical diffusion causes the temperatures to follow the mixolimnion signal with a depth dependent time shift. E.g., in the profile of 20 January 2009, the temperature has a local maximum at ~15.5 m while the mixolimnion is at its coolest values of less than 4 °C. Towards the bottom, the profiles continue to be inversely stratified with much less variation, ending up at a virtually constant temperature of ~7.3 °C. This indicates a continuous heat flux from the sediments.

METHODS

All profiles shown were measured by lowering an automatic CTD-probe (Idronaut Ocean Seven 319, Brugherio, Italy) with a speed of 10-20 cm/s. Accuracy of electrical conductivity and temperature were 1 µS/cm and 0.01 °K, respectively. The resolution of the sensors were 0.1 µS/cm and 0.001 K, the resolution of the pressure sensor was 0.02 dbar (~2 cm). Several consecutively taken CTD-profiles were averaged afterwards to reduce scattering.

Formulas to calculate water density specific for the investigated lakes were developed (Boehrer et al., 2009). The temperature dependence of electrical conductivity $C(T)$ was evaluated from epilimnion and monimolimnion samples over the temperature interval of 1.5°C to 30°C. A linear regression of the form $C(T) = mT + n$ was fitted to the data, see Fig. 1. Hence electrical conductivity at a reference temperature of 25°C could be evaluated from:

$$\kappa_{25} = \frac{C(T)}{\alpha_{25}(T - 25) + 1}, \quad (1)$$

where $\alpha_{25} = 1/(25 + n/m)$ (e.g. Karakas et al., 2003; Boehrer and Schultze, 2008). Based on the specific temperature dependence of the density in the mixolimnion ($\rho_{mixo}(T)$) and monimolimnion water ($\rho_{moni}(T)$) which was measured in two samples, and on conductivity profiles from CTD-probes, the density was calculated:

$$\rho(T, \kappa_{25}) = \rho_{mixo}(T) + [\rho_{moni}(T) - \rho_{mixo}(T)] \cdot \frac{(\kappa_{25} - \kappa_{mixo})}{(\kappa_{moni} - \kappa_{mixo})}, \quad (2)$$

where κ_{mixo} and κ_{moni} are representative values of κ_{25} in the mixolimnion and monimolimnion, respectively, separately for the two lakes and for the study period. From that we derived the local stability N^2 and the stability ratio R_ρ

$$N^2 = -\frac{g}{\rho} \frac{\partial \rho}{\partial z} = -\frac{g}{\rho} \left(\frac{\partial \rho}{\partial T} \frac{\partial T}{\partial z} + \frac{\partial \rho}{\partial \kappa_{25}} \frac{\partial \kappa_{25}}{\partial z} \right), \quad (3)$$

$$R_\rho = \left(\frac{\partial \rho}{\partial \kappa_{25}} \frac{\partial \kappa_{25}}{\partial z} \right) \Big/ \left(\frac{\partial \rho}{\partial T} \frac{\partial T}{\partial z} \right), \quad (4)$$

to quantify the density stratification and to highlight the sensitivity to double diffusive effects.

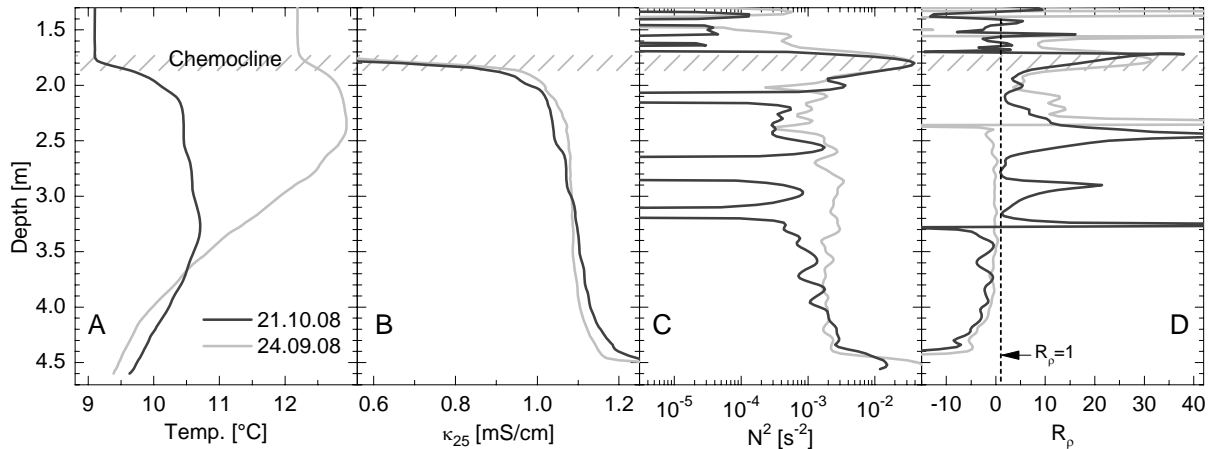


Figure 4. Exemplary profiles for the monimolimnion in Lake Waldsee: temperature, electrical conductivity (panels A and B), local stability N^2 and stability ratio R_p (C and D), calculated after eqs. (1-4).

RESULTS AND DISCUSSION

At the time when cooling pushes the mixolimnion temperature below the values in the chemocline and upper monimolimnion, the net heat flux turns to the upward direction, but at the level of only the molecular diffusion (von Rohden et al., 2009). The gradient by solutes in the chemocline is strong enough to stabilise the stratification throughout the cool period. At a certain layer at the bottom of the chemocline where the salt gradients pass towards the much smaller monimolimnion gradients, the stratification becomes unstable, when “inverse” temperature gradients become locally stronger due to the ongoing upward heat loss.

Lake Waldsee. The observations in Lake Waldsee confirm that local convective mixing started at this depth and migrated downwards during the next weeks or months. In autumn 2006, no staircases developed. Instead, the monimolimnion was successively mixed in October, reaching the bottom after ~1 month (Boehrer et al., 2009). In autumn 2008, however, up two four staircases with variable sizes ranging from ~1 dm to ~1 m and in variable depths were detected. In Fig. 4, an example of the situation before and after onset of double diffusive mixing is shown (panels A and B). Panels C and D show the local stability N^2 and the density ratio R_p as calculated with eqs. (1-4). Note that before the mixing event

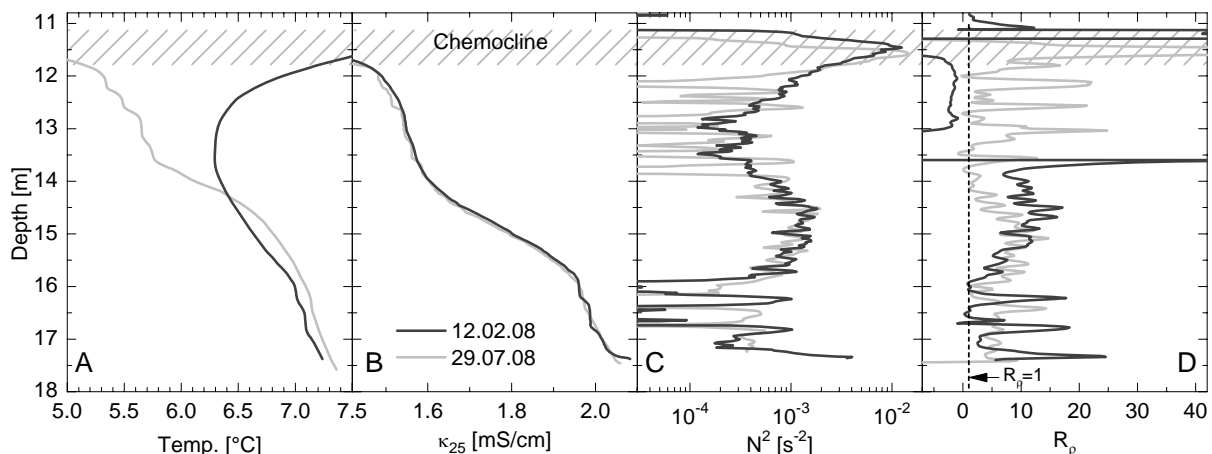


Figure 5. Exemplary profiles for the monimolimnion in Lake Moritzteich: temperature, electrical conductivity (panels A and B), local stability N^2 and stability ratio R_p (C and D), calculated after eqs. (1-4).

(24 September 2008), R_p values in the range of ~ 5 were present at a depth of ~ 2 m short below the chemocline, whereas the deeper monimolimnion still was completely stable (negative R_p).

Lake Moritzteich. Fig. 5 shows a typical situation in winter and summer (examples from 12 December and 29 July 2008). Autumnal cooling of the upper part of the monimolimnion ($\sim 12\text{--}14$ m, see also Fig. 3) induced double diffusive convective mixing, starting short below the chemocline. Between one and six staircases were observed here (four in the plotted example from 12 February) with typical step sizes in the range of a few decimetres. Interestingly, in summer (exemplary in the profile from 29 July 2009, i.e., about half a year later), we found staircases in the lowest part between 15.5 and 17.5 m, whereas the upper part of the profile was smooth and stably stratified at this time (negative R_p). This suggests that the steps arise in the deeper layer with a time lag, according to the speed to which the thermal signal from the upper layer proceeded downwards. Assuming that the permanently stably stratified intermediate layer between the layers, where the steps arose, extended from ~ 13.9 m to ~ 15.6 m (Fig. 5), then the time scale for the propagation of the signal was $\Delta\tau = \Delta z^2/D \cong 240$ days, with D the coefficient of molecular diffusion of heat. This might explain the temporal pattern of the observations. Thus, cooling at the chemocline in late autumn drives double diffusive convection in the upper half of the monimolimnion, which occurs until the following spring months, and in the deepest part with a delay of more than half a year. Here, even in late autumn 2008, staircases were still observed, while the new cooling period has started once again. The overall two-layered structure in the monimolimnion (Fig. 3) can be considered to be the result of the temporal occurrence of double diffusive convection separate in the upper and lower part of the monimolimnion.

The thicknesses of the observed staircases in both lakes are highly variable according to the comparatively quick temperature changes at the upper boundary of the monimolimnia, but nevertheless in the same order of magnitude as reported from other lakes, e.g., Lake Nyos (Schmid et al., 2004). That is, the vertical heat flux is variable as well. Furthermore, the convective mixing might occur intermittently rather than continuously. For this reason, the interfaces appear somewhat smoothed. However, the staircase patterns are strongly homogeneous in the horizontal in both lakes as confirmed by CTD casts from different sites at the same measurement date.

CONCLUSIONS

The observations show that convective mixing triggered by double diffusive processes in monimolimnia of meromictic lakes can be part of the seasonal mixing regime in temperate climates. On the one hand, the occurrence of double diffusion confirms that the exchange between monimolimnion and mixolimnion and within the monimolimnion must in general be as low as molecular. On the other hand, bottom heated monimolimnia can, at least in parts, undergo convective mixing, considerably enhancing the vertical redistribution of solutes. This must be taken into account in assessments of the ecologic development of such lakes. The stability of the stratification within the chemocline, however, is not degraded by these processes.

In principle, preconditions and forcing of the observed double diffusive mixing is similar to other systems (e.g., Lake Nyos (Schmid et al., 2004)). However, the magnitudes of the forcing, i.e., the extent of the seasonal temperature variation at the monimolimnion surface as well as the strength of the stabilising salt and destabilising temperature gradients are

considerably higher. Note that in our examples the water column is sensitive to double diffusive mixing, whereas the overall stability in the respective depth regions is at a rather high level of $N^2 \sim 10^{-3} \text{ s}^{-2}$ (Fig. 3). We attribute the relative discontinuity of the number and thickness of staircases to these continuously changing conditions, to which they should be sensitive.

It seems obvious that these mechanisms are more widespread among meromictic lakes in temperate climates than hitherto thought, as many of them might meet the described preconditions. This should especially be appropriate for existent but also arising pit lakes from open-cast mining, because such lakes are above-average prone to meromixis.

ACKNOWLEDGMENT

This work was financially supported by Deutsche Forschungsgemeinschaft (DFG).

REFERENCES

- Boehrer, B., and M. Schultze (2008). Stratification of lakes, *Rev. Geophys.*, **46**, RG2005, doi:10.1029/2006RG000210.
- Boehrer, B., S. Dietz, C. von Rohden, U. Kiwel, K.D. Jöhnk, S. Naujoks, J. Ilmberger, and D. Lessmann (2009). Double-diffusive deep water circulation in an ironmeromictic lake. *Geochem. Geophys. Geosyst.* (in press), doi:10.1029/2005GC001164.
- Findenegg, I. (1933) Alpenseen ohne Vollzirkulation. *Internationale Revue der Gesamten Hydrobiologie Und Hydrographie*, **28**, 295–311.
- Hoare, R.A., (1966). Problems of Heat Transfer in Lake Vanda, a Density Stratified Antarctic Lake. *Nature* **210**, 787–789, doi:10.1038/210787a0.
- Karakas, G., I. Brookland, B. Boehrer (2003). Physical characteristics of Acidic Mining Lake 111. *Aquatic Sciences*, **65**, 297–307, doi:10.1007/s00027-003-0651-z.
- Kelley, D.E., H.J.S. Fernando, A.E. Gargett, J. Tanny, and E. Özsoy (2003). The diffusive regime of double-diffusive convection. *Prog. Ocean.*, **56**, 461–481.
- Newman, F.C., (1976). Temperature Steps in Lake Kivu: A Bottom Heated Saline Lake. *J. Phys. Ocean.* **6**(2), 157–163.
- Osborn, T.R. (1973). Temperature microstructure in Powell Lake. *J. Phys. Ocean.*, **3**, 302–307.
- Schmid, M., A. Lörke, C. Dinkel, G. Tanyileke, and A. Wüest (2004). Double-diffusive convection in Lake Nyos, Cameroon. *Deep-Sea Res.*, Part I, **51**, 1097–1111.
- Schmitt, R.W. (1994). Double diffusion in oceanography. *Ann. Rev. Fluid Mech.*, **26**, 255–285.
- Stevens, C., and G. Lawrence, (1998). Stability and meromixis in a water-filled mine pit. *Limn. Ocean.*, **43**, 946–954.
- Turner, J.S. (1973). Buoyancy effects in fluids, Cambridge University Press, Cambridge.
- von Rohden, C., J. Ilmberger, B. Boehrer (2009). Assessing groundwater coupling and vertical exchange in a meromictic mining lake with an SF₆-tracer experiment. *J. Hydr.* **372**, 102–108
- Wüest, A., W. Aeschbach-Hertig, H. Baur, M. Hofer, R. Kipfer, and M. Schurter (1992). Density structure and tritium-helium age of deep hypolimnetic water in the northern basin of Lake Lugano. *Aquat. Sci.*, **54**, 205–218

Basic modelling of double diffusive processes in meromictic lakes

Johann Ilmberger and Christoph von Rohden

Institute of Environmental Physics, University of Heidelberg, Im Neuenheimer Feld 229, D-69120 Heidelberg, Germany

*Corresponding author, e-mail Johann.Ilmberger@iup.uni-heidelberg.de

ABSTRACT

The main feature of a meromictic lake is the monimolimnion, a bottom water layer with relatively high density caused by solutes. Because of the density gradient the monimolimnion water is separated from the mixolimnion. Due to groundwater inflow and/or geothermal heat flux the temperature of monimolimnia are frequently well above the temperature of maximum density. The inverse temperature tends to destabilize the water column, but in general this is overcompensated by the stabilizing effect of the dissolved matter. Depending upon the density gradients in the interior of the monimolimnion the system could be susceptible to double diffusive convection, i.e. enhanced vertical mixing due to the two orders of magnitude higher molecular diffusivity of heat compared to solutes.

Double diffusive convection is modelled with a one dimensional model, using only one free parameter: The model includes the molecular diffusion of heat and substances. Vertical mixing is performed when the density instability exceeds a certain level. For the convection only this threshold has to be introduced to get the main feature, the ‘step’ structure of the profiles of temperature and conductivity. The sizes of the steps depend upon the initial density structure, with decreasing size on increasing overall stability. Applying the model upon the small meromictic Lake Waldsee shows that the basic features of the measured profiles are reproduced.

KEYWORDS

Double diffusion, lake, meromixis

INTRODUCTION

In the ocean and deep African lakes the effect of double diffusive convection and the resulting staircase profiles are well known since years (e.g. Turner 1973, Newmann 1976, Schmid et al. 2004 , overview: Kelley et al. 2003).

Observations of double diffusion in temperate zone lakes are rare. Wüest et al. 1992 suspected double diffusive enhanced fluxes in Lake Lugano. Boehrer et al. 2009 describe double diffusive convection in the meromictic Lake Waldsee.

A meromictic lake has layers of water, which do not intermix during the cold season. The bottom water (monimolimnion), which is separated from the mixolimnion by a pycnocline, has a high density due to dissolved matter (ionic, non-ionic, gas, DOC) and therefore doesn't take part in the seasonal mixing. An overview is given by Boehrer and Schulze 2008.

The lower layers of the monimolimnia often show temperatures well above the temperature of maximum density. This is due to the rather slow heat transport through the chemocline and within the monimolimnion and (possibly) a heat flux from the sediment.

During the warm period, the overall water column is stable, because both, the temperature and dissolved matter stabilise. Even on cooling the mixolimnion below the monimolimnion

temperature, the destabilising effect of the temperature is initially overcompensated by the stabilising density gradient due to solutes in the monimolimnion. Further on, when the temperature just above the chemocline is as low as the temperature of the maximum density or even lower, heat diffuses out of the monimolimnion. Now, due to the enormous difference in molecular diffusivities of heat and substance, the water column can get unstable and in the monimolimnion double diffuse convection might occur. The double diffusive convection creates a ‘step like’ structure in the profiles of temperature and salinity in the monimolimnion. Because of its high stability the pycnocline is not affected i.e. the monimolimnion is not affected.

METHODS

The model is a straight forward one dimensional diffusion model with a vertical grid size of 2 cm. The coefficients of diffusion were chosen as $D_H = 1.4 \cdot 10^{-7} \text{ m}^2/\text{s}$ for heat and $D_S = 10^{-9} \text{ m}^2/\text{s}$ for salinity (conductivity κ_{20}) respectively. The time step is adjusted to perform stable calculations.

All effects of increasing (turbulent) diffusion, as e.g. horizontal velocity shear, turbulence production due to convection etc. are assumed to be of minor importance and thus ignored. The only process, besides the diffusion, regarded here, is mixing in case of instability of the water column (see Fig. 1). The model mixing is performed, if a certain threshold of negative buoyancy is exceeded (in general a density difference of -0.0001 kg/m^3 was used). So, if the water column gets unstable for example due to surface cooling, it is successively mixed till it is stable (or neutral in case of complete mixing).

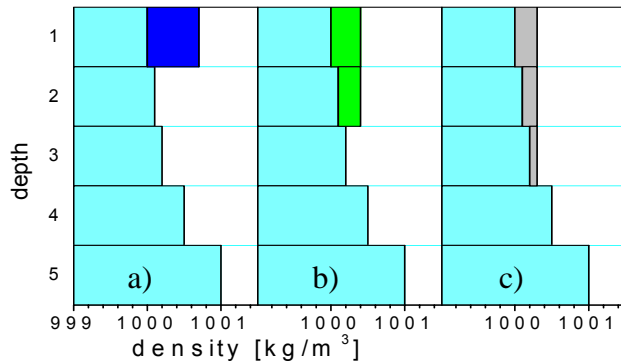


Figure 1. The model’s mixing procedure:

- a) the initial density profile and the increase in density in the first layer (due to cooling),
- b) the first two layers mixed,
- c) after the upper three layers are mixed, the water column is stable.

For the model test runs an initially stable vertical profile for salinity (conductivity) was chosen. The destabilising (inverse) temperature profile was constructed to get a constant (negative) density gradient in the water column. That is, the temperature profile is slightly bent because the density – temperature relation is nonlinear. To calculate the density the relation proposed by Bührer and Ambühl 1975 (expanded for the dissolved substances by $0.705 \cdot 10^{-6} \kappa_{20}$, where κ_{20} is the conductivity at 20°C) was used. Although this is not the appropriate density relation for the lake investigated, for this principal study it might suffice. The sum of the density gradients was kept positive in order to have a stable profile in the beginning.

At the top and the bottom a very stable layer was established in order to have solely molecular diffusion as boundary conditions. This gradient at the top was used to calculate the heat and buoyancy flux into/out of the double diffusive region. For the setup see Fig. 2.

The model run starts with decreasing temperature starting from 7°C and reducing it by 5 degrees to 2°C and keep this temperature for the duration of the run.

RESULTS AND DISCUSSION

MODEL TESTS

The model was run with different salt-stabilities, an inverse temperature profile and a driving temperature of 2°C at the upper boundary.

Figure 2 shows the starting conditions of the model runs. The temperature ranges from 7.1°C at the top and 8.2°C at the bottom of the modelled region (red dotted line). The temperature profile is adjusted to get a constant density gradient ($-4.25 \cdot 10^{-3} \text{ kg/m}^4$). The conductivity profiles shown in figure 2 have constant density differences in the main modelled region and very high values above and below that region. The values for the density gradients are given in Table 1.

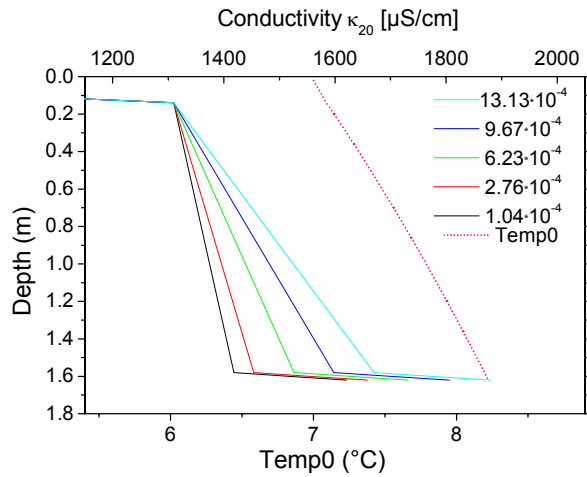


Figure 2. Starting profiles of the temperature (destabilizing) and the salinity (stabilizing). The legend gives the values for the resulting density gradients in kg/m^4

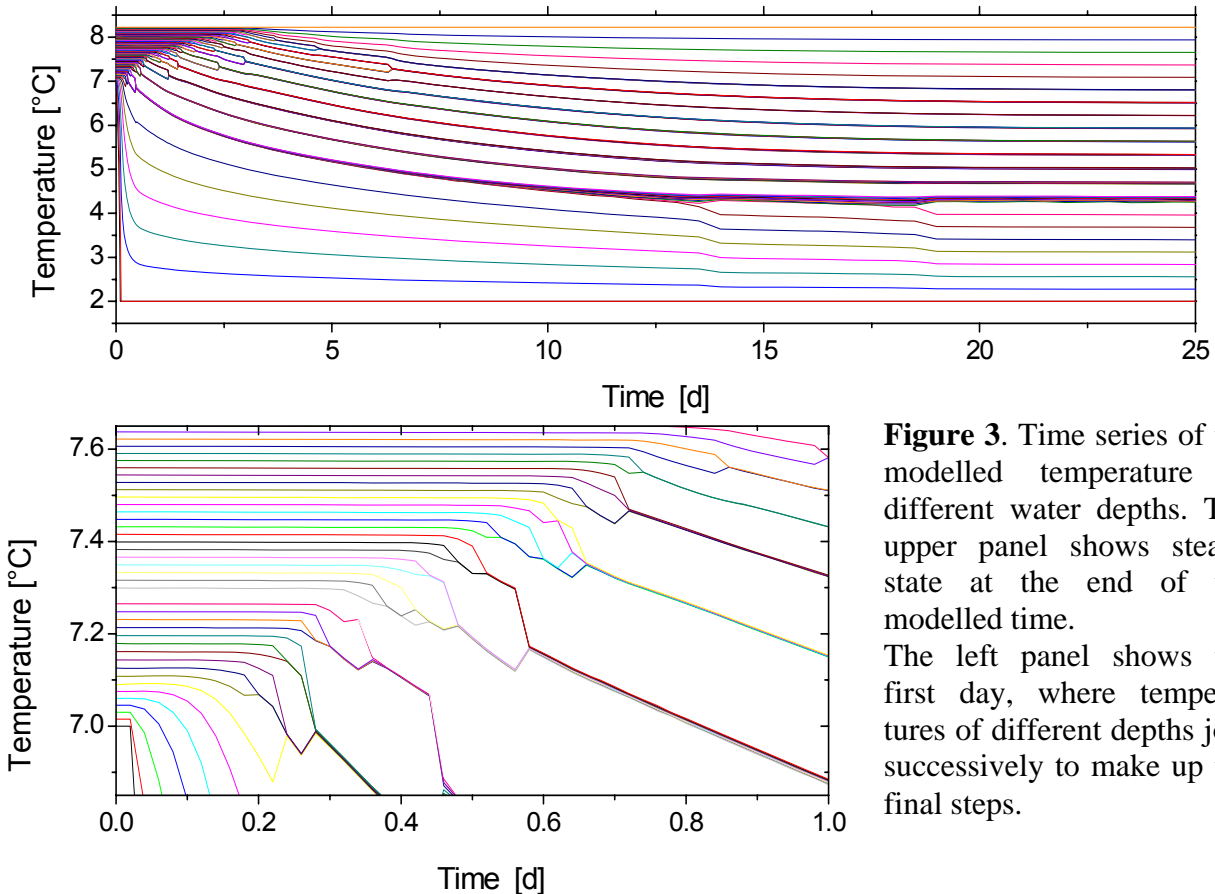


Figure 3. Time series of the modelled temperature at different water depths. The upper panel shows steady state at the end of the modelled time. The left panel shows the first day, where temperatures of different depths join successively to make up the final steps.

The development of the temperature at all depths of the model run 3 ($6.23 \cdot 10^{-4} \text{ kg/m}^4$) is displayed in figure 3. As a 2cm grid was used for the calculations every line represents the temperature of a certain depth and is 2 cm apart from the next line. The lower panel shows the first day of the model run. The joining of temperature lines shows the formation of the steps. The upper panel displays the whole modelled time. At the end of the 25 days period we get constant temperatures, i.e. the system is close steady to state.

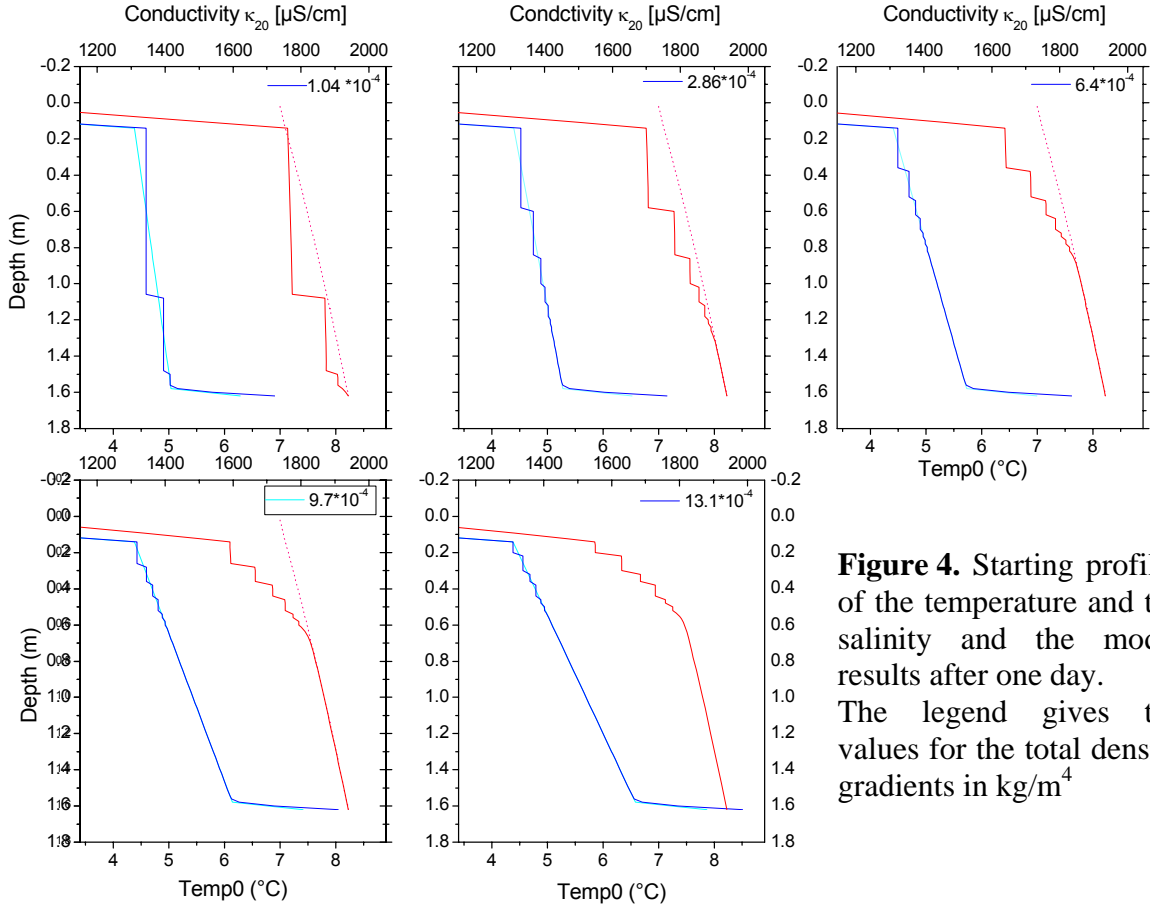


Figure 4. Starting profiles of the temperature and the salinity and the model results after one day. The legend gives the values for the total density gradients in kg/m^4

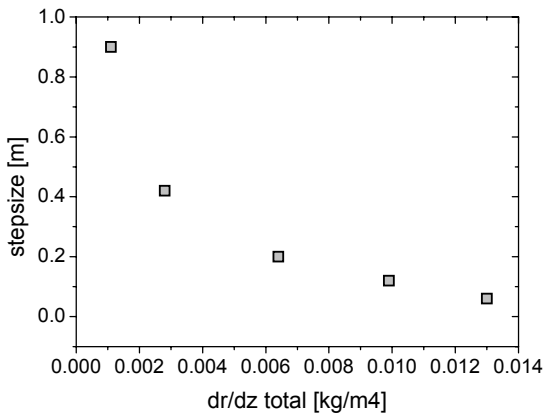


Figure 5. Size of the first step as function of the initial stability.

dp/dz total	dp/dz temp	dp/dz sal	stepsize	R _p	j _{heat}
[kg/m ⁴]	[kg/m ⁴]	[kg/m ⁴]	[m]		W/m ²
1.1E-03	-4.2E-03	5.3E-03	0.90	1.3	23.3
2.8E-03	-4.2E-03	7.1E-03	0.42	1.7	22.9
6.4E-03	-4.2E-03	1.1E-02	0.20	2.5	20.7
9.9E-03	-4.2E-03	1.4E-02	0.12	3.3	19.0
1.3E-02	-4.2E-03	1.8E-02	0.06	4.2	17.8

Table 1. The first column shows the resulting stability, the sum of the second and third column. The stability ratio and the heat flux are displayed in the 5th and 6th column.

The model output of the temperature and conductivity (salinity) profiles after one day are shown in figure 4. The initial stability was lowest in panel a) and highest in panel e). Result of the double diffusive mixing is the step structure of the profiles. At high initial stability we get small steps and when the initial stability is low, the step size is bigger, at least in the top part of the modelled region. In table 1 the results are summarized. The stability ratio, i.e. the ratio of the stabilizing and the destabilizing density gradient, is rather low and ranges from 1.3 to 4.2 which is a strong indication for the occurrence of double diffusion. But these values are calculated from the initial profiles and our system here is driven by the decreasing of the surface temperatures and though the destabilisation is even forced. The Heat flow due to the double diffusive convection is enhanced Table 1 shows the values from ~ 18 to 23 W/m^2 (compared to $\sim 0.5 - 1 \text{ W/m}^2$ for heat conduction). Figure 5 shows the size of the first step as function of the initial total stability of the water column in terms of the resulting initial density gradient.

MODEL APPLICATION: LAKE WALDSEE

The model is applied to the meromictic Lake Waldsee, a very small ($50\text{m} \times 120\text{m}$, 4.7m deep) mining lake. Despite its small depth the lake is meromictic with a chemocline at a depth varying from 0.8 m to $\sim 2\text{ m}$. The meromixis is most probably caused by the “iron-cycle” (oxidising dissolved iron in the mixolimnion, sedimentation and re-dissolution of the iron hydroxide in the monimolimnion). The model run was performed from 24/09/2008 till 21/10/2008, a period of 26 days with an essential heat loss from the mixolimnion to the atmosphere. As the mixolimnion is not modelled, a temperature record at a depth of 1.7 m was used as boundary condition just above the chemocline. In the model the lake ends at a depth of 4.4 m and is forced to follow the temperature record there (see Fig. 6 for the boundary time series, data UFZ Magdeburg).

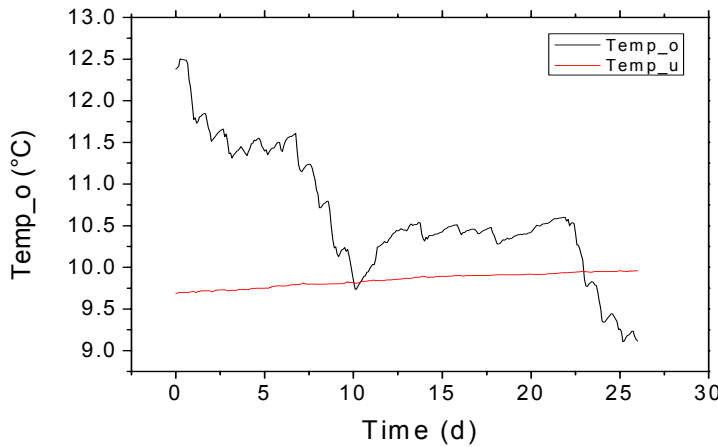


Figure 6. Time series of water temperature at a depth of 1.7 m and 4.4 m as upper and lower boundary condition for the model calculation. The series started at the 24/9/2008.

As starting and target values for temperature and conductivity, measured profiles are used. Fig. 7 shows the profiles from the 24/9/2008 and 21/10/2008 measured with a CTD-probe (IDRONAUT) at high vertical resolution ($\sim 2\text{ cm}$). The starting profiles are only shown in the modelled region, which extends from 1.7 m to 4.4 m water depth.

Figure 8 shows the target profiles (21/10/2008) and the model output after the 26 days period. The calculated profiles display surprisingly well the main features of the measured profiles, the loss of heat and the mixed region of the monimolimnion. The difference of $\sim 0.3\text{ }^\circ\text{C}$ in the temperature –the model temperature is too warm- could be an effect of the low vertical heat

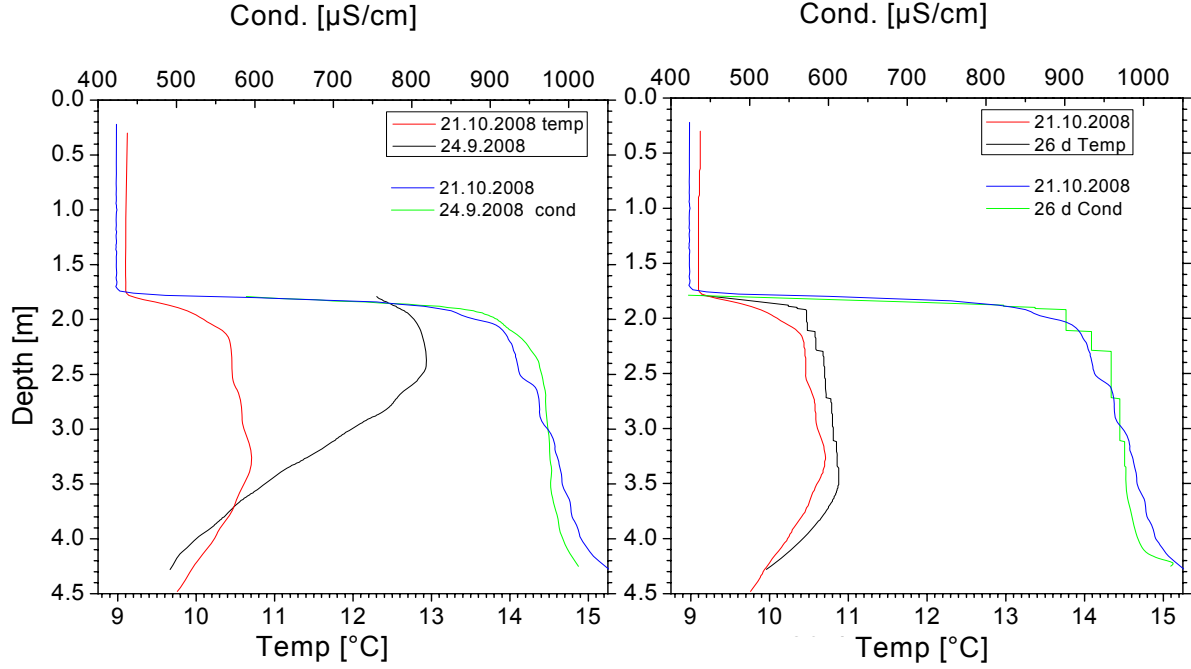


Figure 7. Temperature and conductivity profiles at the beginning (24/9/2008) and the end (21/10/2008) of the modelled period. The profiles used as starting profiles in the model are only drawn below 1.7 m, because the upper part is not modelled.

Figure 8. Temperature and conductivity profiles at the end (21/10/2008) of the modelled period and the model output. Note that the model depth range is from 1.7 m to 4.4 m water depth.

transport, as there is only heat conductance and no turbulence at all in the model. And/or there is a heat loss due to groundwater flushing. The groundwater renewal is about 100% per year, but neither the temperature nor the conductivity of the inflowing water is known (vonRohden et al. 2009) and therefore no estimation is possible. The deviation of about 20 $\mu\text{S}/\text{cm}$ in the conductivity profile is most probably also due to inflow of groundwater or/and re-dissolution of iron hydroxides.

CONCLUSIONS

Modelling double diffusive convection, using solely heat conduction, molecular diffusion of solutes and mixing of the water column due to instabilities, reproduces astonishingly well the principal features of the observed phenomena. The instabilities are caused by the about two orders of magnitude higher molecular diffusivity of heat compared to solutes, i.e. the heat flux out of the monimolimnion causes a destabilisation of the water column in regions, where the density gradients due to solutes is comparatively low and so convective mixing occurs.

The simple approach, using as the only parameter a threshold of negative buoyancy for vertical mixing, produces the stepwise structure of the temperature and conductivity profiles. Of course nature is much more complicated and other processes have to be included in the calculations in order to get a good reproduction of the observed profiles.

Further work has to include appropriate density – conductivity relation, which could improve the results.

ACKNOWLEDGEMENT

This research was granted by the Deutsche Forschungsgemeinschaft (DFG)

REFERENCES

- Boehrer, B., and M. Schultze (2008). Stratification of lakes, *Rev. Geophys.*, **46**, RG2005, doi:10.1029/2006RG000210.
- Boehrer, B., S. Dietz, C. von Rohden, U. Kiwel, K.D. Jöhnk, S. Naujoks, J. Ilmberger, and D. Lessmann (2009). Double-diffusive deep water circulation in an ironmeromictic lake. *Geochem. Geophys. Geosyst.* (in press), doi:10.1029/2005GC001164.
- Bührer, H. and H. Ambühl (1975). Die Einleitung von gereinigtem Abwasser in Seen. *Schweiz. Z. Hydrol.*, **37**:347–369.
- Kelley, D.E., H.J.S. Fernando, A.E. Gargett, J. Tanny, and E. Özsoy (2003). The diffusive regime of double-diffusive convection. *Prog. Ocean.*, **56**, 461–481.
- Newman, F.C. (1976). Temperature steps in Lake Kivu: a bottom heated saline lake. *J. Phys. Oceanogr.*, **6**:157–163.
- Schmid, M., A. Lorke, C. Dinkel, G. Tanyileke, and A. Wüest (2004). Double-diffusive convection in Lake Nyos, Cameroon. *Deep-Sea Res., Part I*, **51**, 1097–1111.
- Turner, J.S. (1973). *Buoyancy effects in fluids*. Cambridge University Press, Cambridge.
- von Rohden, C., J. Ilmberger, B. Boehrer (2009). Assessing groundwater coupling and vertical exchange in a meromictic mining lake with an SF₆-tracer experiment. *J. Hydr.* **372**, 102–108
- Wüest, A., W.Aeschbach-Hertig, H. Baur, M. Hofer, R. Kipfer, and M. Schurter (1992). Density structure and tritium-helium age of deep hypolimnetic water in the northern basin of Lake Lugano. *Aquat. Sci.*, **54**, 205–218

Sediment methane emission: Sources and fate in the water column

D. F. McGinnis^{1,2*}, L. Rovelli^{1,2}, S. Sommer¹ and P. Linke¹

¹ IFM-GEOMAR, Leibniz Institute of Marine Sciences at the University of Kiel, East Shore Campus, Wischhofstrasse 1-3, D-24148 Kiel, Germany

² Eawag: Swiss Federal Institute of Aquatic Science and Technology, Seestrasse 79, CH-6047 Kastanienbaum, Switzerland

*Corresponding author, e-mail dmcginnis@ifm-geomar.de

ABSTRACT

In situ methane emission measurements from sediments are combined with water column backscatter anomalies recorded with an Acoustic Doppler Current Profiler (ADCP) integrated on a benthic observatory. The methane concentration in the flux chamber reached 3-fold higher concentrations. Simultaneous to the sudden methane increase, a significant backscatter anomaly was recorded and persisted for 30 min and covered the entire depth range (100 m) of the upward looking ADCP. Data analyses revealed that a plume outburst likely occurred during this time. A second data set was obtained during lander deployments at Rock Garden where visual observations by ROV confirmed the transient pattern of free gas injection into the water column. Acoustic flares and methane concentration increases in the bottom water hint towards a pressure (tidal) induced discharge mechanism. Using plume modeling, we speculate that the observed water column methane signals are likely due to methane-rich fluid outburst, and not methane bubbles, as too much gas would be required. We further suggest that bubble release from the sediment may be an indication of recent plume outburst activity. The presented data demonstrate the temporal and spatial variability of seabed methane emission, and very short methane signal lifetime in the water column (hours) due to turbulent diffusion. Both have to be considered when methane budgets are extrapolated from single methane emission rates.

KEYWORDS

Hikurangi Margin, cold seeps, methane, physical control parameters, plume, bubbles

INTRODUCTION

Seabed fluid flow, also known as submarine seepage, is the migration of gases and liquids through the seabed and into the marine environment. Submarine seepage affects seabed morphology (forming pockmarks and mud volcanoes), benthic carbon turnover and ecology (Levin, 2005). Because of the biological dependency, it is expected that the chemical environment and the local hydrodynamics (diffusive, advective, gas bubble transport) influence the species composition and their activity.

Little is known about sediment release of CH₄, and currently, only a few in situ measurements of seabed CH₄ emission exist (Torres *et al.*, 2002; Linke *et al.*, 2005; Sommer *et al.*, 2006; Sommer *et al.*, 2009). Moreover, methane expulsion and seep distribution are extremely variable (Greinert, 2008; Naudts *et al.*, *in press*), and can be triggered from short-term physical forcing, e.g. tidal oscillations and waves, and episodic events such as tsunamis, gas discharge, and seismic strain (Tryon *et al.*, 2002; Brown *et al.*, 2005; LaBonte *et al.*, 2007).

Fluid and free gas release (bubbles) around cold seeps may be related to gas hydrate deposits, mud volcanoes, pockmarks or a mixture of those (Judd and Hovland, 2007). Released bubbles can be easily detected by hydroacoustics because of the density difference between gas and water (Greinert, 2008). The hydroacoustic bubble-release signature can sometimes be viewed as a “flare”, which refers to the flame-like image produced on hydrographs or backscatter plots. Acoustic flares only indicate the presence of scatterers (bubbles, particles) in the water, but reveal nothing about the hydrodynamics. However, a large gas release can create a “plume”; a vertical upwelling flow driven by a positive buoyancy source (i.e. bubbles, heat, less saline water, dissolved CH₄, or any combination).

We present data from landers and water column data from Hikurangi Margin cold seep sites (RV SONNE SO191, February/March 2007; Bialas *et al.*, 2007) and show evidence of large-scale outburst activity at two different sites. We analyze a signal in the water column, and constrain the source boundary conditions. These deployments provided a unique combination of biological, chemical and physical data collected simultaneously at the BBL and enable new perspectives on methane source strength of cold seep sites, its controls and the monitoring of the fate of methane in the water column.

Regional Setting

The Hikurangi Margin at the east coast of New Zealand’s North Island is characterized by the oblique subduction of the Pacific plate beneath the Australian plate (Figure 1). A detailed description of the tectonic and geologic framework for gas hydrates and cold seeps on the Hikurangi margin is provided by Barnes *et al.* (*in press*).

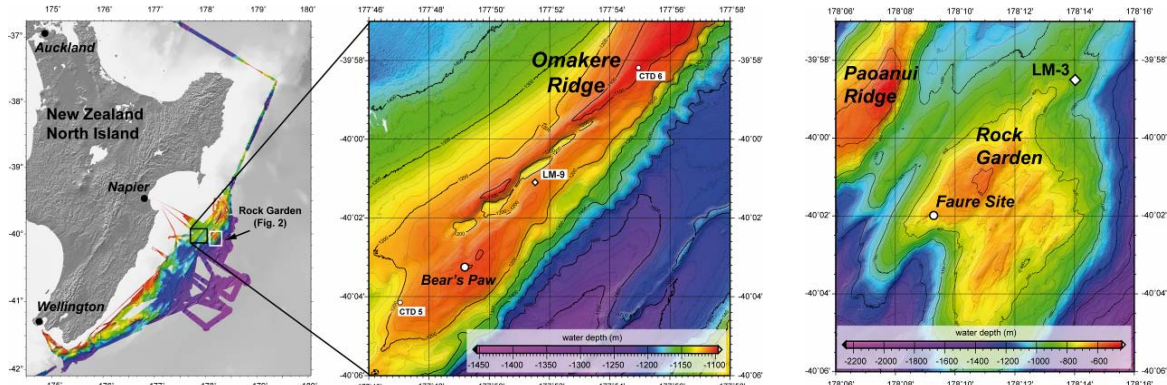


Figure 1. LEFT: Overview map showing the bathymetry of the Hikurangi Margin mapped during SO191. CENTER: Omakere Ridge and the Bear’s Paw cold seep site. RIGHT: Rock Garden area. (left; map courtesy J. Greinert).

This study focuses namely on: 1) *Bear’s Paw (Omakere Ridge)*: Bear’s Paw is a cold seep structure on the Omakere Ridge (Figure 1, center) that was discovered in 2007 during SO191 (Jones *et al.*, *in press*) and 2) *Faure Site (Rock Garden)*: Rock Garden (Figure 1, right), is the southern termination of Ritchie Ridge uplifted by the subduction of a seamount beneath the outer margin bank (Barnes *et al.*, *in press*).

MATERIAL AND METHODS

In-situ Flux Measurement

Benthic landers provide a stationary study environment decoupled from the movement of the ship, and simultaneously measure several physical, chemical and biological parameters across the sediment water interface. The Biogeochemical Observatory (BIGO) and the Fluid Flux

Observatory (FLUFO) (Pfannkuche and Linke, 2003; Sommer *et al.*, 2006) were deployed for in-situ flux measurements of methane and oxygen. For more detailed information see Figure 2 and Linke *et al.* (2009).

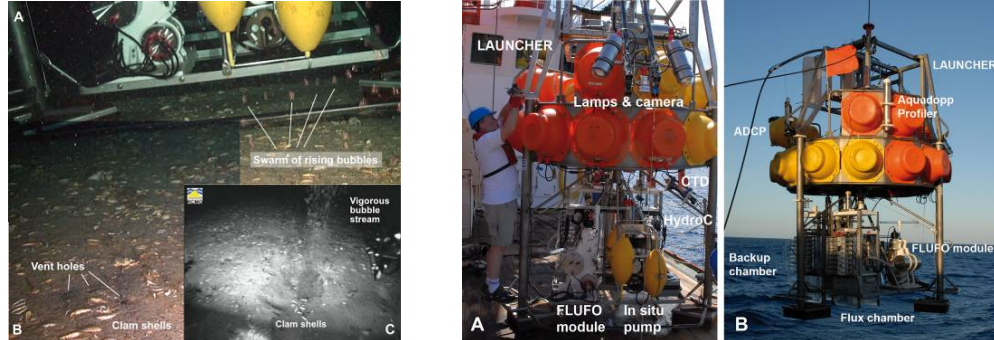


Figure 2. LEFT: Images from video recorded during ROV dive. A) FLUFO-4 is deployed at the Faure Site in immediate vicinity to BIGO-4. B) In front of the observatory shells of vesicomyid clams and vent holes discharging gas bubbles are visible. C) Screen capture of vigorous gas bubbles discharge at Faure bubble site (picture courtesy L. Naudts). RIGHT: Fluid Flux Observatory (FLUFO) prepared for video-guided deployment with the Launcher. A) The front and (B) back view show the different modules integrated into FLUFO.

Each observatory is equipped with two circular chambers (internal diameter 28.8 cm), each covering a sediment area of 651.4 cm². A TV-guided launching system allowed smooth placement of the observatories at selected sites on the sea floor (Figure 2, right). Sampling details and analytical procedures are described by Linke *et al.* (2009).

Measurement of Physical Control Parameters

FLUFO (Figure 2, right) was also equipped with a 300 kHz Workhorse Sentinel ADCP and a small CTD (XR420, RBR Ltd.) mounted 1.2 m above the seafloor. The CTD was also equipped with an optical backscatter sensor (SeaPoint) which measures light scattered by particles suspended in water. The ADCP was mounted on the lander upward looking in 2.5 m distance from the seafloor and deployed in standard profiling mode (mode 1). Details of the data processing and analysis are given by Linke *et al.* (2009).

CTD profiles were obtained with a *SeaBird 911plus* (CAPSUM METS sensor, dissolved oxygen (DO), conductivity, temperature). The CTD samples at 24 hz with a temperature accuracy better than 0.001°C. CH₄ analyses determined by GC on-board using mainly a head-space equilibration extraction method and also a vacuum extraction system. The rosette holds twenty four 10 litre Niskin bottles. The success of the CTD operations during this scientific voyage is undoubtedly indebted to the CAPSUM METS sensor, possibly the only one of a kind, that is very sensitive to change (by as low as 3-5 nM) in water CH₄ content and a relatively rapid recovery after exposure to high concentrations.

FLARE OBSERVATIONS

Lander Deployment at Bear's Paw

A substantial ADCP flare was recorded at around hour 34 (Figure 3A). The ‘flare’ (presumed to be bubbles) persisted for 30 min and covered the entire acoustic depth range (100 m) of the ADCP. During this period, there is an associated increase in vertical velocity at 34 hours (Figure 3D - green line), though this may be an artifact from the large backscatter signal in a single beam. The flare does not seem to be related to a tidal hydrostatic pressure drop (Figure

3C). In fact, the onset of this outburst occurred during high tide and at maximum current velocities of more than 20 cm s^{-1} (Figure 3D). As there is no increase in suspended particles (inferred from the turbidity data), the ADCP flare is almost definitely attributed to a gas or fluid outburst. Simultaneous to the flare, the CH_4 flux of the flux chamber jumped 3-fold to a flux rate of $0.9 \text{ mmol m}^{-2} \text{ d}^{-1}$, provide further evidence toward methane outgassing. At this site, no active gas emission has been previously detected in the water column by any other acoustic device during cruise SO191. However, signatures of shallow gas at the seep sites including gas blanking and acoustic turbidity were captured with sub-bottom profiles (Jones *et al.*, *in press*), suggesting the presence of subsurface gaseous pockets.

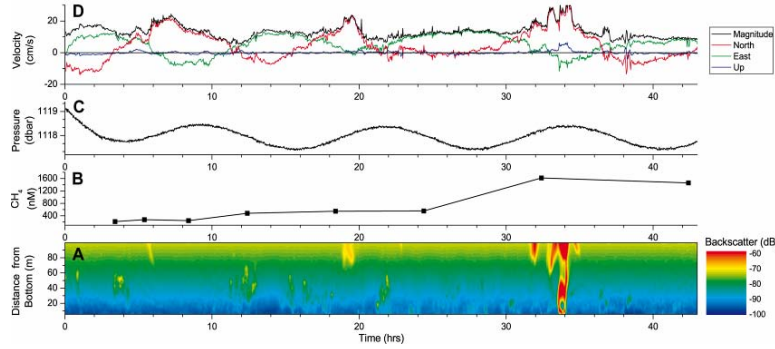


Figure 3. FLUFO-1 observations. Bottom to top: A) ADCP backscatter intensity (Beam 2), B) time series of CH_4 concentrations in the flux chamber, C) pressure and D) depth averaged velocity time series.

Lander Deployment at Faure Site

Visual inspection of the landers by ROV (Naudts *et al.*, *in press*) showed that the deployment sites were indeed in the immediate vicinity of vent holes discharging free gas (Figure 2 left), which is clearly reflected in the backscatter data of the uplooking ADCP mounted on FLUFO (Figure 4A). The backscatter data show pulses of activity that lasted for 2-4 hours and reached up to $\sim 90 \text{ m}$ above the seafloor. These pulses correlate to a decreasing slope of the pressure readings (Figure 4B) from the storage CTD mounted on the lander, that is, flares occur during negative slopes of the pressure curve. These flares occur every ~ 12 hours along with tides. Flares also occur as east velocity is changing from negative to positive (which may account for the “bended” appearance of the flare), further indicating tidal influence

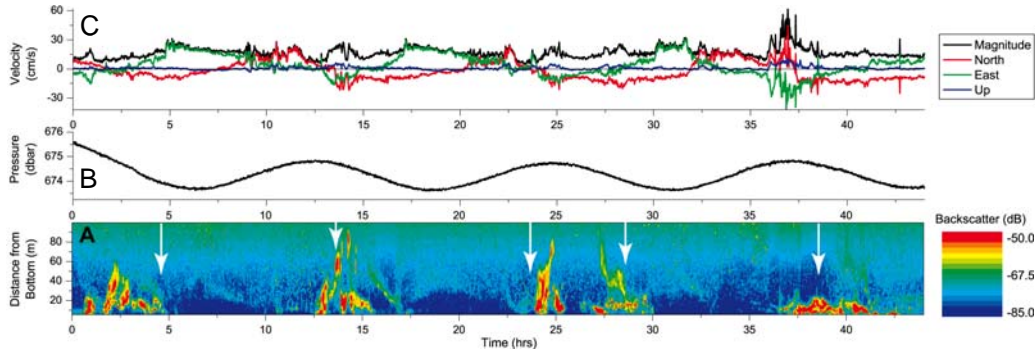


Figure 4. Physical measurements obtained simultaneously to the changes in CH_4 concentration during deployment of FLUFO-4. Bottom to top: A) ADCP backscatter (beam 4), B) local hydrostatic pressure with changes, and C) depth-averaged velocity time series.

DISCUSSION

Bear's Paw Flare

As first shown in Figure 3, we presented observations of the flare which roughly corresponded to the increase in CH₄ flux in the benthic chamber. Figure 5 is a close up of the backscatter for all four beams. We believe Figure 5 shows the effects of a long-term plume (> 4 hours), and speculate that the buoyancy sources are from a combination of high concentrations of dissolved methane in the porewater, perhaps coupled with higher porewater temperatures (Linke *et al.*, 2009). The varying intensity of the backscatter signal suggests fluid and intermittent bubble release as well as some light sediment particles. The phenomenon is measured in all four beams, but the long-term “belt” is almost always present in Beam 1. The very large flare recorded at 33.5 – 34.5 hours is thought to be a large bubble outburst associated with the plume source. The flare(s) seems to wander, which is probably due to changing currents, and perhaps spatial variation of the source.

The belt-like feature is evident for almost the entire period on panel Figure 5D (Beam 1). Remarkably, a corresponding local CH₄ peak of 300 nM was measured within the belt at about 31.3 hrs during CTD cast 18 (Overlaid on Figure 5 contour). This methane peak is certainly due to a plume intrusion. While it is difficult to speculate about the source of buoyancy, we will perform model simulations to try to better define driving forces.

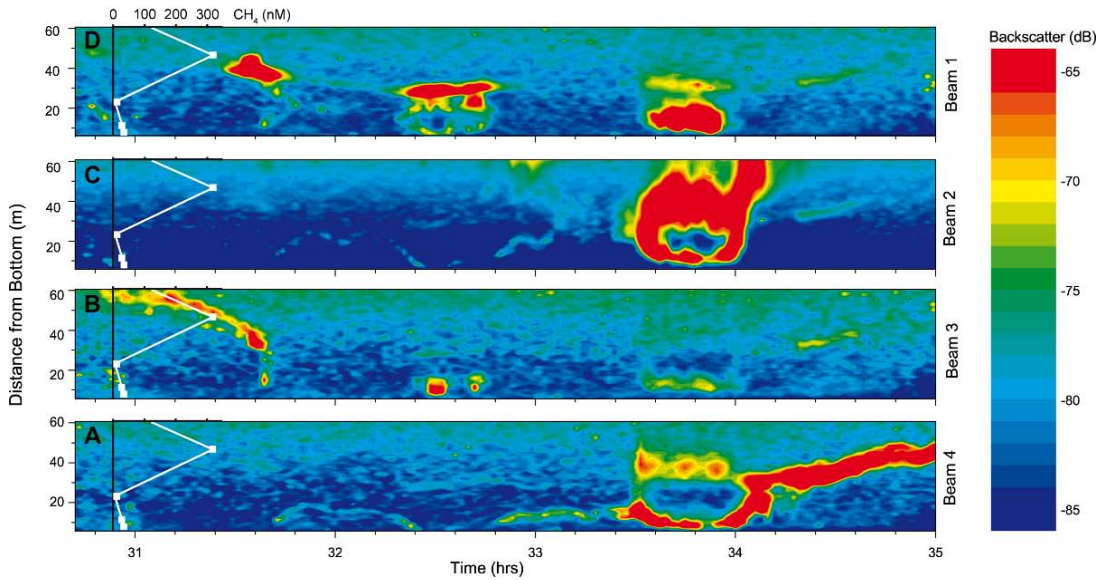


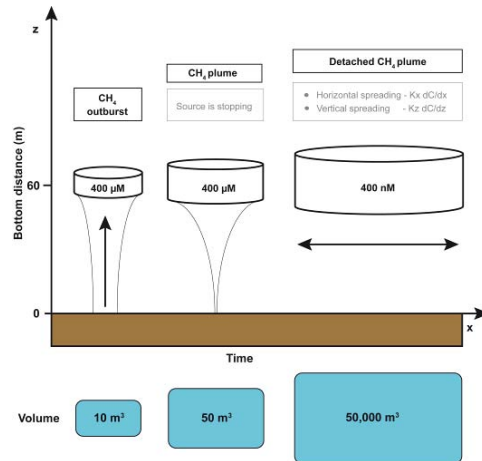
Figure 5. Close up of the ADCP backscatter measurements at Bear's Paw. Bottom to top: ADCP backscatter A) beam 4, B) beam 3, C) beam 2, and D) beam 1. Overlaid in white on all panels, CH₄ values of CTD cast 18 (conc. values are shown as small numbers ranging for 0 – 300 nM). These are arranged so that the peak point (~ 300 nM) is shown at the exact time it was taken in relation with the ADCP data.

Plume Source: Plume Modeling

A plume model was used to constrain possible types and strengths of buoyancy sources was investigated using a plume model (Linke *et al.*, 2009). The model combines the freshwater plume model (Wüest *et al.*, 1992) with the marine, CH₄ bubble model (McGinnis *et al.*, 2006). We simulate a (1) methane bubble source, (2) a heat source, (3) a dissolved methane source and (4) dissolved methane source using observed concentrations in the ambient bottom water (c.f. Figure 5). The plume simulation results are summarized in Table 1.

Table 1. Results of plume simulations.

Plume Start Conditions	Run 1	Run 2	Run 3	Run 4
Plume source depth (m)	1092	1092	1092	1092
Plume radius (m)	2	2	2	2
Initial bubble diameter (mm)	6	-	-	-
delta plume CH ₄ conc. (μM)	0		4200	200
delta plume temperature (°C)	0	2	0	0
Gas flux (Mol s^{-1})	6			
Gas flux (L s^{-1})	1.3			
Plume Stop Conditions				
Max. plume rise height (m)	1045	1045	1045	1082
Rise height (m)	47	47	47	3-10
Final plume CH ₄ conc. (μM)	370	N.A.	463	140

**Figure 6.** Schematic model illustrating the fate of an outburst which injects a CH₄ plume into the water column.

Run 1 demonstrates that a huge amount of gas is required to produce a plume that rises ~50 meters high. An gas outburst of ~1 L/s methane would be required, however, at 1,100 m depth, this is equivalent to 6 Mol/s, or a gas release rate of 8 Ton/day (however, only for a short period). Run 2 shows a heat source equivalent to a local 2°C temperature increase is required to provide the same plume rise height as in Run 1. The following explanation for Run 3 is diagramed in Figure 6. Similar to Runs 1 and 2, for Run 3 we adjusted the initial dissolved CH₄ concentration and found that 4.2 mM (roughly 2% local saturation) was necessary to provide the same plume rise height. This surprising low initial concentration produced a plume rise of ~50 m with a small source area of 2 m radius. The final plume concentration in Run 3 is about 463 μM at the terminal plume rise height (equilibrium depth), which is distributed over the predicted final plume area of $\sim 50 \text{ m}^2$. Water column methane concentrations of ~400 nM (Faure *et al.*, accepted) were measured in the water column above Omakere Ridge. The final plume in Run 3 would therefore have to be diluted due to horizontal turbulent diffusion and advection to match these concentrations. Diluting the plume by a factor of 1,000 (assuming only horizontal turbulent diffusion/dispersion and no oxidation), would imply it spread over an area 1,000 times larger. This would mean concentrations in the range of 400 nM over $50,000 \text{ m}^2$ or a circle with radius 126 m (diameter 250 m). Therefore, if a plume ‘eruption’ or outburst occurred, we would have to sample it within 250 meters to obtain the concentrations observed. This seems on the order of what we could reasonably catch with CTD sampling and in the range of this study (Figure 7). Of course, higher concentrations resulting in larger eruptions (final concentrations) means we could likely find the methane signals up to a few kilometers away.

If there is no density stratification, then it takes very little buoyancy, and hence, a very low initial CH₄ concentration, to cause a plume to rise in the water column as the only resistance is friction (and not density) in this case. This is demonstrated with Run 4 using a well-mixed BBL, where an initial dissolved CH₄ concentration of only 200 μM could result in a plume rising 3 – 10 meters from the sea floor.

In these cases, we speculate that the observed outbursts are likely relatively short, intermittent plumes that rise to some distance, which depends mainly on the buoyancy strength and ambient density stratification. The buoyancy source is then depleted, and the plume

subsequently detaches from the seafloor. The plume signature (or injection depth), such as high CH₄ concentrations, will persist for a certain time (~hours to days) in the water column, but will ultimately be advected away or horizontally and vertically diffusively smeared, depending on the local hydrodynamics. Deciphering the flux pathway of methane across the sediment-water interface is the key in linking physical driving forces, dilution, chemical and microbial oxidation.

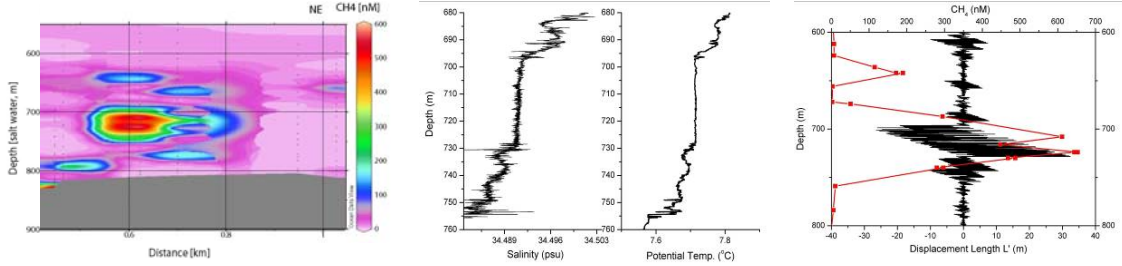


Figure 7. LEFT: The transect of CH₄ concentrations shows that an observed peak at nearby Tui occurs much higher in the water column (from Faure *et al.*, accepted). CENTER: In the corresponding profiles, a remarkable completely well-mixed step (in T and Sal) is observed at this location which is ~35 m thick. RIGHT: Thorpe displacement analysis shows substantial overturns of ~30 m at around 720 m depth that perfectly corresponds with the large peak (~600 nM) of CH₄ (Right).

Plume Fate: Water Column Properties

Once the methane reaches the water column, it is transported via turbulent diffusion. In stratified environments, the density gradient suppresses vertical mixing. As there are typically no horizontal gradients, horizontal diffusivities are several orders of magnitude larger than vertical. Figure 7 (left) shows such a signal from a plume emission. The CTD data showed a 30-meter thick deep mixed layer corresponding almost exactly with the peak of ~600 nM at round 700-730 meters (Figure 7 center, right). Figure 7 (right) shows the methane concentration profile plotted over the Thorpe displacement, L'.

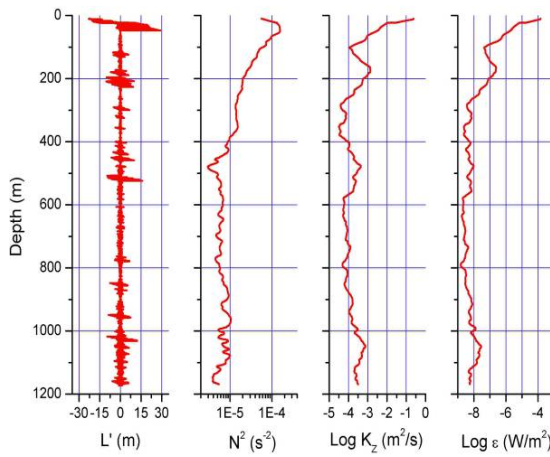


Figure 8. Water column energetics inferred from a slow-profiling (30-50 cm/s) CTD (24Hz). Assuming Thorpe scale is equal to Ozmidov scale, then energy dissipation is $\varepsilon = L_o^2 N^3$ (W/kg). Using a mixing efficiency $\gamma = 0.15$, then the vertical diffusion is defined as $K_Z = \gamma \varepsilon / N^2$ (m²/s). N² is water column stability.

Using Thorpe scale, rough vertical diffusivities (K_z) were estimated from CTD profiles to be $\sim 10^{-4} \text{ m}^2 \text{ s}^{-1}$ (Figure 8; Dillon, 1982). Horizontal diffusivities, K_x , are more difficult to determine, but K_x values obtained in the literature range from 0.3 to over 1,000 $\text{m}^2 \text{ s}^{-1}$ (Sundermeyer and Price, 1998). Methane peaks are therefore diffusively ‘smeared’ over time. In the vertical, the lifetime of such a 30 m thick peak can be estimated as $t = Z^2/K_z = 30^2/(1E^{-4}) \sim 100$ days (Linke *et al.*, 2009). In the horizontal, if we consider our plume example, the residence time of such a signal is $t = 250^2/(0.3 - 1,000) = 60$ seconds to about 2 days, supporting the highly ephemeral nature of the methane signals, which disappeared within hours.

Biological Implications of Water Column Methane

The observatories that recorded the sudden CH_4 increases had been placed at the transition zone between carbonates and dark sediment patches with dense heterotroph ampharetid polychaete beds. These sites, containing mixed chemotroph and heterotroph benthic communities, demonstrate CH_4 flux and oxygen uptake rates, which are of the same magnitude as other cold seep systems where chemotroph communities dominate (Linke *et al.*, 2005; Sommer *et al.*, 2006). We also discovered that these transition zones exhibit large spatial and temporal variability in the supply of fluids and gases from deeper or neighboring sediments. CH_4 may then be discharged into the water column as plumes in an eruptive or outburst pattern that almost completely bypass the benthic filter (e.g. CH_4 discharged as free gas would effectively bypass microbial oxidation). Once released into the bottom water this plume is affected by physical processes (turbulent diffusion) which act to dilute and transport it away.

Methane reaching the BBL in dissolved form (via ‘plume outbursts’ or flux across the sediment-water interface) can be further oxidized aerobically in oxygenated surface sediments or in the BBL where methylotrophic microorganisms might live attached to suspended particles. In general, there are very few measurements of open ocean methane oxidation rates using tracers, so our understanding of the kinetics of microbial methane oxidation in the oxic ocean, particularly in subsurface maxima and plumes, is poorly constrained (Reeburgh, 2007). However, open ocean water column methane oxidation rates are generally viewed as being quite low, but fractional turnover rates of months (Valentine *et al.*, 2001) and days (de Angelis *et al.*, 1993) have been observed with methane concentrations of $\sim 20 \text{ nM}$. Faure *et al.* (accepted) calculate a removal rate in the range of 11 to 19% per day (or $\sim 40 \text{ nM/day}$) from the actual variation in CH_4 concentrations ($< 200 \text{ nM}$) at one site taking all contribution factors into account. Our model results fall in the same range of magnitude and provide insights into the various processes that come into play when methane is injected into the water column.

CONCLUSIONS

We present results using a combined approach to understand the impact of different driving forces on the flux pathway of methane across the sediment-water interface into the water column. Acoustic techniques have been previously used for the efficient location and identification of submarine gas emission, providing a valuable tool for plume detection; we now implement ADCP technology as a survey tool for transient plume emissions. These acoustic surveys were accompanied by physical, biological, chemical and optical data obtained from in situ lander measurements in the BBL. Together with plume model results, we could demonstrate the spatial and temporal variability of natural seabed methane emission and highly ephemeral nature (hours) of the methane signals in the water column. Furthermore, the data provide a hint towards the impact of a change from a fluid-driven system towards a

system with episodic gas discharge which bypass microbial oxidation. In the former case, the plume model strongly supports first evidence of a dissolved CH₄ fluid source and not bubbles, as far too much methane gas would be required (tons per day). We attribute the occurrence of bubbles in the second case likely as only an indicator of recent plume events, and not as the plume buoyancy source. Additionally, high horizontal diffusivity make the transport and ‘smearing’ of CH₄ surprisingly rapid and difficult to follow with single standard oceanographic sampling tools.

Obviously, these issues must be considered when budgets of CH₄ emission rates are extrapolated from single deployments. In view of a limited amount of water samplers, novel methane sensor technology is needed to resolve this unpredictable variability. Multi-disciplinary long-term observatories are needed to understand the processes and driving forces involved. The unique combination of various measurements and modeling results presented in this paper provide a first step to link physical driving forces, dilution, chemical and microbial oxidation in our endeavor to understand the fate of CH₄ injected into the water column.

ACKNOWLEDGMENT

We are grateful for the support of chief mate L. Mallon, officers and crew of RV SONNE (SO191). Many thanks are due to B. Bannert, A. Petersen, W. Queisser and M. Türk for their indispensable technical assistance on board and the operation of the landers. We thank B. Domeyer, M. Haeckel, S. Kriwanek, K. Krieger, and R. Surberg for performing the biogeochemical analyses. Thanks to the ROV team of L. Naudts, D. Boone, M. DeBatist and J. Greinert and the journalist D. Cordts we were able to visually inspect and document the deployment sites of the landers. Special thanks to K. Faure and J. Schneider von Deimling for their assistance with CTD data collection and onboard methane analysis.

REFERENCES

- Barnes, P.M., Lamarche, G., Bialas, J., Henrys, S., Pecher, I., Netzeband, G.L., Greinert, J., Mountjoy, J.J., Pedley, K., Crutschley, G. (in press). Tectonic and geological framework for gas hydrates and cold seeps on the Hikurangi subduction margin, New Zealand. *Mar. Geol.*
- Bialas, J., Greinert, J., Linke, P., Pfannkuche, O. (2007). FS Sonne Fahrbericht/Cruise Report SO 191 New Vents. IFM-GEOMAR, Leibniz-Institut für Meereswissenschaften, Kiel, Germany. 190 pp.
- Brown, K.M., Tryon, M.D., DeShon, H.R., Dorman, L.M., Schwartz, S.Y. (2005). Correlated transient fluid pulsing and seismic tremor in the Costa Rica subduction zone. *Earth Planet. Sci. Lett.*, **238**, 189–203.
- de Angelis, M.A., Lilley, M.D., Baross, J.A. (1993). Methane oxidation in deep-sea hydrothermal plumes of the endeavour segment of the Juan de Fuca Ridge. *Deep-Sea Res. I*, **40** (6), 1169–1186.
- Dillon, T.M. (1982). Vertical overturns: a comparison of Thorpe and Ozmidov length scales. *J. Geophys. Res.*, **87**, 9601–9613.
- Faure, K., Greinert, J., Pecher, I.A., Graham, I.J., Massoth, G.J., de Ronde, C.E.J., Wright, I.C., Baker, E.T., Olson, E.J. (2006). Methane seepage and its relation to slumping and gas hydrate at the Hikurangi Margin, New Zealand. *N.Z. J. Geol. Geophys.*, **49**, 503–516.
- Faure, K. et al. (accepted). Free and dissolved methane in the water column and the sea surface: Geochemical and hydroacoustic evidence of bubble transport. *Mar. Geol.*
- Greinert, J. (2008). Monitoring temporal variability of bubble release at seeps: the hydroacoustic swath system GasQuant. *J. Geophys. Res.*, **113**, C07048.
- Jones, A.T., Greinert, J., Bowden, D., Klaucke, I., Petersen, J., Netzeband, G., Weinrebe, W. (in press). Acoustic and visual characterisation of methane-rich seabed seeps at Omakere Ridge on the Hikurangi Margin, New Zealand. *Mar. Geol.*
- Judd, A., Hovland, M., 2007. Seabed Fluid Flow. Cambridge. 475 pp.
- LaBonte, A.L., Brown, K.M., Tryon, M.D. (2007). Monitoring periodic and episodic flow events at Monterey Bay seeps using a new optical flow meter. *J. Geophys. Res.*, **112**, B02105.
- Levin, L.A. (2005). Ecology of cold seep sediments: interactions of fauna with flow, chemistry and microbes. *Oceanogr. Mar. Biol. Ann. Rev.*, **43**, 1–46.
- Lewis, K.B., Marshall, B.A. (1996). Seep faunas and other indicators of methane-rich dewatering on New Zealand convergent margins. *N.Z. J. Geol. Geophys.*, **39**, 181–200.

- Linke, P., Wallmann, K., Suess, E., Hensen, C., Rehder, G. (2005). In situ benthic fluxes from an intermittently active mud volcano at the Costa Rica convergent margin. *Earth Planet. Sci. Lett.*, **235**(1-2), 79–95.
- Linke, P., Sommer, S., Rovelli, McGinnis, D.F. (2009) Physical limitations of dissolved methane fluxes: The role of bottom layer processes. *Mar. Geol.*
- McGinnis, D.F., Greinert, J., Artemov, Y., Beaubien, S.E., Wüest, A. (2006). The fate of rising methane bubbles in stratified waters: how much methane reaches the atmosphere? *J. Geophys. Res.*, **111**(C9), C09007.
- Naudts, L., Greinert, J., Poort, J., Belza, J., Vangampelaere, E., Boone, D., Linke, P., Henriet, J.-P., De Batist, M. (in press). Active venting sites on the gas-hydrate-bearing Hikurangi Margin, Off New Zealand: Diffusive versus bubble-released methane. *Mar Geol.*
- Pfannkuche, O., Linke, P. (2003). GEOMAR landers as long-term deep-sea observatories. *Sea Technol.*, **44** (9), 50–55.
- Reeburgh, W.S. (2007). Oceanic methane biogeochemistry. *Chem. Rev.*, **107**, 486–513.
- Sommer, S., Pfannkuche, O., Linke, P., Luff, R., Greinert, J., Drews, M., Gubsch, S., Pieper, M., Poser, M., Viergutz, T. (2006). Efficiency of the benthic filter: biological control of the emission of dissolved methane from sediment containing shallow gas hydrates at Hydrate Ridge. *Glob. Biogeochem. Cycles*, **20**(2), GB2019.
- Sommer, S., Linke, P., Pfannkuche, O., Schleicher, T., Schneider v. Deimling, J., Reitz, A., Haeckel, M., Flögel, S., Hensen, C. (2009). Seabed methane emissions and the habitat of frenulate tubeworms on the Captain Arutyunov mud volcano (Gulf of Cadiz). *Mar Ecol Prog Ser.*, **382**, 69–86.
- Sundermeyer, M.A., Price, J.F. (1998). Lateral mixing in the North Atlantic tracer release experiment: observations and numeric simulations of Lagrangian particles and a passive tracer. *J. Geophys. Res.*, **103** (C10), 21481–21497.
- Torres, M.E., McManus, J., Hammond, D.E., de Angelis, M.A., Heesch, K.U., Colbert, S.L., Tryon, M.D., Brown, K.M., Suess, E. (2002). Fluid and chemical fluxes in and out of sediments hosting methane hydrate deposits on Hydrate ridge, OR, I: hydrological provinces. *Earth Planet. Sci. Lett.*, **201**, 525–540.
- Tryon, M.D., Brown, K.M., Torres, M.E. (2002). Fluid and chemical flux in and out of sediments hosting methane hydrate deposits on Hydrate Ridge, OR, II: hydrological processes. *Earth Planet. Sci. Lett.*, **201**, 541–557.
- Valentine, D.L., Blanton, D.C., Reeburgh, W.S., Kastner, M. (2001). Water column methane oxidation adjacent to an area of active hydrate dissociation, Eel River Basin. *Geochim. Cosmochim. Acta*, **65**, 2633–2640.
- Wüest, A., Brooks, N.H., Imboden, D.M. (1992). Bubble plume modeling for lake restoration. *Water Resour. Res.*, **28**, 3235–3250.

Gas exchange and deep water renewal in Lake Van (Turkey) estimated by inverse modelling of transient tracers

Heike Kaden¹, Frank Peeters², Rolf Kipfer³, Yama Tomonaga⁴

¹ Environmental Physics, University of Konstanz, Mainaustr. 252, 78464 Konstanz, Germany,
Heike.Kaden@uni-konstanz.de

² Environmental Physics, University of Konstanz, Mainaustr. 252, 78464 Konstanz, Germany,
Frank.Peeters@uni-konstanz.de

³ Dept. of Water Resources and Drinking Water, Swiss Federal Institute for Environmental
Science and Technology (EAWAG), 8600 Dübendorf, Switzerland and Isotope Geology, Swiss
Federal Institute of Technology (ETHZ), 8092 Zürich, Switzerland, *rolf.kipfer@eawag.ch*

⁴ Dept. of Water Resources and Drinking Water, Swiss Federal Institute for Environmental
Science and Technology (EAWAG), 8600 Dübendorf, Switzerland, *tomonaga@eawag.ch*

*Corresponding author, e-mail: *Heike.Kaden@uni-konstanz.de*

ABSTRACT

The level of closed basin Lake Van (salinity: 21 g kg⁻¹, pH = 9.7), Turkey, rose by about 2 m in the time period between 1988 and 1995 and decreased again until 2003. The lake level rise resulted in the reduction of the deep-water renewal and the development of an anoxic deep-water layer. To simulate the temporal and spatial evolution of the concentrations of the transient tracers SF₆, ³He, ⁴He, ³H and CFC-12 simultaneously and to describe the vertical water exchange, we developed a one-dimensional vertical transport model using the program AQUASIM (Reichert 1994). The model includes the tracer input by precipitation and rivers, evaporation, gas exchange, the vertical transport by turbulent diffusion, ³H decay to ³He, ³H flux, ³H fractionation during evaporation and the influx of helium from sediment. Data from 1989 / 1990 (Kipfer et al. 1994) and 2004 - 2006 was used to validate the model. The actual vertical exchange rates, vertical turbulent diffusion coefficients and the helium flux from the sediment were estimated by inverse modelling. These rates are simultaneously fitted by modelling the tracers from 1900 to present. We show that our model is capable to reproduce the evolution of the transient tracer.

Release and distribution of methane in lakes

H. Hofmann and F. Peeters

¹ Environmental Physics Group, Limnological Institute, University of Konstanz, D-78465 Konstanz, Germany, hilmar.hofmann@uni-konstanz.de

ABSTRACT

Lakes provide an important source of atmospheric methane, but internal pathways responsible for methane emissions are not yet clear. The methane produced in lake sediments can be either oxidized or emitted to the atmosphere. In oxic water bodies, lake littoral zones may form a major pathway, because these zones are highly disturbed by surface waves that interact by their currents with the sediment surface in terms of particle resuspension and pore water exchange. Simultaneous, high-resolution measurements of the surface wave field, wave-induced currents, the acoustic backscatter strength, and the concentration and distribution of dissolved methane were conducted in oligotrophic Lake Constance. These measurements gave evidence that waves enhance the release of dissolved methane in the shallow littoral zone by burst releases of methane that inhibited oxidation at the sediment-water interface. Thereby the amount of released methane is highly related to the production in the anoxic zone of the littoral sediments, which depends on water temperature, and the course of the present surface wave field. Parallel to the near-shore investigations, we conducted measurements to describe the spatial and temporal distribution of dissolved methane between the littoral and the pelagic zone.

Exchange Flow between Open Water and an Aquatic Canopy

Xueyan Zhang^{1*} and Heidi M. Nepf²

¹ *The Parsons Laboratory for Environmental Science and Engineering, Department of Civil and Environmental Engineering, Massachusetts Institute of Technology, 15 Vassar Street, Cambridge, MA 02139, USA*

² *The Parsons Laboratory for Environmental Science and Engineering, Department of Civil and Environmental Engineering, Massachusetts Institute of Technology, 15 Vassar Street, Cambridge, MA 02139, USA*

*Corresponding author, e-mail xyzhang@mit.edu

ABSTRACT

Differential solar heating can result from shading by aquatic plants, producing a temperature difference between vegetated and unvegetated regions of a surface water body. This spatial heterogeneity in water temperature generates gradients in water density that may drive an exchange flow between the vegetation and open water. In lakes, these exchange flows may play an important role in the transport of nutrients and other chemicals, and thus may impact the lake-scale chemistry and ecology. Drag associated with the submerged portion of the plant modifies the exchange, specifically, controlling the velocity scale. In this paper we consider two distinct cases, specifically the exchange generated 1) near rooted vegetation, which occupies the full water depth, and 2) near floating vegetation, which occupies a limited depth of water column at the water surface. Laboratory experiments describe the exchange flow and confirm a scaling analysis. Particle Imaging Velocimetry (PIV) was used to quantify the velocity field. The intrusion velocity was observed to decrease with increasing stem density. When the vegetation is floating, the intruding flow bifurcates, with only a fraction of the flow entering the vegetation layer, and the remainder is displaced downward, below the vegetation layer.

KEYWORDS

Drag; exchange flow; thermally-driven flow; vegetation.

INTRODUCTION

Spatial heterogeneity in water temperature can generate gradients in water density, which in turn can produce convective exchange flows. In lakes, these thermally-driven exchange flows play an important role in the transport of nutrients and other chemicals, and thus can have a significant effect on the lake-scale chemistry and ecology (James and Barko, 1991; MacIntyre and Melack, 1995).

Temperature differences that occur between the shallow and deep regions of a water body are well known. During the daytime, uniform solar radiation causes the temperature within the shallow region to rise more rapidly than that in the adjacent deeper region, because the same heat flux is distributed over a smaller water depth. Similarly, during the night, as the heat leaves the water, the temperature in the shallow region drops more rapidly than that in the deeper region. This diurnal cycle of temperature difference has been observed to generate diurnally-varying exchange flows between the littoral zone and the main body of a lake (Adam and Wells, 1984; Monismith *et al.*, 1990; James *et al.*, 1994). Under weak wind conditions, this exchange flow controls the flushing of the littoral zone, reducing the flushing time by several orders of magnitude from turbulent diffusion alone.

Shading by vegetation can also cause differential heating (Chimney *et al.*, 2006; Ultsch, 1973). For example, dense vegetative stands can reduce incident light by 50 to over 90% (Wetzel, 2001). Lightbody *et al.* (2008) reported that the daytime temperature within the marsh region of a constructed wetland remained 2°C cooler than the adjacent open water areas. Further, Coates and Ferris (1994) showed that the density differences generated by shading from floating plants can generate an exchange flow. However, the flow is displaced downward, beneath the root layer. As an extension to Coates and Ferris (1994), this paper begins with an examination of rooted vegetation, for which the root obstruction extends over the entire depth, so that the intrusion must enter the vegetated layer. Later we also consider the displacement of flow beneath a floating vegetation layer.

Rooted vegetation provides a significant amount of drag, such that rooted plants both promote, through differential shading, and inhibit, through drag, a thermally-driven exchange flow. Tanino *et al.* (2004) studied the impact of canopy drag on exchange flows by generating a lock-exchange within an array of circular cylinders that extended over the entire flow domain. Zhang and Nepf (2008) considered the more natural case of exchange between an emergent canopy and an adjacent region of open water. The velocity of the intrusion entering the canopy, as well as the total discharge between the open water and the canopy were strongly dependent on the canopy drag. Tanino *et al.* (2004) and Zhang and Nepf (2008) considered cases in which the reduced gravity, g' , was constant, set by the density difference between the initial reservoirs. In this work, g' is not constant because it is generated by a steady heat source, mimicking the evolution of shaded and unshaded regions receiving uniform solar radiation. Under a constant heat source, the temperature difference between the shaded and unshaded regions, ΔT , increases linearly with time, such that g' also increases linearly with time.

When solar radiation impinges on a water surface, a significant portion is reflected from the surface and is lost through scattering. The remaining energy penetrates the surface and is absorbed by the water. Due to absorption, the light intensity or irradiance, I , decreases with distance from the water surface following Beer's Law,

$$I(z) = I_0 \exp[-\eta(h - z)]. \quad (1)$$

Here, I_0 is the radiation penetrating the water surface ($z = h$), and $z = 0$ at the bed. The extinction coefficient, η , describes the spatial scale over which light energy is absorbed. We consider a rectangular domain of constant depth, h , and total length, $(L_v + L_o)$, in which L_v and L_o are the lengths of the vegetated and open region, respectively (Fig. 1). We assume that the emergent portions of the plants completely block the incoming solar radiation. Under constant heat flux the water in the open region heats up, and becomes less dense than the adjacent water in the vegetation. This density difference drives an intrusion of warm water into the vegetation at the surface, with a compensating return flow underneath. The intrusion depth, h_i , is expected to scale with $1/\eta$.

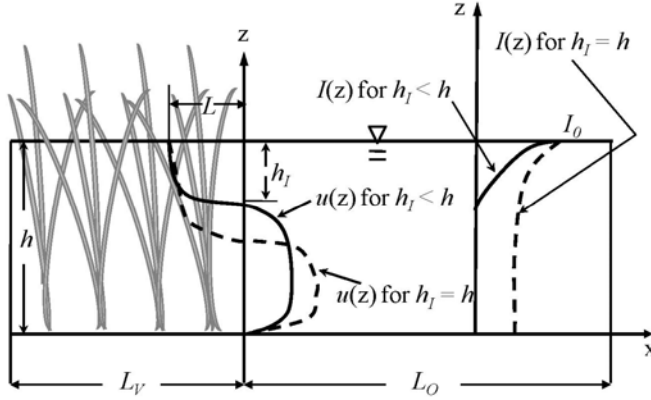


Figure 1. A sketch of thermal and intrusion length scales.

In the littoral regions of a lake, the horizontal length scale is generally much greater than the water depth. The viscous term $\nu \partial^2 u / \partial x^2$ is thus much smaller than $\nu \partial^2 u / \partial z^2$ and can be neglected. The conservation of horizontal momentum in a two-dimensional system is then

$$\frac{Du}{Dt} = -\frac{1}{\rho} \frac{\partial P}{\partial x} - Cau + \nu \frac{\partial^2 u}{\partial z^2}, \quad (2)$$

where u is the horizontal velocity component, P is the pressure, ρ is the fluid density, ν is the kinematic viscosity of water and x and z are horizontal and vertical axis, respectively, and t is time. The second term on the right-hand side characterizes the vegetative drag, and a is the frontal area of vegetation per unit volume. C (m/s) is a linear drag coefficient. A linear drag law is selected based on the expected range of stem Reynolds number.

We introduce the following scales,

$$x \sim L, z \sim h_I, \Delta P \sim \Delta \rho g h_I \sim \rho \alpha \Delta T g h_I, \quad (3)$$

in which L is the horizontal length scale of the intrusion in the canopy (Fig. 1). $\Delta \rho$ is the density difference between the canopy and open water, and ΔP is the resulting pressure difference. α is the coefficient of thermal expansion, and g is gravity. The temperature difference, ΔT , increases with time due to the constant heat flux, I_0 , impacting the water in the open region only. The temperature difference can be expressed as $\Delta T = I_0 t / \rho C_p h_I$, where C_p is the specific heat of water. With the above scaling, (2) can be written,

$$u^2 \sim -\frac{g \alpha I_0 t}{\rho C_p} - CauL + \nu \frac{uL}{h_I^2}. \quad (4)$$

In the initial period after the heat flux has started, the system is controlled by the balance between inertia and buoyancy only. The velocity scale for the inertia-dominated regime, u_i , is

$$u_i \sim \left(\frac{g \alpha I_0 t}{\rho C_p} \right)^{1/2} \sim \sqrt{g' h_I}, \quad (5)$$

where g' is given by

$$g' = \frac{\Delta \rho}{\rho} g = \alpha \Delta T g = \frac{g \alpha I_0 t}{\rho C_p h_I}. \quad (6)$$

As the intruding front lengthens ($L > 0$) over time, both the viscous and vegetative drag become important. For most canopies the vegetative drag will be the more important flow resistance, i.e. $(Cah_I^2 / \nu) \gg 1$. By comparing the terms for vegetative drag and inertia in (4),

we anticipate that vegetative drag will dominate when $u \ll CaL$. Recognizing $L = ut$, the time-scale at which vegetative drag will exceed inertia is

$$T_v \sim (Ca)^{-1}. \quad (7)$$

After this time, the velocity is determined by the balance of buoyancy and vegetative drag. The drag-dominated velocity scale is found to be

$$u_v \sim \left(\frac{g\alpha I_0}{\rho C_p Ca} \right)^{1/2}. \quad (8)$$

It is interesting to see that the velocity is steady in this regime. Although the buoyancy increases with time due to the constant heat flux, $g' = g\alpha I_0 t / \rho C_p h_I$, the vegetative drag also increases with increasing intrusion length, $L \sim t$, and the two effects balance.

The energy balance provides another possible control on the velocity, because the flow cannot carry away more heat than is supplied by the surface flux (Coates and Patterson, 1993). However, under typical conditions, the drag-dominated regime will occur first, and control the dominant velocity scale (Zhang and Nepf 2008).

METHODS

To test the above scaling analysis, a series of experiments were conducted in a Plexiglass tank with dimensions of $70(L) \times 15(W) \times 40(H)$ cm. The tank consisted of two separate chambers, shown in Fig.2. Two 600-Watt spotlights were used to produce a uniform heat source. Particle Imaging Velocimetry (PIV) was used to quantify the flow field within the model vegetation. Pliolite particles with a density of 1.02g/cm^3 were added to the water. A 2-cm wide gap starting at 8 cm from the edge of the canopy was left within the model canopy as a window for the PIV. The width of the gap was chosen to be the same order of magnitude as or smaller than the distance between dowels. A laser sheet entering through the bottom of the tank illuminated the gap. The laser power was kept low enough (0.3 watts) to prevent thermal plumes from being generated due to the heating of the tank's bottom wall.

Additional experiments were conducted with a floating vegetation model (Fig.3). For these cases the exchange was modeled as a lock exchange, as in Zhang and Nepf (2008), for which the reduced gravity, g' , was constant, set by the density difference between the initial reservoirs. The velocity distribution was measured using PIV, as described above.

RESULTS

PIV measurements confirmed that after the intrusion has passed the PIV window, the velocity was predominantly horizontal. This is consistent with previous experimental observations by Coates and Patterson (1993) and Coates and Ferris (1994) for thermally-driven flow, and Zhang and Nepf (2008) for lock-exchange flow.

The intrusion depth, h_I , was extracted from each velocity profile, and the variability within each experimental run used as an estimate of uncertainty. The normalized intrusion depth, ηh_I , for each run is shown in Fig. 4. There is no systematic correlation between the normalized intrusion depth, ηh_I , and ah , implying that the surface intrusion depth is not controlled either by the total water depth, h , or the canopy density, a . Using all available runs, $\eta h_I = 0.28 \pm 0.06$, which is shown by the solid line in Fig. 4. For similar heating conditions, Coates and Patterson (1993) found $\eta h_I = 0.65$.

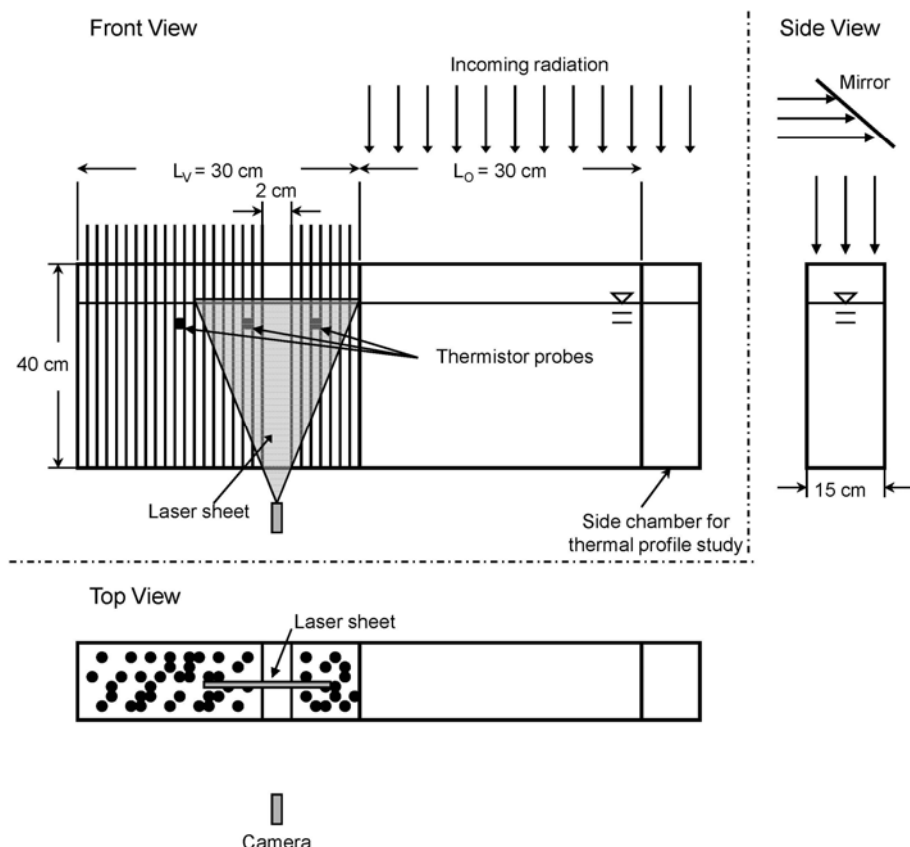


Figure 2. A sketch of the experimental setup. The sketch is not plotted to scale. Specifically, the PIV gap is the same or smaller than the distance between dowels.

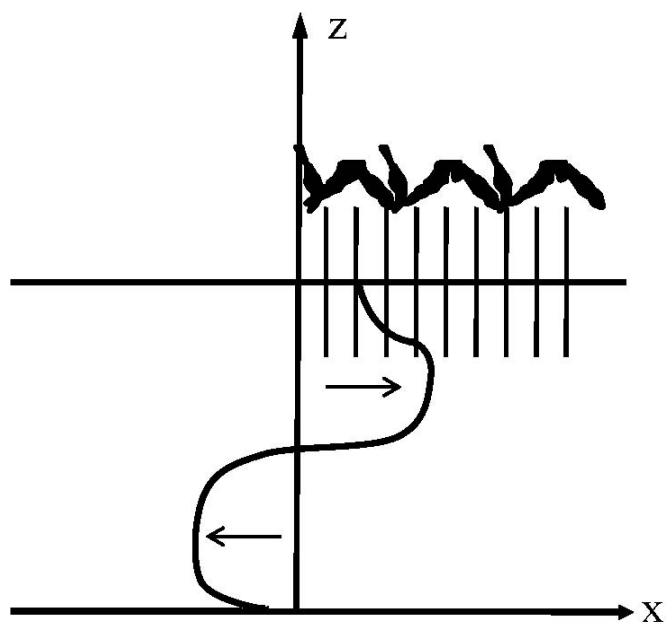


Figure 3. A sketch of an exchange flow between open water and a floating vegetation canopy.

The drag-dominated velocity, u_V , given in (8) is normalized by the viscous-dominated velocity scale, which was derived in Coates and Patterson (1993). This velocity ratio is proportional to the ratio of viscous stress to vegetative drag, as shown by the third term in (9),

$$u_V^* = u_V / \left[\frac{g \alpha I_0 h_L^2}{\rho C_p v} \right]^{1/2} \sim \left[\left(\frac{Cah_L^2}{v} \right)^{1/2} \right]^{-1}. \quad (9)$$

To normalize the measured velocity using (9), the linear drag coefficient C was interpolated from the numerical results of Koch & Ladd (1997), who reported drag for ϕ between 5% and 40% and Re_d between 0.2 to 180, conditions that correspond to those studied here. The normalized U_{mean}^* is plotted against $(Cah_L^2 / v)^{1/2}$ in a log-log coordinate (Fig. 5). The intrusion velocity decreases as the vegetative drag increases. The fitted slope, -1.2 ± 0.2 (with 95% confidence), agrees with our theoretical prediction of -1, based on (12). We anticipate that as the vegetative drag decreases further and becomes comparable with the viscous drag, *i.e.* $(Cah_L^2 / v)^{1/2} \rightarrow 1$, the normalized velocity U_{mean}^* should become $O(1)$; the intrusion velocity is then controlled by viscous drag.

For the case with floating canopy, the intruding flow into the vegetated region bifurcates due to the presence of the floating vegetation. The surface flow is retarded by the vegetation layer and thus the flow velocity is smaller than the flow velocity underneath. In Fig.6, we show a typical horizontal velocity profile of an exchange flow for the case with a floating canopy. The flow velocity within the vegetation (above 12 cm) is less than 1 cm/s, while the flow velocity outside the vegetation layer is between 3-4 cm/s. The velocity profile clearly shows the bifurcation of flow. For comparison, the velocity profile of an exchange flow in the absence of vegetation, but the same g' is also shown. The exchange velocity for the unobstructed case agrees with the theoretical value predicted by Shin (2004). Note that the presence of the floating vegetation changes the structure of the velocity profile in the upper layer.

CONCLUSION

This paper has examined the thermally driven exchange flow generated by the differential shading between open water and an adjacent emergent canopy under a constant light source. Scaling analyses described the expected flow regimes and associated velocity scales. The drag dominated velocity scale was confirmed by experiment. While our model can be used to estimate the magnitude of the exchange flow driven by thermal forcing, there are still challenges in applying our model in the field. First, the application of the model requires an input of the drag coefficient C , which is generally unknown *a priori*. We have also observed that, with a floating vegetation layer, the intruding flow will bifurcate. The flow within the vegetation layer is slower than the flow right underneath. This velocity differential is due to the drag provided by the floating vegetation. Our ongoing research is to develop a predictive theory for the velocity in each layer and the layer depths.

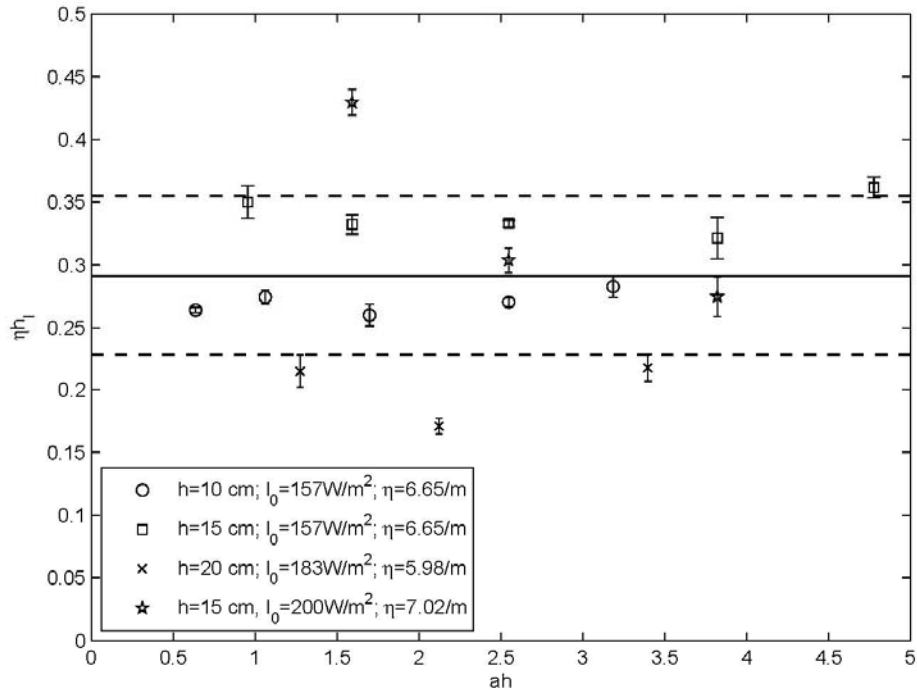


Figure 4. Variation of the normalized intrusion depth ηh_i with ah . The error bars show the standard error for each run. The solid line is the average of ηh_i for all cases. The dashed lines are one standard deviation from the average.

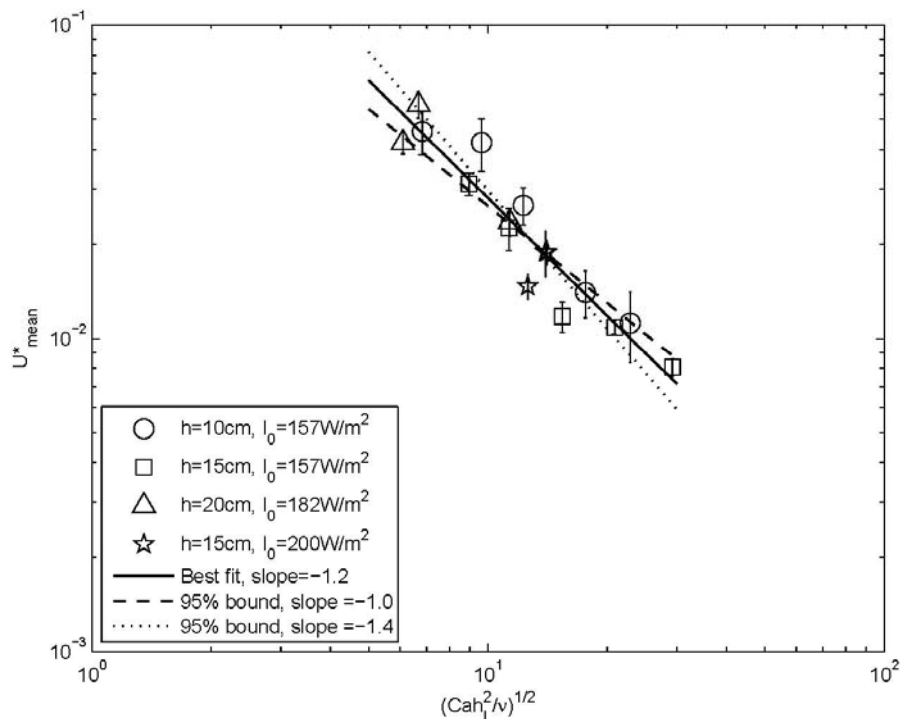


Figure 5. Normalized mean intrusion velocity against normalized canopy drag. The error bars show the standard error for each case. The solid line is the theoretical prediction based on (8).

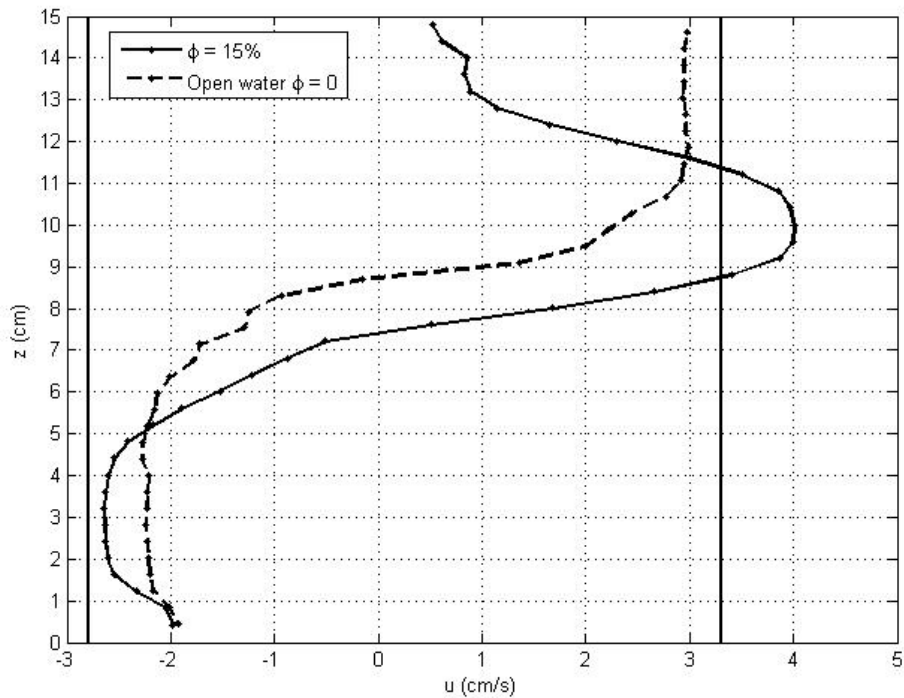


Figure 6. Comparison of the horizontal velocity profiles of exchange flows with floating vegetation and without vegetation (solid line: with floating vegetation; dashed line: pure open water). The two solid lines show the theoretical toe value for the exchange velocity in the absence of vegetation, predicted by Shin (2004).

REFERENCE

- Adams, E. E. and Wells, S. A. (1984), Field measurements on side arms of Lake Anna, VA.. *J. Hydraul. Eng.*, 110 (6), 773-793.
- Chimney, M. J., Wenkert, L. and Pietro, K. C. (2006), Patterns of vertical stratification in a subtropical constructed wetland in south Florida (USA). *Ecol. Eng.*, 27, 322-330.
- Coates, M. J. and Patterson, J. C. (1993), Unsteady natural convection in a cavity with non-uniform absorption of radiation. *J. Fluid Mech.*, 256, 133-161.
- Coates, M. and Ferris, J. (1994), The radiatively driven natural convection beneath a floating plant layer. *Limnol. Oceanogr.*, 39 (5), 1186-1194.
- James, W. F., & Barko, J. W. (1991), Estimation of phosphorus exchange between littoral and pelagic zones during nighttime convection circulation. *Limnol. Oceanogr.*, 36 (1), 179-187.
- James, W. F., Barko, J. W. & Eakin, H. L. (1994), Convective water exchanges during differential cooling and heating: implications for dissolved constituent transport. *Hydrobiologia*, 394, 167-176.
- Koch, D. L. and Ladd, A. J. C., (1997), Moderate Reynolds number flow through periodic and random arrays of aligned cylinders, *J. Fluid Mech.*, 349, 31-66.
- Lightbody, A., Avener, M. & Nepf, H. M. (2008), Observations of short-circuiting flow paths within a constructed treatment wetland in Augusta, Georgia, USA. *Limnol. Oceanogr.*, 53 (3), 1040-1053.
- Monismith, S. G., Imberger, J. & Morison, M. L. (1990), Convective motions in the sidearm of a small reservoir, *Limnol. Oceanogr.*, 35 (8), 1676-1702.
- MacIntyre, S. and Melack, J. M., (1995), Vertical and horizontal transport in lakes: linking littoral, benthic and pelagic habitats. *Journal of North America Bentholological society*, 14(4), 599-615.
- Shin, J. O., Dalziel, S. B. and Linden , P. F. (2004), Gravity currents produced by lock exchange. *J. Fluid Mech.*, 521, 1-34.
- Tanino, Y. Nepf, H. M. & Kulis, P. S., (2004), Gravity currents in aquatic canopies, *Water Resour. Res.*, 41 (12), W12402, DOI: 10.1029/2005WR004216
- Ultsch, G. (1973), The effect of water hyacinth (*Eichhornia crassipes*) on the microenvironment of aquatic communities. *Archiv. Hydrobiologia*, 72, 460-473.
- Wetzel, R. G., (2001), Light in inland water, in Limnology 3rd Ed. Academic Press, San Diego, CA.
- Zhang, X. & Nepf, H. M., (2008), Density driven exchange flow between open water and an aquatic canopy, *Water Resour. Res.*, 44 (8), W08417, doi:10.1029/2007WR006676.

Particle tracking in a gap of aquatic vegetation meadow

G. Ciraolo¹, C. Costa¹, G. B. Ferreri^{1*}, A. M. Folkard² and A. Maltese¹

¹ Dipartimento di Ingegneria Idraulica e Applicazioni Ambientali, Università degli Studi di Palermo (Department of Hydraulic Engineering and Environmental Applications, University of Palermo), Viale delle Scienze – Ed. 8, 90128 Palermo, Italy

² Catchment & Aquatic Processes, Lancaster Environment Centre, Lancaster University, United Kingdom

*Corresponding author, e-mail giofer@idra.unipa.it

ABSTRACT

Aquatic vegetation considerably affects the flow field in water bodies, with an increasing influence as the depth decreases. As a consequence, vegetation also affects the suspended particle transport. Meadows of *Posidonia oceanica* are widespread in the Mediterranean Sea in inshore sandy beds shallower than 40 m. This plant is constituted by a tuft of very thin and flexible ribbon-like leaves about 1 cm wide and up to 1.5 m long; the meadow areal density can reach 1000-1200 plants per square metre. Frequently, such vegetation meadows are not continuous but are interrupted by sandy strips. These discontinuities noticeably affect the flow field and can actually act as particle traps. In this paper, the flow field measured in past experiments is used for studying the behaviour of a gap in an artificial *Posidonia oceanica* canopy towards suspended particle transport. A simple particle tracking model assuming no-slip condition and random velocity fluctuations is adopted. A large number of single-particle tracking was performed taking into account several release elevations of particles as well as a number of settling velocities. The examination of the whole tracks allows one to recognize the particle fate as the simulation parameters vary. In spite of the model simplifying assumptions, the study gives useful indications on the behaviour of a gap towards the suspended particle transport.

KEYWORDS

Aquatic vegetation; suspended transport; particle tracking; turbulence; shallow water.

INTRODUCTION

Aquatic vegetation meadows considerably affect flow field and flow resistance with as more dramatic effects as shallower is the water column. Vegetal mantle, in fact, on the one hand considerably reduces the velocity in the lower flow layer with respect to a bare bottom, as well as, on the other hand, it interacts with the flow causing intense eddy activity near the vegetation top (Ghisalberti and Nepf, 2002; Ciraolo *et al.*, 2007; Okamoto and Nezu, 2009). The flow velocity reduction inside the canopy is caused by conversion of mean kinetic energy into turbulent kinetic energy effected by the plants (Nepf, 1999); along with the mean velocity reduction, a decrease in turbulent length scale occurs. In marine environment, the reduction of mean velocities and turbulent length scale effects the bed protection from erosion by heavy seas, tidal and currents. The conversion of mean kinetic energy into turbulent kinetic energy, moreover, dampens the total sea kinetic energy available for shore erosion.

Besides mitigating bed erosion, vegetation also reduces suspended transport through two distinct mechanisms which can occur individually or simultaneously (Purich, 1996): direct



Figure 1. *Posidonia oceanica* meadows: the left panel shows a meadow at the natural habitat of the lagoon *Stagnone di Marsala* ($12^{\circ}28'E$, $37^{\circ}52'N$, Sicily, Italy), the right panel shows a meadow discontinuity.

capture and sedimentation. The former consists in removal of suspended particles from the flow as they collide with leaves and stems being capturing by adhesion to a sticky periphyton layer (Palmer *et al.*, 2004); the latter is due to the lower velocities which cause more particles to sink while resuspension is considerably reduced (Gacia *et al.*, 1999). The importance of both the mechanisms in reducing suspended transport is documented in the technical literature (*e. g.*, Agawin and Duarte, 2002).

The sediments transported by the flow can have a nature both inorganic (sand, silt, etc.) and biological (pollens, aquatic micro-fauna, animal and vegetal fragments, etc.). The size and density of suspended particles can vary considerably and this has consequences on the fate of particles. Inorganic sediments usually have a diameter ranging between 2 and $2000\text{ }\mu\text{m}$ with a density of about $2650\text{ kg}\cdot\text{m}^{-3}$, whereas typical biological particles have a diameter between a few micrometres and some millimetres and a density between a little more than 1000 and about $1400\text{ kg}\cdot\text{m}^{-3}$ (*e. g.*, Purich, 1996).

In addition to the effects on erosion and sediment transport, aquatic vegetation meadows play an important role in biological equilibrium of marine environment, as they produce a considerable oxygen quantity as well as they are ideal habitats for breeding and growing of numerous animal species, many of which find nourishment in sediments captured by meadows.

In inshore waters of the Mediterranean Sea, up to 40 m deep, *Posidonia oceanica* (Figure 1, left panel) is widespread. This phanerogam consists of roots, a short stem (“rhizome”) and leaves. The rhizome grows in both the vertical and the horizontal directions, forming “mattes”, peculiar terrace formations constituted by a weave of many root beds filled by sediments entrapped within them. The leaves are ribbon-like and very flexible, about 1 cm wide and up to 1.5 m long; they are arranged in tufts, usually composed of six leaves with age and length decreasing from outside to inside. *Posidonia oceanica* settles on sandy beds forming vast meadows even very dense (usually from 500 up to $1000\text{-}1200\text{ plant}\cdot\text{m}^{-2}$). Frequently, *Posidonia oceanica* meadows are not continuous but vegetated areas alternate with sand strips (Figure 1, right panel). The presence of such discontinuities in the meadows noticeably affects the flow field and, consequently, the sediment transport. The effects of a *meadow discontinuity* on the sediment transport has been little studied up to now, although it is an important topic recognizing whether a discontinuity operates as a “trap” for the sediments having passed the upstream vegetated area or, on the contrary, as a “source” of suspended sediments for the flow downstream of the discontinuity.

Some experiments were carried out at the *Dipartimento di Ingegneria Idraulica e Applicazioni Ambientali* (Dept. of Hydraulic Engineering and Environmental Applications) of the University of Palermo (Italy), in a flume equipped with an artificial canopy of *Posidonia oceanica* presenting a gap. The experiments, actually, aimed at studying the flow field within

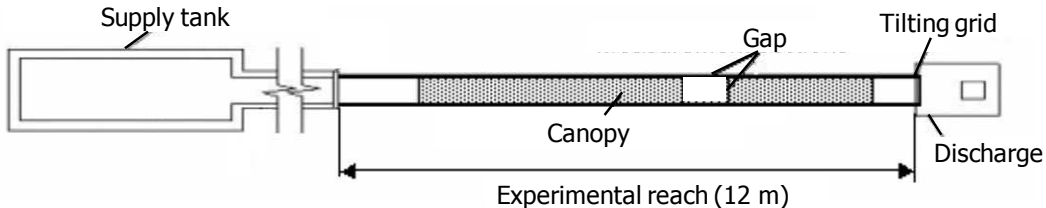


Figure 2. Experimental flume with the discontinuous canopy placed within the final 12 m reach.

the gap as well as in the upstream and downstream canopy stretches (Maltese *et al.*, 2005; Maltese *et al.*, 2007). In the present paper the experimental flow field of one of those runs is adopted as the base to simulate the tracks of single particles within the canopy gap. The aim is to examine the fate of particles as the settling velocity and the initial height of the particle vary as well as, consequently, to recognize whether the gap mainly operates as a trap or a source of sediments.

In the following sections, the experimental equipment is firstly described; then the instantaneous velocities, measured in the selected measurement points, are processed by an interpolation technique to describe more closely the whole velocity field; the model adopted for particle tracking is presented in the next section; finally, the results of the simulations as the settling velocity and the initial height of the particle vary are discussed.

EXPERIMENTAL EQUIPMENT

The experimental set up was presented in detail by Maltese *et al.* (2007), here only the essential information is given. The experiments were performed in a level laboratory flume 26.2 m long (Figure 2) having a rectangular section $77.2 \times 60.0 \text{ cm}^2$. The bottom was marble while the bearing structure was part iron and part concrete; in the final 12 m reach, used for the experiments, the walls were glass. The flume was supplied by a concrete tank which received water from two pipes, of 350 and 150 mm, each equipped with a flow-rate meter. At the flume downstream end there was a tilting grid for control of sub-critical flows.

In the final 12 m reach an artificial *Posidonia oceanica* canopy was placed, which was 9.60 m long and started 1.70 m from the reach beginning (Fig. 3, left panel). The plants were made by assembling six strips of low density polyethylene 1 cm wide and 0.2 mm thick (Fig. 3, middle panel). The outer couple of leaves was 50 cm long, the middle one 25 cm and the inner one 12.5 cm. The plants were arranged on steel-wooden panels, each 76.7 cm wide (Fig. 3, right panel). The planimetric distribution chosen for the plants produced an areal density of 1037

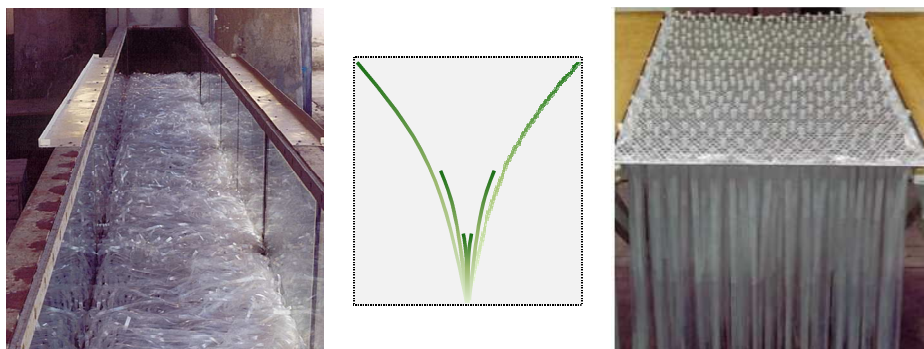


Figure 3. Artificial canopy: view of the canopy upstream of the gap (left panel), sketch of a plant, made by assembling six polyethylene strips (middle panel), and plants arranged in a pre-pierced steel plate before the latter was fixed to a wooden panel (right picture).

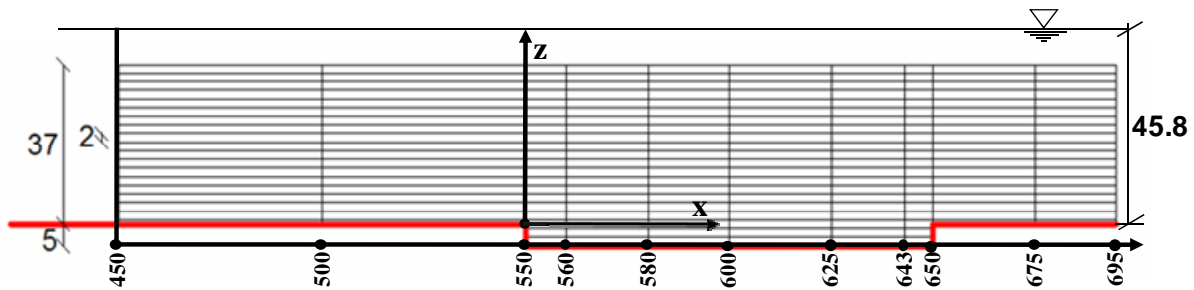


Figure 4. Sketch of the vegetated stretch between secs. 450 and 695 showing the gap (between secs. 550 and 650) as well as the gauging verticals and horizontals in the stretch.

plants·m⁻². Upstream and downstream, the vegetated bed was linked to the marble bottom of the flume by concrete slides.

Between the sections located at 550 and 650 cm from the canopy beginning no panel was set, so that a 1 m gap was realized (Figure 4); the drop between the canopy bed and the flume marble bottom was 5 cm. The drop mirrored the natural situation as in the vegetated areas the bed is higher than in the unvegetated ones because of the rhizome weave and the sediment accumulation. In Figure 4 the sections are indicated by their distance in centimetres from the canopy beginning.

The run whose measurements are used in this paper had a depth $h = 45.8$ cm, taken in a section located a little downstream of the gap, and an average velocity in the same section $U = 5.5$ cm·s⁻¹. The measurements regarded the velocities along several verticals on the flume axis, between sections 150 and 695. The verticals were chosen at steps of 50 cm between sections 150 and 550, whereas between sections 550 and 695 variable steps were adopted according to Figure 4. Along each vertical the measurement points were taken at steps of 2 cm (Figure 4). Instantaneous velocities were gauged by a down-looking 3D ultrasonic instrument of ADV type made by Nortek. Since ADV takes measurements in a sample volume located about 5 cm far from the probe, which had to be immersed below the free surface, in practice the velocities could be acquired up to 37 cm over the vegetated bed. At each point the acquisition time was ≈ 4 min with a frequency of 25 Hz. The frame reference was assumed as in Figure 4, with the x -axis being stream wise and the z -axis vertical and upward.

In order to restrict gauging problems due to leaves being in physical contact and pressing up against the probe, for taking measurements along a given vertical the probe was first placed at the lowest gauging location, after the foliage had been opened, and it was then moved upwards up to the highest location. When a time series exhibited excessive noises (which was judged subjectively from real-time plots displayed during data collection) it was discarded and the acquisition was repeated. According to Maltese *et al.* (2007), specific experiments proved that, although polyethylene moving leaves could act as scatterers of the ADV signal, reliable water velocity measurements could be obtained by filtering out data having correlation values lower than 70% and signal to noise ratio $SNR < 15\%$.

DATA PROCESSING AND FLOW FIELD CHARACTERISTICS

The instantaneous measurements of the velocity components u , v and w , respectively along x , y and z , gauged at each node were first filtered on the basis of the signal to noise ratio and of the correlation parameter, in order for the disaggregated measurements to be discarded. As the measurements were taken along the flume axis the component v was practically null. The filtered data were then used to determine the time-averaged values \underline{u} and \underline{w} , the fluctuations u' and w' , the standard deviations and the frequency distributions of u' and w' , the Reynolds stress $\underline{u'w'}$ as well as to carry out the quadrant analysis. For the sake of brevity, some results

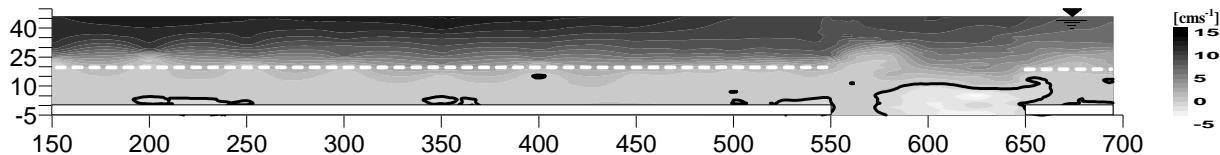


Figure 5. Representation by means of a gray scale of time-averaged velocity u [$\text{cm} \cdot \text{s}^{-1}$]; the dotted white line indicates the mean height of the inflected vegetation.

only of the turbulence analysis are reported here while more extensive analysis of the turbulence characteristics will be made in further papers.

The above point data were then interpolated in space to obtain values in the nodes of a closer grid than the gauging one, for which we chose a 2 cm x -step and a 1 cm z -step. The point data were also extrapolated up to the free surface adopting the same grid. Among the interpolation techniques we selected that based on the *Radial Basis Function* (Franke, 1982) with the *Multiquadric method*, as it is an interpolator of type “exact” having a basis kernel function analogous to variograms in Kriging, which defines an optimal set of weights to be assigned to the point data when interpolating the value at a grid node. Following a semi-variogram analysis, anisotropy was set equal to 2, while, according to Carlson and Foley (1991), the smoothing factor was chosen between the average sample spacing and one-half the average sample spacing. Figure 5 shows the distribution of the mean velocity u , whose intensity is highlighted by means of a gray scale. The horizontal bold broken line indicates the mean height of the vegetation. The bold lines contour the zones having negative u (*i. e.*, towards upstream). The picture shows that inside the vegetation considerably lower velocities occur compared to those outside the vegetation, which is consistent with results of the technical literature (*e. g.*, Nepf and Vivoni, 2000; Ciraolo *et al.*, 2006; Ciraolo *et al.*, 2008). In the first part of the gap the low-velocity zone noticeably expands but then it contracts. As the flow experiences the effects of the downstream vegetated reach and it tends to reassume the upstream velocity distribution, which occurs after section 695 reported in the figure, the low-velocity zone again expands upwards.

Figure 6 shows the velocity vector field in the gap and in its upstream and downstream neighbourhoods. In the second part of the gap a large clockwise eddy is observed, which accounts for the upwards expansion of the low-velocity zone in the first part of the gap as well as for the velocities directed upstream close to the bottom. As further consequences of the eddy, at the gap beginning the upper flow “rears up” to climb over the eddy as well as the related velocities noticeably increase compared with those of the vegetated reach. In the highest layer, however, the velocities are analogous to those in the vegetated reach.

The analysis of the distributions of the Reynolds stress and the dominant quadrants (not reported for brevity) leads to results consistent with the aforesaid ones. In particular, an increase in the Reynolds stress is observed within the gap, with a peak close to the eddy centre, as well as sweep events are dominant in most part of the gap while ejection events only in the upper part of the gap.

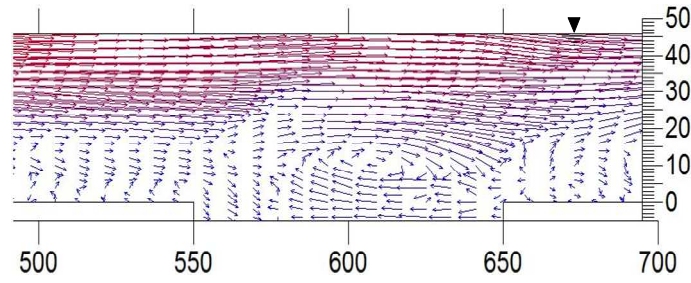


Figure 6. Velocity vector field in and around the gap.

STUDY OF THE GAP BEHAVIOUR

The interpolated flow field was used to investigate the behaviour of the gap towards the suspended sediment transport. Simulation of suspended particle transport is, in general, a very complex topic as this phenomenon depends on the flow characteristics (turbulence included) as well as on the particle characteristics (geometrical, physical, chemical, etc.) and the particle behaviour during the transport (decay, coalescence, etc.) (Shirolkar *et al.*, 1996). Particle transport and turbulence actually influence each other as the mere presence of a particle locally modifies the turbulence as well as a big particle mass load may effect global modification of the turbulence; furthermore, a large particle number density makes particle-particle interactions (such as collisions and coalescence) have to be taken into account (Berlemont *et al.*, 1998). By contrast, as the concentration of particles is very low, their influence on the global turbulence is negligible; particle-particle interactions can be ignored and the whole particle transport can be studied as the “sum” of transport of the single particles (Shirolkar *et al.*, 1996). As long as the particles are small enough, they follow the fluid motion and, in practice, no slip velocity there exists between the two phases, which, therefore, can be treated as a sole homogeneous flow with appropriately changed physical properties (Durst *et al.*, 1984).

Modelling of the particle trajectories

It is known (*e. g.*, Durst *et al.*, 1984; Shirolkar *et al.*, 1996) that suspended particle transport can be modelled following two approaches, Lagrangian and Eulerian. The Eulerian models treat the particulate phase as a *continuum* as if two fluids are present within the flow field. The concentration of the “particle fluid” in the “carrier fluid” has to be considered. The particle transport is monitored by the variations in the concentration within each fixed differential control volume as the particle fluid flows through the control volumes. No trajectories of single particles are carried out. The Lagrangian models, by contrast, treat the particulate phase as it actually is, as a *discrete* system, and each particle is tracked as it moves in the flow field. At each time, the position reached by a particle is a function of the point from where the particle originated and of the time elapsed and it accounts for particle history effects. These models highlighting the non-continuum behaviour of the particulate phase are particularly right for simulating transport of diluted particulate phases.

In the present paper aimed at recognizing the *qualitative* behaviour of the gap rather than at quantifying the sediment transport along the gap, a simple Lagrangian model was adopted. The particle concentration was assumed to be low enough so that inter-particle collisions as well as changes in the measured properties of the turbulent flow field due to the particle transport could be neglected. The particle characteristics were just globally taken into account by the settling velocity V_s , which for small particles is given by the Stokes’ law

$$V_s = \frac{1}{18} \frac{(\rho_p - \rho_w)}{\mu} g D^2 \quad (1)$$

where ρ_p is the particle density, ρ_w the water density, μ the water viscosity, g gravity acceleration and D the particle diameter. A no-slip condition was assumed for the particle motions driven by the flow field, which is acceptable for small particles with a low inertia to drag force ratio (Willgoose, 1997). In this scheme, the only cause of deviation of the trajectory of a sediment particle from that of a water particle, both originating from the same point at the same time, was the gravity force through the settling velocity V_s . The particle motion during each time step was split in three stages: the first stage was the particle advection due to the local mean flow velocity; the second one was caused by gravity; the third stage accounted for the local velocity fluctuation. The no-slip condition concerned the first

and the third stages. The velocity fluctuations u' and w' were determined randomly on the basis of their experimental statistic properties at the point reached by the particle. The coordinates at time t_{i+1} of the particle which at time t_i passed at point A were given by

$$x_{i+1} = x_{A,i} + \Delta t (u_{A,i} + M_x u'_{SD_{A,i}}) \quad (2)$$

$$z_{i+1} = z_{A,i} + \Delta t (w_{A,i} + M_z w'_{SD_{A,i}} - V_s) \quad (3)$$

were Δt is the time step between times t_i and t_{i+1} , u'_{SD} and w'_{SD} are the standard deviations of the fluctuations u' and w' respectively, M_x and M_z are random weights generated by means of the frequency distribution of the experimental velocity fluctuations; the subscript A indicates a quantity at point A and the subscript i a quantity at time t_i . Actually, at each gauging point in the gap, the frequency distributions of the normalized fluctuations u'/u'_{SD} and w'/w'_{SD} were practically coincident each other; indeed, the frequency distributions proved also to be practically *unchanged* over all the gauging points. Therefore, a *sole* mean frequency curve was adopted for u'/u'_{SD} and w'/w'_{SD} over the whole gap. This result indicates a strong correlation exists among the statistical properties of the velocity fluctuations in the points of the gap. This interesting issue will be stressed in a further paper. At each time step, two distinct random values in the range (0, 1) were generated which produced the weights M_x and M_z . A constant time step $\Delta t = 0.15$ s was assumed for all the realizations, without accounting for eddy lifetime and eddy transit time at each point reached by the particle (Shirodkar *et al.*, 1996). The model further assumed the settling velocity to be independent on the local velocity fluctuations, whereas theoretical as well as experimental studies showed that this velocity in vertically oscillating flow is actually lower as compared with that in still water (Willgoose, 1997). The model adopted is conceptually rough but it is simple to handle; however, it appears to be sufficient for a qualitative analysis of the gap behaviour.

Particle tracking and gap behaviour

Many trajectory realizations were carried out releasing particles at the first section of the gap (sec. 550). One particle only was released each time at a release height h_r varying between 1 and 40 cm from the canopy bottom, at steps of 1 cm. The settling velocity V_s was assumed equal to 0.2, 0.4, 0.6, 0.8, 1, 1.5 and 2 $\text{cm}\cdot\text{s}^{-1}$. Note that, according to the Stokes' law (Eq. 1), a higher settling velocity does not imply a higher particle density. For each couple of h_r and V_s values, 1000 realizations were carried out to account for stochastic effects on the trajectories. However, it is to be noted that no considerable deviations there occurred from a realization to another; therefore, the results of the simulations will be shown taking a "typical" realization only for fixed h_r and V_s values. Each realization went on until the particle reached the boundary of the computational domain (*i. e.*, either the upstream or downstream gap end sections or the gap bottom or the free-surface). If the particle reached the gap bottom it was considered definitively *settled* as no resuspension was considered.

Figure 7 shows, as examples, the trajectories simulated as h_r varied, for V_s fixed at 2, 1 and 0.2 $\text{cm}\cdot\text{s}^{-1}$. With the highest settling velocity $V_s = 2 \text{ cm}\cdot\text{s}^{-1}$ (Figure 7, upper panel) all the particles settle, most of them in the first third of the gap and only a few in the second half. Particles released at h_r up to 20 cm (which is about the height of the vegetation inflected) follow trajectories having a roughly constant slope, which is consistent with the low and quasi-constant flow velocities in that part of the gap (Figure 6). The particles released above 20 cm experience eddy effects and follow more or less curved trajectories. The middle panel of Figure 7 relates to the settling velocity $V_s = 1 \text{ cm}\cdot\text{s}^{-1}$. Decreasing in the settling velocity

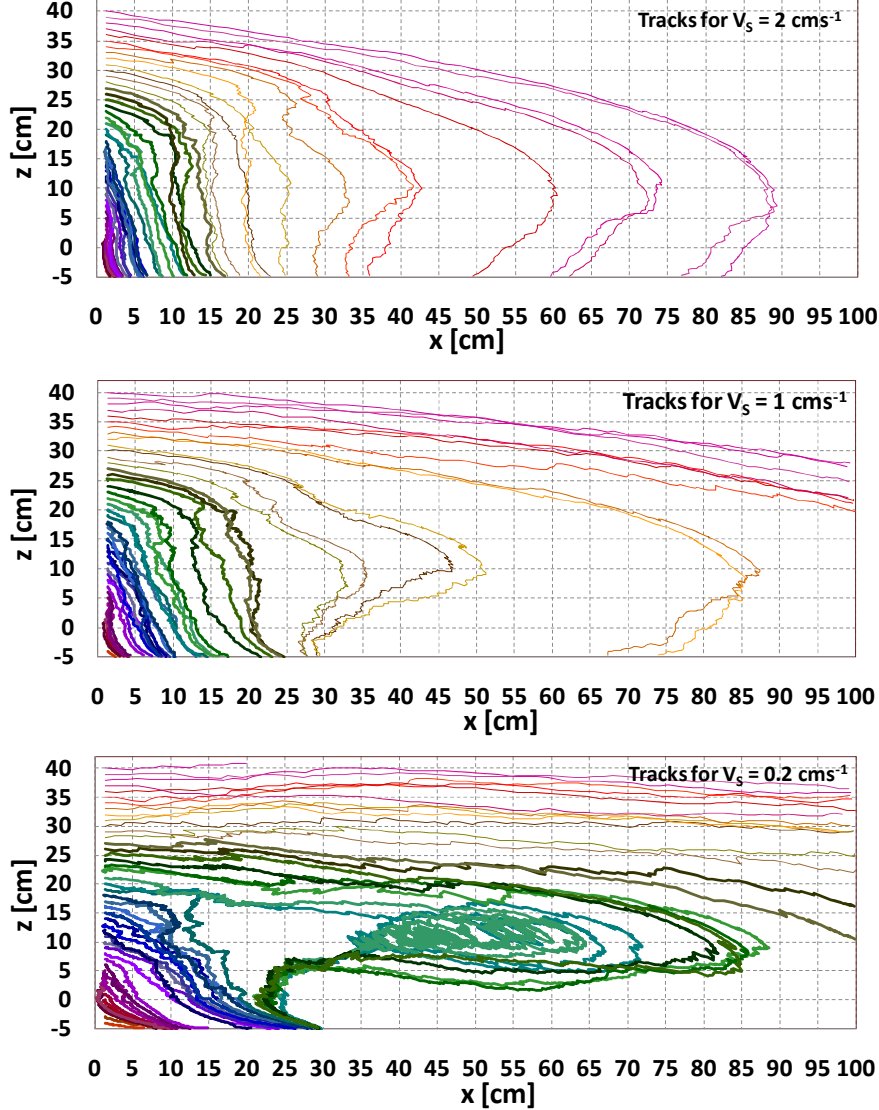


Figure 7. Typical trajectories simulated assuming the settling velocity V_s equal to $2 \text{ cm}\cdot\text{s}^{-1}$ (upper panel), $1 \text{ cm}\cdot\text{s}^{-1}$ (middle panel) and $0.2 \text{ cm}\cdot\text{s}^{-1}$ (lower panel).

allows the particles released at the higher h_r now to reach the downstream vegetated stretch. However, most of the particles settle in the gap, the most part again within the first third whereas only two in the second half. Note that, because of the random simulated turbulence, some couples of close tracks intersect several times. Further decreasing of V_s down to the minimum value considered of $0.2 \text{ cm}\cdot\text{s}^{-1}$ (Figure 7, lower panel) produces a considerable increase in the number of particles reaching the downstream vegetated stretch. Most of the particles, however, again settle in the gap and namely within the first third of the gap. The particles released up to $h_r = 18 \text{ cm}$ follow trajectories roughly rectilinear, whereas those released at $h_r = 19\text{--}25 \text{ cm}$ are entrained by the eddy, in which they remain entrapped at most for a few rounds before go out and then settle on the bottom.

In short, the numerous simulations performed showed that both the settling velocity and the release height considerably affect the particle fate. Only the lower settling velocities make it possible particles to reach the downstream vegetated stretch, but this occurs only for the higher release heights for which the particles are driven downstream by the upper flow layer, which get over the eddy and is characterized by more intense velocities than in the lower part of the flow. Particles released at median heights can be entrapped in the eddy for the lower settling velocities only but within one or a few rounds they go out and settle. Particles

released up to about the vegetation height, which move in the “vegetation shade” characterized by very low velocities, always settle following roughly rectilinear trajectories. On the whole, the realizations showed that the most frequent particle fate is settling within the gap, mainly in the first third of it. According to this result, sediment deposition has to be expected close to the end of the upstream canopy. Of course, for practical applications detailed indications are necessary on the actual distribution of the particles in the first section of the gap as well as on their characteristics, which implies targeted field investigations to be carried out.

CONCLUSIONS

The behaviour of a gap in aquatic vegetation meadow towards suspended sediment transport was examined by means of numerical simulations. The simulations were carried out on the basis of the flow field measured in past laboratory experiments in a flume with an artificial canopy of *Posidonia oceanica*. A close description of the flow field was first obtained by means of interpolation in space of the point measurements. A simple Lagrangian model was adopted for sediment transport, which assumed a so diluted particulate phase that inter-particle interactions could be neglected and no changes in the global turbulence were produced; the model also assumed a so small particle diameter that no-slip condition could be adopted. Three stages were considered for the particle motion during each time step, respectively accounting for advection, gravity and turbulence. The turbulent fluctuations were determined randomly on the basis of their experimental statistical properties. The particle characteristics were globally accounted for by means of the settling velocity. Many particle tracking realizations were carried out releasing single particles at the first section of the gap for several values of the release height and the settling velocity.

The whole realizations showed that only particles having the lower settling velocities and released at the higher heights reached the downstream vegetated stretch. Most of the particles, by contrast, settled in the gap, usually in the first third of it. As these particles were released at heights below the vegetation top they settled following roughly rectilinear trajectories; when released above the vegetation top, the particles experienced the effects of the big eddy which formed in the gap and followed noticeably curvilinear trajectories.

In conclusion, despite the conceptual approximations the model adopted allowed us to have some useful indications for understanding the gap operates as a *sediment trap*. Of course this knowledge has to be integrated with field results concerning the actual distribution along the vertical as well as the physical characteristics of particles in marine environment.

Next steps should concern model improvement in order for dynamics of particle to be accounted for (elimination of *no-slip* hypothesis) and more appropriate turbulent fluctuations to be given at each time step which, although being random, should exhibit satisfactory coherence both in time and in space as particle goes along its trajectory. Generation of coherent fluctuations by appropriate processing of no-synchronized point measurements is a prominent topic for particle tracking.

ACKNOWLEDGMENTS

The authors of the present paper contributed equally to this work, and their names appear in alphabetical order. The writers wish to thank Dr. Giovanni Lombardo and Dr. Eleanor Cox for their dedication and systematic work in setting up the experimental equipment and carrying out the measures as well as for making the measurements available for the present paper.

REFERENCES

- Agawin, N. S. R. and Duarte, C. M. (2002). Evidence of direct particle trapping by a tropical seagrass meadow. *Estuaries*, 25(6A), 1205-1209.
- Berlemont, A., Chang, Z. and Gouesbet, G. (1998). Particle Lagrangian tracking with hydrodynamic interactions and collisions. *Flow, Turbulence and Combustion*, 60, 1-18.
- Carlson, R. E., and Foley, T. A. (1991). The parameter R^2 in multiquadric interpolation. *Computers and Mathematics with Applications*, 21(9), 29-42.
- Ciraolo, G., Ferreri, G. B. and La Loggia, G. (2006). Flow resistance of *Posidonia oceanica* in shallow water. *Journal of Hydraulic Research*, 44(2), 189-202.
- Ciraolo, G., Ferreri, G. B. and La Loggia, G. (2007). Flow resistance of a very dense *Posidonia oceanica* grassland in shallow water. *Proc. of the 5th International Symposium on Environmental Hydraulics – ISEH V*, Tempe, Arizona (U.S.A.), Dec. 4-7, 1-6, CD-ROM.
- Ciraolo, G., Ferreri, G. B. and La Loggia, G. (2008). Influence of *Posidonia oceanica* meadow density on flow resistance in shallow waters. *Proc. of the 2nd International Symposium on Shallow Flows*, Hong Kong, China, Dec. 8-12, 1-6, CD-ROM.
- Durst, F., Milojevic, D. and Schönung, B. (1984). Eulerian and Lagrangian predictions of particulate two-phase flows: a numerical study. *Applied Mathematical Modelling*, 8, 101-115.
- Franke, R. (1982). Scattered data interpolation: test of some methods. *Mathematics of Computations*, 33(157), 181-200.
- Gacia, E., Granata, T. C. and Duarte, C. M. (1999). An approach to measurement of particle flux and sediment retention within seagrass (*Posidonia oceanica*) meadows. *Aquatic Botany*, 65(1-4), 255-268.
- Ghisalberti, M. and Nepf, H. M. (2002). Mixing layers and coherent structures in vegetated aquatic flows. *Journal of Geophysical Research*, 107(C2), 1-11.
- Maltese, A., Folkard, A. M., Ciraolo, G., Cox, E. and Ferreri, G. B. (2005). On the influence of flexible vegetation on flow fields in shallow water: a flume experiment. *Proc. of the 9th Workshop on Physical Processes in Natural Waters*, Lancaster, United Kingdom, Sep. 4-6, 195-202.
- Maltese, A., Cox, E., Folkard, A. M., Ciraolo, G., Lombardo, G. and La Loggia, G. (2007). Laboratory measurements of flow and turbulence in discontinuous distributions of ligulate seagrass, ASCE, *Journal of Hydraulic Engineering*, 133(7), 750-760.
- Nepf H. M. (1999). Drag, turbulence, and diffusion in flow through emergent vegetation. *Journal of Water Resources Research*, 35(2), 479-489.
- Nepf H. M. and Vivoni E. R. (2000). Flow structure in depth-limited, vegetated flow. *Journal of Geophysical Research*, 105(C12), 28,547-28,557.
- Okamoto, T. and Nezu, I. (2009). Turbulence structure and “Monami” phenomena in flexible vegetated open-channel flows. *Journal of Hydraulic Research*, 47(6), 798-810.
- Purich A. (2006). The capture of suspended particles by aquatic vegetation. Environmental Engineering Project Dissertation, School of Environmental Systems Engineering, The University of Western Australia.
- Palmer, M. P., Nepf, H. N. and Petterson, T. J. R. (2004). Observations of particle capture on a cylindrical collector: Implications for particle accumulation and removal in aquatic systems”. *Limnology and Oceanography*, 49(1), 76-85.
- Shirokar, J. S., Coimbra, C. F. M. and McQuay, M.Q. (1996). Fundamental Aspects of Modeling Turbulent Particle Dispersion in Dilute Flows. *Progress in Energy and Combustion Science*, 22, 363-399.
- Willgoose, G. (1997). A hydrodynamic particle tracking algorithm for simulating settling of sediment. *Mathematics and Computers in Simulation*, 43, 343-349.

Hydrodynamics of heterogeneous mussel beds: Laboratory flume experiments

A.M. Folkard^{1*}, J. Gascoigne², T. Bouma³, D. McGovern¹

¹ Lancaster Environment Centre, Lancaster University, Lancaster LA1 4YQ, UK.

² School of Ocean Sciences, Bangor University, Menai Bridge, Anglesey, LL59 5AB, UK.

³ Netherlands Institute of Ecology (NIOO-KNAW), Centre for Estuarine and Marine Ecology,
Korringaweg 7, 4401 NT Yerseke, The Netherlands.

*Corresponding author, e-mail a.folkard@lancaster.ac.uk

ABSTRACT

Whilst the interaction of hydrodynamics with homogeneous communities of benthic organisms is becoming well understood, the hydrodynamics of the fragmented structures that many such communities exhibit remains little known. Of specific interest here are beds of common mussels (*Mytilus edulis*), which often exhibit distinctive spatial patterning. Ecological theories have been forwarded to explain this, but hydrodynamics may also play an important role, and the interactions of flows with patterned mussel beds have not been studied in detail. Moreover, complex patterns of mussel beds create an interesting hydrodynamic modelling problem, in that their spatial scale is typically much smaller than model grid sizes, raising the question of how best to parameterize their roughness.

In an effort to address some of these issues, we performed two laboratory flume experiments. In both, we considered 1-dimensional patterns: the mussel beds extended uniformly across the whole flume, but were discontinuous along-stream. In the first experiment, relatively short ($\leq 1\text{m}$) patches were used. Flow profiles were measured at locations across a single patch at five flow speeds, and at the centres of patches and gaps in multiple-patch runs. Results are compared to previous work on flow over bed roughness transitions, and demonstrate complex feedbacks between the mussel beds and the flow, which may have significant influence on the mussels' food supply.

In the second experiment, longer mussel beds were used and we focussed our measurements on their wakes. The results indicate that, for longer mussel beds, upstream flow and bed structures become irrelevant downstream, as the mussel beds "reset" the flow. Secondly, although the flow readjusts to an apparently equilibrium state shortly downstream of the mussel bed, the turbulence in the downstream profiles is significantly enhanced compared to the upstream flow conditions, far beyond the re-adjustment zone.

KEYWORDS

Common mussel (*Mytilus edulis*); spatial patterning; hydrodynamics; laboratory flume experiments; one-dimensional patterns, patches & gaps.

INTRODUCTION

This study is concerned with blue mussels (*Mytilus edulis*), benthic organisms which feed on suspended particulate matter in the water column. They are found in inter-tidal zones, on hard and soft substrates. On the latter, they may occur naturally or be commercially sown and farmed. In both cases, they typically form extensive beds, individuals attaching to each other and to the substrate via byssal threads. Soft-substrate mussel beds often organise themselves into patches or stripes at multiple scales from $\sim 10^{-1}$ to $\sim 10^2$ metres (e.g. Gascoigne et al. 2005). Attempts to explain this patterning have drawn hitherto almost exclusively on ecological theory, via analogies with other patterned ecosystems, notably semi-arid and peatland vegetation. They are theorised to be due to scale-dependent feedback mechanisms (Rietkerk et al. 2004), i.e. a combination of short-range facilitation – neighbouring organisms' mutual protection from stresses – and long range competition for limited food resources. In mussel beds, both of these are linked to hydrodynamics. The primary stress experienced by mussels is drag which may remove them from the bed, and food is supplied by horizontal advection and vertical turbulent diffusion. Thus the spatial patterning is a response to the hydrodynamics, and conversely, the patterning determines the hydrodynamics by setting the bed roughness conditions. The configuration of the mussel bed-hydrodynamics complex is thus an emergent form arising out of these non-linear interactions. Consequently, the functioning and resilience of soft-substrate mussel beds cannot be understood until these interactions are.

Previous work on the hydrodynamics of mussel beds has concentrated on homogeneous conditions (e.g., van Duren et al. 2006), and on the hydrodynamic effects of exhalant jets, which mussels emit vertically during feeding (e.g. Jonsson et al. 2005; Crimaldi et al. 2007). In contrast, to elucidate the bio-hydrodynamic interactions of patchy mussel beds, the present work investigated the evolution of mean flow and turbulence across and downstream of single mussel patches and arrangements of multiple mussel patches, under different flow velocities.

The key issue here is how the flow responds to mussel-patch edges and recovers downstream of them. At these edges, both the bed roughness and the bed height change as we move from the bare substrate to the raised mussel beds whose roughness elements are the mussels' shells. Hence, we can draw on understanding developed in the literature of both flow over bed roughness transitions (e.g. Chen & Chiew 2003; Chamorro & Porté-Agel 2009) and classical work on boundary roughness patterns (Morris 1955) to inform the interpretation of our results.

The experiments had the following objectives:

- To determine the evolution of mean flow and turbulence over and downstream of mussel patches, and how this evolution varies as a function of flow speed
- To determine how varying the spatial pattern of mussel beds affects their hydrodynamics

The first experiment focussed on flow over a single mussel patch and within arrangements of patches, whilst the second experiment focused on measurements of wakes downstream of mussel patches. A more detailed presentation of the first experiment is given by Folkard & Gascoigne (in press), and the results of the second experiments will be presented in more detail by Folkard et al. (in prep.). We re-present some of the results of each experiment here to allow a synthesising discussion of their findings.

METHODS

Experiment 1

Our first experiment was performed in a rectilinear, flat-bottomed flume 11m long, 0.30m wide and 0.40m high, which the flow filled to a depth of 0.27 ± 0.0025 m. Mussel patches were simulated by placing dead mussel shells, at a density of $\approx 800 \text{ m}^{-2}$, in a self-hardening resinous substrate from which they extended 2-3cm. The combination of substrate and shells extended ~4cm above the bed of the flume. Dead mussels were used because the flume operated only with fresh water, precluding the use of live ones.

The mussel patches were secured onto the bed of the flume, starting 5.5m from its upstream end. Three mussel patch configurations were used (Figure 1). The first, a single, 1-metre long patch, was tested under five mean incident flow speeds ($U_0 = 4.8, 8.9, 12.1, 18.4$ and 23.1 cms^{-1}). The second comprised two 0.80m patches separated by a 0.60m gap. The third comprised four 0.40m patches separated by three 0.20m gaps. Thus, the second and third cases occupied the same total length (2.20m) and contained the same total length of mussels (1.60m). A single flow speed – 18.4 cms^{-1} – was used in these two cases. Using the first configuration, we studied both the effects of varying flow speed, and how the flow changes across a patch. The second and third configurations were used in combination to study the effects of changing the spatial distribution of the mussel bed.

Vertical profiles of 3D flow data were measured with two Nortek Acoustic Doppler Velocimeters (ADVs), which were tested under identical conditions at the start of each experiment to ensure that they gave consistent measurements. Each profile consisted of points 2cm apart from 1-15cm above the bed. Data was recorded at each point for 90s at 25Hz.

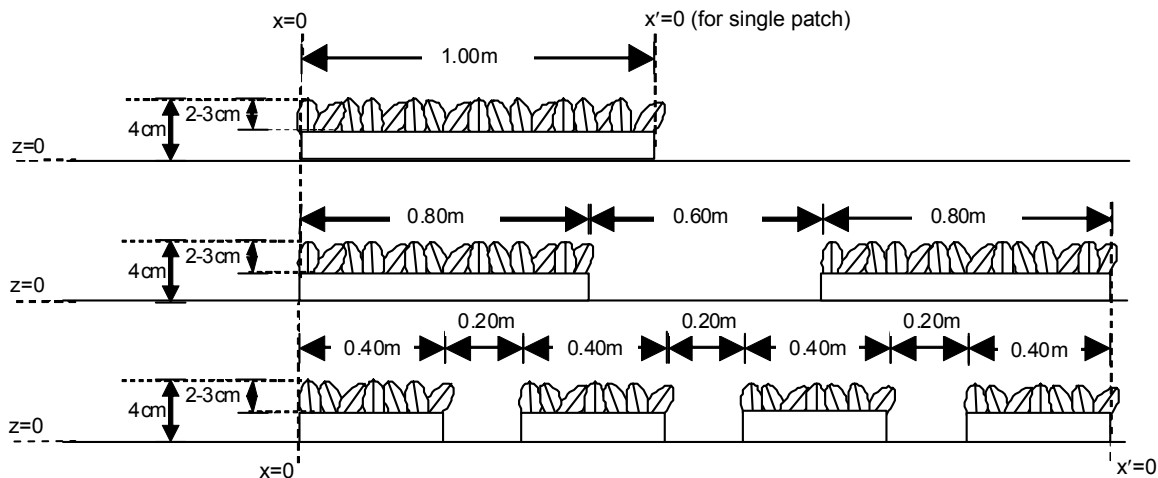


Figure 1. Schematic diagrams of the three mussel patch configurations tested in Experiment 1

Experiment 2

Our second experiment was performed in a race track flume with a test section 10.8m long and a rectilinear cross-section 0.60m wide, filled with water to a depth of 0.35 ± 0.001 m. This flume was able to operate with salt water, so the mussels were live, and actively feeding and exhaling jets of filtered water during the experiment. They were placed on plastic boards 1m long, 1cm thick, equal in width to the flume, and secured to its bed, and allowed to arrange and secure themselves. Their density – $860 \pm 40 \text{ m}^{-2}$ – was such that they completely covered

the boards, and in places sat on top of each other. Thus, although the individual mussels' longest axes were measured as 5.49 ± 0.69 cm (mean \pm 1S.D., $N = 100$), the mussel beds extended on average ≈ 9 cm above the flume bed.

Eight mussel patch configurations were used (Figure 2), as well as a control run with no mussels in the flume. Four consisted of two 1-metre long mussel patches separated by a gap of varying length, three of longer, continuous patches and one of a single 1-metre long patch, with double the mussel density ($1720 \pm 80 \text{ m}^{-2}$) of all the other cases. A single flow speed – 21.1 cms^{-1} – was used throughout. Vertical profiles of 3D flow data were measured with a Nortek Vectrino. Each profile consisted of points at 5, 20, 35, 50, 65, 80, 100, 125, 150, 200, 250 and 300 mm above the flume bed. Data was recorded at each height for 120 s at 25 Hz.

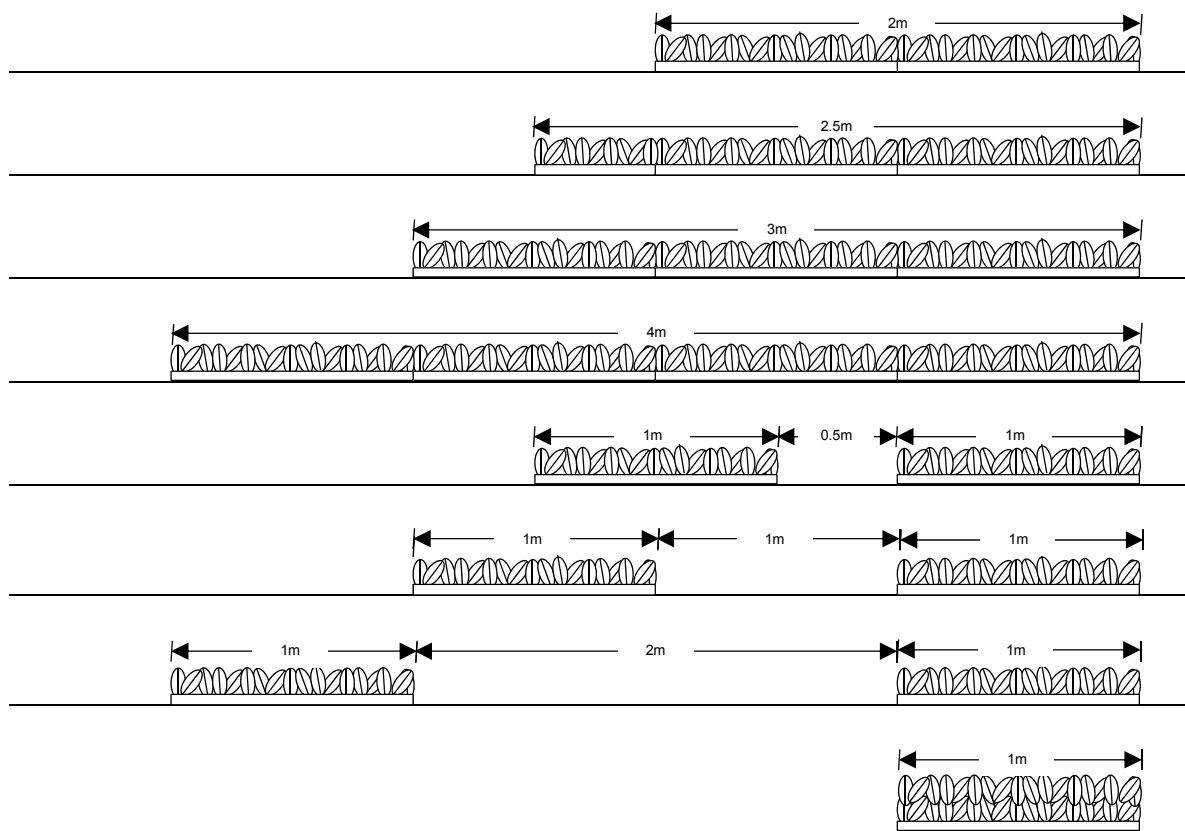


Figure 2. Schematic diagrams of the eight mussel patch configurations tested in Experiment 2

Data processing and analysis

In both experiments, similar data checking, processing and analyses were performed. Upstream flow profiles at multiple positions confirmed that the flow incident on the mussel patches had a semi-logarithmic boundary layer profile and was both approximately uniform (<5% difference between velocity measurements at each height between profiles) and unidirectional (transverse and vertical flow speeds respectively ~2% and ~3% of the average downstream flow speed). Standard procedures for noise and bad data removal were performed following Voulgaris and Trowbridge (1998). Uncertainties in the turbulence data were calculated by determining the effective sampling rate – see Folkard & Gascoigne (in press) for details. This gave uncertainties of 2–3% and 15–16% in the mean flow and turbulence parameters respectively.

We analysed the hydrodynamics using a number of relevant variables. We quantified downstream advection, which may provide horizontal fluxes of food, via vertical (z -) profiles of the mean downstream velocity component U at given along-channel positions x (locations of $x=0$ and $z=0$ shown in Figure 2). Vertical mixing, which may provide vertical fluxes of food, is caused by turbulence, which we quantified in terms of the turbulent kinetic energy (TKE) per unit volume k , and the downstream-vertical Reynolds shear stress component $-\bar{u'w'}$. The hydro-mechanical stresses on the mussels were quantified in terms of bed shear stress, as the shear velocity u^* and the roughness length z_0 . These were calculated using the classical von Karman-Prandtl semi-logarithmic boundary layer equation.

RESULTS

Experiment 1

Single patch configuration. Figure 3 shows the evolution of the depth-integrated TKE k_I , profile maximum Reynolds shear stress component $-\bar{u'w'}_{max}$, u^* and z_0 across the single patch used in the first configuration when $U_0=18.4 \text{ cms}^{-1}$. The most notable changes in k_I are at the patch edges, where it increases significantly, suggesting that these are the primary sites of turbulent energy generation. There is a similar increase at the upstream edge in $-\bar{u'w'}_{max}$, though unlike k_I , it decreases in the patch centre, and there is no clear jump at the downstream edge. The shear velocity u^* also increases sharply at the upstream edge, but not at the downstream edge, and z_0 behaves similarly.

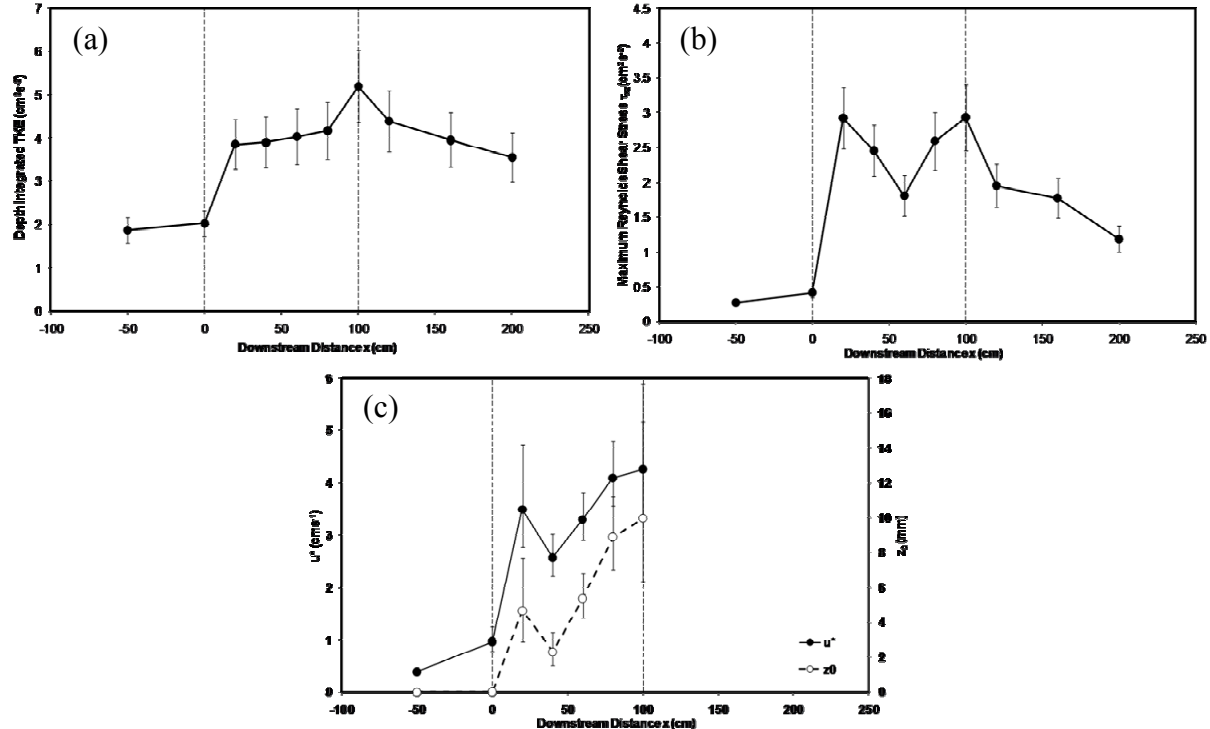


Figure 3. Variation of (a) k_I , the depth-integrated TKE (b) $-\bar{u'w'}_{max}$, the maximum Reynolds shear stress component; and (c) shear velocity u^* and roughness length z_0 along the single patch configuration in Experiment 1 when $U_0 = 18.4 \text{ cms}^{-1}$ case. Dotted lines show the positions of the patch edges.

Two- and four-patch configurations. Figure 4a shows profiles of U at the centre of each patch, and the centre of the gap between the patches in the 2-patch configuration. Although the gap-centre profile has an internal boundary layer, the patch-centre profiles are very similar, suggesting that the velocity profile is able to adjust fully to the changing bed conditions over the length scales used here, at this flow speed. Figure 4b shows profiles of U at the centre of each patch and each gap in the 4-patch configuration. Although internal boundary layers are still evident in the gap profiles, the picture is more confused than the 2-patch case. This suggests that the flow is unable to adjust fully after the previous patch-gap change when it encounters the next one in this configuration, at this flow speed. The overall effect of this difference between the configurations on U downstream of the mussel patches is shown in Figure 4c. Despite having passed over the same total amount of mussels in the same space, the flow in the 4-patch case is slower below $\ln(z) \approx 4$ ($z \approx 55\text{mm}$) than in the 2-patch case. This implies that the increase in patch-gap boundaries reduces the mean flow energy. Furthermore, k is more concentrated near the bed in the 4-patch case: $\approx 70\%$ of k_l in the 4-patch case is in the bottom 5cm of the profile, compared with $\approx 55\%$ for the 2-patch case. This is consistent with our theory that, in the 4-patch case, major turbulence generation events at the bed occur more often, and thus there are fewer opportunities between these for the turbulence to diffuse vertically.

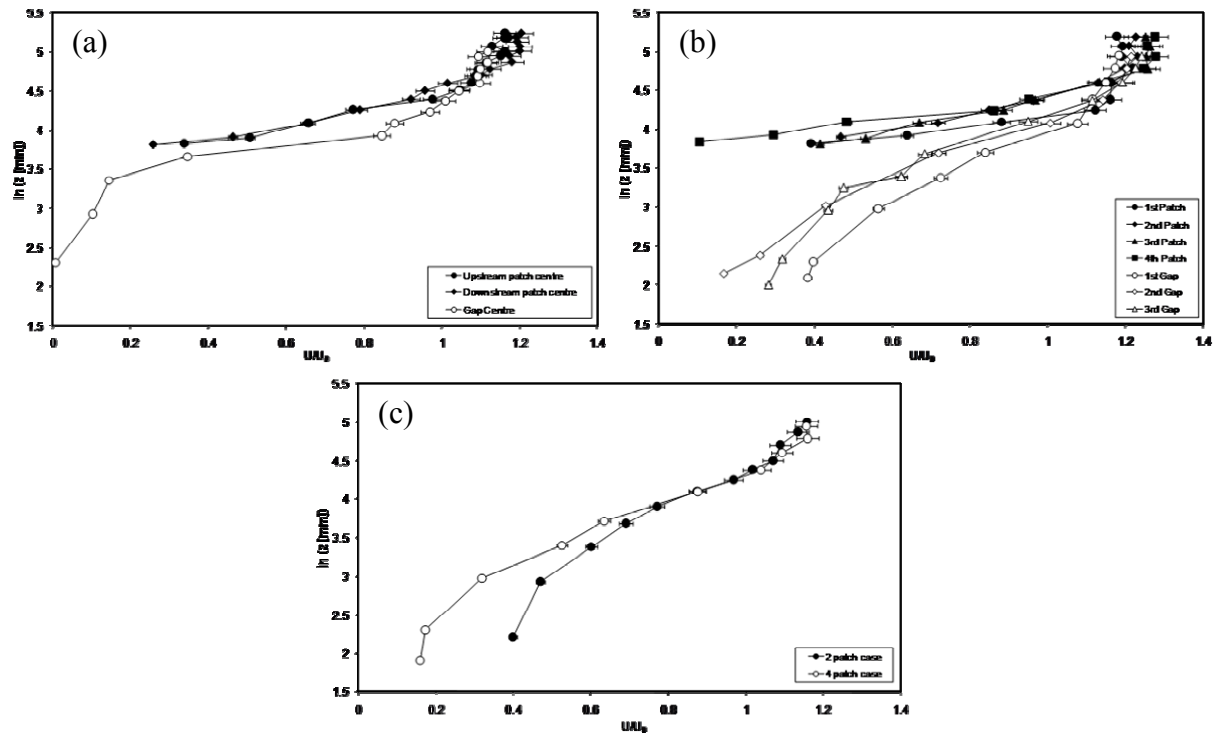


Figure 4. Mean downstream velocity profiles (a) over the centres of patches and gap in the 2-patch case; (b) over the centres of patches and gaps in the 4-patch case; and (c) downstream of the 2-patch and 4-patch configurations

Experiment 2

Figure 5a and b show, respectively, (semi-logarithmic) flow profiles at $x=0$ and the mean of profiles between $x=3\text{m}$ and $x=5\text{m}$, where x is defined, for this experiment, as the distance downstream of the mussel patches. These profiles have three layers: the uppermost, freestream region, where flow is independent of depth, the boundary layer formed by the

flow's passage over the mussels, and the internal boundary layer, formed as the flow adjusts back to the smooth flume bed. At $x=0$ (Figure 5a) there is little difference between profiles from the first seven configurations in Figure 2. The only distinctive profile is that from the "double-density" configuration, which has a more sheared boundary layer and slower flow in the lower part of the profile – evidently due to the increased drag of the double density of mussels. Further downstream (Figure 5b), this distinction has largely disappeared, and all the profiles have converged close to that from the control run.

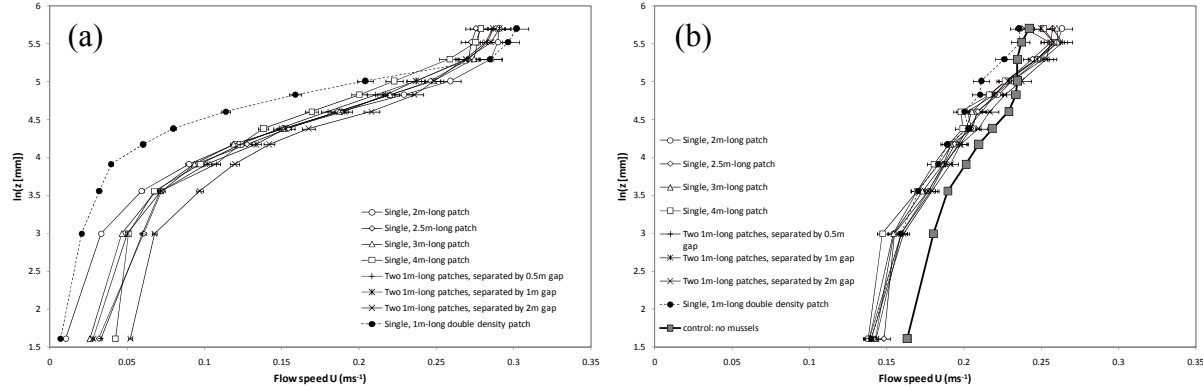


Figure 5. Vertical profiles of U for the eight configurations used in Experiment 2 (a) immediately downstream of the mussel beds; and (b) far downstream (see text for details).

Figure 6 shows the downstream evolution of flow profile parameters. In all three plots, the first seven configurations are essentially indistinguishable, while the double-density configuration case is anomalous at $x=0$ but becomes coincident with the others before $x=5m$. The most striking aspect of these plots is that, whereas u^* and z_0 (Figures 6a and b) converge approximately to their control run values, k_l remains significantly higher and, given the flatness of the data beyond $x\approx 3m$, appears to remain so further downstream still. Thus, although the flow profile has returned to its upstream form, it retains a memory of passing over the mussels in the form of enhanced turbulence levels.

DISCUSSION

The results demonstrate the influence of small-scale patchiness of mussel beds on hydrodynamics, and provide reasons why more patches, and thus edges, are beneficial for mussels: they enhance turbulence, aiding diffusion of food down the water column. The increased near-bed TKE may also increase food supply from benthic sources. The key role of patch-gap edges is apparent in Figure 3. We hypothesise that this is due to the rapid adjustment imposed on the flow at these points. We propose a mechanism whereby, at upstream patch edges, acceleration of the freestream flow (to adjust for the partial blockage of the mussel bed), and deceleration of the near bed flow (due to the mussels' drag) lead to a sudden increase in shear and turbulence generation. As the flow moves downstream, this is ameliorated by vertical turbulent transfer of momentum. At downstream patch edges, we hypothesise that sudden acceleration of the near bed flow due to relaxation of the rough bed conditions leads to enhanced turbulence generation.

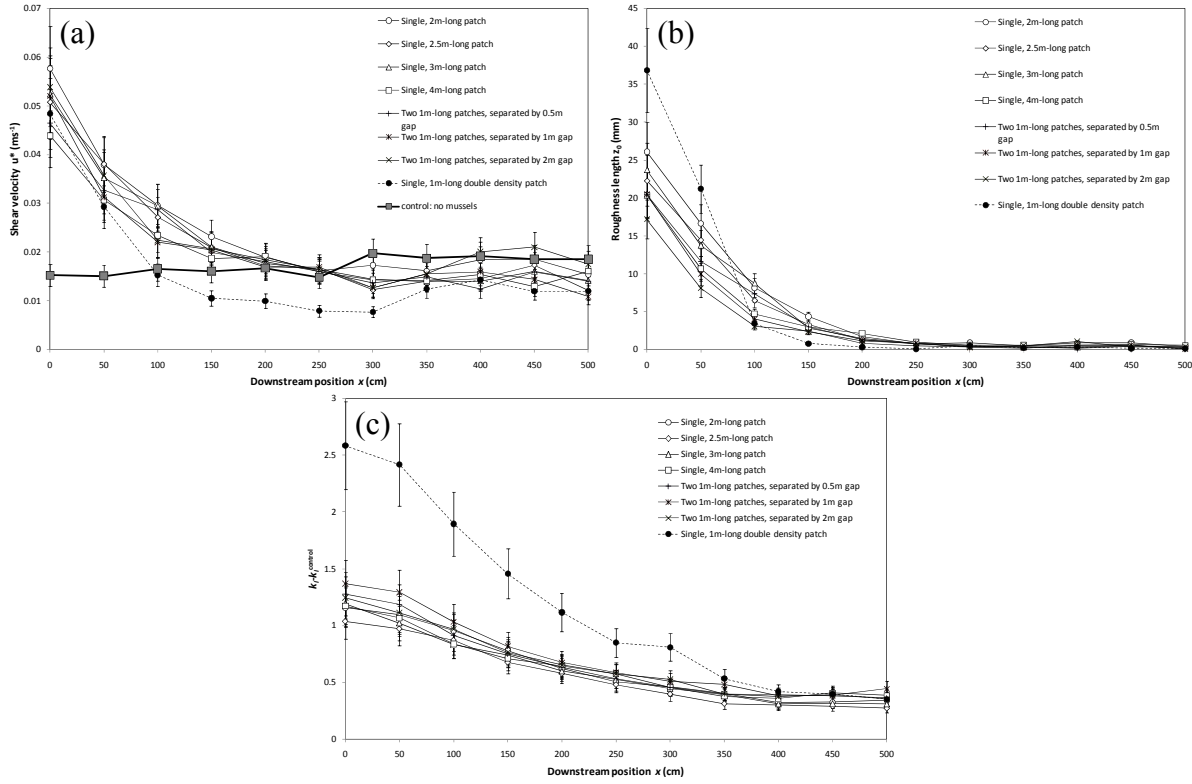


Figure 6. Downstream development of (a) shear velocity u^* (control run values also shown); (b) roughness length z_0 (control run values not shown, since they were $<1\text{mm}$); and (c) turbulent kinetic energy k_t (normalised by subtracting the corresponding turbulent kinetic energy levels from the control run, $k_t^{control}$).

These phenomena are known as “overshooting” and are well documented (e.g. Chen & Chiew 2003). However, Chen & Chiew (2003) did not observe them in open channel flow experiments where the change in roughness was accompanied by only a small change in bed height ($\approx 0.3\text{cm}$). They suggested that this was because of readjustments of the water surface height which were able to compensate for changes in bed roughness. Indeed, the extensive research on the adjustment of velocity profiles over roughness transitions (see Chamorro & Porte-Agel (2009) for a brief but lucid summary) has tended to ignore the coincidence of changes in bed height and roughness. Such a combination occurs in the present experiments, and the outcome is very different from Chen & Chiew’s experiments. This implies that the effect on hydrodynamics of simultaneous changes in bed height and roughness, which are common in many environmental flows, need to be more closely studied.

The strong generation of turbulence at patch edges has important implications for mussel feeding. Concentration boundary layers, where near-bed chlorophyll is depleted above suspension-feeding communities, are much-reported (e.g. Jonsson et al. 2005; Crimaldi et al. 2007; Riisgard et al. 2007), although they tend to be restricted to slow flow conditions. Multiple patch edges would give multiple boosts to turbulence levels and thus rates of chlorophyll diffusion down the water column. Thus, this may be an important benefit to mussels in patchy distributions. This adds to the conclusion of van de Koppel et al. (2005), that gaps in mussel beds enable replenishment of near-bed chlorophyll due to continued (we argue, enhanced) vertical supply in the temporary absence of losses due to mussel feeding.

Others (L. van Duren, pers. comm.) have noted reductions in Reynolds shear stresses in the centre of mussel patches, as is suggested in the present work (Figure 3b). Poor growth rates and die-off of mussels near patch centres have also been observed in the field (Okamura 1986, Gascoigne, pers. obs.) and since $-\bar{u'w'}$ may be taken to represent vertical turbulent fluxes, these two observations may be linked: reduced turbulent fluxes at patch centres exacerbates chlorophyll depletion there, reducing mussel growth and survival.

The results of the 2-patch and 4-patch runs, notably their different downstream flow profiles (Figure 4c) and the observation of enhanced near-bed turbulence levels in the latter, illustrate the manifestation of the patch-edge turbulence generation phenomenon identified in the single patch runs. The flow regime in these environments can be categorised following Morris (1955) and predicted using thresholds proposed by Oke (1988). In both the 2- and 4-patch runs, the height to width (H/W) ratio of the gaps lie in the “isolated roughness flow” regime ($H/W < 0.3$), as opposed to the wake interference flow regime ($0.3 < H/W < 0.7$) and the skimming flow regime ($H/W > 0.7$). Skimming flow, in which there is little advection of fluid within gaps, has been widely studied at the organism scale for benthic filter feeders since Nowell & Church (1979), but there has been much less consideration of flow regime at patch scale. Changes in patch-scale flow regimes may imply significant changes in deposition, flushing and supply of particulates, so this is a topic which merits further research.

In contrast to Experiment 1, where different mussel bed configurations produced different downstream flow profiles (Figure 4c), the results from Experiment 2 showed essentially identical outcomes for different mussel distributions (Figure 5a). The only anomalous profile in Experiment 2 was for the “double-density” configuration (the bottom sketch in Figure 2). The reason for this similarity appears to be that, in Experiment 2, the final mussel patch is always $\geq 1\text{m}$ long, so the flow adjusts fully to this, and any “memory” of upstream patterning is erased from the flow profile. However, although all the profiles in Experiment 2 become essentially identical to the control case after 2–3m, the turbulent kinetic energy remains enhanced significantly further downstream. Since local shear stresses are the same as in the control case, (because the flow profiles are the same) local turbulence production cannot explain this difference. Hence, we theorise that advection of turbulence generated by the mussels continues beyond the point where the flow has adjusted back to equilibrium with the flume bed. Thus, within the flow profile, although memory of upstream mussel distributions is erased by one-metre lengths of mussel bed, memory of having passed over mussel beds persists for $> 5\text{m}$ in the form of enhanced turbulent kinetic energy.

CONCLUSIONS

Results have been reported of two laboratory flume experiments, in which flow profiles over and downstream of a range of mussel distributions have been studied. Our findings are that:

- Mussel patch edges are important sites of turbulence generation. We theorize that this is due to the overshooting phenomenon, exacerbated here by the coincidence of transitions in bed roughness and height
- Hence, patch edges boost turbulent energy, which may benefit mussels by increasing diffusion rates of their food down the water column
- We observed reductions in Reynolds shear stresses at the centre of a mussel patch only 1m long, and suggest that this may be linked to field observations of poor mussel growth at patch centres
- We argue that flow regimes (*sensu* Morris, 1955 and Oke, 1988) at patch scale may strongly affect benthic filter feeder communities, and that this requires further research

- Finally, we found that “memory” of upstream mussel distributions in flow profiles is erased by one-metre long mussel patches, but memory of having passed over mussel beds may persist for >5m downstream in the form of enhanced turbulent kinetic energy

ACKNOWLEDGEMENTS

We are grateful for funding to Lancaster University Geography Department, for technical support to the technical staff of the School of Ocean Sciences, Bangor University and NIOO-CEME, and to John Simpson and Phil Wiles for loan of the ADVs and help with set-up.

REFERENCES

- Chamorro, L.P., Porté-Agel, F., 2009. Velocity and surface shear stress distributions behind rough-to-smooth surface transition: a simple new model. *Boundary-Layer Meteorology* **130**: 29-41.
- Chen, X., Chiew, Y-M., 2003. Response of velocity and turbulence to sudden change of bed roughness in open-channel flow. *Journal of Hydraulic Engineering* **129** (1): 35-43.
- Crimald, J.P., Koseff, J.R., Monismith, S.G., 2007. Structure of mass and momentum fields over a model aggregation of benthic filter feeders. *Biogeosciences* **4**: 269-282.
- Folkard, A.M., and Gascoigne, J.C., (in press). Hydrodynamics of discontinuous mussel beds: laboratory flume simulations. *Journal of Sea Research*.
- Gascoigne, J.C., Beadman, H.A., Saurel, C., Kaiser, M.J., 2005. Density dependence, spatial scale and patterning in sessile biota. *Oecologia* **145**: 371-381.
- Jonsson, P.R., Petersen, J.K., Karlsson, O., Loo, L-O., Nilsson, S., 2005. Particle depletion above experimental bivalve beds: in situ measurements and numerical modeling of bivalve filtration in the boundary layer. *Limnology and Oceanography* **50** (6): 1989-1998.
- Morris, H.M., 1955. A new concept of flow in rough conduits. *Transactions of the American Society of Civil Engineers* **120**: 373-398.
- Nowell, A.R.M., Church, M., 1979. Turbulent flow in a depth-limited boundary layer. *Journal of Geophysical Research* **84**: 4816-4824.
- Okamura, B., 1986. Group living and the effects of spatial position in aggregations of *Mytilus edulis*. *Oecologia*. **69**: 341-347.
- Oke, T.R., 1988. Street design and urban canopy layer climate. *Energy and Buildings* **11**: 103-113.
- Rietkerk M, Dekker S.C., de Ruiter P.C., van de Koppel J., 2004. Self-organised patchiness and catastrophic shifts in ecosystems. *Science* **305**: 1926-1929.
- Riisgard, H.U., Lassen, J., Kortegaard, M., Møller, L.F., Friedrichs, M., Jensen, M.H., Larsen, P.S., 2007. Interplay between filter-feeding zoobenthos and hydrodynamics in the shallow Odense Fjord (Denmark) - earlier and recent studies, perspectives and modeling. *Estuarine, Coastal and Shelf Science* **75**: 281-295.
- van de Koppel, J., Rietkerk, M., Dankers, N., Herman, P.M.J., 2005. Scale-dependent feedback and regular spatial patterns in young mussel beds. *The American Naturalist* **165** (3): E66-E77.
- van Duren, L.A., Herman, P.M.J., Sandee, A.J.J., Heip, C.H.R., 2006. Effects of mussel filtering activity on boundary layer structure. *Journal of Sea Research* **55**: 3-14.
- Voulgaris, G., Trowbridge, J.H., 1998. Evaluation of the Acoustic Doppler Velocimeter (ADV) for turbulence measurements. *Journal of Atmospheric and Oceanic Technology* **15**: 272-289.

Partial-depth exchange flow between canopy and open water

M. Jamali* and S. Marvi

Department of Civil Engineering, Sharif University of Technology, Teheran, Iran

*Corresponding author, e-mail jamali@sharif.edu

ABSTRACT

Emergent vegetations in littoral zones block light, and as a result a density flow forms between the canopy and open area. This exchange flow is limited by the depth of light penetration in the open water. A partial-depth lock exchange model is used to study the problem theoretically and experimentally. The interface profile is almost linear in the canopy area and wavy in the open area. The flow rate and the interface height at the junction and their dependency on a dimensionless drag parameter and light penetration depth are investigated. In general the flow rate is lower for thicker vegetation and smaller depth of light penetration. It is also shown that the flow rate can be predicted from the interface height at the junction.

KEYWORDS

Exchange flow, vegetation, light penetration, numerical model, laboratory model.

INTRODUCTION

Wetlands and aquatic systems are abundant on the earth. Since many biological and chemical processes take place in aquatic regions, an understanding of hydrodynamics of flow in these areas is essential. Exchange flows or gravity currents driven by horizontal density gradients constitute a significant transfer mechanism in many lentic systems and play an important role in chemical characteristics of aquatic regions. Light blockage by emergent vegetations, which is a common feature of littoral zones, leads to a horizontal density gradient. This results in an exchange flow between the vegetated and the open area (Jamali et al., 2008).

Lock exchange models have been widely used to study the gravity currents in both laboratory and numerical experiments, e.g., see Shin (2004). Tanino et al (2005) studied gravity currents in uniform canopies using a laboratory lock-exchange model. The interface had an almost linear shape, and the flow regime changed from inertial to drag-dominated as the experiment proceeded. Jamali et al. (2008) investigated numerically and experimentally the lock exchange flow driven by temperature difference between canopy and uniformly-heated open water. They showed that the flow is characterized by a dimensionless drag parameter, and the flow rate can be obtained directly from the flow depth at a control point close to the junction of the open water and canopy.

In reality, turbidity limits the depth of light penetration. In this study, we consider the problem of lock-exchange flow between canopy and partially-heated open water modeled as a two-layer fluid. The objective is to study the effects of vegetation drag and light penetration depth on the flow. The numerical and experimental results are discussed and compared.

NUMERICAL MODEL

We use partial-depth lock exchange flow as a simple model to study the exchange flow between a homogenous canopy and partially-heated open water. The open water is modeled as a two-layer fluid. Emergent vegetation is considered as an array of randomly-distributed circular cylinders having diameter d . The porosity n represents the volume fraction occupied by water and is given by $1 - \frac{\pi}{4}ad$, where a is frontal area of the cylinders per unit volume.

A two dimensional coordinate system $x^* - z^*$ is used, see figure 1, with the origin located at the junction of the two areas. The general fluid density is denoted by ρ^* . The initial densities of the canopy fluid and the lower layer of the open water are ρ_1 . The density of upper layer in the open area is represented by ρ_2 . Both fluids are assumed to be incompressible and viscous with kinematic viscosity of ν . h_w^* is the dimensional light penetration depth, and H^* is the total water depth. The interface height above the bed is denoted by η^* . Time is denoted by t^* and velocity vector by $\vec{V}^* = (u^*, w^*)$.

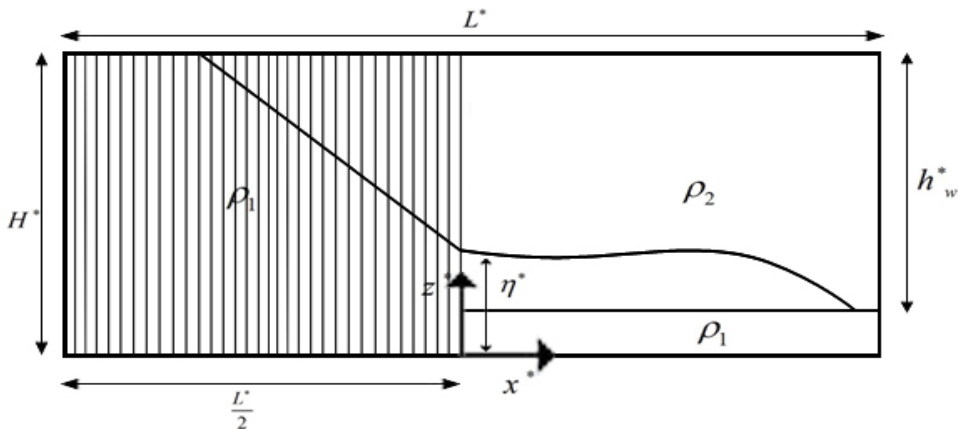


Figure 1. Schematic illustration of partial depth lock exchange flow in a half canopy.

Normalization of the equations is done using H^* as the characteristic length scale and N^{-1} as the characteristic time scale, where $N = \sqrt{g'/H^*}$ and $g' = g(\rho_1 - \rho_2)/\rho_1$ is the reduced gravitational acceleration. As a result, $U = NH^*$ becomes the characteristic velocity scale. Physical variables are normalized as follows:

$$(x, z) = (x^*/H^*, z^*/H^*), (u, w) = (u^*/U, w^*/U), t = t^*N \quad (1)$$

$$h_w = h_w^*/H^*, \eta = \eta^*/H^*, \gamma = (\rho^* - \rho_1)/(\rho_1 - \rho_2)$$

The dimensionless form of a parameter having an asterisk is shown with the asterisk dropped. (x, z) and t are dimensionless independent variables while γ and η are dependent variables.

In the normalized form, the governing equations are:

$$\frac{\partial \gamma}{\partial t} + u \frac{\partial \gamma}{\partial x} + w \frac{\partial \gamma}{\partial z} = 0 \quad (2)$$

$$\frac{D\zeta}{Dt} = \frac{\partial \gamma}{\partial x} - \frac{1}{2} \bar{C} \left(\frac{\partial(Vu)}{\partial x} - \frac{\partial(Vw)}{\partial x} \right) + Re^{-1} \nabla^2 \zeta \quad (3)$$

Equation (2) describes incompressibility and (3) is the vorticity equation, which is obtained from combining momentum and continuity equations using Boussinesq approximation. In (3), $\zeta = \nabla^2 \psi = \partial u / \partial z - \partial w / \partial x$ is vorticity where ψ is a stream function, $\nabla^2 = \partial^2 / \partial x^2 + \partial^2 / \partial z^2$, and $\text{Re} = UH / \nu$. $\bar{C} = C_D aH / n$ is the dimensionless drag coefficient with C_D being drag coefficient. For canopies with very high porosity we can use the empirical relation $C_D = 1 + 10 \text{Re}_d^{-2/3}$ for $1 \leq \text{Re}_d \leq 10^5$ for an isolated circular cylinder (white, 1991, p. 183). In this equation $\text{Re}_d = V^* d / \nu$ is the cylinder Reynolds number. However, in most real canopies and for those considered here, this equation underestimates the drag coefficient. Using some calibration tests, Jamali et al (2008) found that the equation $C_D = 1 + 50 \text{Re}_d^{-2/3}$ gives satisfactory results. We use the latter here.

The governing equations are subject to the initial conditions $\zeta = \psi = 0$ everywhere, $\gamma = 0$ for light fluid, and $\gamma = -1$ for heavy fluid. The boundary conditions are $\psi = u = 0$ at the bed, and $\psi = \zeta = 0$ at $z = 1$ and the side-walls. The equations of motion are solved using a finite-difference technique. The details are given in Jamali et al. (2008).

Figures 2 compares the numerical results with the experimental data for experiment F; the experiments are discussed in the next section. It is seen that the numerical predictions for the toe positions and the interface shape match well the measurements at two different instances. Hence, we use the equation $C_D = 1 + 50 \text{Re}_d^{-2/3}$ for the simulations to follow.

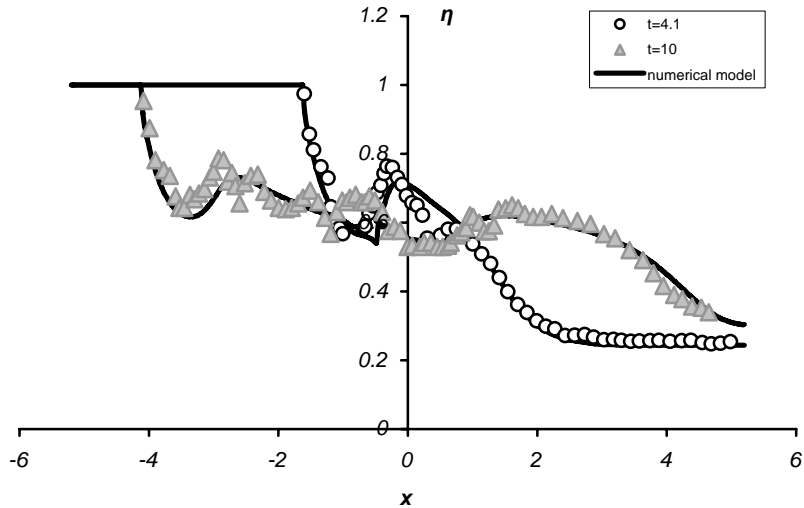


Figure 2. Comparison of the experimental measurements and the numerical predictions for the interface profile in experiment F ($h_w = 0.75$, $\bar{C} = 0.45$).

Re , n , \bar{C} and h_w are the dimensionless constants of the problem. Since the drag force in a canopy usually dominates the viscous force, there is only a weak dependency on Reynolds number Re . According to Kadlec (1990) and Kalff (2002), the observed range for ad in natural canopies is 0.01 to 0.1 and thus n is very close to unity. We ignore the effects of n

and Re on the flow, and so the flow is characterized by h_w and \bar{C} . Later, we present a parametric analysis of the problem based on these two parameters.

EXPERIMENTS

Experiments were conducted in a flume 200 cm long, 20 cm wide, and 35 cm high. The flume was separated into two reservoirs by placing a removable gate in the middle. In order to model the canopy area, white circular cylinders were randomly distributed on a perforated Plexiglas sheet at the bottom of one of the reservoirs. Each cylinder was 6mm thick and 33cm high. The canopy reservoir was filled with dyed salt water to model the cold heavy fluid. The adjacent reservoir was first filled with fresh water up to height h_w^* and then the dyed salt water of the same density as of the canopy water was slowly injected underneath the fresh water. We used a digital camera to record the flow development. By analyzing the results, the interface profile, the flow rate, and the toe velocities in both canopy and open areas were calculated.

Table 1 lists two of the experiments. In the table, \bar{C} is an average value for the canopy region, and C_D was calculated from the equation $C_D = 1 + 50 \text{Re}_d^{-2/3}$ with fluid velocity taken to be $\approx 0.5\sqrt{g'H}$ in calculation of Re_d . Note that in general velocity varies throughout the domain, so does C_D . In numerical simulations of the experiments C_D was calculated locally.

Table 1. List of experiments.

Run	$H(\text{cm})$	h_w	$g'(\text{cm/s}^2)$	ad	n	C_D	\bar{C}
F	19.2	0.75	6.6	0.007	0.994	2.00	0.45
K	16.0	0.5	7.3	0.007	0.994	0.95	0.19

DISCUSSION

In full-depth exchange flow, the interface is nearly linear in the canopy area and resembles the classic gravity current profile (nearly horizontal) in the open area (Jamali et al., 2008). However, here the flow in the open area is characterized by a large propagating internal wave. This is seen in figure 3 which shows development of flow in experiment K with $\bar{C} \approx 0.194$. In the moments following the removal of the gate, flow is dominated by inertia in the whole domain and the force balance is between inertia and buoyancy (gravity). However, the flow regime in the canopy area changes to drag-dominated as the flow velocity increases and the force balance shifts to between drag and buoyancy. At $t=12.2$ a nearly linear interface is seen in the canopy area, while in the open area a large internal wave is observed.

Jamali et al. (2008) showed that in the fully-heated open-water case, there is a control point in the open area very close to its junction with the canopy where the flow depth in the lower layer is minimum, and the internal Froude number is unity. A similar point exists in the partial-depth case; however it differs from the full-depth case in the sense that the corresponding internal Froude number is not unity here. In a full-depth case, the flow velocity u at the control point is equal to the velocity $c = \sqrt{\eta_0(1-\eta_0)}$ of the long internal wave. Hence, the flow rate at the control point can be calculated from $q_0 = u\eta_0 = \sqrt{\eta_0^3(1-\eta_0)}$ where η_0 is the corresponding lower layer depth (Jamali et al., 2008). Figure 4a presents the time variation

of the flow rate at the control point when $h_w = 1.0$ and $\bar{C} = 5.2$. The good agreement between the numerical model and the formula supports the hypothesis of existence of control point for the full-depth case. However, in the partial-depth case should be taken in deriving the relation between the flow rate and the flow depth as the internal Froude number is not unity anymore. Instead the flow velocity can be calculated assuming that the flow field in the open area corresponds to internal wave motion. Using a linear wave theory, one may show the fluid velocity under the internal wave is given by $u = \frac{(\eta_0 - 1 + h_w)}{\eta_0} c$.

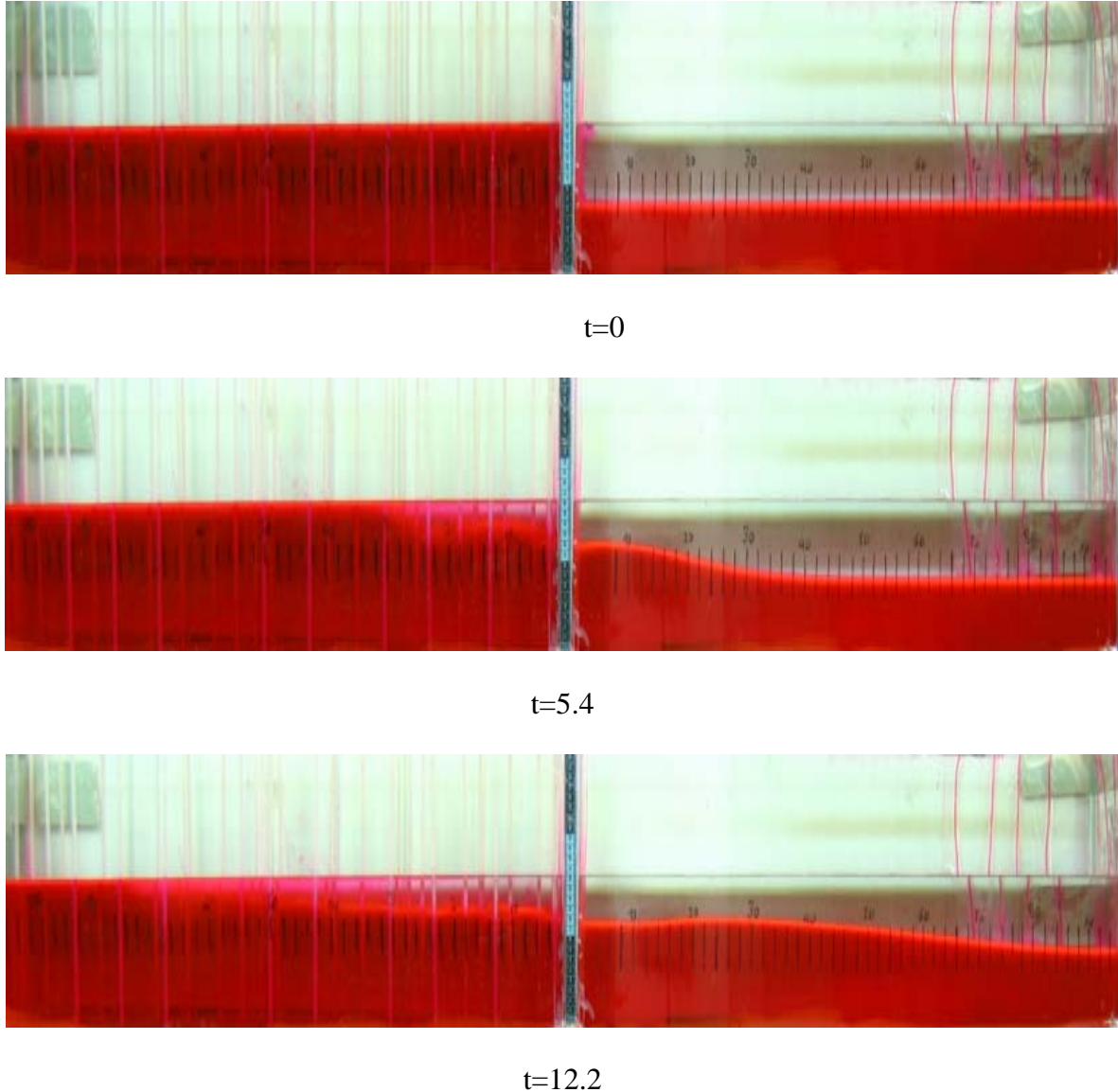


Figure 3. Development of flow in experiment K ($h_w = 0.5$, $\bar{C} = 0.194$)

As a result, the flow rate $q_0 = u\eta_0$ at the junction (control point) is given by

$$q_0 = (\eta_0 - 1 + h_w) \sqrt{\eta_0(1 - \eta_0)} \quad (4)$$

The calculated flow rates from (4) are compared with the numerical results in figure 5b for $h_w = 0.25, 0.5, 0.75$ when $\bar{C} = 5.2$. A good agreement between the numerical model and the formula is observed.

The above hypothesis is also supported by the experiments. We can obtain the flow rate in the experiments by measuring the volume of exchanged fluid in short time intervals. Figures 5 presents the calculated time variations of the flow rate and the interface height at the control point in experiment K. Comparing the results with those from equation 4 supports the existence of the control point.

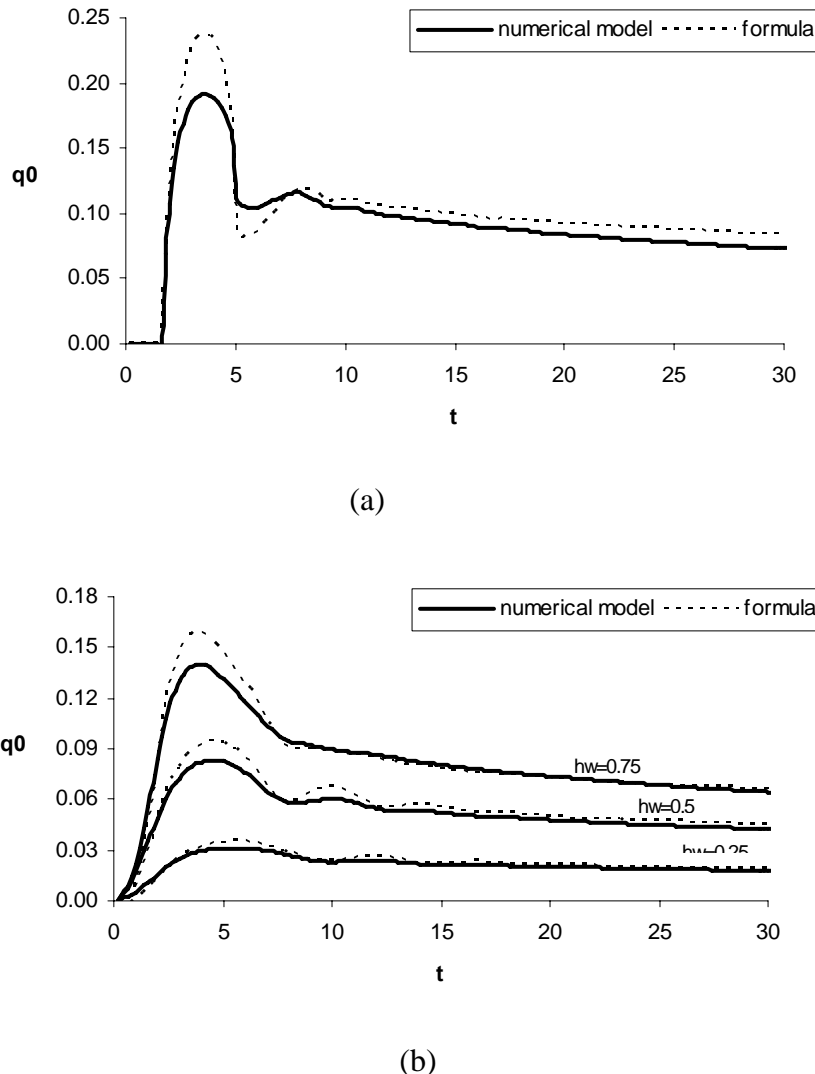


Figure 4. Comparison of the flow rate at control point derived from the numerical model (solid line) and the theoretical formula (dotted line) for $\bar{C} = 5.2$ and a) $h_w = 1$ and b) $h_w = 0.25, 0.5$, and 0.75 .

For each experiment, the toe velocity in the open area, $V_{toe,o}$, is estimated by the crest displacement of the wave in two consecutive images divided by the time difference. By measuring the height of the wave, η_w , we can estimate the speed of the wave from

$c = \sqrt{\eta_w(1-\eta_w)}$. Figure 6 compares the instantaneous velocity of the wave from the equation with the mean velocity from analyzing the images in experiments F. The good agreement between the results suggests that the front moves at the speed of long internal wave.

As stated earlier, the drag parameter \bar{C} is one of the two characteristic parameters of the problem. Here we evaluate the dependency of flow properties on it. Figures 7a-b illustrate the temporal variations of the flow rate and the interface height at the control point for different drag parameters when $h_w = 0.5$. It is seen that, as expected, the flow becomes slower and the interface height gets lower as vegetation drag increases. The peaks in figures 7a and b mark the end of inertia-dominated regime and the start of transition to a drag-dominated flow. For canopies with high vegetation drag, say when $\bar{C} \gg 1$, a drop in the flow rate at the start of the transition period is observed. This can be attributed to the rapid increase in retarding effect of vegetation drag, which is proportional to the square of velocity. The interface height follows almost the same trend. For the case $\bar{C} = 0.05$, since drag is very low, the drop in the flow rate is not observed. For very sparse canopies, the flow is inertia-dominated for a long period. According to figure 7, the sudden drop in the flow rate and interface height for $\bar{C} = 52.4$ takes place sooner than for $\bar{C} = 5.2$. This is because for canopies with higher vegetation density, the inertia regime is shorter and the drag dominates the flow sooner.

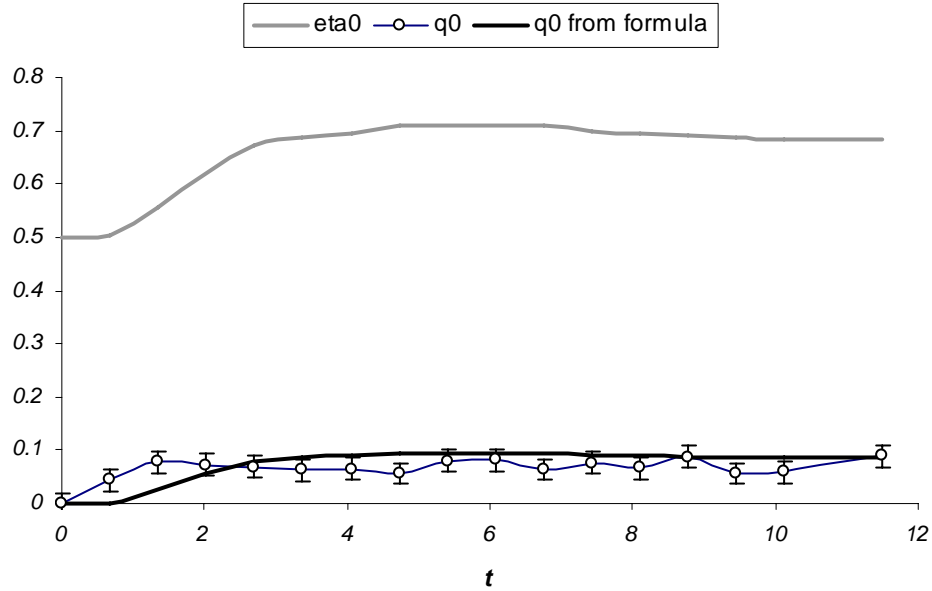


Figure 5. Comparison of the experimental results for the flow rate with that from the equation $q_0 = (\eta_0 - 1 + h_w) \sqrt{\eta_0(1-\eta_0)}$ for experiment K ($h_w = 0.5, \bar{C} = 0.194$)

Using the numerical model we can derive empirical equation for q_0 and η_0 at the quasi-steady state as a function of the drag parameter and light penetration depth. For this purpose, the flow rate at the control point at $t = 18$ is plotted as a function of \bar{C} for different light penetration depths in figure 11. At $t = 18$, the flow has passed the initial stage and is almost at a quasi-steady state. In general, the flow rate decreases with \bar{C} but increases with h_w as discussed before. Using a regression analysis, power curves are fitted to the data points with

$\bar{C} > 1$ in figure 8. The data for smaller drag parameter is excluded from the regression analysis as the flow is not drag-dominated for $\bar{C} \ll 1$, see figure 7. For $\bar{C} > 1$, from regression the flow rate at control point as a function of h_w and \bar{C} may be obtained from

$$q_0 = (0.1508h_w - 0.0021)\bar{C}^{(-0.0626h_w - 0.2468)} \quad (5)$$

For $h_w = 1$ the exponent of the drag parameter is -0.3, which is the same as obtained by Jamali et al. (2008).

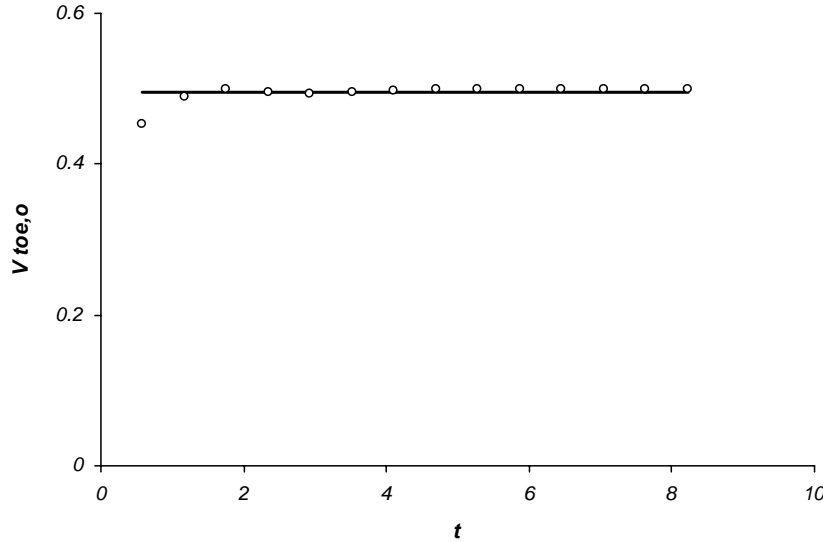


Figure 6. The instantaneous velocity of the wave (in the open area) from the equation $c = \sqrt{\eta_w(1-\eta_w)}$ using the measured wave height η_w (circles) in experiments F ($h_w = 0.75$, $\bar{C} = 0.45$) and comparison with the mean velocity (solid line) from the image analysis of the crest displacement.

In the same manner, using the numerical model, the interface heights at the control point at $t = 18$ for different h_w and \bar{C} are plotted in figure 9. The interface height decreases as h_w and \bar{C} increase. Equation of the best curve fit to the numerical data is:

$$\eta_0 = (-0.7137h_w + 1.0122)\bar{C}^{(-0.2122h_w + 0.0485)} \quad (6)$$

for $\bar{C} > 1$. For $h_w = 1$, \bar{C} has the exponent of -0.16, which is comparable to $-0.18 \pm 9\%$ as obtained by Jamali et al. (2008). The above equations may be used for estimates of the flow in a real situation. A glance at figures 8 and 9 shows that in general the change in the light penetration depth than the drag parameter has a more profound effect on the flow properties.

CONCLUDING REMARKS

The exchange flow due to a thermal density gradient between open and vegetated area was theoretically and experimentally studied. The partially-heated open area was modeled as a two layer fluid. The light penetration depth and drag parameter are the two important parameters that characterize the flow. The flow rate and the interface height at the junction of the two

areas are smaller for a greater drag parameter. On the other hand, for a deeper light penetration, the flow rate is higher but the interface height is lower.

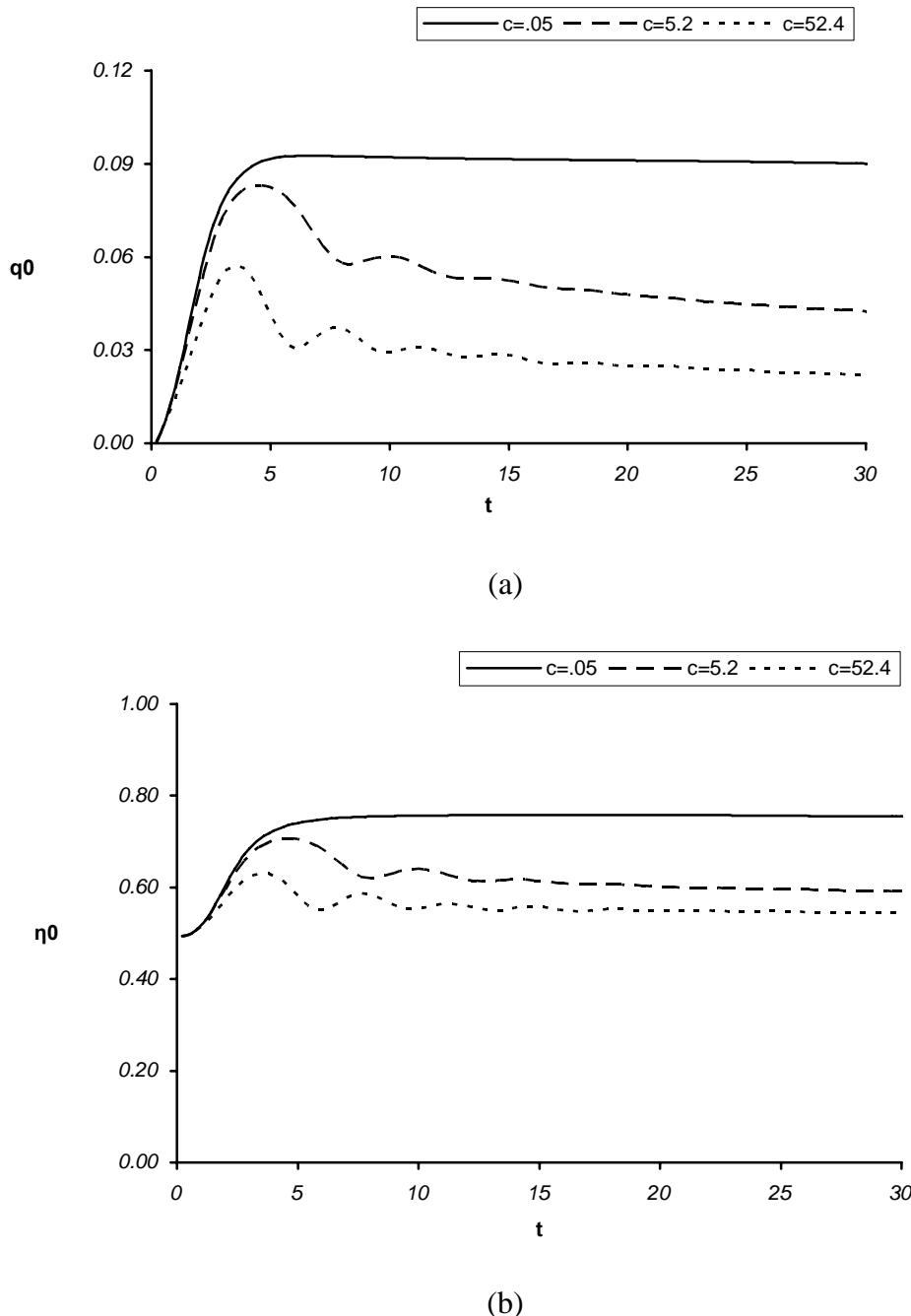


Figure 7. Time variations of a) flow rate at control point, and b) interface height at control point for different drag parameters when $h_w = 0.5$.

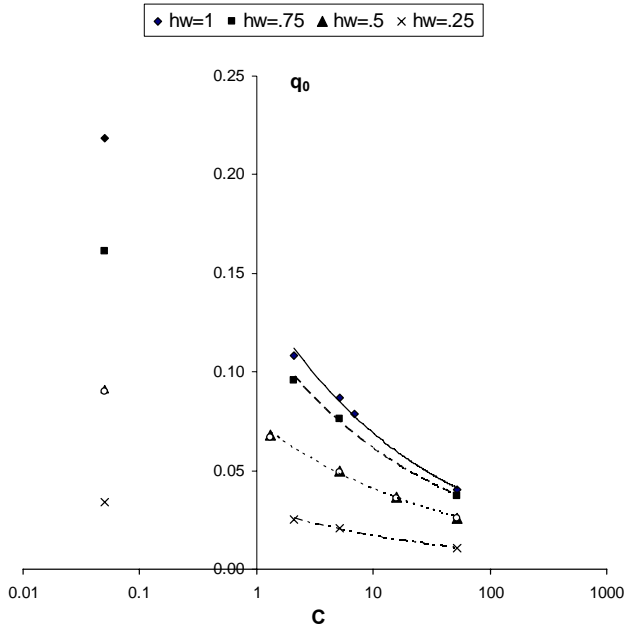


Figure 8. Variation of the flow rate with \bar{C} for different values of h_w .

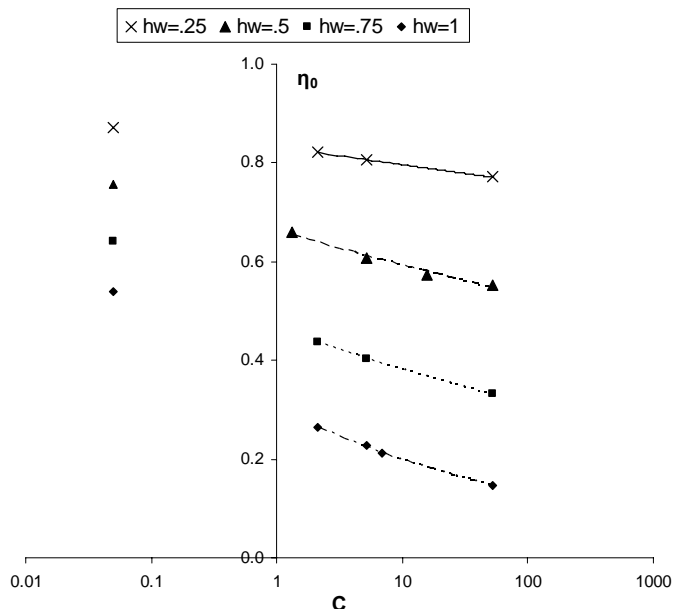


Figure 9. Variation of the interface height at the junction with \bar{C} for different values of h_w .

REFERENCES

- Jamali, M. , Zhang, X. & Nepf, H. (2008), "Exchange flow between canopy and open water". *Journal of Fluid Mechanics* **611**, 237-254.
- Kadlec, R.H. (1990), "Overland flow in wetlands: Vegetation resistance". *J. Hydraulic Engineering* **116**, p 691.
- Kalff, J. (2002), *Limnology: inland water ecosystems*. Prentice-Hall, Upper Saddle River, NJ.
- Shin, J.O., Dalziel, S.B. & Linden, P.F. (2004), "Gravity currents produced by lock exchange". *J. Fluid Mechanics* **521**, p 1.
- Tanino, Y. (2003), *Aquatic Gravity Currents through Emergent Vegetation*. Department of Civil and Environmental Engineering, M.S. Thesis, Massachusetts Institute of Technology.
- Tanino, Y., Nepf, H. M., and Kulis P.S. (2005), "Gravity currents in aquatic canopies". *Water Resour. Res.* **41** W12402, doi:10.1029/2005WR004216.
- White, F. M. (1991), *Viscous Fluid Flow*, 2nd ed., McGraw-Hill, New York.

Wind- and tide-induced currents in the Stagnone Lagoon (Sicily)

G. Ciraolo, M. De Marchis*, C. Nasello and E. Napoli

Department of Hydraulic Engineering and Environmental Applications, University of Palermo, viale delle Scienze 90128, Palermo, IT

**Corresponding author, e-mail demarchis@idra.unipa.it*

ABSTRACT

The Stagnone is a coastal lagoon located in a natural reserve of about 2200 ha characterized by: shallow water (the mean depth is about 95 cm), two openings connecting the lagoon with the open sea, the northern and the southern mouths, presence of islands within the lagoon, presence of a submerged road connecting the Mothia Island with the coast and submerged seagrasses. In this paper, the results of numerical simulations of the hydrodynamic fields in the Stagnone lagoon are compared with experimental measurements of velocities and water levels, carried out in several points using an electromagnetic velocimeter (2D) and two ultrasound ADV sensor (3D). The comparison shows the ability of the code to capture the hydrodynamic behaviour of shallow water coastal lagoons. The simulations are performed using a three-dimensional non-hydrostatic numerical model based on the finite-volume method to discretize the Reynolds-averaged momentum and mass balance differential equations. The numerical model, which is second-order accurate both in time and space, employs the k- ϵ model to represent the turbulent Reynolds stresses. In order to analyse the wind and of the tide effects of on the hydrodynamic flow field two set of simulations were performed: 1) the analysis of the contribution of the wind stress acting on the water surface and 2) the tidal motion, dominated by semi-diurnal components with supplementary contributions of the diurnal one. These simulations reveal that the tidal forces dominate in the North-South direction, whereas wind plays a fundamental role in the East-West water currents.

KEYWORDS

Coastal lagoon; tidal hydrodynamics; shallow water; seiche; wind-driven flow.

INTRODUCTION

Several researches, focused on the understanding of the physical processes that affect the hydrodynamic in coastal lagoons, have been conducted during the last decades. Despite the extensive studies, a number of issues are still open and require further efforts (D'Alpos and Defina, 2007). Several elements are, in fact, responsible of the flow hydrodynamic, among others the bathymetry, the tidal oscillations, the wind field or the aquatic vegetation distribution. A number of experimental observations (see Alpar and Yuce, 1996 and literature therein cited) as well as numerical simulations have been performed in coastal lagoons.

Coastal water are often characterized by shallowness, thus two-dimensional shallow water numerical models have been extensively developed. Suursaari et al., 2002, simulating the sea level in a sub-basin of the Baltic Sea using a 2D hydrodynamic model, observed that the sea level is strongly connected with several forcing and morphological factors, but the most important factor is a very high wind velocity over the free surface. Krámer and Józsa, 2005

used a 2D shallow water equation model in order to analyse the wind-induced steady-state circulation in a lake and unsteady currents in one bay of this lake. A comparison with field observations were performed. Due to the peculiar case of study, anyway, only the wind force was considered. Umgieser et al., 2004, concentrated their efforts on the hydrodynamic in the Venice Lagoon. Unfortunately they limited their analysis to the comparison of the water level, the salinity and the temperature with the gauge data. Vethamony et al., 2005 predict the tides and tidal currents in the Gulf of Kachchh, India, employing a calibrated 2D shallow water equations of mass and momentum, considering the tide force only, even if Babu et al., 2005 demonstrated that in the Gulf of Kachchh seasonal wind variations significantly can modify the hydrodynamic. Ferrarin and Umgieser, 2005 using a 2D finite element model, that resolves the vertically integrated shallow water equations, analysed the contemporary effect of both the wind and the tide forces on the hydrodynamic in the Cabras lagoon, showing that the wind is the main force responsible of the circulation, while the tide determines the discharges through the inlet mouth and modulates the circulation driven by the wind. More recently, Niedda and Greppi, 2007, with the aim to investigate on the relative importance of the different mechanisms that determine the circulation in a small lagoon of the Mediterranean sea, performed numerical simulation with a two-dimensional (2D) horizontal model and compared the numerical results with experimental observations. Their analysis pointed out that the balance of the tidal, the atmospheric and the seiche forces is responsible of the circulation in a small lagoon.

Coastal waters, anyway, are frequently characterized by 3D features that require 3D numerical models. Balas and Ozhan, 2002 carried out 3D numerical simulation in the Göksu Lagoon, finding that the current is mainly driven by the wind force, coherently with the specific geometry of the lagoon. They pointed out that, even if the water depth is quite shallow, some recirculation phenomena in the vertical plane can be found, thus a computed 3D numerical model seems to be the right tool.

Recently, Marinov et al., 2006 analysed the surface elevation and flow pattern, in a coastal lagoon of the Adriatic Sea, considering a variety of tide and wind forces. The numerical simulations were performed through the 3D CHOERENS model. Grifoll et al., 2009 studied the hydrodynamic conditions within the Bilbao Harbour, by means of 3D numerical simulation using the Regional Ocean Modelling System. The analysis shows that the circulation pattern is affected from the tide, the wind and the presence of freshwater as well. The understanding of the hydrodynamic regimes and of the forces that dominate the circulation patterns in a coastal lagoon is of great interest for solving environmental and engineering problems or for the preservation of water quality and coastal resources. The numerical modelling of these processes, jointly with experimental data, represent a powerful tool in order to identify the relative contribution of the previous parameter on the hydrodynamic.

The main purpose of this paper is to analyse the relative contribution of the different forces (tide, wind, etc.) that affect the hydrodynamics and the circulation pattern in coastal lagoons. In order to do this, the lagoon Stagnone di Marsala, located in the north-western part of the Sicily, was analysed through the comparison between 3D numerical simulation and experimental observations.

MATERIALS AND METHODS

Study area

The Stagnone Lagoon is a natural reserve located in the North-Western part of the Sicily in front of the Marsala city. The lagoon, shown in Figure 1, is connected to the open sea through the northern and the southern mouths. The northern mouth (400 m wide, 0.3-0.4 m deep) is characterized by very shallow water that dramatically reduces the water exchange. In order to

overcome this problem in some way a 20 m wide, 1 m deep channel was dredged, enhancing the local flushing capability. On the contrary, the southern mouth, characterized by a wide opening of about 2900 m and depth of about 1.0 - 1.50 m, ensures the transport of mass between the open sea to the lagoon and the water mixing. Inside the lagoon the mean water depth is of about 1.00 m, spanning between 0.20 m and 3.00 m, as shown in Figure 2. Two main islands, Motia and Santa Maria, are located in the center and in the northern part of the lagoon respectively. A very small island, called Scola, is also located in the central region of the lagoon. An ancient submerged road connects the Motia island with the coast in the south-north direction.

Due to the absence of freshwater discharges, the hydrodynamic mixing is influenced predominantly by tide and wind. Seagrasses cover the sandy bottom, the northern part is characterized by the presence of *Cymodocea nodosa*, while the central-southern region is covered by *Posidonia oceanica*, sometimes emerging during low tide. The lagoon is certainly of great naturalistic interest in the Mediterranean sea, due to the presence of typical vegetal and animal species. Due to the particular topography, the hydrodynamic of the lagoon is real complex, requiring a lot of attention in the analyses and suggesting to use a 3D numerical code.

The monitoring data

The tidal data have been acquired using a float-operated Shaft Encoder (Ott Thalimedes), located in a box connected with the dredged channel of the northern mouth (station TD, Fig.1). The sea level is measured since 2002 every minute and the mean value is recorded every 5 minutes.

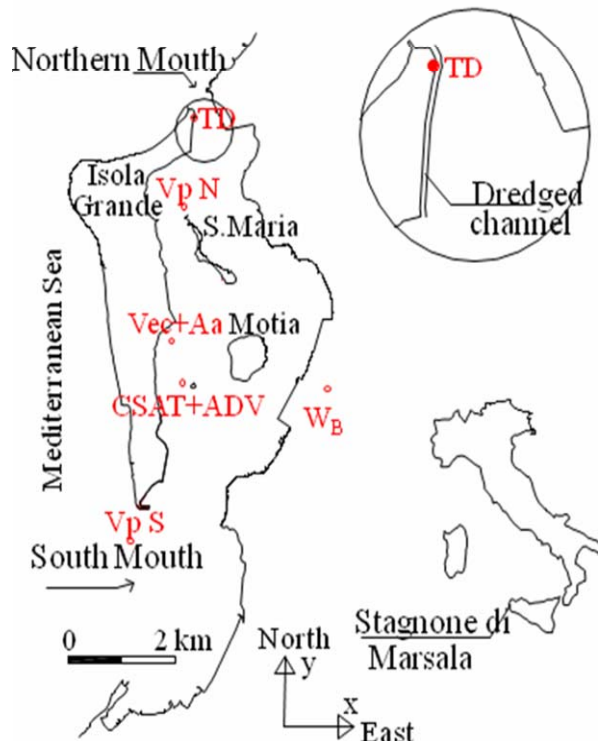


Figure 1. The *Stagnone di Marsala* lagoon. TD, point of measurement of the mean sea level in the northern mouth; VpS, point of measurement of the mean sea level in southern mouth; Aa, W_B and CsAT, wind velocity measurement points; Vec, ADV and VpN, current speed measurement points.

The meteorological gauge (W_b of Fig.1) is located over a building at about 10 m above the ground in the mid lagoon. This weather station is able to record several climatic data: in particular wind speed and direction are measured every 5 seconds and the mean values for each sector are recorded every 15 minutes.

Two bidimensional electromagnetic velocimeters (Veast and Vnorth) (Valeport 808 EM) were located in the northern area of S. Maria island and near the southern mouth (Vp N and Vp S of Fig. 1). The maximum acquisition rate is 0.5 Hz, i.e. with velocities recorded every 2 s. The system is able to record water pressure, temperature and salinity with the same frequency. The Vp S was used to record water levels only.

A three-dimensional ultrasonic velocimeters (Vector by Nortek), able to measure velocities and water pressures up to 16 Hz sampling rate, was located west of Motia island (Vec of Fig.1). In the same platform, a wind station (Aa) able to record wind intensity and direction every minute has been mounted.

Finally a 3D Sonic Anemometer able to measure wind speed at high frequency (25 Hz) has been installed together with a 3D ADV (@ 25 Hz) ultrasound current meters (CSAT + ADV of Fig. 1).

All these velocimeters are able to measure the water depth above the pressure sensor and thus to detect and record level oscillations.

The field campaign was carried out from the 4th to the 10th of July 2006.

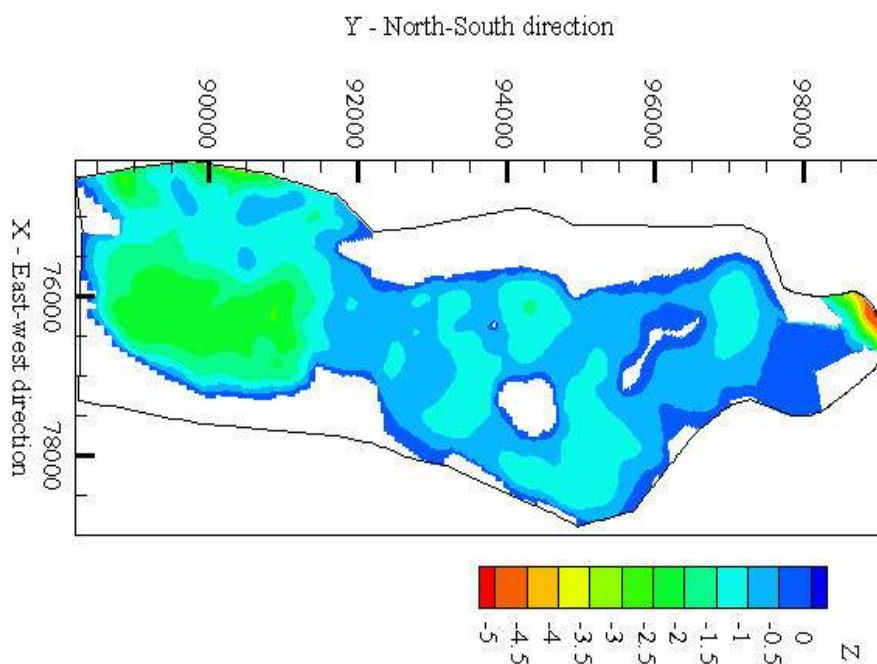


Figure 2. Bathymetry of the *Stagnone di Marsala* lagoon.

The hydrodynamic model and the numerical simulation

To model the fluid flow, the Reynolds averaged continuity and momentum equations were solved, which in the conventional summation approach can be written as:

$$\frac{\partial u_i}{\partial t} + u_j \frac{\partial u_i}{\partial x_j} - \nu \frac{\partial^2 u_i}{\partial x_j \partial x_j} + \frac{1}{\rho} \frac{\partial p}{\partial x_i} - g \delta_{ij} = 0 \quad i, j = 1,..3 \quad (1)$$

$$\frac{\partial u_i}{\partial x_i} = 0 \quad i = 1,..3 \quad (2)$$

where t is the time, x_i the i -th axis (with the east-west, north-south and vertical directions aligned with the axes x_1 , x_2 and x_3 , respectively), u_i the i -th component of the Reynolds

averaged velocity, ρ the water density, p the Reynolds averaged pressure, g the gravity acceleration, ν the kinematic viscosity, δ_{ij} the Kronecker delta and τ_{ij} the Reynolds stresses.

The pressure p can be decomposed into an hydrostatic and a non-hydrostatic pressure part, which is independent of the vertical coordinate:

$$p = \gamma[(z_B + h) - x_3] + q \quad (3)$$

where z_B is the bed elevation from an horizontal plane of reference, h is the depth of the water column and q is the non-hydrostatic pressure.

Introducing equation (3) into equation (1), the Reynolds Averaged Navier-Stokes equations can be rewritten as:

$$\frac{\partial u_i}{\partial t} + u_j \frac{\partial u_i}{\partial x_j} - \nu \frac{\partial^2 u_i}{\partial x_j \partial x_j} + \frac{1}{\rho} \frac{\partial \tau_{ij}}{\partial x_j} + \frac{1}{\rho} \frac{\partial q}{\partial x_i} - g \frac{\partial(z_B + h)}{\partial x_i} = 0 \quad i, j = 1,..3 \quad (4)$$

where the last term is null for $i = 3$, since the independence of z_B and h from x_3 .

The turbulent stresses τ_{ij} are calculated using the $k - \epsilon$ turbulence model in the 'standard' formulation (Launder and Spalding (1974)).

The free surface movements are calculated according to the *kinematic boundary condition*:

$$\frac{\partial h}{\partial t} + u_1 \frac{\partial(h + z_B)}{\partial x_1} + u_2 \frac{\partial(h + z_B)}{\partial x_2} - u_3 = 0 \quad (5)$$

The simulations were performed using a 3D numerical model solver (PANORMUS, Parallel Numerical Open-souce Model for Unsteady Flow Simulation). A second-order accurate semi-implicit method is used for the time advancement of the solution (Crank-Nicolson implicit method for the vertical diffusive and turbulent terms, Adams-Bashforth explicit scheme for the remaining terms). The pressure-velocity decoupling problem typical of incompressible fluids is overcome using a fractional-step method: at each time step RANS equations are solved assuming an hydrostatic pressure distribution without imposing mass conservation (predictor-step); a Poisson-like equation then is solved to obtain a conservative velocity field, to be added to the predictor-step field to obtain the divergence-free velocity field (corrector-step). The free surface elevation is recalculated at each time step according to equation (5). Details on the numerical discretization can be found in Lipari and Napoli, 2008.

In order to isolate the effect of the wind and of the tide on the hydrodynamic flow two different numerical simulation were performed. In the first one (hereafter referred to as TC1), the hydrodynamic flow field is driven by the action of both tidal oscillation, at the southern and northern mouths, and wind velocity field. In the second test case (hereafter referred to as TC2), the numerical simulation were performed imposing the tidal oscillation only, neglecting thus the wind effects.

The computational domain was decomposed with $84 \times 293 \times 12$ cells in the streamwise (east-west direction), spanwise (north-south direction) and vertical direction, respectively. In the vertical direction a non uniform grid was used with a refinement near the bottom and near the free-surface. At the northern and southern mouths respectively, the filtered measured water level were imposed as inflow condition (figure 3). The filtering operation, obtained applying the low-pass Butterworth filter, removed the seiche oscillations from the measured signal. To simulate the flow in the lagoon the no-slip condition is enforced at the bottom, the null normal derivatives are imposed at the northern and southern contour of the mouths, while the free slip conditions are imposed at the land boundaries.

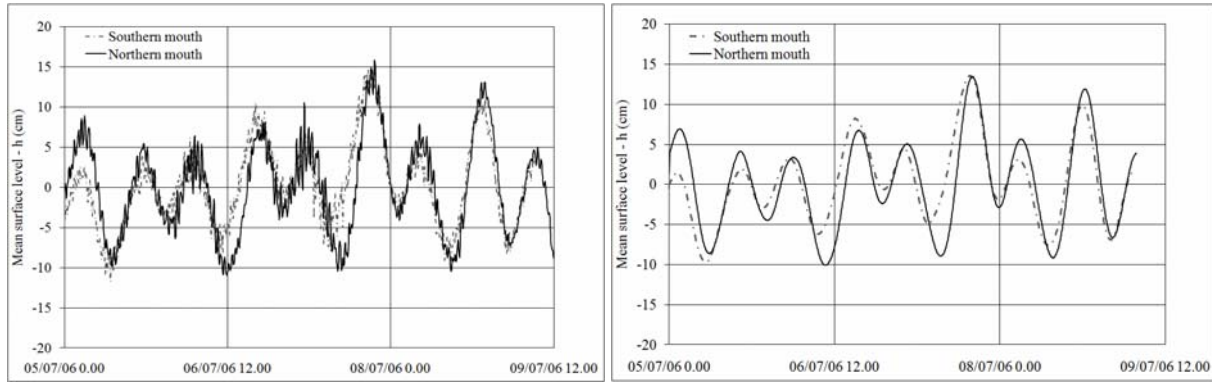


Figure 3. Measured water levels at the north and south mouths. Left, measured data; right filtered water levels imposed as inflow condition.

In the first test case, were both the tidal and the wind force are considered, over the free surface an homogenous, time dependent, measured wind velocity is imposed. The wind speed velocity was measured in three different locations, two of which, identified in figure 1 as Aa and Csat, located inside the lagoon, while the third one, called W_B , over the land. In figure 4 the east-west and north-south measured wind velocity components are plotted. As it can be observed, the general trend of the time dependent wind velocity in the three measurement station is quite similar, suggesting the possibility to impose a constant space distribution of the wind in the simulation. The wind speed at 10 m produces a wind shear stress over the free surface (see Józsa et al. 2007), partially responsible of the hydrodynamic circulation.

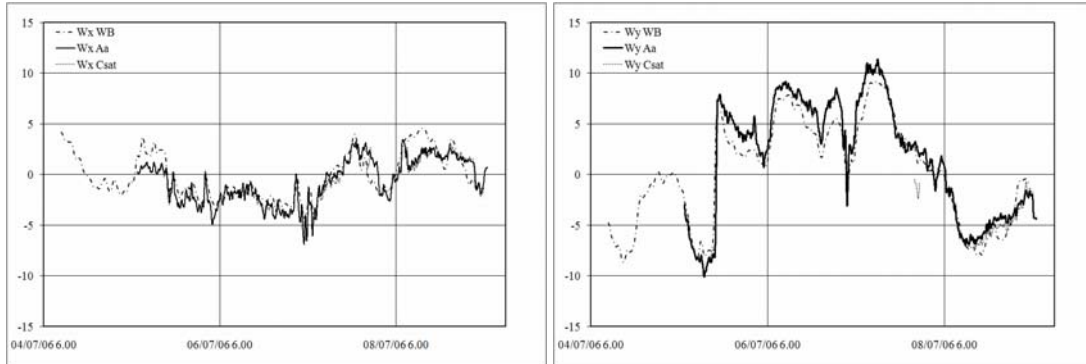


Figure 4. Measured wind velocity components at the W_B , Aa and Csat measurement stations. Left, east-west component; right, north-south component.

RESULTS AND DISCUSSIONS

In the following, in order to validate the applied simulation code, the numerical results obtained imposing both the wind and the tidal forces, and the experimental data in two different monitoring station are compared.

In figure 5 the two component of the experimental and numerical velocities are compared at the ADV measurement station located in a central region of the lagoon (see figure 1). The figure clearly shows a good agreement between measured and simulated north-south velocity component. Both higher and lower oscillations are well reproduced through the numerical code, showing the ability of the PANORMUS model to reproduce the hydrodynamic flow field in coastal lagoon. A lower level of agreement is instead observed for the east-west velocity component. However this component is characterized by very low velocities and the general trend is well captured.

In figure 6 the time series of the east-west velocity and north-south velocity components measured and simulated are compared in correspondence of the *Vec* monitoring station,

located (figure 1) close to the coast of Isola Grande. Again, a quite good agreement between the numerical north-south velocity component and the measured one was achieved for the whole period.

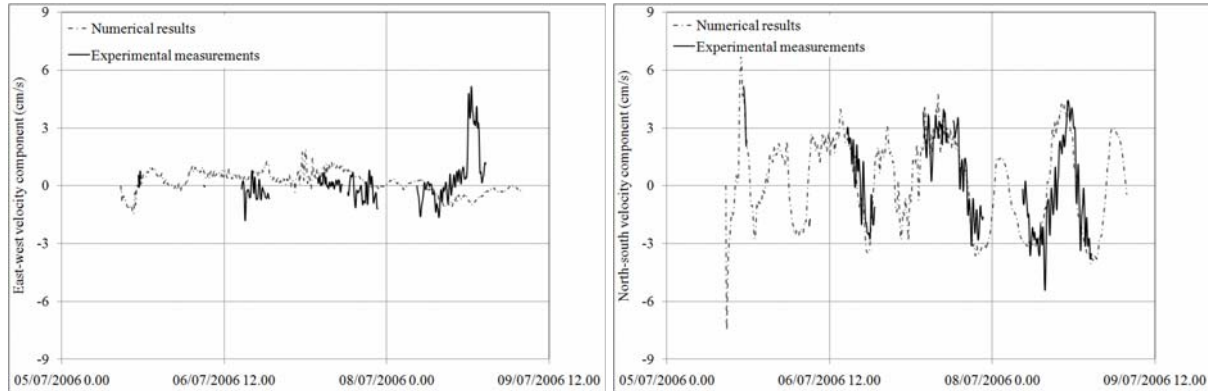


Figure 5. Comparison between measured and simulated velocity components at the ADV measurement station. Left, east-west component; right, north-south component.

Both maximum and minimum values of velocities are well reproduced as well as the small oscillations. The analysis of the east-west velocity component measured and simulated shows, instead, a good agreement in some periods, while some deviation are observed in other periods. Despite of this, also for the east-west component the general trend of the velocity is well captured.

Due to the shallowness and to the presence of vegetated bottom the velocity field is very sensitive with the water level variation, thus the comparison between the measured and the simulated time variation of the water level is shown if figure 7. The comparison was performed in correspondence of the VpN and Vec measurement points located in the northern part of the lagoon respectively, close to the Santa Maria island, and in a central region of the lagoon close to the Isola Grande. In both locations a satisfactory agreement between measured and simulated sea level was found. The range of maximum water level excursion is about 0.25-0.27 m.

The analysis of the Fourier power spectrum of water levels, not reported here, shows that the free surface oscillation are dominated by semi-diurnal period with supplementary contributions from the diurnal (tide oscillation). A second order oscillation, typically of the seiche motion (higher frequency and lower amplitude) of about 0,50 h was also observed. The seiche motion is directly influenced by the wind velocity field acting on the free surface. These results confirm that both the tidal motion and the wind force are responsible of the hydrodynamic circulation inside the lagoon.

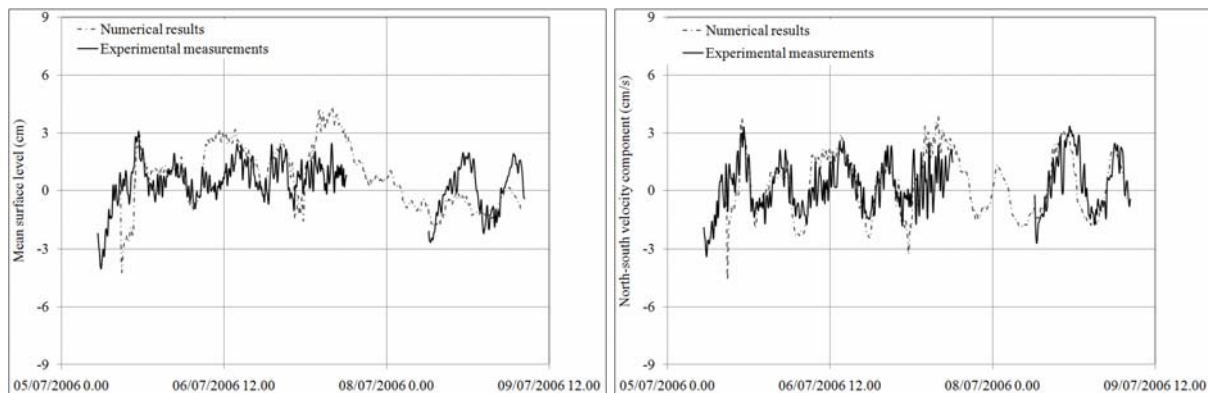


Figure 6. Comparison between measured and simulated velocity components at the Vec measurement station. Left, east-west component; right, north-south component.

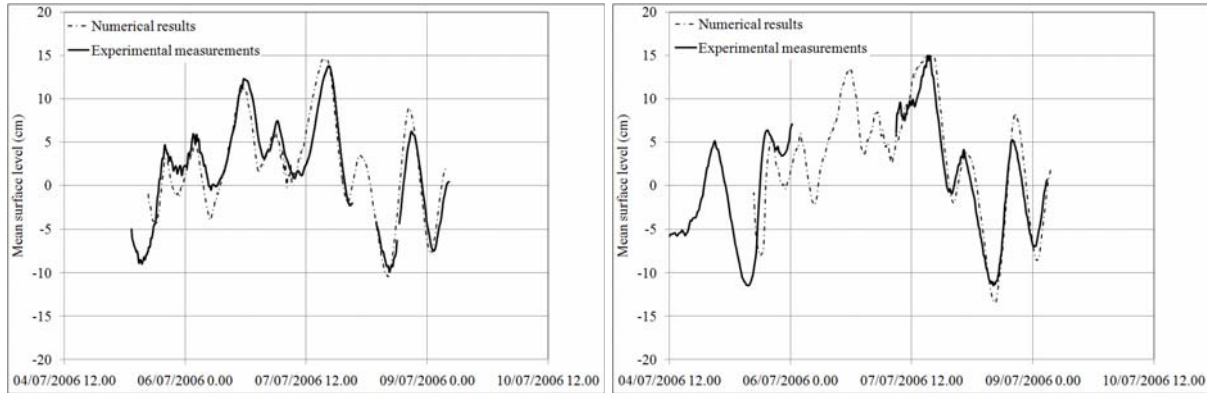


Figure 7. Comparison between measured and simulated water level. Left, Vec measurement station; right, VpN measurement station.

In order to analyse the relative contribution of the tide and of the wind on the circulation pattern, a new simulation was performed neglecting the shear stress at the free surface, thus the imposed filtered tide measurement data become the only one force acting on the flow field.

The numerical results obtained for the TC2 are compared with those obtained for the TC1, where both wind and tide forces were considered. Figure 8 shows the comparison between the east-west and the north-south velocity components obtained in correspondence of the Vec Station. The north-south velocity component has a quite similar trend in both cases and the same values of the velocity were found. The main difference, worthy of attention, is that the small oscillations of the velocity, observed in the TC1, are not reproduced in the TC2. These oscillations are representative of the seiche motion induced by the wind.

The east-west velocity component obtained neglecting the wind field is characterized by lower values of the velocities and some differences were found also for the velocity trend. The results obtained confirm that the hydrodynamic flow field inside the lagoon is affected both by the wind velocity field and the tidal oscillation. More precisely, the tidal force dominates in the north-south direction, while in the east-west direction the wind plays a fundamental role. The same consideration can be made comparing the velocities in correspondence of the ADV station, even if the east-west component of the velocity is certainly negligible with respect to the north-south component (figure 9).

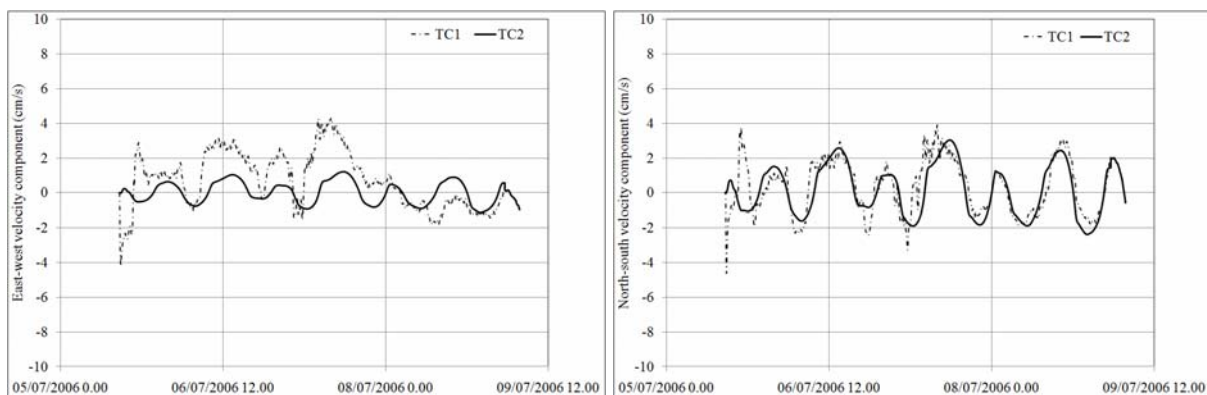


Figure 8. Comparison between the velocity at the Vec point obtained for TC1 and TC2. Left, east-west component; right, north-south component.

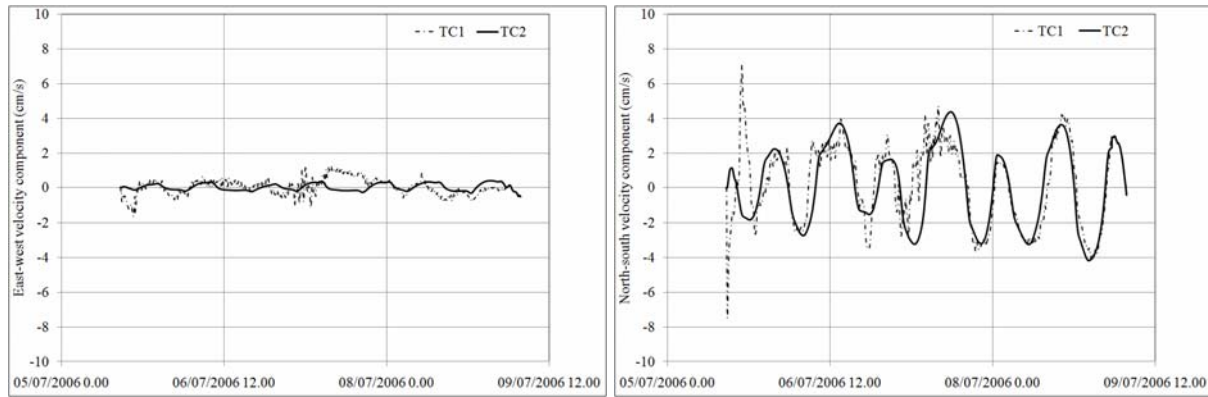


Figure 9. Comparison between the velocity at the ADV point obtained for TC1 and TC2. Left, east-west component; right, north-south component.

The analysis of the figure 5 and 6 showed an unsatisfactory agreement between measured and simulated velocities in the east-west direction. Since these component is mainly driven by the wind action, in further simulations a more accurate wind space-distribution must be taken into account (IBL development due to the different roughness of land and water surface).

CONCLUSIONS

In the present paper a 3D numerical model has been applied in order to simulate the dynamics of the *Stagnone di Marsala* lagoon, located in the west part of Sicily (Italy). The numerical results have been compared with data measured in three different stations. The comparison showed the ability of the code to reproduce the hydrodynamic inside the lagoon. Both the trend and the range of the water level variations have been captured as well as the current velocity. The Panormus model adequately reproduces the free surface elevation and the current speed variation in time generated by the inlet/outlet Mediterranea Sea tide and by the wind velocity field over the lagoon. The numerical model was thus used to separate the effects of the two forces on the flow field. In order to this a second simulation has been performed neglecting the wind shear stresses. The comparison between the two numerical simulations showed that the tidal force dominates in the north-south direction, while in the east-west direction the wind plays a fundamental role. The seiche motion is well reproduced by the model.

Even if the model is able to simulate the hydrodynamic flow field inside the lagoon, a certain level of unsatisfactory agreement in the east-west direction between measured and simulated velocities was found, suggesting that imposing a constant wind acting over the lagoon is not the right way. In further simulations a more accurate wind space-distribution must be taken into account (IBL development due to the different roughness of land and water surface).

REFERENCES

- Alpar B. and Yuce H. (1996). Sea-level variations in the eastern coasts of the Aegean Sea. *Estuarine, Coastal and Shelf Science*, **42**, 509-521.
- Babu M.T., Vethamony P. and Desa E. (2005). Modelling tide-driven currents and residual eddies in the Gulf of Kachchh and their seasonal variability A marine environmental planning perspective. *Ecological Modelling*, **184**, 299-312.
- Balas L. and Ozhan E. (2002). Three-dimensional Modelling of Stratified Coastal Waters Estuarine, *Coastal and Shelf Science*, **54**, 75-87.
- D'Alpos L. and Defina A. (2007). Mathematical modeling of tidal hydrodynamics in shallow lagoons: A review of open issues and applications to the Venice lagoon. *Computers & Geosciences*, **33**, 476-496.

- Ferrarin C. and Umgiesser G. (2005). Hydrodynamic modeling of a coastal lagoon: The Cabras lagoon in Sardinia, Italy. *Ecological Modelling*, **188**, 340–357.
- Grifoll M., Fontán A., Ferrer L., Mader J., González M. and Espino M. (2009). 3D hydrodynamic characterisation of a meso-tidal harbour: The case of Bilbao (northern Spain). *Coastal Engineering*, **56**, 907–918.
- Józsa J., Milici B. and Napoli E. (2007). Numerical simulation of internal boundary-layer development and comparison with atmospheric data. *Boundary-Layer Meteorol.*, **123**(1), 159–175.
- Krámer T. and Józsa J. (2004). An adaptively refined, finite-volume model of wind-induced currents in lake neusiedl. *Periodica Polytechnica Ser. Civ. Eng.*, **49**(2), 111–136.
- Launder B.E. and Spalding D.B. (1974). The numerical computation of turbulent flows. *Comp Meth Appl. Mech. Eng.*, **3**, 269–89.
- Lipari and Napoli (2008). The impacts of the ALE and hydrostatic-pressure approaches on the energy budget of unsteady free-surface flows. *Comput. Fluids*, **37**, 656–73.
- Marinov D., Norro A. and Zaldivar J.M. (2006). Application of COHERENS model for hydrodynamic investigation of Sacca di Goro coastal lagoon (Italian Adriatic Sea shore). *Ecological Modelling*, **193**, 52–68.
- Niedda M. and Greppi M. (2007). Tidal, seiche and wind dynamics in a small lagoon in the Mediterranean Sea Estuarine. *Coastal and Shelf Science*, **74**, 21–30.
- Suursaar U., Kullas T. and Otsmann M. (2002). A model study of the sea level variations in the Gulf of Riga and the Vainameri. *Sea Continental Shelf Research*, **22**, 2001–2019.
- Umgiesser G., Canu D.M., Cucco A. and Solidoro C. (2004). A finite element model for the Venice Lagoon. Development, set up, calibration and validation. *Journal of Marine Systems*, **51**, 123–145.
- Vethamony P., Reddy G.S., Babu M.T., Desa E., and Sudheesh K. (2005). Tidal eddies in a semi-enclosed basin: a model study. *Marine Environmental Research*, **59**, 519–532.

Modeling of the thermal pollution in the lakes-coolers as an example of the Shatura Lakes system (Russia)

E.I. Debolskaya¹, E.V. Yakushev², I.S. Kuznetsov³

¹*Water Problems Institute of The Russian Academy of Sciences (IWP RAS), Gubkina str. 3,
Moscow, 119991, Russia*

²*Norwegian Institute for Water Research (NIVA), Gaustadalleen 21, Oslo, NO-0349, Norway*

³*Leibniz-Institut für Ostseeforschung Warnemünde, Seestrasse 15, D-18119 Rostock,
Germany*

**Corresponding author, e-mail e_debolskaya@yahoo.com*

ABSTRACT

In this study we used three-dimensional hydrodynamic model GETM to simulate the hydrodynamical, thermal and biogeochemical regime of the Shatura Lakes over summer and winter periods. The situated in the Central European Russia Shatura Lakes are used as the lake-coolers of the State District Power Station. The goal of this work was to study the influence of the weather conditions and Station thermal dumps parameters on the Lakes thermal regime, water circulation and the distributions of the basic biogeochemical characteristics, which are responsible for the lakes system ecological state.

This model biogeochemical block (OxyDep) has 4 state variables: dissolved oxygen (DO), total organic matter (OM), biota (BIO) and inorganic nutrient (NUT). Such a simple model allowed to parameterize the main processes responsible for the water column oxygen regime, i.e. synthesis and decay of organic matter and the processes at the boundaries (sea-water exchange and consumption by the sediments). The main goal of OxyDep was to study the processes of the oxygen depletion resulting in the observed formation of suboxic and anoxic conditions in the certain water volumes of the studied lakes.

The application of the model allowed to demonstrate that the thermal dumps regime is the main factor affecting the formation of currents structure, the thermal conditions and the ecological state. The growth of water temperature caused by thermal dump, considerably shifts date of the bloom beginning and its intensity and can lead to intensification of eutrophication and to formation of hypoxic zones.

KEYWORDS

Modeling; thermal pollution; lakes-coolers; hypoxia

INTRODUCTION

Thermal pollution is a harmful increase in water temperature in streams, rivers, lakes, or occasionally, coastal ocean waters. Thermal pollution is caused, for example, by either dumping hot water from factories and power plants or removing trees and vegetation that shade streams, permitting sunlight to raise the temperature of these waters. Like other forms of water pollution, thermal pollution is widespread, affecting many lakes and vast numbers of streams and rivers in all parts of the world. A temperature increase as small as 1 or 2 degrees

Celsius can kill native fish, shellfish, and plants, or drive them out in favor of other species, often with undesirable effects.

The major sources of thermal pollution are electric power plants and industrial factories. In most electric power plants, heat is produced when coal, oil, or natural gas is burned or nuclear fuels undergo fission to release huge amounts of energy. This heat turns water to steam, which in turn spins turbines to produce electricity. After doing its work, the spent steam must be cooled and condensed back into water. To condense the steam, cool water is brought into the plant and circulated next to the hot steam. In this process, the water used for cooling warms 5 to 10 Celsius degrees, after which it may be dumped back into the lake, river, or ocean from which it came. Similarly, factories contribute to thermal pollution when they dump water used to cool their machinery.

Effects of thermal pollution of water bodies cause great harm to natural ecosystems. Dump of heated water can completely change the type of water, make it ice-free in winter and overheated in the summer heat, to cause violent development of organisms, alien this reservoir, to shift time and place of fish spawning, bloom beginning and its intensity and lead to intensification of eutrophication and to occurrence hypoxia and anoxia zones.

Oxygen depletion and anoxia formation are common features observed in the inland waters and the coastal areas. Presence of permanent anoxia and formation of temporal anoxic conditions significantly affect the water quality and ecological status of the water directly (absence of oxygen impair the ecosystem) and indirectly, via changes of nutrient supply from the sediments (initially phosphate). According to recent estimates (Diaz, Rosenberg, 2008), dead zones connected with low oxygen content have spread exponentially since the 1960s. Formation of oxygen-deficient (less than 80% saturation), hypoxic (less than 30%) and anoxic conditions depend on the combined influence of eutrophication (amounts of nutrients loads) and climate (intensity of mixing and water renewal). Thermal pollution considerably reinforces the oxygen depletion.

The goal of this paper was to analyze the process of the construct a model devoted to analyzing of the oxygen regime in the Shatura lake-cooler. Such a model will be able to simulate physical and biogeochemical processes in the lake and to evaluate the effect of the best management practice strategy on improving water quality of the basin.

METHODS

With the increasing of power plants capacity and the use of deep lakes and reservoirs as cooling there is a need to develop new, more accurate methods of numerical simulation.

The calculating of the hydrothermal regime must take into account the effects of wind, density forces and other data of the reservoir-cooler. In addition, to solve practical problems, it is important to know not only the value of average temperature, but also its distribution in the reservoir's volume.

A successful solution can be achieved through mathematical modeling of transport processes and correct statement of the problem, based on adequate natural initial data.

For the calculation of a hydrothermal and biogeochemical regime of lakes-coolers with an estimation of three-dimensional structure we used a coupled hydrophysical-biogeochemical 3-

dimensional model GETM (<http://www.getm.eu>) and OxyDep. The later simplified 4-component biogeochemical model, was specifically elaborated for the calculated of the oxygen content in the simplest possible way (Fig. 1). OxyDep considers 4 state variables:

- BIO, that is all the biota from bacteria and phytoplankton to fish and whales. BIO grows due to photosynthesis, loses inorganic matter due to respiration, and loses total (particulate and dissolved) organic matter due to metabolism, mortality, cannibalism etc.
- NUT, that is the oxidized forms of nutrients (i.e. NO₃ and NO₂ for N), that don't need additional oxygen for nitrification
- OM, that is all kinds of labile organic matter (particulate and dissolved) and reduced forms of inorganic nutrients (i.e. NH₄ and Urea for N).
- OXY, concentrations of dissolved oxygen, that, changed with the formation and mineralization of the organic matter following the Redfield ratio.

Such a simple model allowed to parameterize the main processes responsible for the water column oxygen regime, i.e. synthesis and decay of organic matter and the processes at the boundaries (sea-water exchange and consumption by the sediments). The main goal of OxyDep was to study the processes of the oxygen depletion resulting in the observed formation of suboxic and anoxic conditions in the certain water volumes of the studied lakes

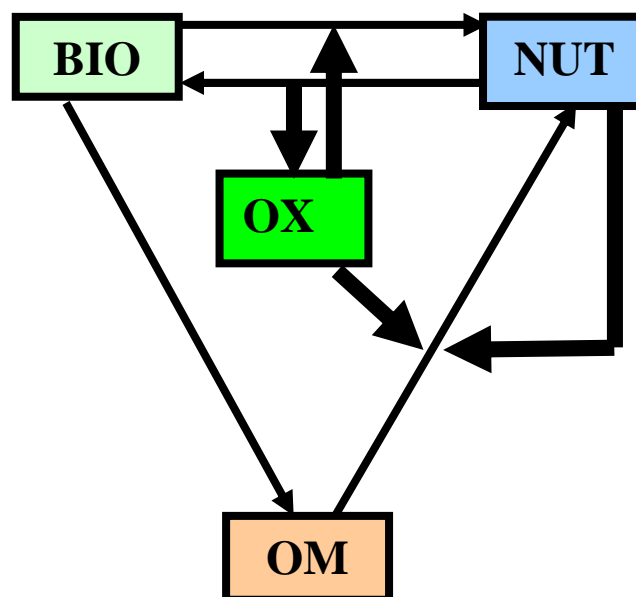


Figure 1. Flow chat of OXYDEP: summarized biogeochemical fluxes and variables: dissolved oxygen (DO), total organic matter (OM), biota (BIO) and inorganic nutrient (NUT).

We parameterized the exchange of the model parameters with bottom as function of the oxygen content following the approach described in (Yakushev et al., 2009, accepted). Besides, we considered air-water exchange of oxygen following (Yakushev et al., 2007).

To describe the dependence of rate of photosynthesis on temperature (LimT) we used a modified dependence (Fig.2):

$$\text{LimT} = 0.5(1+\tanh((t-t_{\min})/s_{\min})) (1-0.5(1+\tanh((t-t_{\max})/s_{\max}))),$$

where: t - water temperature ($^{\circ}\text{C}$), $t_{\min}=15^{\circ}\text{C}$, $s_{\min}=15^{\circ}\text{C}$, $t_{\max}=15^{\circ}\text{C}$, $s_{\max}=15^{\circ}\text{C}$.

RESULTS AND DISCUSSION

Calibration of the model was focused on water temperature and flow velocity. Comparison against observed data obtained during period summer-winter 2008 showed that the model predictions were corresponded well for most of the constituents. The results of measurements of the surface temperature and velocity after 4-hour dump of warm water are shown in the figure 3(left). The results of the modeling of the same regime under the same meteorological conditions are shown in the figure 3 (right). Vertical distributions of temperature and flow velocity calculated on the model, also well coincided with the data of measurements.

To receive the balanced initial conditions for the numerical experiments we performed calculations of the thermal regime dynamics during 2 years.

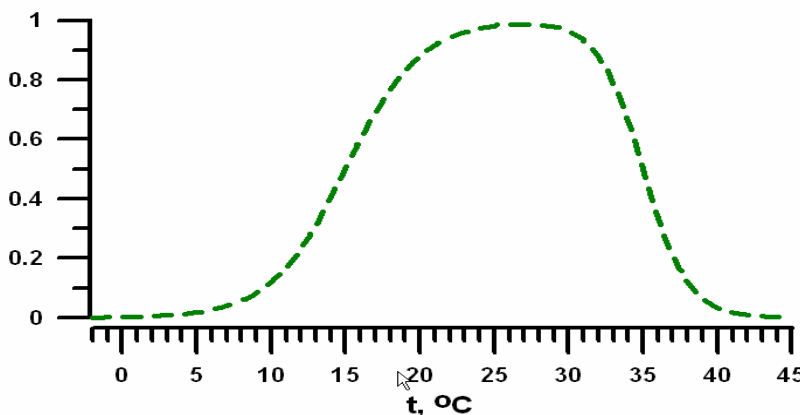


Figure 2. Dependence of the rate of photosynthesis on temperature.

To identify the impact of thermal pollution we modeled the discharge of the warmed-up water with volume of $20\text{m}^3/\text{s}$ and the difference of temperatures in 8°C between the input to the power plants and the dumping place.

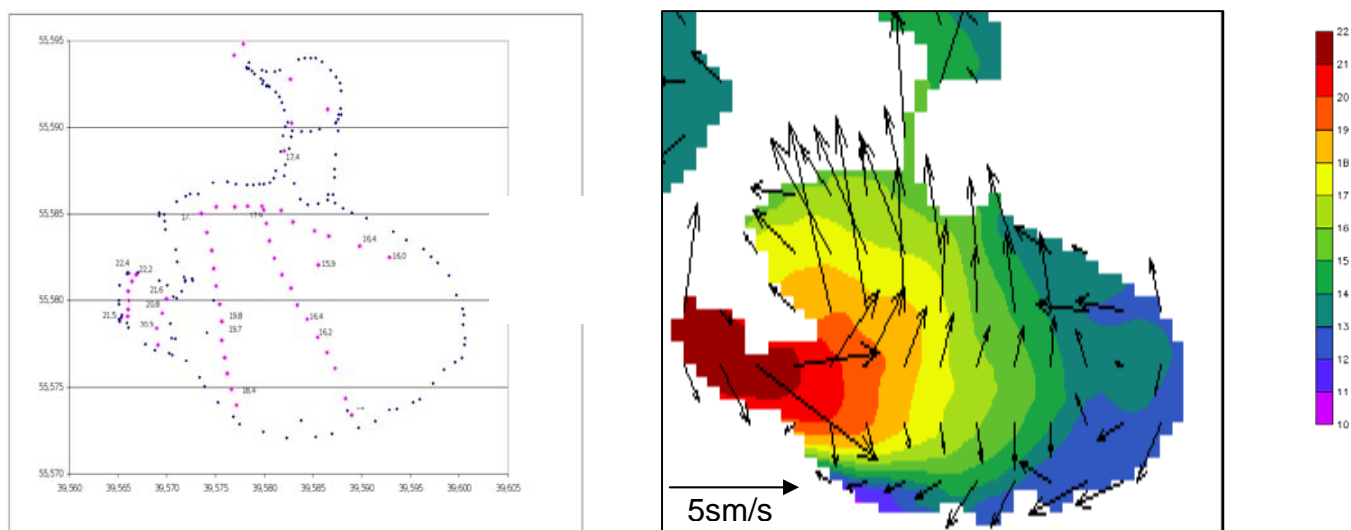


Figure 3. The results of measurements and the calculations on the model of surface temperature after 4-hour dumping of warm water.

Comparison of figures 4 and 5 shows that under the influence of thermal dump biota bloom started a month earlier and the concentration of oxygen considerably decreased that has led to the hypoxia formation.

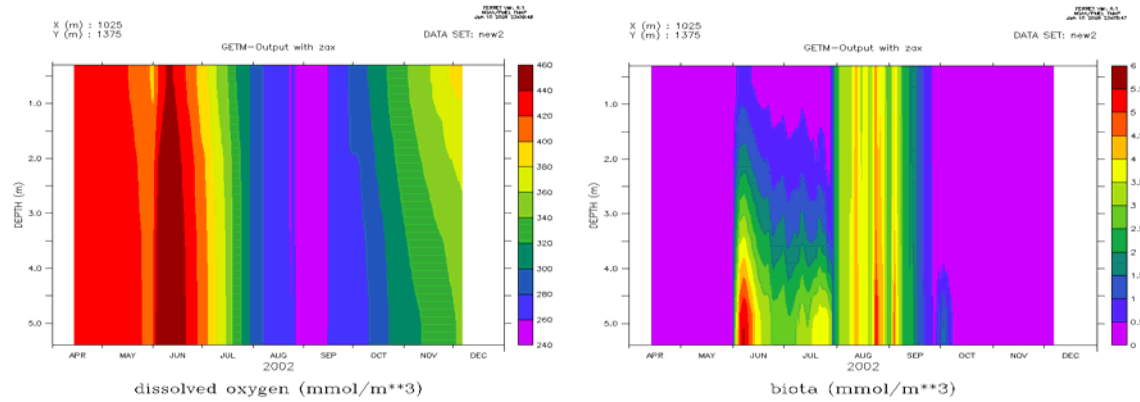


Figure 4. Temporal variability of the vertical distribution of dissolved oxygen and biota in the absence of thermal dumping.

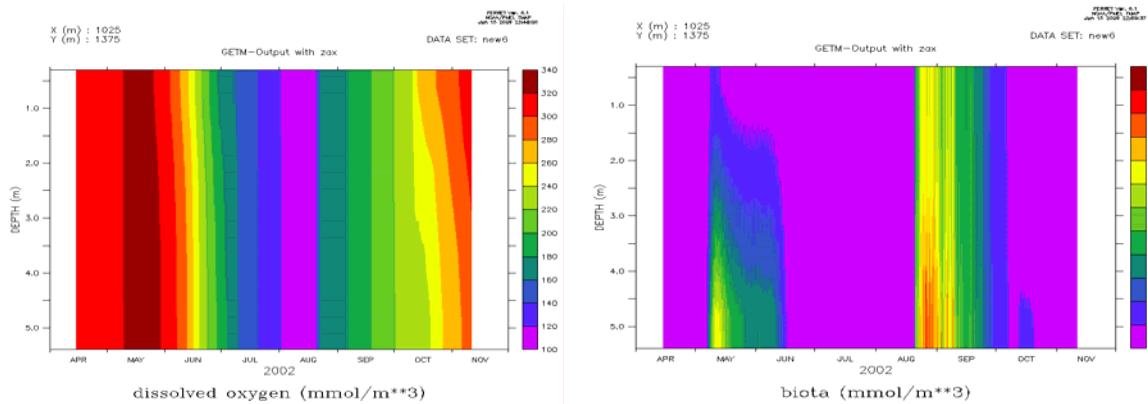


Figure 5. Temporal variability of the vertical distribution of dissolved oxygen and biota under the influence of thermal dump.

CONCLUSIONS

The proposed coupled GETM+OxyDep model can be used for the estimating of oxygen and nutrient regime of the shallow regions with a complex topography.

The increase of a water temperature caused by thermal dump, considerably shifts date of the bloom beginning and its intensity, that can lead to intensification of eutrophication and to formation of hypoxic zones.

In the shallow regions the propagation of the thermal front resulted in formation of the local sites of the biota blooms during the winter-spring period that leaded to the local hypoxia.

ACKNOWLEDGEMENTS This work was supported by the Norwegian Institute for Water Research, Projects 29083.

REFERENCES

- Diaz R.J., Rosenberg R. (2008). Spreading Dead Zones and Consequences for Marine Ecosystems. *Science*, 321, 926-929
- E.V.Yakushev, F.Pollehne, G.Jost, L.Umlauf, I.Kuznetsov, B.Schneider Analysis of the water column oxic/anoxic interface in the Black and Baltic seas with a Redox-Layer Model. 2007. *Marine Chemistry*, 107, 388-410.
- E.V.Yakushev, I.S.Kuznetsov, O.I. Podymov, H.Burchard, T.Neumann, F.Pollehne Modeling of the influence of oxygenated inflows on the biogeochemical structure of the Gotland Deep, Central Baltic Sea: changes in the distribution of manganese. *Computers and Geosciences*, 2009, accepted.

Spring thermal bar in fresh basin: laboratory experiments and numerical simulations

N. Yu. Demchenko¹

¹ P.P.Shirshov Institute of Oceanology of Russian Academy of Sciences, Atlantic Branch,
236000, Prospect Mira, 1, Kaliningrad, Russia

e-mail ndemchenko@mail.ru

ABSTRACT

The thermal bar driven by spring heating over an inclined bottom is an important phenomenon observed in many large basins. It is modelled in a laboratory rectangular tank with an aspect ratio, $H/L \sim 0.1$ (where H and L are the tank height and length, respectively). It is shown, that the thermal bar is to be considered as a process, embracing large horizontal distances, because a basin-wide structure for water circulation develops with time. It is a complicated phenomenon, consisting of a down-slope cascades (which are formed in regions, where $T < T_{md}$), subsurface off-shore jet ($T > T_{md}$) and compensating flow towards to the shallow part of basin, supplying the both in an intermediate layer. The driving factor of this dynamics is destabilizing ($\alpha H < 0$; α – thermal expansion coefficient; H – heat flux) and stabilizing ($\alpha H > 0$) buoyancy flux. Specific features of structure of density and current fields are investigated. It is pointed out, that the speed of propagation of the T_{md} -isotherm and one of the subsurface jet do not coincide: the T_{md} -isotherm propagates faster. The thermal bar front, understood earlier as a convergence zone near the 4°C -isotherm, is associated with the leading edge of the subsurface jet. Increasing with time distance between 4°C -isotherm and subsurface jet is registered in laboratory modeling. This feature can be explained by different driving mechanisms: current is maintained by a horizontal pressure gradient, whilst the surface temperature increases due to heating from surface and advection of heat from shallow part. Results of numerical modeling are shown to be in a good agreement with the laboratory experiments.

KEYWORDS

Spring thermal bar; buoyancy flux; thermal and current structure; limnology.

INTRODUCTION

The “thermal bar” arising in coastal waters is typically considered as “bar, or barrier, for horizontal mixing” (Elliot&Elliot, 1970, Tikhomirov, 1982; Kreiman, 1989). It usually appears in spring and autumn, when water temperature in large basins gradually passes the temperature of maximum density (hereinafter, the T_{md}). Under the same heating conditions at the surface, water at one side of the T_{md} -line is stably stratified, whilst at the other side it is prone to vertical mixing by thermo-gravitational convection. It is commonly accepted, that water masses at the T_{md} -line, being denser than water masses at both sides of it, sink down here; they are replaced by water masses from opposite sides of the bar with temperatures slightly above and below the T_{md} , which mix together to make the next portion of water with T_{md} ; and so on (see, e.g., Tikhomirov, 1982). This way, the thermal bar restricts horizontal

exchange and intensifies vertical mixing. In spring, it keeps warm shallow waters from mixing with the main cold water body, thus favouring to the conditions for spring awakening of aquatic life (Likhoshway et al., 1996).

The phenomenon of the thermal bar was investigated quite intently in field (Tikhomirov, 1982; Mortimer, 2004; Wüest et al., 2005) and in several theoretical studies (Zilitinkevich et al., 1987), laboratory experiments (Elliot&Elliot, 1970; Kreiman, 1989) and numerical investigations (e.g., Elliot, 1971; Farrow, 1995 a, b).

Despite of those investigations, a number of questions remains still unclear. Farrow (1995 a, b) developed analytical and numerical models, disclosing remarkable features of the thermal bar, which up to now were not yet registered in laboratory experiments. These features are (i) non-coincidence between high-gradient zones (fronts) in fields of density and currents, (ii) existence of surface jet and (iii) down-slope gravity current, appearing at different stages of the thermal bar development.

The main goal of this paper is to investigate field of current in the presence of the temperature of maximum density in fresh basin with inclined bottom under heating from the surface. We demonstrate that the (1) thermal bar is a complicated phenomenon consisting of a downslope cascades, subsurface jet and compensating flow in the intermediate layers; (2) locations of the 4°C-isotherm and of the dynamical front do not coincide.

General characteristics of temperature and velocity field

Principal current and density fields in presence of T_{md} in shallow part of a basin is described in Chubarenko&Demchenko (2008, hereafter CD08). With heating, temperature of surface layer becomes higher than the temperature of subsurface layer (but still lower than 4°C), so, the density of upper most layer increases. Being denser, surface water tends to sink, i.e. the water column mixes down. In shallow part, at the same heat removal, water heats faster than in deeper parts, because the mass involved in vertical mixing is smaller. This way, horizontal temperature/density gradients are formed between shallow and deep parts of the basin. The T_{md} is reached first near the shore, and is indicative for the appearance here of another thermal stratification: with further heating, density of surface water decreases, vertical convection stops, and direct thermal stratification is established. With further heating this area expands towards the deeper parts (CD08).

It is physically evident, that the process is driven by the buoyancy flux through the surface $B = g\alpha H/\rho_0 C_p$, rather than by the heat flux H (W/m^2). (Here, g is the acceleration due to gravity, $\alpha = -1/\rho \cdot dp/dT$ is the coefficient of thermal expansion of the water, ρ_0 is the water density, and C_p is the heat capacity of the water under constant pressure). Thus, if α is positive, the water in the surface layer becomes “more buoyant”, and a stable vertical stratification appears. This occurs if $\alpha H > 0$, i.e., either when heating of warm water (with temperature above the T_{md}) or when cooling of cold water (with temperature below the T_{md}). Areas with $\alpha H < 0$ are embraced vertical convection (unstable vertical stratification).

Detailed dynamics of current during the thermal bar development in laboratory conditions is described in (CD08). Series of experiments were performed in a 5-m long laboratory tank with a sloping bottom of aspect ratio 0.01-0.2, extending over 2 m. Cooling/heating was applied at the free surface and water temperature gradually passed the T_{md} («spring» thermal bar). The resultant current and temperature fields were investigated in three phases: (i) down-slope cascades; (ii) subsurface jet and (iii) transformation of one type of circulation to another while passing the T_{md} .

Horizontal exchange in the presence of 4°C-isotherm has different structure over the top of incline and in the deeper one. Transport of water heated above 4°C from shallows is realized in surface layer by means of light subsurface jet, whilst in deep part of the tank, where water temperature is still below 4°C, down-slope cascades persist. With further off-shore

propagation of the thermal bar, the down-slope currents gradually weaken and finally disappear at all. Common feature for the current fields at both sides is the compensating flow towards the shallows in intermediate layers (see also CD08). It is important, that neither convergence zone nor water sinking in the region of the 4°C -isotherm were not observed in the experiments.

The very beginning of the passing of the T_{md} (when it has just appeared at the top) the currents are very weak, and the 4°C -isotherm is close to the vertical. With the formation of the subsurface jet, the 4°C -isotherm is carried by the jet to the part, where bottom layers did not yet reached the T_{md} , so, the down-slope cascades still exist near the bottom (CD08).

LABORATORY EXPERIMENTS

Experimental set-up

Experiments were performed in a 2-m long water channel with a sloping bottom (aspect ratio ~ 0.1) at the Fluid Mechanics Laboratory of Technical University of Eindhoven (The Netherlands). The tank was filled with tap water, which was cooled down to a temperature of 1°C using a cooling machine (ULTRA KRYOMAT TK-30D) and artificial ice cubes put on the free surface. Subsequently, the temperature of water gradually increased due to the heat-exchange through the surface with warmer ambient air. The sidewalls and the bottom were thermally protected by insulator. Structure of the temperature field was monitored by the set of five verified thermistors at fixed positions (LeCroy 8013A); 1 moveable thermistor was used for vertical profiling. Accuracy of the thermistors is 0.001°C . Information about overall flow structure was obtained by photographing of the deformations of dye lines from potassium permanganate crystals, dropped into the tank. Deformation of the dye pattern was monitored by digital camera. Data processing was performed using CorelDraw, Excel and Surfer.

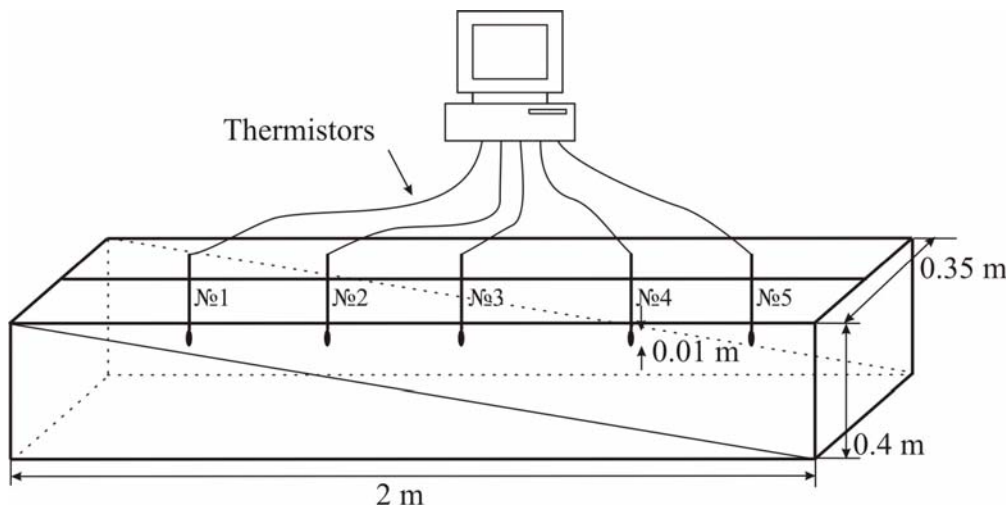


Figure 1. Experimental setup.

The experiments

The experiments presented here reproduced the same development of the thermal bar. The main goal of them was to monitor with finer laboratory tools the difference between the locations of the 4°C-isotherm and of the dynamical front.

Typical structure of temperature and velocity fields is shown on Figure 2.

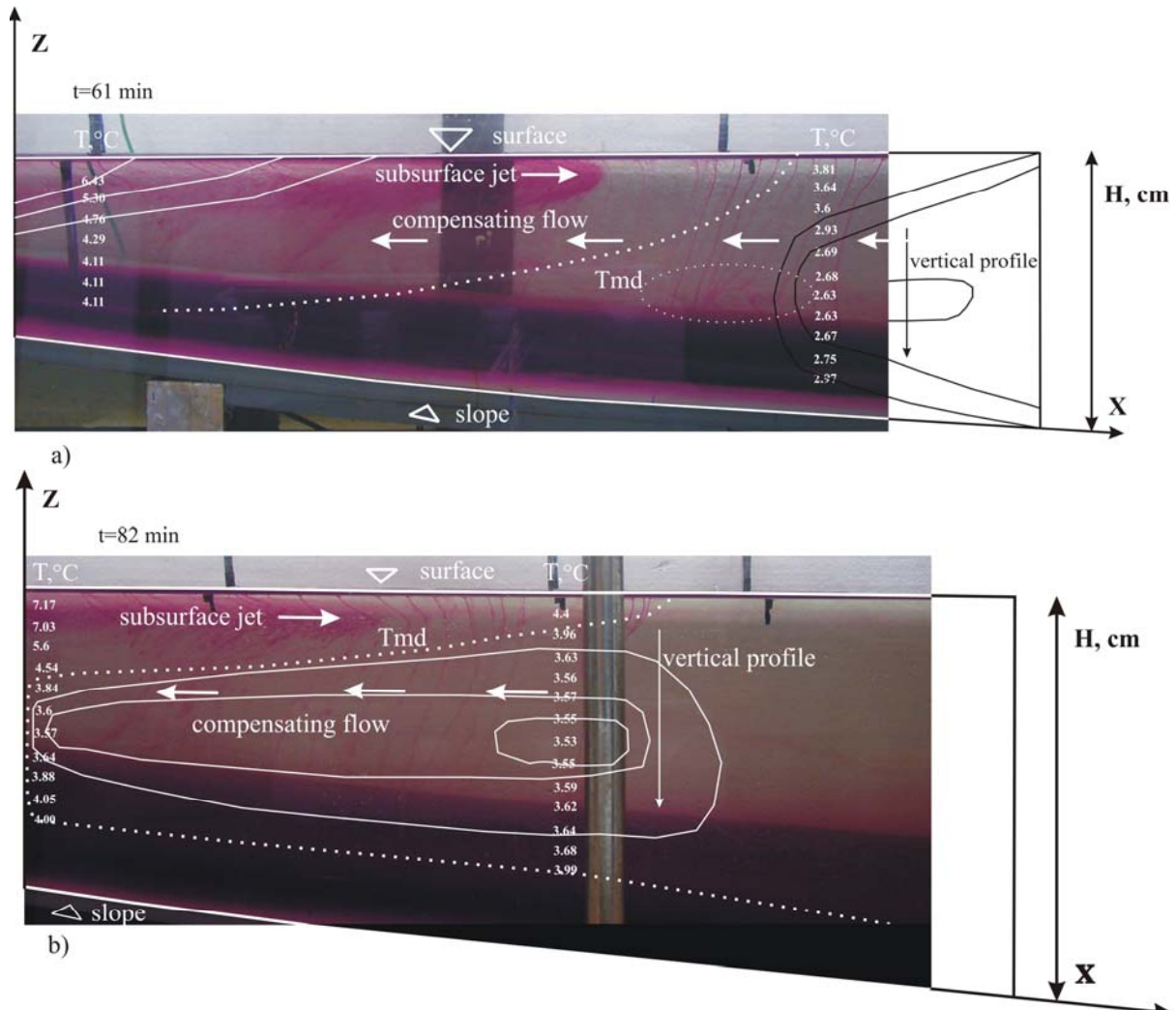


Figure 2. Structure of temperature and current fields in 61 min and 82 min after the beginning of the experiment. Temperature fields are extrapolated from vertical profiles, taken in the vicinity of the head of the subsurface jet, using movable thermistor, namely, at the locations: a) 7, 12 cm and b) 12, 13 cm depths. Numbers in the pictures are water temperatures. Dotted lines mark approximate location of the 4°C-isotherm. Dotted circle on upper panel indicate a region with the down-slope cascades (Demchenko, 2007).

In the deeper part of the basin, there is a well-mixed core and 2 warm (surface and bottom) boundary layers. Their thicknesses are about 0.3D/0.4D ($D=18.5\text{cm}$ – maximum depth of the basin), and vertical temperature difference of 0.8°C/0.3°C, correspondingly. With the development of the process, vertical temperature difference across the boundary layers increases up to 1.5-2°C, thickness of surface layer increases up to 0.5D, whilst the thickness of the bottom layer slightly decreases to the 0.15-0.2D (Demchenko, 2007).

Figure 2 (a,b) demonstrate that, under practically the same heat flux through the surface, shallow waters became more heated than deeper ones. This is because of the same heat H is distributed by vertical convection over water columns of different length. The 4°C -isotherm naturally appears for the first time in the top-most part of the tank, and since that the isotherms become inclined towards the deep part. During rather long initial period, when the 4°C -isotherm already exists in the water-body, top region is still motionless. Since deeper part (which is below the T_{md}) experiences vertical convection due to negative buoyancy flux into surface layer, the iso-therms there are vertical (except for surface and bottom boundary layers).

Figure 2 b shows an instant, when the warm jet is already developed and water particles in the upper-most layer move with almost the same speeds as the subsurface jet does (as referred from video records). Thus, the subsurface jet carries warm water masses from shallow to deep part of the basin, i.e. warm stratified waters are carried into colder open area.

From analysis of Figure 2 a, b, one can conclude, that at the beginning of the experiment, the entire subsurface jet is located within the warm part of the tank and proceeded slower than 4°C -isotherm. The very nose of the jet is associated with the 4°C - isotherm at the water surface. At later stage (Figure 2 b) the leading edge of the jet is well behind the 4°C - isotherm (Demchenko, 2007).

Variation of the buoyancy flux

Since the main external factor, governing the fluid dynamics during the experiments, is a stabilizing and destabilizing buoyancy flux, consider its variation at the given point of the tank with time (Figure 3).

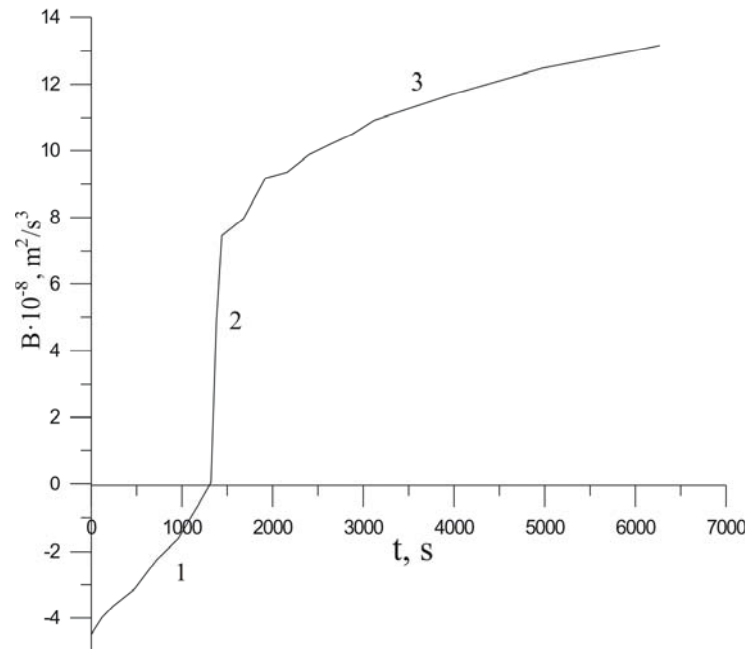


Figure 3. Variation of the buoyancy flux with time during the experiment in one of the points within subsurface layer. Heat flux is practically constant during the experiment. 1 – negative buoyancy flux, which is associated with the down-slope cascades phase; 2 – change of the buoyancy flux sign due to the passing though of the 4°C -isotherm; 3 – positive buoyancy flux, associated with the subsurface jet phase.

Where the temperature is below T_{md} , buoyancy flux under heating from above is destabilizing; it initiates vertical mixing and down-slope cascades, propagating along the bottom slope. In the vicinity of the T_{md} , the buoyancy flux becomes small. After the passing of the T_{md} , it sharply increases, being already a stabilizing factor. Analysis of video-records shows that this jump is associated with arrival of a subsurface jet to the point of the measurement.

Time rate of temperature rise change and horizontal temperature and density gradients in the presence of the T_{md}

Time rate of surface temperature rise in the experiment is presented on Figure 4. Before reaching 4°C strong fluctuations of temperature are observed, which arise due to intense vertical mixing; passing of the 4°C is manifested by the fastest surface temperature rise; and then time rate of surface temperature rise slowly increases.

Thus, as it was shown in the laboratory experiments, the 4°C is associated with the subsurface jet, but does not coincide with it. We may suggest that this faster advancement of temperature is supported by continued heating from above, while the development of real motions in viscous fluids has a certain time lag.

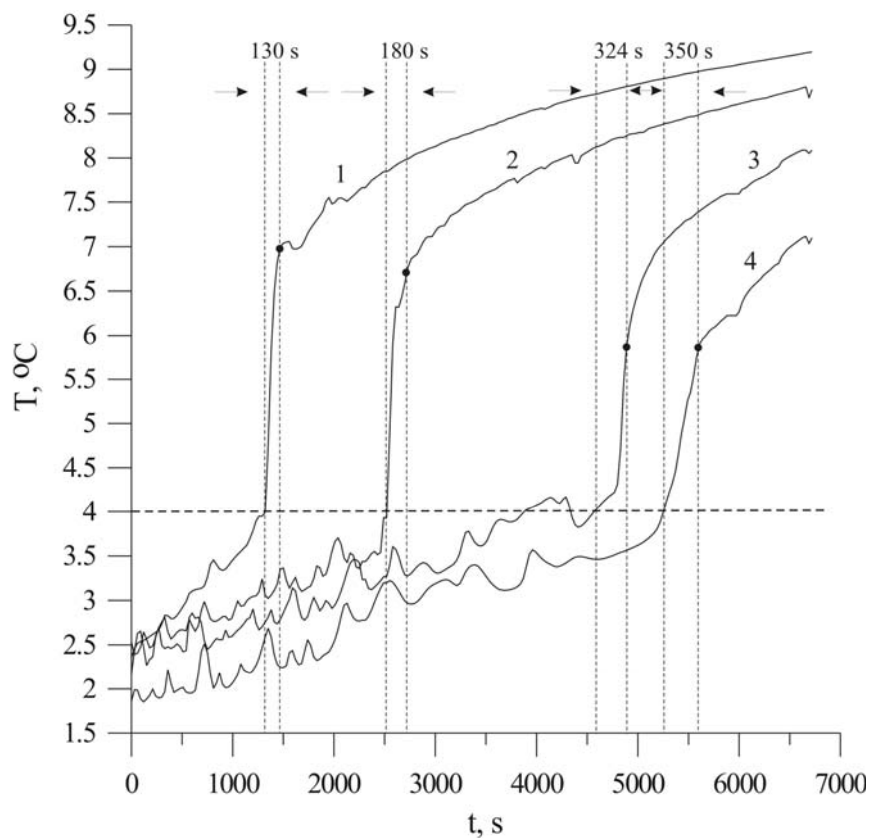


Figure 4. Increase of surface temperature with time for 4 locations along the laboratory tank (distances from the “shore line” are 55, 80, 138, 168 cm). Horizontal dashed line marks the T_{md} . Black points indicate the time, taken from video records, when subsurface jet reaches the location of the given thermistor. The lag between 4°C and subsurface jet appearance at the given point is from 130 to 350 s.

Variation of horizontal surface temperature gradient with time is presented in Figure 5a. At the moment when the T_{md} is registered by thermistor № 2, horizontal gradient between 1st and 2nd thermistors is as big as 15°C/m (stably stratified region) whilst between 2nd – 3rd thermistor – 3.7°C/m (unstably stratified region) (Figure 5a). In about 20 min after that, the same course is repeated by thermistors 3 and 4.

Variation of horizontal surface density gradients with time is presented in Figure 5b. At the moment when the T_{md} is registered by the thermistor № 2, horizontal density gradient between 1st and 2nd thermistors is as big as 0.5 kg/m³/m (stably stratified region) whilst between 2nd – 3rd thermistor – 0.03 kg/m³/m (unstably stratified region). In about 20 min, the same course is repeated by thermistors № 3 and № 4.

In general, horizontal temperature gradients in the stably stratified region are 3-8 times higher than that in the unstably stratified region; horizontal density gradients in the stably stratified region are 20-50 times higher than that in the unstably stratified region, what is in a good agreement with field observations in Ladoga Lake (Naumenko, 1989).

Joint analysis of video records and temperature measurements showed that, before reaching of 4°C by the given thermistor, horizontal temperature/density gradients are small. Intense temperature/density gradient fluctuations characterize vertical thermo-gravitational mixing in region with $T < T_{md}$.

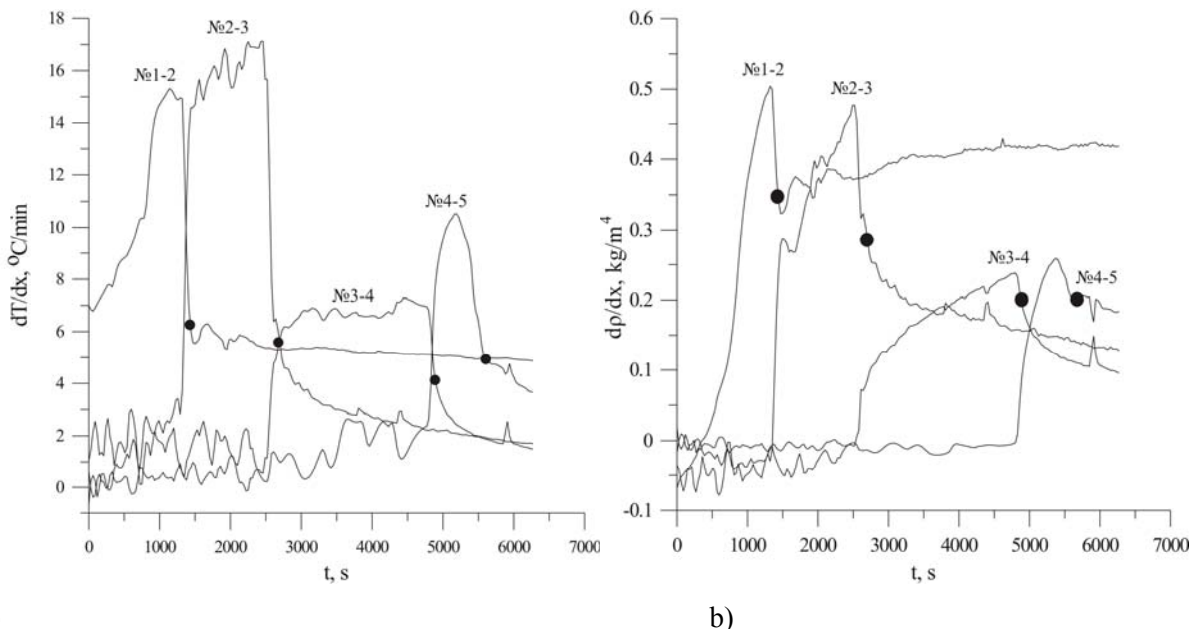


Figure 5. Variation of the horizontal temperature (a) and density gradients (b) between thermistor № 1 and № 2; № 2 and № 3; № 3 and № 4; № 4 and № 5. Black points indicate the time, taken from video records, when subsurface jet reaches the location of the given thermistor.

Horizontal temperature/density gradient jump occurs, when the subsurface jet approaches the location of the given thermistor, but does not yet reach it. With coming of active horizontal subsurface jet to the location of given thermistor, the horizontal temperature/density gradient decreases rapidly and becomes small (but do not vanish at all due to the permanent differential heating). At the same time the temperature/density gradient between the next pair of thermistors increases very quickly. The same course is repeated until the surface water

temperature in the entire basin overcomes the 4°C . So, we can conclude, that the high-gradient zone in field of density propagates faster than that of the dynamical front.

NUMERICAL SIMULATIONS

Numerical modeling of the spring thermal bar was performed using 3D non-hydrostatic MIKE3-FlowModel (DHI Water&Environment, www.dhi.dk/). The flow domain resembled the dimensions of the laboratory tank: 20 cm depth, 320 cm length, 200 cm-long bottom slope with aspect ratio of 0.1. Numerical grid has 80 x 20 cells in horizontal ($0.04 \text{ m} \times 0.04 \text{ m}$) and 20 layers (1 cm each) in vertical; time step of integration was 0.03 s. No wind friction was applied, and heating was modelled as turbulent heat exchange with warmer air.

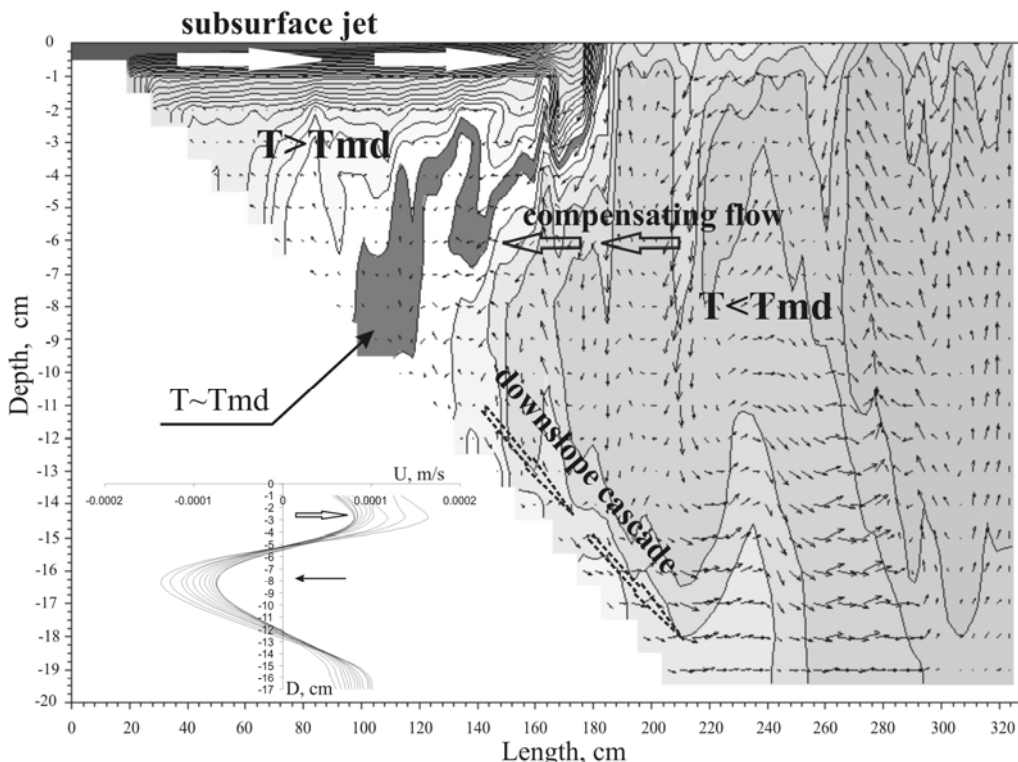


Figure 6. Vertical cross-section of simulated temperature and velocity fields for heating from the surface of an initially homogeneous layer from $T < T_{\text{md}}$. Isotherms are plotted every 0.058°C , and are omitted above 5°C (in the upper-most layer). Velocity vectors show vertical convection due to negative buoyancy flux from above in the entitle region with $T < T_{\text{md}}$. Variation of vertical profiles of horizontal velocity component with time at the position 182 cm off-shore is presented in insert: subsurface jet is marked by white arrow, compensating flow – by the black arrow.

Physical picture in numerical simulations looks quite alike as described on base of laboratory experiments. With the progressive heating, the water temperature over the slope reaches the 4°C (Figure 6) and the light subsurface jet propagates towards to the deep part, whilst the deeper layers are still involved in the down-slope cascades. Deep part of the domain is characterized by still intense vertical mixing. The remarkable feature is the presence of a compensating flow in the intermediate layer.

After the propagation of subsurface jet in the upper layer over the whole length of the tank, there still remain a water masses with $T < T_{\text{md}}$ below the warm upper layer, and down-slope

cascades continues there. It is very important feature for the dynamics in large deep water bodies (Baltic Sea, Ladoga, Onega, Baikal lakes), where spring heating goes the same way: the upper layer is heated above the T_{md} , whilst deeper layers are still below it. This means, that the cold lake interior is involved in down-slope cascading for a long time after the surface is heated above the T_{md} . This may be the reason of deep-water intrusions, reported in Lake Baikal by Wüest et al. (2005).

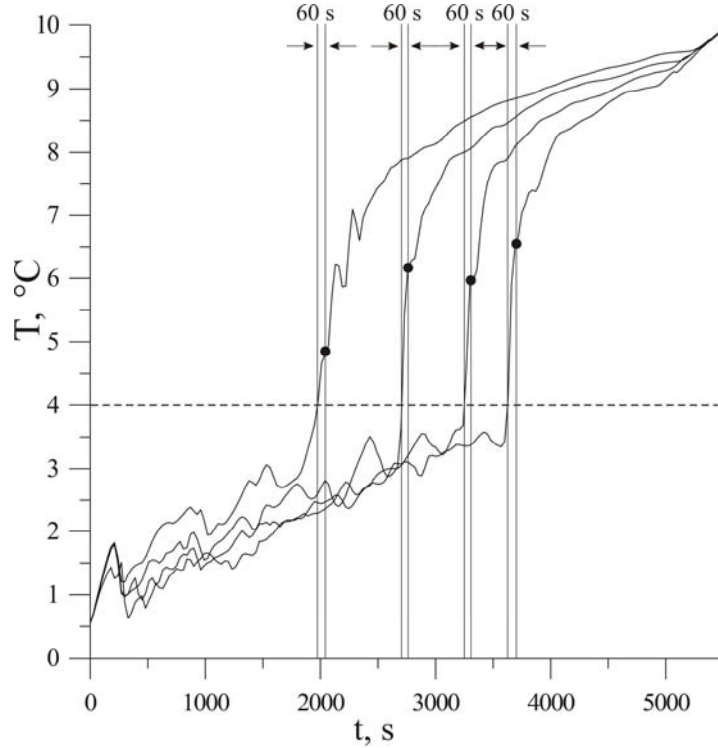


Figure 7. Increase of surface temperature with time for 4 locations along the numerical flume (distances from the shore line are 80, 120, 160, 200 cm). Black points indicate the time, taken from simulated velocity profile, when the sign of the flow velocity becomes positive.

Figure 7 reproduces numerical data in the same manner as Figure 4: surface temperature rise at different locations. Like in laboratory conditions, in the beginning of the process, quite strong fluctuations of the temperature are observed due to the intense vertical mixing before the T_{md} (supported solely by the heat-exchange with the warmer air). When the temperature reaches the 4°C , it increases rapidly, what is associated with the approaching of the subsurface jet. The temperature jump is followed by the velocity increase. Time lag between 4°C and the subsurface jet arrival is about 60 s.

CONCLUSIONS

Important outcome from our experiments is clear understanding, that the thermal bar cannot be considered alone, as just phenomenon/front, taking place in the vicinity of the T_{md} . Both under cooling and heating from above, approaching of the T_{md} begins from the phase of destabilizing surface buoyancy flux, which causes the formation of down-slope cascades over all sloping parts of the bottom. T_{md} appears first at shallow-most locations; however, this does not directly cause any motions: zero thermal expansion implies zero buoyancy flux for any heat supply. This way, horizontal density/pressure gradients have to grow larger, until they are significant enough to drive a surface jet formation. Along with the surface jet formation

and off-shore advancement, the down-sloping flow still exists in the deep part of the basin. Both surface and bottom off-shore flows must be compensated, and this causes the return flow towards to the shallow in intermediate layers, which is common for both deep and shallow regions, and supplies both the down-slope cascades in an unstably stratified region and the subsurface jet in a stably stratified one. Particularly important, that on the later stage of its development, the thermal bar intensifies the horizontal water exchange rather than restricts it.

Series of experiments showed that the passing of the 4°C is associated with the fast surface temperature jump, occurring because of the subsurface jet approaching the given point. However, the speed of propagation of 4°C-isotherm and speed of the jet do not coincide: the 4°C –isotherm propagates faster. So, the thermal bar front, understood earlier as a convergence zone near the 4°C-isotherm, is in fact associated with the leading edge of the subsurface jet.

ACKNOWLEDGEMENTS

The investigations are supported by grants RFBR-07-05-00850a, 09-05-00446 and RFBR-09-05-90740-mob_st.

REFERENCES

- Chubarenko, I.P., Demchenko, N.Yu. (2008). Laboratory modelling of horizontal water-exchange in a basin with sloping bottom while passing the temperature of maximum density, *Oceanology*, **48**(2), 1-14.
- Demchenko, N.Yu. (2007). On a speed of subsurface jet propagation in the presence of temperature of maximum density: Laboratory experiments, *Monog. Volume of Inst. Geophys PAN*, **E-7**(401), 81-87.
- Elliot, G.H., Elliot, J.A. (1970). Laboratory studies on the thermal bar. Proc. 13th Int. Conf. Great Lakes Res., 413-418.
- Elliot, G.H. (1971). A mathematical study of the thermal bar. Proc. 14th Int. Conf. Great Lakes Res., 545-554.
- Farrow D.E. (1995a). An asymptotic model for the hydrodynamics of the thermal bar. *J. Fluid. Mech.*, **289**, 129-140.
- Farrow D.E. (1995b). A numerical model for the hydrodynamics of the thermal bar. *J. Fluid. Mech.*, **303**, 279-295.
- Kreiman, K.D. (1989). Thermal bar based on laboratory experiments. *Oceanology*, **29**, 695-697.
- Likhoshway, Y.V., Kuzmina, A.Y., Potemkina, T.G., Potyemkin, V.L. & Shimaraev, M.N. (1996). The distribution of diatoms near a thermal bar in Lake Baykal. *J. Great Lakes Res.* **22**, 5-14.
- Mortimer, J. (2004). Lake Michigan in motion. University of Wisconsin Press, USA, 299.
- Naumenko, M.A., Karetnikov, S.G. (1998). On a speed of propagation of the thermal front in Lake Ladoga, *Meteorol. and Hydrol.*, (4), 107-115.
- Tikhomirov, A.I. (1982). Thermics of large lakes. Publishing house Nauka, Leningrad, 232.
- Wuest A, Ravens T., Granin N., Kocsis O., Schurter M., Sturm M. (2005) Cold intrusions in Lake Baikal: Direct observational evidence for deep-water renewal, *Limnol. And Oceanogr.*, **50**(1), 184-196.
- Zilitinkevich, S.S., Kreiman, K.D. & Terzhevik, A.Y. (1992). The thermal bar. *J. Fluid Mech.*, **236**, 22-47.

The dynamics of internal wave resonance in periodically forced lakes

L. Boegman^{1*} and G.N. Ivey²

¹ Department of Civil Engineering, Queen's University, Kingston, ON, K7L 3N6, Canada

² School of Environmental Systems Engineering, University of Western Australia, Crawley, WA, 6907, Australia

*Corresponding author, e-mail leon.boegman@civil.queensu.ca

KEYWORDS

Lake hydrodynamics, internal waves, turbulence and mixing, resonance, laboratory experiments.

INTRODUCTION

The periodicity in weather patterns creates over-lake wind fields that occur at regular frequencies. When the wind forcing frequency matches that of one of the natural frequencies of the basin-scale internal seiche modes, resonant amplification of the seiche will occur. Previous work has considered deep rectangular systems with $h_2/L \sim 1$, where h_2 is the hypolomnion thickness and L the basin length (Thorpe 1968), and a shallow circular domains with $h_e/L \sim 0.1$, where h_e is the equivalent depth (Wake et al. 2007). To understand the resonant response of long and shallow lakes and reservoirs ($h_e/L \sim 0.01$) is the objective of the present study. Details on this work can be found in Boegman & Ivey (2009).

METHODS

Laboratory experiments were conducted in a sealed rectangular acrylic tank ($L = 600$ cm, $H = 29$ cm and $B = 30$ cm) filled with a two-layer stratification of fresh and saline water. The system was subjected to periodic forcing, over a wide frequency range, along the longitudinal axis about a central pivot point using an eccentric crank and arm attached to an electric motor.

RESULTS, DISCUSSION AND CONCLUSIONS

The primary modal response is a horizontal mode one (H1) seiche at the same frequency (σ_f) as the forcing. The forcing amplitude and ratio of σ_f to the H1 internal seiche frequency (σ_1) governed the system response (Figure 1). For $\sigma_f > \sigma_1$, higher-mode internal seiches were observed; for $\sigma_f < \sigma_1$, a non-resonant forced H1 internal seiche was observed; and for $\sigma_f \rightarrow \sigma_1$, a resonant H1 internal seiche was observed. For the resonant regime, progressive nonlinear internal waves (NLIWs) formed upon the H1 seiche. Over the $0.8 < \sigma_f / \sigma_1 < 1.2$ bandwidth, resonant amplification also increases the nonlinear and dispersive energy flux to the internal surge and NLIWs, respectively. Under resonant conditions the H1 seiche, nonlinear surge and high-frequency NLIWs contain as much as 10, 2.5 and 3.5 times the energy introduced in the first (non-resonant) forcing cycle, respectively (Boegman & Ivey 2009). These results show that the phase and frequency of the wind forcing relative to the internal wave field must be considered when modelling mixing as a function of wind stress (e.g., using the Wedderburn and/or Lake Numbers) because the relative phase and frequency greatly influence the effectiveness of energy transfer from the wind to the internal modes.

When the NLIWs amplitudes were large, Kelvin-Helmholtz instabilities formed within the wave troughs leading to significant diapycnal mixing within the basin interior (Boegman & Ivey 2009). Resonant amplification was most pronounced for small forcing amplitudes (inverse Wedderburn number, $W^{-1} < 0.2$), because weakly forced waves have the most potential for growth prior to nonlinear energy flux to NLIWs and ultimate turbulent dissipation and mixing through Kelvin-Helmholtz instabilities that form within progressive NLIWs and boundary layers along the tank walls. This observation suggests that each mode has a maximum energy density that, when exceeded, leads to a nonlinear energy cascade. In agreement with field observations under similar forcing conditions, we find the mixing efficiency $0.03 < R_f < 0.18$ and diapycnal diffusivity $1.8 \times 10^{-5} < K_p < 1.2 \times 10^{-3} \text{ m}^2\text{s}^{-1}$ (Boegman & Ivey 2009).

The resonant wave response was modelled as a driven underdamped harmonic oscillator, where the damping coefficient was interpreted as the sum of mixing and dissipation. The results may be generalized to other systems by modelling the H1 seiche amplitude, R_f and K_p as a function of σ_f / σ_1 using the general equations for driven underdamped harmonic oscillators.

ACKNOWLEDGMENTS

The experiments were funded by the Australian Research Council (ARC). A draft of the paper was written while L.B. was visiting at the University of Western Australia under the support of the ARC and the Queen's University Principal's Development Fund (Category A-4).

REFERENCES

- Boegman, L., and Ivey, G.N. 2009. The dynamics of internal wave resonance in periodically forced lakes. *J. Fluid Mech.* (Submitted).
- Thorpe, S. A. 1968 On standing internal gravity waves of finite amplitude. *J. Fluid Mech.* 32, 489–528.
- Wake, G. W., Hopfinger, E. J. & Ivey, G. N. 2007 Experimental study on resonantly forced interfacial waves in a stratified circular cylindrical basin. *J. Fluid Mech.* 582, 203–222.

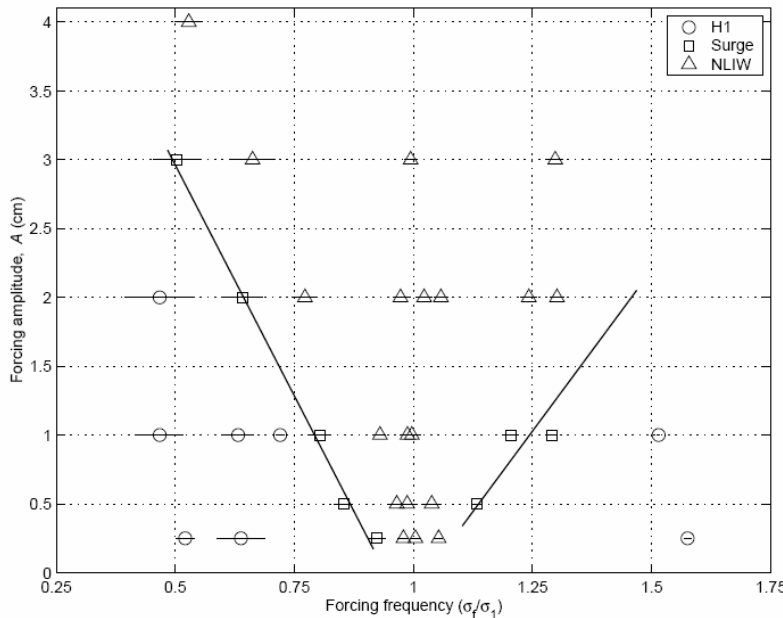


Figure 1. Regime diagram showing the dominant internal wave response under periodic forcing conditions. In all experiments: $h_1 = 8.7 \text{ cm}$, $h_2 = 20.3 \text{ cm}$, $\rho_1 = 1000 \text{ kgm}^{-3}$ and $\rho_2 = 1020 \text{ kgm}^{-3}$. The density difference between the upper and lower layers $\rho_2 - \rho_1 = 20 \text{ kgm}^{-3}$ ($\pm 2 \text{ kgm}^{-3}$), $c_o = 0.11 \text{ ms}^{-1}$, $g' = 0.20 \text{ Nkg}^{-1}$ and $T_i = 2L/c_o = 110 \text{ s}$.

Basin-scale internal waves in the bottom boundary layer of an ice-covered lake.

Georgiy Kirillin*, Christof Engelhardt and Sergey Golosov

Leibniz-Institute of Freshwater Ecology and Inland Fisheries, Berlin

*Corresponding author, e-mail kirillin@igb-berlin.de

ABSTRACT

Unusually cold winter of 2005/2006 in Germany has allowed us to perform high-resolution temperature measurements under ice cover in Lake Müggelsee. Intense seiche-like temperature oscillations developing just after the ice-on have been encountered in a thin water layer above the sediments. The weak density stratification under ice ensures long periods of the basin-scale internal wave, exceeding the inertial period for the lake latitude. Periods of the oscillations differ from theoretical estimations for simple internal gravity seiches, but agree well with theoretical periods for Kelvin-type inertia-gravity waves in a circular basin. The wave is initiated immediately after lake freezing by the release of the potential energy of the thermocline slope and exists for several weeks without external forcing. The rotational character provides long dissipation times of the wave. It allows oscillations to persist in lake during several weeks and longer, affecting biological activity in upper sediment layers. In contrast to ordinary seiches, the Kelvin wave energy is concentrated at the lateral boundaries that can result in essential lateral inhomogeneity of the bottom boundary mixing. Seiche-driven pore-water convection in upper sediments can strongly intensify release of the dissolved matter, such as nutrients, to the lake water. Existence of the basin-scale waves in the benthic boundary layer during several weeks after lake freezing suggests strongly variable external conditions for benthic communities and can play essential role in development of the winter hypolimnetic oxygen depletion.

KEYWORDS

winter limnology, seiches, Kelvin waves, pore convection, water-sediment boundary.

INTRODUCTION

There is still a lack of knowledge on temperature regime in the bottom boundary layer of ice-covered lakes. Existing studies on the water-sediments heat exchange, starting from the seminal work of Birge *et al.* (1927), were concerned mostly with estimation of the sediments contribution into the seasonal heat budget of lakes (Mortimer and Mackereth 1958; Pivovarov 1972; Petrov *et al.* 2006). The temperature regime in the bottom boundary layer is especially important during the ice-covered period. In contrast to the summer time, the layer is not only the energy sink but also one of the major energy sources for the lake body on account of the heat flux from the warmer sediments. The heat and mass exchange across the water-sediments boundary is also an important facet of lake ecology, since it sets up the initial conditions for the spring plankton development, such as nutrients content and bottom temperatures.

Motivated by this, a field study was performed on winter temperature evolution at the water-sediment interface in Lake Müggelsee. Six temperature loggers were installed inside the upper sediment and in the overlying water with vertical resolution of several centimeters. They

registered temperature with 10 seconds sampling time during the entire ice-covered period of 2005-2006 that allowed resolving short-period temperature dynamics overlying the seasonal course. The most outspoken temperature variability with quasi-periodical oscillations revealed itself in the first weeks of the ice-covered period. The apparent mechanism of this variability is a free basin-scale inertia-gravity wave traveling along the lake shore. The resulted temperature oscillations occasionally produced vertical density instability across the upper sediment. According to the estimations of the vertical heat transport, the instability was strong enough to produce vertical convective motions, which suggest significant effect on the dissolved matter exchange between sediment and lake water and can have far-reaching consequences for the ecological state of lakes under ice.

METHODS

Data on the temperature regime at the water-sediments boundary were collected during the winter 2005/2006 in shallow polymictic Lake Müggelsee (Fig. 1) located in Berlin, Germany (Driescher *et al.* 1993). The cold winter (mean air temperature in January was as low as -4.2°C compared to -0.35°C climatic mean for 1961-2002) resulted in the permanent ice cover at the lake surface from 31 December until 1 April 2006. The freezing had started on 31 December, when the first ice appeared at the lake shore, and the lake surface was completely frozen since 10 January 2006. The ice thickness achieved its maximum of 33cm in the beginning of February. During the ice-covered period the ice and snow thickness measurements were performed every 1-3 days.

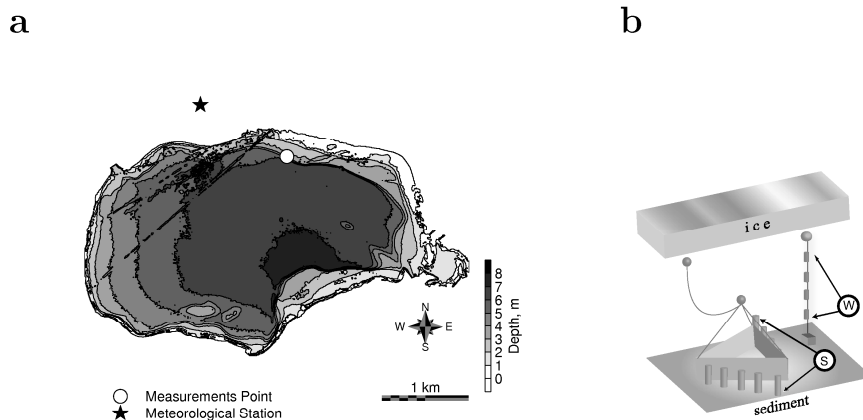


Figure 1. (a) Lake bathymetric map with location of the measurements site and meteorological station. Isobaths are drawn every 1 m. (b) Schematic drawing of the measurement platform installed in sediment (S) and thermistor chain in the water column (W).

The measuring platform (Fig. 1 b) was designed as an equilateral triangle constructed from three 1.25m long and 0.25m high L-bars. The concave sides of the L-bars were directed inside the platform, so that the faces of the L-bars formed the platform's bottom and sidewalls. Six temperature loggers (TR-1050, RBR Canada, accuracy 0.002°C) were attached to the outer faces of the platform's sidewalls with 2-4cm vertical indentation between temperature sensors. The platform was deployed on the lake bottom on 7 December 2005 at 5 m water depth and was withdrawn on 5 May 2006. Sidewalls of the platform were equipped with few stripes of two-sided adhesive film, so that after platform withdrawal the sediment particles remaining on

the film allowed to control depth and position of the platform inside the sediment. Additional information about vertical position of the platform relative to the water-sediments boundary was achieved from the presence/absence of turbulent fluctuations in the temperature records. Both estimations provided with following positions of temperature recorders with respect to the water-sediments boundary (positive upward): -8, -4, 0, 2, 6, and 10 cm. The instrumental error of the estimation did not exceed 1cm. That is, after deployment, the platform sunk into the sediment such that only three of six thermistors finally remained in water. Sinking continued during about two days after deployment; after that the position of the platform remained stable that was demonstrated by the unchanged position of the water-sediments boundary between the 3rd (0cm) and the 4th (2cm) loggers.

A thermistor string with the loggers of the same type was installed in the water column above the platform, registering temperatures at levels 2.5, 3.0, 3.5, 4.0, and 4.5 m above the sediments. The sampling time of all loggers was set to 10 s. The uppermost logger resided at 0.5 m depth below the water surface, where the effect of the logger heating by direct solar radiation is inconspicuous. Also, the RBR temperature loggers have white colored plastic casing, which minimizes the effect of the solar heating on the registered temperature. During periods of complete vertical mixing, temperature readings from the uppermost logger coincided with those from deeper water layers suggesting no essential measurement error was introduced by radiative heating of the logger case. Accompanying meteorological data were collected from the station of the Leibniz-Institute for Water Ecology and Inland Fisheries, located near the lake shore.

RESULTS AND ANALYSIS

Even though the ice cover efficiently isolated the lake water column from external forcing, such as air-lake heat fluxes and wind mixing, the winter temperature evolution at the water-sediment boundary demonstrated a wide spectrum of temporal variations. Figure 2 reproduces the temperature course within the upper sediments and in 10 cm of the overlying water with relation to dynamics of the ice and snow cover at the lake surface. The temperature evolution can be divided into several stages characterized by different governing frequencies and amplitudes of the temperature variability. These stages are closely connected to the variation of the ice and snow thickness on the lake surface. The first month of the ice-covered period (31 December to 24 January) is characterized by high-frequency oscillations of the temperature at the water-sediment interface (stage I in Fig. 2). These quasi-periodic oscillations with amplitudes up to 1°C are clearly expressed in the lower 10 cm layer above the sediment, whereas the most of the water column remains quiescent. Periodic character and localization in a thin interfacial layer suggest wave origin of the temperature variations. The oscillations were cancelled by the increase of the ice thickness associated with cold anticyclone passing over the lake. During one day on 24 January the atmospheric pressure raised rapidly to 1040 mbar and the air temperature decreased from +3°C to -19°C. As a result, the snow and the melting water lying over the primary ice formed a superimposed layer of non-elastic snow ice. The concurrency of the elasticity loss and ceasing of the near-bottom temperature oscillations indicates the linkage between the two phenomena and allows suggesting the near-bottom variations to be caused by oscillations of the ice cover. Afterwards (stages II and III in Fig. 2), no outspoken short-term temperature variability was observed in the water-sediments boundary layer. Small temperature variations exist in the upper part of the water column during the second stage (see Fig. 2 b), driven apparently by the solar heating under the ice. The gradual heating of the upper part of the water column by solar radiation penetrating the ice cover becomes a distinctive feature of the temperature evolution in the concluding phase of the ice-covered period (stage III in Fig. 2 a,b), ending up in the ice break up. Absorption of solar radiation under ice is the well-known heating mechanism in ice-

covered lakes in early spring. Increase of upper layer temperatures produced by it leads to vertical instability and results in vertical convective mixing (Farmer 1975; Mironov *et al.* 2002). The temperature record reveals slow heating of the water column and development of the vertical instability (cf. Fig. 2 a, the 2.5°C isotherm in the upper part of the water column, 2.5-4.0 m above the sediment) starting from the end of February. At the same time, convection remains relatively weak on account of snow cover preventing penetration of the solar radiation, such that weak thermal stratification still exists in the water column (Fig. 2 b, last three temperature profiles). The water column heating is followed by gradual temperature increase at the water-sediment interface. As soon as the snow cover disappears, convection develops much faster and reaches the lake bottom within days. To the moment of ice melting, the water column and the upper sediment have the uniform temperature close to that of the maximum density for fresh water.

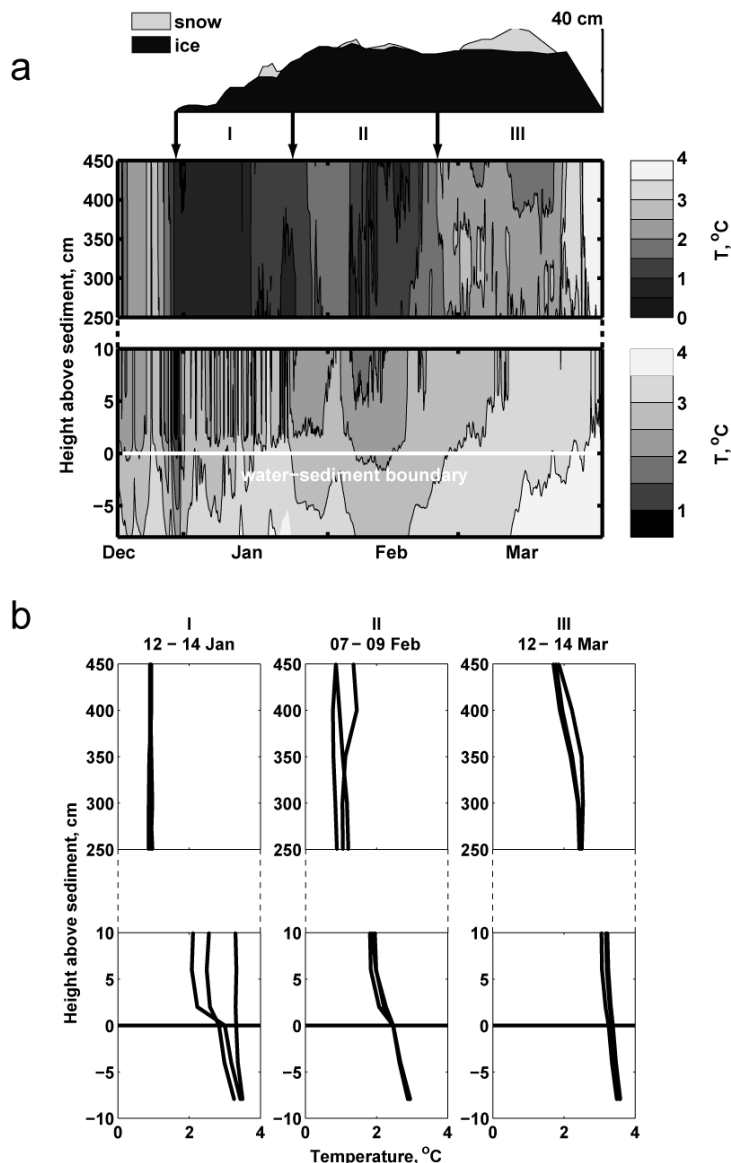


Figure 2. Temperature record at the water-sediments boundary and ice and snow cover thickness in Lake Müggelsee during the ice-covered period 2005-2006. (a) Isotherms map with three stages of the temperature development marked by roman numerals I, II and III. (b) Temperature profiles characteristic for each of three stages. Three profiles with daily time step are drawn for every stage.

Apart from the initial phase (stage I), the temperature evolution follows the typical seasonal course. Processes of the conductive heat release from sediments to water (stage II) and those of the radiative heating of the water column by penetrating solar radiation (stage III) are relatively well investigated (see Pivovarov 1972 on the first subject and Mironov *et al.* 2002 on the second one). There is, however, little knowledge about internal waves under lake ice, especially at synoptic time scales, i.e. with periods long enough compared to the inertial period. Therefore, we confine the following analysis with characteristics and possible mechanisms of internal waves variability during the stage I.

After freezing of the lake surface and developing of the temperature stratification in the sediments vicinity the quasi-periodic temperature oscillations emerged in the sediments vicinity (Fig. 3). The oscillations were not present in the well-mixed part of the water column that allows associating them with internal waves developing at the density interface between the cold layer occupying the bulk of the water column and warmer bottom boundary layer. Two periods, one about 24 hours and another of 11 hours can be distinguished in the oscillations. The fact that the periods are close to the diurnal time scales could suggest generation of the temperature oscillations by solar forcing, e.g. by means of the convective flow of the shallow warmer water along the bottom slope. However, the character of the temperature variations does not support such suggestion: they are close to purely harmonic oscillations without an appreciable trend in the mean temperature. The harmonic behavior and existence of more than one spectral peak in the oscillations indicate rather the wave origin of the motions. Such wave motions shall exist in form of basin-scale internal waves at the density interface between denser bottom water layers and the colder (and lighter) bulk of the overlying water, provided that some initial energy is lent to the wave, e.g. during the surface freezing. Both spectral peaks reside at frequencies close to the inertial frequency f (dotted vertical line in Fig. 3), implying an appreciable effect of the Earth rotation on the oscillations, i.e. the waves have geostrophic inertia-gravity character. One frequency is slightly higher and another one is slightly lower than the inertial frequency, revealing a typical picture of the splitting of the inertia-gravity waves into supercritical and subcritical modes propagating in opposite directions (Gill 1982).

In an infinite channel, the solution for the subcritical mode would result in the well-known Kelvin wave and that for the supercritical mode would be the Poincaré wave. There are several analytical solutions for the inertia-gravity waves in enclosed basins, among them is the classical Lamb's (1932) solution for the long surface waves in a circular lake of constant depth, extended by Csanady (1967) on the case of internal basin-scale waves. The inertial wave frequencies ω in the solution are the functions of the Burger Number

$$S = C(fL)^{-1}, \quad (1)$$

where,

$$C = (gh_{eq}\Delta\rho/\rho_0)^{1/2}, \quad (2)$$

is the phase speed of the planar wave, h_{eq} is the equivalent depth defined as $(H-h)hH^{-1}$. The characteristic lateral length scale L is represented by the radius of the circular basin. The frequencies $\omega(S)$ are found as solutions of the transcendental equations,

$$\begin{aligned} \phi I'_n(\phi) + \sigma^{-1} n I_n(\phi) &= 0 \quad \text{at} \quad \sigma < 1 \\ \phi J'_n(\phi) + \sigma^{-1} n J_n(\phi) &= 0 \quad \text{at} \quad \sigma > 1 \end{aligned} \quad (3)$$

where,

$\sigma = \omega f^{-1}$; $\phi = S^{-1} |1 - \sigma^2|^{1/2}$, J_n , I_n are the Bessel function and the modified Bessel function of order n , correspondingly. The solution for the subcritical ($\sigma < 1$) Kelvin-type, and that for the supercritical ($\sigma > 1$) Poincaré-type wave differ only by replacing the modified Bessel function

I_n with the Bessel function J_n , n being the azimuthal mode of the wave. That is, any stratification/rotation ratio (expressed by the Burger Number S) is associated with an exact pair of wave frequencies. If the two frequencies corresponding to the spectral peaks (Fig. 3) are due to free basin-scale oscillations then their substitution in Eqs. (3) should provide with the same value of S .

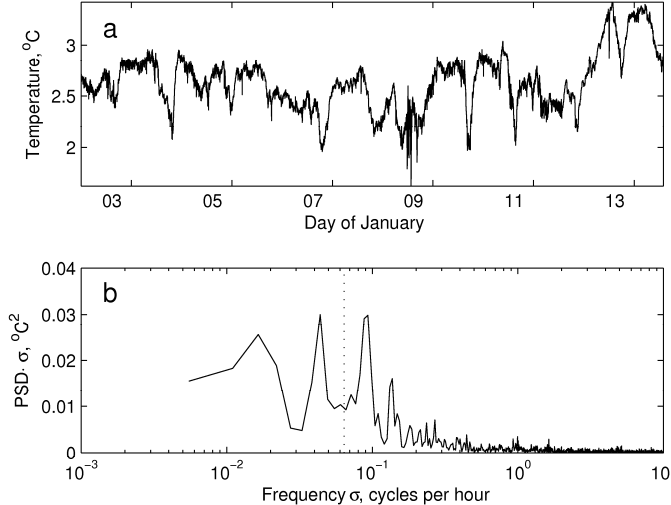


Figure 3. (a) Temperature at the water-sediment boundary after lake freezing and (b) its normalized power spectral density (PSD) estimation. The dotted line in the panel b marks the inertial frequency.

Some uncertainty can be expected on account of the departure of the lake shape from the circular one, the irregular lake topography and the internal friction. More accurate estimation can be achieved by using analytical solutions for waves in basins of elliptic form (Jeffreys 1925; Goldstein 1929; Antenucci and Imberger 2001), which approximates the real shape of Lake Müggelsee better than a circle. In this case, the expressions for the wave frequencies are similar to (3) but involve the elliptic Mathieu functions instead of the Bessel functions J_n , and I_n . We utilize the tabulated form of solution for an elliptic lake with aspect ratio 2:3, provided by Antenucci and Imberger (2001) in form of the polynomial approximations $\omega(S)$. Resolving the inverse problem $S(\omega)$ in graphical form (Fig. 4 a) yields the values $S = 0.42$ and $S = 0.35$ for the observed frequencies 0.04 and 0.10 cph. The two Burger Number estimations are really close to each other and, taking into account simplifications underlying the analytical solution, can be assumed to represent the same value $S \approx 0.4$. Thus, the inverse problem solution $S(\omega)$ for the two frequency values validates the suggestion about the wave origin of the temperature oscillations.

In addition, the achieved Burger Number allows estimating the planar wave phase speed C directly from Eq. (1), without estimating h_{eq} from the vertical density profile. An additional parameter arising here is the lateral length scale L , which is the half-length of the lake ellipse major axis. The density interface could be approximately located in the depths range between 2.0 m and 4.0 m, then the value of L derived from 2-4 m isobaths amounts at 1000 ± 200 m (Fig. 1 a). This yields the Rossby radius

$$R = f^{-1} C = S L \approx 400 \text{ m}, \quad (4)$$

which corresponds to the phase speeds C of about 0.02 to 0.04 ms^{-1} .

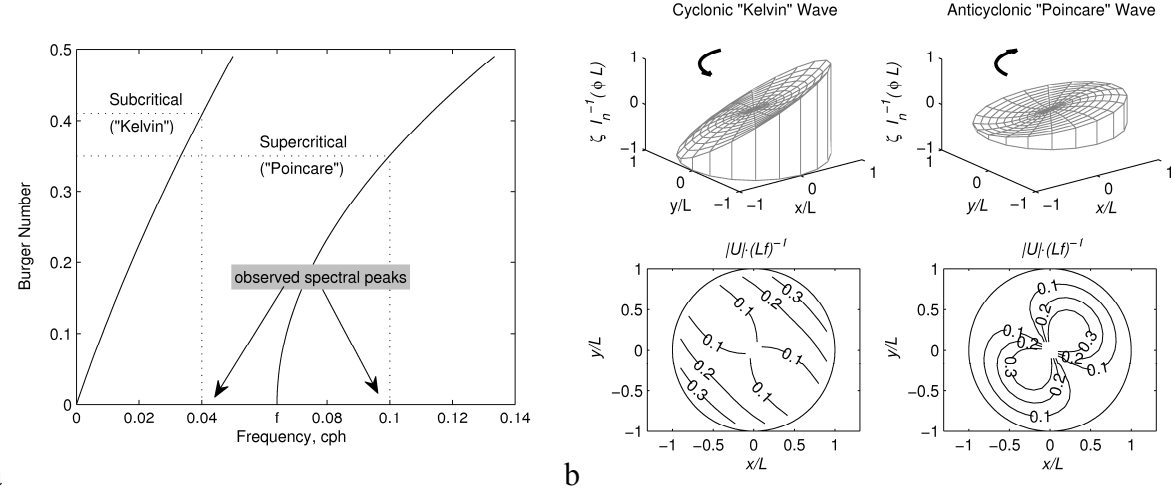


Figure 4. (a) The wave frequency vs. Burger Number diagram for analytical rotational waves in an elliptic lake of 2:3 aspect ratio. Observed spectral peaks from Fig. 3 and corresponding Burger Numbers are marked with dotted lines; f stands for the inertial frequency. (b) Dimensionless surface elevations and velocity fields for subcritical (cyclonic) and supercritical (anticyclonic) waves of the gravest mode in a circular basin with Burger Number 0.4.

The geostrophic character of the internal basin-scale oscillations has important consequences for the lake dynamics under ice. The distinctive feature of the Kelvin wave is the exponential decrease of the wave amplitude and, as a result, of the orbital velocities from the boundary to the basin interior. The Rossby radius (4) represents the e-folding scale of the Kelvin wave amplitude and can be interpreted as the width of the lake bottom area in the vicinity of the density interface, where the wave-driven currents are concentrated. In this sense, the Kelvin wave should more strongly affect the water-sediment exchange at the bottom slope, than the Poincaré wave, which produces water movements mostly in the middle of the lake. The distribution of the wave characteristics across the lake can be illustrated based on the solution for the circular basin; the picture produced by the elliptical solution would be essentially the same. The wave surface is described in polar coordinates by the following relations

$$\zeta_{m,n} = \begin{cases} J_n(r_*\phi) \cos(m\theta + f\sigma t) \\ I_n(r_*\phi) \cos(m\theta + f\sigma t), \end{cases} \quad (5)$$

where m, n are the radial and azimuthal mode, correspondingly, $r_* = rL^{-1} \in [0..1]$ is the dimensionless radius-vector, $\theta \in [0..2\pi]$ is the azimuthal angle, other notations are the same as in (7). The velocity field for the Poincaré wave is given by

$$\frac{U^r}{fL} = -[\sigma\phi^{-1}J_{n-1}(r_*\phi) - nr_*^{-1}\phi^{-2}|\sigma-1|J_n(r_*\phi)] \sin(m\theta + f\sigma t),$$

$$\frac{U^\theta}{fL} = -[\phi^{-1}J_{n-1}(r_*\phi) + nr_*^{-1}\phi^{-2}|\sigma-1|J_n(r_*\phi)] \cos(m\theta + f\sigma t). \quad (6)$$

Replacing J_n by I_n in Eqs. (6) yields the velocity expressions for the Kelvin wave. The characteristic wave shapes and velocity distributions are achieved by substituting of the value $S = 0.4$ into Eqs. (5)-(6) (see Fig. 4 b). Here, as above, we confine us with the gravest wave modes $m = n = 1$. The surface elevation for the Kelvin wave is almost an order of magnitude higher than that of the Poincaré wave and has its maximum at the side boundary, represented in the real lake by the bottom slope. The speeds of the Kelvin wave are also maximal at the side walls, whereas Poincaré speeds at the boundaries are close to zero. Thus, currents produced by the Kelvin wave can essentially contribute to the shear turbulence and

resuspension in the near-shore areas of the lake. The temperature oscillations at the water-sediments boundary are produced by both waves, whereas the effect of the Kelvin wave on temperatures at the bottom slope is much stronger.

It is known that introducing of rotation changes the ratio between the potential and the kinetic energy in waves (Gill 1982) in favor of the potential energy. As a result, the waves have longer dissipation time scales than the simple seiches. Antenucci and Imberger (2001) have estimated the dissipation times for Kelvin-type waves in an elliptic basin to amount at one week based on values for stratification and bottom boundary kinetic energy dissipation typical for Lake Kinneret, Israel. In our case, no information exists that would allow estimation the energy loss due to bottom boundary mixing. In our case, the spatial dimensions of the wave are much smaller than in Lake Kinneret, but the wave speeds are much slower, that allows assuming the dissipation time scales to be comparable to those reported by Antenucci and Imberger. This assumption explains the wave existence during the beginning phase of the ice-covered period without apparent strong external forcing: the bulk of the energy was provided to the wave during the lake freezing by the release of the density interface, when the lake was isolated from the wind stress by the ice cover. However, additional energy feeding of the waves by occasional wind disturbances of the ice surface cannot be a priori excluded from consideration. In basin-scale baroclinic wave motions, the oscillations of the density interface are balanced by the counterphase oscillations of the free surface (see Gill 1982).

The amplitude of the free surface oscillations can be estimated based on the observed density gradient at the interface $\Delta\rho/\rho$, as

$$\frac{\Delta\zeta}{\Delta\eta} = \frac{h}{H} \frac{\Delta\rho}{\rho_0}. \quad (9)$$

Assuming the density gradient $\Delta\rho/\rho = 7 \cdot 10^{-5}$ and the amplitude of the internal wave $\Delta\eta \approx h \approx 1\text{m}$, Eq. 5 yields very small value of 0.1mm for the surface oscillations amplitude $\Delta\zeta$. Disturbances with such small amplitudes can be easily provided by wind variations over the young elastic ice surface and would maintain the wave motions in the bottom boundary layer. Neither the snowfall on 17 Jan 2006, nor the subsequent melting of snow during 20-22 Jan 2006 have affected the oscillations in the bottom boundary layer. The fact that the alteration of the amount of radiation under ice by the snowfall did not affect the temperature oscillations supports our previous suggestion that the oscillations are not connected to the diurnal cycle of solar heating. The oscillations were suddenly cancelled by freezing of melted water over the ice and by increase of ice thickness on 24 Jan 2006. An obvious explanation for it is the ceasing of the surface oscillations at the new non-elastic and thick ice surface followed by damping of the oscillations at the density interface (as soon as $\Delta\eta = 0$ if $\Delta\zeta = 0$, see Chapter 6.3 of Gill (1982) for detailed discussion).

DISCUSSION AND CONCLUSIONS

There are only few studies dedicated to internal basin-scale motions under ice. Perhaps the first assumption on existence of the long-period internal seiches under ice was made by Sir George Darwin and was reported later by Murray (1911). Observed pressure oscillations under the ice of the McMurdo Sound, Antarctica exhibited periods about 3 days and were ascribed by Darwin to internal “seiches”. It is obvious, however, that such long periods would involve rotational effects and the oscillations were, in all likelihood, generated by an inertia-gravity Kelvin-type wave, traveling around the McMurdo Sound. Several studies have recently reported excitation of short-period external (barotropic) seiches in ice-covered lakes forced by wind-induced oscillations of the ice surface (Bengtsson 1996; Malm *et al.* 1998; Petrov *et al.* 2007) and only a couple of studies presented the evidence of the baroclinic basin-scale motions (Kenney 1996; Baer and Degrandpre 2002; Petrov *et al.* 2006). In the latter two

studies internal oscillations were reported with periods of about one week and one month, correspondingly, i.e. at time scales suggesting noticeable effect of the earth rotation.

To our knowledge, this study is the first attempt to consider basin-scale oscillations in ice-covered lakes in context of the geostrophic balance. The fact that the Coriolis force changes characteristics of the basin-scale internal waves has important consequences for energy and mass transport under ice. Thus, localization of the wave currents at bottom slopes in near-shore areas increases bottom shear mixing, which can impact the exchange by dissolved matter between sediments and water column that is important for the internal nutrients loading into the lake. Appreciable effect of seiching on the water-sediments gas exchange has been reported by Baer and Degrandpre (2002). Seiche-driven temperature variations in the upper sediments can affect sediments microbiology, and, as a result, the sediments oxygen demand. The latter is the main process governing development of the oxygen deficit under ice, the phenomenon affecting the plankton dynamics in winter and early spring, and resulting, under certain conditions, in winter fish kills (Golosov *et al.* 2007). Several short periods of convection developed immediately after “switching off” of the wind, which released the deflected interface surface. Although no convection was revealed at the measurement point during the subsequent Kelvin wave oscillations, it could potentially develop at the shallower part of the bottom slope, where the wave-driven temperature oscillations have higher amplitudes. Pore-water convection driven by advection of warmer water over colder sediment can have far-reaching consequences for the ecological state of lakes under ice, such as enrichment of the water column by dissolved nutrients (Lappalainen 1982). The quantitative effect of the water-sediments convective mass exchange on lakewide scales is still poorly investigated and needs additional information on biogeochemical interactions in the upper sediments.

ACKNOWLEDGEMENTS

This study is the part of the research project “Climatic impact on temperature and mixing regime of polymictic lakes and its consequences for lake ecosystems” performed in frames of the priority program AQUASHIFT of the German Science Foundation (DFG, project KI-853-3/1). Partial financial support was provided by the NATO collaborative linkage grant, ref. ESP.NR.NRCLG 982964.

REFERENCES

- Antenucci JP, Imberger J (2001) Energetics of long internal gravity waves in large lakes. Limnol Oceanogr 46:1760-1773
- Baer MM, Degrandpre MD (2002) Under-ice CO₂ and O₂ variability in a freshwater lake. Biogeochemistry 61:95-113
- Bengtsson L (1996) Mixing in ice-covered lakes. Hydrobiologia 322:91-97
- Birge EA, Juday C, March HW (1927) The temperature of the bottom deposits of Lake Mendota; A chapter in the heat exchanges of the lake. Trans Wisconsin Acad Sci 23:189-231
- Csanady GT (1967) Large-scale motion in the Great Lakes. J Geophys Res 72:4151–4162
- Driescher E, Behrendt H, Schellenberger G, Stellmacher R (1993) Lake Müggelsee and its environment – natural conditions and anthropogenic impact. Int Rev ges Hydrobiol 78:327-343
- Farmer DM (1975) Penetrative convection in the absence of mean shear. Quat J Roy Met Soc 101:869-891
- Gill AE (1982) Atmosphere-Ocean dynamics. Academic, NY
- Goldstein S (1929) Tidal motion in rotating elliptic basins of constant depth. Monthly Notices R Astron Soc (Geophys Supp) 2:213-231
- Golosov S, Maher OA, Schipunova E, Terzhevik A, Zdorovenko G, Kirillin G (2007) Physical background of the development of oxygen depletion in ice-covered lakes. Oecologia, 151, doi: 10.1007/s00442-006-0543-8
- Jeffreys H (1925) The free oscillations of water in an elliptical lake. Proc Lond Math Soc 23:455-476
- Kenney BC (1996) Physical limnological processes under ice. Hydrobiologia 322:85-90
- Lamb H (1932) Hydrodynamics. Cambridge University Press, Cambridge

- Lappalainen,KM (1982) Convection in bottom sediments and its role in material exchange between water and sediments. *Hydrobiologia* 86:105–108.
- Malm J, Bengtsson L, Terzhevik A, Boyarinov P, Glinsky A, Palshin N and Petrov M (1998) A field study on currents in a shallow, ice-covered lake. *Limnol Oceanogr* 43:1669–1679
- Mironov D, Terzhevik A, Kirillin G, Jonas T, Malm J and Farmer D (2002) Radiatively-driven convection in ice-covered lakes: observations, scaling and mixed layer model. *J Geophys Res.* Doi: 10.1029/2001JC000892
- Mortimer CH and Mackereth FJH (1958) Convection and its consequences in ice-covered lakes. *Verh Int Ver Limnol* 13:923–932
- Murray J (1911) The observation of tides and seiches in frozen seas. *Rev ges Hydrobiol Hydrogr* 4:129–135
- Petrov MP, Terzhevik AYu, Zdorovennov RE, Zdorovennova GE (2006) The thermal structure of a shallow lake in early winter. *Water Res* 33:135–143
- Petrov MP, Terzhevik AYu, Zdorovennov RE, Zdorovennova GE (2007) Motion of water in an ice-covered shallow lake. *Water Res.* Doi: 10.1134/S0097807807020017
- Pivovarov AA (1972) Thermal conditions in freezing lakes and rivers, Wiley, NY

The physical control of the size structure of the phytoplankton community in a Mediterranean reservoir

A. B. Hoyer^{1*}, P.I. León-Díaz, J. M. Blanco², J. Rodríguez², F. Jiménez-Gómez³, C. Escot⁴ and F. J. Rueda^{1,5}

¹ Instituto del Agua, Universidad de Granada, C- Ramón y Cajal 4, 18071 Granada, Spain

² Departamento de Ecología y Geología, Universidad de Málaga, Campus Universitario de Teatinos, 29071 Málaga, Spain

³ Departamento de Biología Animal, Biología Vegetal y Ecología, Universidad de Jaén, Spain

⁴ Empresa Metropolitana de Abastecimiento y Saneamiento de Aguas de Sevilla, S. A., EMASESA, C- Escuela Pías 1, 41003 Sevilla, Spain

⁵ Departamento de Ingeniería Civil, Universidad de Granada, Spain

*Corresponding author, e-mail abhoyer@ugr.es

ABSTRACT

The size structure of planktonic organisms in the ocean has been shown to be controlled by circulation patterns and, especially, by the vertical velocity fields associated to these patterns. At a spatial scale of few meters, the combination of rising and sinking water motions within the surface mixed layer, driven by the Langmuir circulation is considered to be responsible for the accumulation of organisms of positive or negative buoyancy, which is a characteristic that is linked to cell size. More recently, Rodriguez et al. (2001) proposed an empirical model that links the magnitude of the vertical velocity with characteristics of the size spectrum of phytoplankton in meso-scale eddies. In lakes and reservoirs, the relationship between circulation and mixing processes and the size structure of the phytoplankton is an aspect that, as far as we know, has still not been sufficiently investigated. This lack of information is partially based on the fact that water motions in these systems tend to be complex and difficult to establish due to their limited dimensions. This work studies the size structure of the phytoplankton community under a variety of hydraulic and meteorological forcing scenarios and analyzes the control exerted by the physical processes on the plankton size structure, through computers simulations using a three-dimensional hydrodynamic and transport model.

KEYWORDS

Phytoplankton size structure, vertical water velocity, Mediterranean reservoir

INTRODUCTION

It is widely accepted in the scientific community that the abundance c and size S of phytoplankton cells are related: the larger the cells, the less abundant they are in the aquatic environment. This relationship between abundance and size of algal cells is referred to as size structure and characterizes the phytoplankton community living under any given environmental conditions in an ecosystem. The graphical representation of number of phytoplankton cells or abundance as a function of their size S (either in terms of mass, biovolume S or equivalent diameter D) is the size spectrum. When plotted in log-log scale, the size spectrum is linear with a slope θ equal to -1 (Sheldon et al. 1972, Rodríguez et al. 2001, León-Díaz 2004). The reasons behind that behaviour are mainly physiological, so that there is the same biomass in form of large cells than in the form of small cells. However, this behaviour is exhibited only in ecosystems where environmental conditions are extremely stable. In environments that are subject to perturbations the theoretical size spectrum is modified and does not exhibit the -1 slope. These changes in the spectrum occur as a consequence of phytoplankton cells of varying size responding differently to changes in the environmental conditions. The size structure of planktonic organisms in the ocean, for example, is determined by circulation patterns and, especially, by the vertical velocity fields associated to this pattern. At a spatial scale of few meters, the combination of ascending and descending water motions in the surface mixed layer associated to Langmuir circulations is considered to be responsible for the accumulation of organisms of positive or negative buoyancy, a characteristic linked to cell size (Smayda 1970). At a larger scale, Semina (1968) already proposed that the mean diameter of the organisms was higher in oceanic regions affected by slightly ascending and descending motions, and smaller in regions where vertical motions are more intense. Observation on the size distribution of fractionate chlorophyll in the equatorial region of the Pacific are more correctly interpreted in terms of circulation (equatorial ascendance and horizontal transport) than in terms of nutrient effects (Peña et al. 1990). Rodríguez et al. (2001) analyzed a large observational data base collected in the Mediterranean under different conditions and demonstrated that the slope of phytoplankton size spectrum was determined by the magnitude of the vertical (ascending and descending) velocities in mesoscale frontal structures. León-Díaz (2004) arrived at those same conclusions through numerical experiments conducted in domains of horizontal and vertical dimensions characteristics of ocean environments. In lakes and reservoirs, the physical control of phytoplankton size structure, however, is an aspect that, as far as we know, has still not been sufficiently investigated. Our general goal is to study the size structure of phytoplankton communities that develop in reservoirs, determining the shape of the size spectrum of such communities and the physical drivers controlling the form of those spectra. In this work, in particular, we hypothesize that vertical velocities associated to wind-driven residual circulation in lakes may induce spatial differences in the size spectrum, depending on the horizontal position where it is determined.

METHODS

Our analysis is based on simulations of transport and mixing processes affecting algal cells in a test basin of rectangular shape. The length and maximum depth of the basin were set to 8000 and 30 m, respectively, which are considered typical of small to medium reservoirs existing in the Mediterranean. These dimensions, in particular, apply to the basin of El Gergal reservoir in southern Spain. The space-time changes in abundance c (expressed as number of cells per unit volume) experienced by phytoplankton cells was modeled with the reactive transport equation

$$\frac{\partial c}{\partial t} + \frac{\partial u c}{\partial x} + \frac{\partial v c}{\partial y} + \frac{\partial(w - w_s)c}{\partial z} = \frac{\partial}{\partial x} \left(K_x \frac{\partial c}{\partial x} \right) + \frac{\partial}{\partial y} \left(K_y \frac{\partial c}{\partial y} \right) + \frac{\partial}{\partial z} \left(K_z \frac{\partial c}{\partial z} \right) + \Phi \quad (1)$$

where, u , v , w are the velocity components of the currents in the x, y and z- direction, w_s is the settling velocity, c is concentration of algal cells, K_x , K_y , K_z represent the diffusion coefficient induced by turbulent motions, and Φ is a source-sink term accounting for phytoplankton growth. Phytoplankton growth is represented using a first order model, i.e.

$$\Phi = r_{\max} f(z)c \quad (2)$$

where r_{\max} is the maximum growth rate, and the function $f(d)$ accounts for differences in growth rates occurring at different depth d . León-Díaz (2004) used a depth function of the form

$$f(d) = e^{-\left(\frac{d-A}{B}\right)^2} \quad (3)$$

where A (depth of maximal growth) and B (width of function) were constants, set equal to 45 and 20, respectively. In our experiments we will use $A=9$, equal to the depth of the seasonal thermocline, and $B=6$. Equation 1 was solved for different algal groups varying in cell size (Table 1).The size spectrum at any time and spatial location can be determined from the model results by representing the concentration of algal cells pertaining to phytoplankton group i , c_i , as a function of cell volume S_i or equivalent diameter D_i . Differences in abundance between groups arise as a result of the dependence of r_{\max} and w_s on the cell volume S (Table 2). This dependence was presumed to follow the model proposed by León-Díaz and Blanco (2009),

$$r_{\max}(D) = 4.4D^{-0.45} \quad (4.1)$$

$$r_{\max}(S) = 4.0S^{-0.15} \quad (4.2)$$

$$w(D) = 0.023D^{1.16} \quad (5.1)$$

$$w(S) = 0.029S^{0.39} \quad (5.2)$$

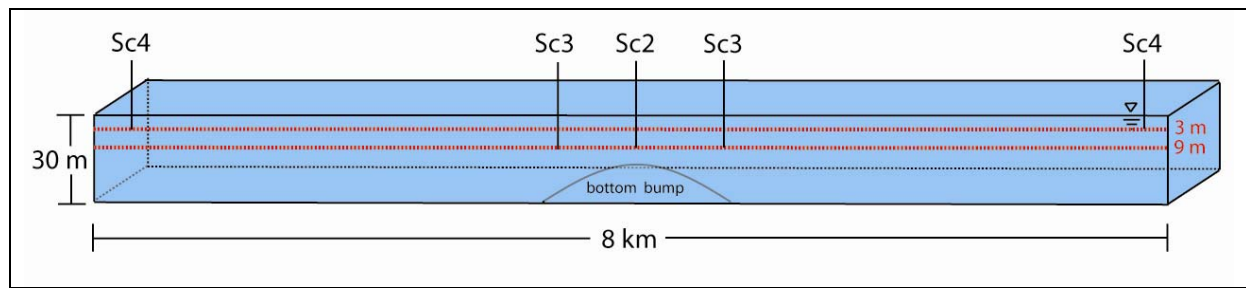
Table 1. Diameters and volumes of algal cells for ten phytoplankton groups, used in our simulations.

Diameter (μm)	Volume (μm^3)	Size group (μm^3)
2	4.2	4
3	14.1	8
5	65.5	64
8	268.1	256
12	904.8	512
20	4188.8	4096
30	14137.2	8192
48	57905.8	32768
76	229849.3	131072
120	904786.9	524288

Table 2. Values/ranges and units of model parameters.

Parameter	Value/Range	Unit
Length x-domain	20	m
Length y-domain	8000	m
Length z-domain	30	m
Time period	10	d
dx	10	m
dy	10	m
Bottom slope	5E-06	-
dz	0.5	m
dt	5	s
Growth rate r_{max}	0.5-3.2	d^{-1}
Settling velocity w	0.05-6.10	md^{-1}
Depth of maximal growth A	9	-
Width of function B	6	-

Numerical solver – Velocity, diffusivity and algal concentration fields were simulated with a three-dimensional (3-D) free surface hydrodynamic and transport model (Smith 2006). The hydrodynamic model has been extensively validated both against analytical solutions and field data (Rueda and Cowen 2005b and references therein). The model is based on the continuity equation for incompressible fluids, the Reynolds-averaged form of the Navier-Stokes equations for momentum, the transport equation for active scalars, and an equation of state relating the concentration of active scalars to fluid density. The governing equations are solved in layer-averaged form using a semi-implicit, three-level, iterative leapfrog-trapezoidal finite difference scheme on a staggered Cartesian grid. Turbulent mixing is represented in the 3-D model using diffusion-like terms. A Laplacian operator with constant mixing coefficients (horizontal eddy viscosity K_z or diffusivity D_h) is used in the model to represent horizontal mixing of momentum and scalars (see below). The quasi-equilibrium turbulent energy model of Galperin et al. (1988), based on the Mellor and Yamada level 2.5 turbulence closure (Mellor and Yamada, 1974) and modified by Kantha and Clayson (1994), is used to calculate vertical turbulent mixing coefficients K_z and A_z . The discrete forms of the two governing equations existing in the turbulence sub-model, one for turbulent kinetic energy and another for an eddy length scale, are only solved during the first iteration during each time step (see Rueda et al. 2005). It is from the estimates of turbulent kinetic energy and length scales that K_z is calculated. Equations (1) through (4) were solved using a two-level semi-implicit scheme, in which only vertical diffusion is discretized implicitly. The advective fluxes in the transport equations are calculated using flux-limiter methods (Durran 1999): the fluxes at the cell faces are constructed with the monotone upstream differencing scheme and the Lax-Wendroff second-order method, using the Roe-superbee limiter (Fringer et al. 2005).

**Figure 1.** Sketch of computational domain with location of data output for scenarios 2-4.

Model setup - The three-dimensional model was set to simulate the space-time changes in the size spectrum occurring as a result of different forcings in our test basin. All algal groups i ($i = 1, N$) were presumed to be uniformly distributed and all had the same concentration ($c_i = 1$, for all i) at the start of the simulations. A period of time of 10 days was simulated in all cases. Four scenarios were simulated with different forcing. In the first scenario, the basin was not subject to any external perturbation and, in consequence, any changes in algal concentrations will be the result of settling and growth (i.e. neglecting advection and diffusion). In this scenario, there are no variations in the horizontal direction and the solution of the 3D model was checked, using a solver coded in Matlab® of the one-dimensional form of Eq. 1, which neglects all advective and diffusive motions. In scenario 2, the bottom of the basin was tilted, with a bottom slope set equal to 5×10^{-6} . In scenario 3, water motion was forced by tilting the lake bottom (as in Scenario 2). In this case, though. The lake bottom was not flat but had a Gaussian bump in the center of the domain, so that water could move up and down within the domain. Both in scenarios 2 and 3, zero-gradient boundary conditions were set on both ends of the domain, in the solution of the reactive transport equation. A fourth scenario was simulated, in which the domain was assumed closed. This scenario represents the case of a lake or a reservoir during periods of low through-flow rates. Mixing and transport was in this case driven by atmospheric forcing. The meteorological data were collected in a Mediterranean water reservoir (El Gergal, Sevilla, Spain) during May 2007. The winds used in our simulations to force the model were the north-south component of the winds observed in the reservoir. In this scenario, we test our working hypothesis. The test basin was discretized using grid cells of size $(\Delta x, \Delta y, \Delta z) = (10, 10, 0.5)$ m. The time step was set to 5 seconds (Table 2). The size spectrum in scenario 1 was constructed at 9m depth; in scenario 2, at 9m depth at a mid-point of the computational domain; in scenario 3, at 9m depth upstream and downstream of the bottom bump (region of vertical advection) and in scenario 4, above the thermocline at 3m depth at both extremes of the domain (regions of vertical advection) at the end of the simulation period (Figure 1).

RESULTS

The spectrum in all cases was linear: smaller cells settled more slowly than larger cells, and grew more rapidly as a result of the depth-dependent growth rate, represented by Eq. 3. The slope of the size spectrum θ , though, varied among scenarios. The slope θ was the same in scenarios 1 (Fig. 3A) and 2 (Fig. 3B). In both cases (scenario 1, Fig.3A and scenario 2, Fig.3B) θ was equal to -4.31. This slope was the largest in magnitude among all scenarios simulated.

The size spectrum changed in response to the vertical motion induced by inserting a bump on the bottom of the basin. The spectrum in regions of ascending motion was flatter than in regions of descending motion (compare Figs.3C and 3D). This difference in slope between regions of ascending and descending motion conforms to the observations of Rodríguez et al. (2001) and the model results obtained by León-Díaz (2004).

Winds along the main axis of the test basin were variable during the simulation period (Fig.2). Winds were predominantly from the north from day 127 to day 130. The maximum speeds during this time occurred during the night. From day 131 to 133, the wind was predominantly from the south with the maximal speeds occurring during the late evening. From night to early morning wind velocities were nearly zero. At the end of the period of study, after day 134, winds were again and consistently from the north. Wind speeds were maximal during the night and early morning, with an overall maximum of 6.78 m/s at the morning of day 135. The residual wind forcing during the study period was from the north.

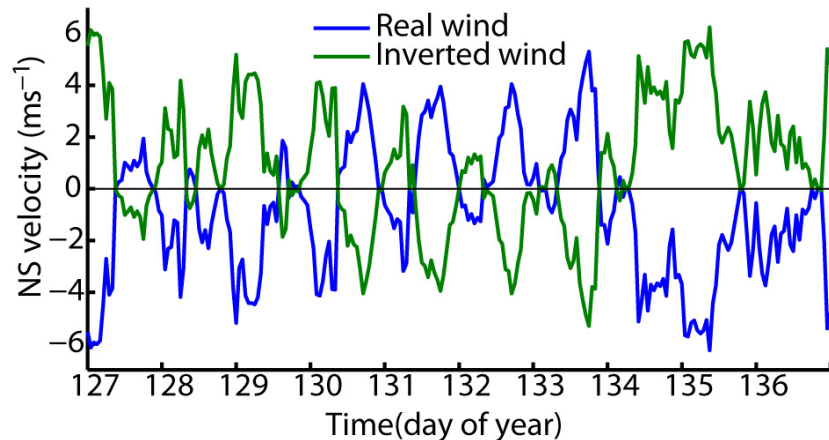


Figure 2. NS wind velocity during the simulation period of Scenario 4.

Under meteorological forcing (scenario 4), differences in the slope were observed between the upwind and the downwind end. The residual circulation driven by the northerly winds is characterized by upwards motions at the upwind (northernmost) end, but downwards near the downwind (southernmost) end. The slope θ of the spectrum was lower in magnitude at the upwind end (Fig.3E) but higher at the downwind end (Fig.3F). If we changed the direction of the winds, i.e. if we considered a residual southerly wind, the upward motion would occur in the southernmost end (S) and the downward residual motion occurred in the northernmost end. Again in this case, the slope in the regions of descending motion (N, Fig.3G) was larger in magnitude than in the areas of ascending movement (S, Fig.3H).

CONCLUSIONS

To study the phytoplankton size structure in Mediterranean lakes and reservoirs four different forcing scenarios were simulated. Our simulation results showed that water motions caused by external (hydraulic or meteorological) forcing determine the phytoplankton size structure. The slope of the size spectrum did not differ between the absence and presence of advection. The spectrum was steeper in the absence of vertical advection. Vertical water motions altered the slope of the size spectrum. The slope of the spectrum was lower in magnitude in areas of ascending motion and larger in areas of downward motion, in accordance with observations in the literature. The residual circulation induced by wind forcing, created areas of residual upward and downward motion in the basin. Spatial variations in the slope of the spectrum appeared as a result of the spatial changes in the upward-downward motion.

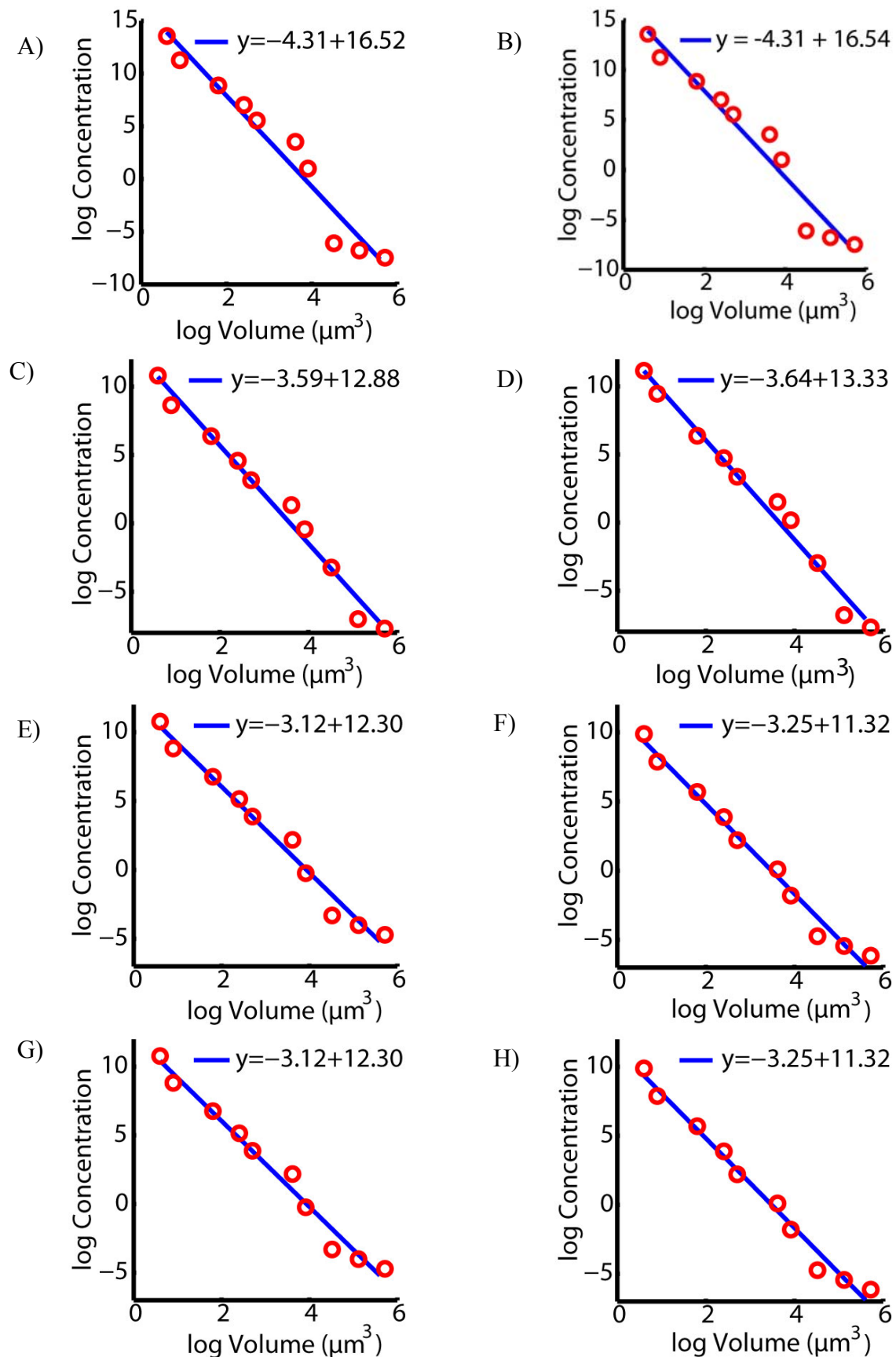


Figure 3. Phytoplankton size spectra. Red circles are model results. Blue lines are regression curves.
 A) Scenario 1, B) Scenario 2, C) Scenario 3, ascending region, D) Scenario 3, descending region, E)
 Scenario 4A, upwind end, F) Scenario 4A, downwind end, G) Scenario 4B, upwind end, H) Scenario
 4B, downwind end

ACKNOWLEDGEMENTS

This work was funded by the Spanish Ministry of Science and Innovation (CGL2005-04070/HID).

REFERENCES

- Durran, D. R. 1999. Numerical Methods for Wave Equations in Geophysical Fluid Dynamics. Springer.
- Fringer, O. B., S. W. Armfield, and R. L. Street. 2005. Reducing numerical diffusion in interfacial gravity wave simulations. *Int. J. Numer. Methods Fluids* 49: 301-329.
- Galperin, B., L. H. Kantha, S. Hassid and A. Rosati. 1988. A Quasi-equilibrium Turbulent Energy Model for Geophysical Flows. *J. Atmos. Sci.* 45: 55-62.
- Kantha, L. H., C. A. Clayson. 1994. An improved mixed layer model for geophysical applications. *Journal of Geophysical Research* 99: 25235-25266.
- León-Díaz, P. I. 2004. Desarrollo de un modelo de proliferación fitoplanctónica asociada a hidrodinamismo vertical y horizontal. Universidad de Málaga.
- León-Díaz, P. I., J.M. Blanco. 2009. Personal communication. 22 January 2009.
- Mellor, G. L. and T. Yamada. 1974. A hierarchy of turbulence closure models for planetary boundary layers. *J. Atmos. Sci.* 31: 1791-1806.
- Moreno-Ostos, E. 2004. Dinámica espacial del fitoplankton en el embalse de El Gergal (Sevilla). Tesis Doctoral. Univserdidad de Granada. 254 pp.
- Peña, A., Lewis, M. R. & Harrison, G. 1990. Primary productivity and size structure of phytoplankton biomass on a transect of the equator at 135 W in the Pacific Ocean. *Deep-Sea Res.* 37: 295-315.
- Rodríguez, J., Tintoré, J., Allen, J. T., Blanco, J. M., Gomis, D., Real, A., Ruiz, J., Rodríguez, V., Echevarría, F. and Jiménez-Gómez, F. 2001. Mesoscale vertical motion and the size structure of phytoplankton in the ocean. *Nature* 410: 360-363.
- Rueda, F. J., E. A. Cowen. 2005. The residence time of a freshwater embayment connected to a large lake. *Limnol. Oceanogr.* 50: 1638-1653.
- Rueda, F.J., S. G. Schladow, S. G. Monismith, and M. T. Stacey. 2005. On the effects of topography on wind and the generation of currents in a large multi-basin lake. *Hydrobiol.* 532: 139-151.
- Semina, H. J. 1968. Water movement and the size of phytoplankton cells. *Sarsia* 34: 267-272.
- Sheldon, R. W., A. Prakash and W. H. Sutcliffe, Jr. 1972. The size distribution of particles in the Ocean. *Limnol. Oceanogr.* 17(3): 327-340.
- Smayda, T. J. 1970. The suspension and sinking of phytoplankton in the sea. *Oceanogr. Mar. Biol. Ann. Rev* 8: 353-414.
- Smith, P.E. 2006. A semi-implicit, three-dimensional model of estuarine circulation. United States Geological Survey, USGS. Sacramento, CA. Open file report 2006-1004.

Simulation of the effects of projected pumped-storage operations on temperature and turbidity in the two affected lakes

M. Schmid^{1*}, D.F. McGinnis^{1,2}, U. Vogel³, A. Wüest^{1,4}

¹ Eawag: Swiss Federal Institute of Aquatic Science and Technology, Seestrasse 79, CH-6047 Kastanienbaum, Switzerland

² IFM-GEOMAR, Leibniz Institute of Marine Sciences at the University of Kiel, East Shore Campus, Wischhofstrasse 1-3, D-24148 Kiel, Germany

³ Limnex AG, Schaffhauserstr. 343, CH-8050 Zürich, Switzerland.

⁴ Institute of Biogeochemistry and Pollutant Dynamics, ETH Zurich, CH-8092 Zurich, Switzerland.

*Corresponding author, e-mail martin.schmid@eawag.ch

ABSTRACT

Thermal stratification and the distribution of fine suspended particles were simulated in two lakes based on several projected pumped-storage operation strategies. The upper lake is an artificial reservoir fed by small rivers from a glaciated catchment and is therefore turbid with inorganic suspended solids concentrations reaching values of ~50 mg L⁻¹ in summer. The lower, natural lake is much clearer and is both a popular tourist destination and a recreational fishery. Simulations were performed using the software CE-QUAL-W2. The two basins were represented by two coupled 2D models. The exercise revealed that in order to minimize the impact on mixing, temperature and turbidity in the lower lake, the extraction and the reinjection points for the pumped-storage operation must be located below the thermocline in both lakes. With this constraint, the major impact on the lower lake is an accumulation of heat and suspended particles below the thermocline, which has limited effects on the biological processes. Surprisingly, the simulation outcomes depended strongly on the exact timing of the pumped-storage operations. Differences in lake surface levels due to different pumped-storage schedules could lead to significantly different amounts of particles entrained from below the thermocline. Such effects may be used to mitigate the impact of the pumped-storage operation by a skilful seasonal regulation of the lake levels.

KEYWORDS

Pumped-storage, two-dimensional lake model, turbidity, lake temperature.

INTRODUCTION

Pumped-storage hydropower schemes are currently evolving on a global scale (Altinbilek et al., 2005), particularly in the central European Alps. The idea of the pumped-storage operations is to move water from a lower basin into an upper basin when excess or low-price power is available and to turbine the water (return to the lower basin) to meet peak demand when power retail-prices are high. Since the efficiency of converting from electrical to potential energy and back from potential to electrical energy is ~90% each way, only about 20% of the energy is lost. This capability is especially valuable for buffering intermittent power production by renewable energy sources such as wind farms (García-González et al.,

2008). Furthermore it has large economic benefits by taking advantage of price differentials on the power market.

Several new pumped-storage schemes are currently under evaluation in the European Alps. The large amounts of transferred water can lead to significant alterations in the stratification of the two basins. Of particular interest is if a basin is a natural lake, when water protection legislation may preclude pumped-storage schemes. For example, according to Swiss legislation, “temperatures, nutrient concentrations and living conditions in lakes must not be negatively affected by the discharge or withdrawal of water”.

There are only a few published studies of models applied to investigate the ecological effects of pumped-storage schemes. For example, Miyanaga (1986) simulated the effects of pumped-storage on stratification and primary production in two reservoirs, concluding that the induced mixing may significantly influence biological productivity. Gailiusis et al. (2003) simulated the impact of different pumped-storage intensities on flow velocities and lake levels in a large shallow reservoir.

The aim of the present study was to predict the effects of the pumped-storage operation on the thermal stratification and the turbidity in the case where the upper basin, an artificial reservoir, is highly turbid due to inflows of fine glacial particles, and the lower basin is a natural lake with relatively clear water and significant touristic importance. The software CE-QUAL-W2 Version 3.2 (Cole and Wells, 2003) was used to simultaneously predict the thermal stratification and the concentrations of mineral particles in the two lakes.

STUDY SITE

The pumped-storage scheme examined intends to use Lago di Poschiavo, a natural lake in the south-eastern part of Switzerland at 962 m a.s.l., as the lower basin, and Lago Bianco, a hydropower reservoir at an elevation of 2234 m a.s.l., as the upper basin. The major properties of the two lakes are given in Table 1. A quarter of the catchment area of Lago Bianco is glaciated. The lake therefore receives large amounts of fine glacial particles. The resulting high turbidity with typical light attenuation coefficients on the order of 2 m^{-1} and the white colour caused by the strong scattering by mineral particles have given the lake its name. Conversely, the light attenuation in Lago di Poschiavo is typically on the order of 0.5 m^{-1} . The surface of Lago Bianco is usually frozen during several months in winter.

Today, most of the outflow from Lago Bianco is used for power generation and discharged into the river Poschiavino which enters Lago di Poschiavo further downstream. Similarly, most of the outflow of the natural lake Lago di Poschiavo is used for hydropower production and the lake level is thus regulated. With the projected pumped-storage scheme, the average water residence times in the two lakes would be reduced from 370 d to 9-32 d (depending on the scenario) for Lago Bianco (upper basin) and from 183 d to 34-85 d for Lago di Poschiavo (lower basin).

Table 1. Properties of the two lakes affected by the projected pumped-storage operation.

	Symbol (unit)	Lago Bianco	Lago di Poschiavo
Volume	$V (10^6 \text{ m}^3)$	22.4 (25.6 ^a)	111
Storage capacity	$V_S (10^6 \text{ m}^3)$	18.6 (21.8 ^a)	15
Surface area	$A (\text{km}^2)$	1.5	2.0
Catchment area	$A_C (\text{km}^2)$	10	199
Glaciated percentage of catchment area	$f_G (\%)$	25	7
Elevation	$h (\text{m a.s.l.})$	2234	962
Maximum depth	$z_{\max} (\text{m})$	53 (56 ^a)	83
Mean depth	$z_m (\text{m})$	15	55
Total outflow without pumped-storage	$Q (\text{m}^3 \text{ s}^{-1})$	~0.7	~7.0
Water residence time	$\tau (\text{d})$	370	183
Residence time ^b pumped-storage scenario 1	$\tau_{PS1} (\text{d})$	32	85
Residence time ^b pumped-storage scenario 2	$\tau_{PS2} (\text{d})$	18	57
Residence time ^b pumped-storage scenario 3	$\tau_{PS3} (\text{d})$	14	46
Residence time ^b pumped-storage scenario 4	$\tau_{PS4} (\text{d})$	9	34

^a after an intended heightening of the dam to a level of 2237 m a.s.l.

^b Sum of natural discharge and pumped volume divided by lake volume

METHODS

A two-dimensional model for the simultaneous prediction of the thermal stratification and the mineral concentrations in the two lakes was implemented using the software CE-QUAL-W2 (W2; Version 3.2). For visualizing inputs and outputs, W2i (W2 interface) and AGPM (postprocessor) were used (Loginetics, Inc.). For both lakes, a grid with a vertical resolution of 2 m was used. The horizontal resolution was 100 m for Lago di Poschiavo and 200-300 m for Lago Bianco (Figures 1 and 2). Several possible discharge and withdrawal depths for the pumped-storage were implemented.

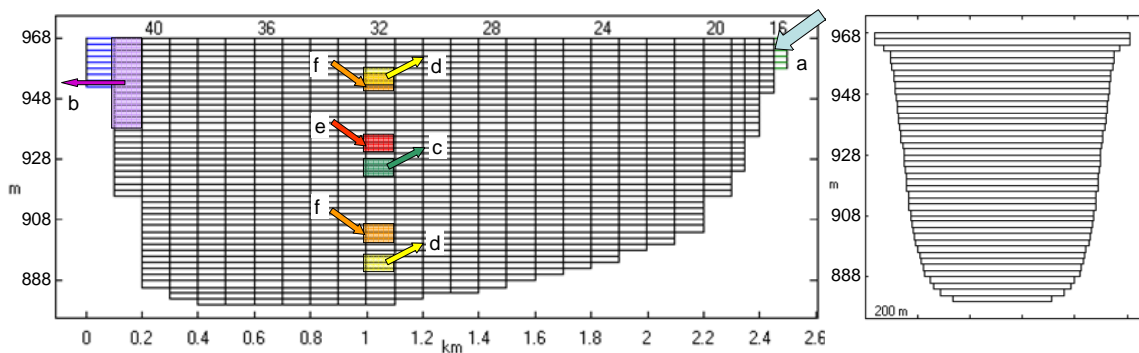


Figure 1. Bathymetry of Lago di Poschiavo (lower basin) as implemented in the model. (a) inflow, (b) withdrawal for downstream hydropower production, (c) withdrawal cells for pumped-storage, (d) alternative withdrawal cells, (e) discharge cells for pumped-storage, (f) alternative discharge cells. On the right hand side a cross section through one of the segments of the lake is shown.

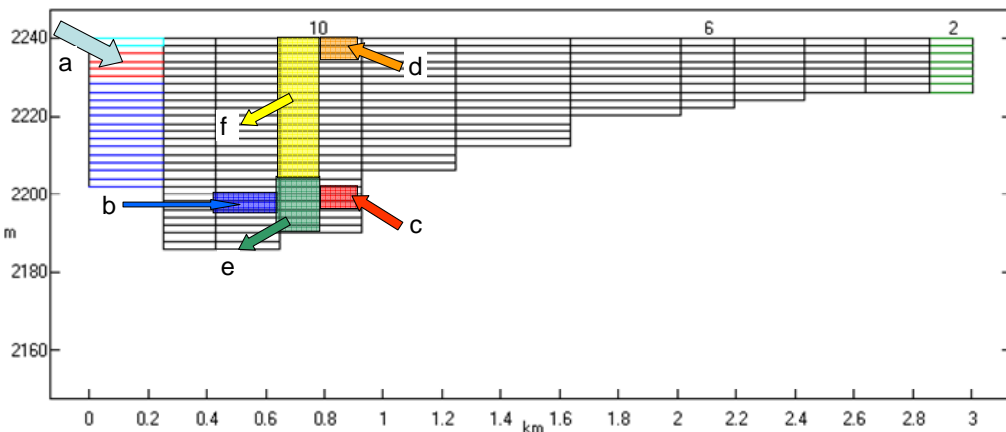


Figure 2. Bathymetry of Lago Bianco (upper basin) as implemented in the model. (a) inflow, (b) discharge of water pumped up from a small lower lake, (c) withdrawal cells for pumped-storage, (d) alternative discharge cells, (e) withdrawal cells for downstream hydropower production (both with and without pumped-storage), (f) alternative withdrawal cells.

The model was driven by meteorological data (air temperatures, wind speed and direction, cloud cover, vapour pressure, and solar radiation) collected either directly on Lago di Poschiavo (for the year 1988) or at the nearest meteorological station of MeteoSwiss in Robbia for Lago di Poschiavo and from the meteorological stations of MeteoSwiss at Bernina and Corvatsch (wind for year 2007) for Lago Bianco.

The total inflows for both lakes were calculated based on observed lake levels and information on turbined water volumes collected by Rätia Energie. Particle concentrations in the Poschiavino, the main inflow of Lago di Poschiavo, were estimated based on a function relating discharge to concentrations developed from observations in 1988/89. Particle concentrations for the inflows to Lago Bianco were not available. These were taken from measurements at Oberaarsee (Arn, 2002), a lake similarly influenced by glacial ablation. Inorganic particles were split into two size classes, particles $>4 \mu\text{m}$ with a sedimentation velocity of 7 m d^{-1} and particles $<4 \mu\text{m}$ with a sedimentation velocity of 0.2 m d^{-1} (for 2007 the sedimentation velocity of the smaller particles was set to 0.1 m d^{-1} in order to better reproduce observed concentrations).

The model was calibrated using observed vertical profiles of temperature and total suspended solids from both lakes from the years 1988 and 2007. The main fit parameters were the wind sheltering coefficient, which determines the efficiency of energy transfer from wind to the lake, as well as the particle sedimentation velocities.

Simulations were performed for 4 different pumped-storage scenarios which were calculated by Rätia Energie based on their “average” hydrologic year 1969 and assumptions on the seasonal and daily dynamics of the energy retail prices. Two of the calculated scenarios are depicted in Figure 3.

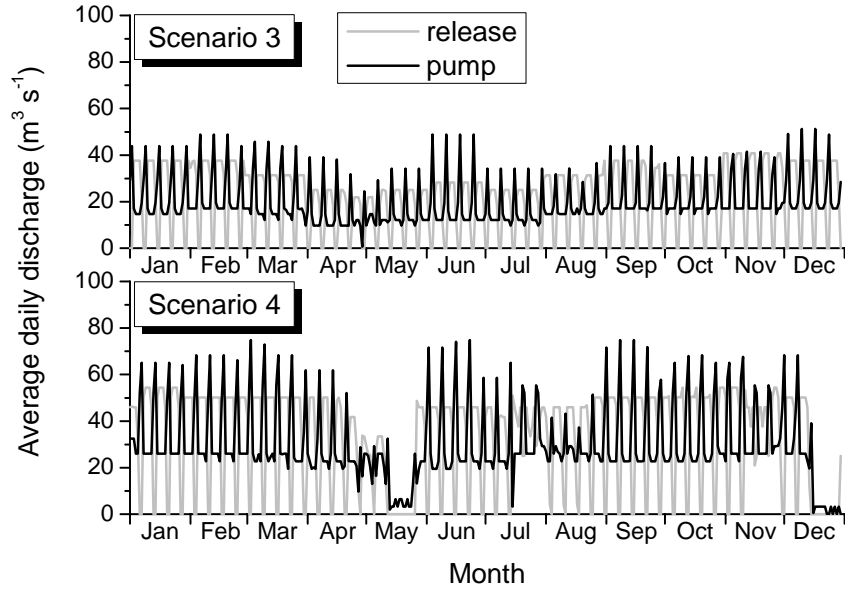


Figure 3. Two of the pumped-storage scenarios used in the simulations.

RESULTS

Temperature

The major effect of the pumped-storage on temperature in the downstream lake was an accumulation of heat below the thermocline during summer (Figure 4). There are two major causes for this warming. First, the water is heated during the pumped-storage operation, since the ~20% of energy lost during the process is transferred as heat to the water. Given the elevation difference of 1270 m between the two lakes, the water temperature increases by about 0.3 °C during both pumping and the generation. This warming effect increases with the amount of water exchanged between the two lakes. In scenario 4 with the highest flow discharge, the difference between a calculation including these frictional heat losses and a calculation neglecting them was ~1.3 °C (Figure 4). Second, the water is more exposed to heating from the atmosphere in upstream Lago Bianco than it is below the thermocline in Lago di Poschiavo. This effect depends not only on the amount of water exchanged between the two lakes, but to a similar extent on the interaction between meteorological conditions and the timing of the pumped-storage operations. In Figure 4, the heating effect of Scenario 3 is smaller than that of Scenario 2 despite on average 35% higher flows. This is mainly due to the timing of the pumped-storage in May and June (Figures 3 and 5). In Scenarios 2 and 4, the pumped-storage discharge is reduced during the month of May when the water in Lago Bianco has not yet heated up, whereas there is no such break in Scenario 3. In addition, in Scenario 2, the lake level of Lago Bianco is lowered during the month of July, leading to a more direct coupling with the atmosphere during the warmest time of the year. Altogether, the average temperature of the turbined water during summer is higher in Scenario 2 than in Scenario 3, which also leads to the simulated convective mixing of a 12 m thick layer below the chemocline in Scenarios 2 and 4 (Figure 4).

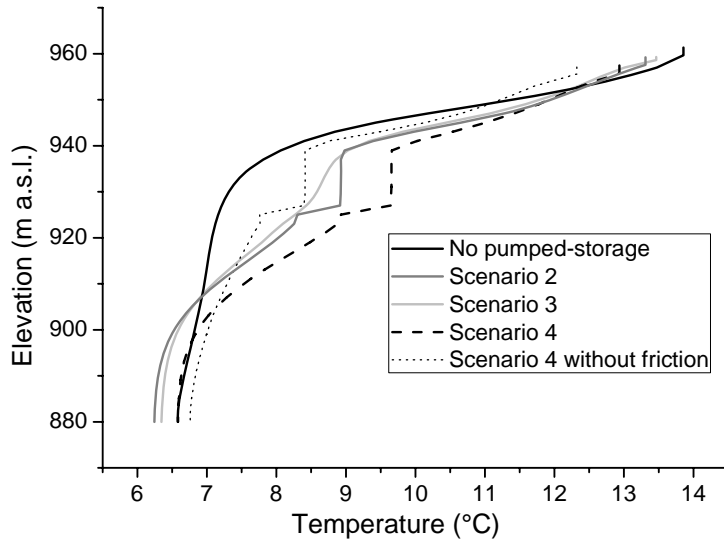


Figure 4. Simulated vertical temperature profiles in the downstream Lago di Poschiavo for 28 August for different pumped-storage scenarios.

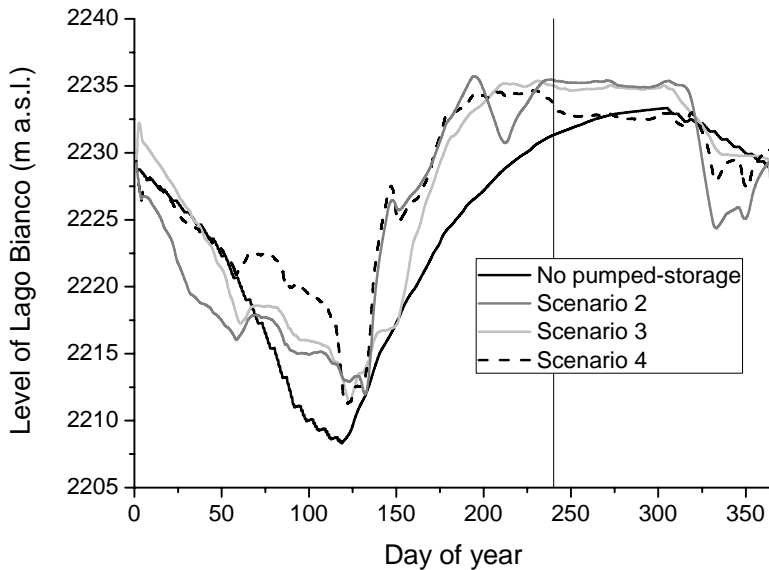


Figure 5. Lake level of Lago Bianco for different pumped-storage scenarios (running averages over one week, in order to remove periodical weekly fluctuations). The vertical line indicates the date (28 August) for which the temperature profiles are shown in Figure 4.

The simulated effect on temperature depends significantly on meteorological and hydrological conditions. The summer deepwater temperatures in Lago di Poschiavo have been observed to range between 4 $^{\circ}\text{C}$ and 6 $^{\circ}\text{C}$ (and probably more in years without observations). This temperature mainly depends on wind conditions during the spring mixing and on the deepwater formation by the major inflow, the river Poschiavino, which is a function of its temperature and particle concentrations. Simulations were performed for a dry (2007), an average (1988) and a rather wet (1969) year, using weather conditions for 2007 (warm and

low wind speeds) and 1988 (cooler and higher wind speeds). The results show a variation of about 2 °C for the summer deepwater temperatures in the scenarios without pumped-storage. The heating effect of the pumped-storage operations is lower in years with high deepwater temperatures (Figure 6), because the temperature difference to the water in Lago Bianco is lower.

The major ecological risk of the temperature increase below the chemocline is an increased probability of mixing down to the base of the warmed layer during summer. Since the temperature and thus the density difference between the lake surface and this depth decreases with increasing pumped-storage discharge, the probability of a cool and windy weather event mixing the whole layer increases. Furthermore, a shortening of the productive season could have been expected as the heated layer facilitates earlier mixing in autumn. However, the simulation results in this respect are not consistent. Depending on the meteorological conditions and the pumped-storage scenarios, the warmed layer is in some cases cooled back to normal temperatures before autumnal mixing as Lago Bianco cools down earlier than Lago di Poschiavo.

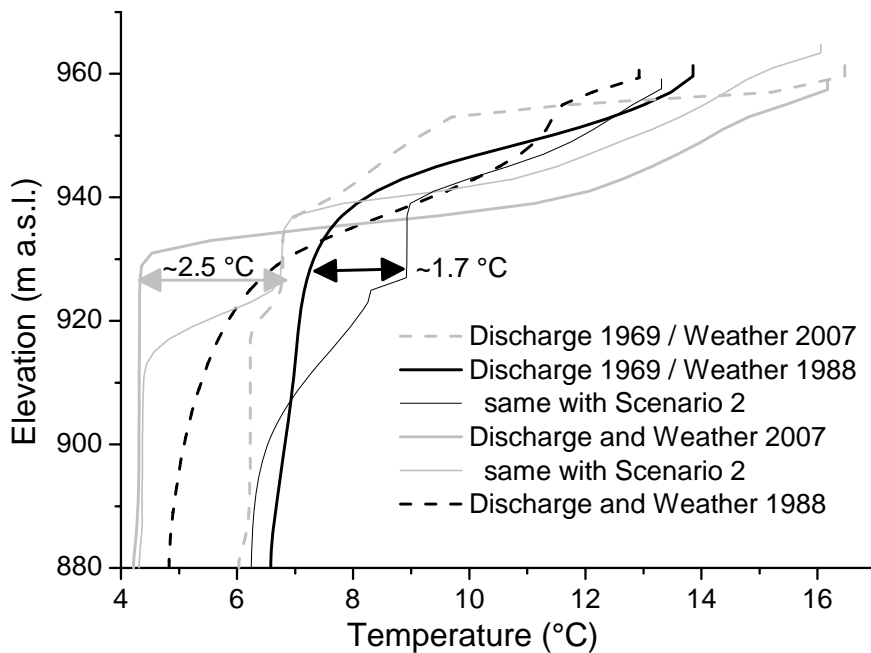


Figure 6. Vertical temperature profiles in Lago di Poschiavo at the end of August in four different meteorological and hydrological cases without pumped-storage and for Scenario 2 in two of the cases.

Particle Concentrations

One of the major expected effects of the pumped-storage operations on the ecological integrity of Lago di Poschiavo is an increased turbidity of the surface layer due to particle inputs from turbid Lago Bianco. Light attenuation and consequently the euphotic depth in Lago di Poschiavo are directly related to particle concentrations (Figure 7). Particle concentrations in Lago Bianco are expected to decrease by a factor of 3 to 4 (data not shown). The differences between the scenarios in average particle concentrations in the top 10 m of Lago di Poschiavo are relatively small (Figure 8). Already the scenario with the lowest discharge reduces the water retention time in Lago Bianco from ~1 year to ~1 month, which has a much larger effect on the fraction of small particles retained in Lago Bianco than any further increase of the discharge. The surface turbidity in Lago di Poschiavo can then be more sensitive to the timing of the pumped-storage operations than to the amount of water exchanged. This is exemplified by Scenario 3 having a higher average impact than Scenario 4 (Figures 7 and 8). The simulated particle concentrations in the surface layer of Lago di Poschiavo reach values comparable to those observed in Lake Brienz for which the effects of upstream hydropower operations on turbidity and primary production have recently been investigated (Finger et al., 2007a; Finger et al., 2006).

The major ecological effect of the increased particle concentrations is a reduction of the euphotic depth by ~2 m during summer. The zooplankton in particular can be very sensitive to reductions in light availability and the respective shortening of the productive period in spring when they need to recover from harsh winter conditions (Finger et al., 2007b). Simulations showed that there is no risk of a long-term accumulation of particles in Lago di Poschiavo thanks to the relatively short water residence time. Less than 10% of additional particles added at the beginning of the year in a simulation still remained in the lake at the end of the year.

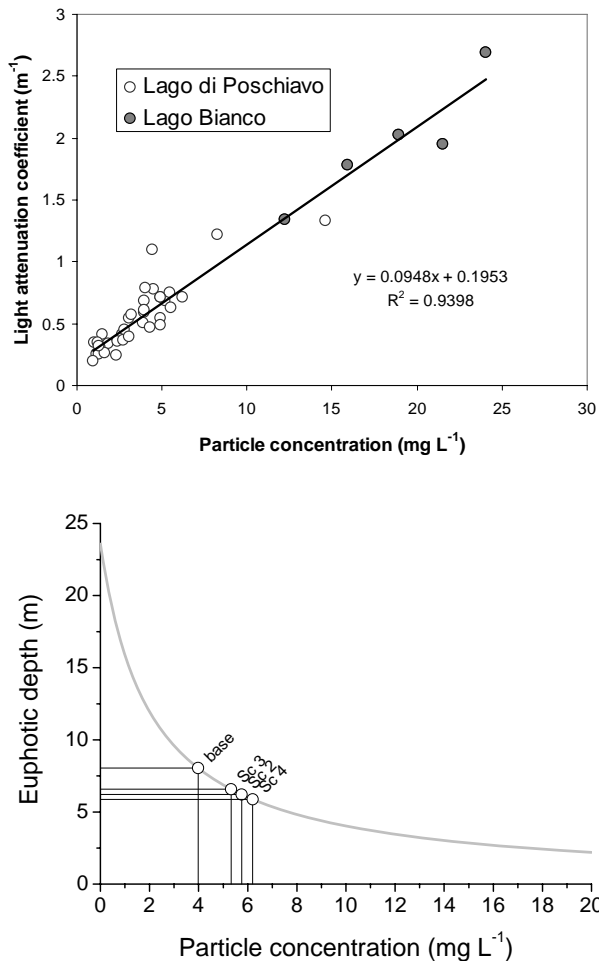


Figure 7. Observed particle concentrations and light attenuation coefficients in Lago di Poschiavo and Lago Bianco (left) and euphotic depth as a function of particle concentration based on the linear regression (right). The circles and drop lines show the average particle concentrations between June and October and the resulting euphotic depths for the base scenario (no pumped-storage) and for the scenarios 2 to 4 (according to Figure 8).

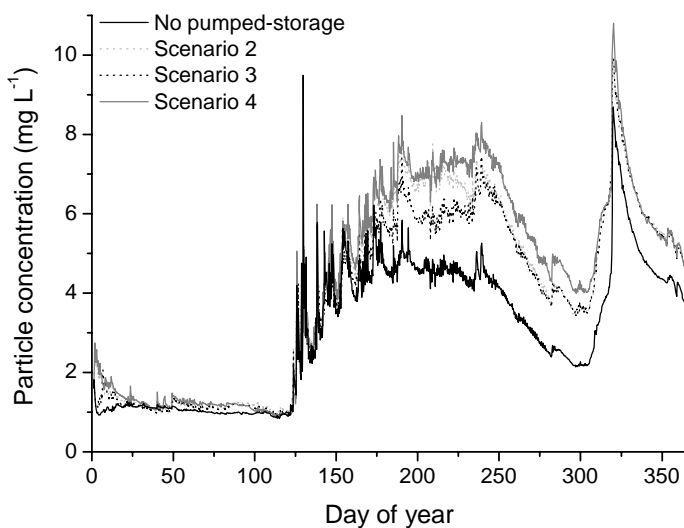


Figure 8. Simulated average particle concentrations in the top 10 m of the water column of Lago di Poschiavo for several different scenarios.

Simulations with different withdrawal and discharge depths in Lago di Poschiavo clearly showed that the water must be both discharged and withdrawn below the main temperature gradient in order to avoid high particle concentrations in the surface layer of the lake (Figure 9). Contrarily, the exact depths of the withdrawal and discharge below the thermocline are less important.

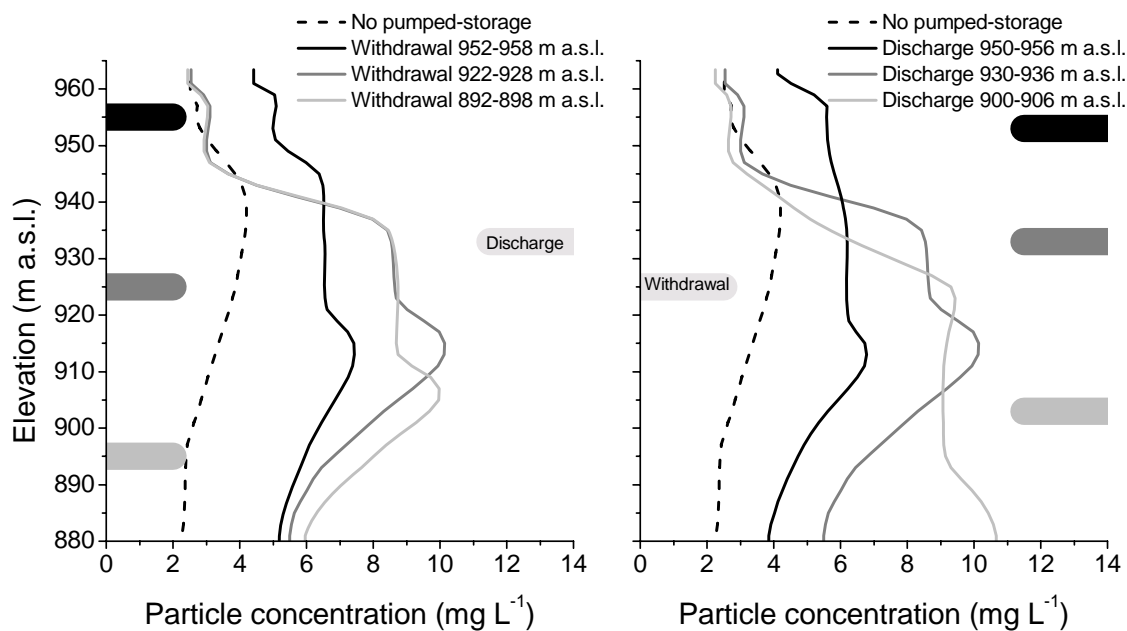


Figure 9. Simulated vertical profiles of inorganic particle concentrations on 2 October 1988 in the pumped-storage scenario 2 for different withdrawal (left) and discharge (right) depths.

CONCLUSIONS

In the present project, the effects of a projected pumped-storage scheme on the temperature and inorganic particle concentrations in the upper and lower basin were simulated with two coupled 2-dimensional models using the software CE-QUAL-W2. The simulations showed that both the withdrawal and the discharge depth in downstream Lago di Poschiavo must be located below the thermocline depth in order to avoid substantial increases in particle concentrations in the surface layer of this lake. If this is implemented, the two major projected effects on downstream Lago di Poschiavo are increased (up to 2-3 °C) summer and autumn temperatures in a depth range of ~20 m below the thermocline as well as increased (by 1-2 mg L⁻¹) turbidity during summer and autumn in the surface layer. The euphotic depth is expected to be reduced by about 2 m. However, the predicted surface turbidity depends strongly on the wind forcing, since particles accumulate at the base of the thermocline during summer and can be mixed into the surface layer by strong wind events. Altogether this leads to a shortening of the productive period due to limited light availability in early spring and in some scenarios due to earlier mixing in autumn. Furthermore, the heat accumulation below the chemocline in Lago di Poschiavo results in some risk for deep mixing occurring during a cold and windy day in summer. Both the effects on temperature and particles are significantly influenced by the timing of pumped-storage operations, which means that there is some potential for mitigating the negative effects on the downstream lake by a careful regulation of the pumped-storage operating mode.

ACKNOWLEDGMENTS

This study was partially financed by a consulting contract with Rätia Energie. The authors would like to thank Scott Wells and Gary Hauser for advice on the CE-QUAL-W2 coupled model setup and Michael Schurter for field work.

REFERENCES

- Altinbilek, D., Seelos, K. and Taylor, R., 2005. Hydropower's role in delivering sustainability. *Energy & Environment*, 16(5): 815-824, doi:10.1260/095830505774478503.
- Arn, K., 2002. Geochemical weathering in the sub- and proglacial zone of the two glaciated crystalline catchments in the Swiss Alps (Oberaar- and Rhoneglacier). PhD Thesis, Université de Neuchâtel, Neuchâtel, 331 pp.
- Cole, T.M. and Wells, S.A., 2003. CE-QUAL-W2: A two-dimensional, laterally averaged, hydrodynamic and water quality model, version 3.2 user's manual., US Army Corps of Engineers., Washington D.C.
- Finger, D. et al., 2007a. Effects of alpine hydropower operations on primary production in a downstream lake. *Aquatic Sciences*, 69: 240-256, doi:10.1007/s00027-007-0873-6.
- Finger, D., Schmid, M. and Wüest, A., 2006. Effects of upstream hydropower operation on riverine particle transport and turbidity in downstream lakes. *Water Resources Research*, 42: W08429, doi:10.1029/2005WR004751.
- Finger, D., Schmid, M. and Wüest, A., 2007b. Comparing effects of oligotrophication and upstream hydropower dams on plankton and productivity in peri-alpine lakes. *Water Resources Research*, 43: W12404, doi:10.1029/2007WR005868.
- Gailiusis, B., Kriauciuniene, J. and Rimaviciute, E., 2003. Modelling the effect of the hydroelectric pumped storage plant on hydrodynamic regime of the Kaunas Reservoir in Lithuania. *Nordic Hydrology*, 34(5): 507-518.
- García-González, J., de la Muela, R.M.R., Santos, L.M. and Gonzalez, A.M., 2008. Stochastic joint optimization of wind generation and pumped-storage units in an electricity market. *IEEE Transactions on Power Systems*, 23(2): 460-468, doi:10.1109/TPWRS.2008.919430.
- Miyanaga, Y., 1986. Modelling of stratified flow and eutrophication in reservoirs. *Ecological Modelling*, 31(1-4): 133-144.

Past and future lake ice covers of the Berlin-Brandenburg area

Juliane Bernhardt^{1*}, Georgiy Kirillin¹, Christof Engelhardt¹ and Jörg Matschullat²

¹ Institute of Freshwater Ecology and Inland Fisheries, Müggelseedamm 310, 12587 Berlin,
Germany

² Technical University Bergakademie Freiberg, Institute for Mineralogy, Brennhausgasse 14,
09599 Freiberg, Germany

*Corresponding author, e-mail bernhardt@igb-berlin.de

ABSTRACT

Ice covers of Brandenburg lakes have been studied with respect to climate variability and change with the help of a one-dimensional physical lake model FLake, which uses time series of meteorological parameters and lake specific parameters as input data.

The model is able to reconstruct the observed past ice phenology (number of ice days and ice start and end dates) of two lakes in the Berlin-Brandenburg area (Lake Müggelsee and Lake Stechlin) very well and with higher accuracy than state-of-the-art linear regression models.

The calibrated and validated model was used to investigate the past and future changes in ice cover timing, intensity and duration of a representative set of Berlin-Brandenburg lakes. For eight lakes covering the range of mean depths and trophic states representative for the region the model predicts its ice phenology until 2100 based on measured meteorology data from the Potsdam station (1947-2007) and simulated meteorology (1961-2100) derived from three regional climate model scenarios (GLOWA, RCAO, WettReg).

Observation and model results showed that deeper lakes had more ice-free winters than shallow lakes. Furthermore, the duration of the ice covered period of shallow, polymictic and turbid lakes was longer than that of deep, dimictic and clear lakes. Thus, shallow and turbid lakes had higher numbers of days per winter covered with ice than deep and clear lakes. Furthermore, mean dates of ice cover formation and break-up of deep and clear lakes are usually later than of shallow and turbid lakes.

Trends with time and increasing temperature of later ice start dates and earlier ice end dates, shortening in ice duration and increasing ice free winters were determined for Berlin-Brandenburg lakes for the past and future climate. For the near future (ca. since 2060) deep and clear Berlin-Brandenburg lakes were predicted to become completely ice free.

FLake is a good tool for forecasting lake ice phenology for lakes differing in morphology and trophic state. This is relevant to predict climate change effects on lake ecosystems and freshwater quality. Decreasing lake ice coverage with further climate warming will affect lakes temperature and oxygen, nutrient and light levels of freshwater bodies, thus it is likely to change species composition, timing and abundance from low to high trophic levels (lake ecosystems).

KEYWORDS

Past and future lake ice, freezing, melting, freshwater lake model FLake, climate.

INTRODUCTION

Climate warming took place during the last decades of the 20th century, and the increase in northern hemispheric temperatures continues, being most pronounced in spring (IPPC 2001). Warmer air temperatures affect water body's temperature, ice cover and lake ecology. Timing of initial ice cover freezing and final thawing and the duration of an ice covered period are referred to as ice phenology. Ice phenology parameters have been widely used for various climate studies (Futter, 2003; Kouraev *et al.*, 2008; Williams *et al.*, 2004) as they are good indicators of regional and large-scale climate variability and change.

Timing, presence and duration of lake ice covers are strongly related to local weather conditions, especially air temperature and wind speed, as they are closely linked to water temperature and stratification of lakes. Snow-depth on lake ice also plays an important role in determining ice break-up dates, but observations on this are rarely available. Other factors that determine ice covers on lakes are exposure to wind, lake volume, lake bottom morphology, mean depth and mean surface area (Adrian and Hintze, 2000; Gao and Stefan, 1999; Kouraev *et al.*, 2008; Livingstone, 1997, 2008; Williams *et al.*, 2004).

Lake ice phenology, ice thickness and snow cover affect substantially chemical and physical lake characteristics and the functioning of the ecosystems in lakes. E.g. timing and magnitude of algal blooms, composition of plankton and fish communities are influenced by lake ice characteristics (Adrian *et al.*, 1999, 2006; Assel and Robertson, 1995; Kalff, 2002; Kouraev *et al.*, 2008). Therefore, changes in ice phenology may have potential effects on lake's food webs and water quality.

Climate change studies based on ice phenology have been conducted for many North American lakes but for a few European lakes only (Magnuson *et al.*, 2000; Liston and Hall, 1995; Ménard *et al.*, 2002; Stefan and Fang, 1997; Varvus *et al.*, 1996; Futter, 2003; Livingstone, 2008; Jeffries *et al.*, 2005; Gao and Stefan, 1999; George, 2007; Shuter *et al.*, 1983; Williams *et al.*, 2004). The sensitivity of ice phenology to climate variability and change has been investigated using observation data from ground and remote sensing and simulation data from computer models and regression models (Jeffries *et al.*, 2005). Many long time series of field observations, taken at coastal stations and during field trips, are available for different regions of North America (e.g., Liston and Hall, 1995; Ménard *et al.*, 2002; Stefan and Fang, 1997; Varvus *et al.*, 1996). Since the 1970s, observations by aerial surveys or satellites provide passive microwave images to study lake ice phenology (Kouraev *et al.*, 2008, Leppäranta and Wang, 2008). Single and multiple variable regression analyses were used to develop regression models that need observed ice data and few correlated input data to predict ice phenology and ice thickness (Gao and Stefan, 1999; George, 2007; Williams *et al.*, 2004). A few physical models have been developed to simulate lake ice (e.g., Bilello, 1964; Palecki and Barry, 1986; Livingstone, 1997; Heron and Woo, 1994; Liston and Hall, 1995; Stefan and Fang, 1997; Varvus *et al.*, 1996) that are applicable for a broader range of lakes and more accurate in forecasting lake ice than regression models.

This study aims at reconstructing Berlin and Brandenburg lake ice covers of the past since 1947, particularly for lakes with no observations. The reliability of FLake for forecasting ice phenology of different lake types is tested. Further purposes are detecting past and future trends in regional lake ice phenology, and quantifying responses of the ice regime in lakes with different morphometry and trophy due to climate variability and change.

METHODS

Sites

Lakes in the Berlin-Brandenburg area are lowland lakes that range from deep and clear lakes with big surface areas to shallow and turbid lakes with small surfaces. Of this region, two well studied lakes with regard to lake ice coverage, namely Lake Müggelsee and Lake Stechlin, were used for models calibration and validation.

Lake Müggelsee is a shallow, eutrophic and polymictic lake in the southeast of Berlin, Germany (52°27' N, 13°39' E). It has a mean depth of 4.8 m, a maximum depth of 8.9 m and covers an area of 7.6 km² (Fig. 1, Table 1).

Table 1. Lake morphology and water quality parameters of the eight Berlin and Brandenburg lakes (Mischke and Nixdorf, 2008)

d = class width		Lake morphology				Water quality	
Lake class mean depth in m	Mean depth in m	Maximum depth in m	Lake area in ha	Mixis	Lakes	Mean Secchi depth in m	Mean extinction coefficient
11 ≥ d < 25	24.2	69.5	412.38	stratified	Lake Stechlin (1)	8.5	0.20
	19.3	36.0	105.97	stratified	Lake Sacrow (2)	1.4	1.26
5 ≥ d < 11	7.1	18.0	162.00	stratified	Lake Nehmitz (3)	6.6	0.27
	5.5	9.8	1482.71	stratified	Lake Wannsee (4)	0.8	2.27
2 ≥ d < 5	4.8	8.9	764.61	polymictic	Lake Müggelsee (5)	1.8	0.80
	2.8	6.3	507.43	polymictic	Lake Selchow (6)	0.4	4.00
0 > d < 2	1.7	4.8	237.21	polymictic	Lake Schwerin (7)	0.6	3.09
	1.5	4.5	96.10	polymictic	Lake Grössin (8)	0.3	5.31



Figure 1. Location of the eight lakes in Berlin and Brandenburg

Full mixing of the lake body often takes place because of its shallowness and relatively big surface area. The lake is flushed by the River Spree and had a mean water retention time of 6–8 weeks. The surrounding topography is flat and the lake basin is oriented from east to west; hence the lake is highly exposed to the prevailing winds from the southwest (Driescher *et al.*, 1993).

Lake Stechlin, situated in the Baltic Lake District in NE Germany ($53^{\circ}09'N$, $13^{\circ}02'E$), about 100 km north of Berlin, has a surface area of 4.1 km^2 . Maximum and mean depths are 69.5 and 24.2 m, respectively (Fig. 1, Table 1). Relatively large depths and small horizontal dimensions cause the dimictic character of the lake. The water level of the oligotrophic lake is regulated by ground water inflow, precipitation (about 590 mm a^{-1}) and evaporation, and temporal runoff through the surrounding sand layers (Casper, 1985; Koschel and Adams, 2003). Relatively weak, predominately westerly winds with average speeds of $2\text{--}3\text{ m s}^{-1}$ characterise the area.

For simulations with the lake model FLake eight Berlin and Brandenburg lakes were chosen in respect to their mean lake depth and turbidity, representing the diversity of lakes in this region (Fig. 1). Four lake depth classes were formed ($0 > d < 2\text{ m}$, $2 \geq d < 5\text{ m}$, $5 \geq d < 11\text{ m}$ and $11 \geq d < 25\text{ m}$), with one turbid and one relatively clear lake in each lake class (Table 1).

The FLake model

The physical lake model FLake (Mironov, 2008) is driven only by few external variables. Lake-specific variables are lake depth, optical characteristics of lake water, temperature at the bottom of the thermally active layer of bottom sediments, and the depth of this layer. The model requires time series of the five meteorological parameters solar radiation, air temperature, air humidity, wind speed and cloudiness as input. The model was run with a daily time step. From these simulation results (daily ice thickness), the number of ice days per winter, freeze-up and break-up dates and the duration of the ice covered period have been calculated. For simplicity, only the findings of the ice phenology parameter “number of ice days per winter” (nd) are shown in the results and discussion section.

Past meteorology and future scenarios

Observed meteorological data from 1947 to 2007 have been used from the Potsdam station (WMO station ID: 10379) of the German Weather Service (DWD). The station's coordinates are $52^{\circ}23'N$, and $13^{\circ}04'E$, and it is situated at an altitude of 81 m a.s.l. on Telegrafenberg. The lake model FLake was driven with measured daily average meteorological data from November the 1st 1947 to October the 31st 2007 (60 hydrological years) to model the ice phenology of the past. Accessible data from DWD were the daily sum of solar radiation (J cm^{-2}), the daily mean air temperature measured in 2 m height ($^{\circ}\text{C}$), the daily relative air humidity (%) and the daily mean wind speed (Bft). Mean daily air temperature at the Potsdam station was 9°C ($\pm 7.8^{\circ}\text{C}$) in the period from 1947 to 2007.

To simulate future ice phenology, and thus the response to the expected climatic changes, meteorology data from three regional climate scenarios (GLOWA, RCAO MPI B2 and WettReg) were used. The first two regional climate scenarios are both based on the same driving global climate model ECHAM 4 (OPYC3-T24) of the Max Planck Institute Hamburg for Meteorology (Roeckner *et al.*, 1996) with the SRES emission scenario B2, but on two different regionalisation procedures and time coverages. The first one is based on the statistical downscaling procedure STAR (Werner and Gerstengarbe, 1997) and run for the period 2001–2055, and the second one is based on the regional climate model RCA (Rummukainen *et al.*, 2001) and run for the time span 2071–2100. In the third scenario, the newer global climate model ECHAM 5 with the more extreme SRES emission scenario A1B (IPCC, 2007) provided the boundary conditions for the regional climate model WettReg (Enke *et al.*, 2005a; Enke *et al.*, 2005b).

In the past, mean annual air temperatures showed an increasing trend of ca. 1°C in 60 years (or 0.017°C per year). The GLOWA regional climate scenario for 2001 to 2055 is based on the prescribed linear temperature trend of a 1.4°C temperature increase per 50 years or a 0.0257°C temperature increase per year. The air temperature increase in the RCAO MPIB2 scenario for 2071 to 2100 is also based on the ECHAM/OPYC3 results of the global circulation modeling and roughly amounts to a 0.03°C temperature increase per year. The statistical model WettReg, based on large scale weather patterns, comprises a temperature increase of approximately 3°C for the period 1961-2100 (or 0.02°C per year) for the south and east of Germany.

Models calibration and validation

As mentioned above, there are only two long time series of lake ice phenology available for the Berlin and Brandenburg area. Calibration and validation of the FLake model, and comparison to the state-of-the-art linear regression models (Gao and Stefan, 1999; George, 2007; Shuter *et al.*, 1983; Williams *et al.*, 2004) were performed at these data sets from Lake Müggelsee and Lake Stechlin. For both lakes, ice observations are available without gaps for the time period from 1961 to 2007 (Fig. 2, grey bars). The calibration period for Lake Müggelsee was from 1976 to 1991 and for Lake Stechlin from 1961 to 1981, and the validation period for Lake Müggelsee was from 1991 to 2007 and for Lake Stechlin from 1981 to 2002.

The model calibration was performed by adjusting lake-specific input parameters (Table 2) in order to obtain the best fit of model results with the observed ice data. Lake parameters (Table 2, dark grey) that fitted best for Lake Müggelsee and Lake Stechlin during the calibration periods were adapted to further selected Berlin and Brandenburg lakes. After that, the model was validated on data from the chosen validation period.

Table 2. Lake specific input parameters to FLake sorted from deep to shallow Berlin and Brandenburg lakes

Lake name	Latitude	Mean extinction coefficient (Apr.-Oct.)	Mean lake depth in m	Ice water heat flux in W m ⁻²	Depth thermal active layer bottom sediment in m	Temperature outer edge bottom sediment in °C	Albedo lake ice cover
Lake Stechlin	53°09'	0.20	24.16	3	3	7	0.1
Lake Sacrow	52°27'	1.26	19.30	3	3	7	0.1
Lake Nehmitz	53°08'	0.27	7.14	5	3	7	0.1
Lake Wannsee	52°27'	2.27	5.50	5	3	7	0.1
Lake Müggelsee	52°27'	0.80	4.80	5	3	7	0.1
Lake Selchow	52°13'	4.00	2.82	5	3	7	0.1
Lake Schwerin	52°12'	3.09	1.68	5	3	7	0.1
Lake Grössin	52°15'	5.31	1.47	5	3	7	0.1

In order to estimate coefficients in the regression models the lake ice phenology observations from both lakes were used. The 11 linear regression models were constructed each including one lake morphological variable (mean lake depth or mean lake area), and one meteorological variable (annual mean air temperature from Potsdam station (DWD) or winter North Atlantic Oscillation Index (mean from Dec-Mar)) (Hurrel, 1995). Table 3 shows selected linear regression equations for predicting the number of ice days (*nd*) and the ice start date (*sd*). The equations obtained with the data from the calibration period were tested on the validation period.

Finally, ice observations, regression and lake model results were compared for Lake Müggelsee and Lake Stechlin in the period from 1961 to 2007 (Fig. 2).

Past and future simulations

Daily lake ice thicknesses of eight Berlin and Brandenburg lakes were modelled for the past from 1947 to 2007 and for the future till 2100. For the eight lakes annual ice phenology data and its means of the modelled past and future time periods were examined (Figs. 3-6). Trends with 1°C rising air temperature were calculated for the past and future ice phenology of Lake Müggelsee and Lake Stechlin (Figs. 7-9).

RESULTS AND DISCUSSION

Calibration and validation

During 1961-2007 shallow and turbid Lake Müggelsee had more winters covered with ice than deep and clear Lake Stechlin. Furthermore, the ice-covered periods of Lake Müggelsee were longer, and the number of ice days per winter was higher than for Lake Stechlin (Fig. 2, grey bars).

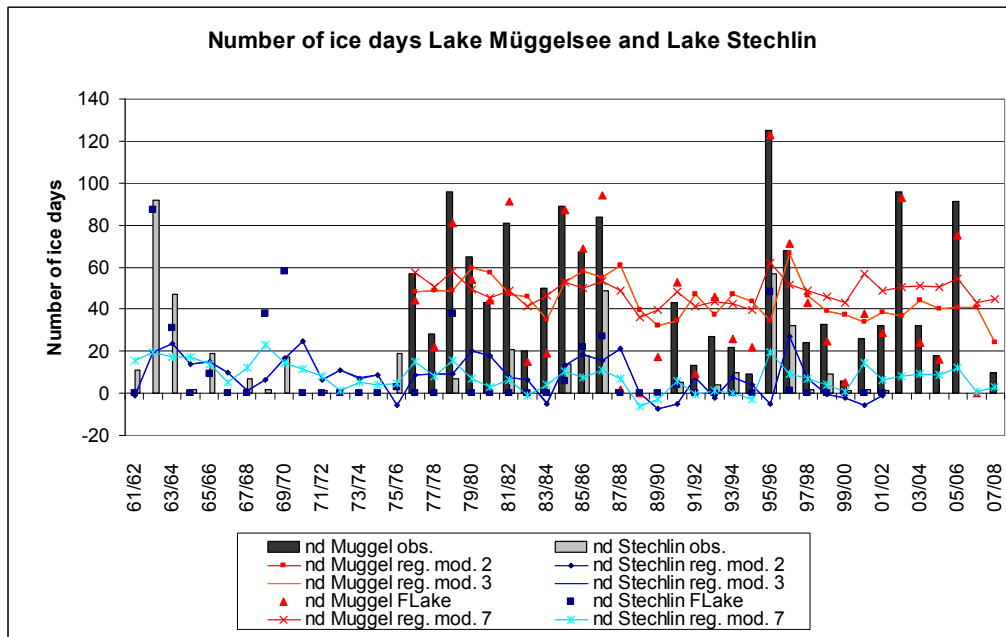


Figure 2. Numbers of ice days for Lake Müggelsee and Lake Stechlin since 1961. Bars show the observed ice data, lines are the numbers of ice days predicted by regression models (Eq. 2, 3, 7, 8), dots mark the numbers of ice days modelled by the FLake

The FLake performed well in predicting lake ice phenology for Lake Müggelsee and Lake Stechlin, with significant linear correlation coefficients between observed and modelled ice phenology parameters for both calibration and validation period. The errors between observed

and simulated ice parameters of the calibration and the validation period are in the same order of magnitude for both lakes. The mean absolute error (MAE) of the number of ice days per winter (*nd*) was between 6.4 and 9.2 days and of the timing of ice break-up (*ed*) between 5.3 and 9.8 days. The MAE of the timing of lake ice freeze-up (*sd*) was with from 6.7 to 18.2 days not as good as for the other two ice phenology parameters. Similar errors are found by Ménard *et al.* (2002). Ice-covered and ice-free winters were well simulated for both lakes. FLake slightly overestimated the number of ice days for Lake Müggelsee and slightly underestimated (yet, in some cases, strongly overestimated) *nd* for Lake Stechlin. For Lake Stechlin strong overestimation of ice days occurred when air temperatures in this year have been low, thus a high number of ice days have been modelled by FLake, but no ice cover or only a few days ice have been observed (Fig. 2, dots).

As a reference, several linear regression models were developed predicting lake ice parameters from meteorology and lake morphology variables. The most important climate parameters for predicting lake ice phenology with regression models were annual mean air temperature and North-Atlantic-Oscillation-Index (NAO-I). The strongest correlations between lake specific parameters and lake ice phenology were found for mean lake depth and mean lake area, which is in agreement with the findings of e.g., Gao and Stefan (1999), Livingstone and Dokulil (2001), Shuter *et al.* (1983) and Williams *et al.* (2004). The regression models constructed here are shown in Table 3.

For the calibration period, two regression equations were significant ($p < 0.05$) for predicting the number of ice days (Eqs. 2 and 3, Fig. 2), three regression equations for the ice start dates (Eqs. 4, 5 and 6) and none of the equations for ice end dates for Lake Müggelsee and Lake Stechlin. For the validation period, the regression models 2, 3, 4, 5 and 6 which used the annual mean air temperature to predict *nd* and *sd*, were insignificant. Regression models predicting *nd* (Eqs. 7 and 8) from the winter NAO-I were significant for both calibration and validation period (Fig. 2). Results of models 2 and 3, as well as those of models 7 and 8, are identical because they use nearly the same input except for depth and area (Table 3, Fig. 2). Number of ice days for both lakes predicted by regression models 2 and 7 are shown in Figure 2 (lines).

Table 3. Linear regression models for predicting ice phenology parameters

Linear regression model	Equation number
$nd = 89.952 - 7.201 * \text{Temp N_O}$	(Eq. 1)
$nd = 153.944 - 10.817 * \text{Temp N_O} - 2.045 * \text{mean depth}$	(Eq. 2)
$nd = 58.309 - 10.817 * \text{Temp N_O} + 11.218 * \text{mean area}$	(Eq. 3)
$sd = 256.569 + 14.728 * \text{Temp N_O}$	(Eq. 4)
$sd = 210.291 + 17.343 * \text{Temp N_O} + 1.479 * \text{mean depth}$	(Eq. 5)
$sd = 279.453 + 17.343 * \text{Temp N_O} - 8.113 * \text{mean area}$	(Eq. 6)
$nd = 61.644 - 2.910 * \text{NAOI (DJFM)} - 2.183 * \text{mean depth}$	(Eq. 7)
$nd = -40.426 - 2.910 * \text{NAOI (DJFM)} + 11.973 * \text{mean area}$	(Eq. 8)

The deterministic model FLake predicted lake ice phenology much better than linear regression models (Fig. 2). The ice data modelled by FLake reflect the high inter-annual variability typical for observed ice phenology (Futter, 2003). In contrast, regression model results reproduce only mean ice phenology on longer time periods. This agrees with the results of Williams *et al.*, (2004) who stated that the best multiple regression analyses cannot account for the full range of annual variability in the historical records, implying the absence of influential factors from these regression models. Simple or multiple linear regression models can be adopted to gain first knowledge on mean ice phenology of lakes in a distinct

region and time window. The predicted data give an overview of ice phenology, if only few input variables are available at a poorer time resolution.

FLake includes more meteorological data with higher temporal resolution than the regression models. Only one meteorological input parameter, the annual mean air temperature or the winter mean NAO-I, was used for the regression models. Five meteorological variables were used with daily resolution to drive FLake. Furthermore, the one-dimensional lake model incorporates more lake specific input data than the regression models. Only mean lake area and mean lake depth were used for the regression models.

Past and future lake ice phenology

FLake was applied to eight different lakes of the Berlin and Brandenburg area for one past period (1947-2007), using observed Potsdam data, and for two future periods (2001-2055; 2071-2100) using simulated data derived from GLOWA-scenarios and RCAO-scenarios. In addition, FLake runs using 20 different simulated WettReg-realisations (1961-2100) were performed only for the lakes Stechlin and Müggelsee providing with minimum and maximum estimates of possible future ice phenology.

Under the same meteorological forcing, the ice characteristics, such as mean number of ice days and percentage of ice covered winters, differed for the eight lakes mostly due to differences in the mean lake depth. The shallower a lake the more days are likely to be covered with ice in each winter (Fig. 3) and the less ice-free winters are likely to occur (Fig. 4).

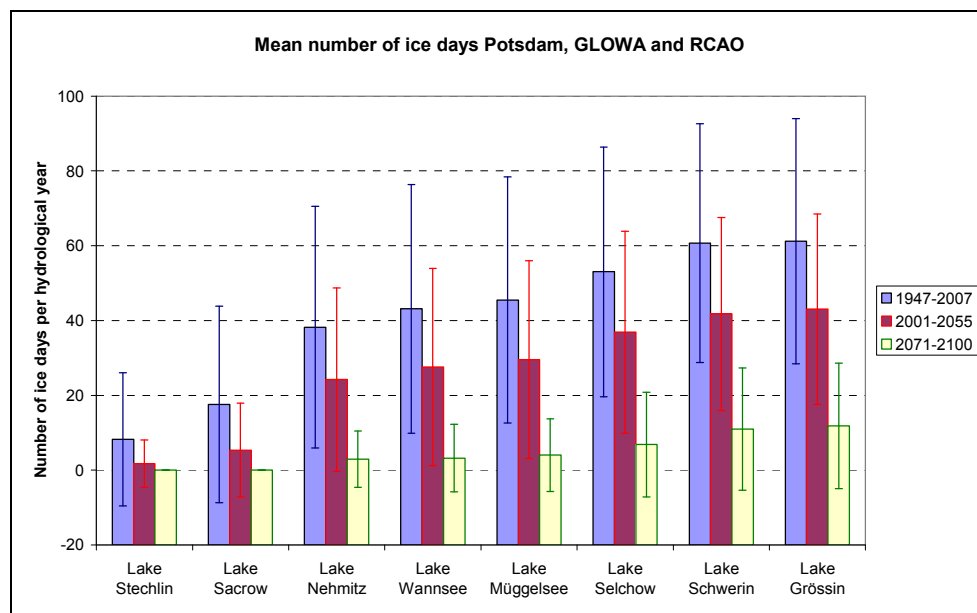


Figure 3. Mean numbers of ice days (\pm standard deviation) for eight Berlin and Brandenburg lakes for periods 1947-207, 2001-2055 and 2071-2100 modelled by FLake.

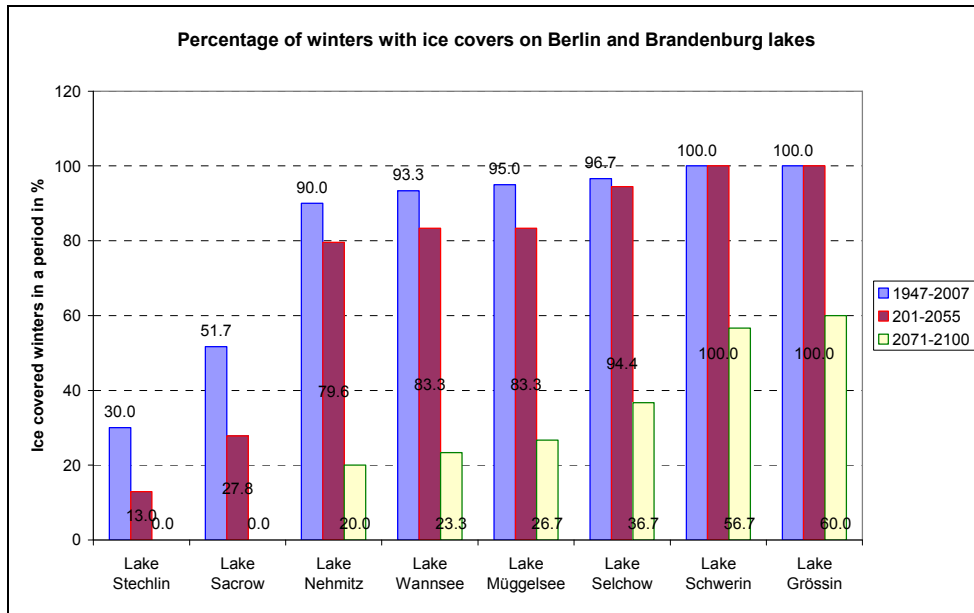


Figure 4. Percentage of ice covered winters for eight Berlin and Brandenburg lakes during 1947-2007 (blue bars), 2001-2055 (red bars) and 2071-2100 (yellow bars), modelled by FLake.

There were significant differences between “number of ice days” means of the modelled time periods, as mean *nd* of the past period (1947-2007) was highest, lower for the closest future scenario from 2001-2055 (GLOWA), finally lowest for the latest future scenario from 2071-2100 (RCAO). The modelled means of *nd* varied in 1947-2007 between 8 and 61 days, in 2001-2055 between 2 and 43 days and in 2071-2100 between 0 and 12 days (Fig. 3). For Lake Müggelsee and Lake Stechlin declining numbers of ice days per winter, modelled using four different scenarios, in the period from 1947 to 2100 are shown in Figs. 8 and 9.

Thus, *nd* decreased with time and increasing air temperature. Trends of *nd* are strongest for the past modelled period and get weaker for the future periods. Thus, modelling results predicted that an increase by 1°C annual mean air temperature caused 16-days (1947-2007) (Fig. 5), 5-days (2001-2055) (Fig. 6) and 2 days (2071-2100) lower numbers of ice days per winter for Lake Müggelsee (Fig. 7). Similar trends in past ice phenology were found e.g. by Magnuson (2008).

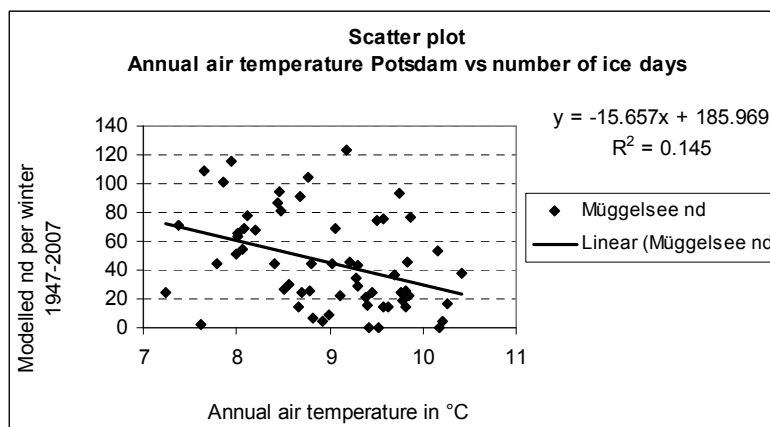


Figure 5. Linear trend of the modelled (FLake) number of ice days (*nd*) for Lake Müggelsee with increasing air temperature 1947-2007

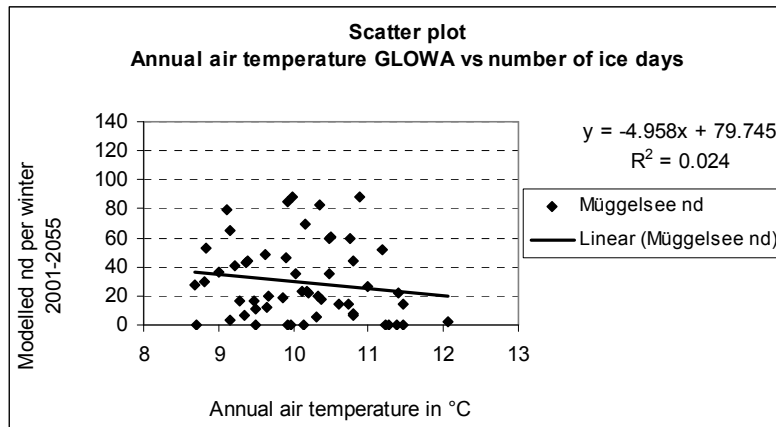


Figure 6. Linear trend of the modelled (FLake) number of ice days (*nd*) for Lake Müggelsee with increasing air temperature 2001-2055

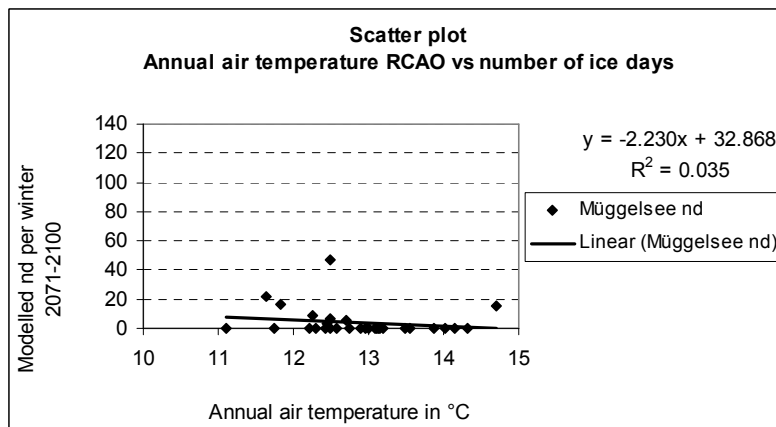


Figure 7. Linear trend of the modelled (FLake) number of ice days (*nd*) for Lake Müggelsee with increasing air temperature 2071-2100

According to FLake-simulations ice-free winters are likely to increase drastically with time and ice covered winters are likely to decrease with increasing mean lake depth (Fig. 4). In the past period 1947-2007 shallow Lake Müggelsee was ice covered 95% of the winters and deep Lake Stechlin 30%. For the future period 2001-2055 (GLOWA-scenario) 83% of the winters are predicted to be ice covered for Lake Müggelsee and 13% for Lake Stechlin. Dramatic reduction in ice cover according to the RCAO-scenario is predicted for the period from 2071-2100 where only 23% of the winters for Lake Müggelsee and no winters for Lake Stechlin are likely to be ice covered (Fig. 4). In the period from 1961-2100 (WettReg) few or no ice-free winters have been modelled for shallow lakes and more ice-free winters than ice-covered winters were simulated for deep lakes (Figs. 8 and 9).

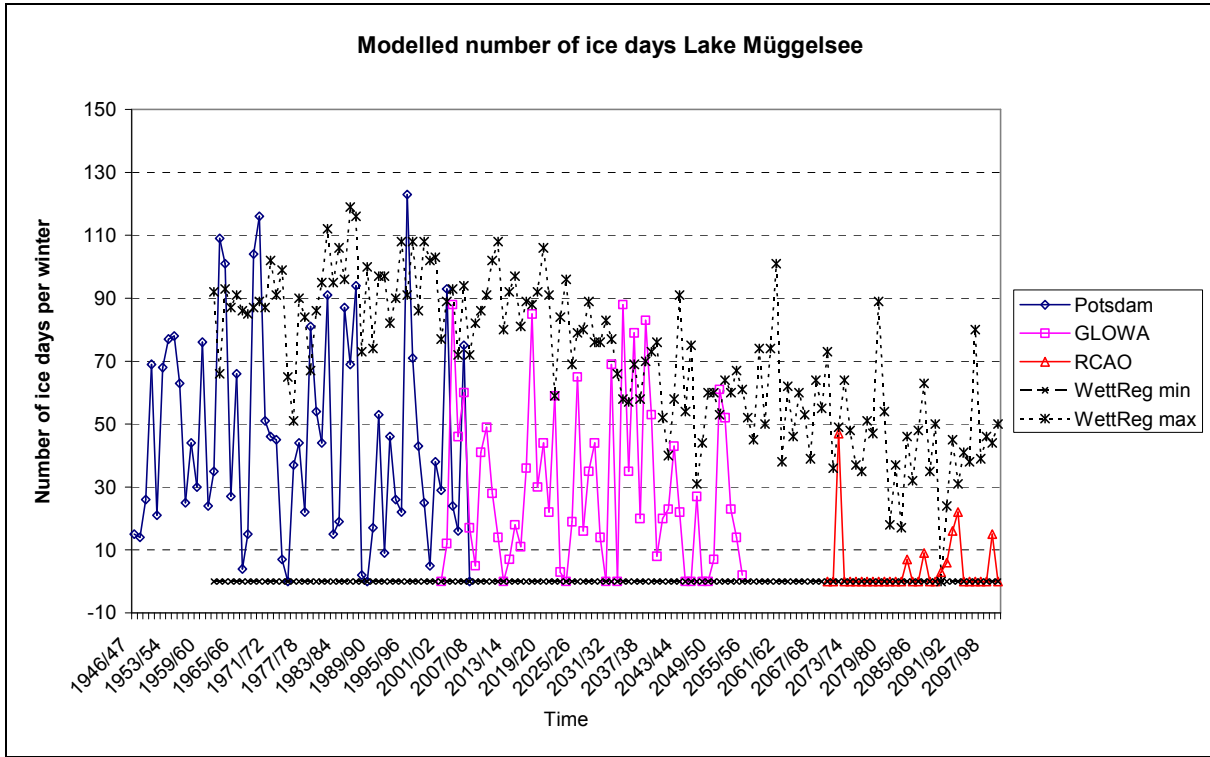


Figure 8. Modelled number of ice days per winter for Lake Müggelsee with 4 different input meteorology time series to FLake (1947-2100): observed data from Potsdam 1947-2007, simulated data derived from the RCMs GLOWA (2001-2055), RCAO (2071-2100) and WettReg (1961-2100). The range of WettReg-realisations is given by the minimum and the maximum numbers of ice days per year

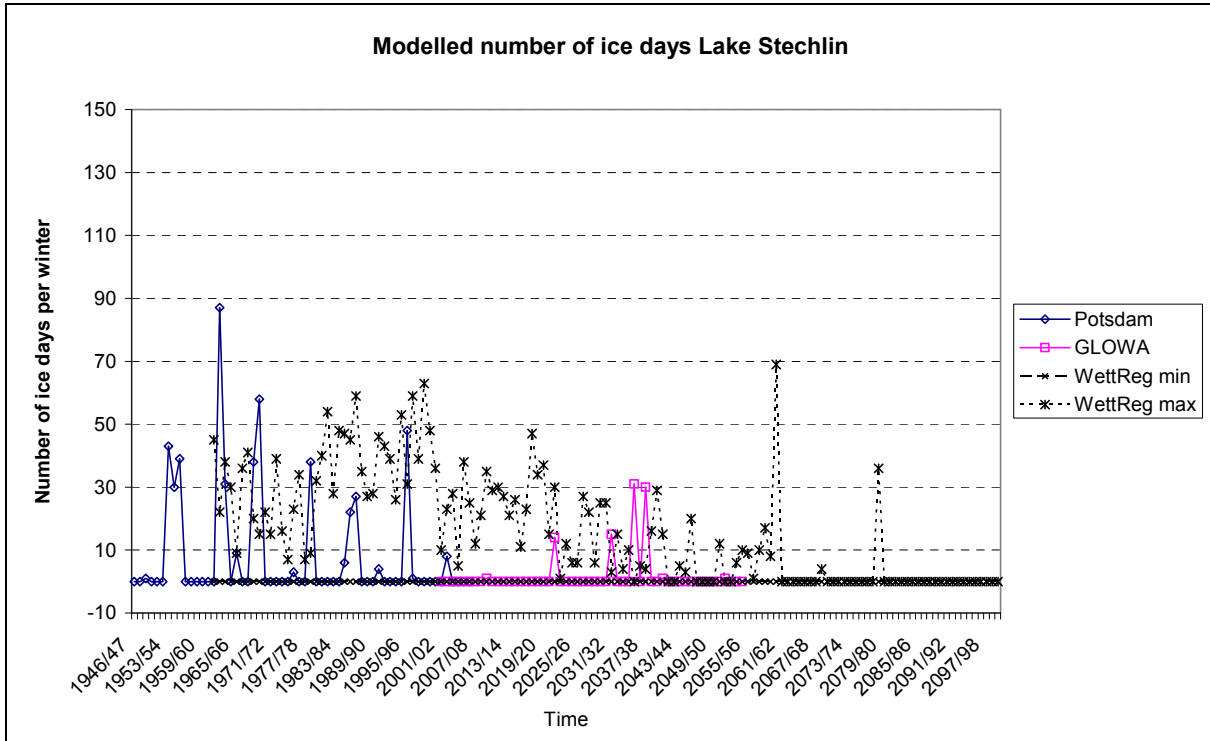


Figure 9. Modelled number of ice days per winter for Lake Stechlin. No ice was modelled for Lake Stechlin using the RCAO input meteorology (further description see Figure 8)

Ice phenology modelling of lakes with a great range of mean lake depth imply that deep, stratified lakes are more strongly affected by climate warming than shallow, polymictic lakes. Duration and intensity of lakes stratification determines lake volume that is directly connected to the water-air-interface (time-dependent). Heat uptake and release of the water body over a year is determined by lake depth, mixed layer depth and duration of stable stratification and mixing. Because the larger lake body can store more and needs longer to release heat (Livingstone, 2008) number of ice covered days of deep lakes was lower than of shallow lakes and mean dates of ice cover formation and break-up were usually later for deep lakes than for shallow lakes. Water body temperature of polymictic shallow lakes is with only a few degrees difference very similar (small time lags) to local air temperature during the year. In contrast, hypolimnion temperature of stratified deep lakes can differ up to 20 degrees to air temperature.

It is likely, that deeper lakes are more strongly affected by the changes in ice phenology than shallow lakes. Thus, a stronger warming trend became more clearly noticeable over the years (climate) for deep lakes than for more shallow lakes that were more affected by current weather conditions.

CONCLUSIONS

The purpose of this study was to model the past ice phenology and to develop future ice scenarios for a variety of freshwater lakes in the Berlin-Brandenburg area. The modelling was aimed at (i) reconstructing the trends in the past ice regime for lakes lacking ice observations, and (ii) estimating the future changes in ice phenology under different climate scenarios, which is important for studying the climate impact on lake ecosystems.

It was shown that the deterministic lake model FLake performs better in reconstructing past lake ice coverage than convenient linear regression models. FLake computes reasonable ice results for shallow, relatively turbid and polymictic, as well for deep, clear and stratified small lakes. The lake model reproduces well the lake ice dynamics, including the high annual variability of ice phenology as well as the intermittent ice coverage per winter. Therefore, the FLake is a reliable tool for studying lake ice phenology and for estimation of the future changes using climate scenarios. Thus, FLake can be applied to model ice covers on lakes all over the world, provided that mean lake depth, water turbidity and meteorological parameters in the lake vicinity are known. Among the major advantages of FLake are: the model is freely available in the internet (open code), is easy to apply by everyone, requires only a few input parameters and is computationally efficient.

Decline in lake ice coverage associated with global climate warming and local air temperature increase could be proved for Berlin and Brandenburg lakes in the past. Past trends of ice reduction are of the same order of magnitude as reported before, (e.g. Magnuson 2008). Further decrease and disappearance of the lake ice coverage in the Berlin and Brandenburg area has been predicted for the future. The overall phenology trends for the past and future climate are: shift to later ice-on and earlier ice-off, with corresponding shortening in the duration of the ice covered period; thinning of ice covers; and increasing number of ice free winters.

ACKNOWLEDGEMENTS

Lake ice phenology data of Lake Müggelsee and Lake Stechlin were provided by Gabriele Mohr, Thomas Hintze and Rita Adrian (IGB). WettReg-scenario data are kindly offered by Frank Kreienkamp (CEC Potsdam) and the German Weather service (DWD) provided Potsdam meteorology data.

REFERENCES

- Adrian R and Hintze T (2000) Effects of winter air temperature on the ice phenology of the Müggelsee (Berlin, Germany). *Verh. Internat. Verein. Limnol.* **27**: 2808-2811
- Adrian R, Walz N, Hintze T, Hoeg S, Rusche R (1999) Effects of ice duration on plankton succession during spring in a shallow polymictic lake. *Freshwater Biology* **41**: 621-632
- Adrian R, Wilhelm S and Gerten D (2006) Life-history traits of lake plankton species may govern their phenological response to climate warming. *Global Change Biology* **12**: 652–661, doi: 10.1111/j.1365-2486.2006.01125.x
- Assel RA and Robertson DM (1995) Changes in winter air temperatures near Lake-Michigan, 1851-1993, as determined from regional lake-ice records. *Limnology and Oceanography* **40**: 165-176
- Bilello M A (1964) Method of prediction of river and lake ice formation. *J. Appl. Meteor.* **3**: 38-44.
- Casper SJ (1985) Lake Stechlin - a temperate oligotrophic lake. In: Junk (ed) *Monographiae Biologicae* **58**: 553pp. Dordrecht, Boston, Lancaster
- Driescher E, Behrendt H, Schellenberger G, Stellmacher R (1993) Lake Müggelsee and its environment – natural conditions and anthropogenic impact. *Int Rev ges Hydrobiol* **78**:327-343
- Enke W, Deutschländer T, Schneider F, Küchler W (2005a) Results of five regional climate studies applying a weather pattern based downscaling method to ECHAM4 climate simulations. *Meteorologische Zeitschrift* **14**: 247-257
- Enke W, Schneider F, Deutschländer T (2005b) A novel scheme to derive optimized circulation pattern classifications for downscaling and forecast purposes. *Theoretical and Applied Climatology* **82**: 51-63
- Futter MN (2003) Patterns and trends in Southern Ontario lake ice phenology. *Environ. Monit. Assess.* **88**: 431-444
- Gao SB, Stefan HG (1999) Multiple linear regression for lake ice and lake temperature characteristics. *Journal of Cold Regions Engineering* **13**: 59-77
- George DG (2007) The impact of the North Atlantic Oscillation on the development of ice on Lake Windermere. *Climatic Change* **81**: 455-468
- Heron R and Woo MK (1994) Decay of a high arctic lake-ice cover - Observations and modelling. *Journal of Glaciology* **40**: 283-292
- Hurrell JW (1995) Decadal Trends in the North Atlantic Oscillation and relationships to regional temperature and precipitation. *Science* **269**: 676-679
- IPCC (2001) Climate Change 2001: The Scientific Basis. Contribution of Working Group I to the Third Assessment Report of the Intergovernmental Panel on Climate Change (IPCC), 944pp. Cambridge University Press, Cambridge, UK
- IPCC (2007) Climate Change 2007: The Physical Science Basis. Contribution of Working Group I to the Fourth Assessment Report of the Intergovernmental Panel on Climate Change (IPCC), 996 pp. [Solomon, S., D. Qin, M. Manning, Z. Chen, M. Marquis, K.B. Averyt, M. Tignor and H.L. Miller (eds.)]. Cambridge University Press, Cambridge, United Kingdom
- Jeffries MO, Morris K, Duguay CR (2005) Lake ice growth and decay in central Alaska, USA: observations and computer simulations compared. *Annals of Glaciology* **40**: 195-199
- Kalff J (2002) Limnology, 592pp. Upper Saddle River, Prentice Hall, New Jersey.
- Koschel R and Adams DD (2003) Preface: Lake Stechlin - An approach to understanding a temperate oligotrophic lowland lake. *Archiv für Hydrobiologie, Special Issues Advances in Limnology* **58**: 1-9
- Kouraev AV, Shimaraev MN, Buharinin PI, Naumenko MA, Crétaux J-F, Mognard N, Legrésy B, Rémy F (2008) Ice and snow cover of continental water bodies from simultaneous radar altimetry and radiometry observations. *Surveys in Geophysics* **29**: 271-295
- Leppäranta M and K Wang (2008) The ice cover on small and large lakes: scaling analysis and mathematical modelling. *Hydrobiologia* **599**:183–189, DOI 10.1007/s10750-007-9201-3
- Liston GE and Hall DK (1995) An energy-balance model of lake-ice evolution. *Journal of Glaciology* **41**: 373-382
- Livingstone D (1997) Break-up dates of alpine lakes as proxy data for local and regional mean surface air temperatures. *Climatic Change* **37**: 407-439
- Livingstone DM and Dokulil MT (2001) Eighty years of spatially coherent Austrian lake surface temperatures and their relationship to regional air temperature and the North Atlantic Oscillation. *Limnology and Oceanography* **46**: 1220-1227
- Livingstone DM (2008) A Change of Climate Provokes a Change of Paradigm: Taking Leave of Two Tacit Assumptions about Physical Lake Forcing. *Internat. Rev. Hydrobiol.* **93**: (4-5) 404-414, DOI: 10.1002/iroh.200811061
- Magnuson JJ, Robertson DM, Benson BJ, Wynne RH, Livingstone DM, Arai T, Assel RA, Barry RG, Card V, Kuusisto E, Granin NG, Prowse TD, Stewart KM, Vuglinski VS (2000) Historical trends in lake and river ice cover in the Northern Hemisphere. *Science* **289**: 1743-1746

- Magnuson JJ (2008) Historical trends in lake and river ice cover in the northern hemisphere. *Science* **289** (5485): 1743-1746
- Ménard P, Duguay CR, Flato GM, Rouse WR (2002) Simulation of ice phenology on Great Slave Lake, Northwest Territories, Canada. *Hydrological Processes* **16**: 3691-3706
- Mironov DV (2008) Parameterization of lakes in numerical weather prediction - Description of a lake model. COSMO Technical Report 11-41. Offenbach am Main, Germany, Deutscher Wetterdienst
- Mischke U, Nixdorf B (2008) Bewertung von Seen mittels Phytoplankton zur Umsetzung der EU-Wasserrahmenrichtlinie. Gewässerreport 10: 263pp. Cottbus, Brandenburgische Technische Universität Cottbus, Fakultät Umweltwissenschaften und Verfahrenstechnik
- Palecki MA and Barry RG (1986) Freeze-up and break-up of lakes as an index of temperature changes during the transition seasons: a case study for Finland. *Journal of Climate and Applied Meteorology* **25**: 893-902
- Roeckner E, Oberhuber JM, Bacher A, Christoph M, Kirchner I (1996) ENSO variability and atmospheric response in a global coupled atmosphere-ocean GCM. *Climate Dynamics* **12**: 737-754
- Rummukainen M, Räisänen J, Bringfelt B, Ullerstig A, Omstedt A, Willén U, Hansson U and Jones C (2001) A regional climate model for northern Europe: model description and results from the downscaling of two GCM control simulations. *Clim. Dyn.* **17**: 339-359
- Shuter BJ, Schlesinger DA, Zimmerman AP (1983) Empirical predictors of annual surface-water temperature cycles in North-American lakes. *Canadian Journal of Fisheries and Aquatic Sciences* **40**: 1838-1845
- Stefan HG and Fang X (1997) Simulated climate change effects on ice and snow covers on lakes in a temperate region. *Cold Regions Science and Technology* **25**: 137-152
- Vavrus SJ, Wynne RH, Foley JA (1996) Measuring the sensitivity of southern Wisconsin lake ice to climate variations and lake depth using a numerical model. *Limnology and Oceanography* **41**: 822-831
- Werner PC and Gerstengarbe FW (1997) Proposal for the development of climate scenarios. *Climate research* **8** (3): 171-180
- Williams G, Layman KL, Stefan HG (2004) Dependence of lake ice covers on climatic, geographic and bathymetric variables. *Cold Regions Science and Technology* **40**: 145-164

Fate of groundwater inflow in Lake Thingvallavatn during early spring ice-breakup

H.Ó. Andradóttir^{1*}, A.L. Forrest² and B.E. Laval²

¹ Faculty of Civil and Environmental Engineering, University of Iceland, 107 Reykjavík, Iceland

² Department of Civil Engineering, University of British Columbia, Vancouver, British Columbia, V5T 1Z4, Canada

*Corresponding author, e-mail hrund@hi.is

ABSTRACT

Sub-artic Lake Thingvallavatn is one of Iceland's largest, deepest and best known lakes. Situated at the rift between the North American and Eurasian tectonic plates, it is part of a world heritage site and a major tourist destination. From a hydrological viewpoint, the lake is unique in that it is predominantly fed by groundwater springs originating from nearby glacier Langjokull. The goal of this study was to establish the near field inflow dynamics of the largest subsurface spring Silfra, contributing approximately 30% of the total inflows to the lake, during early spring ice-breakup. A ten day field study was conducted in February 2009. The groundwater inflows were found to have higher temperature, conductivity, and pH than the receiving lake water. Using temperature as a tracer, the groundwater fate, and mixing regimes were assessed both in open water and under ice, as ice was breaking up and shifting in and out of the study area during the study period. Initial results from moored thermistor chains, CTD profiles, ADV measurements, weather stations and Autonomous Underwater Vehicle (AUV) borne CTD will shed a stronger light on the interaction of river inflows, ice cover and meterological forcings during winter ice cover and early spring break-up. The use of an AUV platform to collect horizontal CTD profiles characterizes horizontal variability of water properties in open and ice-covered water, something that cannot be obtained using conventional techniques.

KEYWORDS

Groundwater fate; ice-breakup; autonomous underwater vehicle; Thingvallavatn; limnology.

INTRODUCTION

Under-ice mixing dynamics in lakes, and particularly sub-arctic and arctic lakes, are poorly understood. With some notable exceptions (Farmer, 1975; Mironov et al., 2002), this results from a lack of field data being collected during the winter months, especially during the early and late winter when then ice is being initially formed and thawing respectively; times when the water body is experiencing significant mass transport (Petrov et al., 2006) but is logically difficult to sample. In lake systems that are ice-covered from a portion to the majority of the year, determining these mixing regimes is essential for examining chemical and nutrient transport.

It has long been recognized that different density inflows (e.g. temperature, conductivity or turbidity) will result in varying insertion points into a water body (Wells and Wettlaufer, 2007); however, the influence of ice on such a system has generally not been studied. The largest challenge of studying this problem is the combination of significant horizontal

variability of water properties and thin ice-cover. The horizontal variability cannot be adequately captured by moored instruments and a transect of vertical profiles cannot be safely obtained.

This objective of this study was to examine the fate of the dominant groundwater inflow (negatively buoyant in the winter months) and the ice-edge interactions in the relatively shallow waters using a variety of conventional (moorings and profilers) and non-conventional techniques (*UBC-Gavia*, an Autonomous Underwater Vehicle). During the course of the study, this system was complicated by intense storm (and associated mixing) events that broke up the ice cover over the 10-day period. This paper will present the initial results during those days with full and partial ice cover and discuss the potential implications for mixing during winter thaw and ice-cover break-up.

METHODS

Site description

Lake Thingvallavatn is one of Iceland's largest (83 km^2) and deepest lakes, with a mean depth of 34 m and maximum depth of 114 m. The lake and its 1000 km^2 catchment area are almost entirely situated on the North Atlantic rift zone. From a hydrological standpoint, this lake is unique in that an estimated 90% of its $100 \text{ m}^3/\text{s}$ average discharge originates from underwater springs, composed of surface run-off and glacial melts from nearby Langjokull and Thorisjokull glaciers. This water percolates through basaltic glacial deposits and lavas before entering the northern shore of the lake through a series of underwater cracks (Adalsteinsson et al., 1992; Saemundsson, 1992). The study area in this paper is the 1.5 km^2 and 2-10 m deep northwestern bay, into which the largest groundwater spring Silfra, with an estimated $30 \text{ m}^3/\text{s}$ of flow, enters the lake (Vatnaskil, 2000). The temperature of this groundwater is typically $2.8\text{-}3.5^\circ\text{C}$ (Adalsteinsson et al., 1992).

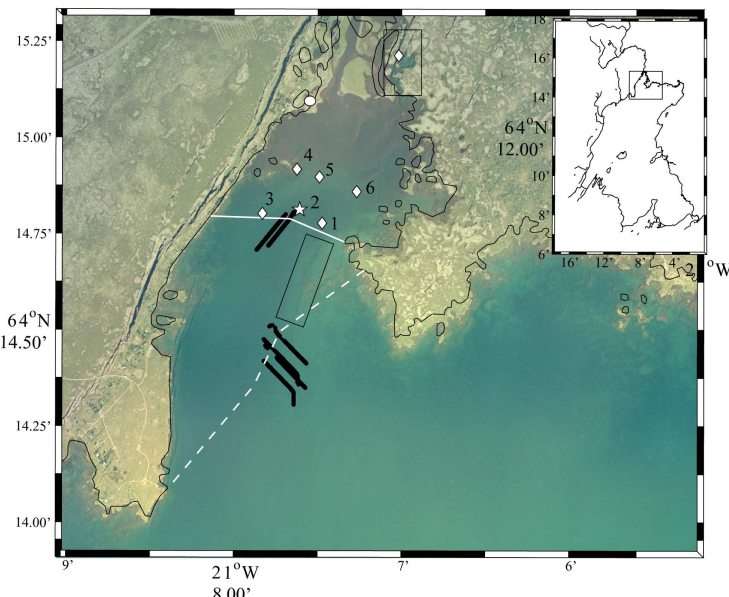


Figure 1. Aerial view of the Silfra groundwater inlet bay (rift approximately delineated by lower box in image) in Lake Thingvallavatn (overview inset) with the overland Oxara river and part of the Silfra inflow (upper box in image) shown at the bay inlet: solid white line - ice edge on Feb. 20, 2009; dashed white line - ice edge Feb. 22, 2009; upper black lines - *UBC-Gavia* mission tracks on Feb. 20, 2009; lower black lines - *UBC-Gavia* mission tracks on Feb. 22, 2009; numbered diamonds - temperature moorings; diamond - source monitoring; star - ADV and temperature mooring; and, circle - weather station.

Ice coverage

Ice cover formation over the lake varies from year to year. In the winters between 1951-1990, the lake was ice-covered continuously for 3 months every winter, typically starting in early January and lasting to early April (Rist and Olafsson, 1986). The water temperature during ice formation ranges typically from 0.2 to 1.7 °C, and 2-3°C at ice-breakup (Adalsteinsson et al., 1992). In the past 7 winters, however, the winter ice-cover has been typically intermittent in space and time for 5 weeks (on average), and two years have been completely ice free (Sveinbjornsson, in review).

Field techniques

A comprehensive field monitoring program was undertaken Feb. 18-28, 2009. Air temperature, relative humidity, wind speed and direction were measured by the Icelandic Meteorological office at 10 minute intervals approx. 6 km northeast inland of the study area. For higher precision of local weather wind and solar radiation conditions, an Onset weather station was temporarily installed at 1.7 m height ~ 10 m from the lake shoreline and within about 600 m leading ice edge on Feb. 20, 2009. Water quality tests were conducted with a handheld Oakton pH-Conductivity-Temperature meter at various locations in groundwater cracks including Silfra, Oxara River and in the lake on Feb. 26-27, 2009.

Water temperatures were continuously monitored at six moored stations along two lateral transects in the bay (see Fig. 1): The first three stations were situated at the ice edge on Feb. 19, 2009 in 4.7-5.1 m deep water. The latter three stations were positioned in a parallel manner in 1.7-2.3 m shallow water. RBR TR-1050 single channel temperature loggers were placed at 0.5-1 m depth intervals from bottom sampling at 1 Hz at each of the six stations. The top loggers were situated approximately at 0.8-1.5 m depth. Vertical conductivity-temperature and depth profiles were taken in open water at various locations in the bay using a Seabird SBE-19plus.

High-resolution CTD measurements were made with a Seabird Electronics SBE-49 mounted on *UBC-Gavia*, a small Gavia-class AUV owned and operated by the University of British Columbia. As configured for freshwater operations, the vehicle is approximately 2.4 m in length, 0.2 m in diameter, and 55 kg dry weight. For the runs beneath the ice edge, a 3 mm monofilament line (deployed at the vehicle speed of ~ 1.4 m s⁻¹) was used as a backup AUV retrieval system since the ice was both too thin to safely work on and too thick to break through with the deployment boat. Mission design was for the vehicle to traverse and return on a parallel line (~ 50 m spacing) 300 m underneath the ice edge at a constant depth where a tolerance of 20 cm (i.e. ±10 cm away from the depth set point) was used.

Water speeds were monitored over a 2.5 day period at moored station No. 2 (Fig. 1) at 0.2 m intervals from the bottom using a Nortek Aquadopp ADV. Water speeds were averaged over 10 minutes in order to ensure sufficient signal strength for reliable velocity readings in this extremely clear water. Results from the bottom 3.6 - 4 m are presented in this paper.

RESULTS AND DISCUSSION

Weather and ice coverage

During the first week of February, air temperature dropped below -10 °C accompanied with low winds, at which time the ice cover started to form. In the beginning of the second week of February, the air temperature rose to 0 °C and the average wind rose to 5 m s⁻¹, but in the latter half of the week extremely cold and calm conditions resumed. By Feb. 16, the entire lake was ice covered, with a few small near shore open areas around the Silfra inlet.

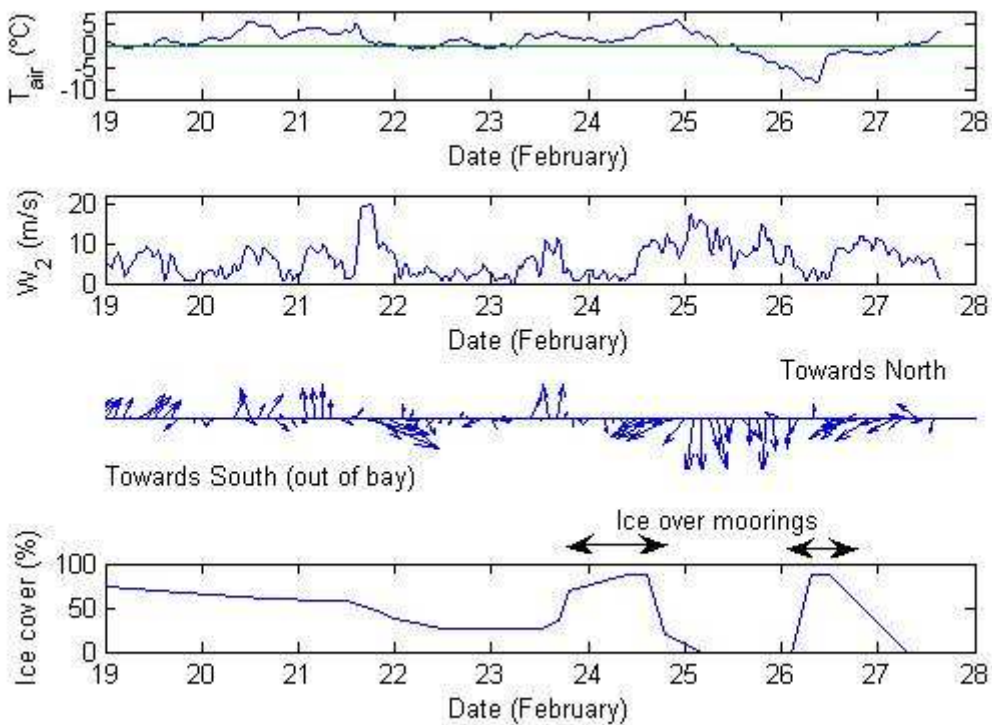


Figure 2. Air temperatures, wind speed, wind direction and ice coverage Feb. 19-28, 2009.

From Feb. 13, 2009 throughout the end of the month, air temperatures remained mostly above 0°C and wind speeds fluctuated from 0-15 m s⁻¹ (see Fig. 2). The combination of high winds and warmer air temperatures broke up, pushed and shifted the ice inside the bay during the field study, and by Feb. 25, 2009 the entire lake was ice-free. Thin ice reformed on Feb. 26, 2009 after a short-lived cold spell, but was gone by the next day. A comparison between temporary near lakeshore and long-term inland weather stations show excellent correlation in the meteorological data except for wind speeds that were consistently 2 m s⁻¹ higher at the lake shore, and higher yet when both wind speed data sets are corrected to 10 m elevation.

Water characteristics

Near surface water quality sampling clearly demonstrate that groundwater inflows have fundamentally different properties than surface and lake water. As summarized in Table 1, the groundwater is basic with pH exceeding 9.7, whereas surface river water is more neutral with pH of 7.6. The specific conductivity of groundwater was found to be ~20 µS cm⁻¹ higher than that of Oxara river. These differences can be explained by the fact that the groundwater interacts with the basaltic and porous volcanic soil on its 50 km long journey from glacier Langjokull to the lake.

In addition, during the cool winter season in which the study was undertaken, groundwater inflow measured around 3.5 °C whereas the surface river water hovered around the freezing point as a result of the soil providing a buffering effect from seasonal meteorological fluctuations. These results conform to the previously published findings of Rist and Olafsson (1986), also summarized by Adalsteinsson et al. (1992).

Table 1. Near-surface water quality results in Lake Thingvallavatn, Feb. 26-27, 2009

Locations	pH	Sp. Cond. ($\mu\text{S}/\text{cm}$)	Temperature ($^{\circ}\text{C}$)	Sample size
Groundwater cracks	9.8 ± 0.1	89 ± 5	3.5 ± 0.1	5
River Oxara	7.6 ± 0.1	66 ± 1	0.3 ± 0.2	7
Lake water	8.7 ± 0.1	80 ± 7	2.0 ± 1.1	6

The water quality sampling provided in Table 1, suggests that specific conductivity and water temperature, may be used as tracers to track the fate of the groundwater inflow in Lake Thingvallavatn. This notion will be explored further in following sections.

Groundwater plume and mixing at moored stations

Continuous temperature measurements and vertical CTD profiles at moored stations in the bay shed light onto the fate of the groundwater plume and mixing regimes. The upper panel in Fig. 3 illustrates the near surface and near bottom temperatures measured in the shallow central mooring (No. 5 in Fig. 1). The fact that the two temperatures are almost the same, suggests that the water column is predominantly well mixed in the shallows. But the temperatures across the three shallow stations are not identical suggesting that the groundwater is not equally strong: the highest temperatures are most often measured at the central station (No. 5 in Fig. 1), generally correlated with the North or Northwesterly winds. In Southerly or Northeasterly winds, the warmest temperatures are measured in the western shallow station (No. 4 in Fig. 1; data not shown). This suggests that the wind influences the lateral trajectory of the groundwater plume entering the lake.

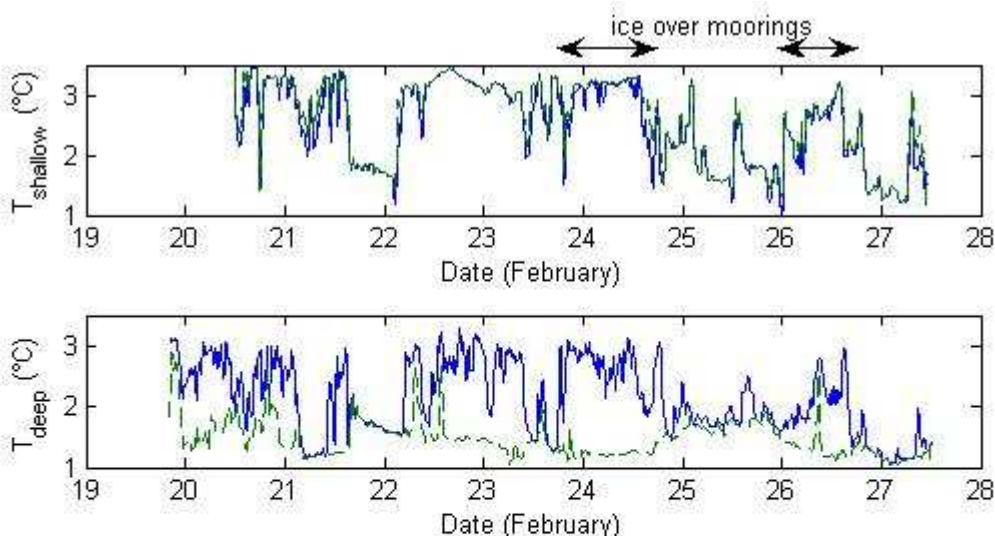


Figure 3. Vertical and temporal variability in water temperature at central shallow station (No. 5) and central deep station (No. 2). Solid line represents temperatures at 0.5 m distance from bottom, while dashed line near surface temperature (1.2-1.6 m deep).

In contrast, the deeper moored stations in the lake exhibit periods of inverse stratification, followed by periods of fully mixed conditions. As shown on the lower plot on Fig. 3, the bottom water is often 3 °C while the surface water is 1-2 °C. This indicates that in the deeper section of the bay, the groundwater plume at 3°C is heavier than local environment, and hence plunges as it enters the lake. The inverse stratification is particularly strong on days where the majority of the bay is ice covered (see Feb. 19-22, 24, 26 of Fig. 3). Vertical

profiles at the three deep moorings illustrated on Fig. 4 suggest that the groundwater plume is confined within the bottom 0.5-1.7 m of the water column, while the upper 2-3 m are relatively well mixed. Lateral variability is evident between the east, central and west moorings on the windy Feb. 20, 2009.

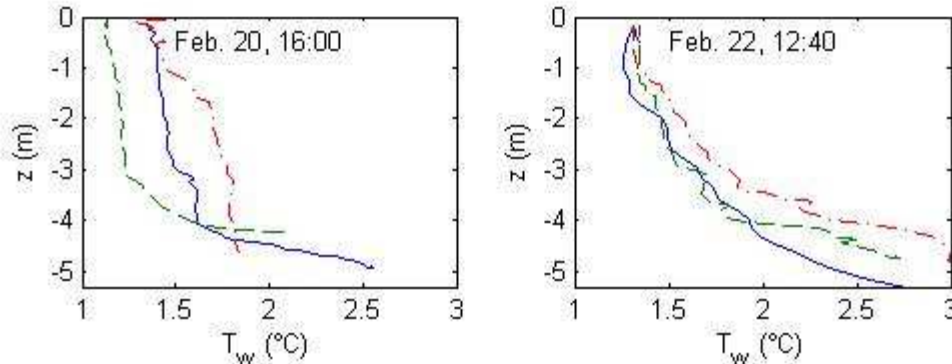


Figure 4. Vertical temperature profiles measured at central (solid), east (dashed) and west (dot-dashed) stations on February 20 and 22, 2009.

While the water column at the deeper stations is predominantly stratified, there are 5 distinct periods when the water column becomes vertically mixed. The meteorological conditions during these events (see Figure 2) suggest that the periods of vertical mixing occur: (1) if wind blows at high wind speeds from the North, pushing water and ice out of the bay in cold or cooling air temperatures, indicating that convective mixing may also contribute; or, (2) if wind blows along the greatest fetch (from the South) along the main body of the lake into the bay. Air temperatures are above zero in the latter scenario, suggesting that convective cooling may not have been an important contributor to vertical mixing. This suggests that the mixing regime is not only influenced by ice cover as discussed earlier, but also by meteorological forcings.

Water Column Velocities

The acoustic Doppler velocity (ADV) measurements taken at station No. 2 (see Fig. 1) on Feb. 22-24 reveal a multilayer flow. The bottom 1.8 m of the water column moves consistently at 6 cm/s downslope towards Southwest (see Fig. 5). This corresponds to the upper boundary of the 0.5-1.7 m deep groundwater plume observed from temperature measurements (see Fig. 4). The fact that the direction is towards Southwest, as opposed to South where the first crack of Silfra reaches the lake, may suggest that the groundwater inflow is not confined as a localized point source, but rather a continuous line source along the series of cracks located along the entire eastern side of the bay (see Fig. 1). Just above the plunging groundwater inflow at 1.8-2.0 m over the bottom, strong echo was found in the water producing invalidly high flow components along the East-West and vertical axes throughout the entire time period. These unstable readings coincide with the direction of shear turbulence generated by the plunging inflow into the bay, and may be a signal of an interference zone between groundwater inflow and baywater

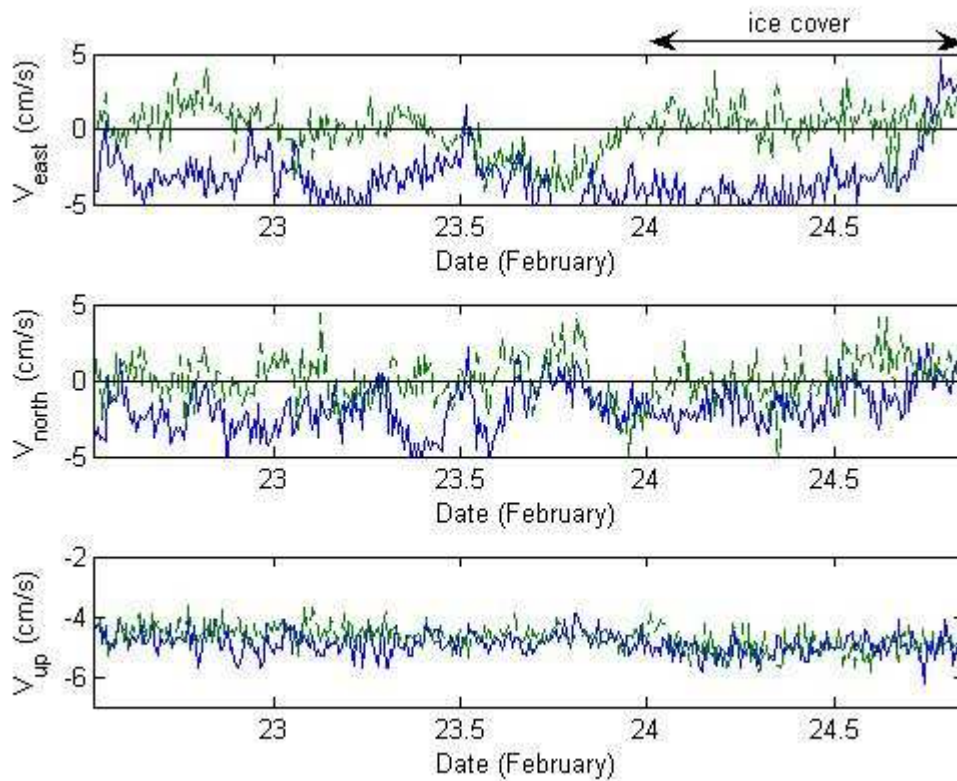


Figure 5. Water speeds in East, North and up directions at 0.6 m (solid blue) and 3.2 m (dashed green) from bottom at moored station 2, Feb. 22-24 2009.

As summarized in Table 2, the flow in the mid and upper layers are consistently around 5 cm s^{-1} moving mostly in the westerly direction. In the upper most layer, the flow is moving in all directions during ice free conditions. In contrast, in the absence of wind during ice cover conditions, the upper layer moving towards northeast, or in the opposite direction to the bottom groundwater intrusion possibly indicating a return flow.

Table 2. Flow speeds in directions at different depths at moored station No. 2, Feb. 22-24, 2009

Zone	Distance from bottom (m)	Average water speed (cm s^{-1})	Prevalent flow direction	
			No ice	Ice cover
Bottom layer (groundwater)	0.2 – 1.6	6 ± 1		SW
Interference zone	1.8 – 2.0	Invalid		E (and W)
Mid layer	2.2 – 2.6	5 ± 1	NW-SW	NW-S
Upper layer	2.8 – 3.6	5 ± 1	All	NE, S

Lastly, it is interesting to consider more closely the time variations in the velocity components along the East and North axes (upper two panels on Fig. 5). Both near bottom (solid line) and upper layer (dashed line) records exhibit oscillations with periods on the order of several hours up to a day during ice free conditions. Once ice covers the mooring on Feb. 24, 2009 these long-term oscillations in the bottom layer appear to be reduced, suggesting that they may be wind driven.

Under ice heterogeneity

During the ice coverage period (Feb. 20 - Feb. 22, 2009), AUV missions were focused on conducting transects under the leading ice edge at a constant depth of 2.0 m in the well-mixed layer (see Fig. 4). As the ice cover was evolving during this time period, these missions were run in different areas (see Fig. 1). On Feb. 20, 2009, two horizontal temperature profiles were collected at the mouth of the bay at the approximate position of the incoming groundwater (upper group of black lines in Fig. 1). Vertical temperature profiles collected in the bay show that the average surface water temperature was approximately 1.5°C when not in the zone of influence of the incoming, warmer groundwater.

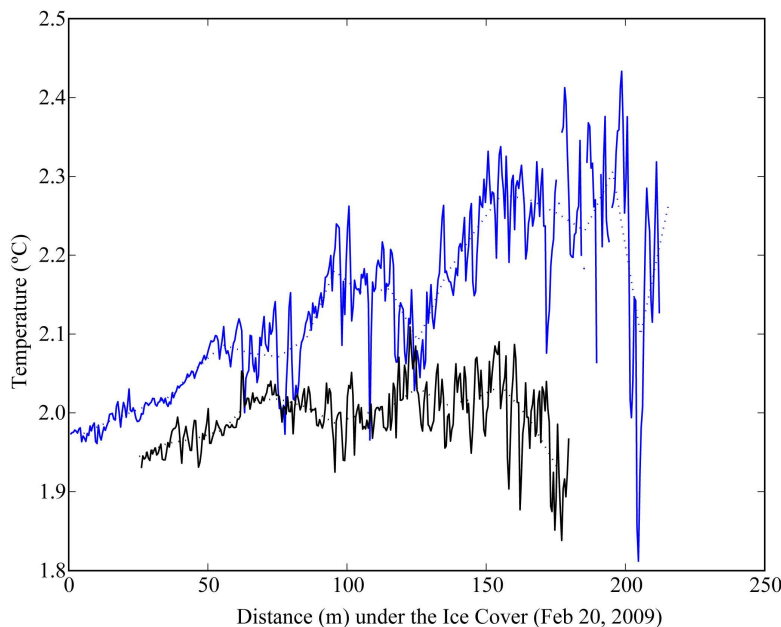


Figure 6. Horizontal temperature profiles at 2 m constant depth (± 10 cm) under the leading ice edge on Feb. 20, 2009 showing transects closer (upper blue) and farther (lower black) from the source water rift (solid and dashed lines represent 50 cm and 10 m horizontal bin average respectively).

As shown in Fig. 6, there are two approximate mixing regimes underneath the ice characterized by relatively constant temperatures from 0 - 50 m (max. deviations of ~ 0.03 °C) and then largely fluctuating temperatures from 50 - 200 m (max. deviations of ~ 0.38 °C). It is proposed that the water is relatively well-mixed in the surface layer above the plunging groundwater plume in the ice-free area as a result of the wind action and that this regime dominates in the near ice edge regime. In the far ice edge regime, the system is subject only to the forcings of the incoming groundwater and not wind. It is conjectured that the observed temperature deviations at 2 m depth under the ice are a localized effect of heterogeneous currents resulting from the groundwater plume flowing along the bottom (at 4-5m) rather than other physical processes such as surface heating. This is because the temperature fluctuations measured here are greater than observed in other ice-covered systems with no groundwater inflows (Forrest et al., 2008). The slight offset between the two transects (~ 0.05 °C in the near ice edge region) is thought to reflect the positioning of the lines to the source water; warmer temperatures representing relative proximity.

This theory is reinforced two days later when further AUV missions were conducted at the ice edge on Feb. 22, 2009. In the interlude, a 20 m s^{-1} windstorm pushed most of the ice off the bay so the deployments were undertaken much further out into the lake (see lower black lines on Fig. 1). Figure 7 shows a complex mixing regime under the ice which varies laterally in 2D under the ice. Similar to the initial missions of Feb. 20, 2009, the water closest to the ice edge is characterized by low temperature fluctuations.. In 50-100 m distance from the ice edge, temperature deviations of about 0.025°C are observed. Thermal deviations continue to be present until 150-250 m under the ice edge, but with variable strength. The most dominant temperature fluctuations (max. deviations 0.08°C) are measured in the third transect 200 m under the ice. This is likely the signal of an additional source of groundwater into the lake, because, as seen from Fig. 1, underwater cracks extend into the lake and are therefore likely to have localized effects. In general, however, the thermal deviations are much smaller than previously observed in the shallower inlet region (recall $\pm 0.38^\circ\text{C}$ on Feb 20, 2009). This indicates that the water 2 m under ice further into the lake is less heterogeneous. The likely reasons for this difference are related to the geographical positioning of the AUV missions: First, the transects were conducted closer to the main body of the lake, suggesting that water column is more influenced by cold lake water. Second, the water depth was $\sim 10 \text{ m}$ depth as compared to $\sim 4 \text{ m}$ at the initial deployment site, such that impacts of bottom flowing groundwater are not as strong near the water surface. Third and last, the AUV missions were conducted further from the source waters on the eastern side, also suggesting less groundwater influence.

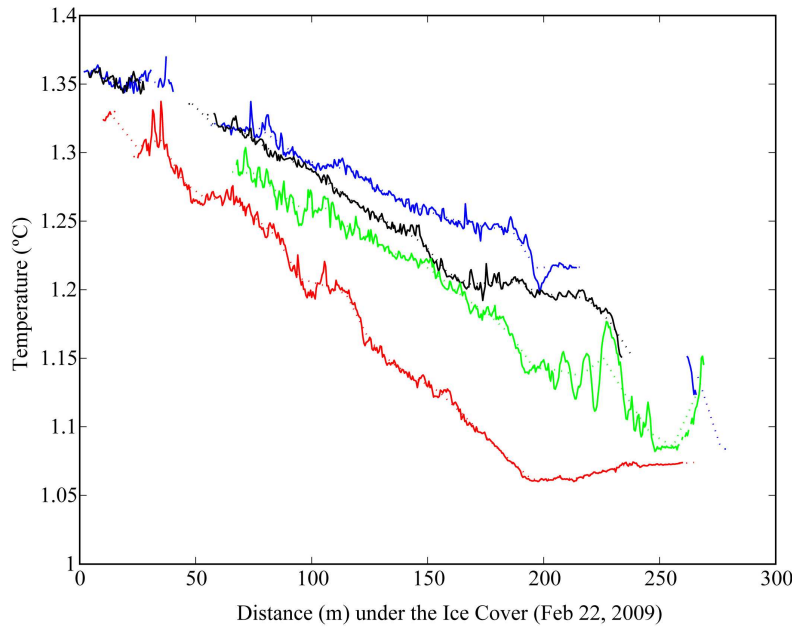


Figure 7. Horizontal temperature profiles at 2 m constant depth ($\pm 10 \text{ cm}$) under the leading ice edge on Feb. 22, 2009 showing transects closest to the groundwater source (upper blue) successively until furthest from shore (lower red) (solid and dashed lines represent 50 cm and 10 m bins respectively).

Focusing next on temperature trends, Fig. 7 shows that the farther away from the source water located in the eastern part of the bay, the lower the overall temperature became. This is in accordance with the AUV missions conducted on Feb. 20 (Fig. 6). In contrast, the further under the ice that was profiled, the lower the measured temperature. This different trend

could be due to these AUV missions being further into the lake. The surface water in the lake measured a few days later were 1 °C, so the fact that the water measured 200 m under the ice being 1.05-1.10°C is consistent. But this downward temperature trend could also be brought by the large windstorm on the preceding day. As the wind blew from open to ice-covered waters during the windstorm, warmer water (left side on Fig. 7) was likely pushed from shallower section under the leading ice edge, generating a cooler lake water return flow (right side on Fig. 7). Lastly, it is unlikely that the decreasing temperature could be a result from vehicle motion and vertical stratification of the water column, because as Fig. 4 shows that the top 2-2 meters are relatively well mixed. In the worst-case scenario where the vehicle was operating directly along the thermocline, the vertical gradient is only $\sim 0.1 \text{ }^{\circ}\text{C m}^{-1}$. In a 20 cm depth tolerance window, the greatest expected variation would be 0.02 °C, which is an order of magnitude less than the overall difference observed from 50 m to 250 m below the ice (e.g. 0.2 °C along the first transect).

CONCLUSIONS

This study collected data in the near-shore region of Lake Thingvallavatn during a dynamic period of late winter ice break-up and explored the fate of the incoming groundwater. Initial datasets (including temperature moorings, vertical profiling, horizontal profiling, and velocity profiling) indicate that the groundwater is a negatively buoyant line source along the underwater cracks situated on the entire eastern side of the bay. This denser groundwater plunges into the lake and travels as a gravity current along the bottom slope. During ice free conditions, the direction of the groundwater plume varies in space and time, depending on local weather conditions. These meandering effects appear to be reduced during ice covered conditions.

The use of *UBC-Gavia* provides a unique dataset that is unable to be gathered with any other technique. Initial results demonstrate a unique and previously unseen heterogeneity under the ice edge. In the shallow, near delta region, large thermal fluctuations are observed in the horizontal at 2 m below the ice ($\pm 0.38 \text{ }^{\circ}\text{C}$), believed to be an interaction between the groundwater plume and ice cover in the absence of mean wind-shear. In the deeper delta regions, the impacts of cold lake water become more prominent, and lateral heterogeneity is dampened, except at localized spots of groundwater inflows.

ACKNOWLEDGEMENTS

This project was funded by the Canadian Northern Scientific Training Program (NSTP) and the University of Iceland Research Fund. Alexander Forrest was supported by a Canadian National Scientific and Engineering Research Council (NSERC) postgraduate scholarship-doctorate (PGS-D) scholarship. The Thingvellir National Park Rangers Einar Saemundsen and Scott Riddell are thanked for their assistance and continuous watching over the project. The efforts of our field crew working at times in difficult weather conditions, that is Pasquale Amendola, David Chretien, Lukas Eggler, Matthieu Fillon, Anna Lefering, Marie Mortamet, and Gudbjorg Esther Vollertsen, are greatly appreciated. The Institute of Biology at the University of Iceland and Finnur Ingimarsson at the Natural History Museum of Kopavogur are thanked for boat lending for the field study. Hafmynd ehf, the manufacturer of *UBC-Gavia*, and specifically Richard Yeo and Eggert Magnusson, receive specific thanks continuous help in these efforts. Icelandic Meteorological Office is thanked for providing reference weather data for the study. Sveinn Oli Palmarsson and Einar Sveinbjornsson are thanked for their sharing of information on the inflows and ice cover of Lake Thingvallavatn.

REFERENCES

- Adalsteinsson H., Jónasson P.M. & Rist S. (1992), Physical characteristics of Thingvallavatn, Oikos, **64**, 121-135.
- Farmer D. M. (1975). Penetrative convection in the absence of mean shear. Q. J. R. Meteorol. Soc. **101**: 869–891.
- Forrest A.L., Laval B.E., Pieters R. and Lim D.S.S. (2008), Convectively driven transport in temperate lakes. Limnology and Oceanography **53(5, part 2)** 2321-2332.
- Mironov D., Terzhevik A., Kirillin G., Jonas T., Malm J., and Farmer D. (2002), Radiatively driven convection in ice-covered lakes: Observations, scaling and a mixed layer model. J. Geo. Res. **7**: 1 - 16.
- Petrov M. P., Terzhevik A.Y., Zdorovenkov R. E., and Zdorovenkova G. E. (2006), The thermal structure of a shallow lake in early winter. Water Resources **33**: 135 - 143.
- Rist S. & Ólafsson G. (1986), Ísar Þingvallavats (e. Lake Thingvallavatn ice cover), Náttúrufræðingurinn, **56** (4), 239-258.
- Saemundsson, K. (1992), Geology of the Thingvallavatn area, Oikos, **64**, 40-68.
- Sveinbjörnsson E., (in review), Vetrarís á Þingvallavatni – gagnlegur veðurfarsmælir (e. Ice cover on Lake Thingvallavatn – practical weather monitoring), Náttúrufræðingurinn.
- Vatnaskil Consulting Engineers (2000), Þingvallavatn. Rennslislíkan. 78 p
- Wells M. G. and Wetlaufer J. S. (2007), The long-term circulation driven by density currents in a two-layer stratified basin. Journal of Fluid Mechanics **572**: 37-58.

Modeling climatological circulation in Lake Michigan

Dmitry Beletsky^{1*} and David Schwab²

¹ University of Michigan, Ann Arbor, MI 48108, USA

² NOAA Great lakes Environmental Research Laboratory, Ann Arbor, MI 48108, USA

*Corresponding author, e-mail dima.beletsky@noaa.gov

ABSTRACT

Climatological circulation in Lake Michigan is presented. It is based on continuous modeling of 3D lake circulation and thermal structure from 1998-2007 using observed meteorological data as the forcing function. Model results show a large-scale cyclonic circulation pattern during both stratified and unstratified conditions with current speeds of several cm/s. Model results are compared with long-term current observations. Mechanisms driving long-term lake circulation are discussed.

KEYWORDS

Lake Michigan, circulation model, climatology.

NOTE:

This paper was published in the Geophysical Research Letters and available online. The following code is both the login ID and password: 55714634. Click this link to access the article: <http://www.agu.org/journals/gl/gl0821/2008GL035773/>

Summertime Inter-hypolimnetic Thermal Differences in a Small Multi-basin Lake

Y. Imam^{1*}, B. Laval¹, D. Lim², and G. Slater³

¹ Department of Civil Engineering, University of British Columbia, 6250 Applied Science Lane, Vancouver, BC, Canada, V6T 1Z4.

² NASA Ames Research Center, Mail-Stop 245-3, Moffett Field, CA, USA, 94035-1000.

³ School of Geography and Earth Sciences, McMaster University, 1280 Main Street West, Hamilton, ON, Canada, L8S 4K1.

* Corresponding author, e-mail yehya@civil.ubc.ca

ABSTRACT

The hypolimnia of the three basins composing a small, dimictic lake (Pavilion Lake, British Columbia, Canada), have been observed to vary in temperature during the ice-free stratified period. The difference is significant; the hypolimnion of the deepest basin, the Central Basin (60m deep), was colder by up to 1.5°C than the hypolimnion of the South Basin and by up to 0.8°C than the North Basin hypolimnion, as revealed by CTD profiling in 2006. The three basins of the 5.8km long lake are connected by shallow and constricted sills. The saddle-shaped North Sill is 195m wide and crests 9m below the water surface. The South Sill is broader (420m wide) and more irregular with multiple peaks and inter-channels ranging between 5m and 23m deep.

Lim et al. (2009) suggested the thermal differential between the basins hypolimnia may be attributed to variability in groundwater influx and temperature. The suggestion partly stems out of the characteristic Karst hydrology of the region and that no perennial surface source feeds into Pavilion Lake. Information on groundwater quantities and distributions were not available to substantiate this hypothesis. In this paper, we provide further observations of the hypolimnetic thermal differences in Pavilion Lake. The hypothesis of groundwater influence is investigated and additional causes are proposed. These include differing morphometric characteristics and variability in wind-driven circulations, and subsequently mixing. The latter hypothesis is tested via a three-dimensional hydrodynamic and transport model that is only forced by spatially uniform meteorological conditions (i.e. no groundwater inflow). The model reproduced the trends in hypolimnetic thermal differences but not the full magnitude. The features and associated processes described for Pavilion Lake can be transferred to other similar multi-basin groundwater-fed lakes in temperate zones.

KEYWORDS

Groundwater; hypolimnion; multibasin; numerical modeling; Pavilion Lake; wind-driven.

INTRODUCTION

Owing to the verticality of both surface heat fluxes and the gravitational field, lakes generally exhibit pronounced horizontal thermal layering. On seasonal time-scales, basin-wide horizontal gradients (variability) of water temperature are insignificant in single-basin

lakes or even lakes with multiple branches but whose connections are not particularly restrictive. Contrastingly, significant horizontal differences have been reported in multi-basin lakes. For instance, Schlatter et al. (1997) have studied, using tracer release, the thermal structure variability between two-sill separated basins in Lake Lucerne. They attributed the observed differences to a spatially variable wind field and to differences in the dissolved solids loading of the tributaries. In Amisk Lake, at the peak of summer stratification, hypolimnetic temperature in the smaller basin (averaged over multiple years) was warmer than the second larger and deeper basin by $\sim 1.5^{\circ}\text{C}$ (Lawrence et al., 1997). During the early 1990s, operation of an oxygen diffuser in the earlier basin raised the temperature difference to about $\sim 3.8^{\circ}\text{C}$ (Lawrence et al., 1997). Another example, a small subbasin of Quesnel Lake exhibited higher hypolimnetic temperatures than the deeper main basin. The difference was around 0.55°C below 100m of depth (unpublished data from July 2003). Finally, similar observations were made in Pavilion Lake as described below.

CTD casts were collected in each of the three basins of Pavilion Lake approximately once every eight weeks between late April and mid-October, 2006 (Figure 1). Less than two weeks after ice-removal (Lim et al., 2009), the late April profiles show slight differences in hypolimnetic temperatures between the three basins (Figure 1a). Below 30m of depth, the south and north basins were warmer than the central basin by 0.16°C and 0.04°C , respectively. These temperature differences grew significantly such that in the latter half of June, the south basin was warmer than the central basin by 1.3°C and warmer than the north basin by 0.7°C (Figure 1b). The same trend was also observed in the temperature profiles of August and October (Figure 1c,d). However, the thermal differential increased at much slower rates towards autumn turnover as we see in the October profiles that, at 30m depth, the south basin was 1.5°C and 0.8°C warmer than the central and north basins, respectively.

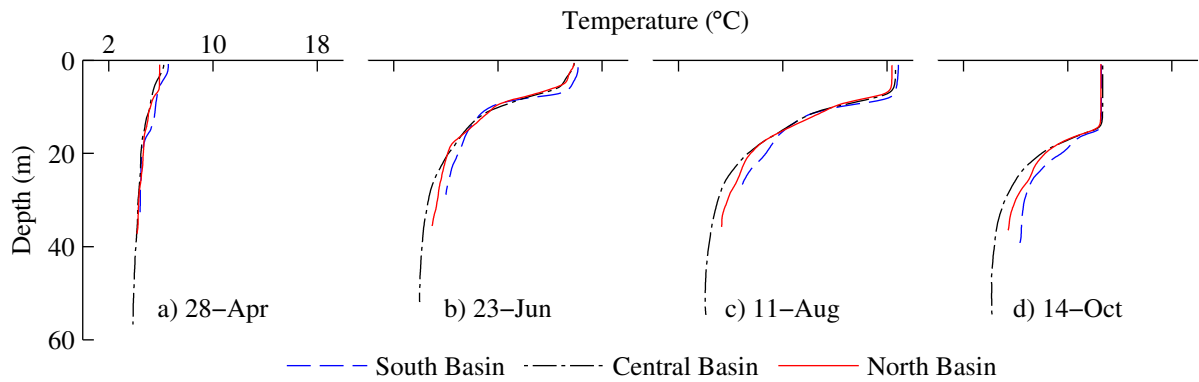


Figure 1. Temperature profiles from CTD casts in each of the three basins of Pavilion Lake. Profiles are for (a) 28-April, (b) 23-June, (c) 11-August, (d) 14-October, 2006 (data published in Lim et al., 2009, except panel c). Note the temperature difference between the three basins below 20m depth.

Lim et al. (2009) suggested the hypolimnetic temperature differences were caused by variabilities in groundwater influx and/ or temperature. In this paper, we elaborate on observations of hypolimnetic thermal differentials in 2006 and 2007 and attempt to explain the cause(s). Four possible causes are discussed. The first considers morphometric characteristics of the basins under uniform meteorological conditions. The second concerns

the likelihood of spatially variable heat flux exchange at the surface of the basins. The third explores the hypothesis of groundwater influence. Finally, the fourth cause involves differing wind-induced mixing between the basins. This is addressed by means of a three-dimensional numerical model.

METHODS

Site Description

Three basins combine to form the body of Pavilion Lake, in the interior plateau of British Columbia, Canada (Figure 2). The multibasin lake is small; 5.8km long and 60m deep. From north to south, the basins have maximum depths of 39.3m, 60.3m, and 41.7m, respectively. The North Basin (NB) is connected to the Central Basin (CB) via a constricted sill. This North Sill is saddle-shaped cresting as shallow as 9.3m (relative to outlet spillway crest level) (Figure 6). The South Sill connecting the CB to the South Basin (SB) is broader (420m wide) and more irregular with marl shoals projecting as shallow as 4.5m below the surface and 23m deep interchannels.

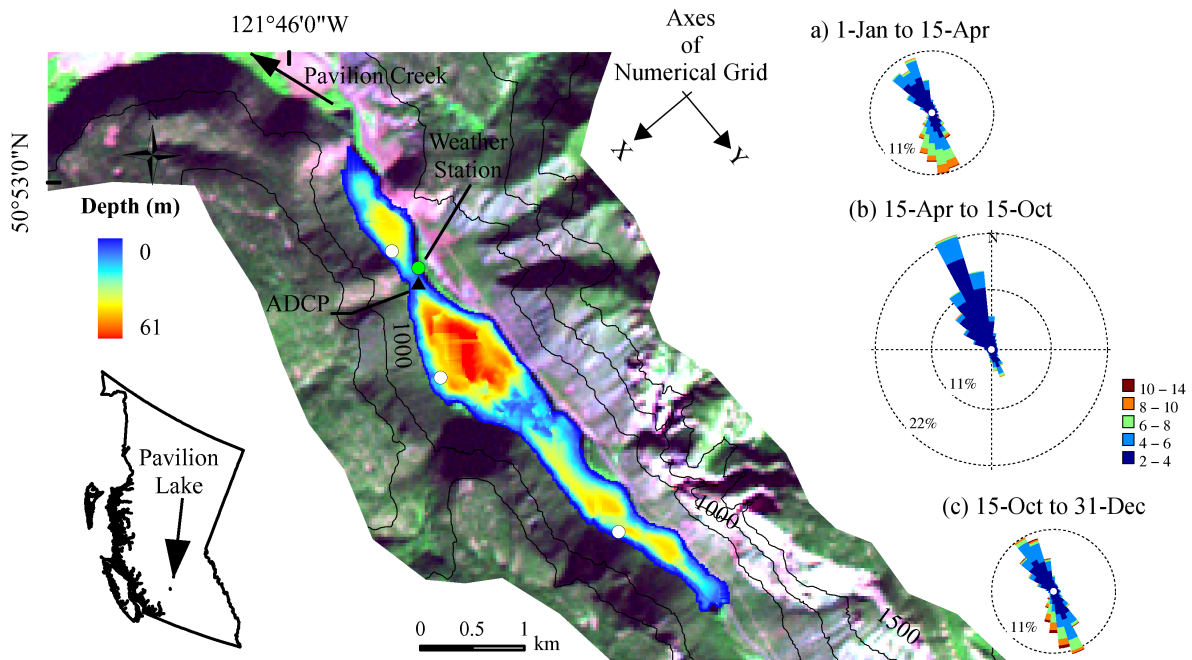


Figure 2. Map of Pavilion Lake. Bathymetry is overlaid on a Landsat 7 ETM+ image (composite of bands 7,4,3). With the lake surface at around 801m above mean sea level, surrounding relief is indicated by the 1000, 1200, and 1400m elevation contours. Lower left insert shows the location of Pavilion Lake in the interior plateau of British Columbia, Canada. Polar histograms on the right (a,b,c) show the distribution of relative occurrences of wind blowing from different directions. These wind roses cover 3.5, 6, and 2.5 months of 2006, respectively. Axes displayed at top center indicate the orientation of the cartesian grid utilized in numerical simulations.

Pavilion Lake develops ice cover for three to four months in a given year. With removal of ice-cover, typically occurring around mid-April, spring turnover homogenizes the lake waters in all three basins (Lim et al., 2009). The lake soon rapidly develops thermal

layering as the incident solar insolation intensifies. By early August, stratification reaches its peak and the water column evolves into three distinct layers (Figure 1c). From the surface, a 5m thick layer forms that is well-mixed by wind action. Underneath, within the metalimnion, temperature drops sharply from its surface value ($\sim 19^{\circ}\text{C}$). The temperature gradient reaches its maximum of $-2.2^{\circ}\text{C}/\text{m}$ at about 8.5m depth thereafter the gradient diminishes rapidly to less than $-0.8^{\circ}\text{C}/\text{m}$ below 12m of depth. In the lower portion of the metalimnion, temperature decreases more slowly with depth but differently between the basins leading to the thermal differential between the basins' hypolimnia, as introduced earlier. As of late summer, the net thermodynamic fluxes through the lake's surface reverse sign and heat is lost to the overlying atmosphere. The surface layer steadily cools and deepens by convective mixing. Differences in hypolimnetic temperatures between basins slightly grow during early autumn. The entire lake is brought to isothermal conditions by the end of November.

Entrenched in the Marble Canyon, Pavilion Lake is mainly subjected to winds along its medial axis (Figure 2). The overlooking cliffs immediately rise in excess of 500m above the lake surface and effectively channels the wind. During the summer, prevalent winds are daytime upvalley breezes that regularly reach maximum speeds of 5m/s. In winter and autumn, winds are episodic and more intense. These storms are apparently synoptic scale flows that break in or are channeled along the Marble Canyon. Wind occurrences are almost equally distributed from the two directions; NNW and SSE but with stronger storms from the latter direction.

The hydrology of Pavilion Lake is not fully understood but is presumed to be karstic commensurate with the regional dominance of karst geology (Lim et al., 2009). Between spring and autumn turnovers, no persistent stream inflows could be identified and direct rainfall over the lake amounts to about 180 mm per unit area of the lake (as measured on site). The lake is drained by withdrawal through Pavilion Creek, utilized for downstream irrigation and ranching, and by evaporation. As indicated earlier, Lim et al. (2009) provide and discuss evidence related to groundwater recharge of the lake. According to those authors, groundwater seeps into the lake from multiple scattered sources rather than gushing through few distinct springs. The locations of these sources remain largely unknown.

Field Observations

Most of the field observations reported here cover a period at least five months prior to the end of 2006. On the east shore of the North Sill, a weather station measured wind speed and direction, PAR quantum flux, air temperature, relative humidity, and precipitation. Atmospheric pressure was tracked by means of an absolute pressure sensor. Readings, or averages of multiple readings, were logged at 30min intervals. Water temperatures were monitored by two means; CTD profilers and self-contained loggers. Temperature profiles shown in Figure 1 were collected using a SBE19plus SEACAT profiler with a calibrated accuracy of $\pm 0.005^{\circ}\text{C}$. For continuous monitoring, self-contained loggers were deployed at several locations in the lake. Because of mooring restrictions, the loggers, at different depths, had to be deployed on the lake floor by divers rather than attached to anchored vertical strings. Of interest here are pairs of loggers deployed in each basin at depths of 27.4m and 33.5/ 36.6m. Five loggers were RBR TR1050 (accurate to $\pm 0.002^{\circ}\text{C}$) and logged at 1min intervals. The deepest logger in the Central Basin was a RBR TR-

1000fs (accurate to $\pm 0.05^{\circ}\text{C}$) logging once every 3min. Additional water velocity and temperature data on the North Sill was used to validate the numerical model but are not presented in this paper.

Numerical Modeling

The Estuary, Lake, and Coastal Ocean Model (ELCOM) was selected for simulating the three-dimensional hydrodynamics in Pavilion Lake (see Hodges et al., 2000, for a detailed description of ELCOM). ELCOM's unique vertical mixing scheme proved proficient in simulating the hydrodynamics and transport in several stratified natural systems; e.g. Lake Kinneret (Laval et al., 2003; Marti and Imberger, 2006); Lake Constance (Appt et al., 2004); Lake Maracaibo (Laval et al., 2005); and Lake Biwa (Shimizu et al., 2007). The model has not been used to model natural multi-basin lakes and ours seems to be the first such application. Principal inputs to ELCOM include the numerical grid, wind forcing information, meteorological parameters specifying surface thermodynamic and mass fluxes, and stream inflows and outflows.

RESULTS

Observed Hypolimnetic Thermal Evolution

Temperature records from deep thermistors in the three basins are shown in Figure 3. The records are one year long excluding the winter and early spring (about four months). We first consider the onset of stratification in 2007 till the end of July (Figure 3b). In all three basins, temperatures recorded at a common depth of 27.4m clearly reveals differences between the thermal evolution in each basin's hypolimnion as was indicated by the CTD profiles of Figure 1. Following spring turnover, each hypolimnion warms varyingly from the two other basins but seemingly with interannual consistency. At 36.6m depth, the South Basin (SB) rapidly warms over the Central Basin (CB). The difference grew at an average rate of $0.031^{\circ}\text{C}/\text{day}$ over May and June but decreased by a factor of four over July. By early August, the difference had reached 2.10°C . A similar pattern is observed by comparing the temperature in the North Basin (NB), at the slightly shallower depth of 33.5m, to the 36.6m deep record in the CB. By the end of July, NB is warmer by 1.25°C over CB. At the shallower depth of 27.4m, comparison of all three basins yields corresponding differences but of smaller magnitudes. By late July, 2007, the CB is colder than the SB and NB by 1.45°C and 1.05°C , respectively.

Turning our attention back to August, 2006, and the subsequent three months, changes in temperature differentials between the hypolimnia were very slight. This seeming thermal plateau continued up til the autumn turnover when convective cooling rapidly mixed the surface layer downward and homogenized the water column in each basin. Comparing corresponding depths, downward mixing appear to have progressed faster in the SB than in the rest of the lake.

Simulated Hypolimnetic Thermal Evolution

A two-month long simulation was conducted using ELCOM. The run was initialized with the temperature profiles of Figure 1a (April 28th, 2006) and maintained to June 24th for comparison with the profiles of Figure 1b. The modelled epilimnion temperatures exceeded the observed values by about 2°C (Figure 4a,b,c). However, the depth to the base of the epilimnion was well reproduced. As for the hypolimnia, the SB's temperature

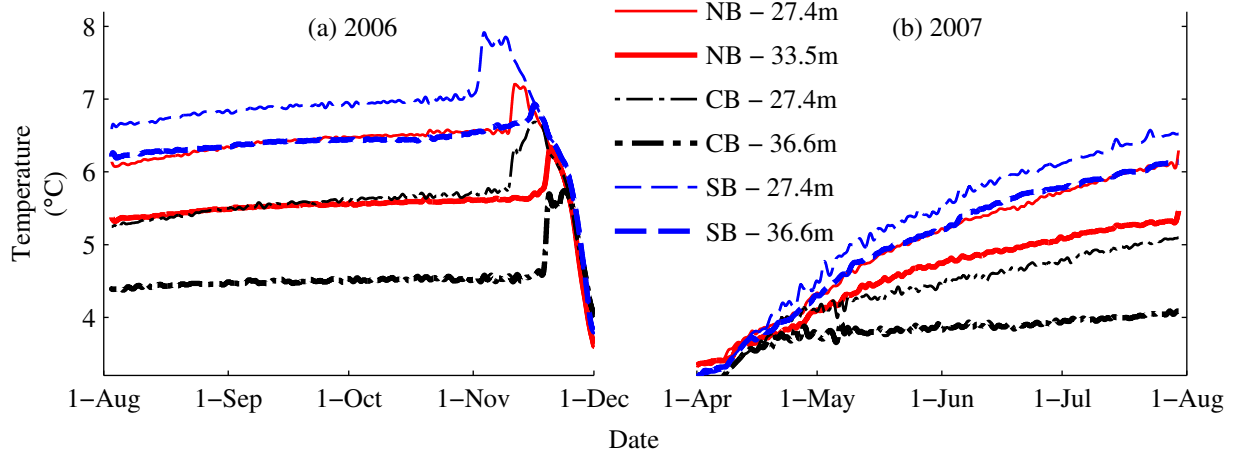


Figure 3. Temperature recorded by deep thermistors in the three basins from early August, 2006, to the end of July, 2007. As we are only interested in the season of normal thermal stratification, data between autumn and spring turnovers is not shown. For clarity, temperature records have been low-pass filtered with a 48hr cutoff. As per the legend, a different line style and color is used for each basin with data of deeper thermistors shown thicker.

was 1.5°C below the measured while that of NB was slightly better varying by about 1.1°C off the field temperature (Figure 4c,a). The best reproduction is the temperature of CB's hypolimnion although that is probably because the actual temperature did not rise as much from its initial value (Figure 4b). As it stands, the model results overestimate the epilimnion temperature while underestimating the temperatures in the lower parts of the metalimnion and in the basins' hypolimnia. The model seems to exchange the appropriate thermal fluxes at the surface but not to distribute the (gain in) heat content as observed in the field; apparently, mixing is underestimated in the model.

What is remarkable though is the reproduction of the thermal differentials - pattern-wise - between the hypolimnia (Figure 4d). The CB hypolimnion slightly warmed from its initialization value but those of the SB and NB witnessed significant rise in temperature. The magnitudes of these rises were however about two thirds less than observed. At 30m depth, the modeled SB and NB temperatures were warmer than the CB by about 0.44°C and 0.24°C, respectively.

Exploration of a Groundwater Source

Between August 5th to 7th (Julian days 217.8 to 219.5), a short-termed experiment was undertaken in which two conductivity-temperature loggers (RBR XR-420-CTf; accurate to $\pm 3\mu\text{S}/\text{cm}$) were deployed on the eastern slope of the Central Basin (Figure 5a,b). The loggers were placed in a spot, 8m deep, where groundwater is suspected to seep into the lake. This was suggested by the floor being bare of weed growth. One logger (H) was deployed lying on the floor with its probe facing the growth ends. The second logger (V) was mounted upright on a short rebar with its probe pointed upwards projecting above the surrounding weeds. Engulfed within the thermocline, logger H anticipatedly recorded colder temperatures than logger V (Figure 5c). Contrastingly, conductivity corrected to 25°C at logger H was significantly higher than at logger V (Figure 5d). Hence, the higher conductivity (proxy for total dissolved solids) indicates the possibility of groundwater

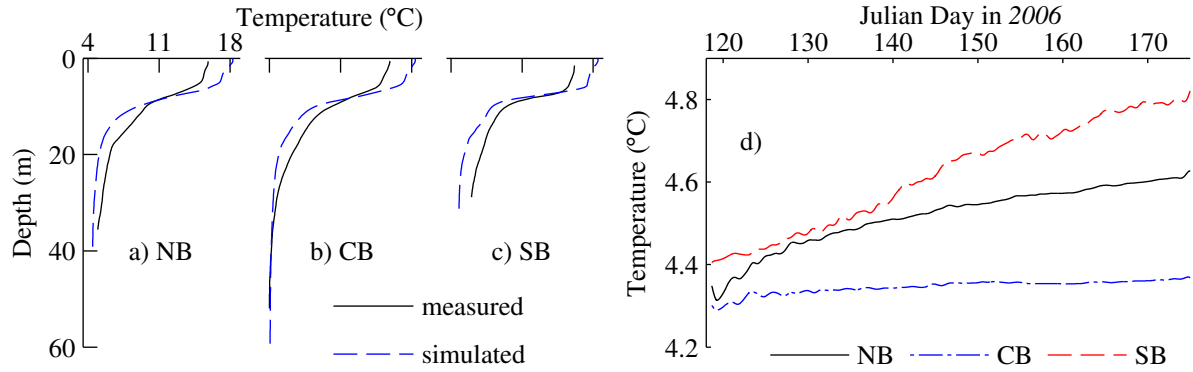


Figure 4. Panels (a,b,c) compare ELCOM simulated temperature profiles to profiles from CTD casts in the NB, CB, and SB, respectively. Panel (d) show the continuous record of simulated temperatures in the three basins at a depth of 30m.

inflow diffusing through the lake side and flowing downslope in a seemingly well defined path.

DISCUSSION

It is now evident that hypolimnetic temperature differences between the three basins of Pavilion Lake persisted during the ice-free stratified season in 2006 and 2007 (temperature profiles in Lim et al., 2009, also show this is the case for 2005). The question is why do these differences arise and what mechanisms or processes contribute to their evolution. In an attempt to provide an explanation, we discuss four possible causes below.

Changes in the heat content ΔH , of a control volume, and hence changes in its temperature ΔT , is a function of the thermal fluxes Q_H exchanged with the ambient. In lakes, the principal thermal fluxes are exchanged at the surface and penetrate vertically through the water column such that at any depth, the change in heat content underneath equates to the net spatially-averaged heat flux times area of the lake A at that level. The corresponding change in temperature;

$$\Delta T = \frac{\Delta H}{mc}$$

where $m = \rho V$ is the water mass (average density by underlying volume), and c the specific heat capacity. Simplifying;

$$\Delta T = \frac{Q_H}{\rho c} \frac{1}{V/A} \propto \frac{1}{d_{avg}}$$

Thus, the change in temperature is inversely proportional to the average depth ($d_{avg} = \frac{V}{A}$) underlying a level of interest. If we carry this to the basins of Pavilion Lake and first assume thermodynamic fluxes are spatially uniform over the surface and down through the water column (Figure 6a), we find plausible explanation as to why CB is colder than the other two basins. Figure 6b shows the average depth as a function of level above bottom and indicates CB has lower area to storage ratio. However, the NB and SB have comparable average depths. As such, at least another factor is involved in setting the hypolimnetic temperature differences between the two basins. As we pass the argument

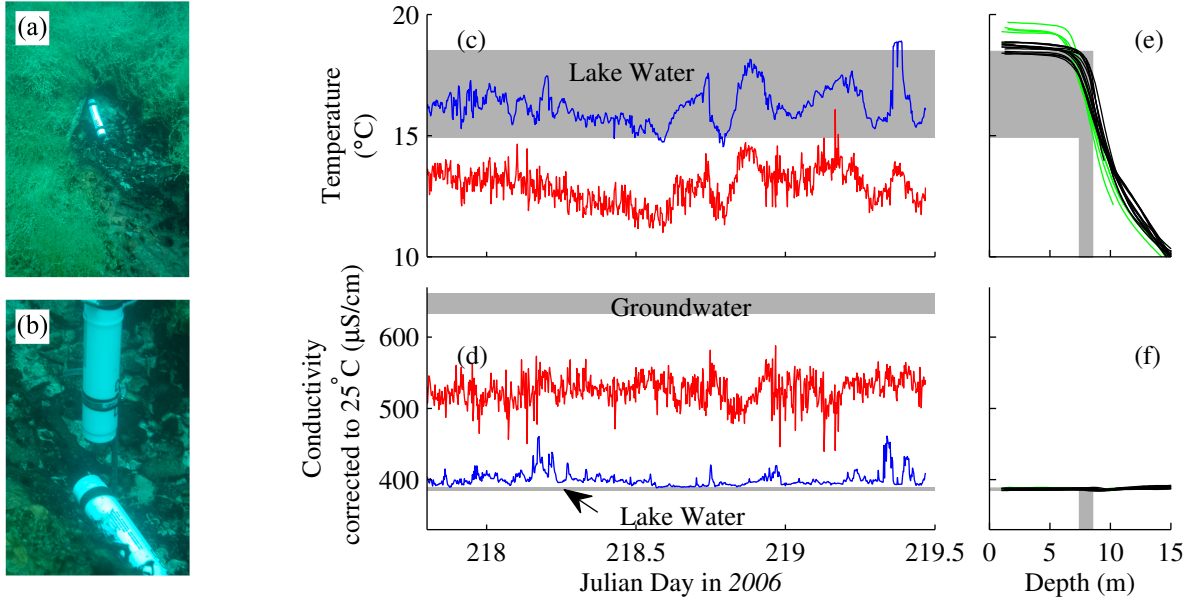


Figure 5. (a,b) Conductivity-Temperature Loggers deployed near the eastern shore of the Central Basin (courtesy of Donnie Reid). Picture (a) was taken before the second logger was deployed and shows the growth-free patch meandering downslope. (c,d) Temperature and specific conductivity measured by the horizontal (red) and vertical loggers (blue). (e,f) Temperature and specific conductivity profiles from CTD casts collected on 1-Aug (green) and 11-Aug (black) in 2006. Note that depth is shown on the horizontal axis and that only the top 15m are shown. Lake water characteristics indicated on panels (c) and (d) are inferred from the profiles of (e) and (f), respectively.

above regarding the CB, it is noteworthy that this morphometric factor seem to also support the similar observations in Amisk Lake (before oxygen injection) and Quesnel Lake.

Moving on to the next possible cause which is concerned with Q_H being non-uniform over the domain. For Pavilion Lake, the expectation is that surface Q_H is spatially uniform given the lake is of small geographical extent. Moreover, topography shadowing, with the almost N-S orientation of the lake and canyon, is likely to instill cross- rather than along-thalweg gradients in solar irradiance, the principal component of the thermal budget.

As to the role of groundwater, the experiment utilizing temperature-conductivity (CT) sensors provide evidence of groundwater inflow. Sampling of the nearest well to the experiment site, which is within 20m, gave a multi-year average temperature-corrected conductivity, C_{25} , of $651 \pm 16 \mu\text{S}/\text{cm}$ in August (Lim et al., 2009). On the other hand, based on 18 CTD casts (four on 1-Aug and 14 on 11-Aug), lakewater C_{25} within a depth range of 7.4-8.5m, encompassing the two CT sensors and allowing for depth-determination errors, was bound between 384 and $389 \mu\text{S}/\text{cm}$ (Figure 5f). Conductivities measured by the CT sensors and corrected to the same reference temperature lie within the basin-wide lakewater - groundwater limits. Readings of the horizontal logger (H) is mid-way between the lake and well waters while that of the vertical logger (V) is slightly higher than the lake's conductivity. The temperature signal provides further confirmation. Based on the 18 CTD casts mentioned above (Figure 5e), lake-wide temperature within the depth range

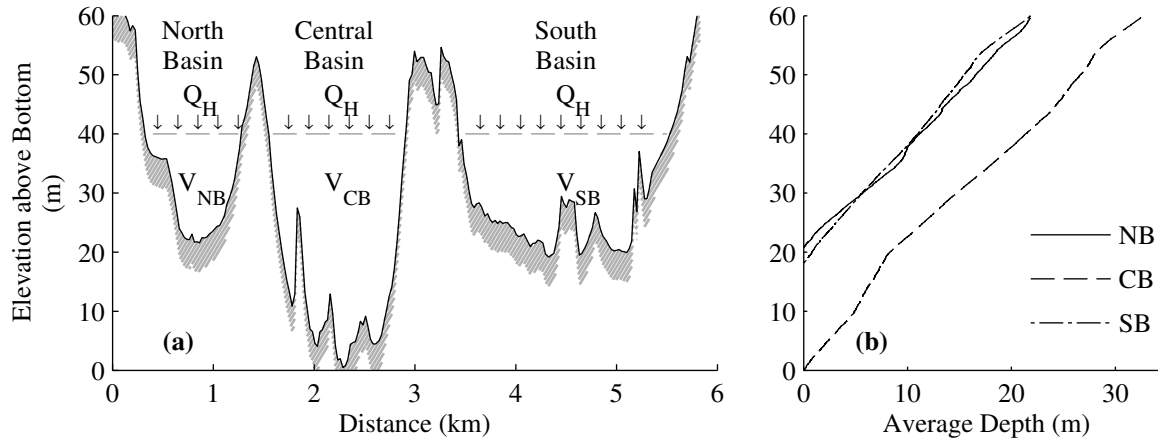


Figure 6. (a) Longitudinal profile of Pavilion Lake. Profile starts at the North tip of the lake. In box models of the hypolimnia, heat fluxes Q_H at an arbitrary level are distributed uniformly over the respective areas and affect the underlying volumes. (b) Hypsometric curves for the three basins.

of 7.4–8.5m was bound between 14.9°C and 18.5°C. The mean temperature of logger V is $16.23 \pm 0.77^\circ\text{C}$, towards the lower end of the range of ambient metalimnetic temperatures. For the horizontal logger (H), the mean temperature was $12.91 \pm 0.75^\circ\text{C}$, fairly below the ambient temperatures. Further insight is obtained by calculating the temperature gradient between the two loggers over their separation distance; 0.6m. The average temperature gradient amounts to $5.5 \pm 0.9^\circ\text{C}/\text{m}$, corresponding to about 3-fold the maximum gradient in the thermocline. The emerging picture is that groundwater seeps into the lake and is rapidly diluted with lake water. Groundwater is of higher conductivity (as measured in the surrounding wells; Lim et al. 2009) and lower temperature (as anticipated during summertime and also concluded above). The effect of groundwater is such as to raise the ambient conductivity and lower the temperature at its point of entry. Quantification of the groundwater influence is however an intensive exercise not only necessitating monitoring of seepage rates and temperatures but identifying the sources in the first place. This latter task involves thorough mapping of the lake bottom and sides. Currently, we can only conclude that groundwater ‘may be’ playing a role in setting the hypolimnetic differences, particularly, between the NB and SB. If that is so, then, speculating, the SB could be receiving less groundwater than the other two basins leading to its higher hypolimnetic temperature.

Finally, the numerical modeling results show the same pattern of temperature differences between the hypolimnia. The magnitudes are about 65% less though. This is remarkable given that no groundwater inflows were input to the model and that all meteorological conditions, including wind, were specified as uniform over the entire domain. This brings the possibility that differing wind-induced circulations, and the associated shear and mixing, contribute to the observed hypolimnetic thermal variability. In favour of this argument is the increased temperature difference between the two basins of Amisk Lake during the operation of the oxygen diffuser in the shallower basin (rising from a pre-injection value of 1.5°C to 3.8°C). Lawrence et al. (1997) suggest the diffuser-driven circulation within the basin it was deployed in lead to mixing of warmer metalimnetic water with the colder underlying hypolimnion raising the temperature of the latter. The inference for Pavilion Lake is that an external energy source (wind) could drive differing circulation patterns in

the hypolimnia of the basins and could plausibly lead to thermal differences. One factor that might be relevant is the relative wind fetch of each basin (Figure 6a). The South Basin has the greatest fetch of 2.7km compared to 1.5km and 1.7km of the North and Central Basins, respectively. The relation is still to be investigated in the model output.

CONCLUSIONS

We have reported herein observed temperature differences between the hypolimnia of a small temperate multi-basin lake. Three probable causes are proposed. These are differing morphometric characteristics, groundwater inflow, and variability in wind-driven dynamics and mixing. The first factor distinguishes the largest and deepest basin apart from the other two basins. The latter two factors are likely to determine the differences between the hypolimnia of the North and South Basins.

ACKNOWLEDGEMENT

Execution of this field program would not have been possible save the help of the divers; Donnie Reid, Dale Andersen, and Mike Delaney. Harry Bohm contributed greatly to the design of deployments and execution of field operations. We would like to thank Dr. Alfred Wueest for his insight and fresh ideas. We are also grateful to all of the members of the Pavilion Lake Research Project for their continued field and intellectual support, to Linda and Mickey Macri and Ron and Lorna Cook for hosting the project, and to the Pavilion Community in general for all of their goodwill. In particular, we would also like to extend our thanks to Ts'Kw'aylaxw First Nation and British Columbia Parks for their support over the years.

REFERENCES

- Appt, J., Imberger, J., and Kobus, H. (2004). Basin-scale motion in stratified upper lake constance. *Limnology and Oceanography*, 49(4):919–933.
- Hodges, B. R., Imberger, J., Saggio, A., and Winters, K. B. (2000). Modeling basin-scale internal waves in a stratified lake. *Limnology and Oceanography*, pages 1603–1620.
- Laval, B., Imberger, J., and Findikakis, A. (2005). Dynamics of a large tropical lake: Lake maracaibo. *Aquatic Sciences - Research Across Boundaries*, 67(3):337–349.
- Laval, B., Imberger, J., Hodges, B. R., and Stocker, R. (2003). Modeling circulation in lakes: Spatial and temporal variations. *Limnology and Oceanography*, 48(3):983–994.
- Lawrence, G. A., Burke, J. M., Murphy, T. P., and Prepas, E. E. (1997). Exchange of water and oxygen between the two basins of amisk lake. *Canadian Journal of Fisheries and Aquatic Sciences*, 54(9):2121–2132.
- Lim, D. S., Laval, B., Slater, G., Antoniades, D., Forrest, A., Pike, W., Pieters, R., Saffari, M., Reid, D., Schulze-Makuch, D., Andersen, D., and McKay, C. (2009). Limnology of Pavilion lake, B. C., Canada - Characterization of a microbialite forming environment. *Fundamental and Applied Limnology*, 173:329–351.
- Marti, C. L. and Imberger, J. (2006). Dynamics of the benthic boundary layer in a strongly forced stratified lake. *Hydrobiologia*, 568(1):217–233.
- Schlatter, J. W., Wueest, A., and Imboden, D. M. (1997). Hypolimnetic density currents traced by sulphur hexafluoride (SF 6). *Aquatic Sciences-Research Across Boundaries*, 59(3):225–242.
- Shimizu, K., Imberger, J., and Kumagai, M. (2007). Horizontal structure and excitation of primary motions in a strongly stratified lake. *Limnology and Oceanography*, 52(6):2641–2655.

Turbulence Measurements from a Glider

F. Wolk¹*, R.G. Lueck¹, L. St. Laurent²

¹ Rockland Scientific Inc., Victoria, British Columbia, V8Z 1C1, Canada.

² Department of Physical Oceanography, Woods Hole Oceanographic Institution, Woods Hole, MA, 02543-1536, USA

*Corresponding author, e-mail fabian@rocklandsscientific.com

ABSTRACT

To test the feasibility of measuring small-scale turbulence from an ocean glider, a self-contained package carrying velocity shear probes and FP07 thermistors is deployed in a small lake on a *Slocum* ocean glider. The package's turbulence sensors are augmented by a high-resolution pressure sensor and a set of orthogonally mounted accelerometers monitoring the glider's attitude and vibrations. The package is neutrally buoyant and does not limit the glider's manoeuvrability. It attaches to the top of the glider's fuselage with the turbulence sensors positioned just ahead of the glider nose. The package receives power from the glider and can record turbulence data independently for up to 35 days. Data from a test in Ashumet Pond near Cape Cod show that vibration levels of the glider are generally small and do not interfere with the measurement of small-scale turbulence shear. The accelerometer spectra show vibration peaks at 28, 60, and 80 Hz, which are caused by vibrations of the glider's tail fin assembly. These vibrations are stimulated by the action of the glider's buoyancy pump, which acts at the top and bottom turn-around points, and by the action of the rudder, which is activated at regular intervals (~6 seconds) during the flight in order to control the heading of the glider. The vibration peaks have a small magnitude and narrow bandwidth and do not interfere with the shear probe spectrum. The shear probes resolved dissipation rates between $5 \times 10^{-11} \text{ W kg}^{-1}$ in the quiescent layer below the thermocline and $1 \times 10^{-7} \text{ W kg}^{-1}$ in the surface mixing layer. All measured shear spectra fit well with the Nasmyth Empirical Spectrum.

KEYWORDS

Turbulence; shear probes; ocean gliders; mixing

INTRODUCTION

The majority turbulence measurements at dissipation length scales are made using loosely tethered vertical profilers, which are driven by buoyancy and, therefore, provide a nearly vibration-free platform from which to measure the horizontal velocity shear, $\partial u / \partial z$, $\partial v / \partial z$. Lueck *et al.* (2002) give an overview of this “classical” profiler technology. Loosely tethered vertical profilers provide a relatively fast repetition of the measurement, because they can be winched back to the surface at the end of the profile. The tether can also provide a real-time data display, which can guide operational decisions during the experiment. However, the deployment of these profilers requires a considerable amount of experience and skill, as well as dedicated ship time, because it is too risky to operate other over-the-side instrumentation while the profiler is in operation. As a result, the turbulence observations in the world’s oceans remain sparse, despite half a century worth of measurements.

In recent years, the technology of autonomous underwater gliders has matured to provide a new, cost effective infrastructure for observing oceanographic parameters over large areas and over long periods. Approximately 160 commercially available gliders are in operation today, providing measurements of conductivity, temperature, and pressure. Three models of ocean gliders are currently commercially available: The *Slocum Electric Glider* developed by Teledyne Webb Research (Jones and Webb, 2007); the *Seaglider*, developed by the University of Washington (Eriksen *et al.*, 2001); and the *Spray*, developed by Scripps Institute of Oceanography and Woods Hole Oceanographic Institution (Sherman *et al.*, 2001). Similar to ARGO profiling floats, gliders operate by adjusting their buoyancy to move down or up in the water column, while wings and tailfins translate part of the vertical motion into the horizontal component, resulting in a saw-tooth trajectory. Typical vertical-to-horizontal glide ratios are 1:4, resulting in a quasi-vertical, quasi-horizontal measurement. Gliders provide a nearly ideal platform for turbulence measurements because their propulsion does not rely on moving parts, such as propellers, whose vibrations introduce noise into the measured turbulent velocity fluctuations.

Here we present the results from a recent test flight of a *Slocum* glider carrying turbulence shear probes and an *FP07* thermistor. This is the first reported deployment of these sensors on a glider and the data show that the shear probes were able to resolve dissipation rates as low as $5 \times 10^{-11} \text{ W kg}^{-1}$, which is comparable to measurements achieved by the best tethered free-fall profilers. This is encouraging because it shows that gliders are a suitable platform to resolve turbulence levels typically found in the open ocean. The next section describes the instrumentation and experimental setup of the test, followed by a presentation, analysis and discussion of the turbulence data.

INSTRUMENTATION AND EXPERIMENTAL SETUP

Turbulence Package and Glider

The glider is a *Slocum Electric Glider* with a depth rating of 200 m, shown in Figure 1. It has an overall length, including tail fin, of 2.5 m and a hull diameter of 0.21 m. Its mass is 52 kg and the payload capacity is 5 kg. With an alkaline battery pack, the glider's nominal endurance at a 1:4 glide angle and a forward speed of 0.35 m/s is 20 days.

The turbulence package is a *microRider-1000-6* developed by Rockland Scientific Inc. The package is neutrally buoyant and supports two velocity shear probes (Osborn and Crawford, 1980), two *FP07* thermistors, and one SBE7 micro-conductivity probe. These turbulence sensors are mounted on the tapered nose section of the package. Three accelerometers are mounted in an orthogonal configuration on the rear of the pressure bulkhead that separates the nose section from the main pressure housing. The bulkhead also houses the port that connects to a pressure transducer. The main pressure housing contains the signal condition electronics and the data acquisition computer (*Persistor CF2*).

The turbulence package is attached on faired mounting brackets to the top of the glider fuselage, with the turbulence sensors positioned just ahead of the glider nose, outside of the region of flow deformation (Figure 1). In this orientation, the velocity shear probes measure the $\partial w / \partial x$, $\partial v / \partial x$ shear components. The glider/package coordinate system is defined by the orientation of the accelerometers, which, in their nominal configuration, are oriented so that the x -coordinate is forward, y is port, and z is up. The accelerometers pick up a component of gravity and for the given configuration, the glider pitch (θ) and roll (φ) angles are defined as $\theta = \arcsin(a_x/g)$ and $\varphi = \arcsin(a_y/g)$, where g is the gravitational constant and a_x and a_y are

the measured accelerations. Pitch is defined positive when the glider's nose is above the horizontal plane; roll is defined positive when the glider rolls to the left.

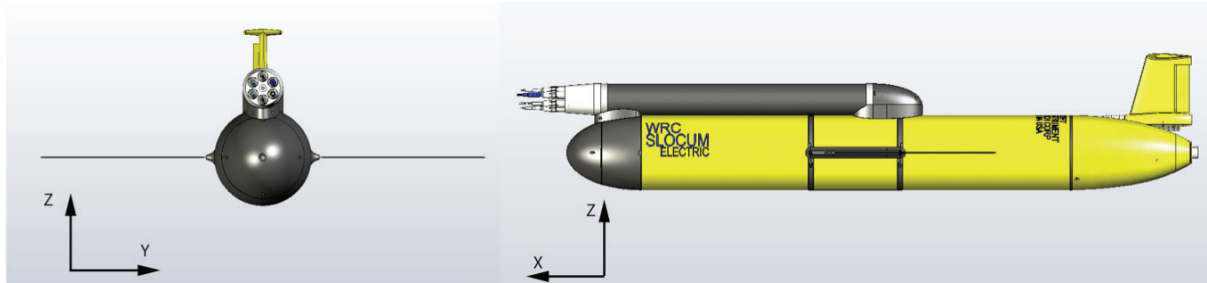


Figure 1: Turbulence package and glider configuration.

Experimental Conditions & Procedures

The test was carried out in Ashumet Pond ($N41^{\circ} 38'2.4''$, $W70^{\circ} 32'5.3''$), a small lake near East Falmouth, MA, which is frequently used by Teledyne Webb Research to test gliders. The lake measures ~ 1350 m north-south by ~ 900 m east-west and has a maximum depth of 20 m. The lack of surface inflow and outflow results in extremely low turbulence levels in the hypolimnion, which makes the lake an ideal site to test the noise level of the glider in terms of the measured dissipation rate.

On the day of the experiment, May 1, 2009, weather conditions were calm with wind speeds less than 5 m s^{-1} and air temperature of 13.5° . The passing of a storm two days prior caused a remnant active surface mixing layer, which was further sustained by convective circulation resulting from latent heat loss to the atmosphere.

Five dives were performed with duration of 500 to 1000 seconds, during which the glider completed between two and four ascent/descent cycles. The glider changes its buoyancy at preset depths by pumping fluid into and out of a cavity. During the ascending and descending portions of the resulting saw tooth path, the glider makes pitch adjustments by shifting the battery pack forward or aft to maintain a straight flight path. During two of the dives (dat_014 and dat_015), this feature was turned off to evaluate the vibrations that result from the battery movement and its possible influence on the shear data. However, due to the absence of large-scale currents in the lake and the relatively short saw tooth cycles, the pitch adjustment was rarely activated. To maintain heading, the glider activates a rudder on the tail fin at regular intervals of approximately 6 seconds. This feature was active in all of the dives.

RESULTS AND DISCUSSION

Glider Attitude and Dynamics

The five separate deployments all gave similar results. Figure 2 shows a summary of the data recorded by the turbulence package during one of the deployments (dat_015). The data are shown after a minimal amount of processing was applied to convert the raw data into physical units. The flight path was a straight line heading west to east, where the glider performed a saw-tooth pattern between 1 m and 12 m depth.

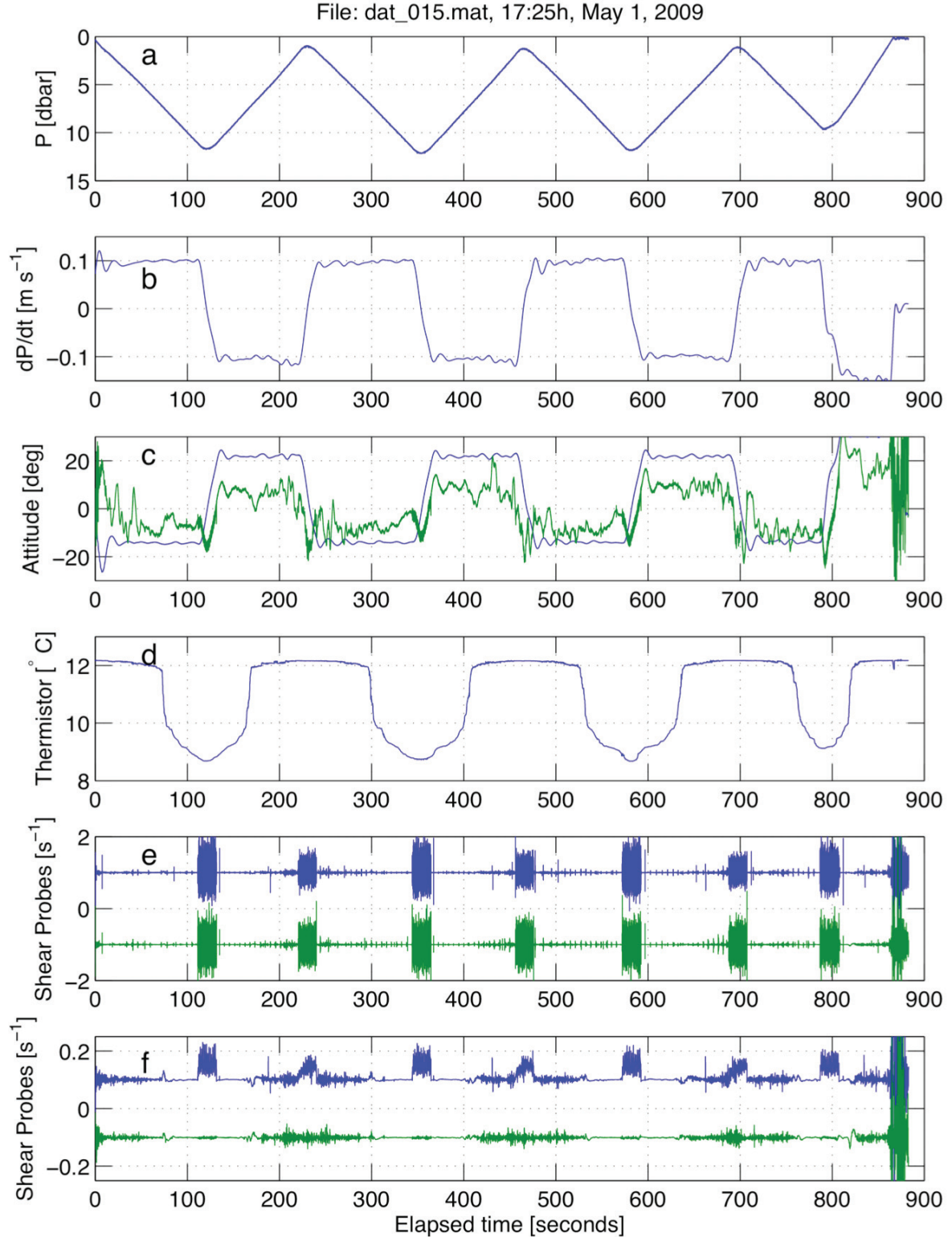


Figure 2: Summary of the data measured by the turbulence package (data file dat_015). All data are shown as elapsed time from the beginning of data file. (a) pressure record; (b) rate of change of pressure, expressed in $\text{dbar s}^{-1} \approx \text{m s}^{-1}$; (c) pitch angle (blue) and roll angle times 10 (green); (d) water temperature measured by the FP07 thermistor; (e) shear probe #1 (blue) and shear probe #2 (green), offset by +1 and -1, respectively; (f) shear probe signals low-pass filtered at 15 Hz.

Three descent-ascent cycles were completed; the fourth cycle starting at 700 s was aborted. The glider's net vertical speed, $W = -dP/dt$, is shown in panel b, and is on average

$9.68 \times 10^{-2} \text{ ms}^{-1}$ ($\sigma = 5 \times 10^{-4}$) during descent and $10.4 \times 10^{-2} \text{ ms}^{-1}$ ($\sigma = 3 \times 10^{-4}$) during ascend. The average pitch angle (panel c) is $-14.1^\circ/22.0^\circ$ during descent/ascent. The pitch angle allows us to estimate the forward speed of the glider along its flight path, $U = W / \sin(\theta)$. Table 1 summarizes the typical speeds and pitch angles observed along the path.

The roll angle is within $\pm 1.5^\circ$. Panel c in Figure 2 shows the roll angle (multiplied by ten). A systematic offset of -27° has been removed from the roll measurement. The offset is the result of misalignment of the turbulence package on the glider.

Table 1. Typical average pitch angle, θ ; vertical speed, W ; and speed along the glide path, $U = W / \sin(\theta)$.

	θ (degrees)	W (m s^{-1})	U (m s^{-1})
Descent	-14.1	-0.096	0.394
Ascent	22.0	0.104	0.280

Angle of Attack

Since the shear probes measure the hydrodynamic lift force created by the turbulent flow, their operation depends on the angle of attack (AOA) of the oncoming flow. Wind tunnel tests with large-scale probe models have shown that the flow over the probe body is laminar for AOA within $\pm 20^\circ$. Outside of this range, the boundary layer separates from the probe and the potential flow theory underlying the operating principle of the probes no longer applies (Osborn and Crawford, 1980).

For the glider, the AOA is the difference between the pitch angle and the angle of the glide path. The manufacturer of the glider states that the average AOA is within $\pm 3^\circ$ during descent and ascent (Teledyne Webb Research, Ben Allsup, personal communication 2009). Simple mathematical models presented by Williams *et al.* (2008) predict an AOA as much as 10° for certain flight conditions. We are in the process of further evaluating the existing data in order to compute the AOA for the glider configuration with the turbulence package used in this experiment. The results of this work will be included in a future presentation.

Vibration Signatures

The possibility of making successful shear probe measurements from the glider depends on the glider's vibration levels, and these were unknown at the onset of this experiment. The shear probes are essentially transverse force sensors and so they are sensitive to rectilinear accelerations. Any vibration of the glider in the 1 to 100 Hz frequency range will show up as a spurious signal in the measured shear signal (Wolk *et al.*, 2002).

An obvious feature in the shear probe signals (Figure 2-e) is vibration contamination when the glider reaches the top and bottom of the saw tooth profile (e.g., at elapsed time 120, 230 s, etc.). The vibrations are caused by the operation of glider's ballast pump, which displaces fluid in order to adjust the buoyancy, but these vibrations are irrelevant. The data at the turning points cannot be interpreted as shear because the forward speed of the vehicle is zero. Additionally, during ascent and descent, numerous smaller vibration signatures are visible at approximately 6-second intervals. These are caused by the glider's rudder, which controls the heading of the glider. The rudder movements are more frequent and stronger at the beginning

of the descent or ascent as the glider accelerates from the turn-around point at the top or bottom of the saw tooth.

Accelerometer spectra (Figure 3) for the x , y , and z directions of the glider (cf, Figure 1) were computed for three conditions: (i) descending glide when neither the buoyancy pump nor the rudder are active (heavy line); (ii) at the bottom of the profile when the buoyancy pump is active (thin solid line); and (iii) descending glide while the rudder is in operation (dotted line).

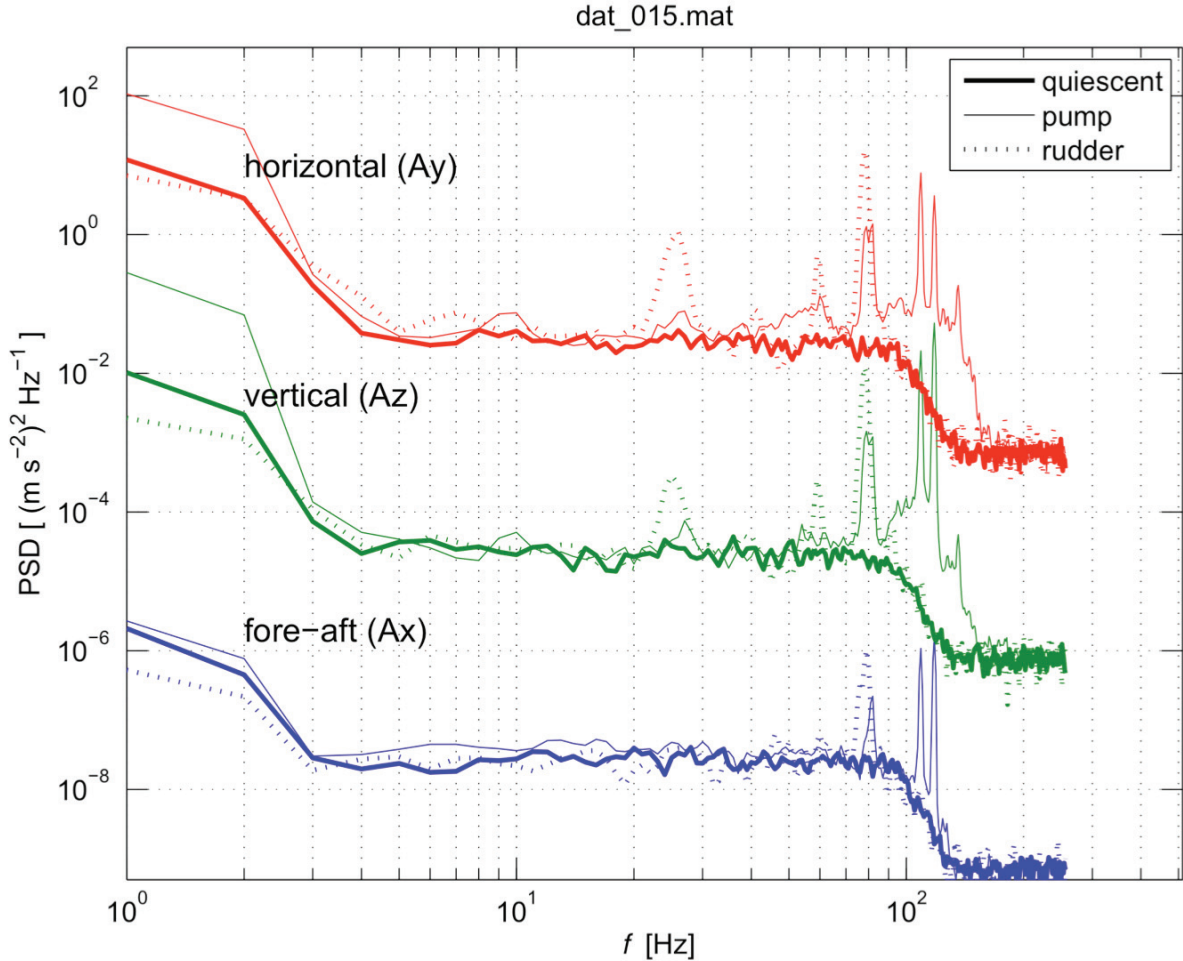


Figure 3: Accelerometer spectra for x -axis (blue), z -axis (green) and y -axis (red) for three conditions: (i) during descent when neither buoyancy pump nor the rudder were active (heavy line); (ii) at the bottom of the profile when the buoyancy pump is running (thin line); (iii) during descent when the rudder is active. The lowest set of spectra is for the x -direction. Spectra for the z - and y -direction are offset by 10^3 and 10^6 , respectively.

For the quiescent condition (heavy line), the spectra are flat throughout the entire frequency band and are at the noise level of the accelerometers. The rise at ~ 1 Hz represents the low-frequency body motions. The anti-aliasing filters suppress the signal variance starting at 98 Hz. The action of the buoyancy pump (thin lines) shows various narrow-banded spectral signatures above 60 Hz. The pump signature is strongest at 80 Hz, with some harmonics at higher frequencies. The vibration signatures are stronger and more broad-banded in the transverse (y , z) directions than in the along-body (x) direction. This is a typical feature of cylindrical bodies, because they are stiffer in the along-axis direction than in the transverse

direction. In the case of the *Slocum* glider, the tail fin, which is mounted on a cantilevered stanchion protruding from the aft of the hull, likely acts as an amplifier for the vibrations. We also note a broader spectral peak centred on 60 Hz in the y direction (horizontal to the glider axis), which is not present in the z component, which is most likely the result of an asymmetry of the glider tail fin, which, by its nature, is more flexible in the y direction than in the z direction.

The action of the rudder (dotted line) shows spectral signatures in the transverse directions at 28, 60, and 80 Hz. The latter corresponds with the 80 Hz vibration excited by the buoyancy pump, and therefore is likely a characteristic frequency of the tail fin assembly. The peak at 60 Hz is more pronounced in the horizontal (y) direction than in the vertical direction (z), because the movement of the rudder is in the x - y plane.

Shear Data

The vibration signatures identified in the accelerometer measurements also show up in the shear data. A segment of data from a descending portion of a dive, between 2.5 m and 11.2 m, is plotted as a “pseudo” vertical profile (Figure 4), showing temperature, temperature gradient, $\partial T_1 / \partial x$, and velocity shear for shear probes #1 and #2, $\partial u_1 / \partial x, \partial u_2 / \partial x$. This representation is practical because it gives a composite view of the measured parameters. It shows small-scale variations along the quasi-horizontal glide path in context with large-scale vertical features. The temperature profile shows a thermocline at ~ 7.5 m depth separating the active surface mixing layer from the quiescent layer below the thermocline. The variance of the temperature gradient and shear signals clearly reflect the different levels of turbulent mixing in the two layers.

The action of the rudder is visible throughout the profile in the unfiltered shear signals (red and green lines). The vibration signature is more pronounced in the $\partial u_1 / \partial x$ signal than in the $\partial u_2 / \partial x$ signal, because the shear probes were orthogonally mounted. The sensitive axis of shear probe #2 was in the horizontal direction, parallel to the movement of the rudder, while the sensitive axis of shear probe #1 was in the vertical direction, perpendicular to the rudder movement. The amplitude of the vibrations decreases over the length of the profile. This is due to the fact that the glider needs to make stronger course corrections at the beginning of the profile, when its speed is slow and the glider is unstable. Similarly, the amplitude of the vibrations signatures is on average larger in the surface mixing layer than in the quiescent layer below the thermocline, because in the turbulence in the surface layer requires stronger rudder action.

In order to reveal the vertical structure in the turbulent velocity, the two rightmost traces in Figure 4 show the shear signals after a 0.15 to 10 Hz band pass filter was applied. The filter effectively removes the high frequency vibration signatures and shows the extremely quiescent conditions below the thermocline. This representation also shows that the shear measurements, on average, have identical signal variance. The single-sided excursion of the shear signals at 7.5 m depth is the result of a pyro-electric effect, which discussed in detail by Lueck (2008). This is a transient effect with a time scale of several 10s of seconds and it occurs when the shear probe’s piezo-ceramic sensing element experiences a change in temperature. The temperature differential can cause an asymmetric expansion of the sensing element, which causes the spurious, transient signal. This effect is most pronounced in large temperature gradients in combination with slow profiling speeds, as is the case here. Because

of the long time scale of the spurious signal, the pyro-electric effect is of no consequence to the shear measurement (Lueck, 2008).

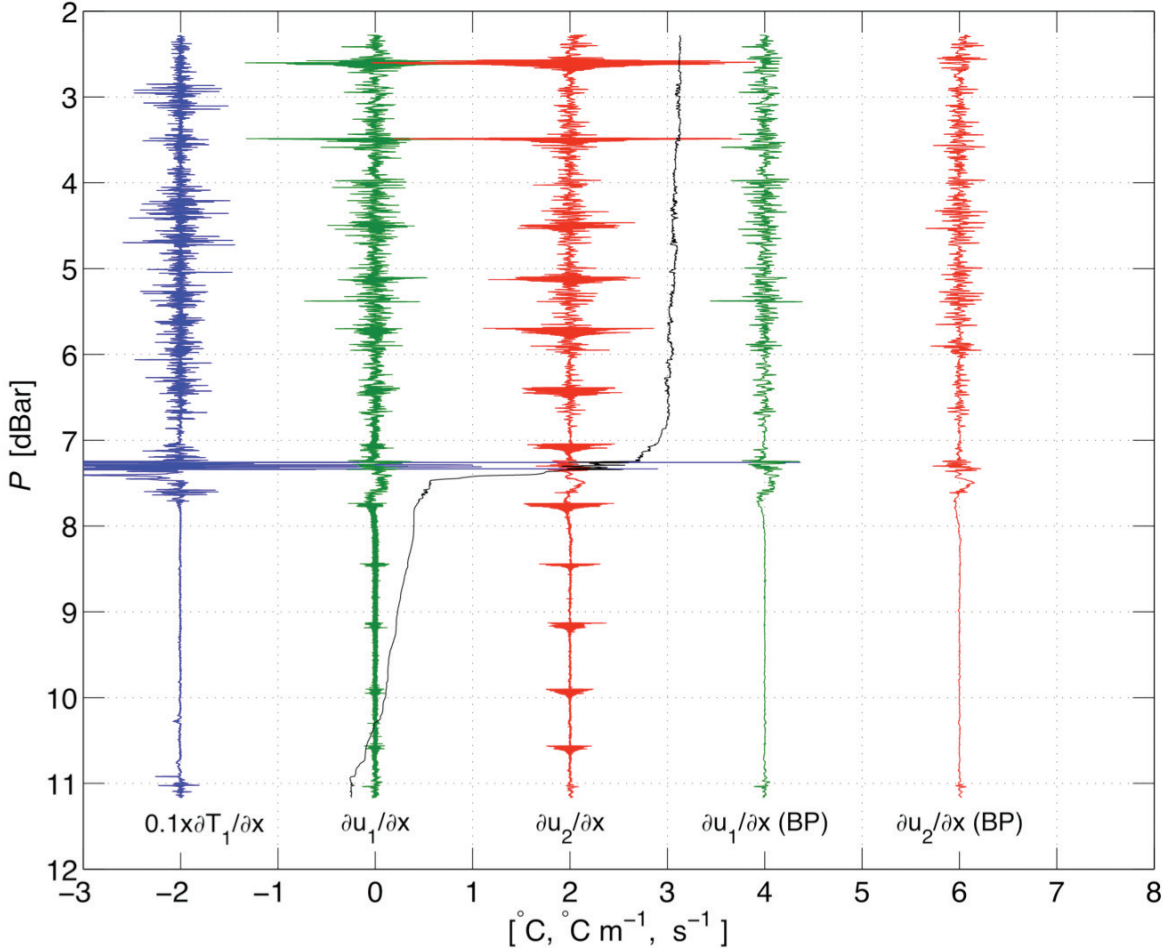


Figure 4: Pseudo profiles of temperature (T_1), temperature gradient ($\partial T_1 / \partial x$), and velocity shear ($\partial u_1 / \partial x, \partial u_2 / \partial x$). Temperature is offset by -9°C . All gradient signals are centred on zero and are offset by integer numbers, as shown. The shear signals $\partial u_i / \partial x, \partial u_2 / \partial x$ are high-pass filtered at 0.15 Hz. The BP labels denote that a 0.15 to 10 Hz band-pass filter has been applied.

Shear spectra were computed for two sections in the turbulent and the quiescent portions of the profile in Figure 4, following the procedure of Goodman *et al.* (2006). The shear signals were high-pass filtered at 0.15 Hz in order to remove low frequency motions of the glider, but this removal of signal content does not affect the calculation of the dissipation rate. For both turbulent and quiescent conditions the measured spectra of both shear probes agree with each other (indicating no systematic biases in the probes' calibration or the electronics of the system) and they agree well with the Nasmyth Empirical Spectrum (hereafter NES; Oakey 1982). Good agreement with the shape of the NES is a measure of the quality of the shear data (Gregg, 1999). The spectra computed from this dive are representative of all other dives that were performed in Ashumet Pond.

The spectra from the turbulent layer (Panel a) were computed from 44 seconds of data. Both spectra for shear probe #1 and shear probe #2 agree with the NES over two decades in wavenumber space, between 1 and 100 cpm. The thin lines are the spectra computed from the

“raw” shear signals ($\partial u_1 / \partial x, \partial u_2 / \partial x$ in Figure 4). The vibration peaks that were identified in the accelerometer spectra are visible in the raw spectra at the higher wavenumbers. For example the peak at 70 cpm corresponds to the 28 Hz peak in the accelerometer data that was associated with the rudder action. Other vibration peaks at higher wavenumbers can be similarly matched with the accelerometer data. Note, however, the vibration peak in the shear probe #1 spectrum at 100 cpm, which corresponds to a frequency of 40 Hz. At this frequency the accelerometer spectra show only a very small vibration signature. The reason is that the shear probes are mounted in front of the pressure case and they tend to amplify vibrations because of the leveraging effect of their protracted position.

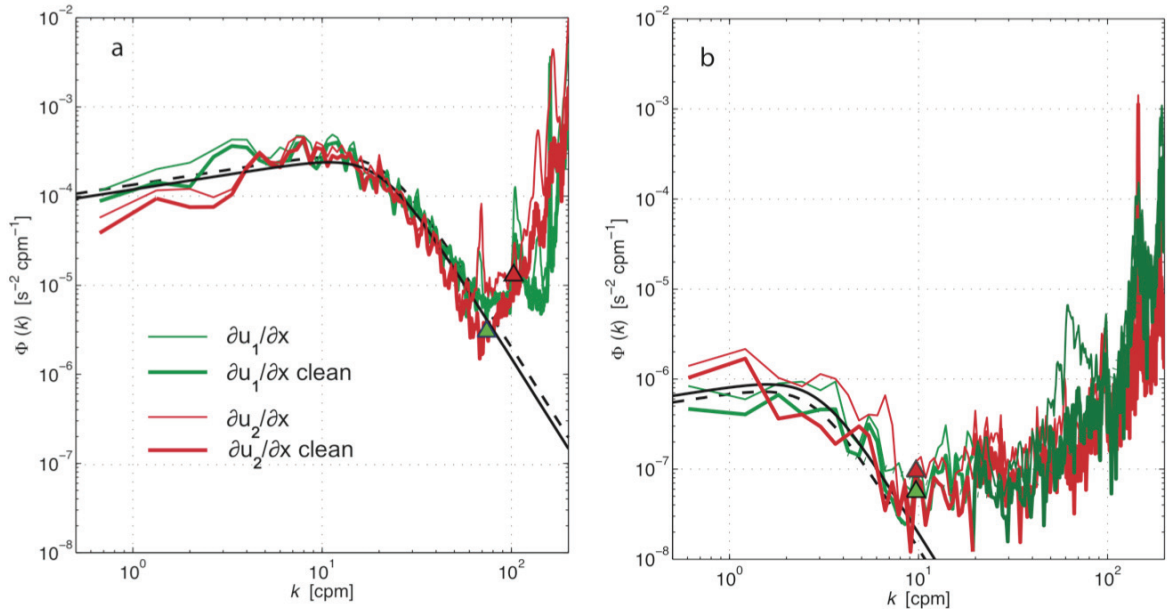


Figure 5: Shear spectra computed from the turbulent surface layer (a) and the quiescent bottom layer (b). Green lines are from shear probe #1 and red lines are from shear probe #2. The thin lines are the spectra computed from the “raw” shear signals, where only a 0.15-Hz high pass filter was applied to remove low-frequency (large scale) motions of the glider. The heavy lines are spectra after signal content coherent with the accelerometer data was removed from the shear signals using the Goodman Method (Goodman *et al.*, 2006). The triangles denote the wavenumber cutoff points used in the computation of the dissipation rates.

The vibration signatures can be very effectively removed from the shear probe data by using the information from accelerometers. This technique was first suggested by Levine and Lueck (1999) and later refined for three dimensions by Goodman *et al.* (2006). By calculating the three-dimensional coherence matrix between a shear probe signal and the (three) accelerometer signals, only signal content that is coherent with that of the accelerometers (i.e., caused by body vibrations) is removed. The “clean” shear spectra are shown as the heavy lines in Figure 5. After this treatment, the dissipation rates are computed from the cleaned shear spectra using

$$\varepsilon = 7.5\nu \int_0^{k_{\max}} \Phi(k) dk ,$$

where ν is the kinematic viscosity and k_{\max} is the maximum wavenumber of integration, indicated by the triangular markers in the figure. For shear probe #1 $\varepsilon_1 = 6.8 \times 10^{-8} \text{ W kg}^{-1}$ with

a viscous cutoff wavenumber (Kolmogorov wavenumber) of $k_v = 81 \text{ cpm}$; and for shear probe #2 $\varepsilon = 5.8 \times 10^{-8} \text{ W kg}^{-1}$ with $k_v = 78 \text{ cpm}$. Note that the vibration peaks are above the viscous cutoff wavenumber, so that the shear spectra are fully resolved.

The spectra from the quiescent layer also show good agreement with the NES. These spectra were computed from only a 16-second segment of data, and so they exhibit a higher statistical uncertainty. Dissipation rates computed for the two shear probes are $\varepsilon_1 = 2.5 \times 10^{-11} \text{ W kg}^{-1}$ with $k_v = 11 \text{ cpm}$ and $\varepsilon = 3.3 \times 10^{-11} \text{ W kg}^{-1}$ with $k_v = 12 \text{ cpm}$. Again, it is worthwhile to note that while the vibration peaks are visible at the higher wavenumbers, none of the noise peaks falls into the wavenumber range of the turbulent shear spectrum. This shows that the glider has extraordinarily low noise levels, which means that the glider can resolve open ocean turbulence levels.

CONCLUSIONS

Data were presented from the first test flight of a *Slocum* glider carrying a turbulence sensor package with velocity shear probes. The test was carried out in a small lake, which provided a practical test location. The lake did not have any strong currents and very low turbulence levels below the thermocline, which made it possible to assess the noise level of the glider in terms of the measured dissipation rate of turbulent kinetic energy.

Three main results from these tests are:

- The flight dynamics of the *Slocum* glider were not negatively affected by the presence of the turbulence package. Typical vertical speeds of the glider were 0.1 m s^{-1} , which corresponded to 0.4 m s^{-1} of forward speed along the glide path. This is a nearly ideal speed from shear probe measurements.
- The glider's sources of vibration noise are the ballast pump, battery shifting for pitch control, and the rudder action for course control. The pump noise is significant but it occurs only at the turn-around points of the saw tooth profile and, therefore, is irrelevant for the shear probe measurements. The noise resulting from the battery shifting was not detectable in this test. The noise from rudder action occurs at high wavenumbers and does not affect shear measurement.
- Dissipation rates from $\sim 10^{-7} \text{ W kg}^{-1}$ in the surface mixing layer of the lake down to $\sim 5 \times 10^{-11} \text{ W kg}^{-1}$ below the thermocline were measured. This shows that the glider matches the performance of the best vertical profilers in terms of the resolved dissipation rate.

Future work will be directed towards assessing the angle of attack, which is the difference between the glider's pitch angle and its glide path. More tests will be carried out to assess the additional drag introduced by the turbulence package, in order to estimate the impact on the glider's power consumption and endurance.

Acknowledgements: Ben Allsup and Peter Collins of Teledyne Webb Research and Ken Decoteau of FSU supported the fieldwork at Ashumet Pond. The glider and microstructure work of LS is supported by the US Office of Naval Research Physical Oceanography Program. The instrument system described here was funded through ONR contracts N00014-05-1-0360 and N00014-09-1-0289.

REFERENCES

- Eriksen, CC, T.J. Osse, R.D. Light, T. Wen and T.W. Lehman (2001). Seaglider: A long-range autonomous underwater vehicle for oceanographic research. *IEEE Journal of Oceanic Engineering*, **26**, 424–436.
- Gregg, M.C., 1999: Uncertainties and Limitations in Measuring ε and χ . *T. J. Atmos. Oceanic Technol.*, **16**, 1483–1490.
- Goodman, L., E.R. Levine and R.G. Lueck (2006). On Measuring the Terms of the Turbulent Kinetic Energy Budget from an AUV. *J. Atmos. Ocean. Tech.*, **23**, 977–990.
- Jones, C. and D. Webb (2007). Slocum Gliders, Advancing Oceanography. In: *Proceedings of the 15th International Symposium on Unmanned Untethered Submersible Technology conference (UUST'07)*, Durham, NH, USA, 19 to 20 August 2007. Autonomous Undersea Systems Institute.
- Levine, E.R., and R.G. Lueck (1999): Turbulence Measurement from an Autonomous Underwater Vehicle. *J. Atmos. Oceanic Technol.*, **16**, 1533–1544.
- Lueck, R. (2008). Testing of the EAWAG VMP-500-028 in Harry Lake. Application Note AN-017, Rockland Scientific Inc., Victoria, B.C., Canada. Available at <http://www.rocklandsscientific.com> (July 2009) or through info@rocklandsscientific.com.
- Lueck, R., F. Wolk, and H. Yamazaki (2002). Oceanic velocity microstructure measurements in the 20th century, *J. Oceanography*, **58**, 153 – 174.
- Oakey, N. (1982). Determination of the Rate of Dissipation of Turbulent Energy from Simultaneous Temperature and Velocity Shear Microstructure Measurements. *J. Phys. Oceanogr.*, **12**, 256–271.
- Osborn, T. R., and W. R. Crawford (1980). An airfoil probe for measuring turbulent velocity fluctuations in water. *Air–Sea Interaction: Instruments and Methods*, L. H. F. W. Dobson and R. Davis, Eds., Plenum, 369–386.
- Sherman, J., R.E. Davis, W.B.Owens and J.Valdes (2001). The autonomous underwater glider Spray. *IEEE Journal of Oceanic Engineering*, **26**, 437–446.
- Williams, C.D., R. Bachmayer and B. deYoung (2008). "Progress in Predicting the Performance of Ocean Gliders from At-Sea Measurements", Proceedings of the OCEANS'08 MTS/IEEE, September 15 to 18, 2008, Québec City, Québec, Canada.
- Wolk, F., H. Yamazaki, L. Seuront, and R. Lueck (2002). A new free-fall profiler for measuring biophysical microstructure. *J. Atmos. Ocean. Tech.*, **19** (5), 780–793.

In-situ measurements of turbulence in fish shoals

Andreas Lorke^{1,2*} and W. Nikolaus Probst¹

¹ Limnological Institute, University of Konstanz, D-78457 Konstanz, Germany

² Institute for Environmental Sciences, University of Koblenz-Landau, D-76829 Landau, Germany

* corresponding author: lorke@uni-landau.de

ABSTRACT

Turbulence was measured *in-situ* within shoals of juvenile perch *Perca fluviatilis* with a self contained autonomous microstructure profiler near an artificial reef in Lake Constance, Germany. Depth-averaged dissipation rates of turbulent kinetic energy (TKE) correlate with the density of shoaling fish, providing evidence for fish induced turbulence in a large and stratified lake. The magnitude of the fish induced turbulences was comparable to the magnitude of turbulence typically caused by internal waves or wind forcing and could only be observed during periods of low background turbulence and high fish abundance. The observed rates of dissipation of TKE are about two orders of magnitude smaller than production rates of TKE estimated from empirical models and based on observed fish size and swimming speed. The results of the present study for the first time proof the presence of fish induced turbulences in a natural aquatic habitat and strongly suggest that further research on the interaction between animal behavior and water column turbulence is required.

.

Field observations of breaking high-frequency internal waves

Martina Preusse ¹, Frank Peeters ², Andreas Lorke ³

¹*Limnological Institute Uni Konstanz, martina.preusse@uni-konstanz.de*

²*Uni Konstanz, Frank.Peeters@uni-konstanz.de*

³*Uni Landau, lorke@uni-landau.de*

* corresponding author: *martina.preusse@uni-konstanz.de*

ABSTRACT

Internal waves are a common phenomenon in lakes and in the ocean. To explore their changing properties in the near-shore zone, the temperature and current velocity in the littoral zone of a large lake (Lake Constance) were measured with high-resolution methods during several weeks in summer 2008. The data frequently reveal small-scale density inversions in the water column of the otherwise strongly stratified lake. A comparison between the passage of the basin-scale internal Kelvin wave and the occurrence of inversions demonstrates a pronounced phase relationship due to high-frequency internal waves. Nonlinearity and amplitude of the high-frequency waves play an important role for the increase in the total amount and the extreme values of density inversions. The small-scale unstable stratifications, generated by high-frequency waves, indicate the breaking of the waves outside the boundary layer.

Hydrodynamics and Salinity of the Future Sacramento-San Joaquin Delta

Wm. E. Fleenor^{1*}, J. R. Lund¹, E. E. Hanak², J. F. Mount³

¹ Civil and Environmental Engineering Department, Center for Watershed Sciences, University of California, One Shields Avenue, Davis, CA, USA 95616

² Public Policy Institute of California, Senior Fellow Director of Research, 500 Washington St, Suite 600, San Francisco, CA, USA 94111

³ Geology Department, Center for Watershed Sciences, University of California, One Shields Avenue, Davis, CA, USA 95616

**Corresponding author, e-mail wefleenor@ucdavis.edu*

ABSTRACT

An initial assessment of the salinity implications of four broad strategies for managing future Sacramento-San Joaquin Delta water exports is presented. The four strategies include: (1) continued pumping of exports through the Delta (the current policy), (2) diverting water upstream and conveying it around the Delta through a peripheral canal, (3) combining the current through-Delta pumping strategy with a peripheral canal (so-called “dual conveyance” or “dual facility”), and (4) ending exports altogether. Salinity implications of two main aspects of change in the Delta over this century: 30.48 and 91.44 cm of sea level rise and increased island flooding are considered. The focus is on salinity, the water quality characteristic of primary interest to water users and the one most easily represented in most models.

Change will occur in the Delta, with outcomes of export possibilities depending on what conveyance strategy is chosen, how the system is operated, and how sea level and climate conditions evolve. With sea level rise predicted over the next century, initial model simulations suggest significant increases in salinity in the Delta, eventually pushing Delta salinity beyond reasonable levels for drinking water and irrigation unless large (and costly) increases in Delta outflows or reductions in upstream use and exports are made. Similarly, permanently flooded western islands significantly increase salinity intrusion into the Delta. In contrast, some islands elsewhere in the Delta might be pre-flooded without long-term effects on Delta salinities. Modeling concurrent sea level rise and island flooding was not done, but these two effects would be at least additive, making Delta salinity conditions difficult indeed for both urban and agricultural users.

The approach represents a first cut at predicting trends and magnitudes of likely changes with different export management strategies and changed natural conditions. The analysis also points to many areas that require more detailed modeling work to more thoroughly evaluate issues related to sea level rise, island flooding, and the effects of operational changes (notably varying the timing of exports and the operation of upstream reservoirs) both now and in the future.

KEYWORDS

Hydrodynamic; estuary; limnology; sea level rise; shallow water; stratified.

INTRODUCTION

The Sacramento-San Joaquin Delta once encompassed over 2,023.5 km² of intertidal marsh and floodplains. Before the significant management of upstream releases of water from dam construction, Delta hydrodynamics and water quality underwent anthropogenic modification. With the discovery of gold in 1848, the intertidal wetlands and floodplains of the Delta underwent separation from the aquatic ecosystem by dike and levee construction. As the Delta was being channelized, upstream hydraulic mining began sending large quantities of sediment into the Delta and reducing channel depths until banned by the late 1890s. At the same time modifications were being made to widen and deepen channels for shipping while some new channels were dug to straighten the sinuous rivers (Thompson 1957).

Salinity intrusion into the Delta was an early problem as upstream irrigation diversions reduced Sacramento River inflow, although intrusion in dry years was significant before diversions (Young 1929). Beginning with the completion of Shasta Dam on the Sacramento River, upstream releases and diversions took control of Delta inflows. Dam construction and diversions have reduced the San Joaquin River to an even greater extent. Delta flow management was further increased and complicated with the early 1950s implementation of the Federal Central Valley Project (CVP) to export water from the southern Delta to irrigate part of the central valley. Sacramento River water entering in the north was pulled down through the Delta to the pumps. Additional exports began with the completion of the State Water Project (SWP) to supplement southern California drinking water and irrigation needs, also pumped from the southern Delta. The sum of these changes produced a system that manages the water quality in the Delta to the benefit of agriculture and urban water needs while pulling most exported water down through the Delta from the Sacramento River to the southern pumps (see Figure 1). To assist the management of Delta water quality, multiple gates and barriers are permanently or annually installed.

In spite of more recent efforts to manage water releases for the benefit of the ecosystem, fish populations have continued to decline (Lund *et al.* 2007). The issue of ecosystem viability has become of increasing interest as 5 native species are now listed as either endangered or threatened. A recent court decision to reduce some of the negative flows produced by through-Delta pumping has required significant export reductions. Should the delta smelt populations not improve, there will likely be additional court ordered management changes.

The risks to 1,770 km of dikes and levees, many protecting the below sea level subsided farm land, are becoming increasingly apparent. The seismic potential of the area is considered significantly great to be able to breach multiple islands with various levels of probability. Sea level rise has been steady over the last 100 years and the rate of increase is predicted to rise (IPCC 2007). The IPCC (2007) report also predicts increasing winter storms with more rain and reduced snow pack increasing the likelihood of higher winter and spring flood flows. Continued subsidence of the interior farm land adds to the stress of the dikes and lessens the ability to raise and reinforce the dikes to keep up with sea level rise and climate change.

The California Department of Water Resources (DWR) implemented the Delta Risk Management Strategy (DRMS) program to assess the current risks and produce strategies in dealing with the future failures (DRMS 2006a). One of the projects to provide needed information was the development of a simplified, one-dimensional hydraulic and water quality model (Water Analysis Module) to use to predict water quality (salinity) changes to the Delta for use by decision management systems (DRMS 2006b). Model results would be

used to determine if export pumping needed to be reduced or halted and how much upstream water might need to be released to hold back salinity intrusion or mix it out of the Delta if salt was pulled in by levee failure.

Here, the WAM model and others are used to examine the range of viable Delta export options identified by Lund *et al.* (2007) with the possibility of clarifying the available options.

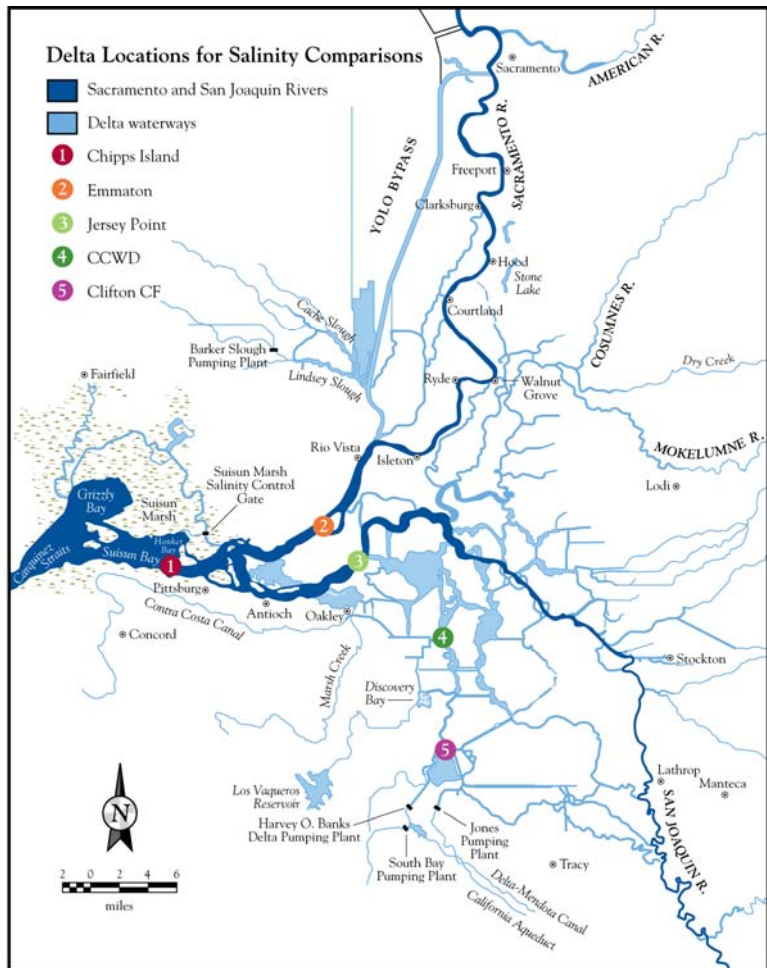


Figure 1 Sacramento-San Joaquin Delta.

METHODS

Two existing computer models were employed to conduct this analysis. The first is a computationally efficient one-dimensional, tidally averaged model called WAM (water analysis module), which was developed by Resource Management Associates, Inc. for modeling work in the Delta Risk Management Strategy (URS Corporation and Jack R. Benjamin and Associates, 2007a). WAM incorporates dispersion characteristics based on 3-D modeling performed with UnTRIM (Gross *et al.* 2007). The WAM model was used to explore the effects of sea level rise and of Delta water management alternatives including the four export options discussed above (through-Delta pumping, no exports, and several capacities of peripheral canal or dual conveyance facilities) and a scenario with “unimpaired flows” (with neither exports nor upstream diversions). These simulations covered historical water conditions for 20 water years, from 1981 to 2000, a period including considerable diversity in precipitation, with both one of the wettest periods and one of the longest droughts

in recent history. To explore the effects of permanent island-flooding, a second, more detailed two-dimensional finite element model developed by Resource Management Associates, Inc., for the DRMS flooded-island modeling work (URS Corporation and Jack R. Benjamin and Associates 2007b) was used. Because the 2-D model takes considerably longer to run (480 hours, versus 15 minutes for WAM), the study relied on existing simulations for the island-flooding scenarios. Flooded-island simulations use conditions for a shorter period: the two and a half years between April 12, 2002, and December 31, 2004.

RESULTS AND DISCUSSION

Continued Exports through the Delta. The historical boundary conditions as defined by Dayflow data (<http://www.iep.water.ca.gov/dayflow/>) as input for simulations of 1981-2000 water years are used as the “Base Case” scenario. To examine a range of effects for agricultural, urban, and environmental water uses, output is focused on five locations within the Delta (Figure 1): (1) Chipps Island on the Delta’s western edge used to monitor salinity regulations for fish during the springtime, (2) Emmaton, a northwestern location on the Sacramento River where irrigation water standards are in effect, (3) Jersey Point an irrigation standard on the western Delta on the San Joaquin River, (4) the Contra Costa Water District’s (CCWD) pumping plant in the southwestern Delta with stringent urban standards, and (5) the Clifton Court Forebay (Clifton CF) in the southern Delta representing exports for the State Water Project (SWP) and the Central Valley Project (CVP) with year-round urban standards and seasonal irrigation standards.

No Exports and Unimpaired Flows. Two separate simulations were made eliminating the water exports from the southern Delta. The first was performed with the same inflow conditions as the “Base Case” but with no exports from the Delta. The second was performed using the ‘unimpaired’ inflows provided by DWR. Unimpaired flows route the water flowing into the reservoirs as though the dams no longer existed. They are not ‘natural’ flows since current watershed and river systems do not dampen the flows like would have occurred.

The results of these simulations are summarized in Figure 2, which compares the “Base Case” to scenarios with “no exports” and with “unimpaired” Delta flows (i.e. flows without exports, upstream diversions or surface storage). For the ‘no exports’ simulation the “Base Case” was modified to set the exports of CCWD, SWP, CVP and the North Bay Aqueduct to zero. Shaded areas are periods when compliance with salinity standards is prescribed, although compliance levels vary by location and across water year types. Each graph location provides the compliance level (in parenthesis), but exceedance of the compliance level is not necessarily an actual violation since standards are based on varying short-term averages (State Water Resources Control Board 2000).

Although ending water exports would substantially increase Delta outflows, it would not uniformly freshen Delta waters, and likely be best for the ecosystem (Lund *et al.* 2008). Salinity decreases in the northern and western Delta (Emmaton and Jersey Point), but increases significantly in the southern Delta (Banks) without exports. South Delta exports reduce South Delta salinities. Without exports, higher salinity San Joaquin River water is no longer diluted by the fresher Sacramento River water currently pulled south to the pumps.

In contrast, for “unimpaired” flows without upstream or export diversions or surface storage releases, dramatic reductions occur in salinity at all Delta locations, except at Emmaton and Chipps in the fall. Because the unimpaired flows were estimated using monthly averaged

inflow and water quality data, the results are somewhat muted relative to results that would have been obtained using daily data. However, this simulation presents salinity conditions under pre-development flows for the current Delta network and landscape, not for the “natural” Delta that existed before the dredging and diking of the Delta’s marshlands in the second half of the 19th century.

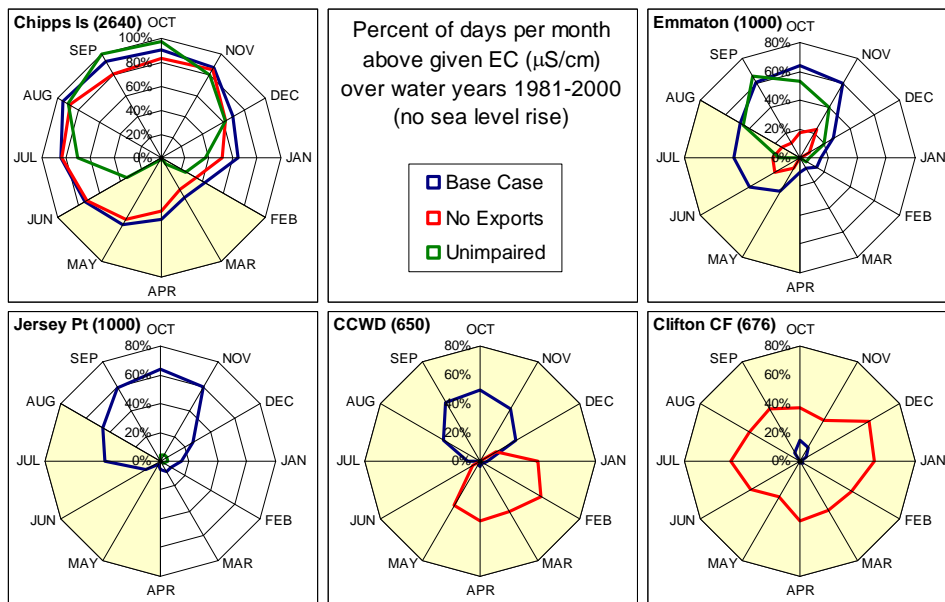


Figure 2 Simulated percentage of days each month exceeding the specified EC ($\mu\text{S}/\text{cm}$) at locations in the Delta with no exports and unimpaired flows. Values presented are the average monthly value over the simulation period 1981–2000.

Consequences of Sea Level Rise. Sea level at the Golden Gate Bridge of California has increased by 0.2 cm per year over the past century. Most climate models project an increase in the rate of sea level rise during the next century (IPCC 2007). For planning purposes, the CALFED Independent Science Board (ISB) has recommended that the Delta Vision effort use mid-range values for sea level rise of 20.3-40.6 cm by 2050 and 71.1-103.1 cm by 2100 (http://calwater.ca.gov/science/pdf/isb/meeting_082807/ISB_response_to_ls_sea_level_090707.pdf). Only very recently have examinations begun of the consequences of sea level rise for Delta salinity distributions.

With sea level rise, and all other conditions being equal, the ocean pushes its higher salinity (higher density) water farther into the Delta (Hansen and Rattay 1965; Fischer *et al.* 1979). Less clear are potential effects of deeper water, which may reduce vertical mixing of salinity (with fresh water at the top, and more saline water at lower depths). To simulate sea level rise, the downstream boundary and initial water elevation throughout the Delta were increased by 30.48 and 91.44 cm. These simulations all assume continued south Delta exports.

The result is an increase in salinity at all five locations compared with the “Base Case” (Figure 3). With 30.48 cm of sea level rise, salinity in the Delta may still be low enough for irrigation during the growing season, but levels in the southern Delta would significantly increase costs of drinking water treatment. On average, annual salinity at Banks increases by approximately 4 to 26 percent and CCWD by approximately 35 to 49 percent. With a 91.44 cm sea level rise, salinity would greatly increase the cost of drinking water treatment and Delta water may be unsuitable for agricultural irrigation. In very dry years, the salinity problems are particularly acute, even with 30.48 cm of sea level rise (see Figure C.11 in Fleenor *et al.* 2008).

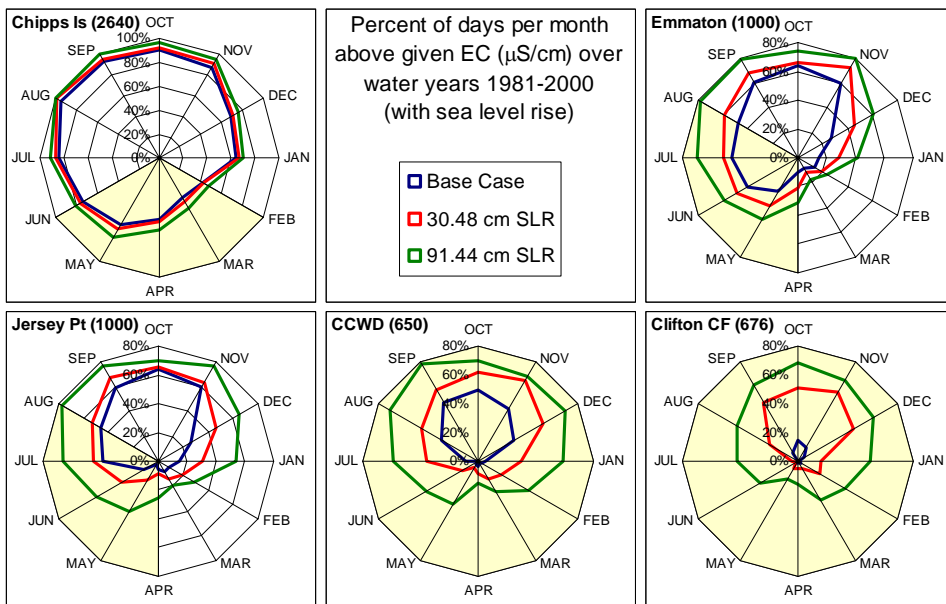


Figure 3 Simulated percentage of days each month exceeding the specified EC ($\mu\text{S}/\text{cm}$) at locations in the Delta with sea level rise. Values presented are the average monthly value over the simulation period 1981–2000.

Consequences of Island Failure. Over the last 100 years there have been 166 dike and levee failures in the Delta. As a consequence of continued sea level rise, periodic flood flows, deteriorating levees and earthquakes, islands will continue to fail; and with earthquakes and floods, many could fail simultaneously. Some flooded islands may not be worth reclaiming based on the economic value of the activities on the islands themselves (Lund *et al.* 2008; Suddeth *et al.* 2008). It is important to model the salinity consequences of leaving islands permanently flooded following failure, to see whether they have strategic value for maintaining long-term Delta salinity.

In the simulations shown here, the islands are “pre-flooded” - filled with water of salinity equaling that in surrounding channels. This depiction represents conditions for an island that has already been flooded for some time; it could also result if the initial flooding occurred during the winter or spring, when significant river flows are available. Four island flooding scenarios are compared with the base case (labeled “Intact”) and shown in Figure 4.

- Five western islands (Sherman, Twitchell, Bradford, Brannon-Andrus and Jersey),
- Five eastern islands (Venice, Mandeville, MacDonald, Jones and Bouldin),
- Five southern islands (Palm-Orwood, Bacon, Woodruff, Jones and Victoria islands), and
- Twenty islands (all preceding islands plus five in the Central Delta: Byron, Bethel, Webb, Holland and Quimby).

As with the other scenarios, these simulations assume continued south Delta exports. The results, shown in Figure 5, suggest some striking differences in strategic value of Delta islands for maintaining salinity levels. The permanent flooding of five western islands increases salinity intrusion to the pumps in the southwest and southern Delta and would significantly affect drinking water treatment costs between August and December.

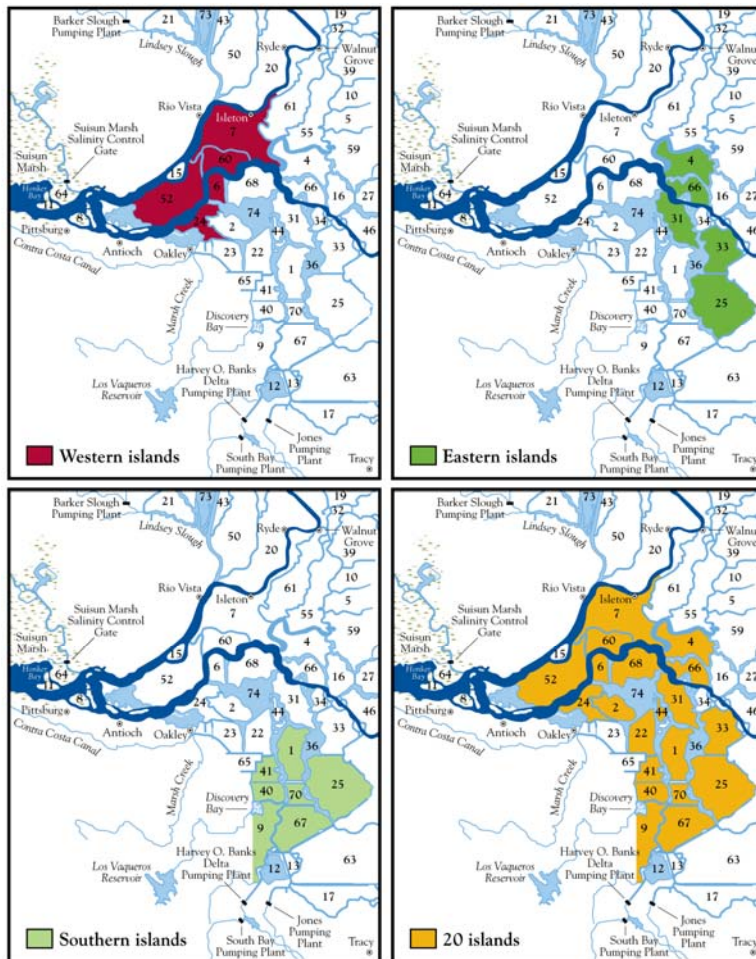


Figure 4 Four separate flooded island simulations.

In effect, the long-term consequences of permanent western island failures are almost as problematic for export water salinities as the immediate consequences of levee breaches. These failures result in little change at Chippis Island and Emmaton, in part since no breaches were included on the Sacramento side of the islands. Only modest changes occur at Jersey Point, because without the “big gulp” of a sudden levee failure, most salt water is pulled southward toward the pumps. For the western island failures more saline water is drawn in from the eastern Bay on flood tides and is then released by the islands during ebb tides into fresher river water increasing dispersion of the salts.

In stark contrast, the permanent flooding of eastern or southern islands shows little, if any, long-term salinity effects on the Delta. There are even short periods when the failed islands improve southern Delta salinity (CCWD and Clifton CF) by facilitating the flow of Sacramento River and eastside streams (Calaveras, Mokelumne, and Cosumnes) through the Delta toward the southern pumping plants. Since the flooded areas are farther from the Bay than are the western islands, they do not draw as much saline water in from the Bay. There is also considerable eastward infiltration of sea salt from the filling and emptying of flooded western islands with each subsequent tide.

The catastrophic failure scenario, with permanent failures of 20 islands, produces very similar results to the failure of the five western islands, highlighting the importance of the five western islands in maintaining the current conveyance system for water exports. As discussed

in Lund *et al.* (2008), this is a particularly risky prospect, given the high probabilities of failure of these islands by mid-century from flood and seismic activity.

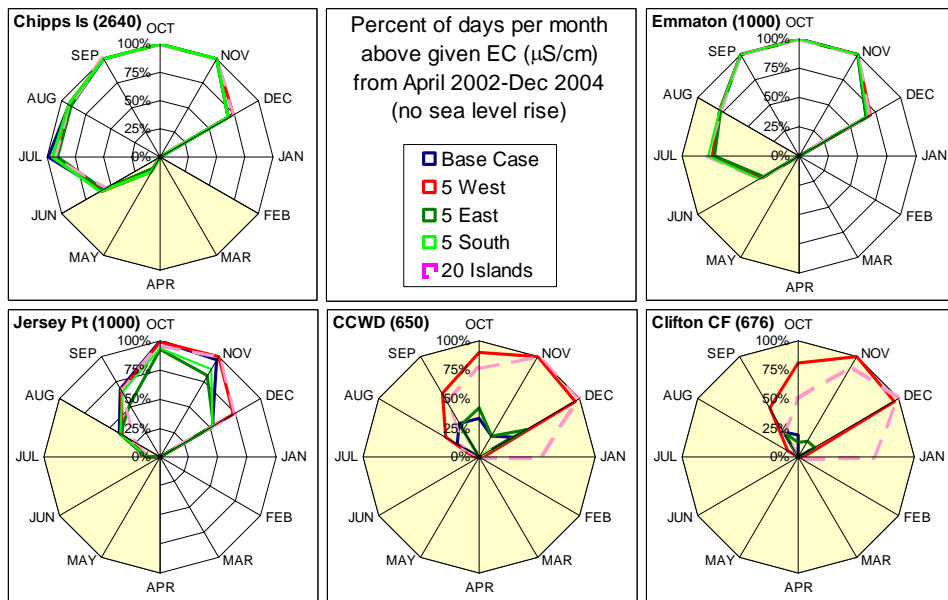


Figure 5 Simulated percentage of days each month exceeding the specified EC ($\mu\text{S}/\text{cm}$) at several locations in the Delta with island failures. Un-shaded areas of April to August are when irrigation standards are in effect but actual limits vary with water year type.

Consequences of Peripheral Canal Exports. The potential water quality effects of rerouting some or all export volumes from Delta channels to a peripheral canal has been hotly debated for over 30 years. One justification for a canal has been that exporters could benefit from lower salinity water by tapping into Sacramento River flows upstream of the Delta. However, water users in the Delta have been concerned that these diversions would increase salinities within the Delta itself. Although reducing or eliminating south Delta export pumping could benefit Delta fish populations, environmental advocates also have expressed concerns over whether the volume and timing of diversions would sufficiently protect fish.

An earlier peripheral canal was rejected by the voters in 1982, but was a very large facility ($708 \text{ m}^3\text{s}^{-1}$) intended to significantly increase the capacity of water exports from the Sacramento River watershed. Here, a more modest set of alternatives is examined. Assuming stability of export volumes at 1981-2000 levels, several canal capacities were examined, including $56.6 \text{ m}^3\text{s}^{-1}$ (2K PC), $212.4 \text{ m}^3\text{s}^{-1}$ (7.5K PC) and $424.8 \text{ m}^3\text{s}^{-1}$ (15K PC), operated as dual conveyance with some continued south Delta exports. In these scenarios, the canal takes as much of the daily exports as possible, subject to an environmental constraint on the amount of water that can be drawn from the Sacramento River ($283.2 \text{ m}^3\text{s}^{-1}$ minimum flows on the Sacramento River). An alternative without this environmental constraint was examined, operating as an exclusive peripheral canal that does not utilize existing Delta pumps (“PC Only”). Using the “PC Only” with the same environmental constraint would require upstream re-operation to comply and was not done here.

At current sea level, the dual conveyance scenarios examined here have relatively modest effects on salinities in the Delta (Figure 6). Salinity increases for locations along the Sacramento River (Emmaton), as the reduced river flow allows brackish water to move upstream. Salinity decreases slightly for locations near the San Joaquin River outlet (Jersey Point), as less saltwater is pulled from the west with reduced through-Delta pumping. The “PC Only” scenario alone significantly increased salinity at the southwestern (CCWD) and southern (Clifton CF) pumping locations, for reasons similar to the no exports scenario

examined above; with less fresh Sacramento River water being drawn toward the pumps, southern Delta water salinity is dominated by the more saline San Joaquin River flows. For users of export water, the salinity implications of these changes depend on the export blend, because Sacramento River water is so much fresher than San Joaquin River water. At current sea level, continued through-Delta exports with the dual conveyance systems depicted here protect agricultural users in the western Delta along the San Joaquin River (Jersey Point) and the southern Delta (Clifton CF) as well as urban users at the CCWD pumps. However, some additional upstream flow releases would likely be required to maintain agricultural salinity standards at Delta locations along the Sacramento River (Emmaton).

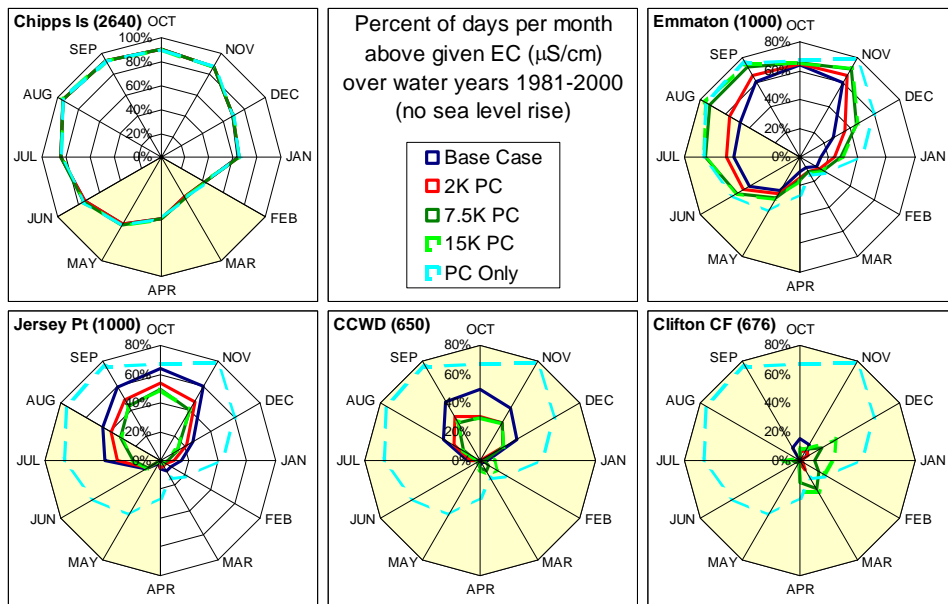


Figure 6 Average percentage of days in each month exceeding the specified EC ($\mu\text{S}/\text{cm}$) at locations in the Delta for different operational scenarios, at current sea level.

CONCLUSIONS

Modeling suggests that large changes are in store for Delta water quality as a result of natural forces acting on the Delta. Sea level rise during the next century will significantly affect salinity in the Delta. Eventually, sea level rise will increase Delta salinities beyond reasonable levels for drinking water and irrigation unless large increases in Delta inflows or reductions in exports are made. Permanently flooded western islands would have a similar effect, even if the islands are pre-flooded to avoid a “big gulp” associated with unexpected levee failures. In contrast, islands elsewhere in the Delta might be pre-flooded without long-term effects on Delta salinities provided the western islands remain intact. Modeling concurrent sea level rise and island flooding was not possible in the time available for this work. However, these two effects would at the very least be additive, making Delta water quality conditions difficult indeed for both urban and agricultural users.

Switching from the current south Delta export pumping strategy to some form of peripheral canal or dual conveyance implies different outcomes for exporters and in-Delta water users. For exporters, a canal offers the possibility of blending in lower salinity Sacramento River water. Even at current sea level, blending offers significant salinity improvements. A canal has different effects for in-Delta pumbers, depending on their location. Even when operated with minimum flow restrictions on the Sacramento River to prevent entrainment of aquatic life, a peripheral canal, operated in a dual conveyance mode, allows salinities to intrude

farther up the Sacramento River, increasing salinity for Delta farmers in these areas. In contrast, salinities in the lower San Joaquin River and the western Delta generally decrease as less water is drawn into the Delta from the saltier Suisun Bay. An exclusive peripheral canal (PC Only), without south Delta exports, substantially increases salinity in the southern Delta, since fresher Sacramento River water is no longer drawn into the Delta from the Sacramento River to dilute San Joaquin River outflows. For South Delta water users, this effect is similar to ending all exports. With sea level rise, the differences among different canal alternatives diminish.

ACKNOWLEDGEMENTS

Modeling assistance was provided by student research assistants Dane Behrens and Kevin Fung. Funding was provided by Stephen D. Bechtel Jr. and the David and Lucile Packard Foundation.

REFERENCES

- DRMS. 2006a. ITF Paper: Upstream Water Management/Delta Water Operations / Delta Island Water Use. Prepared by URS Corporation/Jack R. Benjamin & Associates, Inc., Prepared for Department of Water Resources. September, 2006.
- DRMS. 2006b. Delta Risk Management Strategy (DRMS). Initial Technical Framework Paper: Hydrodynamics / Water Quality. Prepared by URS Corporation/Jack R. Benjamin & Associates, Inc. Prepared for Department of Water Resources. September, 2006.
- Fischer, H.B., List, E.J., Koh, R.C.Y., Imberger, J., and Brooks, N.H., 1979. *Mixing in Inland and Coastal Waters*. New York: Academic Press Gross, E.S., Koseff, J.R., and Monismith, S.G., 1999. Three-dimensional salinity simulations of South San Francisco Bay. *Journal of Hydraulic Engineering*, 125 (11), 1199-1209.
- Fleenor, W., Hanak, E., Lund, J., and J. Mount. 2008. Technical Appendix C: Delta Hydrodynamics and Water Salinity with Future Conditions. Public Policy Institute of California, San Francisco, CA, 51 pp.
- Gross, E. S., M. L. MacWilliams, and N. Nidzieko, "Three-Dimensional Salinity Simulations of Sea Level Rise Scenarios," Delta Risk Management Strategy, Department of Water Resources, Sacramento, California, 2007.
- Hansen, D.V., and Rattray, M., 1965. Gravitational circulation in straits and estuaries, *Journal of Marine Research*, 23, 104-122.
- Intergovernmental Panel on Climate Change, *Climate Change 2007: Synthesis Report*. Contribution of Working Groups I, II and III to the Fourth Assessment, Report of the Intergovernmental Panel on Climate Change [Core Writing Team, Pachauri, R.K and Reisinger, A. (eds.)]. IPCC, Geneva, Switzerland, 104 pp., 2007.
- Lund, J., E. Hanak, W. Fleenor, R. Howitt, J. Mount, and P. Moyle. 2007. Envisioning Futures for the Sacramento-San Joaquin Delta. Public Policy Institute of California, San Francisco, CA, 300 pp.
- Lund, J., Hanak, E., Fleenor, W., Howitt, R., Mount, J., Moyle, P., and W. Bennett. 2008. Comparing Futures for the Sacramento-San Joaquin Delta. Public Policy Institute of California, San Francisco, CA.
- State Water Resources Control Board, Revised Water Right Decision D-1641, Sacramento, California, March 15, 2000. Available at: <http://www.waterrights.ca.gov/Decisions/D1641revs.pdf>.
- Suddeth, R., Mount, J., and J. Lund. 2008. Technical Appendix B: Levee Decisions and Sustainability for the Delta. Public Policy Institute of California, San Francisco, CA, 39 pp.
- Thompson, John, Settlement Geography of the Sacramento-San Joaquin Delta, California, dissertation, Stanford University, 1957.
- Young, Walker R., Report on Salt Water Barrier Below Confluence of Sacramento and San Joaquin Rivers, California, Bulletin 22, Vols. I and II, Division of Water Resources, California Department of Public Works, Sacramento, California, 1929.
- URS Corporation and Jack R. Benjamin and Associates, Inc., Technical Memorandum, Topical Area: Water Analysis Module, prepared for the California Department of Water Resources, 2007a.
- URS Corporation and Jack R. Benjamin and Associates, Inc., Delta Risk Management Strategy (DRMS) Phase 1 Risk Analysis Report, draft, prepared for the California Department of Water Resources, 2007b.

Shear-induced bottom boundary layer convection in stratified basins: A modeling study

J. Becherer^{*1, 2}, L. Umlauf^{1, 3}

¹*Leibniz-Institute for Baltic Sea Research (IOW), Warnemünde, Germany*

²becherer@io-warnemuende.de, ³lars.umlauf@io-warnemuende.de

ABSTRACT

Recent studies have shown evidence of inverse stratification inside turbulent bottom boundary layers (BBL) on the slopes of stratified basins. These data suggest that the near-bottom vertical current shear acting on the cross-slope buoyancy gradient may create unstable stratification and therefore strongly modify turbulence and mixing in the BBL. In addition to shear production, this mechanism provides an extra source of turbulent kinetic energy with a yet unknown impact on the basin-scale mixing. Here, we present results from a process-oriented modeling study investigating this effect in lakes, where the near-bottom shear and turbulence result from internal seiching motions. Simulations have been performed with a three-dimensional high-resolution numerical model using topography-following coordinates and a state-of-the-art second-moment turbulence model. In agreement with available data our results suggest that mixing occurs in a BBL of a few meter thickness, and dominates the basin-scale mixing for the system we have investigated (Lake Alpnach, Switzerland). Turbulence during BBL convection was found to be strong with diffusivities approximately one order of magnitude larger than during stable stratification. However, because of the weak stratification, the contribution of unstable boundary layers to overall mixing was found to be small. Conversely, during periods of downwelling, the stabilizing effect of the shear greatly enhances the mixing efficiency thus leading to strong mixing in spite of the comparatively small diffusivities.

KEYWORDS

Bottom boundary layer; sloping bathymetry; internal waves; seiches; diapycnal mixing; convection.

INTRODUCTION

A number of studies have shown that mixing processes in the bottom boundary layer (BBL) of lakes, fjords and oceanic sub-basins may significantly contribute to the net basin-scale mixing (Ledwell et al. 1995, Goudsmit et al. 1997, Wüest et al. 2000). The BBL is generally characterized by weak vertical density gradients due to enhanced turbulence and mixing in the near-bottom region. In most cases, the source of this turbulence is believed to be shear-production of turbulent kinetic energy resulting from the strong current shear associated with the lower boundary condition. Turbulence for near-bottom mixing can be provided by other sources as well, e.g. by critical reflection of high-frequency internal waves (Thorpe et al. 1997), or the interaction of currents with rough topography elements (Rudnick et al. 2003). Here, we focus on the interaction of cross-slope stratification and an oscillating vertical near-bottom shear. Depending on the direction of the instantaneous cross-slope velocity, this configuration may lead to alternating periods with strong stable stratification and weak unstable stratification, where in the latter case a reversal of the vertical buoyancy flux

provides an additional source of near-bottom turbulence. Necessary for the occurrence of this effect are three circumstances: a sloping bathymetry, oscillating near-bottom velocities, and a stratified water body. In this process-oriented study, focusing on a small lake, oscillating near-bottom velocities are generated by low-frequency standing internal waves (internal seiches) generated by resonance with the temporally varying wind field. It was shown in former studies (Lorke et al. 2002, 2005) that the vertical shear associated with the upslope velocities due to such internal seiching may result in unstable stratification, creating a convective layer of several meter thickness that provides an extra source of turbulent kinetic energy for the BBL (Lorke et al. 2008). On the other hand, during times of downwelling, the vertical near-bottom shear was shown to increase vertical stratification in the BBL, leading to a suppression of turbulence.

Previous field investigations have provided valuable insight into the basic mechanisms of shear-induced convection but, due to their localized nature and technical limitations, some important questions regarding the basin-scale impact and the modification of BBL turbulence due to periodic stratification could not be resolved. Here, we employ a three-dimensional lake model in order to study these effects in greater detail, and to estimate the impact of BBL mixing on the overall mixing in a small lake.

METHODS

In order to study the process of shear-induced period stratification we employ a three-dimensional circulation model based on the shallow water equations (GETM, see Burchard and Bolding 2002) that has previously been shown to successfully reproduce the basin-scale internal wave pattern in other lakes (Umlauf and Lemmin, 2005). For the representation of the near-bottom processes investigated here, the main advantage of this model is the topography-following coordinate system, allowing for a sufficient vertical resolution of the turbulent BBL that would not be achievable with geopotential (i.e. z -level) coordinates. The complex effects of turbulent mixing were parameterized here by a second-moment turbulence closure model with prognostic equations for the TKE and the dissipation rate (see Umlauf et al. 2005, Umlauf and Lemmin, 2005). Our investigation focuses on a small Swiss lake, Lake Alpnach, an almost independent side-basin of Lake Lucerne with a length of about 5 km, a width of 1.5 km, and maximum depth of ca. 35 m (see Fig. 1).

Model setup

We used a uniform horizontal resolution of 20 m and 50 topography-following vertical layers. The vertical layer spacing was strongly zoomed into the near-bottom region, resulting in a minimum layer thickness of approximately 10 cm close to the bottom, which we found necessary to resolve the complex structure of the BBL. The lake was initialized with a realistic temperature profile, obtained from a field campaign in summer 2007 (see Fig. 1). Since our main goal here is a short-term process study of the BBL behaviour we used a highly idealized surface forcing. The model was forced by a homogenous sinusoidal wind field, directed along the main axis of the lake, with a period of 24 hours and a maximum wind stress of 0.02 Pa, of the order of the observed peak wind stresses during stable weather conditions in the summer.

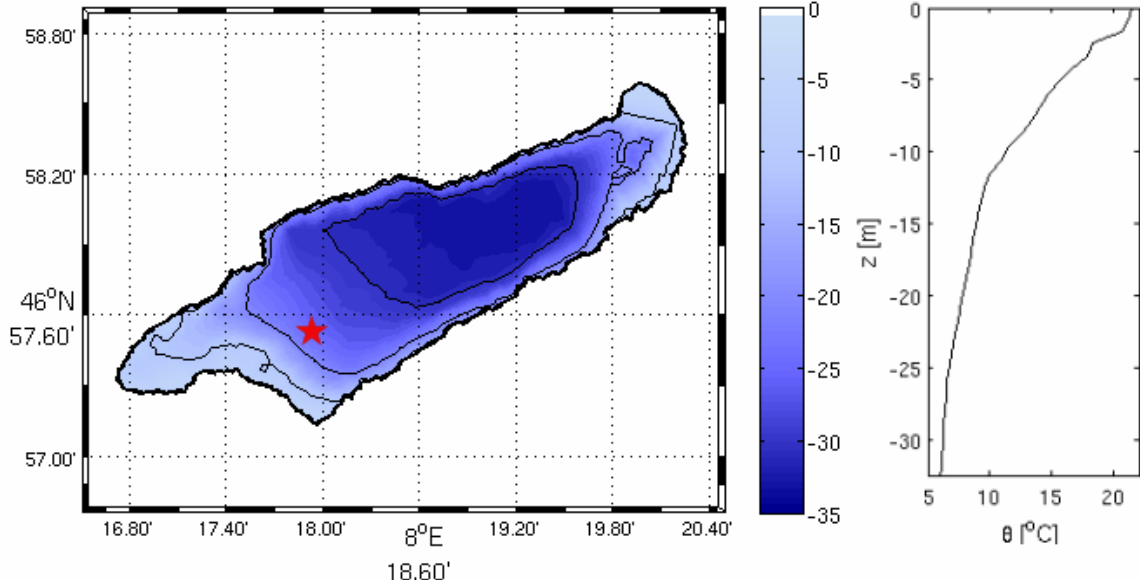


Figure 1. The left panel shows the bathymetry of Lake Alpnach, where the red star indicates the position of the slope station displayed in Fig. 3. The right panel shows the initial temperature-profile obtained from a measurement campaign in 2007.

Quantification of mixing

In order to investigate the contribution of BBL mixing to overall mixing it is necessary to define a sufficiently general measure for mixing, applicable also during periods of unstable stratification, where a quantification of mixing relying on the heat flux fails (due to a reversal of the direction of the heat flux). Our analysis will be based on the destruction of temperature variance, χ , which, by definition, is positive definite and well defined in both stable and unstable stratification. The balance of temperature variance is given by

$$\frac{\partial \langle \theta'^2 \rangle}{\partial t} + D^\theta = P^\theta - \chi,$$

where the local change and transport of temperature variance, D^θ , are balanced by production,

$$P^\theta = -2 \langle w' \theta' \rangle \frac{\partial \theta}{\partial z},$$

and molecular destruction,

$$\chi = D_m \left\langle \left(\frac{\partial \theta'}{\partial x_i} \right)^2 \right\rangle.$$

Here, D_m is the molecular diffusivity and θ the potential temperature. The primes indicate fluctuating quantities, and $\langle \dots \rangle$ the ensemble average. Consistent with the closure assumptions invoked in turbulence modelling (Umlauf et al. 2005) and the usual techniques used for the analysis of temperature microstructure profiles (Thorpe, 2005) we assume that the production and dissipation are in balance,

$$P^\theta = \chi.$$

RESULTS

Internal seiching

It has previously been shown by Munnich et al. (1992) that internal seiching in Lake Alpnach is somewhat special compared to most other lakes since the second vertical mode is often the dominant. This is due to the fact that the strong thermal winds, frequently observed under stable weather conditions in summer, create a clear 24 hour signal, which happens to be in approximate resonance with the natural period of the 2nd-vertical mode. The three-dimensional model results show that this internal seiche exhibits the typical characteristics of a Kelvin-wave (see Fig. 2) with the temperature crest moving counterclockwise and the current velocities directed parallel to the coast. The strong rotational effects are consistent with the observation that the internal Rossby radius is comparable to the size of the basin, a fact that has previously been ignored (Munnich et al. 1992).

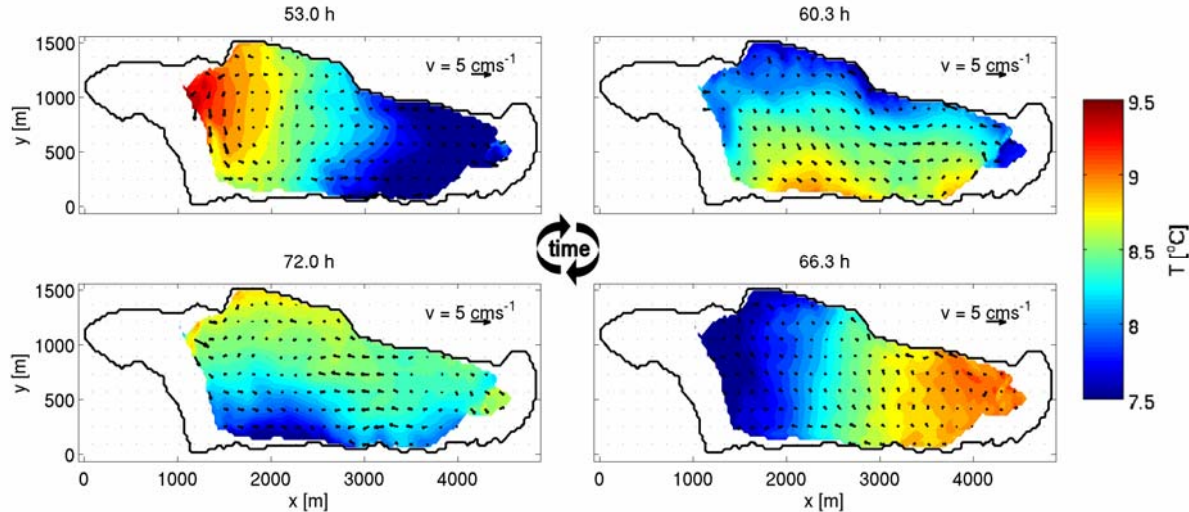


Figure 2. Horizontal transect through Lake Alpnach at a depth of 20 m at different times. The colour-scale indicates the temperature and the arrows the velocity field. The four frames show different snapshots during the internal seiching period ($T=24$ h).

Mixing in the BBL

Fig. 3 illustrates the structure of the turbulent BBL during periods of up- and downwelling, respectively. The creation of stable and unstable stratification associated with the direction of the cross-slope currents can be clearly seen. Although the turbulent diffusivity for unstable stratification is about one order of magnitude higher than that during downwelling (stable stratification), almost no mixing of temperature variance in the unstably stratified layer is observed due to the comparably small inverse temperature gradient. Only in the entrainment layer, located above the instability, significant mixing is seen to occur. The flux Richardson number in the convective region is negative and reaches peak values around $R_f = -1$, indicating that buoyancy production substantially contributes to the budget of turbulent kinetic energy.

On the other hand, during periods of down-slope flow, a relatively strong stable temperature gradient is observed. The flux Richardson number is close to a value of about 0.2, indicating that mixing is highly efficient. Therefore, although the observed diffusivities are approximately one order of magnitude smaller than during unstable stratification, a much stronger mixing of temperature variance occurs in the interior of the BBL (Fig. 3).

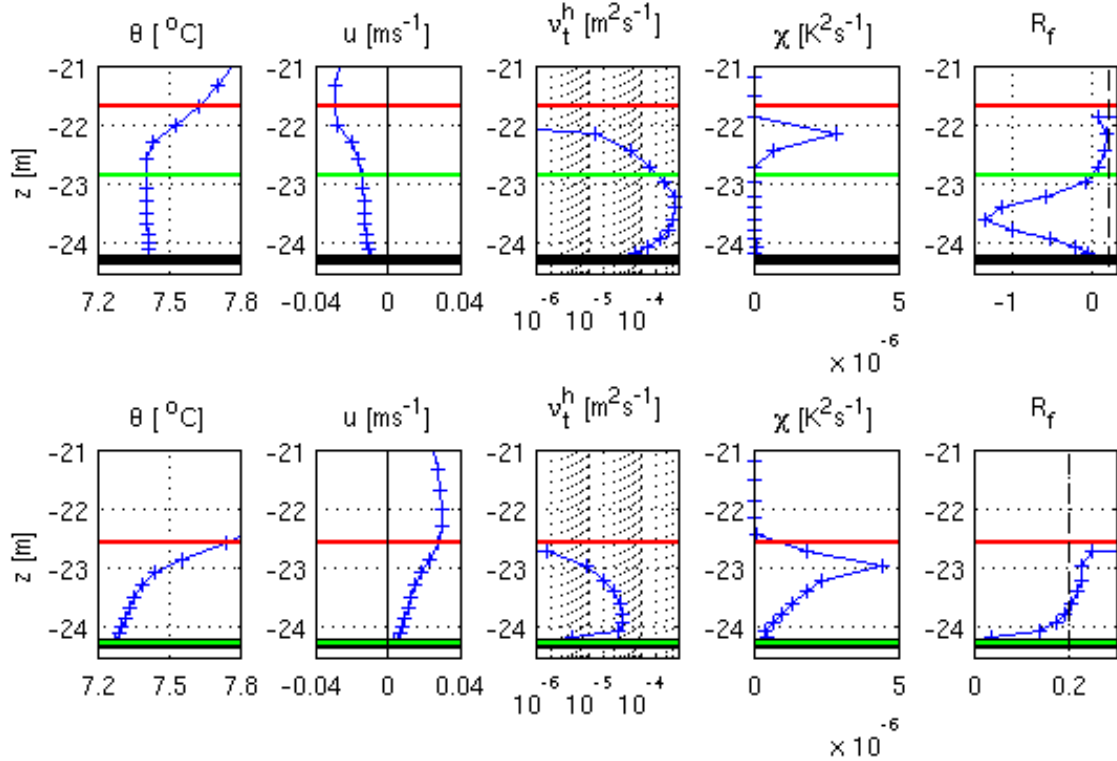


Figure 3. First row: Temperature, down-slope velocity, turbulent diffusivity, destruction rate of temperature variance, and flux Richardson number at $t=156$ hours (unstable stratification). Second row: The same, but now for $t=146$ hours (stable stratification). Shown are the first 3 m above the ground on the south-western slope of Lake Alpnach (see Fig. 1). The black line denotes the depth of the bottom, the green line the height of the convective layer, and the red line indicates the height of the bottom boundary layer, defined by a minimum threshold for the turbulent kinetic energy.

Basin-scale effect

The contribution of these effects to the basin-wide mixing is illustrated in Fig. 4. BBL-mixing is found to be the dominant part in overall diapycnal mixing in this lake, consistent with the analysis of the spreading of tracer cloud in this lake described by Goudsmit et al. (1997). The magnitude of boundary mixing is seen to oscillate with twice the seiching period, which is easily understood from the fact that periodically enhanced mixing occurs on *both* slopes of the elongated basin of Lake Alpnach. Interestingly, and consistent with the analysis discussed in the context of Fig. 3 above, mixing peaks occur during downwelling flow on the respective slopes, where the shear has a tendency to create stable stratification in the BBL, and thus increase the mixing efficiency. The contribution related to mixing in the unstable parts of the BBL is relatively small (Fig. 4), which leads us to the main conclusion of this paper: the major part of the basin-scale mixing is due to turbulence provided by bottom shear during periods of downwelling motion on the slopes, where the diffusivity is small compared to unstable periods but mixing is rather efficient.

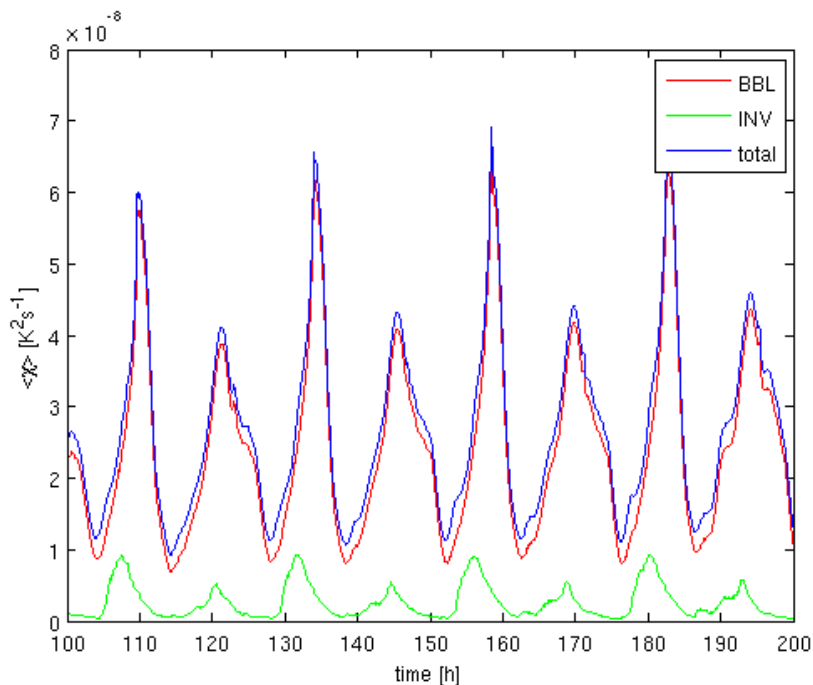


Figure 4. Dissipation of temperature variance in Lake Alpnach. The blue line indicates the average of χ for the volume below 10 m depth, i.e. excluding all contributions from direct surface wind mixing. The red line denotes the contribution of BBL-mixing, and the green line is the part associated with convection caused by BBL-instabilities.

REFERENCES

- Burchard, H., Bolding, K., 2002, GETM – a general estuarine transport model. Scientific documentation. Technical Report EUR 20253 EN, European Commission
- Gloor, M., Wüest, A. and Münnich, M., 1994, Benthic boundary mixing and resusension induced by internal seiches , *Hydrobiologia* 284, 59-68, 1994
- Goudsmit, G.-H., F. Peeters, M. Gloor, and A. Wüest, 1997, Boundary versus diapycnal mixing in stratified natural waters. *J. Geophys. Res.* 102: 27903-27914.
- Lewell, J.R., and B. M. Hickey, 1995, Evidence for enhanced boundary mixing in the Santa Monica Basin. *J. Geophysical Res.* 100: 20655-20679.
- Lorke, A., L. Umlauf, T. Jonas, and A. Wüest, 2002. Dynamics of Turbulence in Low-Speed Oscillating Bottom-Boundary Layers of Stratified Basins. *Environmental Fluid Mechanics* 2: 291-313
- Lorke, A., F. Peeters, and A. Wüest, 2005, Shear-induced convective mixing in bottom boundary layers on slopes. *Limnol. Oceanogr.* 50(5), 1612-1619
- Lorke, A., L. Umlauf, and V. Mohrholz, 2008, Stratification and mixing on sloping boundaries. *Geophys. Res.*, 35
- Münnich, M., Wüest, A. and Imboden, D., 1992, Observation of second vertical mode of the internal seiche in an alpine lake, *Limnol. Oceanogr.* 37, 1705-1719
- Rudnick, D. L. and others. 2003. From tides to mixing along the Hawaiian Ridge. *Science* 301: 355-357
- Thorpe, S. A., 1997. On the interaction of internal waves reflecting from slopes. *J. Phys. Oceanogr.* 27: 2072-2078.
- Thorpe, S. A., 2005. The Turbulent Ocean. Cambridge University Press, Cambridge, UK.
- Umlauf, L. and Burchard, H. (2005), Second-order turbulence closure model for geophysical boundary layers. A review of recent work, *Continental Shelf Research*, 25 (2005), 795-827
- Umlauf, L., and U. Lemmin. Inter-basin exchange and mixing in a large lake. The role of long internal waves. *Limnol. Oceanogr.*, 50(5), 1601-1611, 2005.
- Wüest, A., G. Piepke, and D.C. Van Senden, 2000. Turbulent kinetic energy balance as a tool for estimating vertical diffusivity in wind-forced stratified water. *Limnol. Oceanogr.* 45: 1388-1400.

An improved numerical solver of the 2D diffusive shallow waters equations over unstructured triangular meshes

C. Aricò*, C. Nasello, M. Sinagra, T. Tucciarelli

Dipartimento di Ingegneria Idraulica ed Applicazioni Ambientali, Università di Palermo, Viale delle Scienze,
90128 Palermo, ITALY

*Corresponding author, e-mail arico@idra.unipa.it

ABSTRACT

A preliminary version of a fast methodology for the solution of the diffusive form of the 2D shallow water equations over irregular domain is presented. The spatial domain is discretized with unstructured triangular meshes. The algorithm is based on a fractional time step decomposition of the original problem in a convective prediction problem plus a diffusive correction problem. A semi-analytical procedure for the solution of the convective equations, defined inside the Marching in Space and Time (MAST) model framework, is developed. The diffusive step is solved according to a formulation that is shown to provide, in the final linear system, the same coefficients given by the lumping Mixed Hybrid Finite Element (LMHFE) method with an edge-centered finite volume formulation. The matrix of the system is sparse, symmetric, positive definite and for acute triangularization preserves the so-called M property. A specific technique is developed to preserve the same property also for obtuse triangles with a small reduction of the second order spatial accuracy.

KEYWORDS

Analytical solution, diffusive model, numerical methods, obtuse triangles, shallow waters, unstructured mesh.

INTRODUCTION

Many important environmental problems require the computation of steady and unsteady state hydrodynamic fields in heterogeneous and irregular domains, with numerical techniques based on discretization schemes preserving the local and the global mass balance. In the present paper we present a time-splitting methodology for the numerical solution of the shallow waters (SW) flow equations written in diffusive form and solved in a domain discretized with an irregular triangular network. The methodology is developed mainly for the real-time simulation of natural floods, but can be easily adapted to all the hydrodynamic problems where a velocity potential does exist.

In the time-splitting approach the governing Partial Differential Equations (PDEs) are split in a prediction system and a correction system. Using the MAST approach (Bascià and Tucciarelli, 2004; Aricò and Tucciarelli, 2007a, b; Aricò *et al.*, 2007) it is possible to obtain a convective prediction system, with only one eigenvalue and one eigenvector following the vertically averaged velocity direction in each x, y, t point. In the MAST approach the prediction problem is solved at each time step as the sequential solution of several Ordinary

Differential Equations (ODEs), defined in each computational cell as function of the local geometry and the previously computed potentials.

The remaining correction problem is diffusive and can be solved using any available numerical techniques for parabolic and elliptic problems. In the past decades, Finite Volumes (FV) and Finite Elements (FE) methods have been widely applied. Unlike FV first order and second order methods, in the FE approach the potential continuity is guaranteed across the elements, but velocity is calculated by differentiation of the potentials inside the elements. This implies that the discrete normal fluxes are discontinuous across inter-element boundaries and the local mass conservation is not warranted. One way to circumvent this problem is to proper exploit the local subdomains where the mass conservation property is satisfied. For example, in the Galerkin technique applied on 2D triangulation, the subdomains can be defined as the Voronoi (or Thiessen) polygons. Application of this approach in 3D is very complicated and provides a strong increment of the computational time. On the other hand, the Finite Volume (FV) approach is locally mass conservative because the subdomain where the mass balance is applied is the same mesh element. The Mixed Finite Element (MFE) methods provide and attractive framework for these types of problems: by simultaneously approximating the potential head and normal fluxes, the computed normal fluxes are continuous across inter-element edges and the local and global mass balance is automatically achieved. MFE methods have been extensively used for the solution of parabolic problem in many application fields (groundwater flow problems, petroleum reservoir problems, potential flow problems, ...), but in elliptic problems (i.e. steady state problems) the matrix of the system becomes ill-conditioned (Bergamaschi and Putti, 1999). An improved technique is represented by the Mixed Hybrid Finite Element (MHFE) method. The MHFE spatially discretizes the flow equations in a set of continuity equations across all the edges of the mesh, using the average potentials along these edges as unknowns and leads to final linear algebraic systems that are always symmetric and positive definite.

In the following, two major advances are introduced in the MAST formulation. The first one is the use of a semi-analytical solution of the solution of the ODEs in each computational cell. The semi-analytical solution allows to get in the prediction step a second order accuracy in time, but also to guarantee a very small error when very large time steps are used.

The second contribution is about the solution of the correction problem. This is solved by simply assuming the linearity of the potentials inside the elements and enforcing the mass balance in the computational cells, located in the middle of each edge. The proposed technique is shown to be equivalent to the recently proposed (Younes *et al.*, 2006) mass lumping edge-centred MHFE scheme. This procedure has been finally modified in order to maintain the good properties of the final algebraic system when obtuse triangle are included in the mesh.

SEMI-ANALYTICAL SOLUTION OF THE PREDICTION PROBLEM

The prediction momentum and continuity equations, in the context of the MAST approach, can be written as:

$$\frac{\partial p}{\partial t} + gh \left(\nabla_x H^k + \frac{n^2 p \sqrt{p^2 + q^2}}{h^{10/3}} \right) = 0 \quad (1), \quad \frac{\partial q}{\partial t} + gh \left(\nabla_y H^k + \frac{n^2 q \sqrt{p^2 + q^2}}{h^{10/3}} \right) = 0 \quad (2),$$

$$\frac{\partial h}{\partial t} + \frac{\partial p}{\partial x} + \frac{\partial q}{\partial y} = 0 \quad (3),$$

where $p = uh$, $q = vh$, u and v are the vertically averaged velocity components in the x and y directions, h is the water depth, g is the gravity acceleration, n is the Manning coefficient, $\nabla_{x(y)} H^k$ is the spatial gradient of the piezometric head in $x(y)$ direction, at time level t^k .

Call P_j^m the j^{th} node of triangle m and \vec{l}_j^m the edge vector following in counterclockwise direction. Call P^m the intersection of the three lines normal to each edge \vec{l}_j^m and passing through P_{jm}^m , the node opposite to \vec{l}_j^m (Figure 1). Assume the computational cells to be located in the middle of each side. Assuming a linear variation of the piezometric head inside the triangle, it is possible to compute the flux through each side \vec{l}_j^m as the sum of the fluxes trough the $P_{jp}^m - P_m$ and the $P_m - P_j^m$ intervals, named respectively $Fl_{j,jp}^m$ and $Fl_{j,jm}^m$. Because the line through cells i and im is orthogonal to the interval $P_{jp}^m - P_m$, the crossing flux $Fl_{j,jm}^m$ is proportional to the difference between the two potentials. It comes out that:

$$Fl_{j,jm}^m = -rc_{j,jm}^m h^{5/3} (H_{im} - H_i) \quad (4a), \quad rc_{j,jm}^m = -\frac{2d}{l_{jp}^m} T_{j,jm}^m \quad (4b),$$

$$T_m^k = \frac{n^{-1}}{\left((\nabla_x^m H^k)^2 + (\nabla_y^m H^k)^2 \right)^{1/4}} \quad (4c),$$

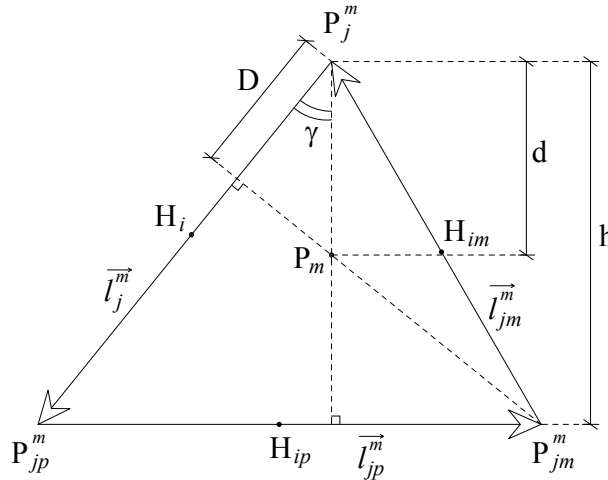


Figure 1. Triangular element scheme and notations.

where jm is the index of the node preceding j in counterclockwise direction, the scalar product in Eq. (4b) is between the edge vectors sharing node P_j^m , A^m is the area of triangle m , $H_{im(i)}$ is the piezometric heads in cell im (i), located in the middle of edge \vec{l}_{jm}^m (\vec{l}_j^m), n is the Manning coefficient and \bullet is the symbol of scalar product. The expression of coefficient $rc_{j,jm}^m$ in Eq. (4b) can be more easily computed as:

$$rc_{j,jm}^m = -\frac{2d}{l_{jp}^m} T_{j,jm}^m = -\frac{2D}{l_{jp}^m \cos \gamma} T_{j,jm}^m = -\frac{2Dl_j^m}{l_{jp}^m l_j^m \cos \gamma} T_{j,jm}^m = -\frac{2Dl_j^m}{l_{jp}^m h} T_{j,jm}^m = -\frac{\vec{l}_j^m \cdot \vec{l}_{jm}^m}{A^m} T_{j,jm}^m \quad (4d).$$

The computational domain can be spatially discretized as a 1D network of cells located at the middle point of each edge and linked by fictitious channels, with a flow discharge equal to the flux $F\ell_{j,jm}^m$ in Eq. (4a). The storage capacity is assumed to be concentrated only in the cells, in the measure of one third of the area of each triangle (one or two) sharing the edge of the cell. Observe that the coefficient $rc_{j,jm}^m$ in Eq. (4b) becomes positive if the triangle m is obtuse. In this case, the oriented fluxes given by Eq. (4a) inside the triangle m can form a loop. This is inconsistent with the irrotationality of the velocity field and hampers the sequential solution of the ordinary differential equations in each cell (see an example in Figure 2). To avoid this inconvenient, a special treatment of the obtuse triangles is required, as better described in section “*Adaptation to obtuse triangles*”.

Assuming cell i to be shared by elements m and n , the ODE in a given cell i becomes:

$$\sum_{p \neq j} rc_{j,p}^m h^{5/3} (H_i^k - H_{ip}^k) + \sum_{s \neq j} rc_{j,s}^n h^{5/3} (H_i^k - H_{is}^k) = A_i \frac{dH_i}{dt} \quad (5),$$

where j is assumed to be the local index corresponding to cell i in both triangles, ip and is are the index of the cells corresponding respectively to the local indices p and s in elements m and n , and A_i is the sum of 1/3 the area of each element. In Eq. (5) coefficients $r_{j,p}^m$ and $r_{j,s}^n$ are multiplied by a power of the water depth h , that we take as the value in the upstream node of each channel. Eq. (5) can be written as:

$$K_i^k h_i^{5/3} + A_i \frac{dH_i}{dt} = Ft_i \quad (6),$$

where

$$K_i^k = \sum_{u \neq j} \delta_{j,u}^{k,m} r c_{j,u}^m (H_{iu}^k - H_i^k) + \sum_{s \neq i} \delta_{j,s}^{k,n} r c_{j,s}^n (H_{is}^k - H_i^k) \quad (7a),$$

$$Ft_i^k = \sum_{u \neq j} (1 - \delta_{j,u}^{k,m}) r c_{j,u}^m (H_i^k - H_{iu}^k) + \sum_{s \neq j} (1 - \delta_{j,s}^{k,n}) r c_{j,s}^n (H_i^k - H_{is}^k) \quad (7b),$$

where $\delta_{j,p}^{k,m} = 1$ if $H_{ip}^k < H_i^k$, $\delta_{j,p}^{k,m} = 0$ otherwise.

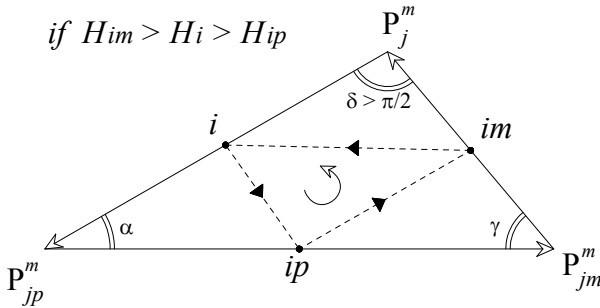


Figure 2. Example of obtuse triangle with oriented fluxes inconsistent with the velocity irrotationality.

A semi-analytical solution of Eq. (6) along each time step can be found by changing the time value of the entering flux with its mean value along the time step, that is:

$$K_i^k h_i^{5/3} + A_i \frac{dH_i}{dt} = \overline{Ft}_i^k \quad (8).$$

Define h_i^k the water depth at the beginning of the time step and h_i^{kf} its asymptotic value according to Eq. (8), that is:

$$h_i^{kf} = \left(\frac{\overline{Ft}_i^k}{K_i^k} \right)^{3/5} \quad (9).$$

Eq. (8) can be written in dimensionless form as:

$$\frac{d\xi}{d\tau} = 1 - \xi^{5/3} \quad (10a), \quad \xi = \frac{h_i}{h_i^{kf}} \quad (10b), \quad \tau = \frac{dt \overline{Ft}_i^k}{A_i h_i^{kf}} \quad (10c), \quad \text{if } h_i^{kf} > h_i^k$$

$$\frac{d\xi}{d\tau} = \xi_f^{5/3} - \xi^{5/3} \quad (11a), \quad \xi = \frac{h_i}{h_i^k} \quad (11b), \quad \tau = \frac{dt \overline{Ft}_i^k}{A_i h_i^k} \left(\frac{h_i^k}{h_i^{kf}} \right)^{5/3} \quad (11c), \quad \text{if } h_i^{kf} < h_i^k$$

Closed form solutions of Eqs. (10) and (11) do not exist, due to the non integer value of the power exponent in the right hand side of Eqs. (10a) and (11a). A series solution is possible, but a good approximation can also be found with a smaller computational time by setting:

$$\xi = \frac{\exp(c_1\tau) + c_2}{\exp(c_1\tau) + c_3} \quad (12a), \quad \text{if } h_i^{kf} > h_i^k, \quad \xi = 1 + (\xi_f - 1) \frac{\exp(c_1\tau) + c_2}{\exp(c_1\tau) + c_3} \quad (12b), \quad \text{if } h_i^{kf} < h_i^k,$$

with a proper choice of the c_1 , c_2 and c_3 coefficients. Using any c_3 value it is possible to match the initial value ξ_0 and its first derivative ξ'_0 by setting:

$$c_2 = \xi_0 (1 + c_3) - 1 \quad (13a), \quad c_1 = \xi'_0 \frac{(1 + c_3)^2}{(c_3 - c_2)} \quad (13b), \quad \text{if } h_i^{kf} > h_i^k$$

$$c_2 = \frac{(\xi_0 - 1)(1 + c_3)}{(\xi_f - 1)} - 1 \quad (14a), \quad c_1 = \xi'_0 \frac{(1 + c_3)^2}{(c_3 - c_2)} \frac{1}{(\xi_f - 1)} \quad (14b), \quad \text{if } h_i^{kf} < h_i^k$$

The first derivative ξ'_0 can be computed as the r.h.s. of Eqs. (10a) and (11a), for $\xi = \xi_0$. This choice guarantees a second order reduction of the error around the $\tau = 0$ value. Because the time step, in the MAST approach, is not restricted by the Courant condition, it is also important to select a c_3 coefficient that provides a small error for any possible τ value.

The numerical minimization of the maximum ξ error for any possible positive τ value leads, in the two cases $h_i^{kf} > h_i^k$ and $h_i^{kf} < h_i^k$ to the $c_3(\xi_0)$ and $c_3(\xi_f)$ functions shown in Table 1 and in Figure 3.

Table 1. c_3 coefficient that provides the smallest error for any possible τ value.

ξ	$h_i^{kf} > h_i^k$		$h_i^{kf} < h_i^k$	
	c_3	c_3	c_3	c_3
0.0	0.746910	-0.817120		
0.1	0.579450	-0.605480		
0.2	0.460290	-0.473940		
0.3	0.366280	-0.374090		
0.4	0.288870	-0.293430		
0.5	0.223400	-0.226030		
0.6	0.166990	-0.168420		
0.7	0.117660	-0.118360		
0.8	0.074026	-0.074301		
0.9	0.035066	-0.035129		

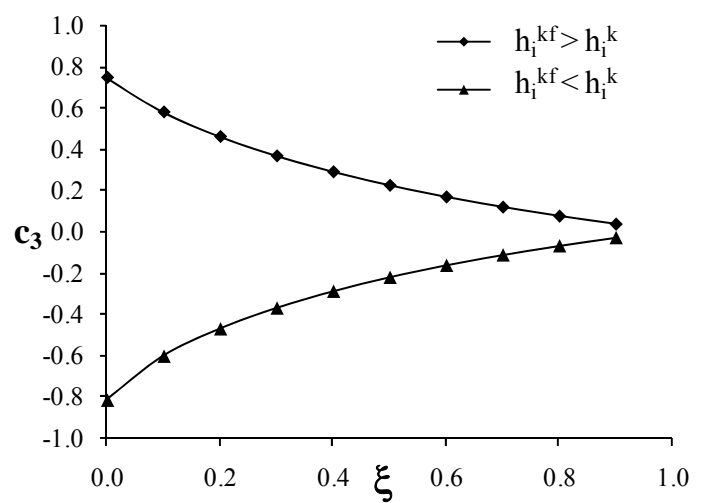


Figure 3. Function c_3

See in figg. 4a and 4b the finite difference solution of Eqs. (10a) and (11a) in the case of respectively $\xi_0 = 0$ and $\xi_f = 0$, compared with the semi-analytical solutions (12a) and (12b) corresponding to the optimal c_3 values (respectively 0.7469 and -0.8171). The maximum error computed with the initial conditions $\xi_0 = 0$, for $h_i^{kf} > h_i^k$, or $\xi_f = 0$, for $h_i^{kf} < h_i^k$, is the worse one and it is smaller than 10^{-3} . See also, in the same figure, the semi-analytical solutions corresponding to $c_3 = 0$ and $c_3 = 1$. These two solutions are equivalent to the analytical closed form solution of equations (10a) and (11a) when the power exponent is approximated respectively to 1 or 2.

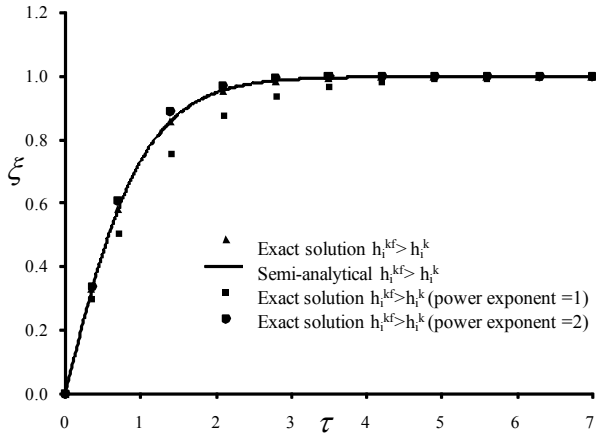


Figure 4a. Comparison of the solution obtained by the semi-analytical method and the exact solution (case $\xi_0 = 0$).

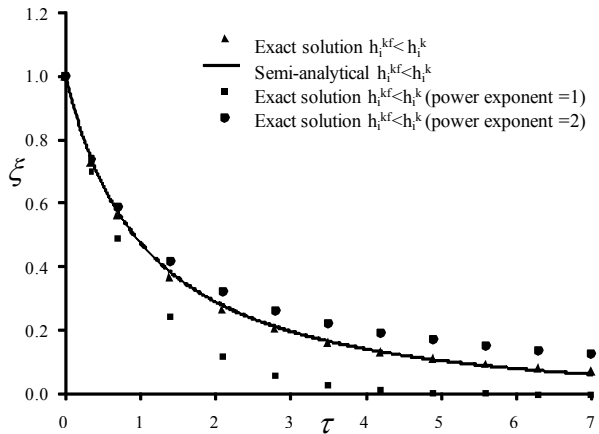


Figure 4b. Comparison of the solution obtained by the semi-analytical method and the exact solution (case $\xi_f = 0$).

SOLUTION OF THE CORRECTION PROBLEM

In the contest of MAST approach, the algebraic system of the correction problem can be written in the form:

$$\begin{aligned} & \sum_{u \neq j} r d_{j,u}^m \left(h_{i,iu}^{k+1/2} \right)^{5/3} \left(\eta_i^{k+1} - \eta_{iu}^{k+1} \right) + \sum_{s \neq j} r d_{j,s}^n \left(h_{i,is}^{k+1/2} \right)^{5/3} \left(\eta_i^{k+1} - \eta_{is}^{k+1} \right) \\ &= \sum_{u \neq j} r d_{j,u}^m \left(h_{i,iu}^{k+1/2} \right)^{5/3} \left[\left(H_i^{k+1/2} - H_{iu}^{k+1/2} \right) - \left(H_i^k - H_{iu}^k \right) \right] + \quad i = I, \dots, N \quad (15), \\ & \sum_{s \neq j} r d_{j,s}^n \left(h_{i,is}^{k+1/2} \right)^{5/3} \left[\left(H_i^{k+1/2} - H_{is}^{k+1/2} \right) - \left(H_i^k - H_{is}^k \right) \right] + A_i \frac{d\eta_i^k}{dt} \end{aligned}$$

where N is the cell number, $r d_{j,u}^m = r c_{j,u}^m h_{i,iu}^{5/3}$, $\eta_i^{k+1} = H_i^{k+1} - H_i^{k+1/2}$, $\eta(0) = 0$ and

$$h_{i,iu}^{k+1/2} = \frac{h_i^{k+1/2} + h_{iu}^{k+1/2}}{2} \quad (16).$$

Boundary conditions are zero corrective flux passing through the upstream cells where entering fluxes are assigned in the prediction step. In the downstream cell i , where the piezometric head is constant and known, the assigned correction is:

$$\eta_i^{k+1} = H_i^k - H_i^{k+1/2} \quad (17).$$

System (15) is solved by applying a preconditioned conjugate gradient method. After simple manipulations, it is easy to show that, if the water depth is constant inside the triangles, the

coefficients of system (15) are the same provided by the lumping MHFE with an edge-centred finite volume formulation (see for example Younes *et al.*, 2006). This procedure produces a M-matrix (a non-singular matrix where the diagonal terms are always positive and the off-diagonal terms are negative or null) for acute triangulation; the M-property guarantees that local maxima or minima not appear in the solution in a domain without sinks or sources (Younes *et al.*, 2006). In presence of obtuse triangles in the computational mesh, the M-property is not guaranteed and the system matrix is no more positive definite. The procedure described in the following subsection is developed to maintain the M-property also in presence of obtuse triangles, with a small reduction of the second order spatial accuracy.

Adaptation to obtuse triangles

Assume j to be the vertex of the obtuse triangle m corresponding to the maximum angle, jp and jm respectively the following and the preceding one in counterclockwise direction. Call i , ip and im the index of the corresponding cells. Define two auxiliary internal sides $\overrightarrow{l_{j_1}^m}$ and $\overrightarrow{l_{jm}^m}$, respectively orthogonal to sides $\overrightarrow{l_j^m}$ and $\overrightarrow{l_{jm}^m}$ sharing vertex j (see figure 5). In the case shown in figure 5, the coefficient $rc_{j,jm}^m$ is positive, while the other two coefficients are negative. Assume $rc_{j,jm}^m = 0$, so that the fluxes through the edges $\overrightarrow{l_j^m}$ and $\overrightarrow{l_{jm}^m}$ are proportional only to the difference $(H_i - H_{ip})$ and $(H_{im} - H_{ip})$ respectively. The fluxes Fl_{j,jp_1}^m and Fl_{j,jm_1}^m through sides $\overrightarrow{l_{j_1}^m}$ and $\overrightarrow{l_{jm}^m}$ are given by:

$$Fl_{j,jp_1}^m = -r'_{j,jp_1} (H_i - H_{ip}), \quad r'_{j,jp_1} = \frac{2l_{j,jp_1}^m}{l_{jm}^m} T_m^k h^{5/3} \quad (18a),$$

$$Fl_{j,jm_1}^m = -r'_{j,jm_1} (H_{ip} - H_{im}), \quad r'_{j,jm_1} = \frac{2l_{j,jm_1}^m}{l_j^m} T_m^k h^{5/3} \quad (18b).$$

On the other hand, since a linear variation of the piezometric heads has been assumed inside each triangle m , flow velocity is constant along all side $\overrightarrow{l_j^m}$. For instance, assume the flow velocity direction shown in figure 5, call P_{np}^m the intersection point between the velocity vector drawn from point jp_1 and side $\overrightarrow{l_j^m}$, l_j^m the distance of P_{np}^m from P_j^m and l_{np}^m the distance of P_{np}^m from P_j^m measured in counterclockwise direction. Position of point P_{np}^m depends on the direction of the element velocity and is updated after each time step. Flux through side $\overrightarrow{l_{j,np}^m}$ (between points P_j^m and P_{np}^m) is equal to Fl_{j,jp_1}^m . Because velocity is constant along the all side $\overrightarrow{l_j^m}$, the total flux Fl_j^m can be computed as:

$$Fl_j^m = Fl_{j,jp_1}^m \frac{l_j^m}{l_{j,np}^m} = -(H_i - H_{ip}) \frac{2l_{j,jp_1}^m}{l_{jm}^m} T_m^k h^{5/3} \frac{l_j^m}{l_{j,np}^m} = -r''_{j,jp_1} (H_i - H_{ip}) \quad (19a),$$

$$\text{where } r''_{j,jp_1} = r'_{j,jp_1} \frac{l_j^m}{l_{j,np}^m} \quad (19b).$$

Coefficient r''_{j,jp_1} tends to infinity as point P_{np}^m approaches node j and takes a positive value if the velocity direction is between the directions of $\overrightarrow{l_j^m}$ and $\overrightarrow{l_{jp_1}^m}$. In this case, a flux estimation error (and a corresponding reduction of the solution accuracy) is unavoidable if a mesh with

constant geometry is adopted. To guarantee the computational efficiency and the $r''_{j,np}$ negativity, the following approximation is made:

$$l_{j,np}^m \approx \max(\varepsilon, |l_{j,np}^m|) \quad (19c),$$

where the two arguments of the max function are a small positive number and the absolute value of the $l_{j,np}^m$ distance.

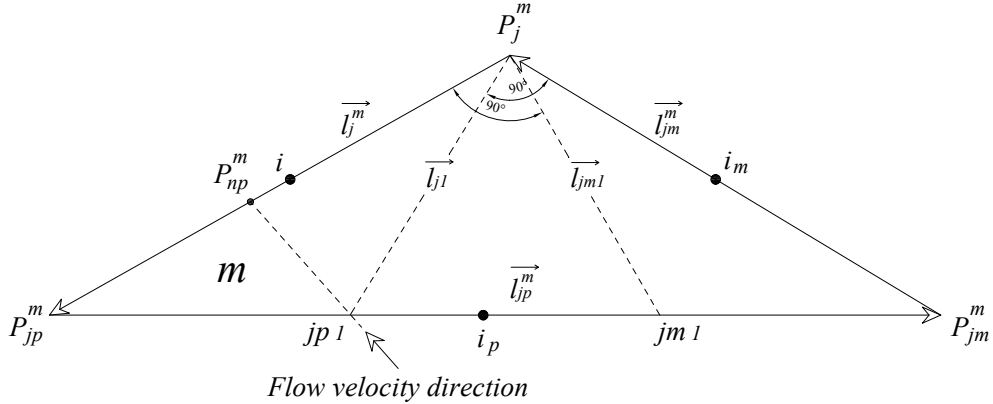


Figure 5. Triangular element scheme and notations for obtuse triangle.

NUMERICAL TESTS

A 10 m x 10 m domain has been assumed with the computational mesh shown in figure 6. The Manning n coefficient is 0.025 s/m^{1/3} and dry conditions are initially assumed in the domain. Four different cases have been considered by changing the slope of the domain. In each case the maximum slope is 0.01, but the gradient direction follows in each case a different diagonal orientation. Neumann and Dirichlet boundary conditions respectively on the two connected upstream and downstream sides, according to the direction of the bottom slope, have been given. The Dirichlet water depth is $h = 0.25$ m and a unitary Neumann boundary flux equal to the uniform flow conditions corresponding to the Dirichlet value is distributed along the two upstream sides. After transient conditions, a uniform water depth value should be reached in all the domain, equal to the Dirichlet value. This value is exactly attained using any acute triangulation of the domain.

In figure 6 the transient conditions for three simulation times are shown for flux injection from the upper left corner of the square. In figure 7 the errors of the computed asymptotic water depths, with respect to the exact values, are shown. The errors are measured as the difference of the computed value and the uniform flow one in each cell. In all the investigated tests, higher errors occur approximately near the incoming flux boundaries and next to the obtuse triangles (pointed out in the figures). During the transient flow small time oscillations occur near obtuse triangles; in stationary conditions, the relative error with respect to the exact solution is always smaller than 0.1%.

CONCLUSIONS

Two advances of the MAST formulation, previously proposed, have been introduced with the present paper. The first one is the use of a semi-analytical solution of the ODEs defined in each computational cell in the prediction step. The second one is the solution of the correction problem through the recently proposed mass lumping edge-centred MHFE scheme, here

formulated by means of simple geometrical assumptions. The proposed procedure has been modified in order to maintain the good properties of the final algebraic system when obtuse triangle are included in the mesh. The result of preliminary tests is very encouraging for extensions to cases with strongly heterogeneity of geomorphologic parameters and real-time applications.

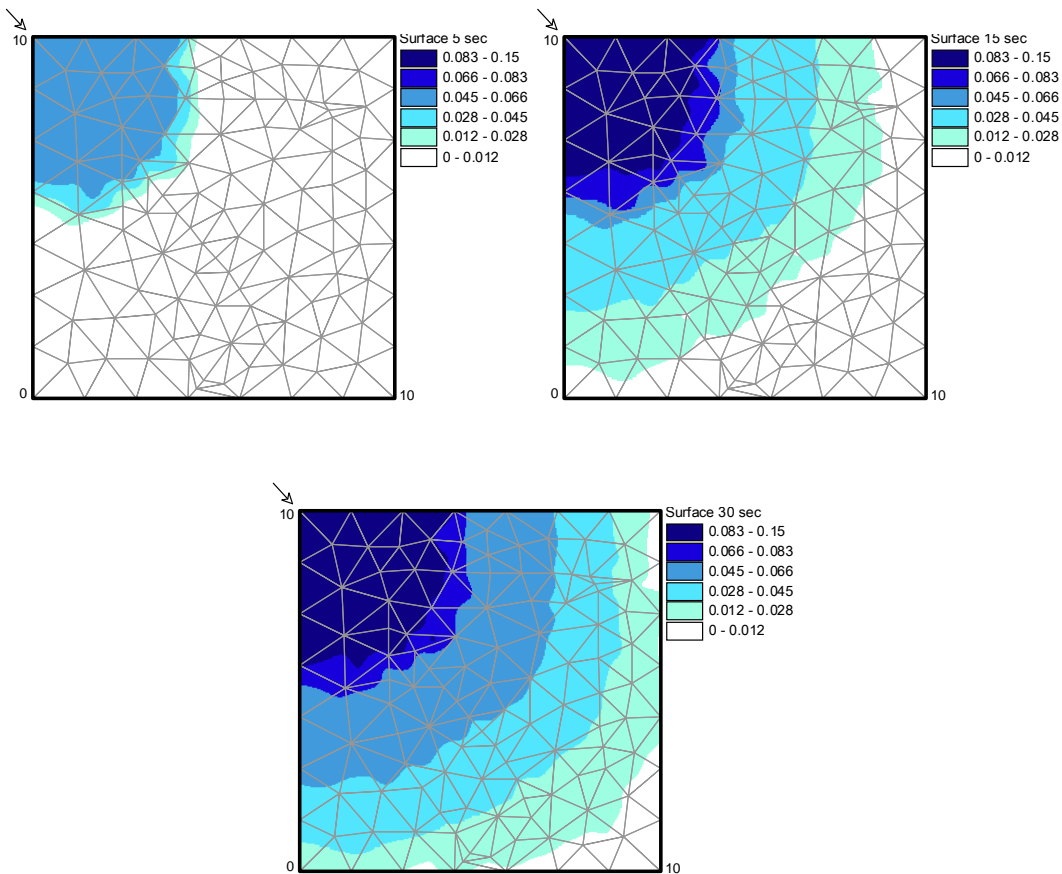


Figure 6. Transient conditions. Computed water depth at 5, 15 and 30 s.

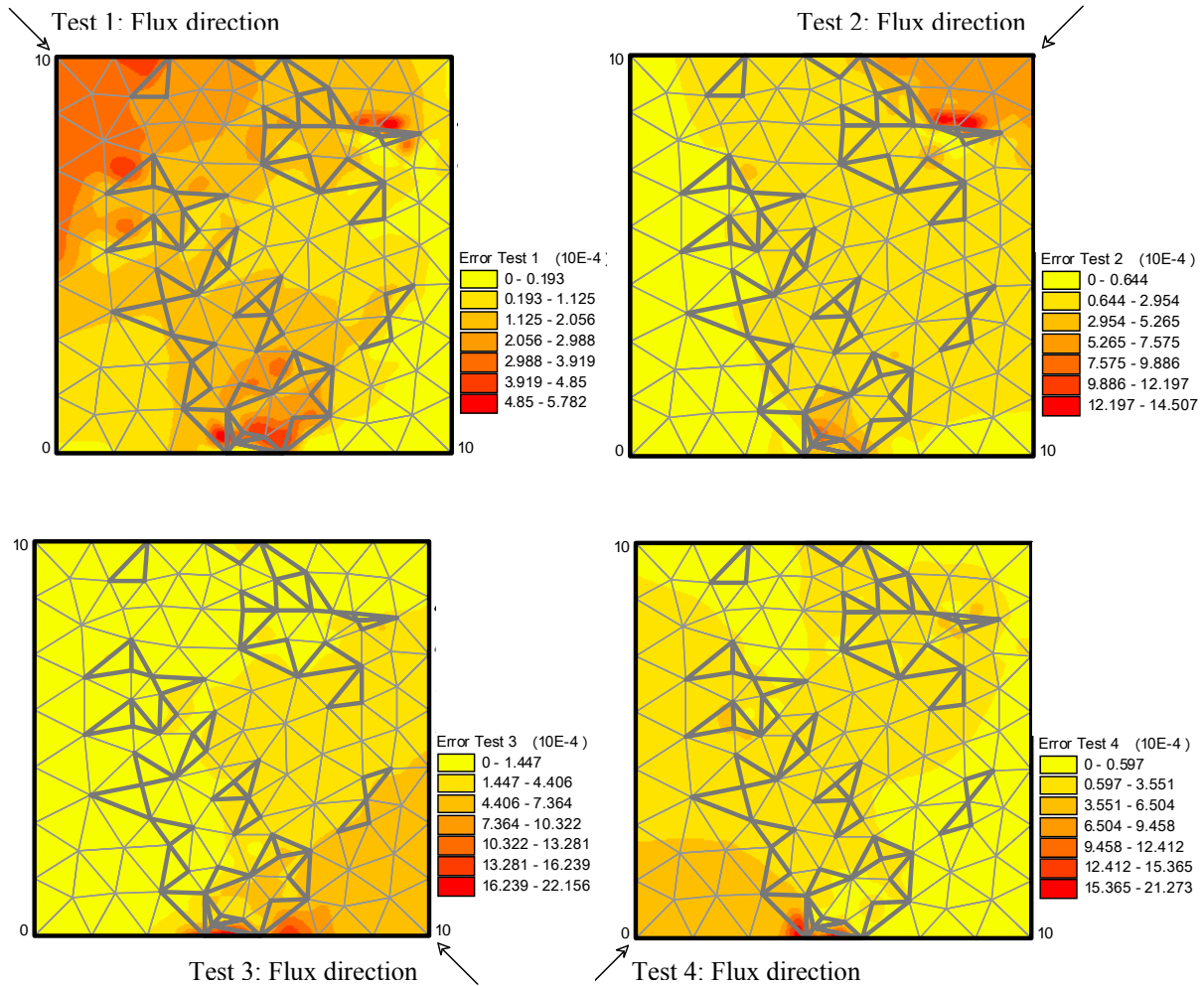


Figure 7. Steady-state conditions. Errors of the numerical solution respect to the exact one.

REFERENCES

- Aricò C. and Tucciarelli T. (2007). MAST solution of advection problems in irrotational flow fields, *Adv. Wat. Res.*, **30**(3), 665-685.
- Aricò C. and Tucciarelli T. (2007). A Marching in space and time (MAST) solver of the shallow water equations. Part I: The 1D case. *Adv. Wat. Res.*, **30**(5), 1236-1252.
- Aricò C., Nasello C. and Tucciarelli T. (2007). A Marching in space and time (MAST) solver of the shallow water equations. Part II: The 2D case, *Adv. Wat. Res.*, **30**(5), 1253-1271.
- Bascià A. and Tucciarelli T. (2004). An explicit unconditionally stable numerical solution of the advection problem in irrotational flow fields, *Wat. Res. Res.*, **40**(6), W06501, 2004.
- Bergamaschi L. and Putti M. (1999). Mixed Finite Elements and Newton-type linearizations for the solution of Richard's equation, *Int. J. Num. Met. Eng.*, **45**, 1025-1046.
- Younes A., Ackerer P. and Lehmann F. (2006). A New Mass Lumping for the Mixed Hybrid Finite Element Method, *Int. J. Num. Met. Eng.* **67**, 89-107.

Hydrodynamic and Hydraulic Modeling of the Huron-Erie Corridor

David J. Schwab^{1*}, Eric J. Anderson¹, Gregory A. Lang¹

¹ NOAA Great Lakes Environmental Research Laboratory
4840 South State Road - Ann Arbor, MI 48108, USA

* corresponding author: David.Schwab@noaa.gov

ABSTRACT

The Huron-Erie Corridor (HEC) serves as a major waterway in the Great Lakes and is the connecting channel between Lake Huron and Lake Erie. The system consists of the St. Clair River, Lake St. Clair, and the Detroit River, and serves as a recreational waterway, source of drinking water for Detroit, MI and surrounding cities, as well as the only shipping channel from the ocean and the lower lakes to Lakes Huron, Michigan and Superior. Typical stage difference from Lake Huron to Lake Erie is 1.5 m along the 150 km corridor. Typical mean transport through the river system is 5000 cubic meters per second. A three-dimensional unstructured hydrodynamic model (FVCOM) has been applied to the HEC to provide operational nowcasts and forecasts of physical conditions as well as hindcasts for scenario testing and contaminant tracking in the system. Nowcasts are performed eight times per day and 48-hour forecasts are performed two times per day. Comparisons between model simulations and observed values show average differences of 3 cm for water levels and 12 cm/s for along-channel currents in the St. Clair River (compared to mean current values of 1.7 m/s). In addition, hindcasts of conditions using 1985 meteorology are compared with current observations at twelve mooring stations in Lake St. Clair. In general, the uncertainty in computed currents in the lake is much greater than in the rivers simply because of the associated uncertainty in boundary conditions. In the western and central regions of the lake, currents compare well with observations in both mean and time-variable flow (normalized Fourier norms range between 0.18 and 0.75). Currents in the eastern part of the lake are an order of magnitude smaller and yield higher uncertainty between computed and observed values (normalized Fourier norms range between 0.83 and 1.13).

Temporal evolution and spatial heterogeneity of ecosystem parameters in a subtropical lake

I. Ostrovsky* and Y. Z. Yacobi

Israel Oceanographic & Limnological Research Ltd. Yigal Allon Kinneret Limnological Laboratory P.O. Box 447, Migdal 14950, Israel

*Corresponding author, e-mail ostrovsky@ocean.org.il

ABSTRACT

Biological production in the warm, monomictic, Lake Kinneret (Israel) strongly depends on allochthonous and autochthonous nutrient supply. Localization of areas where nutrient supply (e.g. phosphorous) is higher may be visualized using the distribution of chlorophyll *a* (CHL) as a tracer and also be explored by carbon uptake potential (CUP) measured at standardized light and temperature conditions. Spatial variability of these parameters was studied at several stations over an annual cycle. In winter and spring the maximal algal biomass occurs near the entrance of the main tributary, Jordan River and follows the dispersion of riverine water in the lake. The massive allochthonous nutrient (phosphorous and nitrogen) load from Jordan River resulted in the highest values of CHL (proxy of algal biomass) and CUP in the inlet area. In summer-autumn higher concentrations of CHL occurred at the lake periphery, where seiche-induced boundary mixing enhanced the upward transport of dissolved nutrients through the thermocline to the euphotic zone. Rapid deepening of the thermocline in the autumn created proper conditions for a massive phosphorous supply from the peripheral phosphorous-rich sediments directly to the upper productive layer and thus caused distinguishable heterogeneity in CUP. Our study indicates that analysis of the spatial variation of primary productivity and algal abundance may be a useful tool to study processes of nutrient load and their localization.

KEYWORDS

Spatial heterogeneity; seasonal variability; nutrient supply; chlorophyll; primary productivity; resuspension; seiching; Lake Kinneret; Jordan River; FluoroProbe.

INTRODUCTION

Spatial variability in aquatic ecosystems is caused by physical (upwelling, fronts, seiches, turbulence, inflows, etc.), chemical (e.g. unequal nutrient loads), and biological processes (grazing, migration, etc.) and their interactions (Kalikhman *et al.*, 1995; Metaxas and Scheibling, 1996; Knauer *et al.*, 2000; Wuest and Lorke, 2003; Kratz *et al.*, 2005; Reynolds, 2006). In eutrophic lakes, where primary productivity is controlled by nutrient availability (bottom-up regulation), factors affecting nutrient loads may induce temporal and spatial variability of algal abundance. In stratified aquatic ecosystems, measurements of limiting nutrient concentrations in the upper productive layer are often problematic. Episodic supply of new nutrients across a strong thermocline fuels the new production by the growth of phytoplankton species (Goldman, 1988). It is usually minute and cannot be measured by standard analytical methods. In lakes, such injections (diapycnal transport) take place predominantly at the marginal zones near the sloped bottom (Ostrovsky *et al.*, 1996, MacIntyre *et al.*, 1999), but rapid uptake of dissolved nutrients makes direct detection of the

small, but persistent, upward fluxes a difficult task. On the other hand, analysis of spatial distribution of primary producers at specific seasons may pinpoint the locations where nutrient enrichment was most extensive, and thus be used as a proxy for nutrient enrichment pattern.

The relative importance of various sources and mechanisms controlling nutrient supply (load from watershed basin, diffusion from the bottom, diapycnal mixing, destratification, etc.) for the generation of spatial heterogeneity in lake productivity is an important subject of modern limnology. In stratified lakes boundary processes can generate intense turbulent mixing, resuspension (Imboden and Wuest, 1995; Ostrovsky and Yacobi, 1999, Wuest *et al.*, 2000; Lorke *et al.*, 2005) and upward fluxes of nutrients (Ostrovsky *et al.*, 1996; MacIntyre *et al.*, 1999). Presently the role of various phenomena in formation of spatial variability of chemical fluxes is poorly understood. It seems that finding the relationships between localized enhancement of biological productivity and physical processes may elucidate the relative role of those processes/factors in development of spatial heterogeneity in nutrient load. One of the most promising outcomes of the analysis of spatial variability is the “visualization” of mechanisms that control lake eutrophication and determine local importance of internal vs. external loading of nutrients.

In this paper we investigated processes that may be responsible for spatial variability of phosphorous (limiting nutrient) supply during various seasons in the subtropical Lake Kinneret (Israel). We hypothesized that the distribution schemes of primary producers correspond to spatial variability of the limiting nutrient load. This led us to study the correspondence of the observed seasonal patterns of spatial variability of primary productivity (measured at standardized light and temperature conditions) and chlorophyll *a* (CHL) concentration to the foreseen schemes of phosphorous supply.

STUDY SITE: LAKE KINNERET

Lake Kinneret is a subtropical monomictic lake. It is 22 km long and 12 km at maximum width. The main water inflow (60 – 70% of the total) is the River Jordan, which enters at the northern part of the lake. The Jordan River is the main source of allochthonous nutrients to the lake. Nutrient contents (SRP, NH₄, NO₃, etc.) strongly correlate with total suspended load in river water (Avnimelech, 1980). The most intensive water discharge occurs during January-April. At the early beginning of the flood, the large proportion of the cold river water flows just above the bottom. In late winter and spring the river flows into the upper part of the lake and mixes with the lake water. In the lake the general counterclockwise circulation diverges the incoming water toward the western shore (Serruya, 1974) and the solid load then transported along the western part of the lake (Serruya *et al.*, 1974).

Lake Kinneret is steadily stratified from April-May till the beginning of winter, with surface temperatures approaching 30°C. Anoxic conditions develop in the hypolimnion in early summer. During summer months, the almost daily stress of the westerly wind applied to the lake surface induces large basin-scale internal seiches (Antenucci, 2000). Isotherm displacements approach up to 10 m at the lake periphery (Serruya, 1975). In summer and early autumn, the average position of the thermocline is most steady. In the epilimnion the concentration of soluble inorganic nitrogenous ions (NO₃+NH₄) is mostly <0.050 mg L⁻¹, and that of SRP is commonly <0.002 mg L⁻¹, (Serruya 1978; Berman *et al.*, 1995). At the end of the stratification period, the concentrations of dissolved phosphorous (mainly SRP) and nitrogen (mainly NH₄) in the hypolimnion are at least order of magnitudes higher than those in the epilimnion. SRP is preferentially accumulated within the turbulent BBL below 30-m depth, while its concentration above 30-m isobath is close to detection limits (Nishri *et al.*, 2000). The anoxic bottom in the lake center is the most important source of SRP, and turns into an effective source of that nutrient when the deepening thermocline crosses the water

layers which are >30m. With the temperature decrease in the autumn the thermocline deeps. The eradication of thermal stratification is accompanied by an increase of the concentration of major nutrients in the upper part of the lake, as the result of mixing epilimnetic and nutrient-rich hypolimnetic waters. The stratification is destroyed completely in and homothermy lasts from December-February until February-March. Internal load of nutrients supposed to play a key role in the total nutrient supply (Smith *et al.*, 1989; Markel *et al.*, 1994).

The algal biomass and CHL are usually minimal between August to December, and in January initiate to increase following thermal destratification and holomixis. When the lake fully destratified (January-February) inorganic phosphorous and nitrogen concentrations are the highest in the euphotic zone, the biomass of algae rapidly begins to rise, and in March-May it reaches its maximum. The large dinoflagellate *Peridinium guatunense* was the dominant species during the spring bloom between 1968 and 1995. From 1996 it was often substituted by other species, that resulted in a prominent reduction of the spring biomass but not in primary productivity (Yacobi, 2006).

MATERIALS AND METHODS

Algal abundance (chlorophyll concentration, CHL) and potential primary productivity (carbon uptake potential, CUP) were measured in samples collected at seven stations in Lake Kinneret, Israel (Fig 1A). In the deeper pelagic and sublittoral stations (A, D, G, and K) the samples were a composite of water collected from the uppermost 8 m, at 1-m intervals with a 5 L sampler. In three littoral stations (LN, LW, and LS) water was collected by a hose-sampler that sampled the entire 3-m water column. The water samples were withdrawn using dark bottles and brought to the lab within 2h. In the laboratory, CHL was estimated fluorometrically on duplicated 25-ml sub-samples filtered onto GF/C filters, and extracted in 90% acetone (Holm-Hansen *et al.*, 1965). Another set of duplicate sub-samples (50 ml) was collected in clear polycarbonate bottles for the determination of carbon uptake. Those sub-samples were incubated for 2h at 23 °C under light flux of approximately $80 \mu\text{Einst m}^{-2} \text{s}^{-1}$. Carbon uptake was measured with a modified ^{14}C uptake technique (Steeman-Nielsen, 1952). A spike of about 10 μCi of $[^{14}\text{C}]$ -bicarbonate was added to each bottle. After incubation, the water samples were filtered under a light vacuum ($<1.3 \times 10^4 \text{ Pa}$) onto 25-mm 0.45-mm filters (Millipore), rinsed with 15 ml of filtered lake water, and briefly fumed in HCl vapor to eliminate remaining traces of inorganic ^{14}C . Control samples poisoned by Lugol's iodine at zero-time were run with each experimental series to compensate for non-biological adsorption to filters. The average difference between duplicates was <10%. The concentration of bicarbonate in lake water was determined in an additional sub-sample by measurement of alkalinity and pH (Standard Methods for the Examination of Water and Wastewater, 1995), in each sampling station.

To relate the values of primary productivity obtained in the laboratory experiments at permanent conditions with those measured *in situ*, we used water samples collected at 2-m depth at station A for the parallel estimations of ^{14}C uptake in laboratory and *in situ* experiments. The comparison shows that in the laboratory carbon uptake rate was an average of nearly 70% of that in the lake. The higher values measured in the lake samples are expected, as the irradiance flux at the 2-m incubation depth in the lake was an average higher than the light used in the laboratory. The data confirmed that our laboratory measurements provided fairly adequate assessments of primary productivity in the lake. Such a unified laboratory approach led us to determine spatial variability of primary productivity potential.

To indicate the bottom regions that were the most disturbed by physical forces, sediment resuspension was studied using sedimentation trap technique. Sedimentation fluxes were monitored at stations A and F (Fig. 1A) with the traps moored 2.5 m above the bottom.

Accumulated material was collected biweekly. Dry matter content was determined by weighing of the samples after heating at 80 °C for 24 h (Koren and Ostrovsky, 2001).

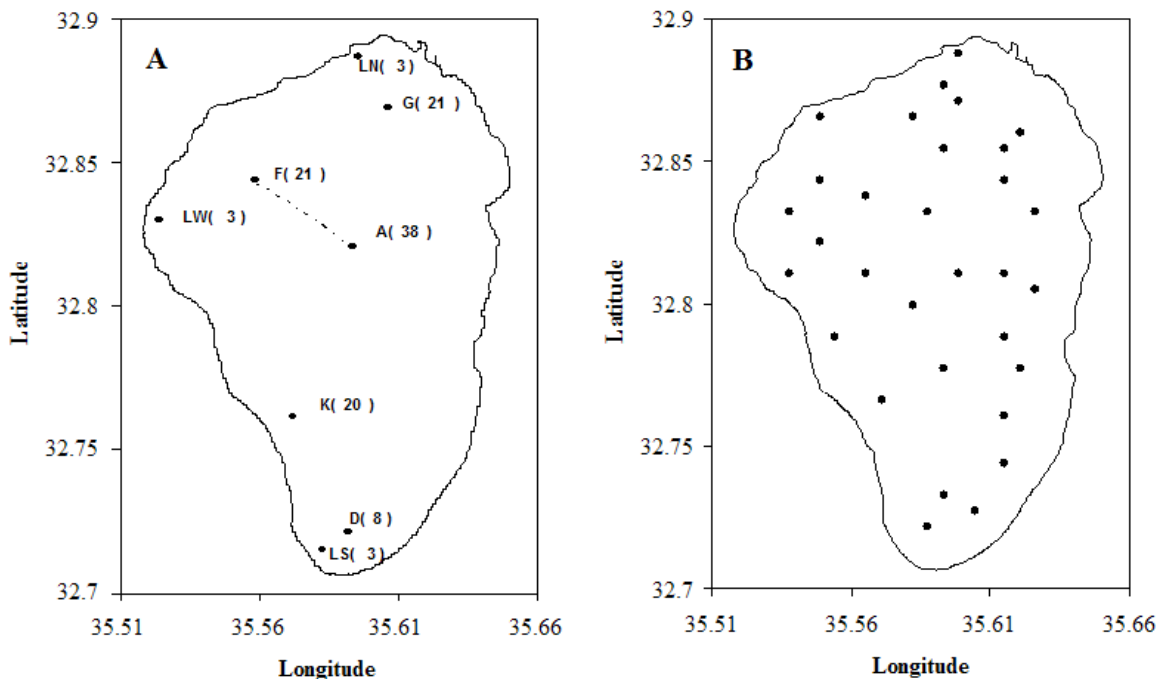


Figure 1. Maps of Lake Kinneret with location of stations. A. Locations where primary productivity (as carbon uptake potential) and chlorophyll *a* concentration were measured. B. Locations of chlorophyll *a* sampling with FluoroProbe. Numbers in brackets indicate the mean station bottom depths during the sampling period. At stations A, F, G, and K the bottom was covered by hypolimnetic water during most of stratification period. At stations D, LN, LS, and LW the bottom was overlying by epilimnetic water. St LN is located near the Jordan outlet zone. Sedimentation traps were deployed at stations A and F (connected by a line). Longitude and latitude scales are given in decimal numbers.

The general scheme of dispersion of the Jordan River water in the saltier Kinneret water was determined from conductivity measurements that were carried out at the end of the flood season of 1998. Vertical profiles of conductivity were measured with DataSonde 4 (Hydrolab Co) at 27 stations in the northern and central parts of the lake. The proportion of the Jordan water (J, %) at each point (location, depth) was calculated using the following formula:

$$J = (C_i - 1.095)/(0.480 - 1.095) * 100 ,$$

where C_i is the conductivity at given point of the lake at the end of the flood season, $0.480 \pm 0.018 \text{ mS cm}^{-1}$ is the average conductivity of the river water during the flood period, and $1.095 \pm 0.013 \text{ mS cm}^{-1}$ is the volumetric average conductivity of the lake water just before the intense flooding (at the beginning of December 1997). At each location the volumetric contribution of the discharged water per unit lake surface area was calculated based on J vertical profiles. Because conductivity of other incoming water sources (which contribute about 40% of the total inflow) differs from the volumetric average conductivity, this formula gives just an approximate assessment of the proportion of the Jordan water at specific locations.

Chemical concentrations of various solutes, such as total phosphorous (P_{tot}), total dissolved phosphorous (TDP), soluble reactive phosphorous (SRP), NO_3 , and NH_4 in Lake Kinneret and Jordan River water were measured according to standard analytical procedures

(Standard Methods for the Examination of Water and Wastewater 1995). These parameters have been weekly monitored during the last few decades and were taken from the databases of the Kinneret Limnological Laboratory and Mekorot Water Company (Watershed Unit). Jordan River discharge has been monitored daily by Hydrological Service of Water Commission.

Wind velocity and direction were measured hourly by a Yonng anemometer at an offshore meteorological station located about 50 m from the western edge of the lake (close to stn. H) and positioned 10 m above the water level. The mean kinetic wind energy transferred to the water (P_w , W m^{-2}) was calculated as follows:

$$P_w = \kappa \rho_{\text{air}} C_d W^3$$

where κ is the wind factor (1.8×10^{-2}), ρ_{air} is the air density (1.2 kg m^{-3}), C_d is the drag coefficient (1.1×10^{-3}), W is the wind speed (m s^{-1}). Temperature and chemical profiles were measured weekly at the central station A.

The vertical profiles of CHL and temperature were also measured by a submersible FluoroProbe (bbe Moldaenke, Kiel, Germany), at 31 stations (Fig. 1B). Each sampling camping was accomplished within about 5-h time span (Yacobi and Schlichter, 2004). The surveys reported here were done carried out in different years.

RESULTS AND DISCUSSION

Thermal structure

The measurements made in this study were designed to determine spatial changes in algal productivity and to pinpoint possible physical and chemical processes that influence the variability of limiting nutrient (phosphorous) supply to the upper productive water layer. This approach assumes that algal productivity reflects seasonal-specific load of phosphorous, which cannot be directly measured due to its low concentration in the water. Consideration of the predominant physical phenomena in specific seasons allowed us to outline the anticipated scheme of heterogeneity in phosphorous load and then to compare it with the actual distribution of algal abundance and productivity.

The thermal regime and seasonal changes of the upper mixed layer thickness in 1999-2000 closely corresponded to those in typical years (cf. Serruya, 1975). From July to October 1999 the epilimnion thickness, measured down to the upper edge of the thermocline, sluggishly increased from 14 m to 16 m. The basis of the epilimnion began to deepen fast with the intense cooling of the lake surface in November (Fig. 2). During that time the sharpest temperature gradient ($3 - 4 \text{ }^{\circ}\text{C m}^{-1}$) was observed at the most upper part of the metalimnion. Complete holomixis took place from mid January until the beginning of March 2000. The thickness of the upper mixed layer slowly extended from 7 to 15 m from March until November 2000; then, the basis of the epilimnion began to deepen faster reaching nearly 28 m at the end of December. The respective changes in bottom area underlying the complete mixed water are shown on Fig. 3B.

Internal load of phosphorous

Below we will mainly consider changes in TDP concentrations. Both TDP and SRP concentrations are very similar in the deep hypolimnion (SRP composed more than 90% of TDP). In the epilimnion TDP concentrations were normally very low (close to the level of detection limit). From August and until the end of the stratified period the concentration of P_{tot} gradually increased only in the deepest part of the anoxic hypolimnion, primarily below 30-m isobath (Fig 2). During that period 70-80% of hypolimnetic P_{tot} was TDP and their seasonal dynamics were identical.

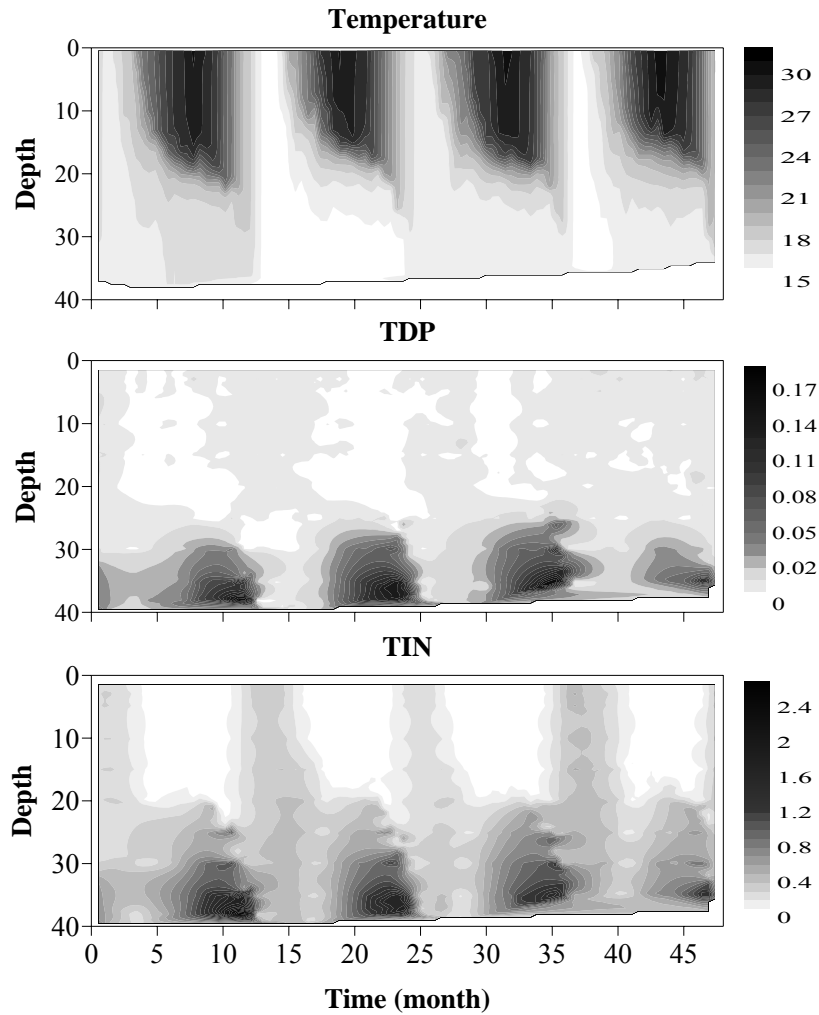


Figure 2. Seasonal dynamic of temperature, total dissolved phosphorous (TDP) and total inorganic nitrogen (TIN) concentrations in the water column at central station in Lake Kinneret. Time scale started from the beginning of 1999 (zero time).

The average rate of P_{tot} increase in the water ranged from $0.5 \text{ mg P m}^{-3}\text{d}^{-1}$ at 30-m depth to $1.0 \text{ mg P m}^{-3}\text{d}^{-1}$ at 38-m depth. Since the bottom sediment is a major source of hypolimnetic P, one may estimate an approximate rate of P flux from the bottom. To do this, the rate of P_{tot} increase rate at each depth was multiplied by the respective ratio of volume of 1-m thick water layer to the bottom area with which this layer is directly in contact. Such an approach suggests that vertical fluxes between water layers are small (which is true for stratified waters) and horizontal transfer of solutes is fast enough to maintain horizontal chemical homogeneity. The diffusive fluxes from the deep bottom sediments to the water, calculated on the basis of area-specific rate of P_{tot} increase, were surprisingly invariable between 30-m and 38-m bottom depth. For instance, in summer-autumn 1999 and 2000 these rates were $4.57 \pm 0.22 \text{ mg P m}^{-2} \text{ d}^{-1}$ and $4.07 \pm 0.2 \text{ mg P m}^{-2} \text{ d}^{-1}$, respectively. Those values were close to the fluxes measured in laboratory from sediment cores collected from 23-m and 40-m bottom depths (Eckert and Nishri, 2000). For instance, in mid December 1999 (just before destratification), when TDP and P_{tot} reached their maxima in the hypolimnion, the inventory P_{tot} and TDP below the 27-m isobath were as high as 36.5 and 27.5 tones, respectively. Immediately after the establishment of holomixis, the concentrations of the nutrients were equally distributed within the entire water column. Therefore, the supply of hypolimnetic TDP to the upper 10-m upper layer, based on the volumetric relationship, was estimated as

14.5 tones. This value is an approximation of the internal TDP supply to the upper productive layer.

Although the annual TDP load from the Jordan River in 1999-2001 (see below) was notably lower than the multi-annual mean, it constituted half the internal TDP that was supplied to the upper 10-m productive layer. The calculated proportion between the external and internal loads of TDP underlines the importance of the former in the provision of the bio-available phosphorous into the productive part of the water column.

Wind energy pattern

Recent investigations showed that wind energy may be an appropriate measure of turbulent mixing in stratified lake, since the efficiency of the energy transfer into the stratified part of the water body via internal seiching and related mixing are nearly constant for various lakes (Wuest *et al.*, 2000). Because wind is the dominant source of turbulent energy in Lake Kinneret during the period of its stable stratification (Hodges *et al.*, 2000), the dynamics of wind energy suppose to reflects the changes of the diapycnal mixing. The mean kinetic wind energy transferred to the water and available for turbulent mixing was the highest in June-September (Fig. 3A), when thermal stratification was strongest. Since the diapycnal mixing takes place primarily near the lake boundaries and the vertical flux through the metalimnion is almost negligible at the lake interior (Imberger, 1994; Nishri *et al.*, 2000; Saggio and Imberger, 2001), the most prominent upward flux of nutrients may be expected at the lake circumference. The lowest mean wind energy was observed from mid October until the end of March. This time span covered the last months of the stratified period (when the thermocline deepened as a result of lake cooling), entire holomixis, and beginning of the next stratified period.

Sediment resuspension

The contribution of the re-suspended particles in the total sedimentation flux was studied to indicate the locations and timing of massive resuspension. Assuming that the newly-produced particles settle down almost equally all over the lake and taking into account that the contribution of resuspended material to the total flux at the lake center is minor (< 20%) in summer (Ostrovsky and Yacobi, 1999), the ratio between sedimentation rates at peripheral Station F (22-m depth) and central Station A (F/A ratio) should indicate the dynamics of resuspension near the Station F.

Despite large variation of the mean wind energy between July and October, no clear relationship was found between that variable and F/A ratio (Fig. 3). This suggests that during these months the changes in find energy did not affect the resuspension below the thermocline. The F/A ratio of 1—2.5 at that time could be attributed to the lateral transportation of sediments, which were resuspended at the shallower areas (Ostrovsky and Yacobi, 1999). Rapid increase in F/A ratio occurred in November-December, when thermocline approached Station F. This indicates the massive resuspension of sediments in proximity to that station. The rapid decrease in losses on ignition of the trap material at the Station F, as compared to the Station A (data not shown), also indicated that the proportion of the resuspended material in the sedimentation flux was high. An increase (by factor 2 – 6) in total suspended matter concentration in the near-bottom water at Station F also suggests massive resuspension at that time. The resuspension was apparently caused by interaction between internal waves of 1-2 m height, which were populated the gradually deepened metalimnion, and the fragile sediments that were accumulated below the thermocline during previous months. Since in November-December the wind was rather weak, it is doubtful that turbulent motions in the epilimnion were energetic enough to support resuspension in deep enough areas.

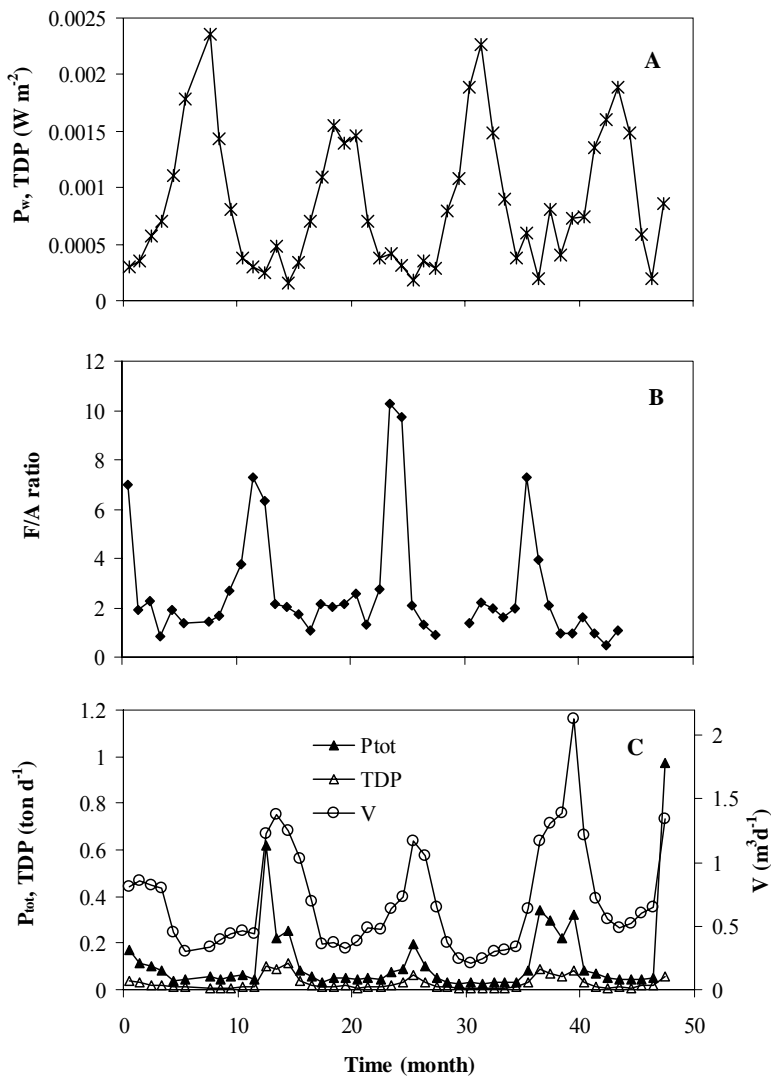


Figure 3. Temporal changes in A) wind energy (P_w), F/A ratio is the ratio of sedimentation rates at peripheral Station F (22-m depth) to sedimentation rates at central Station A in Lake Kinneret, B) F/A ratio is the ratio of sedimentation rates at peripheral Station F (22-m depth) to sedimentation rates at central Station A in Lake Kinneret, C) monthly water inflow (V), total phosphorous (P_{tot}), and total dissolved phosphorous (TDP) load from the Jordan River sedimentation rates between stations F and A. Time scale started from the beginning of 1999 (zero time).

Dispersion of Jordan River water in the lake

The dispersion of the Jordan River water in the lake was used to outline spatial changes in supplement of the allochthonous TDP. At the end of the winter-spring 1998 runoff the Jordan water entering the lake was diverted westward (Fig. 4), which agree with the general pattern of water movement in the lake (Serruya, 1974). The volumetric contribution of the discharged water per unit lake surface declined from $1.7\text{-}2.0 \text{ m}^3 \text{ m}^{-2}$ near the Jordan outlet area to $1.28\text{-}1.36 \text{ m}^3 \text{ m}^{-2}$ at the lake center. The last number was close to the average contribution of river water in the lake ($1.43 \text{ m}^3 \text{ m}^{-2}$), as it can be obtained from the total volume of the Jordan that entered the lake between December 1997 and March 1998 ($233 \times 10^6 \text{ m}^3$) and the lake surface ($163 \times 10^6 \text{ m}^2$). The proportion of the floodwater that entered to the upper 10-m productive

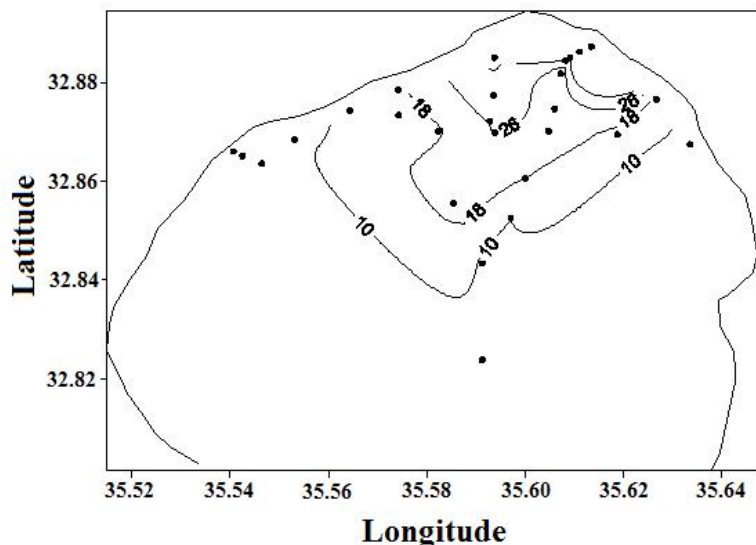


Figure 4. The dispersion of the Jordan River in the upper 10-m water stratum of Lake Kinneret in April 1998 (the end of winter-spring runoff). Isolines indicate the percentage of the River Jordan water. Points show location of sampling stations where conductivity profiles were measured.

layer gradually decreased with distance from the Jordan River entrance and with depth of the water column. At the shallow northern stations (12-m – 16-m bottom depth) it was 84%, at deeper stations (19-m – 22-m bottom depth) – 72%, and at the lake center (40-m bottom depth) – 56%. Therefore, the actual contribution of the riverine water to the upper 10-m strata declined in 2.5 folds, from the Jordan outlet ($1.7 - 2.0 \text{ m}^3 \text{ m}^{-2}$) to the lake center ($0.72 - 0.76 \text{ m}^3 \text{ m}^{-2}$).

Assuming that about 2/3 of the Jordan water enters to the upper 10-m layer, the external load of TDP there was about 7 tones. The allochthonous TDP supply to the upper biologically productive layer should be more pronounced in the northern and western parts of the lake than in other regions, since the contribution of the P-rich riverine water to the Jordan intake zone was much higher than that at the lake center. The average TDP supply in January-March 2000 was about 6-9 times as higher as the summer-autumn averages in 1999 and 2000. In summer and autumn months Jordan River temperature is cooler than the epilimnetic water, therefore, some part of the incoming phosphorous was probably not available for the primary producers for that time span.

Spatial distribution of chlorophyll *a* and primary productivity in relation to P supply

The spatial variability of algal abundance and primary productivity (measured as carbon uptake potential, CUP) was investigated during the following time periods: July-September 1999, June-September 2000, October-December 2000, and March-April 2000. The first two periods represent typical summer conditions with windy weather, the most steady average thermocline depth, and ordinary post-spring-bloom algal community. The third period was featured by fast deepening of the thermocline position due to cooling of the upper mixed water layer and weak wind. The fourth period was characterized by the most intensive algal bloom of 2000, maximum inflow of the nutrient-rich water from the watershed, and weak wind forcing.

As seasonal changes in the ecosystem may not occur synchronously in different parts of the lake, the momentary snapshots of CHL and CUP distributions can be influenced by

asymmetric successive changes in the planktonic community (species change, local losses of biomass, etc.). Therefore, averaging of the data was used to detect seasonal-characteristic patterns of spatial variability of the measured parameters. The frequency of our measurements

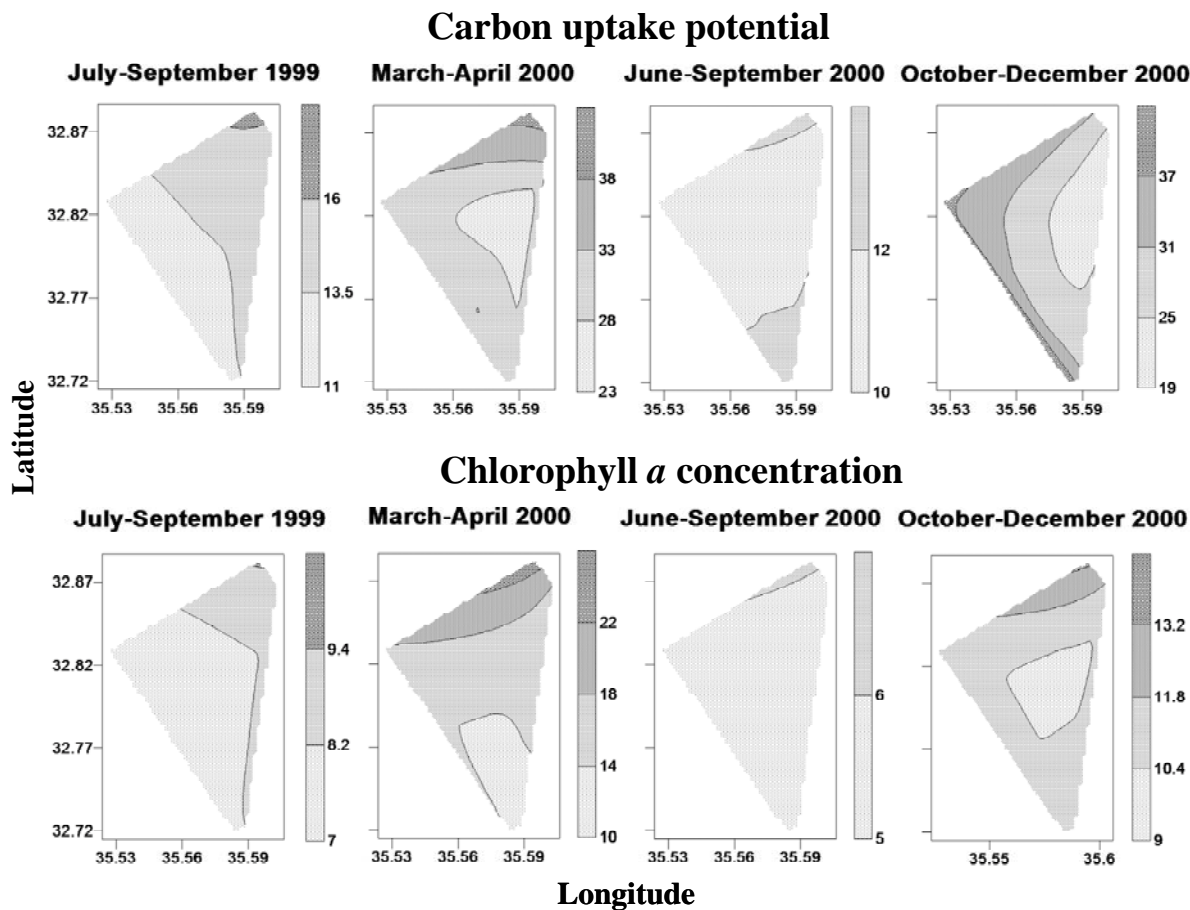


Figure 5. Spatial distribution of chlorophyll *a* concentration (mg Chl m^{-3}) and carbon uptake potential ($\text{mg C m}^{-3} \text{ h}^{-1}$) at various seasons. Each plot represents span-averaged parameters over several (at least five) surveys. The plots reflect significance of parameter change over sampling area: the difference in value is significant ($P<0.05$, paired t-test) over one scale level. Latitude and longitude is given in decimal units.

let us combining from five to seven consecutive data collections for each period of interest. The distributions of the parameters showed different patterns in various seasons (Fig. 5).

From June-July to September 1999 and 2000 no significant differences ($P>>0.05$) in distributions of CHL and CUP were found between the chosen stations. The only exception was noticed at the northernmost tip of the lake, where slight loads of allochthonous phosphorous remained even in the driest season (Fig. 3C) and could sustain higher level of CHL and CUP. The virtual similarity in CHL concentrations and CUP between shallow and deep stations did not allow supporting the anticipated enhancement of algal biomass and primary productivity at the lake periphery in the summer. This suggests that the upward flux of phosphorous due to diapycnal mixing in the shallow areas was rather small due to low SRP concentration in the metalimnion and upper hypolimnion (i.e. in the strata from where the nutrient could be transported upward, cf. Nishri *et al.*, 2000). Still, our measurements carried out with FluoroProbe showed negative correlation ($r=-0.86$, $P<0.001$) between spatial variability in CHL concentrations and temperature, while standard variations in CHL were small (< 20%, Fig. 6). The later imply that in areas of intense water mixing (upwind side of the lake), which are attested by lower temperature, CHL concentrations were noticeable

higher than in other locations. This supports the hypothesis that upwelling and seiche-initiated diapycnal mixing, which persistently occurs in the shallow lake regions, causes upward fluxes of limiting nutrient and thus augments localized algal abundance (Ostrovsky *et al.*, 1996; MacIntyre and Jellison, 2001; Steissberg *et al.*, 2005). In fact, in summer an energetic afternoon wind induced large internal waves in the lake. Propagation of these waves at the sloping boundary produces intense turbulence, shear-induced convection near the bottom (Lemckert *et al.*, 2004; Lorke, 2007), enhanced diffusive transport across the sediment–water interface (Lorke *et al.*, 2003), strong resuspension (Ostrovsky and Yacobi, 1999), and diapycnal mixing at the lake periphery (MacIntyre *et al.*, 1999). Still, the low algal abundance and productivity, as compared with other seasons (Fig. 5), suggests negative balance of phosphorous in the epilimnion prevailed in the summer and early autumn, such that seiche induce mixing could not cover phosphorus losses through sedimentation.

During the autumn of 2000 the average CUP and CHL concentrations increased from 10 ± 1 to 33 ± 5 mg C m⁻³ h⁻¹ and from 5 ± 1 to 11 ± 1 mg Chl m⁻³, respectively. The augmentation of algal abundance coincided with the time of fast thermocline deepening, when large fraction of the hypolimnetic water was incorporating into the epilimnion. During October–December 2000, CUP was significantly higher ($P<0.05$) at the lake periphery than at the lake center (Fig. 5). This suggests higher supply of phosphorous at the lake circumference. The average CHL concentrations measured at the lake periphery in the autumn were also slightly higher than those at the center, but the differences were not statistically significant. Elevated concentrations of CHL at the lake circumference were also detected at the end of October 1992 based on analysis of satellite images (Mayo *et al.*, 1995). These findings suggest that prominent supply of phosphorous took place at the lake periphery in the autumn when winds showed relatively low velocity. Phosphorous could be supplied either from the hypolimnetic water or from bottom sediments. It is doubtful that thermocline erosion, as water got cooler (positive buoyancy flux), could be spatially heterogeneous. The average concentration of the TDP between 20-m and 27-m isobaths (ca. 0.010 mgP L⁻¹) was about twice as higher as in the epilimnion. Incorporation of that layer into the epilimnion could provide about 4.7 tones of TDP into the epilimnion and, thus, to contribute to an increase in the new production. On the other hand, the thermocline deepening down to 27 m could not remarkably enlarge concentration of the P_{tot} in the epilimnion, as its concentrations in the upper hypolimnion and epilimnion were nearly identical (0.015 – 0.020 mg P L⁻¹) in October–December 2000.

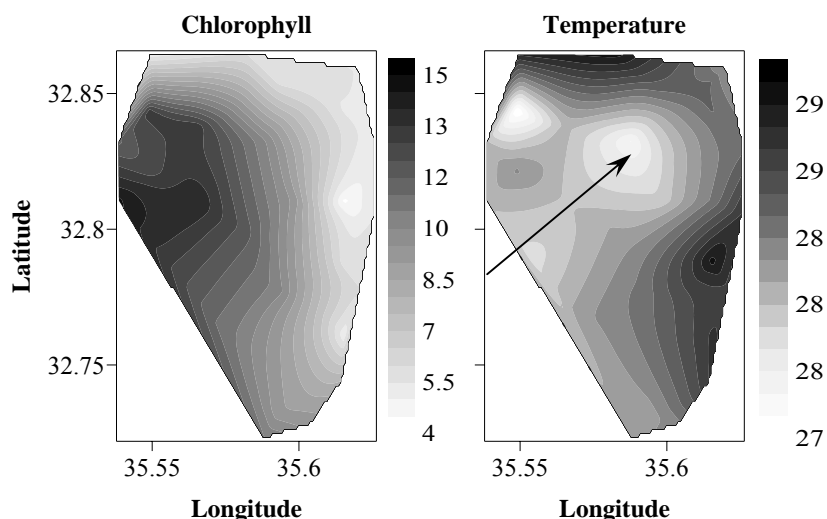


Figure 6. Spatial distribution of chlorophyll *a* concentration (mg Chl m⁻³) and temperature (°C) in September 4, 2001. Measurements were done using FluoroProbe at 31 stations. The dominant direction of strong afternoon wind is shown by arrow.

A potentially rich source of phosphorous is at the bottom sediments residing below the thermocline. The pore water of such sediments contains about two orders of magnitudes higher dissolved phosphorous concentration than concentration of the epilimnetic P_{tot} (Eckert and Nishri, 2000; Eckert *et al.*, 2003). During the time of the fast thermocline deepening, disclosure of those fragile sediments should lead to P release directly to the peripheral part of the epilimnion. A rough assessment of TDP that was released from the bottom belt between 20-m and 27-m isobath, directly to the epilimnion, during half the time of its rapid exposure to the epilimnion (two weeks) was evaluated based on the average diffusive flux from the bottom (see above). The calculated value (two tones of phosphorous) could be significantly underestimated, because both the direct injection of the P-rich sedimentary pore water during massive resuspension of sediments (see above) and enhanced diffusion under highly turbulent conditions in the epilimnion could promote an extra-removal of phosphorous from the bottom during that time. However, even such a lowered estimate shows that the TDP supplied from the peripheral sediment belt could account for at least 40% of the TDP that was incorporated with water due to thermocline erosion (4.7 tones, see above). Thus, the rapid deepening of the thermocline in the autumn and associated massive resuspension at the thermocline-bottom interface could be responsible for spatial heterogeneity in the TDP supply to the upper productive water layer and such a way to stimulate algal productivity in the lake circumference.

In the spring of 2000, at the end of the rainfall season, algal abundance and productivity were much higher at the Jordan outlet area and northwestern part of the lake than at the central and southern areas (Fig. 5). Similar pattern of algae distribution was reported earlier (Pollingher, 1988; Ostrovsky and Sukenik, 2008). Such a pattern closely followed the general scheme of dispersion of the Jordan water and associated allochthonous nutrients in the lake. The increased CHL and CUP near the Jordan outlet zone were also well recognizable during other seasons (e.g. summer and autumn) and may be attributed to the persistent supplement of nutrients with Jordan waters into the upper stratum of the lake. In fact, higher concentrations of inorganic phosphorous and/or nitrogen were registered near the Jordan River, in contrast to other littoral areas where chemical analysis could not revealed reliable augmentation of nutrient concentrations as compared with deep stations (Berman *et al.*, 1989). Whether local augmentation of algal abundance persists depends on the rates at which algae are produced and vanish. Large horizontal circulations of water mass (e.g. dyer-like structures, currents) cannot be obstacles for detection of algal biomass and productivity increase, as the entire nutrient-enriched water mass moves cohesively. An anti-clockwise cohesive movement of nutrient-enriched water from the Jordan outlet zone form zones where algal biomass and productivity are notably higher (Ostrovsky and Sukenik 2009). In contrast, in some cases distribution of algae may not reflect local supply of available nutrients. For instance, wind can induce horizontal patchiness for positively and negatively buoyant algal cells at downwind or upwind (respectively) sides of the lake (e.g. Reynolds 2006). Also fast metalimnetic jets may horizontally disperse nutrients out of locations where they were intensively transported upward (e.g. shallow regions, upwelling zones) and thus mask the area of enriched productivity. These processes should be taken into consideration when the distribution of phytoplankton is cross correlated with nutrient provision.

CONCLUSIONS

The analysis of spatial heterogeneity in CUP may be a good tool to explore spatial changes in nutrient availability. This approach is potentially expedient when standard analytical methods do not permit to quantify spatial changes in limiting nutrients in the upper productive layer, because nutrients are rapidly depleted and recycled. In contrast to chemical analysis, algal productivity assessed by the uptake of the ¹⁴C, enables detection of minute differences in the

growth potential of phytoplankton. Relatively short time of algal biomass doubling (from < 1 – 2 days for most of the algae, Reynolds, 2006, to about a week for *Peridinium*, Berman and Pollingher, 1974) makes CHL concentration also a good measure of the enhanced nutrient supply. Investigation of heterogeneity in phytoplankton distribution can be also an effective supplementary tool to study dominant physical and chemical processes that are responsible for nutrient load and water motions. It should be taken into consideration when reliable monitoring program is planning.

ACKNOWLEDGMENTS

We thank Dr. A. Nishri for making available chemical data of Lake Kinneret. We are indebted to Mekorot Water Company for making chemical monitoring data of the Jordan River available. The authors thank N. Koren, J. Didenko, S. Chava, S. Kaganovsky, J. Easton for assistance in carrying out the laboratory analysis and field sampling. This study was supported by grants from and the German-Israeli Foundation for Research and Development (I-0416-026.08/95, I-711-83.8/2001), the Israel Science Foundation (211/02), and also was based on Lake Kinneret Monitoring Program.

REFERENCES

- Avnimelech, Y. (1980). Studies on Lake Kinneret (Sea of Galilee) watershed. 1: Characterization of water and suspended load in Lake Kinneret Tributaries. *Water, Air, and Soil Pollution* 14, 451-460.
- American Public Health Association. 1992. Standard methods for the examination of water and wastewater. 18th edition. American Public Health Association
- Antenucci, J. P., J. Imberger, and A. Saggio. (2000). A. Seasonal evolution of the basin-scale internal wave field in a large stratified lake. *Limnol. Oceanogr.* 45, 1621-1638.
- Berman, T., L. Stone, Y. Z. Yacobi, M. Schlichter, A. Nishri, and U. Pollingher, (1995). Primary production and phytoplankton in Lake Kinneret: A long term record (1972 - 1993). *Limnol. Oceanogr.*, 40, 1064-1076.
- Berman, T., U. Pollingher. (1974). Annual and seasonal variations of phytoplankton, chlorophyll and photosynthesis in Lake Kinneret. *Limnol. Oceanogr.*, 19, 31-54.
- Berman, T., U. Pollingher, B. Kaplan, and S. Chava. (1989). Limnological characteristics in "deep littoral" waters in Lake Kinneret, p. 305-315. In: Spanier, R., Steinberger, Y., and Luria, M. [eds.], Environmental Quality and Ecosystem Stability, Proceedings of the 4th International Conference of the Israeli Society of Ecology and Environmental Quality Science. IV-A/B. ISEEQS Publishers. Jerusalem.
- Eckert, W. and A. Nishri (2000). Sedimentary phosphorous frux in Lake Kinneret. *Arch. Hydrobiol.* 55, 397-411.
- Eckert, W, J. Didenko, E. Uri, and D. Eldar. (2003). Spatial and temporal variability of particulate phosphorus fractions in seston and sediments of Lake Kinneret under changing loading scenario. *Hydrobiologia* 494: 223-229.
- Hodges, B.R., Imberger, J., Saggio, A., and Winters, K.B. (2000): Modeling basin-scale internal waves in a stratified lake. *Limnol. Oceanogr.* 45, 1603-1620.
- Holm-Hansen , O.C., J. Lorenzen, R.W. Holmes and J.D.H. Strickland. (1965). Fluorometric determination of chlorophyll. *J. Cons. Int. Explor. Mer.*, 30, 3-15.
- Gloor, M., A. Wuest, and M. Munnich. (1994). Benthic boundary mixing and resuspension induced by internal seiches. *Hydrobiol.* 284, 59-68.
- Goldman, J. (1988). Spatial and temporal discontinuous of biological processes in pelagic surface waters, p. 273-296, In B. J. Rothschild [ed.]. Toward a theory on biological-physical interactions in the World Ocean. Kluwer Academic Publishers.
- Imberger, J. (1994). Transport processes in lakes: a review article, p. 99-193, In R. Margalef [ed.], Limnology now, a paradigm of planetary problems. Elsevier.
- Imboden, D., and A. Wuest. (1995). Mixing mechanisms in lakes, p. 83-138, In A. Lerman, D. M. Imboden and J. R Gat [eds.], Physics and chemistry of lakes. Spring-Verlag.
- Kalikhman, Y., I. Ostrovsky, P. Walline, M. Gophen, and Y. Z. Yacobi (1995). Distribution fields for aquatic ecosystem components: method of identification of correlation zones. *Freshwater Biology* 34, 317-328.
- Knauer, K., H.M. Nepf, and H. F. Hermond. (2000). The production of chemical heterogeneity in Upper Mystic Lake. *Limnol. Oceanogr.* 45, 1647-1654.

- Koren, N., and I. Ostrovsky. (2001). Sedimentation in a stratified subtropical lake. Verh. Internat. Verein. Limnol., 27: 2636-2639.
- Kratz, T. K., S. MacIntyre, and K. E. Webster. (2005). Causes and consequences of spatial heterogeneity in lakes. Pp. 329-347 In Lovett, G. M., C. G. Jones, M. G. Turner, and K.C. Weathers (eds.). Ecosystem Function in Heterogeneous Landscapes. Springer, NY.
- Lemckert, C., J. P. Antenucci, A. Saggio, And J. Imberger. (2004). Physical properties of turbulent benthic boundary layers generated by internal waves. *J. Hydraul. Eng.* 130: 58–69.
- Lorke, A., F. Peeters, and A. Wuest. (2005). Shear-induced convective mixing in bottom boundary layers on slopes. *Limnol. Oceanogr.* 50: 1612-1619.
- Lorke, A., B. Muller, M. Maerki, and A. Wuest. (2003). Breathing sediments: The control of diffusive transport across the sediment–water interface by periodic boundary-layer turbulence. *Limnol. Oceanogr.* 48: 2077–2085.
- Lorke, A., F. Peeters, and A. Wuest. (2005). Shear-induced convective mixing in bottom boundary layers on slopes. *Limnol. Oceanogr.*, 50: 1612–1619.
- Lorke, A. (2007): Boundary mixing in the thermocline of a large lake. *J. Geophys. Res.* 112. C09019. doi:10.1029/2006JC004008.
- MacIntyre, S., K. M. Flynn, R. J. Jellison, and J. R. Romero. (1999). Boundary mixing and nutrient fluxes in Mono Lake, California. *Limnol. Oceanogr.* 44, 512-529.
- MacIntyre, S., and R. Jellison. (2001). Nutrient fluxes from upwelling and enhanced turbulence at the top of the pycnocline in Mono Lake, CA. *Hydrobiologia*. 466: 13-29.
- MacIntyre, S., J.O. Sickman, S.A. Goldthwait, and G.W. Kling. (2006). Physical pathways of nutrient supply in a small, ultra-oligotrophic arctic lake during summer stratification. *Limnol. Oceanogr.* 51: 1107-1124.
- Markel, D., Y. Kolodny, B. Luz, and A. Nishri. (1994). Phosphorus cycling and phosphorus sources in Lake Kinneret: tracing by oxygen isotopes in phosphate. *Israel Journal of Earth Science* 43, 165-178.
- Mayo, M., A. Gitelson, Y.Z.Yacobi, and Z Ben-Avraham. (1995) Chlorophyll distribution in Lake Kinneret determined from Landsat Thermatic Mapper data. *Int. J. Remote Sensing*, 16, 175-182.
- Metaxas, A and R.E.Scheibling, (1996). Spatial heterogeneity of phytoplankton assemblages in tidepools: Effects of abiotic and biotic factors. *Mar. Ecol. Prog. Ser.* 130: 179-199.
- Nishri A., J. Imberger, W. Eckert, I. Ostrovsky, and J. Geifman J. (2000). The physical regime and the respective biogeochemical processes in lower water mass of Lake Kinneret . *Limnol. Oceanogr.* 45, 972-981.
- Ostrovsky, I., Y. Z.Yacobi, P. Walline, and Y. Kalikhman. (1996). Seiche-induced water mixing: its impact on lake productivity. *Limnol. Oceanogr.* 41, 323-332.
- Ostrovsky, I., and Y. Yacobi. (1999). Organic matter and pigments in surface sediments: possible mechanisms of their horizontal distributions in a stratified lake. *Can. J. Fish. Aquat. Sci.* 56, 1001-1010.
- Ostrovsky, I. and A. Sukenik (2008). Spatial heterogeneity of biogeochemical parameters in a subtropical lake. In Monitoring and Modeling Lakes and Coastal Environments (P. K. Mohanty, ed.). Springer, 248 p.
- Pollingher, U. (1988). Freshwater armored dinoflagellates: growth, reproduction strategies, and population dynamics, p. 134-174, In C. D. Sundgren [ed.], Growth and reproduction strategies of freshwater phytoplankton. Cambridge University Press.
- Reynolds, C. S. (2006). Ecology of Phytoplankton. Cambridge University Press. 535 pp.
- Saggio, A. and J. Imberger, J. (2001). Mixing and turbulent fluxes in the metalimnion of a stratified lake *Limnol. Oceanogr.* 46, 392-409.
- Serruya, C., M. Edelstein, U. Pollingher, and S. Serruya. (1974). Lake Kinneret sediments: Nutrient composition of pore water and mud exchange. *Limnol. Oceanogr.* 19, 489-508.
- Serruya, C. (1978). Water chemistry, p.185-204. In C. Serruya [ed.], Lake Kinneret. Dr. W. Junk Publ., The Hague.
- Serruya, S. (1974). The mixing patterns of the Jordan River in Lake Kinneret. *Limnol. Oceanogr.*, 18, 175-181.
- Serruya, S. (1975). Wind, water temperature and motions in Lake Kinneret: general pattern. *Verhandlungen Internationale Vereinigung für Theoretische und Angewandte Limnologie* 19, 73-87.
- Smith, S. V., S. Serruya, Y. Geifman, and T. Berman. (1989). Internal sources and sinks of water, P, N, Ca, and Cl in Lake Kinneret, Israel. *Limnol. Oceanogr.* 34, 1202-1213.
- Standard Methods for the Examination of Water and Wastewater (1995). 19th edn, American Public Health Association/American Water Works Association/Water Environment Federation, Washington DC, USA.
- Steeman-Nielsen, E., (1952). The use of radioactive carbon (14C) for measuring organic production in the sea. *J. Cons. Cons. Int. Explor. Mer.*, 18, 117-140.
- Steissberg, T.E., S.J. Hook and S.G. Schladow Steissberg (2005). Characterizing partial upwellings and surface circulation at Lake Tahoe, California-Nevada, USA with thermal infrared images. *Remote Sensing of Environment* 99 (1-2): 2-15.

- Wuest, A., G. Piepke, and D. C. Van Senden. (2000). Turbulent kinetic energy balance as a tool for estimating vertical diffusivity in wind-forced waters. Limnol. Oceanogr. 45, 1388-1400.
- Wuest, A., and A. Lorke (2003), Small-scale hydrodynamics in lakes, Annu. Rev. Fluid Mech., 35, 373–412.
- Yacobi, Y.Z., and Schlichter, M. (2004). GIS application for mapping of phytoplankton using a multi-channel fluorescence probe derived information. In: (Yangbo Chen, Kaoru Takara, Ian D. Cluckie & F. Hilaire De Smedt, eds), GIS and Remote Sensing in Hydrology, Water Resources and Environment, IHAS Publication 289: 301-307, International Association of Hydrological Sciences Press, Wallingford, UK.
- Yacobi, Y.Z. (2006). Temporal and vertical variation of chlorophyll a concentration, phytoplankton photosynthetic activity and light attenuation in Lake Kinneret: possibilities and limitations for simulation by remote-sensing. J. Plankton Res., 28: 725-736.

A Comparison of Parameterized, Simulated and Measured Turbulent Mixing in the Gulf of Finland, the Baltic Sea

M.-J. Lilover ^{1,*} and A. Stips ²

¹ *Marine Systems Institute at Tallinn University of Technology
Akadeemia tee 21, 12618 Tallinn, Estonia*

² *European Commission – Joint Research Centre
Via E. Fermi, 2749 (TP272)
I-21027 Ispra (VA), Italy*

*corresponding author, e-mail madis@phys.sea.ee

ABSTRACT

Three time series of shear microstructure measurements (duration 13, 24 and 14 h respectively) have been performed in 3 different wind forcing regimes as well as in 3 different background density stratification and current velocity shear situations at the entrance to the Gulf of Finland, in July 1998. Vertical shear of current velocity was enhanced by near-inertial waves during the first (A1) and the third (A3) time series, the background stratification weakened continuously from A1 toward A3. We compared eddy diffusivities based on the Richardson number parameterization and eddy diffusivities simulated using the two equation k- ϵ turbulence closure (General Ocean Turbulence Model, GOTM) with the “measured” ones. For two out of the three time series the eddy diffusivities calculated via the Richardson number parameterization and via the k- ϵ model simulation agreed well with the experimental data. However, summing up the discrepancy of all three time series both methods resulted in a remarkable and consistent bias against the measured eddy diffusivity. On the contrary, the calculations with a new parameterization scheme, which considers the internal wave kinetic energy fitted well for all three time series. Similarly the modified k- ϵ simulations which considered the internal wave energy level matched better the measured profiles.

KEYWORDS

Baltic Sea; Gulf of Finland; eddy diffusivity; k- ϵ model; TKE dissipation rate measurements; turbulent mixing;

INTRODUCTION

The Baltic Sea is a brackish semi-enclosed sea having a very limited water exchange with the saline North Sea. The limited water exchange and large river runoff lead to two-layer salinity stratification with a permanent halocline located at about 60-70 meters below the sea surface. The Gulf of Finland is a typically estuarine environment: the salinity in the surface layer ranges from approximately 5-7 PSU at the entrance to nearly fresh water in the eastern end of the gulf. The general circulation is cyclonic in the gulf and varies strongly due to the wind forcing (Palmen, 1930). Inertial oscillations and seiches are also an important part of the non-stationary circulation pattern (Alenius *et al.*, 1998). The tidal oscillations of the sea level have minor importance to the dynamics of the Baltic (Kullenberg, 1981). The seasonal thermocline

is strongest in July-August and is usually observed at the depth of 10-20 m, so effectively restricting nutrient transport to the euphotic layer in summer.

Biological phenomena like bio-diversity or algae blooms are commonly studied in relation to meso- and small-scale physical processes in the last years. Biologists are especially interested in estimating the eddy diffusivity to calculate vertical fluxes of nutrients. Therefore, in interdisciplinary scientific campaigns in addition to the biochemical parameters, also physical parameters like wind, currents, temperature, salinity, density and as a new parameter - turbulent kinetic energy dissipation rate are measured to estimate the eddy diffusivity. Alternatively, the eddy diffusivity can be estimated using parameterization or turbulence modeling. Parameterization schemes relying on mean water density and current velocity (using the Richardson number for parameterization) as well as the parameterization via the two-equation k - ε turbulence model have been usually calibrated for multiannual simulations. Both schemes applied to the Baltic Sea have satisfactorily simulated the temporal development of the seasonal thermocline (Meier, 2001). However, marine biology phenomena like algae blooms are sensitive to nutrient transfer events from the deep water into the euphotic layer (Kononen *et al.*, 2003; Lilover *et al.*, 2003). Therefore, turbulent mixing calculation schemes used to explain the marine biology phenomena have to be able to reproduce short term mixing events (of about 1 day duration), which can cause significant nutrient pulses into the euphotic zone (Lilover *et al.*, 2003).

In the present paper we focus on the capability of different eddy diffusivity calculation schemes to follow short term forcing changes. Finally, we propose a new scheme for the eddy diffusivity parameterization relying on the high frequency constituent of the current kinetic energy. We also suggest to incorporate additionally turbulence generation by internal waves into the k - ε model for the eddy diffusivity simulation. Our study is based on three measurement series conducted under different forcing situations and we compare the estimates of eddy diffusivities derived from direct turbulence measurements, from different parameterization schemes and from the one-dimensional General Ocean Turbulence Model (GOTM, www.gotm.net). We focus on comprehending the turbulence mixing away from boundaries – in the “midcolumn”, where internal waves could play important role in generating the turbulent fluxes. In section 2 we describe our measurements and instruments. In section 3 we present an overview of the background physical conditions, we compare the “standard” parameterization and simulation schemes to calculate the eddy diffusivity and finally we propose a “new” scheme allowing for separation of different observed levels of turbulence intensity.

MATERIALS AND METHODS

The measurements were conducted aboard R/V *Aranda* (Finnish Institute of Marine Research) from 13 to 23 July 1998 at the entrance area to the Gulf of Finland (Figure 1). The data discussed further were gathered at an anchor station A ($59^{\circ}42.5'N$, $23^{\circ}38.0'E$). The basic data-set includes current velocity recorded by a bottom mounted Acoustic Doppler Current Profiler (ADCP) (14-23 July); Conductivity, Temperature, Depth (CTD) and turbulence data collected by a microstructure measuring system (MSS) during anchor station on 14-15 (A1), 16-17 (A2) and 21 July (A3). In addition, the wind data at 10 m height with time interval 10 min were extracted from the R/V *Aranda* weather station data file.

The bottom mounted (at 54m depth) ADCP (RDI Narrow Band 600 kHz) was deployed by Pirkanmaa Regional Environmental Centre (Finland). The mooring position was chosen as

close to the anchor station as possible. The bin size of 1 m and averaging over 15 min time interval were selected to obtain data from 50 to 7 m depths.

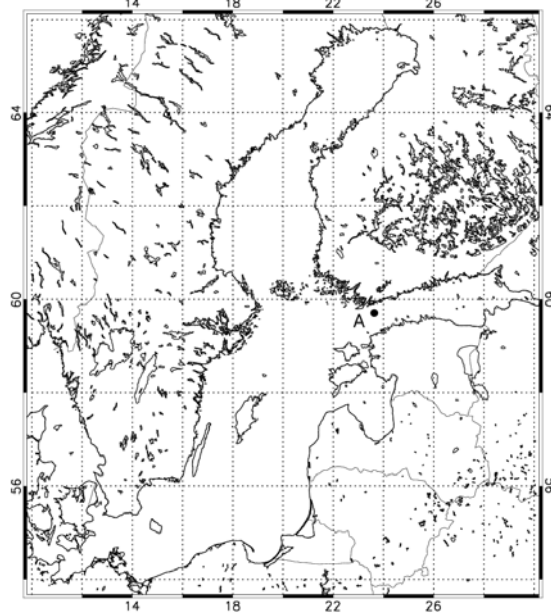


Figure 1. Map showing the positions of the dissipation time series measurements (A ·) onboard R/V Aranda and that of the moored ADCP in the entrance of the Gulf of Finland.

The measurement series with the MSS profiler were conducted on an hourly basis i.e. sub-series consisted of six consecutive profiles per hour. The MSS profiler was equipped with CTD sensors to obtain high-resolution temperature, salinity, density profiles and with a shear probe (time constant approx. 3ms) to measure current velocity fluctuations [15]. From the latter, the viscous dissipation rate of turbulent kinetic energy, ε ($\varepsilon = 7.5 v \langle (\partial u / \partial z)^2 \rangle$, where v is the kinematic viscosity, $\partial u / \partial z$ is the vertical profile of current shear fluctuations and $\langle \rangle$ denote averaging) was calculated with relative error of about 30% as detailed in (Prandke and Stips, 1998). The data were sampled at a frequency of 1024 Hz. To avoid cable-induced disturbances the data were collected in freely sinking mode within depths of 5 to 55 m with a mean sinking speed of 0.6 m s^{-1} . However, to avoid possible disturbances by the ship (although the ship was anchored by 3 anchors and the engine switched off), turbulence data only from below 10 m were taken into account. To reduce the inherent noise and ensure the comparability (turbulence data resolution in time was 1 hour and current data resolution in vertical direction 1 meter), all small- and meso-scale resolving data sets were merged onto 1 m times 1 h grid and then filtered by a low-pass Butterworth filter with 4 m cut-off in vertical direction and 2 h cutoff in time. The filter cut-off scales were determined from current data rotary spectra analysis where white noise appeared at scales less than 4 meter and 1 hour.

RESULTS AND DISCUSSION

Wind forcing, background stratification and currents

With respect to the wind speed the microstructure measurements were performed under three different wind forcing conditions: rising strong wind (A1), weak wind (A2) and decreasing strong wind (A3)). We divided the current velocity into 3 frequency bands: sub-inertial,

inertial (1.33-2.4 cpd) and super-inertial. The series mean kinetic energy and velocity shear ($s = [(\partial u / \partial z)^2 + (\partial v / \partial z)^2]^{1/2}$) behaved in accordance with the mean wind stress: the highest values belonged to A1 and the lowest to the A2 (Table 1). However series A3 had the highest inertial frequency band kinetic energy.

Table 1. Mean characteristics of wind, current kinetic energy, vertical shear and buoyancy frequency in the water column from 10 to 50 m depth during the three time series.

	A1	A2	A3
Mean wind speed (m s ⁻¹)	11	5	8
Mean wind stress (N m ⁻²)	0.20	0.04	0.10
Mean kinetic energy (10 ⁻⁴ J kg ⁻¹)	76.4	15.7	45.8
Mean sub-inertial kinetic energy (10 ⁻⁴ J kg ⁻¹)	59.1	12.6	25.2
Mean inertial kinetic energy (10 ⁻⁴ J kg ⁻¹)	15.1	1.4	18.6
Mean super-inertial kinetic energy (10 ⁻⁴ J kg ⁻¹)	2.1	0.8	2.0
Mean shear squared, s ² (10 ⁻⁴ s ⁻²)	3.7	1.4	2.9
Mean sub-inertial shear squared, s ² (10 ⁻⁴ s ⁻²)	1.9	0.8	1.4
Mean inertial shear squared, s ² (10 ⁻⁴ s ⁻²)	1.2	0.3	1.1
Mean super-inertial shear squared, s ² (10 ⁻⁴ s ⁻²)	0.6	0.3	0.4
Mean buoyancy frequency squared, N ² (10 ⁻⁴ s ⁻²)	6.1	4.5	4.1

For the entire measurement period the sub-inertial current velocity shear was strongest in the upper layer. Below the pycnocline the inertial shear prevailed during the entire current velocity measurement period. The mean stratification was influenced by the meso-scale flow and weakened continuously from A1 toward A3 - during series A3 the stratification was the weakest (Figure 2). Thus, in terms of generation of turbulent mixing, in the case of A2 the mixing was presumably weakly developed because of the weakest wind forcing, the weakest shear and medium stratification.

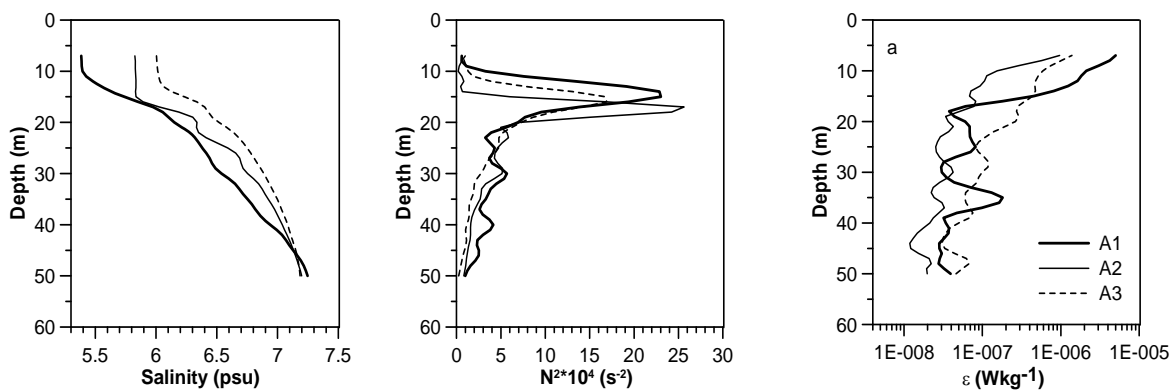


Figure 2. Average profiles of the salinity, squared buoyancy frequency and measured TKE dissipation rate for time series A1, A2 and A3.

In the case of A1, more mixing is expected because of strong shear caused by strong wind forcing. And in the case of A3, the weak stratification and relatively strong shear were the factors supporting the turbulent mixing. In the latter case the relative contribution to the velocity shear from inertial waves was the highest.

“Measured” eddy diffusivity (Osborn model)

The vertical eddy diffusivity of mass based on quantities measured by us (ε , N^2) was estimated on the base of Osborn (1980) model $K_\rho = 0.2\varepsilon/N^2$, where $N^2 (N^2 = -g/\rho\partial\rho/\partial z)$, where g is the gravitational acceleration and ρ is water density) is the buoyancy frequency squared. The model assumes a local production-dissipation balance of turbulent kinetic energy and therefore the eddy diffusivity was calculated for the layer below the maximum of buoyancy frequency where we assume that the Osborn model will apply. Because of the intermittent nature of small-scale turbulence, the mean eddy diffusivity profiles were calculated from the individual profiles (henceforth K_ρ denotes the mean eddy diffusivity).

Below the upper mixed layer (UML) the mean eddy diffusivity profile had its local minimum in the pycnocline at 17-18 m depth and remained moderately variable, within the range of 10^{-5} - $10^{-4} \text{ m}^2 \text{s}^{-1}$, below 21 m depth (Figure 3, upper panel). However, in that layer all three mean profiles corresponding to cases A1, A2 and A3 were significantly separated from each other. Relative to the weakest level of turbulence in the case of A2, an increase of K_ρ was observed in A1 because of the strong current shear and in A3 because of relatively strong shear and the weakest stratification (Table 1). So, the “measured” eddy diffusivities presented here clearly reflect changes of the background fields’ characteristics.

Further we focus on the evaluation of different parameterization schemes in respect to separate the different time series in a similar way as the measured eddy diffusivities reveal.

Parameterization of eddy diffusivity in the form $K_{Ri}=f(Ri)$

Next we discuss the approximation of eddy diffusivity using a Richardson number ($Ri=N^2/s^2$) dependent parameterization scheme. The formula is adopted from Pacanowski and Philander (1981) and Meier (2001) papers:

$$K_{Meier, Pac} = K_0 / (1 + Ri/Ri_0)^q + K_b, \quad (1)$$

here except Ri all other letters denote constants given in Table 2. The scheme by Pacanowski and Philander (Pac) is developed for the Equatorial Pacific Ocean using modeled data and the scheme developed by Meier for the Baltic Sea is also based on modeled data. Actually the constants for these two schemes are derived for a large area and for a long time simulation and are not location specific, but rather object specific (Equatorial Pacific Ocean, Baltic Sea).

Table 2. Constants of the Richardson number dependent mixing parameterization

	K_0 $*10^{-4} \text{ m}^2 \text{s}^{-1}$	K_b $*10^{-4} \text{ m}^2 \text{s}^{-1}$	q	Ri_0	
K_{Meier}	20	0.01	1.5	0.1	Meier
K_{Pac}	v_t^{-1} 1)	0.1	1	0.2	Pacanowski and Philander

1) $v_t = 50/(I+Ri/Ri_0)^2 + 1$

The Ri dependent parameterized vertical profiles of the eddy diffusivity fit better in the case of A2 and are clearly too low in the case of A3 (Figure 3, upper panel). These parameterizations fail to some extent in the lower part of pycnocline (layer 15-21 m) in all three time series. The fit in the layer below (21-47 m) is characterized in the following way: (1) in case A1 K_{Meier} nicely follows the changes in depth but is shifted to smaller values; (2) in case A2 both K_{Meier} and K_{Pac} fits quite well; (3) in case A3 both are strongly shifted towards small values. Relying on series mean vertical profiles (Figure 3, upper panel) we can

summarize here that in the case of our measurements at the entrance of the Gulf of Finland the parameterization scheme by Meier is more sensitive to Ri changes but the discrepancy to the measurement data is larger than for the Pacanovski and Philander scheme. However both these parameterization schemes are not able to describe the mean measured profiles for all three time series – namely A3 has 4-5 times larger bias as A1 and A2 (Figure 3, upper panel). Thus we continue to seek a parameterization and/or simulation scheme which will describe equally well all three time series.

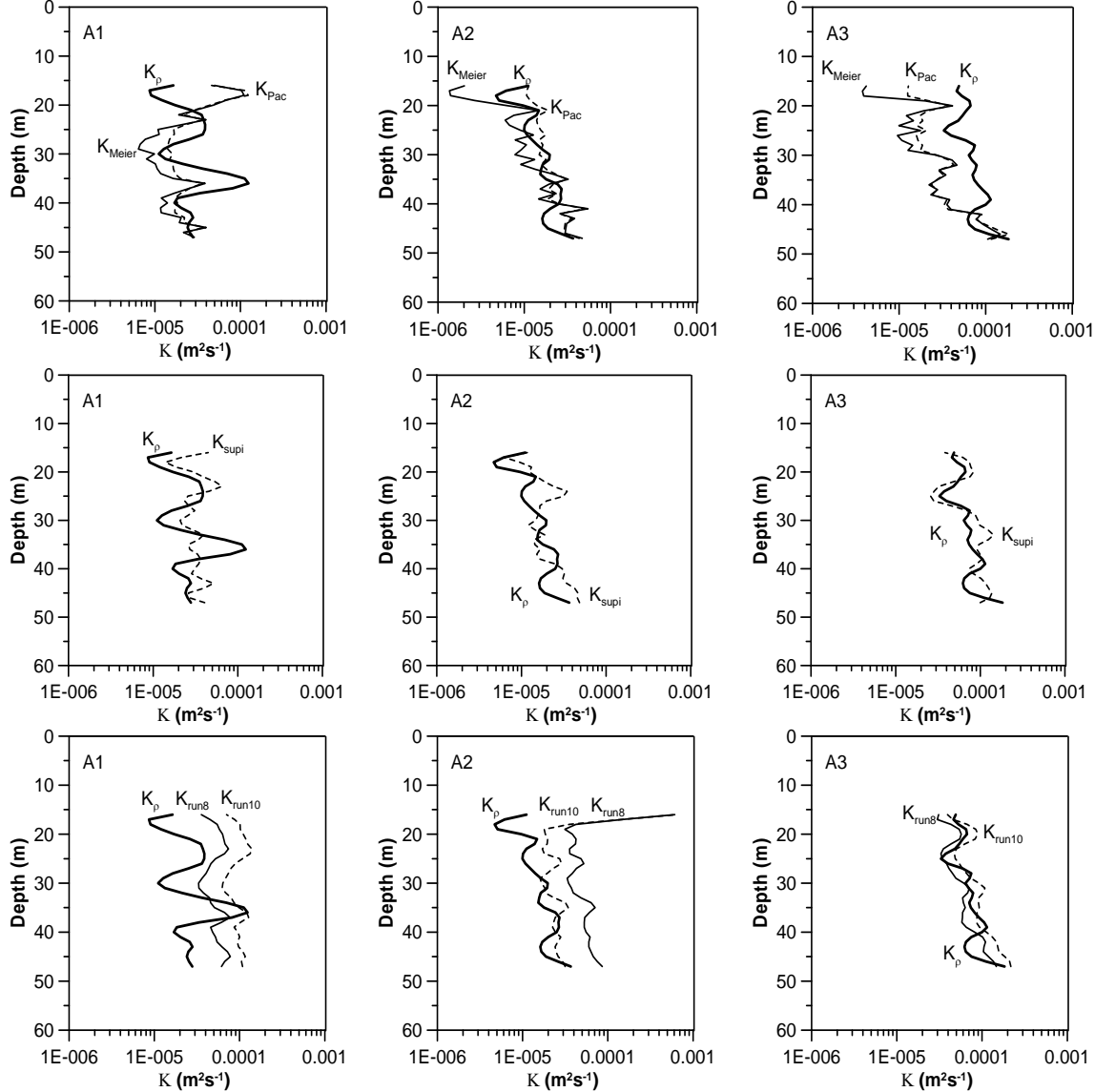


Figure 3. For the three time series A1, A2 and A3 the time averaged profiles of measured eddy diffusivity in reference with parameterized using Pacanowski and Philander and Meier schemes (upper panel), parameterized using the new scheme (middle panel), simulated by standard and new scheme k - ϵ model (lower panel, lines marked as K_{run8} and K_{run10} respectively).

Simulated eddy diffusivity by standard k - ϵ model

We simulated the eddy diffusivity (Figure 3, lower panel) using a two equation k - ϵ turbulence closure (GOTM). Different modeling scenarios were tested, applying either only

meteorological forcing or additional forcing by measured current velocities. It was necessary to relax the simulated temperature and salinity to the measured ones, because advective processes were important in that area. The adjustment of simulated values to the measured reference time series A2 gave large bias for time series A3 and vice versa adjusting the model values to the values of time series A3 produced large biases for A1 and A2 (Figure 3, lower panel, $K_{\text{run}8}$). Therefore here the standard k - ϵ model (GOTM) similar to the schemes described above was not able to simulate equally well all three time series (or in other words to separate time series with diverse mean values) (Figure 3, lower panel, $K_{\text{run}8}$).

New parameterization of eddy diffusivity

For the deep ocean (Gargett, 1984; Gargett and Holloway, 1984) as well as for the Baltic Sea (Stigebrandt, 1987) the parameterization of eddy diffusivity

$$K = aN^l, \quad (2)$$

with a constant a was successfully used. In our case the 3 different measurement series have 3 different mean N values. Still the parameterization (2) does not provide the right order of the time series, as A2 has the smallest mean measured K_ρ but not the largest N to rank the parameterized K in order of the measured K_ρ . Therefore the scheme (2) with constant a value is not suitable for our task to separate time series with diverse mean eddy diffusivity values. However it was proposed (Stigebrandt, 1995; Axell, 1998) that a could depend on energy fluxes of local sources. Axell speculated (2002) about the physical interpretation of a in "(2)" and found that combining the Osborn (1980) model for eddy diffusivity ($K \sim \epsilon N^2$) and the common turbulence scaling (eddy viscosity $v_t \sim k^2 \epsilon^{-1}$ (Rodi, 1980)) the eddy diffusivity should scale as

$$K \sim kN^l, \quad (3)$$

where k denotes turbulent kinetic energy (TKE) density. Relying on "(2)" and "(3)" he concluded that a could be related to the mean background level of the TKE due to unresolved shear resulting from the direct input of wind energy.

Here we propose to parameterize our measured eddy diffusivity using the following equation:

$$K_{\text{supi}} = \gamma E_{\text{kin.supi}} N^l, \quad (4)$$

which is similar to (3) where a is substituted by $\gamma E_{\text{kin.supi}}$. This parameterization separates series A1 and A3 from A2 in the right way (Figure 3, lower panel) and gives reasonably similar vertical profiles compared to the measured eddy diffusivity.

New simulation of eddy diffusivity

Two-equation turbulence models, such as the k - ϵ model (Rodi, 1987) are widely used to model eddy viscosity and diffusivity within the water column. These models are usually only forced by surface momentum and buoyancy fluxes. They have been successfully applied to reproduce turbulence levels in the surface and in the bottom layer (Simpson *et al.*, 1996; Stips *et al.*, 2002). However it is also well established that such models fail to simulate the observed levels of dissipation rate in and below the pycnocline by several orders of magnitude (Stips *et al.*, 2002; Rippeth, 2005).

As the turbulence generation is based on the available TKE resulting from buoyancy and resolved current shear, this fact points to a missing source of TKE in and below the pycnocline. In order to avoid the model predicting unrealistic low dissipation rates at mid-water depth, a lower limit for the TKE is usually introduced (Mellor, 1989; Burchard *et al.* 1998). This practically represents a crude parameterization of additional TKE generation from unresolved internal wave breaking. As it can be expected that spatial and temporal variations

of this background level of TKE really exist, Axell (2002) proposed an improved parameterization. In his parameterization the lower limit of TKE (further TKE_{min}) is made a function of the local wind energy input. He argues that regardless of the exact nature of the generating process the internal wave energy available for deepwater mixing should be correlated with the wind energy. In his paper the energy flux density from the mixed layer is basically considered to be proportional to the cube of the wind friction velocity. This approach is however ignoring the fact that for the generation of internal waves not only the local wind energy is important, but also the change of the wind direction as well as geostrophic adjustment of coastal jets and mesoscale eddies. This is actually indirect supported by Lass *et al.* (2003), who could not find any correlation of the dissipation variability in the deeper interior with the local wind fluctuations. Indeed the respective trial to simulate our measurements using the parameterization according to Axell (2002) was not successful.

We are therefore proposing a different approach, which is in line with the ideas presented above, that this additional source of TKE is derived from super inertial current shear. As stated above internal waves with frequencies higher than the inertial frequency could be responsible for the explained additional turbulence generation which takes place during series A3. We therefore parameterized this energy in the “midcolumn” (excluding upper mixed layer and bottom layer) by making TKE_{min} a function of vertically averaged super-inertial frequency band kinetic energy. Written in a simplified way this parameterization looks for our example like:

$$TKE_{min}(t) = \lambda * E_{kin.supi(20m-45m)}(t), \quad (5)$$

where t shows the time dependency and the exact value of λ could be experimentally determined. For testing our hypothesis we set $\lambda = 0.01$, assuming that at least 1% of the available kinetic energy might be converted to turbulence. It can be seen (Figure 3, lower panel, run10) that this new approach explains the different levels of dissipation rate and eddy diffusivity qualitatively correctly. Especially the separation of low level turbulence case A2 from other cases A1 and A3 with enhanced turbulence is clearly realized which was not reproduced by any of the standard simulations.

To assess qualitatively the ability of the presented schemes to describe equally well all three time series mean eddy diffusivity profiles we introduce the AADB (Averaged Absolute Difference of Biases) (Table 3). The AADB considers the fact that we prefer the schemes which give the bias toward the same direction for all three time series. According to AADB (Table 3) the new parameterization scheme which considers the superinertial waves kinetic energy is the best scheme to get equally well estimates of eddy diffusivities under different forcing conditions. Similarly the modified $k-\epsilon$ simulations which considered the superinertial internal wave energy gave the second smallest overall AADB value (the smallest from the simulations).

CONCLUSIONS

It has been frequently argued that near-inertial oscillations are the most energetic or at least give the highest contribution to the squared vertical shear in the Baltic Sea below the upper mixed layer (Krauss, 1981). However the 9 days ADCP current measurements within the CYANO98 experiment revealed that the described picture did not hold for the entrance to the Gulf of Finland which has an estuary like stratification and is known as an area of nearly permanent fronts. For the full measurement period (9 days) the subinertial energy (kinetic

energy of meso-scale processes) prevailed in the water column. The contributions of the inertial and sub-inertial energy bands were roughly equal for time series A3. Besides these two large energy contributors the super-inertial energy contribution was about 5% of total kinetic energy but its distribution appeared to be proportional to the turbulent kinetic energy dissipation rate (not shown). The sub-inertial current velocity vertical shear square, s^2 , dominated in the upper layer while in the layer below the pycnocline the inertial s^2 prevailed for the full measurement period (9 days). The super-inertial shear square contributed about 17% to the total mean shear square.

The measured turbulence parameters were in accordance with the wind forcing in the UML but not through the entire water column. In the layer below the buoyancy frequency maximum the dissipation rate was successfully parameterized as being proportional to both super-inertial kinetic energy density and buoyancy frequency (not shown). The parameterization of eddy diffusivity as a function of the mean Richardson number did not separate the series mean profiles in the correct order given by the measured eddy diffusivity. The parameterization with the new proposed scheme considering the super-inertial internal waves kinetic energy resulted in the right sequence of mean eddy diffusivity profiles. Only using the modified k - ϵ simulations which consider the additional internal wave energy input a good qualitative correspondence to the measured profiles could be achieved.

Table 3. Statistical characteristics of different eddy diffusivity calculation methods for the three time series.

	bias ¹			mean AV ⁴	AADB ²			RMSD ³	
	A1	A2	A3		A1	A2	A3	mean	
K _{Pac}	-0.07	0.53	-2.30	0.97	1.89	0.42	0.18	0.43	0.34
K _{Meier}	-0.43	-0.48	-2.90	1.27	1.65	0.47	0.29	0.55	0.44
K _{supi}	0.29	0.57	0.35	0.40	0.19	0.27	0.24	0.16	0.22
K _{run 8}	1.11	2.73	-0.37	1.40	2.07	0.40	0.64	0.14	0.39
K _{run10}	2.03	1.25	0.75	1.35	0.85	0.62	0.47	0.18	0.42

1) bias – difference between parameterized or simulated mean and measured mean values

2) AADB = $1/3(|A2_{bias}-A1_{bias}|+|A3_{bias}-A2_{bias}|+|A3_{bias}-A1_{bias}|)$

3) RMSD – root mean squared difference

4) mean AV – mean of absolute values

K_{Pac}, K_{Meier}, K_{supi} – eddy diffusivity parameterization schemes according to Pacanovski and Philander, Meier and this paper respectively;

K_{run 8}, K_{run 10} – eddy diffusivity simulations by GOTM using standard and in this paper proposed setups respectively.

ACKNOWLEDGEMENT

The measurement campaign CYANO98 was funded by EU project MITEC (EU DGXII MAST IC20-CT98-0111). The authors acknowledge the valuable help of many colleagues from several institutions who contributed to the CYANO98 experiment. Thanks go especially to Kaisa Kononen who was an excellent chief scientist and to Timo Huttula who provided the ADCP data. M.-J. Lilover' research was supported by a grant of the Enlargement Action of EU Commission 6th Framework Programme.

REFERENCES

- Alenius, P., Myrberg, K. and Nekrasov, A. (1998). Physical oceanography of the Gulf of Finland: a review. *Boreal Environ. Res.*, **3**, 97-129.
- Axell, L.B. (1998). On the variability of Baltic Sea deepwater mixing. *J. Geophys. Res.*, **103**, 21,667– 21,682.
- Axell, L.B. (2002). Wind-driven internal waves and Langmuir circulations in a numerical ocean model of the southern Baltic Sea. *J. Geophys. Res.*, **107**(C11), 3204, doi:10.1029/2001JC000922.
- Burchard, H., Petersen, O. and Rippeth, T. P. (1998). Comparing the performance of the Mellor-Yamada and the $k-\epsilon$ two-equation turbulence models. *J. Geophys. Res.*, **103**, 10,543–10,554.
- Gargett, A.E. (1984). Vertical eddy diffusivity in the ocean interior. *J. Mar. Res.*, **42**, 359–393.
- Gargett, A.E. and Holloway, G. (1984). Dissipation and diffusion by internal wave breaking. *J. Mar. Res.*, **42**, 15–27.
- Kononen, K., Huttunen, M., Hällfors, S., Gentien, P., Lunven, M., Huttula, T., Laanemets, J., Lilover, M.-J., Pavelson, J. and Stips, A. (2003). Development of a deep chlorophyll maximum of *Heterocapsa triquetra Ehrenb.* at the entrance to the Gulf of Finland. *Limnology and Oceanography*, **48**, 594 - 607.
- Krauss, W. (1981). The erosion of a thermocline. *J. Phys. Oceanogr.*, **11**, 415-453.
- Kullenberg, G.E.B. (1981). Physical oceanography. In: A. Voipio (ed.), *The Baltic Sea*. Amsterdam: Elsivier, pp. 135-181.
- Lass, H.-U., Prandke, H. and Liljebladh, B. (2003). Dissipation in the Baltic Proper during winter stratification. *J. Geophys. Res.*, **108**(C6), 18-1 – 18-20.
- Lilover, M.-J., Laanemets, J., Kullas, T., Stips, A. and Kononen, K. (2003). Late summer vertical nutrient fluxes estimated from direct turbulence measurements: a Gulf of Finland case study. *Proceedings of the Estonian Academy of Sciences. Biology, Ecology*, **52**(3), 193 - 204.
- Meier, H.E.M. (2001). On the parameterization of mixing in three-dimensional Baltic Sea models. *J. Geophys. Res.*, **106**, 30997-31016.
- Mellor, G.L. (1989). Retrospect on oceanic boundary layer modeling and second moment closure. In: Fifth Aha Huliko'a Hawaiian Winter Workshop, Honolulu: Hawaii Inst. of Geophy.
- Osborn, T. (1980). Estimates of the local rate of vertical diffusion from dissipation measurements. *J. Phys. Oceanogr.*, **10**, 83-89.
- Pacanowski, R.C. and Philander, S.G.H. (1981). Parameterization of vertical mixing in numerical models of tropical oceans, *J. Phys. Oceanogr.*, **11**, 1443-1451.
- Palmén, E. (1930). Untersuchungen über die Strömungen in den Finnland umgebenden Meeren. In: *Commenationes Physico-Mathematicae*, 12, Societas Scientiarum Fennica.
- Prandke, H. and Stips, A. (1998). Test measurements with an operational Microstructure-Turbulence profiler: detection limit of dissipation rates. *Aquatic Sciences*, **60**, 191-209.
- Rippeth, T.P. (2005). Mixing in seasonally stratified shelf seas: a shifting paradigm. *Phil. Trans. Roy. Soc. London, A363*, 2837-2854.
- Rodi, W. (1980). Turbulence Models and Their Application in Hydraulics—A State-of-the-Art Review. Int. Assoc. for Hydraul. Res., Delft.
- Rodi, W. (1987). Examples of calculation methods for flow and mixing in stratified flows. *J. Geophys. Res.*, **92**, 5305– 5328.
- Simpson, J.H. , Crawford, W.R., Rippeth, T.P., Campbell, A.R. and Choak, J.V.S. (1996). Vertical Structure of turbulent dissipation in shelf seas. *J. Phys. Oceanogr.*, **26**(8), 1580-1590.
- Stigebrandt, A. (1995). The large-scale vertical circulation of the Baltic Sea. In: Omstedt, A. (ed.): First Study Conference on BALTEX, Visby, Sweden, August 28-Septernber 1, 1995. Geestacht: Int. BALTEX Sect., GKSS Res. Cent., pp. 28-47.
- Stips, A., Burchard, H., Bolding, K. and Eifler, W. (2002). Modelling of convective turbulence with a two-equation $k-\epsilon$ turbulence closure scheme. *Ocean Dynamics*, **52**, 153–168.

Scenarios of multi-annual simulations of the coupled North Sea – Baltic Sea system

Adolf Stips¹, Karsten Bolding², Madis Lilover³

¹ CEC Joint Research Centre, Global Environment Monitoring Unit, TP272, Via E. Fermi, I-21027 Ispra, Italy

² Bolding & Burchard Hydrodynamics, Strandgyden 25, DK-5466 Asperup, Denmark

³ Tallinn University of Technology, Marine Systems Institute, Akadeemia 21, 12618 Tallinn, Estonia.

*Corresponding author, e-mail adolf.stips@jrc.ec.europa.eu

ABSTRACT

The Baltic Sea is a brackish semi-enclosed sea having a very limited water exchange with the more saline North Sea. The limited water exchange and large river runoff lead to typical two-layer salinity stratification with a permanent halocline located at about 60-70 meters below the sea surface.

The aim of the present study is to make scenario simulations of the coupled North Sea - Baltic Sea system using the GETM (<http://getm.eu>) hydrodynamic model. Specifically we want to test the influence of different model settings, parameterization schemes, initial conditions and of a variety of forcing conditions on the occurrences and strength of salt water inflows. The model area covers the connected Baltic Sea and North Sea, therefore no prescribed barotropic sealevel forcing in the Kattegat area is applied. Initial conditions and 3D boundary conditions are derived from climatological data. The tidal forcing is applied at the open boundaries in the English Channel and at the open North Sea. Different relatively coarse data sets for the meteorological forcing were used (ERA40, ERAIN, CLM). Despite of that coarse spatial resolution the main features of the inflow dynamics could be qualitatively reproduced. For the river inflow we used climatological data for the 30 most important rivers within the model area.

Factors that influence the water exchange comprise the large scale air pressure fields, the corresponding wind fields specifically in the channel area, the fresh water run off to the Baltic Sea, water level (filling state) of the Baltic Sea, tides, the exact bathymetry determining the cross sectional area and the related bottom friction as well as the vertical and horizontal mixing processes

A first assessment of the long term effect of the saltwater exchange is performed by comparing the salinity changes at the Gotland Deep from the different simulations. We established that the most critical forcing component is the strength of the actual wind forcing, followed by the importance of the fresh water flux. The role of the air pressure field and of the tidal forcing is smaller, but they cannot be neglected for achieving realistic simulations.

The most important GETM internal model characteristic appeared to be the used internal pressure gradient parameterization scheme, followed by the turbulence parameterization and the applied advection scheme.

KEYWORDS

Hydrodynamic modelling; Baltic Sea; density inflow.

INTRODUCTION

The Baltic Sea is a salinity stratified semi-enclosed basin located in Northern Europe. The permanent salinity stratification is maintained by the surface freshwater supply from rivers and precipitation and by the bottom inflow of high saline water from the North Sea. Until recently it was believed that the bottom water in the deep sub-basins is only replaced after large storm forced mainly barotropic inflow events, so called Major Baltic Inflows (MBIs, Matthäus *et al.* 1992). The importance for the renewal of intermediate layers in the halocline of small and medium strength baroclinic inflows has been demonstrated by (Feistel *et al.* 2006). Mohrholz *et al.* (2006) have shown, that during the past 2 decades the frequency of large barotropic inflows has decreased, whereas the frequency of medium intensity baroclinic inflows has increased.

Many different factors are influencing the water exchange between the North Sea and the Baltic Sea and specifically the inflow of salty and oxygen rich water to the deeper Baltic basins like the Gotland Sea. These factors comprise the large scale air pressure fields over the entire area, the resulting wind fields specifically in the channel area, the fresh water run off to the Baltic Sea, water level (filling state) of the Baltic Sea, tides, the exact bathymetry determining the cross sectional area and the related bottom friction as well as the vertical and horizontal mixing processes which are diluting the inflowing water masses.

Conceptual models (Lass *et al.* 1996 and Gustafsson *et al.* 2001) could qualitatively show that the two major factors determining the occurrence of MBIs are the filling state of the Baltic Sea (as represented by the Landsort sealevel) and the large scale pressure field over the North Sea and Baltic Sea area which determine the strength of the barotropic pressure gradient. Only recently the smaller but nevertheless important role of the baroclinic pressure gradient in driving small salt water inflows was experimentally discovered by Feistel *et al.* (2003)

Contrary to the general understanding of the main processes achieved, until recently the detailed 3D hydrodynamic modeling of salt water inflows was not completely satisfactory. In most personal communications from model studies it was told that despite the adequate reproduction of the general features the inflowing salt water along its way through the different basins (from the Belt Sea via Arkona Sea, Bornholm Sea into the Gotland Sea) became too diluted and therefore lost its density and finally could not enter in sufficient amounts or not deep enough into the Gotland Basin.

As the main reason for this dilution process an unrealistically high numerical diffusion of current state of the art models is suspected (Burchard and Rennau, 2008). Depending on the characteristics of the model used there are at least two different reasons proposed for the occurrence of this excessively high mixing: firstly artificial mixing at the step like bottom topography for z-coordinate models and secondly pressure gradient errors for σ -coordinate models.

Despite the fact that this problem has been known for many years and is investigated by several different research groups extended and systematic studies of the importance of the different factors influencing the salt water inflow to the Baltic Sea have not been done. Even very fundamental questions about the role of the local wind field in driving or preventing salt inflows to the Baltic proper have not been well investigated. Here we will present a first attempt to separate the importance of the different processes and parameters. For doing that we are applying the public domain General Estuarine Transport Model (GETM, Burchard and Bolding, 2002, www.getm.eu), which had been used successfully for performing realistic simulations Stips *et al.* 2004.

MODEL IMPLEMENTATION

General features

GETM solves the three-dimensional hydrostatic equations of motion by applying the Boussinesq approximation and the eddy viscosity assumption. Vertical subgrid scale mixing is parameterized using a turbulence closure with flux boundary conditions. The turbulence scheme for vertical mixing in GETM is selected via the GOTM (General Ocean Turbulence Model, www.gotm.net) turbulence model. In this study we applied the standard k- ϵ turbulence closure. A simple parameterization for considering the additional mixing effect of breaking internal waves can be included. The model allows the application of different schemes for vertical as well as for horizontal coordinates.

Different numerical schemes for tracer advection are implemented and can be used. For this study we mainly used the ULTIMATE quickest algorithm, but we also compared to the simple upstream advection scheme. A background harmonic diffusion of $AH=10 \text{ m}^2 \text{ s}^{-1}$ is applied. For details of the model the reader is referred to Burchard and Bolding, 2002.

Implementation details

The GETM model was implemented for the coupled North Sea Baltic Sea area using different grid sizes of 6 nm, 3 nm and 2'x3' applying cartesian or spherical coordinate systems respectively. These grids have been generated from different sources of bathymetric data, comprising the DYNOCs bathymetry, the IOWTOPO data (Seyfert and Kayser, 1995) and the GEBCO global 1' topographic data set. Further different filters were applied for smoothing the bathymetry, as this is required for terrain following coordinates which have been used for these simulations. As an example the 3'x2' bathymetry generated in such a way is shown in Fig. 1, which also provides an impression of the model area. It should be mentioned that the difficulty of simulating salt water inflows using such a large coupled domain is considerably increased, as the very important Kattegat water level which is determining the barotropic pressure gradient cannot be prescribed.

The barotropic time step had to be adjusted to the respective horizontal resolution. The split factor between barotropic and baroclinic mode was typically 30. Open boundaries of the model domain are existing between the North Sea and the North Atlantic and the English Channel. Climatological river runoff from 33 major rivers was used for the fresh water input. The model was initialized using the climatological temperature and salinity data compiled by Jannssen *et al.* 1999. For the open boundary conditions at the Atlantic these climatological data were also applied via a sponge layer formulation. Meteorological forcing data were provided by the European Centre for Medium Range Weather Forecasting (ECMWF, www.ecmwf.int). The following basic data were extracted from the ECMWF data base: air pressure, air temperature, total cloud cover, wind speed (east and north component), dew point temperature, precipitation and evaporation. The time step of the data is 6 hours and the downscaled spatial resolution is approximately 0.5 degrees. The data are interpolated in space and time to the respective model grid.

For the tidal forcing at the open boundaries the parameterization derived from the TOPEX-POSEIDON data set has been used, see podaac.jpl.nasa.gov/cdrom/tide. The extracted data are linearly interpolated in time and space to the open boundary elevation points.

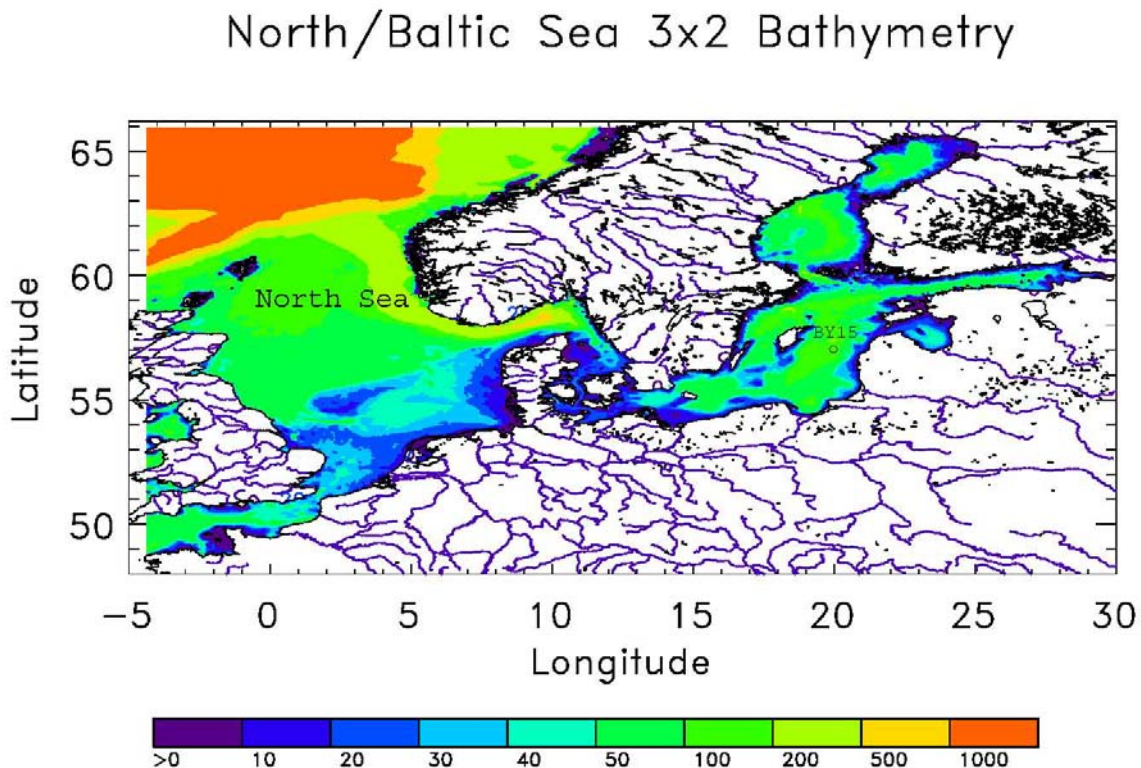


Figure 1. Bathymetry of the coupled North Sea - Baltic Sea setup. The monitoring station BY15 in the central Baltic Proper (Gotland Sea) is indicated by a circle.

Scenario simulations

The main characteristics of the simulations here presented are summarized in Table 1. The standard setup (Run0, r0) used 30 vertical layers, fresh water flux (FWF) from rivers and from the atmosphere, tidal forcing at the open boundaries, complete meteorological surface forcing and a smoothed bathymetry. For the calculation of the internal pressure gradient (IP) the Blumberg-Mellor scheme (Blumberg and Mellor, 1987) was used. For the different scenarios (run1 to run19 here) selected forcings or other features were deactivated, to assess their relative importance to the overall quality of the simulation. For run r4 the number of vertical layers was reduced to 15 and for run19 it was increased to 45.

The simulation r0, starting from climatology in January 1997 represents the basic reference run. The runs usually extend from the year 1997 until the end of 2007, but some runs (r9) were started already in 1986. During the first year (1997) the model has to adapt to the artificial initial density stratification taken from the climatological data. During the first phase of this process the salinity is decreasing at an unrealistically high rate, resulting from strong transport and exchange processes. This adaptation process seems to last about one year for the GETM model. At the end of the first year the bottom salinity in the deep basins has approached the original starting value again.

For the purpose of this investigation we use as a simplified measure of model performance the change of the salinity in the bottom layer at the central station BY15 (57.3° N, 20° E, see Fig. 1) in the Gotland basin. The total change of bottom salinity after 10 years of simulation for the different runs is given in Table 2. In the reference run the salinity increased during these 10 years by 0.34 PSU, which is slightly less than the 0.5 PSU increase resulting from the measured data taken from the monitoring programme. Changing now different components of the forcing and the setup we compare their relative influence with respect to the reference run.

Table 1. Summary and characteristics of the analyzed runs for the scenario simulations.

	Forcing	Start year	Comments
Run00 (r0)	FWF, rivers, tides, wind, air pressure, smoothed, 30L	1986	Reference run
Run01 (r1)	FWF, no rivers, tides, wind, air pressure, smoothed, 30L	1997	No rivers
Run02 (r2)	FWF, rivers, no tides, wind, air pressure, smoothed, 30L	1997	No tides
Run03 (r3)	FWF, rivers, tides, wind, air pressure, unsmoothed, 30L	1997	Unsmoothed bathymetry
Run04 (r4)	FWF, rivers, tides, wind, air pressure, smoothed, 15L	1997	Only 15Levels
Run05 (r5)	FWF, rivers, tides, no wind, air pressure, smoothed, 30L	1997	No wind
Run06 (r6)	FWF, rivers, tides, wind, no air pressure, smoothed, 30L	1997	Constant air pressure
Run07 (r7)	FWF, rivers, tides, wind, air pressure, smoothed, 30L	1997	Different IP scheme 4
Run08 (r8)	FWF, rivers, tides, wind, air pressure, smoothed, 30L	1997	Different IP scheme 6
Run09 (r9)	No FWF, rivers, tides, wind, air pressure, smoothed, 30L, starting earlier	1986	Starting earlier
Run13 (r13)	FWF, rivers, tides, wind, air pressure, smoothed, 30L	1997	Simple turbulence
Run16 (r16)	FWF, rivers, tides, wind, air pressure, smoothed, 30L,	1997	Simple advection (Upstream)
Run17 (r18)	FWF, rivers, tides, wind, air pressure, smoothed, 30L,	1997	Wind=Wind*1.3
Run18 (r18)	FWF, rivers, tides, wind, air pressure, smoothed, 30L,	1997	Wind=Wind*0.7
Run19 (r19)	FWF, rivers, tides, wind, air pressure, smoothed, 30L, 45Levels	1997	45Levels

The expected high importance of the riverine fresh water input not only for the surface salinity, but also for the bottom salinity is evidenced by run r1 (Table 2). The bottom salinity increases after the usual initial drop in almost all the years, with a rate of 2.9 PSU in 10 years, which is about 7.6 times more than the reference run r0. From this high sensitivity it is therefore clear that the usage of the best available river runoff data is essential for adequately simulating the Baltic Sea salinity. This was already shown by Lehmann and Hinrichsen, 2000. The importance of the applied wind forcing is investigated by the runs r5, r17 and r18 applying either no wind or increased/reduced wind during the simulation. The highest overall value for the bottom salinity is achieved by switching off the wind forcing completely (r5), which results in about 9 times higher increase compared to the reference run (Table 2). Figure 2 is showing a visualization of the temporal development of the bottom salinity at BY15 from run r17 using an increased wind speed and run r18 using a decreased wind speed compared to

run r0. The reason for the increased bottom salinity without wind or reduced wind is the strongly suppressed vertical mixing, which allows the high saline water to inflow without much dilution.

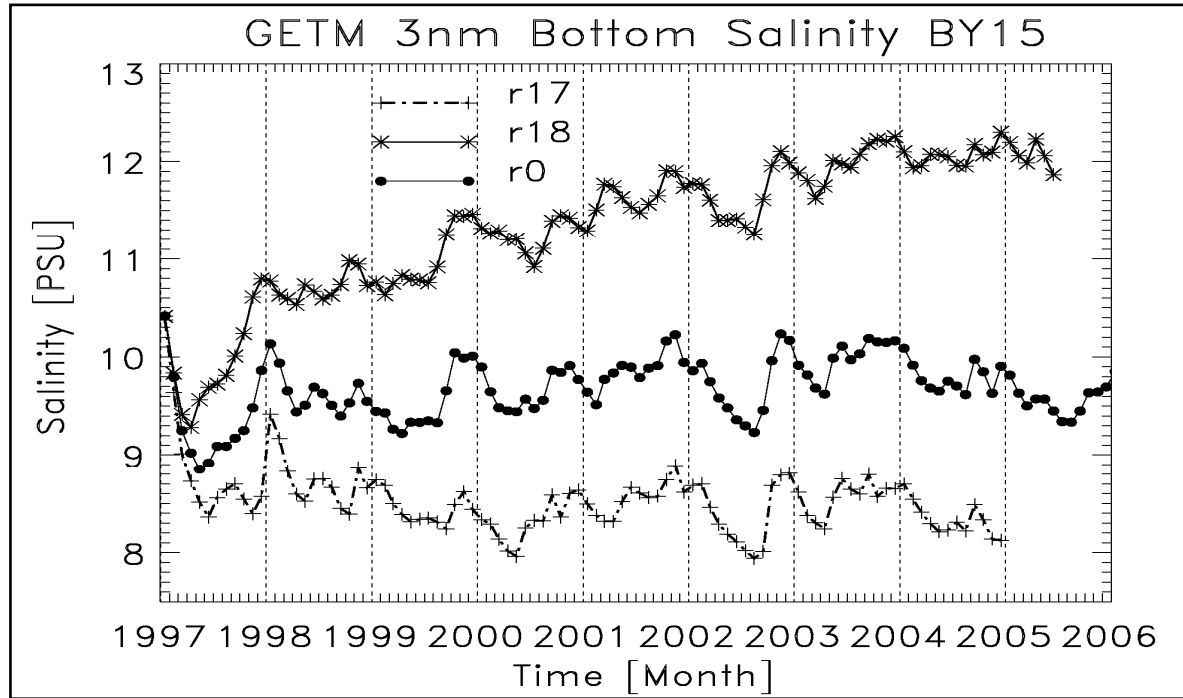


Figure 2. Temporal development of the bottom salinity at station BY15, reference run r0, increased wind speed r17 and decreased wind speed r18.

Usually the role of tides in the Baltic Sea is considered to be small. As can be seen in Table 2 for the run r2 the tidal forcing at the open boundary of the North Sea was switched off. The salinities are increased when switching the tidal forcing off and have a tendency to increase further (increase about 0.5 PSU in 10 years). This underlines the fact that despite the small influence of tidal mixing in the Baltic proper, it cannot be ignored for long term (decadal) simulations. This also demonstrates that doing simulations with all settings being equal but just not applying tidal forcing would give slightly more realistic results, then with tidal forcing, because of the reduced mixing.

The sensitivity of the bottom salinity to the complete ignorance of air pressure fluctuations (at least over such long time scales as considered here) and to a 50% reduction of the number of used layers is surprisingly small (Table 2). In both cases the simulations follow the reference run rather close.

General vertical coordinates as used in this study are terrain following and therefore allow a good representation of dense water inflows Burchard *et al.* 2005, whereas special measures must be applied to achieve equally good results in z-level models Meier, 2007. Unfortunately the disadvantage of using terrain following coordinates is often increased artificial mixing due to numerical errors in the calculation of the internal pressure gradient over steep topography Mellor et al. 1998. Therefore the realistic rough bottom topography is usually smoothed before doing simulations with terrain following models (Martinho and Batten, 2006). Not applying the normal smoothing will lead to a little increased mixing in the model domain and therefore the bottom salinities are reduced, as can be seen in Table 2 run r3.

The simulations are very sensitive to changes in the applied advection scheme. Instead of the total variance diminishing (TVD) scheme used for the reference run we used a simple upstream advection scheme for run16. For a visual impression of the result the temporal changes of the bottom salinity are also shown in Figure 3. Due to the high diffusive character

of the upstream advection scheme the bottom salinity is decreasing quite strong during the simulation period.

A very similar but even more pronounced effect has the substitution of the two-equation $k-\epsilon$ turbulence model by a simple constant background diffusivity (the canonical value of $10^{-4} \text{ m}^2 \text{ s}^{-1}$ has been chosen), as can be seen from run r13 in Table 2. Obviously such a simple turbulence parameterization (still often applied in General Circulation Models), leads again to far too high vertical mixing, thereby diluting the inflowing salt water too much.

Finally we present here also results from the run r8, which uses the more sophisticated internal pressure gradient calculation scheme published by Shchepetkin and Mc Williams, 2003. Unfortunately the result is rather disappointing as the lowest overall bottom salinity after the 10 year simulation period is achieved and the reason for this unexpected behaviour is unclear.

Table 2. This gives a summary of the change of bottom salinity at the central Gotland Sea station BY15 after 10 years of simulation. Given are the absolute change in PSU and the change relative to the reference run r0.

(1998-2007)	Absolute change [PSU]	Relative to r0 [PSU]	Ratio (sensitivity index)	Comment
Run05 (r5)	3.44	3.10	9.1	No wind
Run01 (r1)	2.92	2.58	7.6	No runoff
Run18(r18)	1.64	1.98	5.8	Wind*0.7
Run02 (r2)	0.57	0.23	0.7	No tides
Run06 (r6)	0.38	0.04	0.1	No air pressure variation
Run00 (r0)	0.34	0.00	0.0	Reference
Run04 (r4)	0.31	-0.03	-0.1	15 Levels
Run03 (r3)	0.24	-0.10	-0.3	No bathymetry smoothing
Run16(r16)	-0.91	-1.25	-3.7	Upstream advection
Run13(r13)	-1.29	-1.63	-4.8	Simple turbulence
Run08 (r8)	-1.78	-2.12	-6.2	Sophisticated pressure gradient

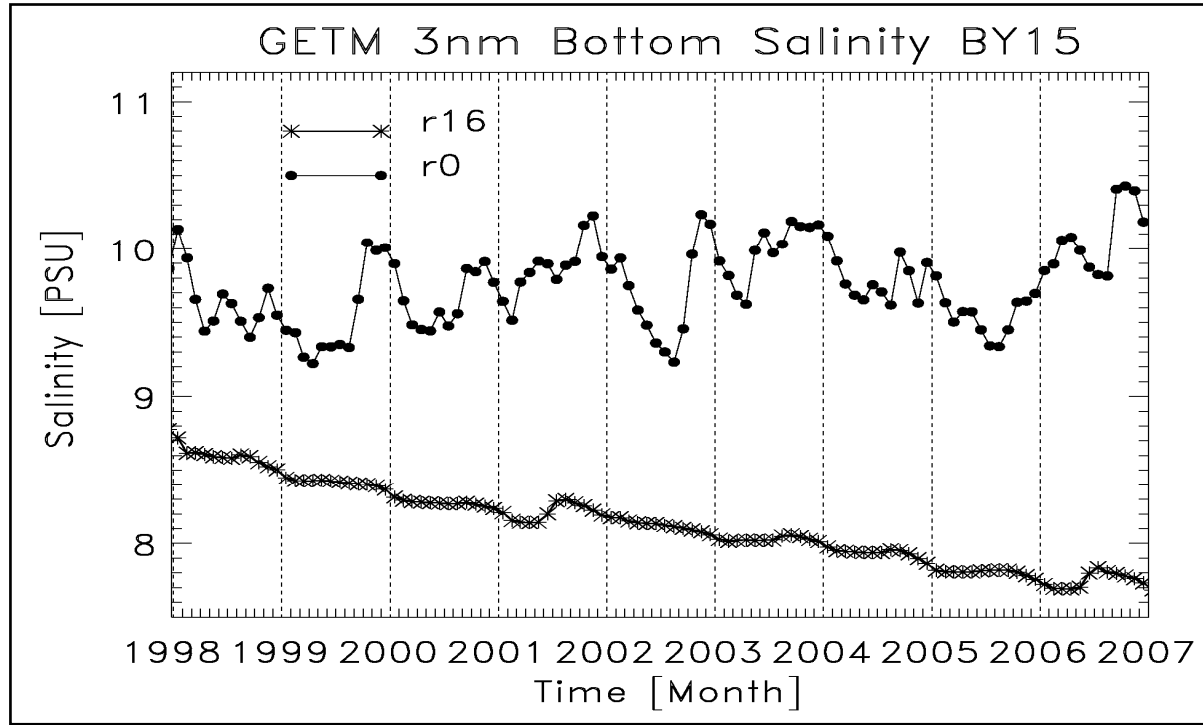


Figure 3. Temporal development of the bottom salinity at station BY15, reference run r0 using a TVD advection scheme compared to run r16 applying a simple upstream advection scheme.

CONCLUSIONS

An attempt was made to investigate some of the factors that influence the quality of multi-annual simulations of the complicated large scale estuarine basin like the Baltic Sea. Despite the fact that many studies have dealt with the circulation in the Baltic Sea experimentally or by simulation, there are still many open questions related to the pathways of the inflowing salt water in the various sub basins. The role of upwelling stirred by the topography and of diapycnal mixing caused by breaking internal waves is still not understood. Here we were able to show that the simulated bottom salinity far away from the Baltic Sea entrance area has its greatest sensitivity with regard to the applied fresh water fluxes, wind field and tidal forcing as external model forcing data. The details of the numerical implementation of the model as the used advection scheme, the turbulence model and pressure gradient scheme are of at least the same importance as the boundary forcing.

It seems still to be necessary to significantly improve current hydrodynamic models to achieve more realistic simulations and to improve the applied boundary conditions. One way in this direction might be to introduce so called adaptive coordinates Burchard and Beckers, 2004, which might be able to avoid some of the major drawbacks of currently used coordinate systems.

ACKNOWLEDGMENT

We thank the GETM development team for their continuous enthusiasm and support in helping to improve and to run the model. The measured data for this study were provided by the Baltic NEST database. Excellent informatics support was given by Philippe Simons and Francesco Andreozzi.

REFERENCES

- Blumberg A.F. and G.L. Mellor, A description of a coastal ocean circulation model, in Three dimensional ocean models, N.S. Heaps, Ed., American Geophysical Union, Washington D.C., 1-16, 1987.
- Burchard H. and K. Bolding, GETM – a general estuarine transport model – scientific documentation, European Commission, Tech. Rep. EUR 20253 EN, 157pp, 2002.
- Burchard H. and J.M. Beckers, Non-uniform adaptive vertical grids in one-dimensional ocean models, *Ocean Modelling*, 6, 51-81, 2004.
- Burchard H. et al., Dynamics of medium-intensity dense water plumes in the Arkona Basin, Western Baltic Sea, *Ocean Dynamics*, 55, 391-402, 2005.
- Burchard H. and H. Rennau, Comparative quantification of physically and numerically induced mixing in ocean models, *Ocean Modelling*, Volume 20, Issue 3, 2008, Pages 293-311
- Feistel R. et al., Warm waters of summer 2002 in the deep Baltic proper, *Oceanologia*, 45, 571-592, 2003.
- Feistel R., G. Nausch, W. Matthäus and E. Hagen, Temporal and spatial evolution of the Baltic deep water renewal in spring 2003, *Oceanologia*, 46, 581-598, 2003.
- Feistel R., G. Nausch and E. Hagen, Unusual Baltic inflow activity in 2002-2003 and varying deep-water properties, *Oceanologia*, 48, 21-35, 2006.
- Gustafsson B.G. and H.C. Andersson, Modeling the exchange of the Baltic Sea from the meridional atmospheric pressure difference across the North Sea, *Journal Geophysical Research*, C106, 19731-19744, 2001.
- Jannssen F., C. Schrum and J. Backhaus, A climatological dataset of temperature and salinity for the North Sea and the Baltic Sea, *Deutsche Hydrographische Zeitschrift*, 9, 245pp, 1999.
- Lass H.U. and W. Matthäus, On temporal wind variations forcing salt water inflows into the Baltic Sea, *Tellus A*, 48, 663-671, 1996.
- Lehmann A. and H. Hinrichsen, On the thermohaline variability of the Baltic Sea, *Journal of Marine Systems*, 25, 333-357, 2000.
- Matthäus W. and H. Franck, Characteristics of major Baltic inflows – a statistical analysis. *Continental Shelf Research*, 12, 1375-1400, 1992.
- Martinho A.S. and M.L. Batten, On reducing the slope parameter in terrain-following numerical ocean models, *Ocean Modelling*, 13, 166-175, 2006.
- Meier H.E.M., Modeling the pathways and ages of inflowing salt- and freshwater in the Baltic Sea, *Estuarine Coastal Shelf Science*, 74, 717-734, 2007.
- Mellor G.L., L.Y. Oey and T. Ezer, Sigma coordinate pressure gradient errors and the seamount problem, *Journal Atmospheric and Oceanic Technology*, 15, 1122-1131, 1998.
- Mohrholz V., J. Dutz and G. Kraus, The impacts of exceptionally warm summer inflow events on the environmental conditions in the Bornholm Basin, *Journal Marine Systems*, 60, 285-301, 2006.
- Seifert T. and B. Kayser, A high resolution spherical grid topography of the Baltic Sea, Scientific report series, Institute Baltic Sea Research Warnemünde, 9, 73-88, 1995.
- Shchepetkin A.F. and J.C. McWilliams, A method for computing horizontal pressure-gradient force in an oceanic model with a nonaligned vertical coordinate, *Journal of Geophysical Research*, 108, 2003.
- Stips A., K. Bolding, T. Pohlmann and H. Burchard, Simulating the temporal and spatial dynamics of the North Sea using the new model GETM (general estuarine transport model), *Ocean Dynamics*, 54, 266-283, 2004.

Flow characteristics in a large amplitude meandering bend

Donatella Termini*

Dipartimento di Ingegneria Idraulica ed Applicazioni Ambientali, Università di Palermo,
Italy e-mail: dony@idra.unipa.it; donatella.termini@unipa.it

*Corresponding author, e-mail dony@idra.unipa.it; donatella.termini@unipa.it

ABSTRACT

Experiments on a large amplitude meandering laboratory channel have been conducted for two values of the width-to-depth ratio. Experiments show that, especially for small width-to-depth ratio, at the apex section a counter-rotating circulation cell forms near the free surface of the outer-bank region. It seems that such counter-rotating circulation cell affects the bank shear stress distribution improving the outer bank stability conditions.

KEYWORDS

Meandering channels; bank erosion; secondary circulation; laboratory flume

INTRODUCTION

A large amount of experimental research on secondary flow motion in bends has been performed.

Studies conducted in constant curved bends have highlighted that an unique secondary circulation cell develops in the central-region of each cross-section (Kikkawa et al., 1976; Zimmerman and Kennedy, 1978).

But, other studies conducted in natural channels (Bathurst et al., 1979; Dietrich and Smith, 1983) and in a strongly constant curved laboratory channel (Blanckaert and Graf, 2001), have shown that an additional counter-rotating circulation cell occurs in the outer-side of the bend. Recent investigations concerning the cross-sectional flow motion at the apex section of a large amplitude meandering flume (Termini, 2004; Termini and Piraino, 2007) have highlighted the formation of both the circulation cells. Thus, the cross-sectional flow motion seems to be obtained by the combination of the central-region cell (i.e. the classical secondary circulation cell) and the counter-rotating circulation cell forming near the free surface in the outer-bank region of the cross-section.

The presence of such counter-rotating circulation cell (Blanckaert and Graf, 1999; Termini and Piraino, 2008) exerts a strong influence on the bank shear stress distribution and, thus, on the bank erosion processes.

For given channel plane-shape and roughness conditions of the walls, the entity of the circulation motion depends on the value of the width-to-depth ratio (Yalin, 1992).

In this work, the variation of the cross-sectional flow motion along the meandering bend is analyzed on the basis of flow velocity data collected in a laboratory channel for two values of the width-to-depth ratio.

EXPERIMENTAL APPARATUS

The meandering laboratory channel, constructed at the Dipartimento di Ingegneria Idraulica ed Applicazioni Ambientali - University of Palermo (Italy), follows the sine-generated curve with a deflection angle of 110°. The channel cross-section is rectangular with width $B=0.50$

m; the banks are rigid and the bed is of quartz sand (medium sediment diameter of 0.65 mm). The initial longitudinal bed slope on the channel centerline is $S=0.371\%$. More details of the experimental installation can be found in previous works (Termini, 2004; Termini and Piraino, 2007). Two runs, characterized respectively by flow rate of $0.012 \text{ m}^3/\text{s}$ (run 1) and $0.007 \text{ m}^3/\text{s}$ (run 2), were conducted. The overall-averaged water depth was $h=0.055 \text{ m}$ (width-to-depth ratio equal to 9.02) and $h=0.03 \text{ m}$ (width-to-depth ratio equal to 16.66), respectively.

During each run the longitudinal, transverse and vertical flow velocity components were measured by using an Acoustic Doppler Velocity Profiler (DOP 2000 - by Signal Processing s.a.), as described in previous works (Termini and Piraino, 2007; 2008). The measures were carried out in many sections, opportunely selected along the channel. In this work only sections A, B, C, D and E of Figure 1 are analyzed.

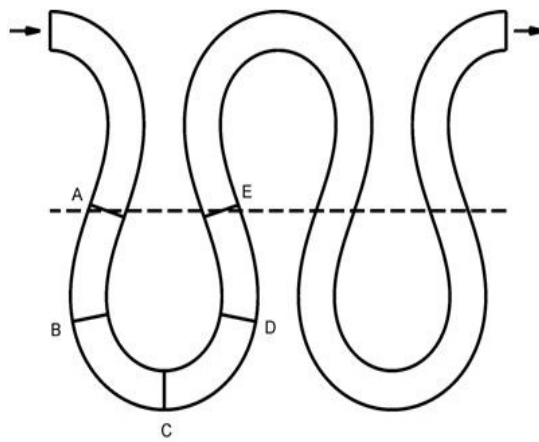


Figure 1. Measurement cross-sections

CROSS-SECTIONAL FLOW MOTION

Distribution of radial velocity component

The distributions of the time-averaged radial velocity component, v_r , estimated, for each run, in sections A÷ E are shown in Figure 2. In this figure, the background painting allows the visualization of the sign of v_r . Three regions can be identified in each cross-section: the inner-bank region ($r<10$), the central region ($10<r<42$) and outer-bank region ($r>42$). It can be observed that: in the inflection section A (see Figure 2), especially for $B/h<10$, the vectors v_r are directed toward the inner bank (negative versus) both in the inner-bank and in the central regions. Because of the local bed deformation, in a thin area of the central region the vectors change the sign near the bed. In the outer-bank region, the vectors v_r are directed toward the outer bank (positive versus). This behavior could be due to the fact that section A is still affected by the inflow conditions. In case of $B/h>10$ (run 2) no reliable data are available in the outer-bank region. At section B (Figure 2), all vectors are directed toward the outer bank for both the considered B/h ratios. At apex section C (see Figure 2), for $B/h<10$, it can be observed that v_r changes the sign: all vectors are directed toward the inner-bank both in the inner-bank region (where deposition occurs) and in the major part of the central region.

Approaching to the outer-bank region the vectors have crossed vertical profiles: near the free surface the vectors are oriented toward the outer bank (positive sign); near the bed they are oriented toward the inner bank. In the case of $B/h > 10$, the crossed vertical profiles of v_r can be found only in the central region (approximately at $r \leq B/2$).

As the channel curvature decreases, i.e. passing from section C to section D (Figure 2), for $B/h < 10$, the crossed vertical profiles of v_r are both in the central region and very close to the outer bank. In the case of $B/h > 10$, the crossed profiles are found only in the outer-bank region (where higher water depths occur). Finally, in the inflection section downstream (section E), for both the investigated B/h ratios, all vectors are oriented toward the inner bank.

It can be concluded that, especially for $B/h < 10$, crossed vertical profiles of v_r are found at the outer-bank region, along the channel reach characterized by high curvature.

Distribution of vertical velocity component

For each run, the distributions of the time-averaged vertical velocity component in the investigated sections (A-E) are shown in Figure 3.

It can be observed that: at the inflection section A, for $B/h < 10$, all vectors v_z are oriented toward the bed (negative sign). In case of run 2 ($B/h > 10$) no reliable data are available in the outer-bank region; in the central region the vectors v_z are oriented toward the bed (negative sign) while in the inner-bank region they are oriented toward the free surface (positive sign). At section B (Figure 3), for $B/h < 10$, the vectors v_z have negative sign (toward the bed) both in inner-bank region and in central region, although local changes of sign can be observed (especially near the bed and in the central-region); in the outer-bank region, except in a thin area near the free-surface, all vectors v_z are oriented toward the free surface (positive sign).

In the case of $B/h > 10$, all vectors v_z are toward the bed (negative sign) both in inner-bank region and in central region; in the outer-bank region local changes of sign of v_z can be observed. At apex section C, for both the B/h ratios, in the major part of the central-region and in part of the outer-bank region, the vectors v_z change the sign passing from the free-surface (v_z is negative) to the bed (v_z is positive).

As the channel curvature decreases, i.e. in section D, v_z changes the sign passing from the free-surface to the bed in the outer-bank region. Such behavior can be observed for both the investigated B/h ratios. In the inflection section downstream (section E), all vectors v_z are oriented toward the bed (negative sign); in the case of $B/h > 10$, they become positive (toward the free-surface) near the bed in the outer-bank region.

The distributions of v_z highlight that, especially for $B/h < 10$, also the vertical profiles of v_z show a crossed trend at the outer bank along the channel reach characterized by high curvature.

Cross-flow streamlines

In order to separate the contribute of cross-stream circulation from the average convective transport motion, the local radial flow velocity component has been decomposed into the sum of the depth-averaged value, \bar{v}_r , and its local deviation, v_r^* , in accordance with other studies (Bachelor, 1970; Bradshaw, 1987; Blanckaert and Graf, 2002).

The cross-stream flow can be visualised by the streamlines function, which is given by (Blanckaert et al., 2008):

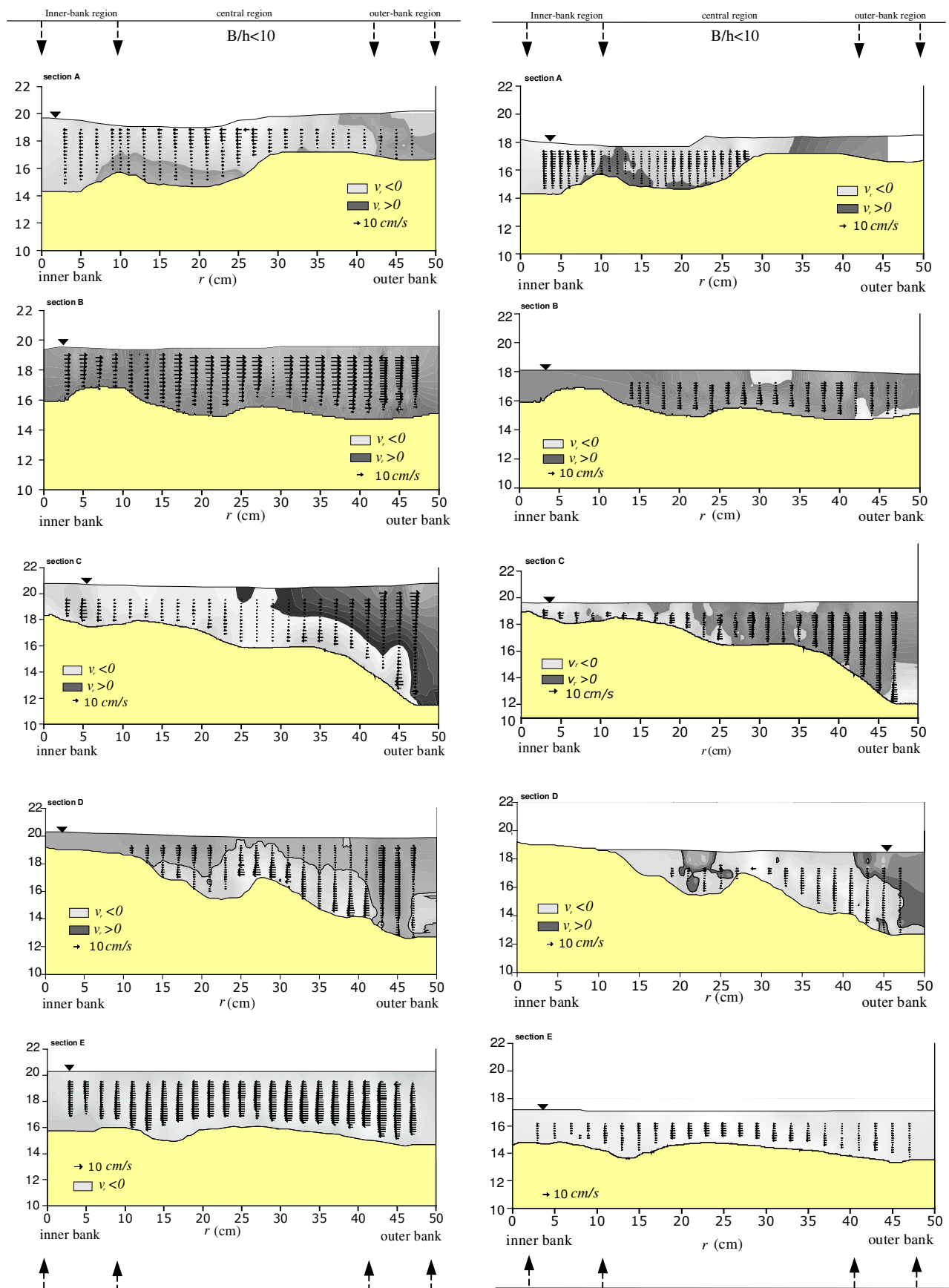


Figure 2. Distributions of time-averaged radial velocity component

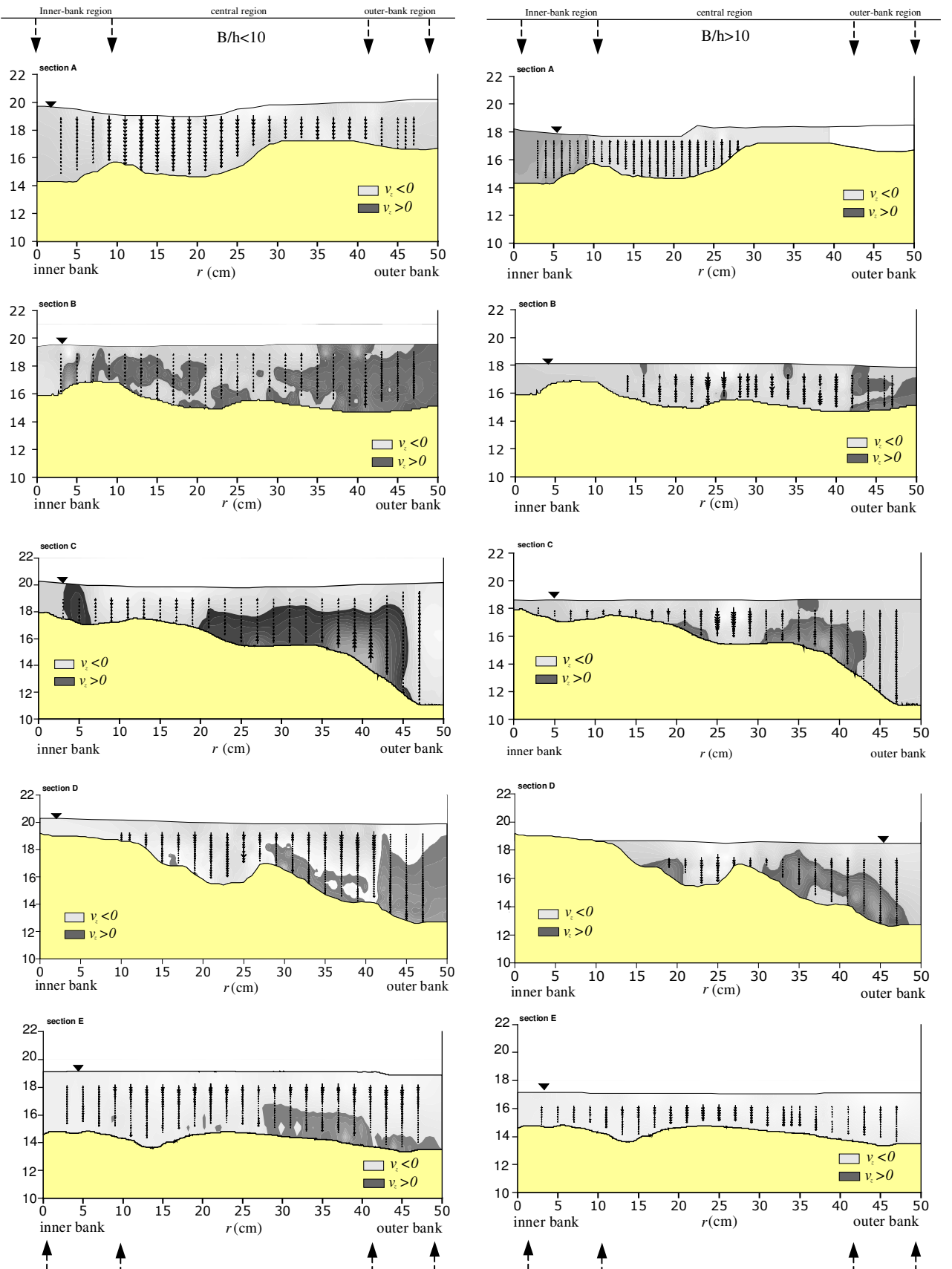


Figure 3. Distributions of time-averaged vertical velocity component

$$\psi = \frac{1}{2}(\psi_r + \psi_z) \quad (4)$$

with:

$$\psi_r = -\left(1 + \frac{r}{R}\right) \int_{z_b}^{z_{sur}} v_r^* dz \quad ; \quad \psi_z = \int_0^r \left(1 + \frac{r}{R}\right) v_z dr + cte \quad (5)$$

where r is the local radius of curvature, R is the radius at the channel axis, z_b and z_{sur} are respectively the local bed and free surface elevations. In Figure 4 the contour-lines of ψ are reported for both the investigated width-to-depth ratios. It can be observed that in section A (Figure 4), for both the B/h ratios, the streamlines do not show evident circulation cells. In the case of $B/h < 10$, a thin circulation cell seems to appear only in the outer-bank region. This is due to the changing of sign of v_r near the outer bank (Figure 2). In section B (Figure 4), the patterns are in general rather smooth for both the width-to-depth ratios. At the apex section C, three circulation cells seem to form in the case of $B/h < 10$: in the outer-bank region a first circulation cell (with negative sign) occurs near the free surface; two circulation cells (with positive sign) seem to form in the central region (but shifted toward the outer-bank region) and very near to the outer-bank. In the case of $B/h > 10$, except in a very small area near the free surface of the outer-bank region where positive contour lines of ψ thicken, no evident circulation patterns can be observed. Passing from section C to section D, i.e. as the channel curvature decreases, it can be observed that the circulation patterns observed in section C (near the free surface at the outer-bank region) extend toward the bed. Finally, in the inflection section downstream (section E), for both the width-to-depth ratios, the contour lines of ψ are again smooth as previously observed in section A.

Thus, the ψ patterns highlight the formation of a secondary counter-rotating circulation cell, especially in the case of $B/h < 10$. This circulation cell initiates approximately at the bend entrance (section B); then it evolves until to reach the apex section (section C) and decays at the bend exit (section D).

EFFECTS ON BANK EROSION

Distribution of bank shear stress

In order to analyze the effect of the cross-sectional flow motion on bank erosion, the distributions of the bank shear stress $\tau_{rs} = -\rho \overline{v'_r v'_s}$ (where v'_i ($i=r,s$) represents the instantaneous fluctuation component in direction i ; the over-bar indicates the time-averaged value) have been examined for the case of $B/h < 10$.

In Figure 5 the horizontal profiles of τ_{rs} , normalized with respect to the mean shear stress $\tau = \rho u_*^2$, (with $u_* = \sqrt{g R_h S}$ - being g is the acceleration of gravity, R_h the hydraulic radius of the cross-section) are reported. In this figure, z indicates the water level with respect to an horizontal reference plane. Figure 5 shows that at section A τ_{rs}/τ increases in value approaching to the outer-bank where it reaches the higher value. At section B τ_{rs}/τ changes the sign near the outer bank; the higher value of τ_{rs}/τ is found at $38 < r < 40$. At the apex section C the higher value of τ_{rs}/τ is also found at $38 < r < 40$ but, approaching to the outer bank, τ_{rs}/τ changes again the sign assuming a peak value at $r=45$ cm, i.e. approximately at

the eye of the outer-bank circulation cell. Very close to the outer bank it rapidly decreases in value. Similar behavior can be observed in section D, but in this section the peak value is smaller than that observed in section C. No evident peak values appear in section E and the horizontal profiles of τ_{rs} / τ have a trend similar to those observed in section A.

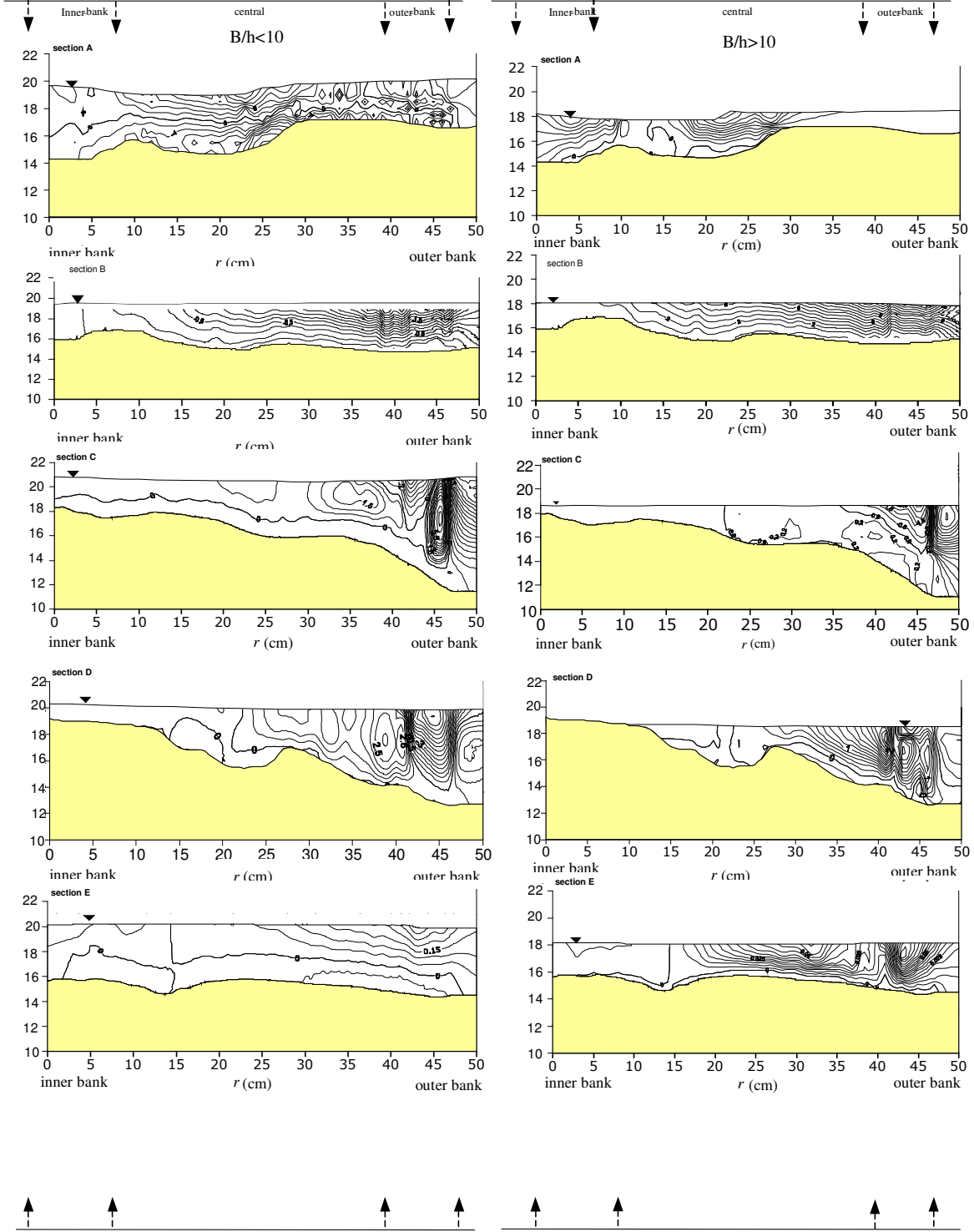


Figure 4. Contour-lines of the stream-line function

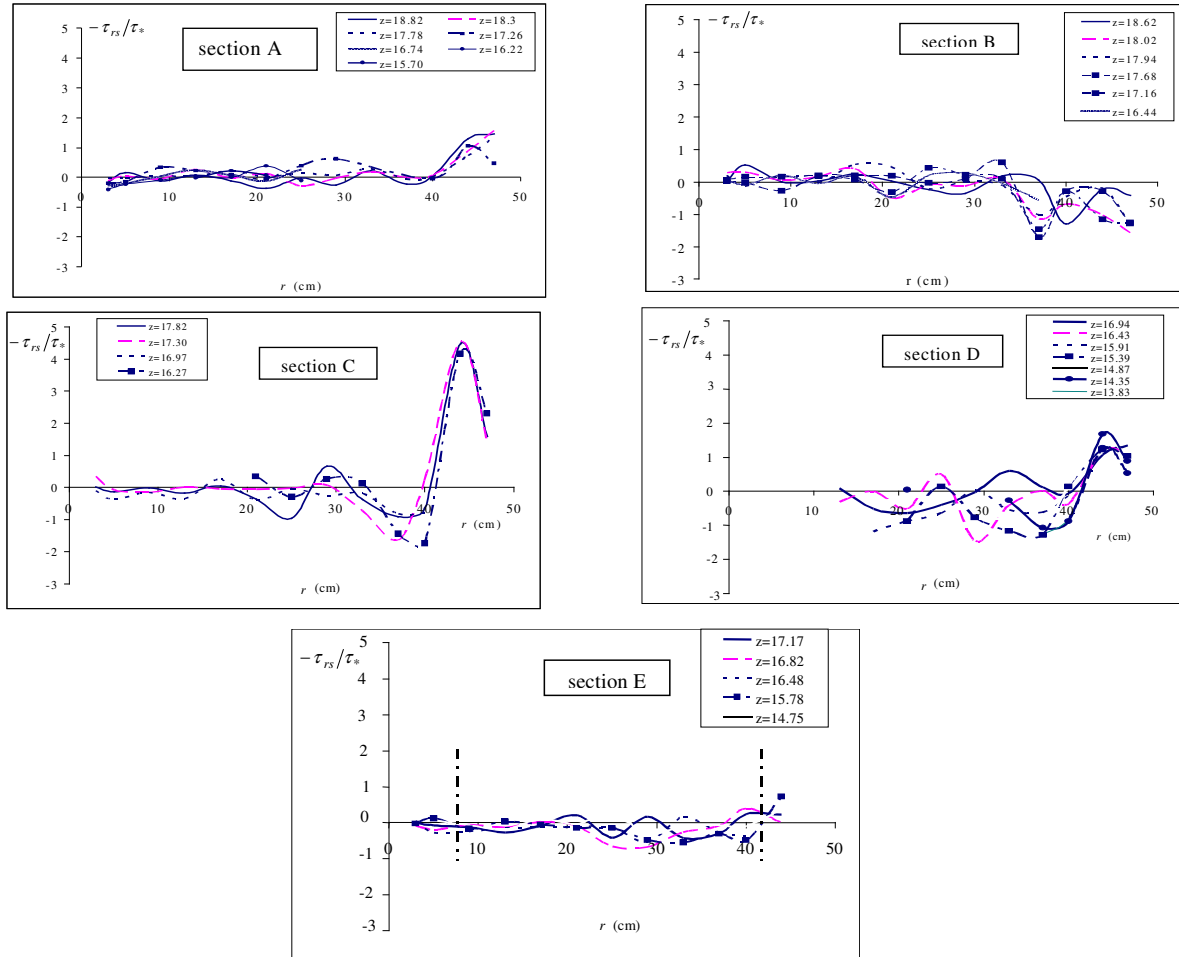


Figure 5. Horizontal profiles of $-\tau_{rs} / \tau_*$

DISCUSSION AND CONCLUSION

Experiments show that, at the bend entrance, besides the central-region circulation cell, a counter-rotating circulation cell forms near the free surface of the outer-bank region. Such outer-bank circulation cell is fully developed at the bend apex and it decays at the bend exit. This flow behaviour can be observed only for $B/h < 10$. For $B/h > 10$ the main circulation cell is not significant and a weak outer-bank circulation cell appears only at the apex section. The presence of the outer-bank circulation cell allows to maintain very low values of the bank shear stress, τ_{rs} , close to the bank. The effect decays at the bend exit.

REFERENCES

- Batchelor, G.K. (1970). An introduction to fluid dynamics. Cambridge Univ. Press. Cambridge U.K.
- Bathurst, J.C., Thorne, C.R., Hey, R.D. (1979). Secondary flow nad shear stress at river bends. *Journal of Hydr. Div.* **105(10)**. 1277-1295.
- Blanckaert, K. & Graf, W.H. (1999). Outer-bank cell of secondary circulation and boundary shear stress in open-channel bends; I.A.H.R. Symposium on River, Coastal and Estuarine Morphodynamics; Genova, September 6-10
- Blanckaert, K. & Graf, W.H. (2001). Mean Flow and Turbulence in Open-channel Bend; *Journal of Hydraulic Engineering*, 127(10), pp. 835-847.
- Blanckaert, K. & Graf, W.H. (2002) Secondary currents measured in sharp open channel Bend. *International congress River Flow 2002*, 4-6 September, Belgium, pp 117-125.

- Blanckaert, K., Buschman, F.A., Schielen, R., Wijbenga, J.H.A. (2008). Redistribution of velocity and bed-shear stress in straight and curved open channels by means of a bubble screen laboratory experiments- *J. of Hydr. Eng.*, **134(2)**, 184-195.
- Kikkawa, H., Ikeda, S. & Kitagawa, A. (1976). Flow and Bed Topography in Curved Open Channels, *J. Hydr. Div.* - ASCE- 102(9), Proceeding paper 12416, 1327-1342.
- Bradshaw, P. (1987). Turbulent secondary flows. *Annu. Rev. Fluid. Mech.* **19**, 53-74
- Dietrich, W.E. & Smith, D. (1983). Influence of the Point Bar on Flow Through Curved Channels, *Water Resources Research*, **19(5)**: 1173-1192.
- Termini, D. (2004). Flow in meandering bends, *International Congress Riverflow*, Napoli 23-25 June, 109-117.
- Termini, D. & Piraino, M. (2007). Secondary circulation motion in the apex section of a large amplitude meandering flume, 32nd Congress of IAHR, The International Association of Hydraulics Engineering and Research, Venice, 1-7 July.
- Termini, D. & Piraino, M. (2008). Experimental investigation of the evolution of secondary motion in a large amplitude meandering flume, *International Congress Riverflow2008*, Izmir-Turkey 3-5 Sept, pp 1279-1288.
- Yalin, M.S. (1992). *River Mechanics*, Pergamon Press, London.
- Zimmerman, C. & Kennedy, J.F. (1978). Transverse Bed Slopes in Curved Alluvial Streams, *J. Hydr. Div.*, **104(1)**, Proceeding paper 13482, 33-48.

Flow velocity and turbulence intensity distribution in a vegetated straight laboratory channel

F.G. Carollo¹, V. Ferro¹, D. Termini^{2*}

¹ Dipartimento di Ingegneria e Tecnologie Agro-Forestali, Università di Palermo, Italy

² Dipartimento di Ingegneria Idraulica ed Applicazioni Ambientali, Università di Palermo, Italy E-mail:

*Corresponding author, e-mail dony@idra.unipa.it ; donatella.termini@unipa.it

ABSTRACT

In this paper the flow over real flexible vegetation is experimentally studied. A 2D-ADV (Acoustic Doppler Velocimeter) is used to measure the local flow velocities, for different vegetation concentrations and varying the flow discharge and the flume slope. The hyperbolic tangent profile of a pure mixing layer proposed by Ghisalberti and Nepf (2002) is tested and the local flow velocity measures are used to evaluate the mixing-layer parameters. Finally a new theoretical law to determine the distribution of the longitudinal turbulence intensity is also presented.

KEYWORDS

Vegetation; flow velocity; turbulence; laboratory experiments.

INTRODUCTION

Natural rivers are characterized by a strong hydraulic and geomorphic complexity. Many studies conducted in this field show that the accurate estimation both of the river morphological changes and of local hydraulic characteristics of flow is necessary for restoration and protection of biodiversity. Vegetation is a key factor to analyze the interrelated system of flow, sediment transport, and morphodynamic in rivers. Effects of vegetation on flow velocity are significant and are of crucial importance for stabilizing sediments and reducing erosion along the channel. In particular, it has been generally agreed that vegetation increases flow resistance and modifies sediment transport and deposition. The analysis of the hydrodynamic conditions in vegetated channels is complex because vegetation is flexible in varying degrees and it oscillates in the flow changing position (Tsujimoto et al., 1992). Furthermore, because of temporal changing of roughness due to natural vegetative growth, the response of vegetation to the flow can change in time. In this work the flow over real flexible vegetation is experimentally studied. An Acoustic Doppler Velocimeter is used to measure the local flow velocities, for different vegetation concentrations and varying the discharge and the flume slope. The influence of both vegetation concentration and depth/vegetation height ratio on the measured velocity profiles is analyzed. The experimental velocity distributions are positively compared with the hyperbolic tangent profile of a pure mixing layer previously verified by Ghisalberti and Nepf (2002). Peculiarly, for different flow and vegetative conditions, fitting of the hyperbolic tangent profile to the experimental velocity distributions has allowed the localization of the inflection point of the velocity profile at a distance from the bed always close to the vegetation height. Furthermore a new expression to interpret the turbulence intensity distribution is proposed.

EXPERIMENTAL APPARATUS

The experimental runs were carried out in a rectangular straight flume constructed at the Dipartimento di Ingegneria Idraulica ed Applicazioni Ambientali of University of Palermo (Italy). The flume, 0.60 m wide and 14.4 m long, has a sloping bed. The water discharge was measured by an orifice plate installed in the feeding pipe. The water depth was measured by a point gauge. The measurement reach, located at 7.9 m from the entrance channel section, was 3 m long (Figure 1). The channel banks were rigid, while the channel bed was of grass, produced by a mixture of stable Loietto (50%), Festuca rubra (40%) and Poa pratensis (10%). The resulting turf was composed by ribbon-like stems large about 4-5 mm (Figure 2). The experimental runs were carried out for four vegetation concentrations, ($\delta = 280, 310, 337, 440$ stems/dm²), determined as the mean of stems per unit area, evaluated by 15 samples along the measurement reach. The flow depth was estimated as the mean of four measurements. The first measurement cross-section was at 90 cm downstream from the beginning of turf reach and the following three cross-sections had a relative distance of 40 cm. The bent vegetation height observed in presence of flow through the transparent walls, k_V , and the non-submerged vegetation height, H_V , were estimated as the mean of three measurements by three decimal rules fixed to flume wall. The experimental runs were carried out varying, for each stem concentration, the flow rate and the flume bed slope. The water depth measurements ranged from 6.1 to 27.2 cm, which corresponded to depth-vegetation height ratio values ranging from 1.02 to 6.04 and Froude numbers varying from 0.22 to 0.73 (see in Carollo et al. 2002). During experimental runs the vegetation was always inflected, both prone and waving, and characterized by an inflection degree, k_V/H_V , ranging from 0.25 to 0.73. A 2D side-looking Acoustic Doppler Velocimeter (ADV) was used for the measurements of longitudinal and transverse flow velocity components. For each measurement point the maximum sampling rate of 25 Hz was used. The local flow velocities were measured in five verticals of a cross-section located in the middle of the measuring reach. The measurements verticals were located at a distance of the wall equal to 4 cm (V1), 7 cm (V2), 14 cm (V3), 22 cm (V4) and 30 cm (axial vertical - Va). The details of the measurement techniques can be found in Carollo et al. (2002). The influence of the depth/vegetation height ratio, h/k_V , and of the stem concentration on velocity have been analyzed for sixteen of the all experimental runs. For such runs, Table 1 lists water depth h , flume slope s , discharge Q , non-submerged vegetation height H_V , stem concentration, δ and bent vegetation height, k_V . During all runs, the vegetation was submerged. Runs 1-14 were carried out with a vegetation which was always prone; while for runs 15 and 16 the vegetation was cut obtaining more rigid stems having a quasi-erect configuration.

LONGITUDINAL FLOW VELOCITY AND TURBULENCE INTENSITY EXPERIMENTAL DISTRIBUTIONS

The velocity profiles were plotted in the plane U/u^*-Y , denoting with u^* the shear velocity and with Y the relative depth equal to the ratio between the distance from the bed z and the water depth h ($Y = z/h$). As discussed in details in a previous work (Carollo et al. 2002), the analysis of the measured velocity distributions highlighted that for each velocity profile three zones, marked by two relative depths, Y_1 and Y_2 , can be identified (see in Figure 3). In zone I, i.e. for $Y < Y_1$, the velocity profile has the concavity turned toward the bottom and tends asymptotically to the vertical axis for $Y \rightarrow 0$; in zone II (for $Y_1 \leq Y \leq Y_2$) the velocity values rapidly increase and the velocity gradient along the vertical assumes its maximum value; zone

III, for distances $Y>Y_2$, is characterized by positive vertical velocity gradients which are progressively decreasing until to become null near the free surface. In other words, near the free surface, the velocity profile becomes vertical (quasi constant values of flow velocity). In zone II the logarithm velocity profile could be fitted, but the shape of the experimental velocity distribution clearly shows that an inflection point, located at a distance from the bed $Y_f=z_f/h < Y_2$ occurs.



Figure 1. Measurement channel reach

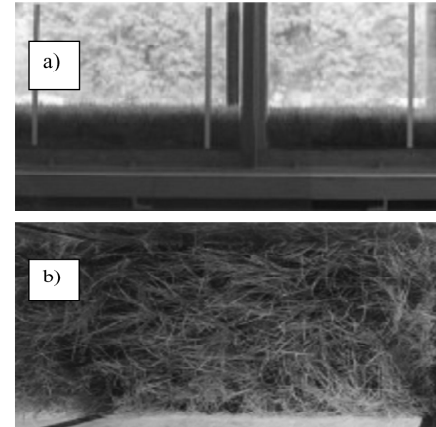


Figure 2. Side (a) and top (b) views of the vegetated bed in the case of 440 stems dm^{-2}

Table 1. Experimental data

Run	h [cm]	s [%]	Q [l/s]	H_v [cm]	δ [stems/ dm^2]	k_v [cm]
1	11.9	1.0	37.6	11.0	310	4.8
2	13.5	1.0	30.1	20.0	440	8.0
3	14.6	0.2	30.1	20.0	440	8.0
4	14.0	0.2	26.9	20.0	440	8.2
5	12.5	1.0	26.9	20.0	440	7.7
6	17.8	0.2	77.6	20.0	440	7.0
7	16.8	1.0	77.6	20.0	440	6.6
8	19.9	0.2	105.9	20.0	440	6.3
9	18.3	1.0	105.9	20.0	440	5.9
10	12.8	0.2	26.9	11.5	280	7.0
11	19.0	0.2	77.6	11.5	280	5.4
12	21.7	0.2	105.9	11.5	280	4.9
13	24.5	0.2	135.0	11.5	280	4.7
14	27.2	0.2	170.8	11.5	280	4.5
15	27.7	0.2	188.7	5.9	337	3.8
16	27.2	0.2	189.2	3.5	337	3.1

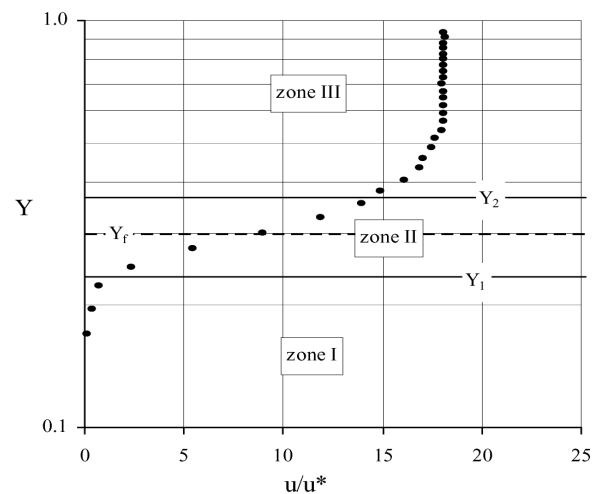


Figure 3. Measured velocity profile-localization of three different zones

For a given value of ratio h/k_v , when the stem concentration decreases, the flow velocity value increases inside the vegetation and decreases above it; furthermore, the thickness of the vertical velocity profile in zone III decreases. As an example, in Figure 4 the velocity profiles obtained for two values of stem concentration are reported.

The localization and the size of zone II are influenced by the depth/vegetation height ratio but are independent on the stem concentration. Stem concentration affects only the shape of the velocity profile (Carollo et al. 2002).

Then, the values of turbulence intensity, U' , have been calculated at each measurement point as standard deviations of the instantaneous measured data. The distributions of the estimated turbulence intensity, normalized by the shear velocity u^* , have been plotted against relative depth Y and have been compared with the distributions of the local mean velocity. As an example, the comparison of the distribution measured in the axial vertical (Va) of run 13 is reported in Figure 5. This figure shows that the turbulence intensity profile has a peak value at a relative water depth $Y_t = z_t/h$, corresponding to the relative depth Y_f at which the inflection point of the velocity distribution occurs. For $Y < Y_t$, the turbulence intensity increases rapidly; but for $Y > Y_t$ the turbulence intensity decreases until $Y = Y_{max}$, being Y_{max} the relative water depth at which the maximum value of velocity is reached. Finally, for $Y > Y_{max}$, the turbulence intensity assumes an almost constant low value.

The peak value of the normalized turbulence intensity U'_{max}/u^* is higher than the peak ($U'_{max}/u^* < 3.6$) observed in non-vegetated beds (Wang et al. 1993, Nezu and Nakagawa 1993, Carollo et al 2005). Figure 6 shows, for a given vegetation concentration ($\delta = 280$ stems/dm²), the trend of the normalized turbulence intensity for different relative vegetation roughness k_v/h . This figure shows that the normalized turbulence intensity presents a peak value for $Y = Y_t$ and that Y_t is almost equal to k_v/h .

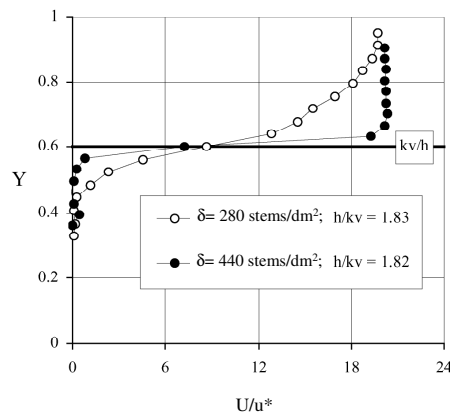


Figure 4. Velocity profiles for different values of vegetation concentration

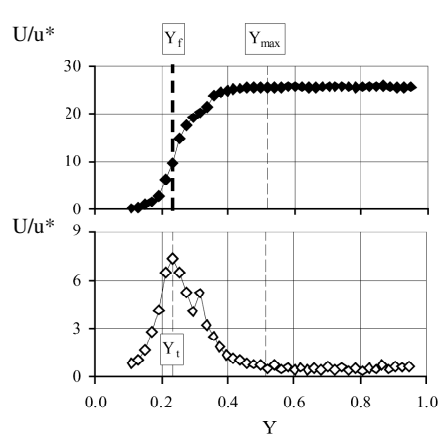


Figure 5. Measured turbulence intensity distribution and corresponding velocity profile

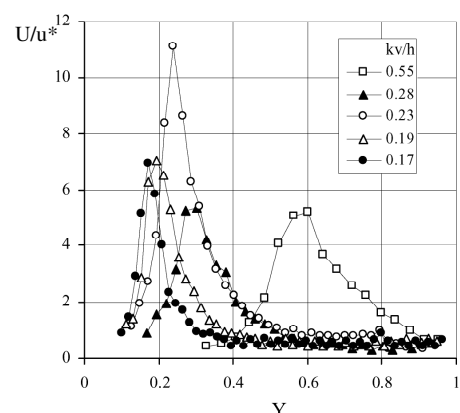


Figure 6. Turbulence intensity distributions measured in the axial vertical for different relative roughness

VERIFICATION OF MIXING LAYER APPROACH

The observed trend of the experimental velocity profiles confirms the analogy with the terrestrial canopies, according with the observations obtained by Raupach et al. (1996). In order to apply the mixing layer theory, the vertical profile could be considered as a composition of two regions of constant velocity separated by a confined intermediate region containing the inflection point.

The velocity profile of a mixing layer is approximated by a hyperbolic tangent (Ho and Huerre, 1984):

$$U = \bar{U} + \frac{\Delta U}{2} \tanh\left(\frac{z - \bar{z}}{2\theta}\right)$$

$$\Delta U = U_2 - U_1 \quad \text{and} \quad \bar{U} = (U_1 + U_2)/2 \quad (1)$$

U_1 and U_2 indicate the lowest and highest values of flow velocity, respectively (where the velocity gradient is approximately zero) and θ is the momentum thickness defined as (Roger and Moser, 1994; Ghisalberti and Nepf, 2002):

$$\theta = \int_{-\infty}^{+\infty} \left[\frac{1}{4} - \left(\frac{U - \bar{U}}{\Delta U} \right)^2 \right] dz \quad (2)$$

Thus, the variables of the mixing layer have been estimated by fitting eq. (2) to the experimental data and by imposing the minimization of the mean of the errors squared (Carollo et al., 2008). In Figure 7 all the experimental velocity profiles are plotted on the plane $((z - \bar{z})/\theta, (U - \bar{U})/\Delta U)$. The same figure reports the velocity profiles measured by Ghisalberti and Nepf (2002) and the curves of equation (1), with parameters estimated as aforementioned. As Figure 7 shows, especially in the mixing region, all profiles collapse in a single curve, confirming that the mixing layer approach is valid.

As discussed in a previous work (Carollo et al., 2008), the velocity profile of eq. (1) can be applied above the distance from the bed z where $U = 0$. For distances z lower than this limit, the longitudinal flow velocity has to be set constantly equal to zero.

The fitting procedure permits to locate the inflection point at a distance from the bed close to k_v , both for the experimental profiles measured by Ghisalberti and Nepf (2002) and for those measured during the investigations reported in the present work. In fact, as Figure 8 shows, for all the experimental profiles, the couple of points (k_v, \bar{z}) arrange around the bisector line. In such a way, the parameter assumes a clear physical meaning allowing the application of the mixing layer theory by knowing the localization of bent vegetation height, k_v .

TURBULENCE INTENSITY DISTRIBUTION

In order to interpret the turbulence intensity distribution, it has been supposed that the mixing layer zone could be considered as composed by two superimposed *boundary layers* (one of which overturned) and delimited by the top of vegetation (Figura 9). Under such hypothesis, in analogy with the expression proposed by Mendoza and Zhou (2001), the following equation has been proposed to define the turbulence intensity distribution:

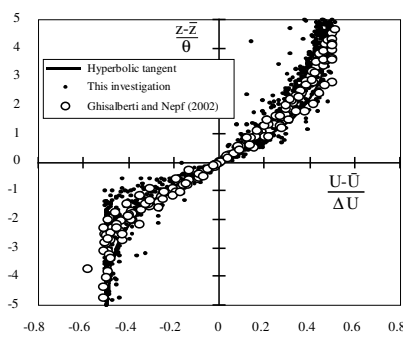


Figure 7. Comparison between all velocity profiles and eq. (1) in the mixing layer

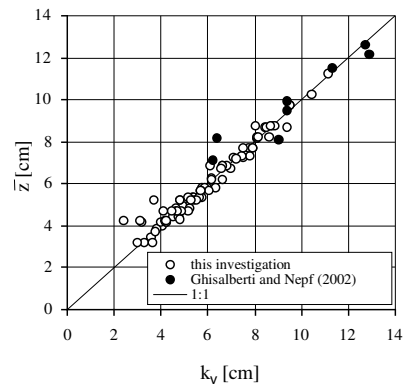


Figure 8. Comparison between parameter obtained by fit eq. (1) to experimental profile and k_v values.

$$U' = b_0 U e^{-b|z-k_v|} + b_1 \left(1 - e^{-b|z-k_v|}\right) \left| \frac{U_2 - U_1}{2} - U \right|^{0.5} \quad (3)$$

where b_0 , b_1 and b are parameters that have to be determined by using measured data. Figure 10 shows the fitting of equation (3) to measured data (at channel axis - measurement vertical va).

It can be observed that equation (3) allows to describe the turbulence intensity both inside and above the vegetation later.

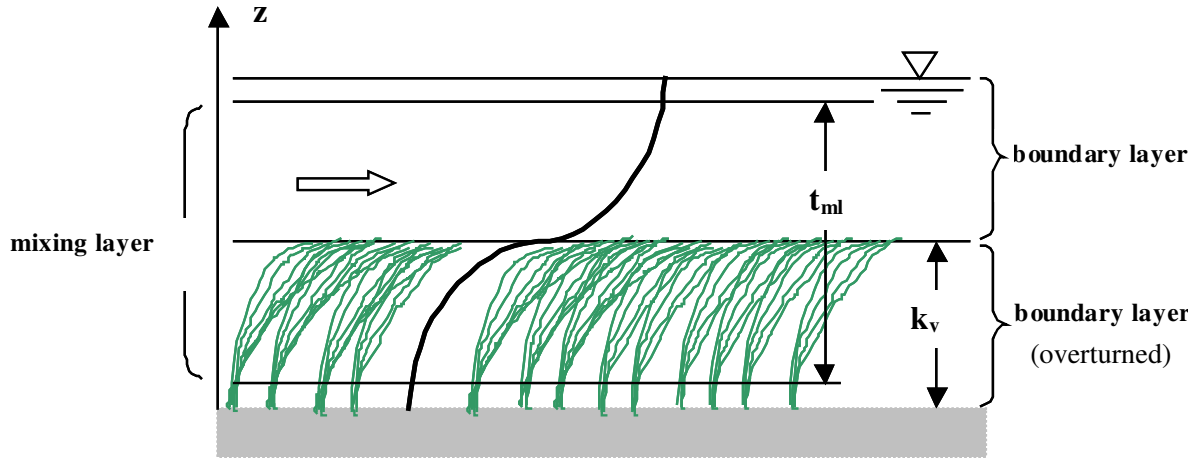


Figure 9. Mixing layer and superimposed boundary layers

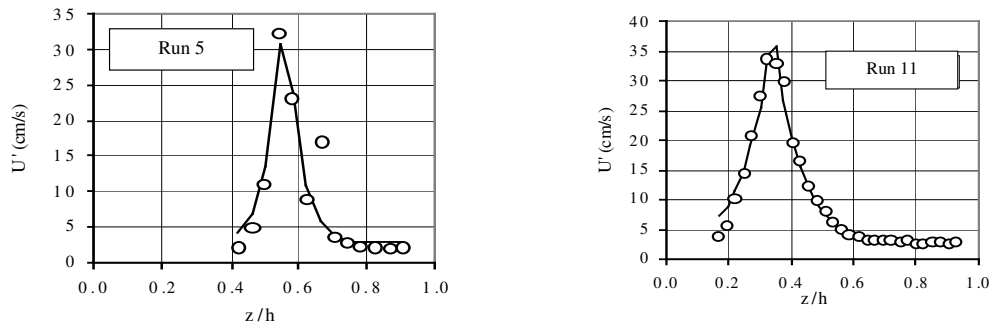


Figure 10 . Fitting of eq. (3) to measured turbulence intensity data

CONCLUSION AND DISCUSSION

The application of the mixing layer approach to interpret the vertical profile of longitudinal velocity component in a vegetated channel has been verified using data collected in a straight laboratory channel with flexible vegetation on the bed. According with Ghisalberti and Nepf (2002), the velocity profile is approximated by a hyperbolic tangent. The variables of the mixing layer have been estimated by fitting the theoretical profile both to the experimental data collected by Ghisalberti and Nepf (2002) and to those presented in the present work. Furthermore, a new expression to interpret the turbulence intensity distribution has been proposed. In order to verify the applicability of the proposed equation, further analyses have to be conducted.

REFERENCES

- Carollo, F. G., Ferro, V. & Termini, D. 2002. Flow velocity measurement in vegetated channels. *Journal of Hydraulic Engineering* 128(7): 664-673.
- Carollo, F.G., Ferro, V., Termini, D. (2005). Flow resistance law in channels with flexible submerged vegetation. *Journal of Hydraulic Engineering ASCE*. 131(7): 554-564.
- Carollo, F.G., Ferro, V., Termini, D. (2008). Flow velocity profile and turbulence characteristics in a vegetated straight flume. International Congress Riverflow 2008- Cesnme - Izmir (Turkey) 3-5 September-1-4
- Ghisalberti, M. & Nepf, H. M. 2002. Mixing layer and coherent structures in vegetated aquatic flows. *Journal of Geophysical Research* 107(2):3-1-3-11.
- Ho, C.M., & Huerre, P. 1984. Perturbed free shear layers. *Annu. Rev. Fluid Mech.*, 16, 365–424.
- Mendoza, C. & Zhou, D. Turbulent intensities in open-channel flows, *Mechanics Research Communication*, 2001, Vol. 28, No. 3, 317-325.
- Nezu, I., Nakagawa, H. (1993). Turbulence in open-channel flows. Balkema: Rotterdam.
- Tsujimoto, T., Shimizu, Y., Kitamura, T. & Okada, T. 1992. Turbulent open-channel flow over bed covered by rigid vegetation. *Jour. Hydroscience & Hydraulic Eng.*, JSCE, Vol.10, No.2, pp.13-25, 1992.
- Raupach, M. R., Finnigan, J. J., & Brunet, Y. 1996. Coherent eddies and turbulence in vegetation canopies: The mixing layer analogy. *Boundary Layer Meteorol.*, 78, 351–382, 1996.
- Rogers, M. M., & Moser, R. D. 1994. Direct simulation of a self-similar turbulent mixing layer. *Phys. Fluids A*, 6(2), 903–923.
- Wang, J., Dong, Z., Chen, C., Xia, Z. (1993). The effects of bed roughness on the distribution of turbulent intensities in open channel flow. *Journal of Hydraulic Research*. 31 (1): 89-98.

The use of high-resolution sismo-acoustic echosounder imaging for Estimation carbon sink in *P. oceanica* dead matte

Filippo Luzzu, Agostino Tomasello, Germana Di Maida, Carla Orestano, Maria Pirrotta, Carmelina Bellavia, Cesare Costantini, Antonino Scannavino and Sebastiano Calvo

Dipartimento di Ecologia, Università di Palermo, Viale delle Scienze, Edificio 16, 90128 Palermo, Italy

Corresponding author e-mail: luzzu@unipa.it

ABSTRACT

A high-resolution echosounder was used to acquire seismo-acoustic records of *P. oceanica* dead *matte* patches in the Gulf of Palermo. Using Seismo-acoustic profiling it was possible to detect dead *matte* structures hidden by variable layers of sandy sediment. The thickness of the dead *matte structure* reaches a maximum of 2.2 m. The mean volume per unit area of seabed surface (MEIx) varies from 0.2 to 2.2 m³/m² with an average value of 1.6 m³/m² and a total volume estimated of 73,000 m³. We estimated 2,484 tons of total carbon accumulated in the *matte* and an age of *P. oceanica* dead *matte* ranging between 3,600 and 530 years. Seismo-acoustic technologies prove to be a powerful, non-destructive method to measure the thickness, extension, volume of dead *matte* and its potential carbon content.

Keywords: *Posidonia oceanica*, dead *matte*, sub-bottom profiler, remote sensing, carbon sink

INTRODUCTION

Posidonia oceanica (L.) Delile is a endemic seagrass key species in The Mediterranean coastal environments, where it forms a very extensive and productive ecosystem [Ott, 1980; Pergent et al., 1995]. This marine phanerogam is the only species able to form *matte*, a biogenic structure resulting from growth of plagiotropic and orthotropic rhizomes intertwined with roots and autochthonous and allochthonous detritus [Boudouresque and Meisnez, 1982]. Due to its highly refractory nature, the *matte* is a long-term organic reservoir that can be preserved over thousands of years, forming structures several meters thick [Mateo et al., 1997] that represent a potential carbon sink [Mateo et al., 2006].

Natural and/or anthropogenic factors can determine the regression of the *P. oceanica* meadow and disappearance of living shoots in the upper part of the *matte* with the formation of a regressive structure, called “dead *matte*”[Pergent et al., 1995].

Acoustic-based geophysical methods are remote-sensing techniques commonly used in aquatic environments [Garcia et al., 2004; Nitsche et al., 2004; Schrottke et al., 2006].

These techniques are able to provide, indirectly, images of seabed features and sub-bottom sediment layers, allowing bathymetry mapping and subsurface information with a cost-effective and non-destructive approach which represents a better alternative to traditional surveys.

Instruments like the Sub-Bottom Profiler (SBP) that uses a combination of sonic and ultrasonic waves, can provide images of the water-sediment interface and underlying

sediment layers by detecting changes in the mechanical impedance through reflections from the sub-bottom stratigraphy [Schock et al., 1989; Ballard et al., 1993; Schock, 2004].

Recently a very high-resolution seismo-acoustic (Sub-Bottom Profiler) technique was successfully applied to assess the volume occupied by the *matte* underlying *P. oceanica* meadows [Lo Iacono et al., 2008].

In particular, the use of the very high-resolution sediment sub-bottom profiler, that use the parametric effect [Grant and Schreiber, 1990; Spieß, 1993], can detect small impedance variations, created by the presence of organic matter [Wunderlich and Müller, 2003] like that stored in the *matte*.

In this study a high resolution seismo-acoustic survey was carried out in the Gulf of Palermo (NW coast of Sicily, Italy) (Fig. 1) where, as a consequence of several decades of multiple pollution sources due to city planning disorder, improper waste disposal and untreated wastewaters [Genchi et al., 1982; Calvo et al., 1994], very extensive *P. oceanica* dead *matte* patches occur [Tomasello et al., 2007].

The aim of this study is to assess the effective extension, volume and the age of dead *matte* by high resolution seismo-acoustic techniques and to estimate indirectly the amount of carbon stored.

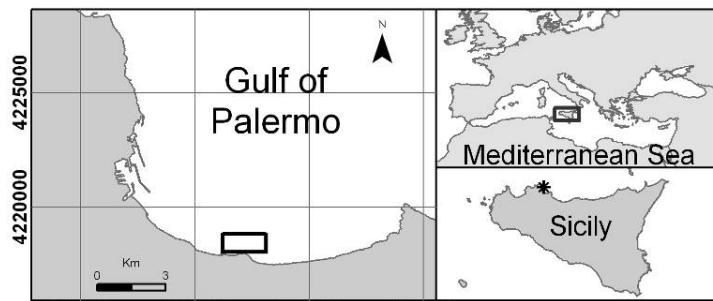


Figure 1 - Study area

MATERIALS AND METHODS

Data acquisition

On summer 2008 in the inner sector of the Gulf of Palermo (Fig. 1) a high-resolution echosounder Innomar SES-2000 compact, was used to acquire seismo-acoustic records of *P. oceanica* dead *matte* patches. The track lines were performed by navigation software using a morpho-bathymetric map previously acquired by a Multibeam Sonar System (Reson SeaBat 8125) as background, on which the dead *matte* emerging from the bottom was previously identified [Luzzu, 2009] (Fig. 2). Seismo-acoustic profiling was carried out using a secondary frequency of 6 kHz. The data was corrected for loss of energy (spreading corrections) by using a linear time-varying gain (TVG). Ship movement was corrected by a TSS/Marhs motion reference unit.

Data processing

Each sub-bottom profiles was processed by Innomar-ISE 2.9 software (Interactive Sediment layer Editor) and upper and lower limits of each acoustic layer were selected.

The top and base of the dead *matte* were reconstructed via GIS by two DTM (Digital Terrain Model) with a pixel size of 1 m².

Matte thickness and volume was calculated. In particular, a *Matte* Edification Index (MEIx) was defined by the ratio between *matte* and sea bottom surface (m³/m²).

RESULTS AND DISCUSSION

The investigated area covers a surface of about 45,000 m², between 14.8 and 20.8 m of depth. The seafloor shows an irregular topography with dead *matte* and circular eroded structures delimited by *matte* walls of up to 1 m high with sand inside(Fig. 2).

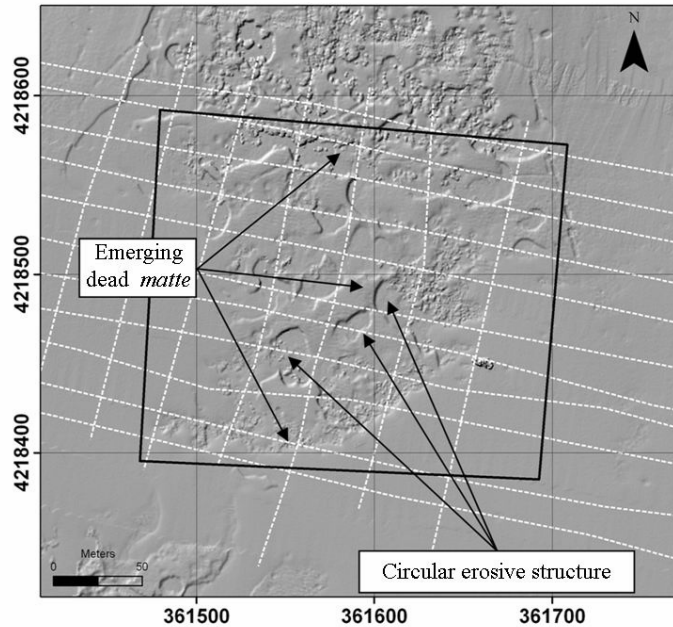


Figure 2 - Seismo-acoustic tracks (white lines) acquired on *P. oceanica* dead *matte* in the Gulf of Palermo. The black square delimits the area in which all the analyses were performed. The morpho-bathymetric map was acquired by Multi Beam Sonar System Reson SeaBat 8125.

About 49% of total area investigated (22,000 m²) is covered by emerging dead *matte*. By high resolution Seismo-acoustic profiling it was possible to identify different acoustic layers, interpreted as sand and rock, which constitute the present-day base of the *matte*. The rocky structure, identifiable by high amplitude reflector, lies between 1.5 and 4 m below the seabed (Fig. 3). This suggests that rock and sand layers are the native substrata on which *P. oceanica* meadow started to settle in the area.

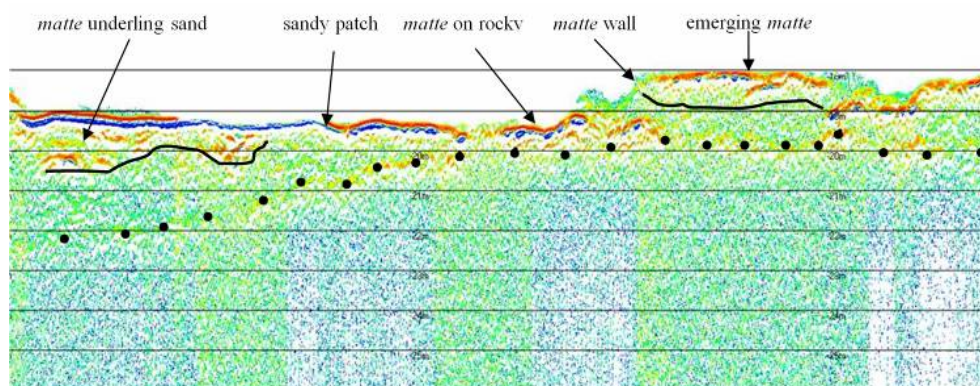


Figure 3 - Example of a seismo-acoustic profile in which the three different layers can be recognized: the base of the *matte* over sand is marked with a black line; the rocky layer is marked with dots through point sequence.

Analysis of Seismo-acoustic profiles showed other hidden dead *matte* structures for a total surface of 19,000 m² which corresponds to 42% of the area investigated. These structures are covered by variable layers of sandy sediment (Fig. 3 and 4) and are invisible to Multibeam sonar or visual inspection.

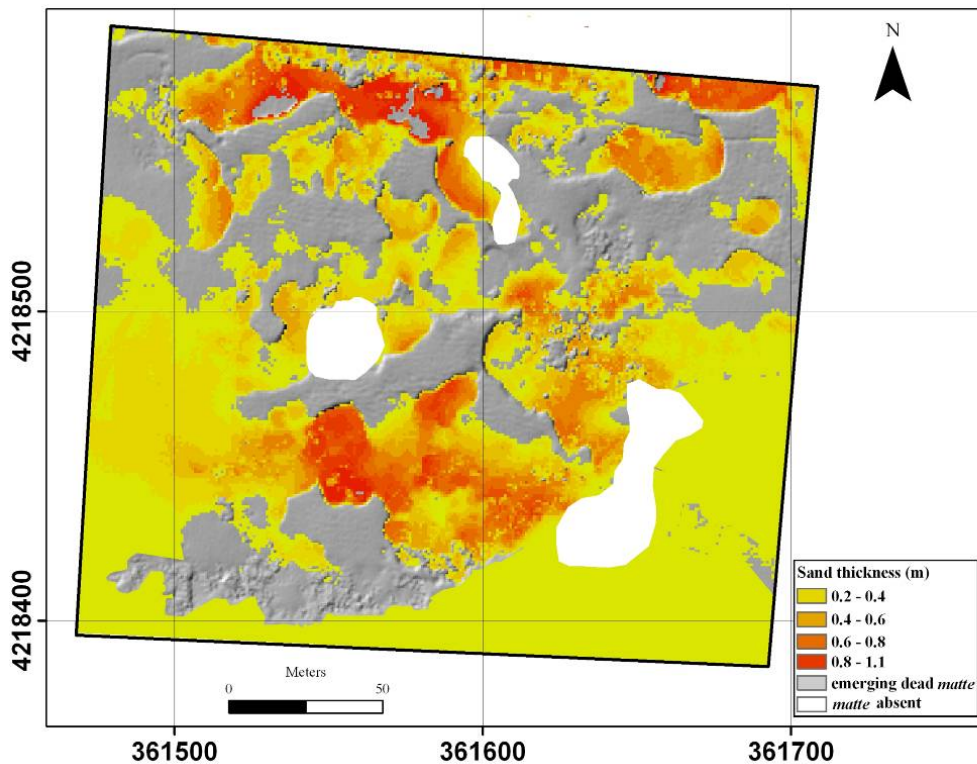


Figure 4 - Map distribution of emerging *matte* (grey) and sediments above the *matte* revealed by a sub-bottom profiler (red and yellow).

The cause of coverage by sandy sediment and complete loss of the meadow was probably the erosion, transport and deposition of inert solid waste that has been discharged along the shoreline of the gulf of Palermo since the end of the second world war.

The maximum thickness of the dead *matte* reaches 2.2 m. The vertical accretion of *matte* is a process that includes production, decomposition and erosion events. This process was estimated over centuries or millennia in several sites of Mediterranean sea, with values that ranging from 0.06 to 0.41 cm year⁻¹ [Mateo et al., 1997; Lo Iacono et al., 2008].

According to these estimates, settlement of the meadow in the area investigated may thus have occurred between 3,600 and 530 years ago.

The Matte edification index (MEIx) varies from 0.2 to 2.2 m³/m² with an average value of 1.6 m³/m² (Fig. 5). Considering the total surface occupied by dead *matte* in the area its total volume was estimated at 73,000 m³.

Literature data indicates that the amount of carbon stored in the *matte* is 0.034 tons/m³ [Lo Iacono et al., 2008], so it is possible to asses the total carbon accumulated in 73,000 m³ of dead *matte* is about 2,484 tons.

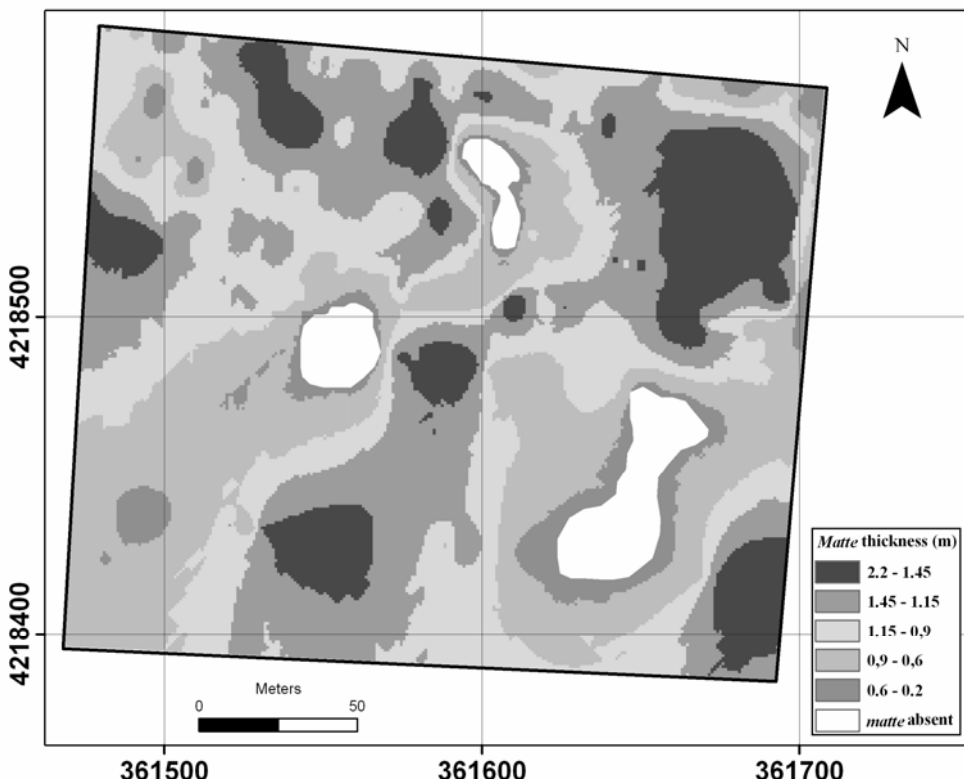


Figure 5 - Distribution map of *Matte* Edification Index (MEIx).

CONCLUSIONS

The use of high resolution seismo-acoustic technology proves to be a powerful, non-destructive method to measure the thickness, age, extension and volume of *matte* [Lo Iacono et al., 2008; Endler, 2009]. This technology can provide information about the *matte* structure and give an accurate assessment of the potential size of the carbon stored in the dead *matte*, confirming the importance of *P. oceanica* as a sink for this element. Moreover, high resolution seismo-acoustic technologies will be applied to larger scales in the future, providing a better understanding of the role of *P. oceanica* in the carbon cycle of the entire coastal marine Mediterranean ecosystem.

REFERENCES

- Ballard R.F., Sjostrom K.J., McGee R.G., Leist R.L. (1993) - *A rapid geophysical technique for subbottom imaging*. Geophysical Techniques for Site and Material Characterization. GA, Atlanta, pp. 117-128.
- Boudouresque C.F., Meisnez A. (1982) - *Découverte de l'herbier de Posidonie*. Parc National de Port-Cros, Parc Naturel Regional de la Corse, Cahier n. 4, pp. 79.
- Calvo S., Galluzzo M., Viviani G. (1994) - *Water pollution problems in the Palermo area*. In: Dellow B. and Puusola T. Editors, Proceedings UETP-EEE Annual Conference "Improving the Urban Environment". London, pp. 73-87.
- Endler R. (2009) - *Sediment physical properties of the DYNAS study area*. J. Marine Syst., 75: 317-329.
- Garcia G.A., Garcia-Gil S., Vilas F. (2004) - *Echo characters and recent sedimentary processes as indicated by high-resolution sub-bottom profiling in Ria de Vigo, NW Spain*. Geo Mar. Lett., 24: 32-45.
- Genchi G., Di Bernardo F., Lugaro A., Calvo S., Ragonese S., Riggio S. (1982) - *Dystrophic and eutrophic states of coastal sea-water in Palermo bay during the summer season (august 1981)*. VI^o Journees Etud. Poll., CIESM. Cannes, pp. 635-639.
- Grant J.A., Schreiber R. (1990) - *Modern swaths sounding and subbottom profiling technology for research applications: the Atlas Hydrosweep and Parasound system*. Mar. Geophys. Res., 12: 9-19.

- Lo Iacono C., Mateo M.A., Gràcia E., Guasch C., Carbonell R., Serrano L., Serrano O., Dan J. (2008) - *Very high-resolution seismo-acoustic imaging of seagrass meadows (Mediterranean Sea): Implications for carbon sink estimates.* Geophys. Res. Lett., 35: L18601, doi:10.1029/2008GL034773.
- Luzzu F. (2009) - Sistemi avanzati a controllo remoto nel monitoraggio ambientale lungo la fascia costiera. PhD Thesis, Università di Palermo. pp. 107.
- Mateo M.A., Cebriàn J., Dunton K., Mutchler T. (2006) - *Carbon flux in seagrass ecosystem.* In: Larkum A.W.D., Orth R.J., Duarte C.M. Editors, *Seagrasses: Biology, Ecology and Conservation.* Springer, The Netherland, 7: 159-192.
- Mateo M.A., Romero J., Pérez M., Littler M.M., Littler D.S. (1997) - *Dynamics of millenary organic deposits resulting from the growth of the Mediterranean seagrass Posidonia oceanica.* Estuar. Coast. Shelf Sci., 44: 103-110.
- Nitsche F.O., Bell R., Carbotte S.M., Ryan W.B.F., Flood R. (2004) - *Process-related classification of acoustic data from Hudson River Estuary.* Mar. Geol., 209: 131-145.
- Ott J.A. (1980) - *Growth and Production in Posidonia oceanica (L.) Delile.* P.S.Z.N.I. Mar. Ecol., 1: 47-64.
- Pergent-Martini C., Leoni V., Pasqualini V., Ardizzone G.D., Balestrieri E., Bedini R., Belluscio A., Belsher T., Borg J., Boudouresque C.F., Boumaza S., Bouquegneau J.M., Buia M.C., Calvo S., Cebriàn J., Charbonnel E., Cinelli F., Cossu A., Di Maida G., Dural B., Francour P., Gobert S., Lepoint G., Meinesz A., Molenaar H., Mansour H.M., Panayotidis P., Peirano A., Pergent G., Piazzi L., Pirrotta M., Relini G., Romero J., Sanchez-Lizaso J.L., Semroud R., Shembri P., Shili A., Tomasello A., Velimirov B. (2005) - *Descriptors of Posidonia oceanica meadows: Use and application.* Ecol. Indicat., 5: 213-230.
- Pergent G., Pergent-Martini C. (1995) - *Dynamique et évolution de l'herbier à Posidonia oceanica en Méditerranée.* G. Bot. Ital., 129(1): 303-317.
- Pergent G., Pergent-Martini C., Boudouresque C.F. (1995) - *Utilisation de l'herbier à Posidonia oceanica comme indicateur biologique de la qualité du milieu littoral en Méditerranée: état des connaissances.* Mésogée, 54: 3-27.
- Rey J., Diaz del Rio V. (1989) - *Cartografía de los fondos marinos de la bahía de Palma (Baleares, España): Distribución de las praderas vegetales y sedimentos superficiales.* In: Boudouresque C.F., Meinesz A., Fresi E., Gravez V. Editors. International Workshop *Posidonia oceanica* Beds, GIS Posidonie. Marseille, France. pp. 28-41.
- Schock S.G., LeBlanc L.R., Mayer L.A. (1989) - *Chirp subbottom profiler for quantitative sediment analysis.* Geophysics, 54(4): 445-450.
- Schock S.G. (2004) - *A method for estimating the physical and acoustic properties of the sea bed using chirp sonar data.* IEEE J. Oceanic Eng., 29(4): 1200-1217.
- Schrottke K., Marius B., Alexander B., Burghard F., Dierk H. (2006) - *Fluid mud dynamics in the Weser estuary turbidity zone tracked by high-resolution side-scan sonar and parametric sub-bottom profiler.* Geo Mar. Lett., 26(3): 185-198.
- Spieß V. (1993) - *Digitale Sedimentechographie - Neue Wege zu einer hochauflösenden Akustostratigraphie.* Ber. Geowiss. Univ. Bremen, 35: 1-199.
- Tomasello A., Calvo S., Di Maida G., Lovison G., Pirrotta M., Sciandra M. (2007) - *Shoot age as a confounding factor on detecting the effect of human-induced disturbance on Posidonia oceanica growth performance.* J. Exp. Mar. Biol. Ecol., 343: 166-175.
- Wunderlich J., Müller S. (2003) - *High-resolution subbottom profiling using parametric acoustics.* International Ocean Systems, 7(4): 6-11.

Application of the Princeton Ocean Model to simulate the fate and behaviour of pharmaceuticals in a shallow urban lake

Sebastian Schimmelpfennig*, Christof Engelhardt, Gunnar Nützmann, Georgiy Kirillin

*Leibniz-Institute of Freshwater Ecology and Inland Fisheries, Department of Ecohydrology,
Müggelseedamm 310, D-12587 Berlin, Germany*

* corresponding author email: schimmelpfennig@igb-berlin.de

ABSTRACT

The increasing occurrence of anthropogenic trace pollutants (e.g. pharmaceuticals, endocrine disruptors, pesticides) in urban water bodies requires a human and eco-toxicological risk assessment. To save the drinking water resources efficiently the fate and behaviour of trace pollutants has to be completely understood.

The Princeton Ocean Model (POM) was used to simulate currents and concentration of pharmaceuticals (from a waste water treatment plant effluent) in a shallow urban lake in Berlin, Germany. The model has to deal with a challenging bathymetry (8 islands, steep bottom slope) as well as with two river inflows which are very different in flow dynamics and temperature patterns.

The pressure gradient error was identified as the main handicap for the application of POM in this small scale environment. Spurious currents which appear in the standard POM configuration obstruct realistic tracer simulations. Therefore, advanced numerical schemes taken from literature are tested to reduce the pressure gradient error. The sixth-order difference scheme (Chu and Fun 1997) shows no improvement, whereas the density Jacobian scheme with monotonized cubic polynomial fits (Shchepetkin and McWilliams 2003) reduces the errors to an acceptable level.

The model will be calibrated and validated with several field measurements, e.g. mounted permanent thermistor chains, monthly temperature, conductivity, and current profiling, meteorological data sampling at a platform in the lake, and comprehensive chemical lab measurements, i.e. trace analysis of pharmaceuticals.

Seagrasses as biological barriers against anthropic input in coastal marine ecosystems

S. Vizzini*, C. Tramati, V.A. Tumbarello, V. Costa and A. Mazzola

*Department of Ecology, University of Palermo, via Archirafi 18,
90123 Palermo, Italy*

*Corresponding author, e-mail vizzini@unipa.it

ABSTRACT

Seagrasses are marine plants that support highly complex and productive ecological systems. The importance of the multiple services provided by these ecosystems highlights the need to preserve their health. Indeed, as a result of increasing global population and human pressure, coastal waters inhabited by seagrasses have been subject to increasing organic matter and contaminant loading. Due to their morphology (i.e. the presence of shoots with long leaves), seagrasses reduce hydrodynamic energy and, at the same time, enhance sedimentation, functioning as traps for fine sediment and as a potential barrier against the transfer of anthropic input from rivers to the open-sea. In this study we analysed sediment features along a stream to sea transect in southern Sicily (Italy) to explore the role of seagrasses in reducing continentally-derived organic matter and contaminant input. Sediment was sampled in five stations and analysed for organic matter content and heavy metals (Cd, Cr, Cu, Hg, Ni, Pb, Zn). A decline in organic matter content and heavy metals was observed along the transect. Four (Cd, Cu, Ni, Hg) out of the seven heavy metals investigated showed the highest values in the stations characterised by sparse and dense *Cymodocea nodosa* meadows. Cr was maximum at the stream station, while Pb and Zn at the mouth of the stream. However, in these last three cases, the station with *C. nodosa* showed much higher metal concentrations than the adjacent sea. As a consequence, seagrasses are involved in biologically-mediated changes in the environment. A decline in the extension of seagrasses may determine the loss of important ecological functions and have several negative effects, not only in terms of significant reduction in secondary production and biodiversity, but also, as suggested by the results of this study, in terms of their role as biological barrier against the transfer of organic matter and contaminants to the open-sea.

KEYWORDS

Marine angiosperms, sediment, heavy metals, estuary, Mediterranean.

INTRODUCTION

Marine-coastal ecosystems and, in particular, their biogeochemical cycles are strongly influenced by input of material from adjoining ecosystems (Ernst, 1987). Indeed, they are characterised by large supplies of continental organic matter and high primary production rates, sustained by river-induced nutrient input, that, in combination with a limited water depth, lead to organic matter enrichment of the sea floor. In many cases, rivers provide also input of contaminants into adjacent marine-coastal ecosystems. For example, human activities

are sources of heavy metals, which are transported to the coastal marine environment via rivers and, to a lesser extent, atmosphere (Dassenakis *et al.*, 1997). The continental contribution of heavy metals to the world's ocean is quite large, as >97% of their mass transport is associated with river sediments (Gibbs, 1977). As a consequence, coastal areas around the river mouths are affected by enrichment in nutrients, organic matter and contaminants (Angelidis and Aloupi, 2000).

Concentrations of heavy metals in the marine environment depends on their reactivity, on the chemical characteristics of the matrix, and on the presence of reactive substrates in the receiving waters. When these particle-reactive pollutants enter coastal waters, many are quickly adsorbed on suspended matter and removed to bottom sediments (De Groot *et al.*, 1976). Sediments therefore provide a temporally integrated indication of environmental quality and act as a major reservoir, containing concentrations orders of magnitude greater than the overlying water column. Trace metals deposited in coastal systems can then become incorporated into the biota, which due to bioaccumulation can have severe negative effects (see Islam and Tanaka, 2004 for a review).

Seagrasses are marine angiosperms that inhabit marine near-shore environments (Butler and Jernakoff, 1999). Generally they colonize soft bottoms, although salinity and turbidity resulting from river discharge are important factors in inhibiting their growth immediately adjacent to river mouths. Seagrasses are widely acknowledged as organisms able to sequester trace metals from the marine environment via both the leaves and roots-rhizomes, indeed their concentrations can be correlated with those of water column and sediments, respectively (Pulich, 1980; Lyngby and Brix, 1982; Neinhuis, 1986; Ward, 1989).

In this paper we analysed sediment features along a stream to sea transect in southern Sicily (Italy) to explore the role of seagrasses in reducing continentally-derived organic matter and contaminant input. In particular, we analysed heavy metal levels (cadmium, Cd; chromium, Cr; copper, Cu; nickel, Ni; lead, Pb; zinc, Zn; mercury, Hg) and organic matter content in five stations along the transect to characterise their distribution.

METHODS

The study was carried out in the mouth of the stream Irminio (Lat. 36°46'20.82" N; Long. 14°35'45.61" E) and the adjoining marine coastal area (Sicily, Italy). The stream arises from Mount Lauro, an ancient volcano, now inactive, of the Ibleo plateau and ends after 55 km in southern Sicily into the Mediterranean Sea. The final part of the stream and its mouth are included in a Regional Natural Reserve that occupies an area of approximately 134 hectares. The reserve embraces a coastal area of natural interest, hosting numerous protected bird species, both sedentary and migratory. The coast presents a typical dune habitat with strips of scrub-forest at the mouth of the stream. The marine ecosystem is characterised by the presence of the seagrasses *Cymodocea nodosa* and *Posidonia oceanica*, the last only in patches.

The sampling was carried out in September and October 2006 in five stations along the stream to sea transect. In particular, a sampling station was located in the final part of the stream (station *Stream*), another in the mouth (station *Mouth*) and the remaining three stations at sea: station *Cym-Edge* represents the boundary between the unvegetated soft bottoms and a *C. nodosa* meadow and is characterised by a sparse meadow, the station *Cym* was positioned in a dense *C. nodosa* meadow, and the station *Bare sand* is a sandy marine control (Figure 1).

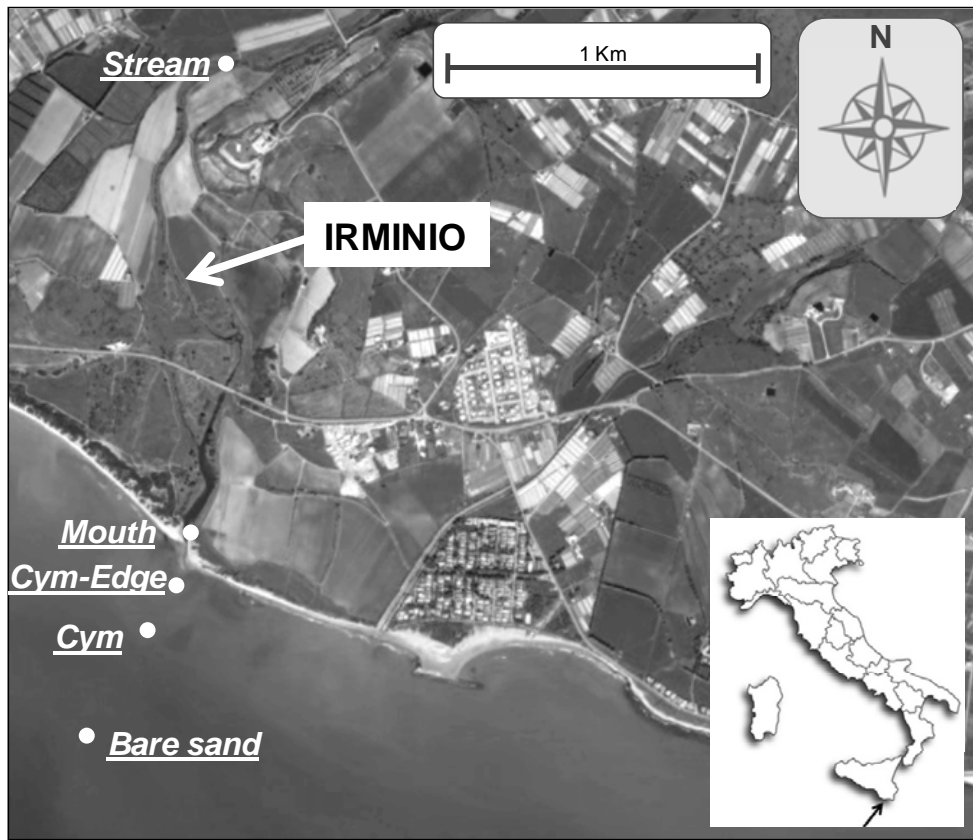


Figure 1. Sampling area with the five (*Stream*, *Mouth*, *Cym-Edge*, *Cym*, *Bare sand*) sampling stations (●).

In each station, samples of sediment were collected in five replicates using PVC cores. Sediment was sieved with a 63 µm sieve prior to the analyses for heavy metal (Cd, Cr, Cu, Hg, Ni, Pb, Zn) and organic matter (OM) content.

Heavy metals

The determination of heavy metals was carried out following the protocols U.S. EPA Method 3052/96 (hotplate digestion technique) and U.S. EPA Method 6010B/96 for digestion and analysis, respectively. The mineralization of the sediment consists in the total digestion of the sample with a mixture of strong acids in a closed microwave system (CEM, Model MARS®). Approximately 0.2 g of dry sediment were mineralized with suprapur acids. For each sample, 9 ml of HNO₃ 67-70%, 3 ml of HF 40%, 0.5 ml of H₂O₂ 30% and 2.5 ml of MilliQ water were added. The metal content was determined by an Optical Emission Spectrometry with Inductively Coupled Plasma (ICP-OES, Varian Vista MPX). For Hg determination, a generator of hydrides (VGA-77) and a reducing solution containing suprapur NaBH₄ 0.3% and NaOH 0.5% and a carrier solution consisting of HCl 5M were used. The analytical control was carried out through the mineralization of a certified material (Marine Sediment MESS-3, National Research Council of Canada). The percentage recovery of the process of mineralization was between 95% and 101%.

Organic matter

The organic matter content was quantified by gravimetry. A few grams of sediment were oven dried (100 °C) to constant weight to estimate total matter (TM). Then the sample was placed in a muffle furnace (450 °C) to constant weight and weighed to estimate the inorganic fraction (IM). The organic fraction (OM) was calculated as the difference between the TM and the IM.

Statistical analysis

The spatial variability in sediment heavy metal levels was investigated through multivariate analyses. In particular, a cluster analysis and a principal coordinate analysis (PCO; Anderson and Willis, 2003) were carried out on normalised Euclidean distances of heavy metal concentrations. The relationship between heavy metals and organic matter content was investigated using distance-based multivariate analysis for a linear model (DISTLM, Anderson 2005).

RESULTS

Heavy metal levels were reported in figures 2-5.

Cd and Hg were accumulated in the station characterised by the presence of a dense *C. nodosa* meadow (*Cym*; Cd=1.339±0.324 mg/kg d.w. and Hg=1.857±0.438 mg/kg d.w.) (Figure 2).

Cr and Zn were more abundant at stations *Stream* (Cr=54.365±5.675 mg/kg d.w. and Zn=63.952±8.763 mg/kg d.w.) and *Mouth* (Cr=53.166±2.607 mg/kg d.w. and Zn=94.820±3.650 mg/kg d.w.) than at *Cym* (Cr=12.931±1.494 mg/kg d.w. and Zn=15.705±3.095 mg/kg d.w.) and *Bare sand* (Cr=11±0.896 mg/kg d.w. and Zn=16.438±1.535 mg/kg d.w.), while *Cym-Edge* showed intermediate values (Cr=40.099±0.920 mg/kg d.w. and Zn=34.130±1.833 mg/kg d.w.) (Figure 3).

Cu showed increasing levels from the *Stream* (19.879±1.186 mg/kg d.w.) to the station *Cym-Edge*, where it reached a peak (56.585±1.669 mg/kg d.w.) and then it decreased seaward with a minimum in the *Bare sand* station (3.262±0.535 mg/kg d.w.) (Figure 4).

Ni showed similar concentrations in four (*Stream*, *Mouth*, *Cym-Edge* and *Bare sand*) out of the five stations (mean values ranged between 17.761 and 26.163 mg/kg d.w.), while it exhibited higher levels in the station *Cym-Edge* (44.012±0.656 mg/kg d.w.) (Figure 4).

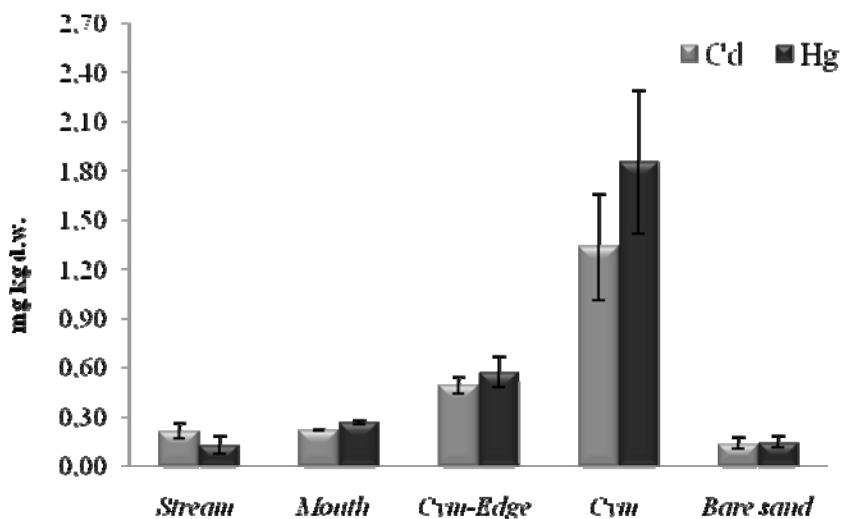


Figure 2. Mean concentrations of Cd and Hg (mg/kg d.w., ±s.d.) in sediments of the five stations.

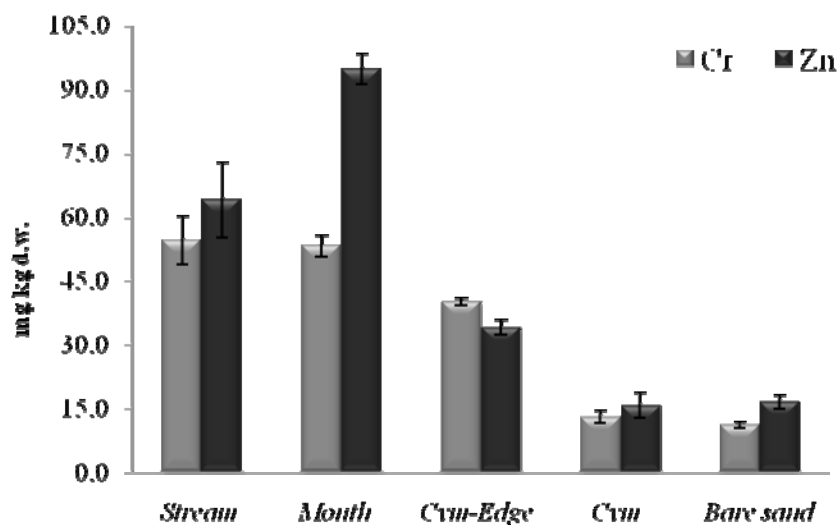


Figure 3. Mean concentrations of Cr and Zn (mg/kg d.w., \pm s.d.) in sediments of the five stations.

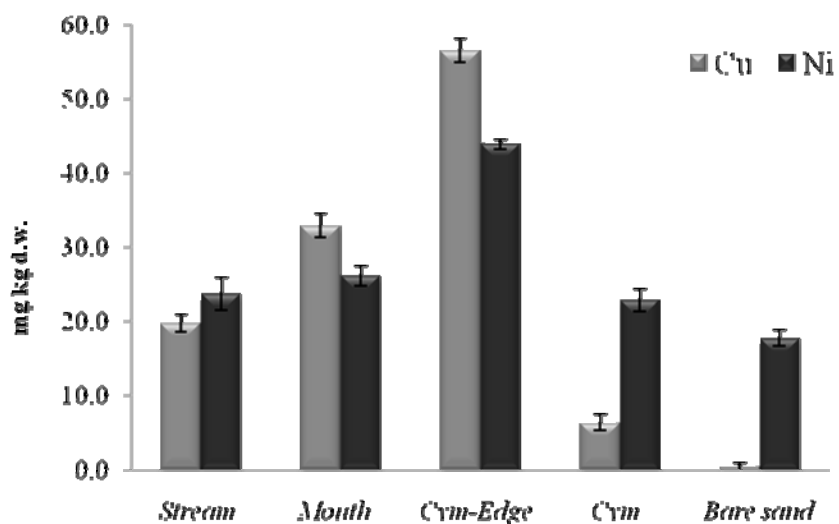


Figure 4. Mean concentrations of Cu and Ni (mg/kg d.w., \pm s.d.) in sediments of the five stations.

Pb increased from the *Stream* (7.193 ± 0.329 mg/kg d.w.) to the *Mouth* (11.113 ± 0.261 mg/kg d.w.) station and gradually decreased from *Cym-Edge* (6.456 ± 1.022 mg/kg d.w.) to *Bare sand* (3.270 ± 0.592 mg/kg d.w.) station.

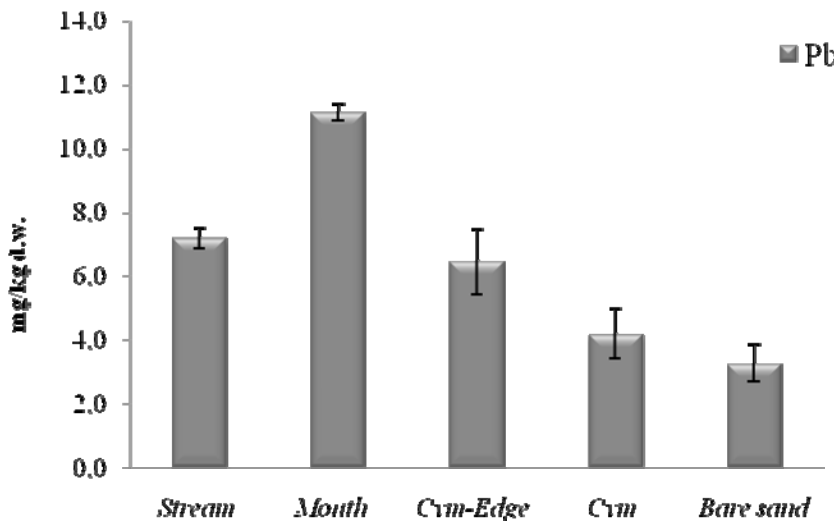


Figure 5. Mean concentrations of Pb (mg/kg d.w., \pm s.d.) in sediments of the five stations.

Organic matter content showed the maximum value in the station *Stream* ($1.099 \pm 0.135\%$) and the minimum in the station *Bare sand* ($0.469 \pm 0.014\%$), while the other three stations (*Mouth*, *Cym-Edge* and *Cym*) fall into a range of concentrations of between 0.583% and 0.844%.

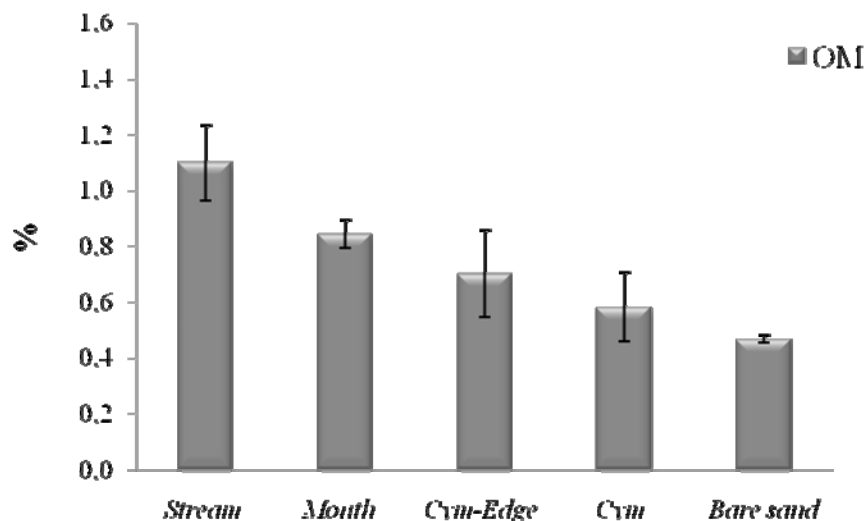


Figure 5. Percentage content of organic matter (\pm s.d.) in sediments of the five stations.

Cluster analysis and PCO ordination sorted the sampling stations into two groups, one included the stations *Stream*, *Mouth* and *Cym-Edge* characterised by higher Cu, Cr, Ni, Pb and Zn concentrations, the other consisted of the stations *Cym* and *Bare sand* characterised by higher Cd and Hg concentrations (Figure 6).

DISTLM procedure highlighted that the relationship between heavy metals and organic matter content was significant (Pseudo-F=4.056, P=0.017).

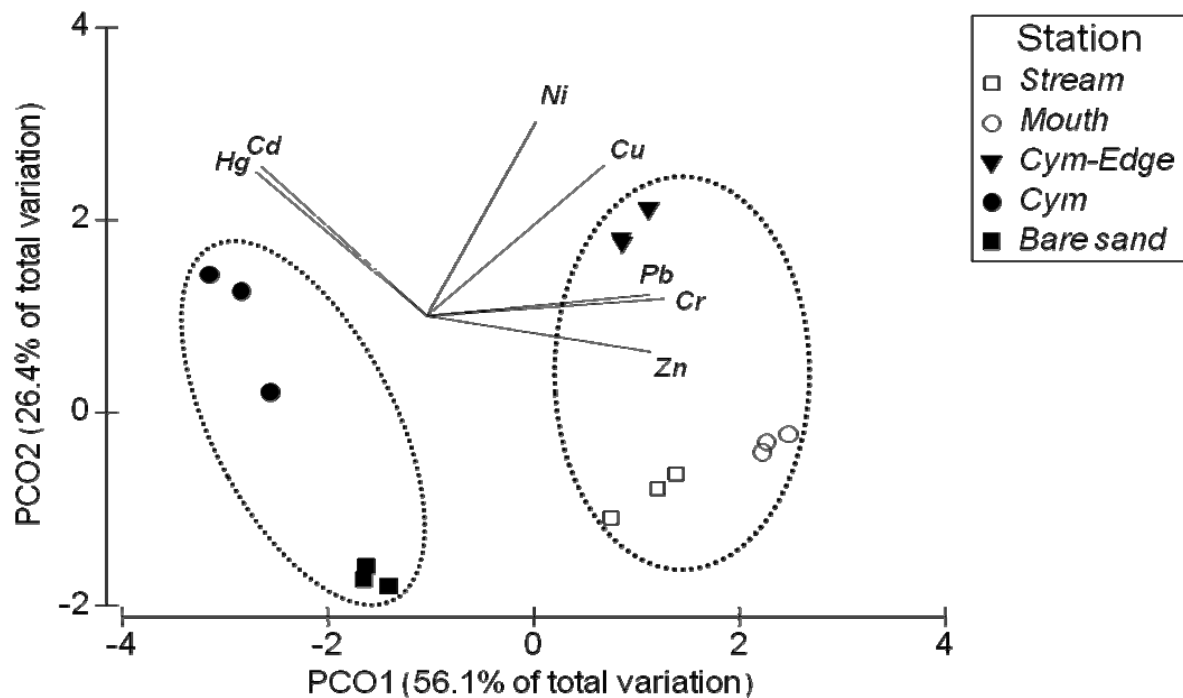


Figure 6. PCO ordination based on normalised Euclidean distances of heavy metal concentrations in sediments. Results of cluster analysis (distance of 4) were overlaid.

DISCUSSION AND CONCLUSION

Most metals had higher concentrations in the stream, its mouth and the sparse *C. nodosa* meadow that represents the boundary between unvegetated soft bottoms and the dense seagrass meadow. The high values of metals can be attributed to the continental input and runoff. Indeed, the stream Irminio is influenced by the agricultural and rural development areas located in the southern Sicily. Many of the metals analysed (Cr, Cu, Pb, Zn, Ni) are components of fertilizers (Förstner and Wittmann, 1981), which may be their source. The high turbidity caused by suspended particulate matter in this area could also act as scavengers for the metals. In addition, the low hydrodynamism in the mouth can favour the sedimentation and the accumulation of heavy metals in the sediments.

The minimum concentrations of almost all metals were found in the stations with a dense *C. nodosa* meadow and marine bare sand. This result can account for the presence of biological barriers (i.e. seagrasses) that act following two distinct mechanisms: they have a physical role by increasing sedimentation of fine particles favouring the accumulation of contaminants in the sediments, but they are organisms able to sequester trace metals and to bioconcentrate them in their tissues (Pergent-Martini and Pergent, 2000; Lafrabrie et al., 2008), acting as biofilters. Indeed, in the study area *C. nodosa* yielded higher heavy metal content in the dense (i.e. station *Cym*) than in the sparse (i.e. station *Cym-Edge*) meadow (data not shown), confirming the major role in reducing the contamination of sediments through biological processes. However, an opposite trend was found for Cd and Hg that were more abundant in the station with a dense seagrass meadow than in those closer to the stream. This can be the result of the lower adsorption of Cd and Hg than other metals (e.g. Lair *et al.*, 2007); as a consequence they accumulate in areas at a higher distance from the source.

Although in the present study low organic matter content was found in all the sampling stations, a significant correlation was observed between this variable and heavy metal level distribution. Indeed, in sediments there is a strong affinity between metals and organic matter (Förstner and Wittmann, 1981). However, the major factor involved in the observed

distribution of heavy metals in the fine fraction of sediments seem to be the distance from the source, local hydrodynamism and the presence of seagrasses.

The heavy metal levels were compared with the limits (0.3 mg/kg d.w. for Cd and Hg, 30 mg/kg d.w. for Ni and Pb, 50 mg/kg d.w. for Cr) proposed by the Italian law 367 (6/11/2003) regarding specifically sediments from marine-coastal areas, lagoons and coastal ponds. On average, three heavy metals exceeded the limit in two stations: Cd and Hg in *Cym-Edge* and *Cym*, and Cr in *Stream* and *Mouth*. Ni exceeded the limit only in *Cym-Edge*. The marine control station (*Bare sand*) showed values consistently lower than the maximum proposed, suggesting the overall good quality of the marine area adjoining the stream Irminio in terms of contamination.

In conclusion, maximum metal concentrations were registered in the transitional area between the continental and marine systems, corroborating the evidence for a buffer role of transitional ecosystems and their crucial importance for reducing contaminant transfer into the open-sea. In the present study, the buffering role seems to be strongly connected with the presence of seagrasses that, at low depth and due to their morphology, enhance sedimentation, functioning as traps for fine sediment and as barriers against the transfer of anthropic input from rivers to the open-sea, allowing a decline in contamination levels and consequent damages to marine organisms and ecosystem health.

REFERENCES

- Anderson M.J. (2005). DistLM v.5: A FORTRAN computer program to calculate a distance-based multivariate analysis for a linear model. Department of Statistics, University of Auckland, Auckland, New Zealand.
- Anderson M.J. and Willis T.J. (2003). Canonical analysis of principal coordinates: a useful method of constrained ordination for ecology. *Ecology*, **84**, 511-525.
- Angelidis M.O. and Aloupi M. (2000). Geochemical study of coastal sediments influenced by river-transported pollution: Southern Evoikos Gulf, Greece. *Mar. Pollut. Bull.*, **40**(1), 77-82.
- Butler A. and Jernakoff P. (1999). Seagrass in Australia: Strategic Review and Development of an R&D Plan. CSIRO, Melbourne, Australia.
- Dassenakis M., Scoullos M. and Gaitis A. (1997). Trace metals transport and behaviour in the Mediterranean Estuary of Acheloos River. *Mar. Pollut. Bull.*, **34**(2), 103-111.
- De Groot A.J., Salomons W. and Allersma E. (1976). Processes affecting heavy metals in estuarine sediments. In: J.D. Burton and P.S. Liss (eds.), *Estuarine Chemistry*. Academic Press, New York, pp. 131-157.
- Ernst W.H.O. (1987). Metal fluxes to coastal ecosystems and the response of coastal vegetation. In: A.H.L. Huiskes, C.W.P.M. Blom and J. Rozema J. (eds.), *Vegetation between land and sea, Structure and processes*. W. Junk Publ., pp. 302-310.
- Förstner U. and Wittmann G.T.W. (1981). *Metal Pollution in the Aquatic Environment*, Springer-Verlag, Berlin.
- Gibbs R.J. (1977). Transport phases of transition metals in the Amazon and Yukon rivers. *Geol. Soc. Am. Bull.*, **88**, 829-843.
- Islam S. and Tanaka M. (2004). Impacts of pollution on coastal and marine ecosystems including coastal and marine fisheries and approach for management: a review and synthesis. *Mar. Pollut. Bull.*, **48**, 624-679.
- Lafabrie C., Pergent-Martini C. and Pergent G. (2000). First results on the study of metal contamination along the Corsican coastline using *Posidonia oceanica*. *Mar. Pollut. Bull.*, **57**, 155-159.
- Lair G.J., Gerzabek M.H. and Haberhauer G. (2007). Sorption of heavy metals on organic and inorganic soil constituents. *Environ. Chem. Lett.*, **5**, 23-27.
- Lyngby E. and Brix H. (1982). Seasonal and environmental variation in cadmium, copper, lead and zinc concentrations in eelgrass (*Zostera marina* L.) in the Limfjord, Denmark. *Aquat. Bot.*, **14**, 59-74.
- Nienhuis P. H. (1986). Background levels of heavy metals in nine tropical seagrass species in Indonesia. *Mar. Pollut. Bull.*, **17**, 508-511.
- Pergent-Martini C. and Pergent G. (2000). Marine phanerogams as a tool in the evaluation of marine trace-metal contamination: an example from the Mediterranean. *Int. J. Environ. Pollut.*, **13**, 1-6.
- Pulich W.M. Jr. (1980). Heavy metal accumulation by selected *Halodule wrightii* Aschers. populations in the Corpus Christi Bay area. *Contrib. Mar. Sci.*, **23**, 89-100.
- Ward T.J. (1989). The accumulation and effects of metals in seagrass habitats In: . W.D. Larkum, A.J. McComb and S.A. Shepherd (eds.), *Biology of Seagrasses: A Treatise on the Biology of Seagrasses with Special Reference to the Australian Region*. Elsevier, Amsterdam, pp. 797-820.

Optical properties of Sicilian lakes during a *Cyanophycea* *Planktothrix rubescens* algal bloom

Vincenzo Pampalone¹, Antonino Maltese^{1*}, Giuseppe Ciraolo¹ and Goffredo La Loggia¹

¹ Dept. of Hydraulic Engineering and Environmental Applications, Università di Palermo (IT),
Viale delle Scienze –Ed. 8, Palermo, 90128, Italy, IT

*Corresponding author, e-mail maltese@idra.unipa.it

ABSTRACT

In December 2006 blooms of *Planktothrix rubescens* were found in the Prizzi reservoir in Sicily. *Planktothrix* is a genus of filamentous alga comprising approximately 6 species, between these the *P. rubescens* is sadly famous since this organism produces microcystins which are powerful hepatotoxins.

Firstly found in Europe in 1825 on Geneva lake, recently (2006) those algae has been find out in Pozzillo, Nicoletti e Ancipa reservoirs (Enna Province), as well as in Prizzi (Palermo Province) and Garcia reservoirs (Trapani Province).

Toxins produced by those bacteria (usually called microcystine LR-1 and LR-2) are highly toxic since they can activate oncogenes cells causing cancer pathologies on liver and gastrointestinal tract.

Even if water treatment plants should ensure the provision of safe drinking water from surface waters contaminated with those toxic algae blooms, the contamination of reservoirs used for civil and agricultural supply highlights human healthy risks. International literature suggests a threshold value of $0.01 \mu\text{g l}^{-1}$ to avoid liver cancer using water coming from contaminated water bodies for a long period.

Since *Planktothrix rubescens* activities is strongly related to phosphate and nitrogen compounds as well as to temperature and light transmission within water, the paper presents the comparison between optical properties of the water of an infested reservoir and those of a reservoir characterized by clear water.

Field campaigns were carried out in February-March 2007 in order to quantify the spectral transparencies of two water bodies through the calculation of the diffuse attenuation coefficient, measuring underwater downwelling irradiance at different depths as well as water spectral reflectance.

Results show that diffuse attenuation coefficient is reduced by approximately 15% reducing light penetration in the water column; coherently reflectance spectral signature generally decreases, exhibiting a characteristic peak **around 703 nm** not present in uncontaminated waters. Latter findings highlight the possibility to detect *Planktothrix rubescens* infestations using their spectral characteristics by means of multitemporal remote sensing techniques.

KEYWORDS: planktothrix rubescens; diffuse attenuation coefficient; visibility depth.

INTRODUCTION

In recent years publications that deal with problems related to rapid increases of cyanobacteria populations in aquatic ecosystems are increasingly appearing.

Cyanobacteria such as the genus *Oscillatoria* release toxins into waterbodies. Jann-Para et al. (2004) studied the *Planktothrix rubescens* species (*Oscillatoria rubescens*). The results of their work suggested that the toxin production increased when the light intensity, temperature, alkaline pH and phosphorus contents were at low levels.

Legnani et al. (2005), describes the seasonal dynamics of the Cyanobacterium *P. Rubescens*, pointing out the environmental factors favoring its dominance during the whole cycle, with particular attention to the role exerted by physical factors in promoting the growth of *P. rubescens*, despite the nutrient reduction. Experimental evidences suggested the involvement of mechanisms already observed in other European lakes, such as the establishment of a metalimnetic niche. Data pointed out high environment sensitivity to hydrological regime changes, probably due the seasonal phytoplankton dynamics. The reddish color of *P. rubescens* blooms rightly alerts media and population. *P. rubescens* is usually confined to the metalimnion as light penetrates to this depth, but during periods of low shortwave irradiance such as winter, when the filaments are poorly irradiated, they float up to the surface, forming red-colored water blooms (Walsby et al. 2004, and Walsby et al., 2005). Within this frame it is important to characterize the water column through its extinction optical properties.

Test sites

Many freshwater lakes at Northern latitudes are dominated by filamentous cyanobacteria of the genus *Planktothrix* that does not always associated with eutrophication. In recent years a toxic bloom of *Planktothrix rubescens* occurred in several Sicilian lakes (e.g. Ancipa Reservoir - Capizzi, Pozzillo Reservoir – Regalbuto, Nicoletti Reservoir – Leonforte, Raia Reservoir – Prizzi, Trinità di Delia Reservoir). The last two were chosen as test-sites (Figure 1), however no algal bloom was present at Raia-Prizzi lake during the field campaign.

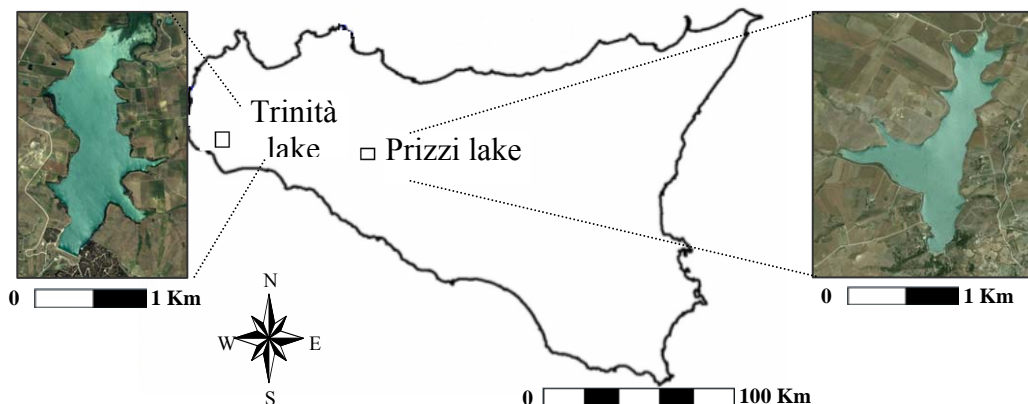


Figure 1. The test site locations in UTM WGS84 33N are, Prizzi lake: 359500E, 4177000N and SS. Trinità di Delia lake: 302000E, 4175000N.

Prizzi reservoir is an artificial lake in the Province of Palermo, Sicily, that resulted from the construction of a hydroelectric dam on the Raia Torrent, is also used for irrigation purposes. It has an average elevation of 638 m a.s.l., its surface area is $0.9 * 10^6 \text{ m}^2$, a mean depth of 10.3 m, and a maximum depth of 45.5 m.

Calvo et al. (1993) reported that total phosphorus concentration indicates eutrophic conditions, while chlorophyll a suggests mesotrophy, low phytoplankton biomass in spring, summer and autumn ($< 1 \text{ mg l}^{-1}$), and higher values in winter (4.1 mg l^{-1}). Phosphorus loadings mainly originate from cultivated soils (~50%); the reported surface loading was $\sim 1.5 \text{ gm}^{-2} \text{ y}^{-1}$. They also reported a zooplankton biomass maximum in summer ($\approx 3 \text{ mg l}^{-1}$) and lower values in the other seasons ($< 1.5 \text{ mg l}^{-1}$).

SS. Trinità di Delia reservoir, close to Castelvetrano in the Province of Trapani, Sicily, has been produced damming the River Delia for irrigation purposes (Figure 2). It has an average elevation of 69 m a.s.l., a surface of approximately $2.4 \times 10^6 \text{ m}^2$, a mean depth of 8.5 m, and a maximum depth of 22.0 m. Calvo *et al.* (1993b) reported that total phosphorus concentrations, chlorophyll *a* and phytoplankton biomass tend to eutrophic conditions. Phosphorus loadings mainly originate from urban centers (~50%), then from cultivated soils (~30%); the reported surface loading was ~6.8 gm⁻²y⁻¹. Water has a zooplankton biomass peak in spring (~9.5 mgL⁻¹), and low concentration of total inorganic nitrogen in the summer-autumn period.

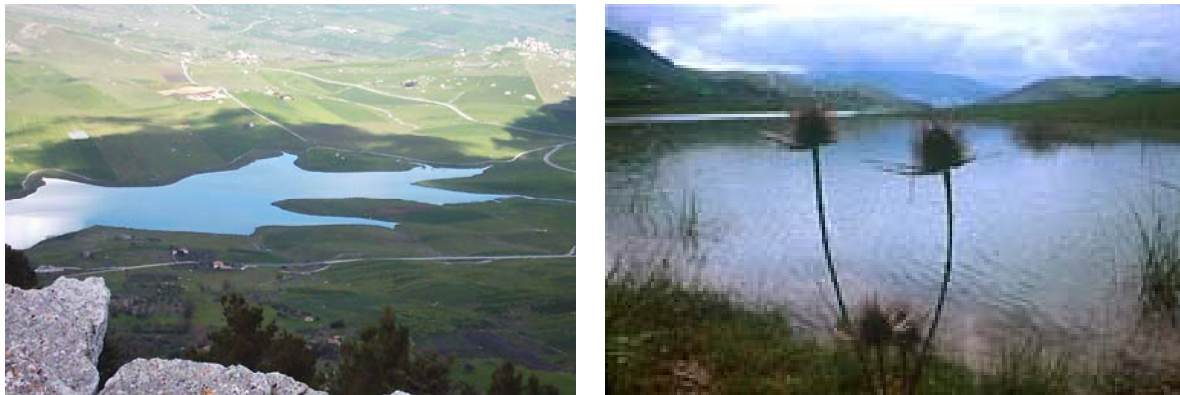


Figure 2. Panoramic view of Raia-Prizzi reservoir (left panel), and clean lake waters (not affected by algal infestation) (right panel).



Figure 3. Field campaign at Trinità reservoir 14th of March 2008. Left panel shows the *Planktothrix Rubescens* algal bloom, while right panel shows spectroradiometric measurements Analytical Spectral Devices FieldSpec® HandHeld spectroradiometer.

MATERIAL

The dataset therefore includes *in situ* data of two campaigns, both carried out in March 2008. All the data were positioned in UTM Zone 33N WGS84 using an EGNOS-enabled Magellan Meridian Platinum GPS unit.

Water samples collection

In order to establish if *Planktothrix Rubescens* algae, effectively infested the lake, a 0.5 l Niskin bottle was used to collect water samples at different depths. It has stoppers on both ends, a 0.5, which are held in place by springs. The bottle mouths are firstly left open, the sampler is then attached to a winch line and lowered to the desired depth, when, a weight is

released reaching the Niskin bottle, a mechanism releases the two stoppers, collecting a sample of the water from that depth.

Spectroradiometric measurements

Underwater spectral irradiances and in-air upwelling spectral radiances were acquired using an Analytical Spectral Devices FieldSpec® HandHeld spectroradiometer operating between 325 and 1075 nm with a spectral resolution of 1.5 nm. A 10 meter long fiber optic cable, fitted with an underwater cosine diffuser probe, was used to acquire underwater irradiances at 11 depths from just below the water's surface, up to 5 meters.

METHODS

Data processing: diffuse attenuation coefficient retrieval

The diffuse attenuation coefficient $K_d(\lambda_i)$ models the irradiance extinction behaviour within the water column. The depth at which a water column can be considered as optically infinite depends on the wavelength, as K_d is a spectral parameter. K_d can be directly measured from underwater measurements of spectral irradiance (Kirk, 1994) as we measured downwelling spectral irradiance (Equation 1). The greater the diffuse attenuation coefficient the more negligible is the contribution of the bottom and the more the water column can be considered optically as infinitely deep.

$$K_d(\lambda, z) = \ln \left(\frac{\frac{E_d(\lambda, z_1)}{E_d(\lambda, z_2)}}{z_2 - z_1} \right) \quad (1)$$

where:

$E_d(\lambda, z_1)$ and $E_d(\lambda, z_2)$ are the *in situ* downwelling spectral irradiance at depths z_1 and z_2 below the water surface, respectively and $K_d(\lambda_i)$ is the diffuse attenuation coefficient;

Assuming z_1 is equal to 0, we obtain:

$$E(z, \lambda) = E_{0^-}(\lambda) * e^{-K_d(\lambda) * Z} \quad (2)$$

where E_{0^-} represents the irradiance just below the water surface and z is a generic depth. Equation (2) describes the vertical irradiance attenuation assuming the coefficient K_d for zenith sun. Neglecting skylight, whose distribution depends on solar elevation, equation (3) takes into account the directional behaviour of the light field in the upper layer of the sea Jerlov, N.G. (1976):

$$E(z, \lambda) = E_{0^-}(\lambda) * e^{-K_d(\lambda) * Z} / \cos j \quad (3)$$

with:

$$\sin i / \sin j = \sin(90 - h_s) / \sin j = 4/3 \quad (4)$$

where h_s is the solar elevation and i, j are the absolute refraction angles for air and water.

RESULTS

The underwater spectral irradiance peak of the Prizzi lake waters was approximately located at 550-580 nm, increasing slightly towards longer wavelengths with increasing depth, while

the analogous measurements on the Trinità lake water gave a spectral maximum in the red region of the spectrum ($\approx 600\text{-}650$ nm).

Wavelength [nm]	MODIS	MERIS	CZCS	$K_d(l) [\text{m}^{-1}]$ Trinità lake	$K_d(l) [\text{m}^{-1}]$ Prizzi lake
412	405-420	402-422	-	1.44	1.53
443	438-448	433-453	433-453	1.32	1.04
490	483-493	480-500	-	1.01	0.69
510	-	500-520	510-530	0.94	0.60
531	526-536	-	-	0.84	0.51
555	546-556	-	540-560	0.65	0.45
620	-	610-630		0.37	-
670	662-672	-	660-680	0.52	0.81
678	673-683	-	-	0.54	0.82
756	743-753	753-758	-	1.23	3.33
865	862-877	845-885	700-800	1.61	3.14

Table 1. Diffuse attenuation coefficient K_d [m^{-1}] of clear and infested waters).

This is due to the high concentrations of *Planktothrix Rubescens* algae. The $K_d(\lambda)$ values were calculated for both sites for the central wavelengths corresponding to MODIS, MERIS and CZCS optical sensors (Table 1). Results were compared with Jerlov classification for which both waters are classified as turbid coastal waters (Water type 7).

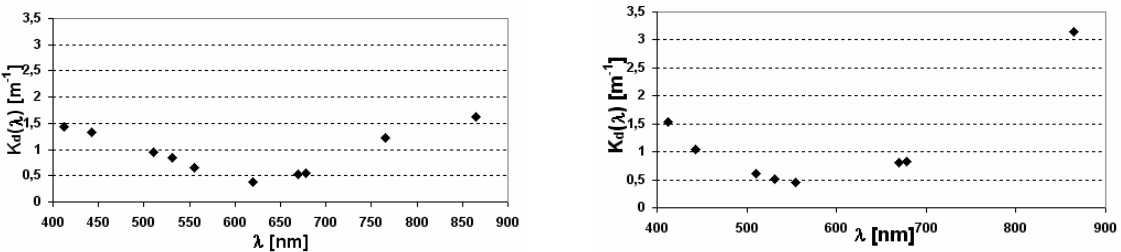
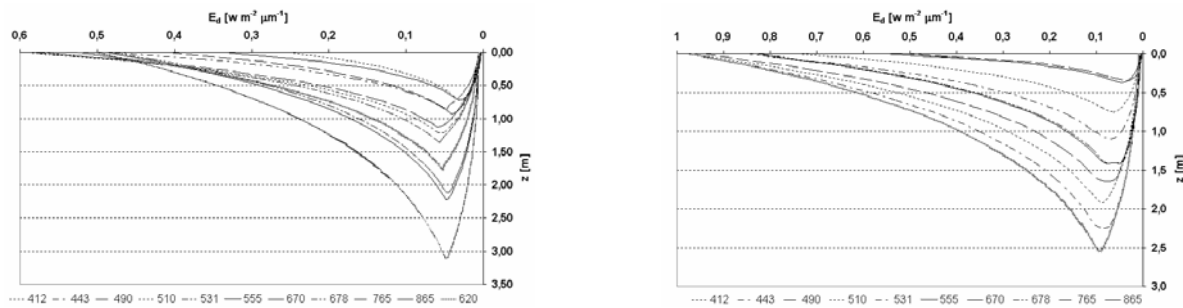


Figure 4. Water diffuse attenuation coefficient values for each wavelength

Left) Trinità lake

Right) Prizzi lake

An exponential law describing the spectral quantity $K_d(\lambda)$ allows us to estimate the virtual depths for which only a small part of the downwelling incoming irradiance (e.g. 1%) re-emerges, after travelling through the water column firstly as downwelling irradiance, then upwelling irradiance. These values give us an idea of the depth of spectral visibility of an optical remote sensor in this type of water. For the clear lake waters has a spectral visibility depth of nearly 3.0 m at 620 nm (Figure 5, left panel), while infested water reaches 2.5 m at 555 nm (Figure 5, right panel).

**Figure 5.** Irradiance decay $E_z(\lambda)$ [$\text{W m}^{-2} \mu\text{m}^{-1}$]*Left) Trinità lake**Right) Prizzi lake*

The analysis of the irradiance decay in the water (Figure 5) shows that the *Planktothrix rubescens* algal bloom attenuates the spectral visibility depth of about 0,5 m (~ 15%). However, has been implicitly hypothesized that the bottom reflects 100% of the downwelling irradiance, while the actual reflection depends on the bottom type and is much lower and as a consequence the visibility depth is actually lower.

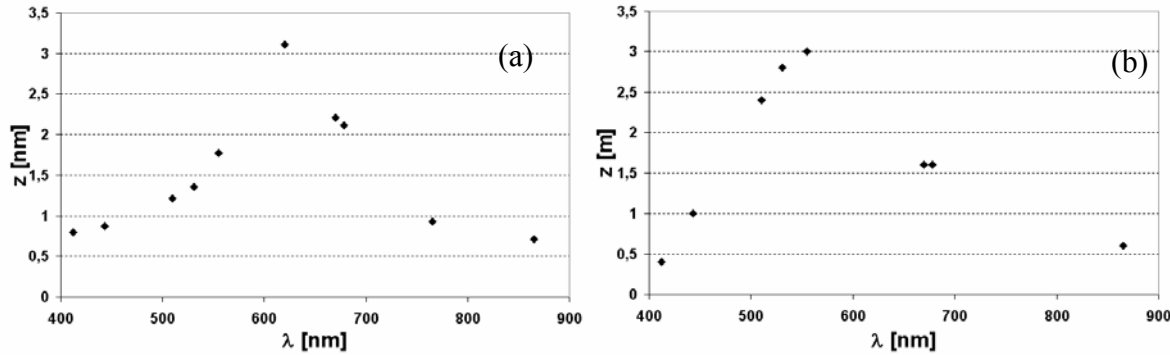
**Figure 6.** Spectral visibility depth z [m]*Left) Trinità lake**Right) Prizzi lake*

Figure 6 shows the depth of maximum spectral visibility for the central band wavelengths described in Table 1. The depth of visibility is quite low in the blue region in Trinità waters due to both absorption and backscattering, and it increases with increasing wavelength reaching a maximum (≈ 3.1 m) at 620 nm, while Prizzi water shows a similar maximum visibility depth (≈ 3.0 m) at lower wavelengths (512 nm). At higher wavelengths the visibility depth decreases in both waters because of strong absorption by the water itself in the near infrared part of the spectrum and because of the algae absorption.

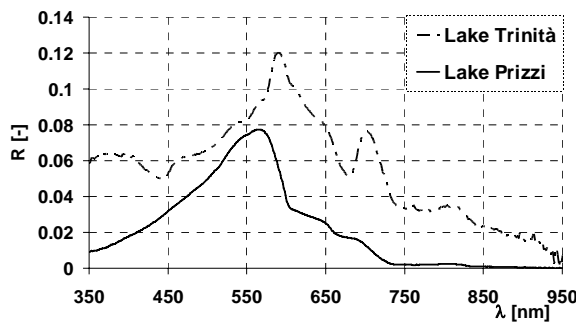
**Figure 7.** Spectral reflectance $R(\lambda)$ [-] of a typical Sicilian lake water (dashed line) and that of a water characterized by a *Planktothrix rubescens* algal bloom (continuous line).

Figure 7 shows that during the bloom the reflectance spectrum is formed under the dominating influence of the *Planktothrix rubescens*; typical features of this spectrum (dashed

line) are a maximum at wavelengths around 703 nm not occurring in the typical lake water (continuous line), a maximum at 592 nm occurring at lower wavelengths (571 nm) and with lower magnitude in the reference water (≈ 0.07 vs. ≈ 0.12), and a minimum at 447 nm and a maximum in the range 376-412 nm also not occurring in the reference water.

CONCLUSIONS

During periods of low shortwave irradiance such as winter, when light weakly penetrates water columns and waters get colder, *P. rubescens* filaments float up to the surface, forming red-colored blooms.

Analyses were carried out on two reservoirs: Prizzi lake and Trinità lake, respectively not showing and showing the *Planktothrix Rubescens* algal bloom during the field data acquisition. The comprehensive examination of all the literature parameters suggests that usually Prizzi reservoir was in a meso-eutrophic conditions, while the Trinità reservoir can be classified as eutrophic.

Underwater spectral irradiances and in-air upwelling spectral radiances were acquired in February-March 2007 by means of a Analytical Spectral Devices HandHeld spectroradiometer in order to characterize the extinction optical properties of the former lake (infested by the red algae) and the latter (not showing an infestation during field data acquisition). Underwater downwelling irradiance at different depths as well as water surface spectral reflectance were measured.

Results shown that optical properties are significantly altered when *Planktothrix rubescens* infests the lake water. Due to the algal bloom lake water the irradiance peak moves towards longer wavelengths (from 550-580 nm to ≈ 600 -650 nm). Spectral visibility depth decreases of about 15% from 3.0 m at 620 to 2.5 m at 555 nm.

The comparison between the reflectance spectrum of a water dominated by the *Planktothrix rubescens* influence and the spectrum of reference lake water shows a higher magnitude of the former case. Maximum and minimum values not occurring in the reference water (e.g. a minimum at maximum at 447 nm and a maximum at 703 nm) and a peak at 592 nm presumably decreasing with the decreasing concentration of the algae filaments.

ACKNOWLEDGEMENT

This research was partially funded by the ARPA (Agenzia Regionale per la Protezione dell'Ambiente) of the Sicilian Regional Government within the “Ricerche e studi finalizzati all'integrazione delle tecniche di telerilevamento per il monitoraggio ambientale dei laghi e per la definizione di un sistema per il rilevamento di fioriture algali” Project (Researches and studies aimed to integrate remote sensing techniques for lakes environmental monitoring and to setup an algal bloom detection system). The authors would like to thank Dr. A. Scordo and Dr. S. Nizza for helping us during field data acquisition.

REFERENCES

- Calvo, S., Barone, R., Naselli Flores, L., Fradà Orestano, C., Dongarrà, G., Lugaro, A. and Morabito, G. (1993a). “Limnological studies on lakes and reservoirs of Sicily”. Il Naturalista Siciliano, Vol. XVII, 189-195.
- Calvo, S., Barone, R., Naselli Flores, L., Fradà Orestano, C., Dongarrà, G., Lugaro, A. and Morabito, G. (1993b). “Limnological studies on lakes and reservoirs of Sicily”. Il Naturalista Siciliano, Vol. XVII, 237-243.
- Legnani, E., Copetti, D., Oggioni A., Tartari, A., Palumbo M.T. and Morabito, G. (2005). “*Planktothrix rubescens*’ seasonal dynamics and vertical distribution in Lake Pusiano (North Italy)”. J. Limnol., 64(1): 61-73.

- Jann-Para, G., Schwob, I., and Feuillade, M. (2004). "Occurrence of toxic Planktothrix rubescens blooms in lake Nantua, France" *Toxicon*, 43(3), 279-285.
- Kirk, J.T.O., (1994). "Light and Photosynthesis in Aquatic Ecosystems", Cambridge University Press, 509 pp.
- Jerlov, N.G. (1976). "Marine Optics. Chapter 4 – Global radiation incident on the sea surface", Elsevier Oceanography Series, 14. New York, pp. 231.
- Mobley, C.D. (1994) "Light and Water. Radiative Transfer in Natural Waters" *Optical properties of Water*, 61-142.
- Sathyendranath, S., Platt, T., 1989. "Remote sensing of oceanic primary production: Computations using a spectral model's" *Deep-Sea Res. I* 36, 431-453.
- .

Study of the accuracy of the mean flow from ADCP

Manel Gutierrez, Jesus Planella*, Elena Roget

*Department of Physics, Environmental Physics Group, University of Girona.
Campus de Montilivi, PII. E-17071, Catalonia, Spain. http://copernic.udg.es/en/r_gfa.php
u1052100@correu.udg.edu, jesus.planella@udg.edu, elena.roget@udg.edu*

ABSTRACT

Time series measured with acoustic Doppler current profilers (ADCP) need to be accurately processed in the time domain to achieve reliable mean velocity profiles. This analysis becomes more complex if currents are slow and the mean velocity in a time length can be affected by turbulence and unsteady processes.

This paper discusses the effect of sampling time length on the accuracy of the mean velocities based on autocorrelation functions. The effect of unsteady processes is investigated using several statistical criteria, such as a run test and a reverse arrangement test, to assess the signal stationarity. Finally the normalized mean square error is also computed to optimize the averaging time, giving an error below a small percentage of the ensemble variance.

A procedure is discussed and applied to data recorded with an ADCP moored at the bottom of Lake Banyoles, in the narrow sill connecting the two lobes of the lake, where a slow baroclinic current (up to 4 cm/s) was present.

KEYWORDS:

Autocorrelation function; Accuracy; Baroclinic current; Mean velocity profile; Sampling time length; Statistical tests

INTRODUCTION:

Acoustic Doppler current profilers (ADCPs) have been used to measure flows in aquatic systems for over two decades now and within the last years they have emerged as an alternative to current meter string measurements. However, to correctly determine that mean flow profile, instrument characteristics are not enough to determine the operational settings which also depend on characteristics of the flow such as its turbulence level.

That is why current commercial instrumentation considers different flow conditions and allows different profiling modes. Accurately determining the time evolution of slow currents is still a challenging task. It requires determining the best averaging to perform for noise reduction and fulfilling the stationarity assumption in order to obtain statistically significant velocities of the flow with the best possible time resolution.

In this study different statistical methods are investigated to find the optimum parameter to improve the ADCP profiling capability for low velocity flows. Also, an example application is presented in section 2 for the case of bottom baroclinic currents in a small lake due to the different cooling rates of its two lobes. In section 3 different statistical tests are considered to better determine the parameters for data processing. Finally in section 4 the measured flow, based on the analysis in section 3, is presented.

MEASUREMENT SITE AND EXPERIMENTAL SET UP

Lake Banyoles is a small, widely-studied lake (see Casamitjana et al. 1996 for a review) with the main inflow ($1 \text{ m}^3/\text{s}$) entering the lake through 12 warm underground sources. At the end of the autumn, when the surface mixed layer has completely disappeared, different cooling rates between the two lobes create a baroclinic current from the northern to the southern lobe which affects the circulation of the entire lake and shifts the residence time of the northern lobe from a few days to almost one year (Roget et al., 1993). Direct measurements of the velocity of this current using a rotor current meter placed at the Station 1 (see Fig 1a) one metre above the bottom showed velocities ranging from 4 to 7 cm/s along the neck connecting the two lobes (see Fig. 1b).

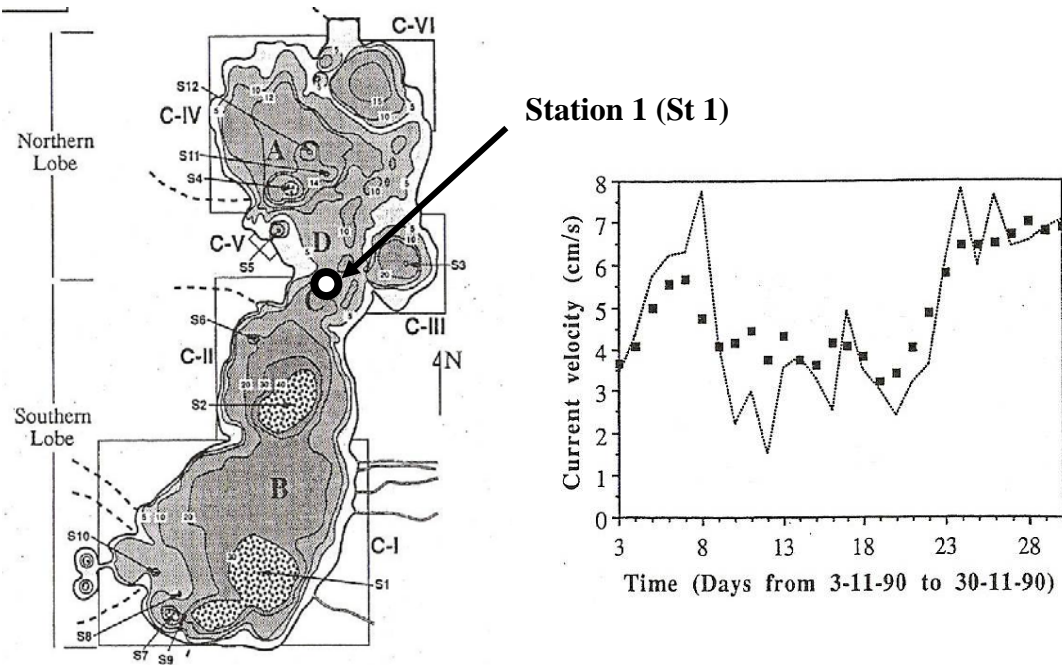


Fig. 1. (Left) Bathymetric map of Lake Banyoles according to Moreno-Amich and Garcia Berthou (1989). The northern and southern lobes are marked on the map together with 4 sub-basins in the northern lobe and two others in the southern lobe. Dotted areas correspond to 12 underground sources (called S1-S12). Station 1 is marked with a circle on the map.

(Right) Graphic of the bottom density currents at St 1 (dotted line) measured during November 1990 and corresponding estimated baroclinic velocities (little squares).

For the present work, in November and December 2008 a broadband 600 kHz ADCP (RDI Instruments) was mounted on the bottom of Lake Banyoles at Station 1 showed in Figure 1. The field campaign was carried out in fair weather conditions: light winds about 5 m/s blowing from the south. Under these conditions, the general circulation of the lake is known to be as presented in Figure 2, that is, the bottom density currents flowing southwards together with the returning surface currents in the upper layer, which at the time is also forced by the wind drag.

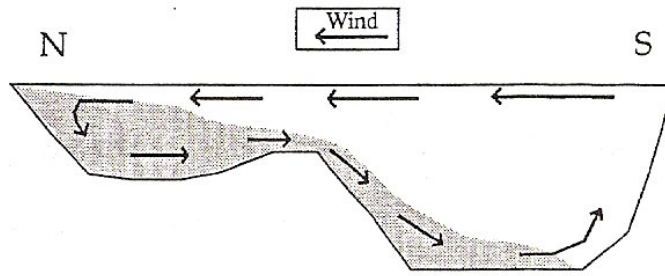


Fig. 2. Schematic of the water circulation in Lake Banyoles when the density current is established and a southern wind blows.

Although standard ADCP deployment structures are fixed, the conditions of Lake Banyoles – small fetch and low winds – allowed us to use a highly buoyant frame placed immediately above the bottom which assured the verticality of the instrument. Because changing tilt angles (pitch, heading and roll) in time leads to changes of the velocity along each beam and causes errors in the estimates of the mean flow (Yu and Lueck, 1999), we collected the data using a single ping configuration and monitored the tilt angle fluctuations. We found a constant value for these angles and small variations in pitch and roll angle values.

Basic ADCP operating parameters were selected using manufacturer specifications and conventional guidelines (RD Instruments, 1996; RD Instruments, 1999) as summarized in Table 1. A single ping configuration at the fastest rate possible (0.41 s per 2.4 Hz) was chosen to study velocity uncertainties due to both internal and external factors (including turbulence). ADCP was operated in mode 1. To reduce statistical errors, the minimum value of the horizontal ambiguity velocity was set as low as possible – 80 cm/s – a speed that largely exceeds the maximum value of the expected current in the lake. Quality parameters such as correlation and percentage of good data were also recorded for the posterior analysis.

**Workhorse Sentinel ADCP (RDI)
Characteristics /Operational
settings**

Frequency	600 kHz
Beam angle	20°
Sampling rate	2.4 Hz
Bin size	0.5 m
Beginning 1 st cell	1.51 m
Ambiguity velocity	0.8 m/s
Operation	WM1, Single ping
St. 1 depth	~9 m

Table 1. Characteristics and operational settings of the Workhorse

DATA PROCESSING AND ANALYSIS

Data collected by the ADCP were stored in a binary file and uploaded into WinADCP software to be exported into a text file for later analysis of the streamwise velocity component, v . Prior to this and based on the correlation magnitude and percent good values bad, false data were flagged for further interpolation. Also despiking was performed in order to remove any value of v larger than 2.5 times the standard deviation of a given segment (Emery and Thomson, 2001).

Streamwise velocities were recorded from 12.00 to 14.20 at Station 1 on November 29 and an 18-min segment starting at 12.20 was chosen for the analysis presented below. A similar analysis was done recursively for the two-hour period showing analogous results.

The mean and the variance of v was computed from an increasing number of data points starting from 1 point (1/2.4 sec) to 27000 points (18 minutes). Results for bins 4 (near the bottom) and 11 (near the surface) are presented in Figure 3 where it can be observed that statistical (mean and variance) values become rather stable after minute 12, approximately.

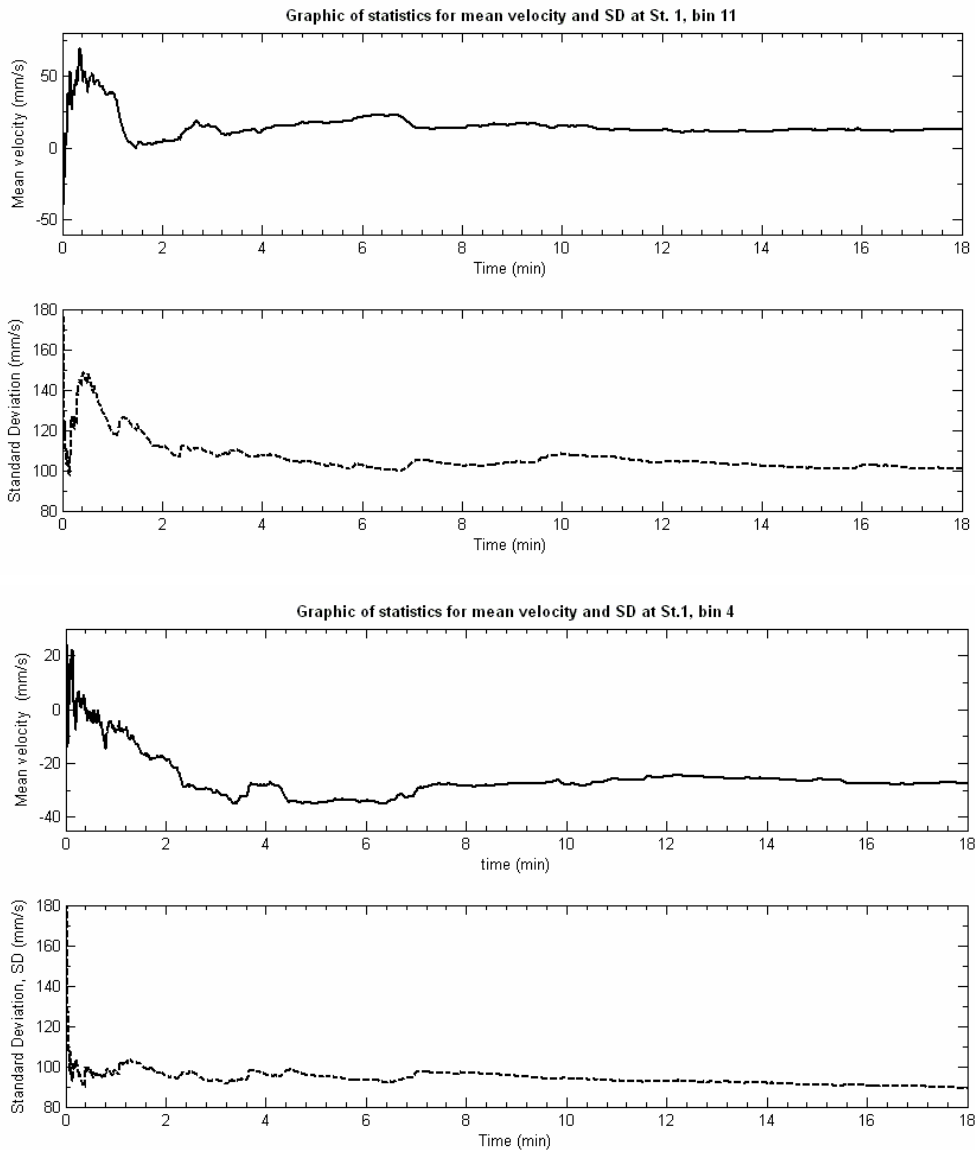


Fig. 3. Stability of the mean and SD of the velocity for bins 4 and 11 of an arbitrary data segment considering a recursive averaging from the measuring interval to 18 minutes.

Stability of the statistical parameters observed in Figure 3 is in agreement with Tenekes and Lumley (1972) who proposed

$$T = \frac{2\tau \overline{u^2}}{\epsilon^2 U^2} \quad (1)$$

as a good estimate of the time series length, T, to obtain accurate values of the mean flow quantities (mean and variance). In formula (1)

$$\epsilon = \sqrt{\frac{(U_T - U)^2}{U}} \quad (2)$$

is the allowable error level, U the estimated mean, U_T is the mean velocity at the record length T and τ is the time integral scale (Muste, 2004). The time integral scale can be obtained by integrating the area below the autocorrelation function (ACF) between zero time lag and that corresponding to the first zero crossing.

For the case discussed here the autocorrelation functions for the data corresponding to four different bins (depths) are presented in Figure 4 and the corresponding estimates of τ are shown in Table 2.

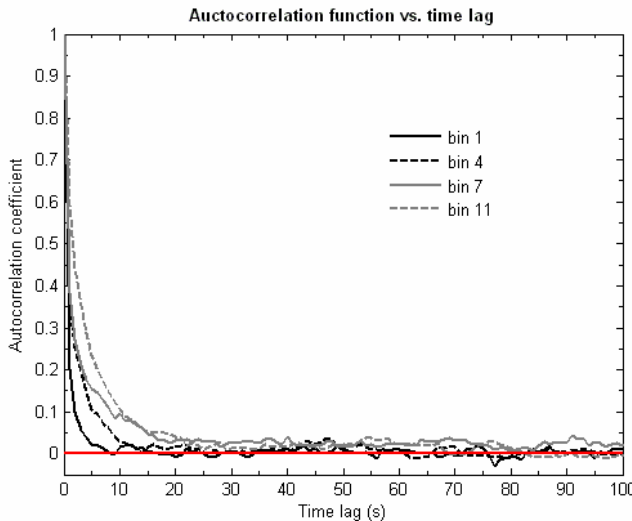


Fig. 4. Autocorrelation function for the streamwise velocity at four different distances from the bottom at St. 1 in the lake.

Table 2. Estimations of the length scale, τ , from ADCP single-ping 18-min records collected at different depths of the water column.

Bin	z/h	τ (s)
1	0.15	0.40
4	0.30	0.85
7	0.45	3.00
9	0.55	2.14
11	0.65	1.94
12	0.70	3.03

As observed in Table 2, for the 18-minute record studied, the integral time scale, τ , ranges between 0.65 and 3.03 s. As a rough approximation, considering a mean integral time scale of 2 s and error level of 10% and estimating from Figure 3a a mean velocity of the order of 50 mm/s and a standard variation of 100 mm/s, the time record length required to obtain the real mean velocity according to formula (1) should be about 20 minutes. These results, which are obtained after knowing the mean statistical properties of the series, are approximately in accordance with the observed stationarity of the statistical parameters of the signal observed in Figure 3 for the 18-minute time series.

In the following stage an accurate analysis of data stationarity was carried out applying different statistical tests (Beck et al., 2006) to determine the length of time to obtain correct mean velocities considering random errors (from internal and external factors) and the stationarity of the interval. With this objective the standard running test (Siegel and Castellan, 1988) has been used together with a reverse arrangement test proposed by Bendat and Piersol (1986). In order to smooth small scale variability, both tests were conducted on the 18-minute time series after averaging for 30 s. As presented in Table 3, for the 18-minute interval shown in Figure 3, for all the bins the z-score has been less than -1.96 or more than 1.96, which are the limits, at a confidence level of 95%, to accept a significant trend. These results confirm the stationarity of 18-minute segment data.

		Number of reverse arrangements in the time series			
		Run Test	Reverse Arrangements		
		Test			
Bins	z/h	z-score (\bar{U})	z-score (SD)	z-score(\bar{U})	z-score(SD)
1	0.15	-0.10	-0.10	-1.85	-0.57
4	0.30	0.51	-0.44	0.74	1.58
7	0.45	-0.93	-1.17	-1.22	0.21
9	0.55	-0.10	-0.82	-0.10	-1.58
11	0.65	-0.15	-0.83	-0.35	0.74

Table 3. Results from the two stationarity tests for five of the time series of the instantaneous velocity at different distances from the bottom of the lake at St.1.

A statistically significant ($p < 0.05$) trend is present when the z-score is ≤ -1.96 or ≥ 1.96 .

Assuming the process to be steady, the accuracy of the data is studied to determine the sampling time necessary to capture the temporal random distribution of turbulence in the process. The normalized mean square error (NMSE) is defined as follows (González-Castro, 2000):

$$\text{NMSE} = \frac{(U(T) - \bar{U})^2}{\bar{u}^2}$$

where \bar{u}^2 is the variance of the streamwise velocity, $U(T)$ is the mean velocity estimate based on a record length and \bar{U} is the ensemble mean velocity.

The NMSE as a function of time span is plotted in Figure 5.

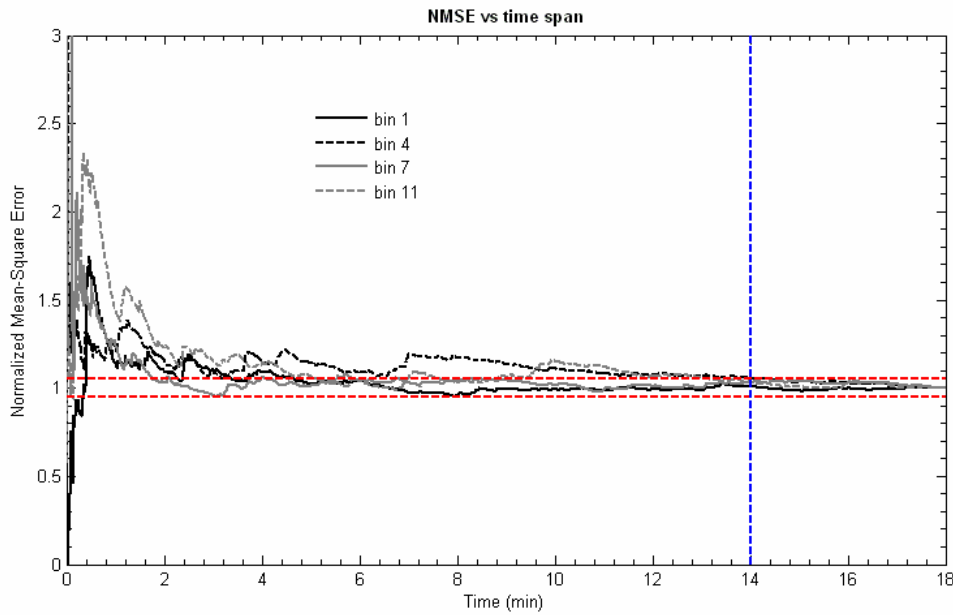


Fig. 5. Normalized mean-square error calculated at different times of averaging. Horizontal lines show the limits of 5% in error of the ensemble variance. The vertical line at 14 min suggests time of averaging when the error stays below 5%.

Observing the graphic of NMSE, 18-minute initial record data could be reduced to a 14-minute average and this average time keeps the error below 5%.

RESULTS

Figure 6 shows the profile of the mean velocity averaged over 14 minutes and Table 4 presents the accuracy of its mean, which is about 0.5 cm/s and is the lowest indeterminacy we can expect according to the bias of the instrument.

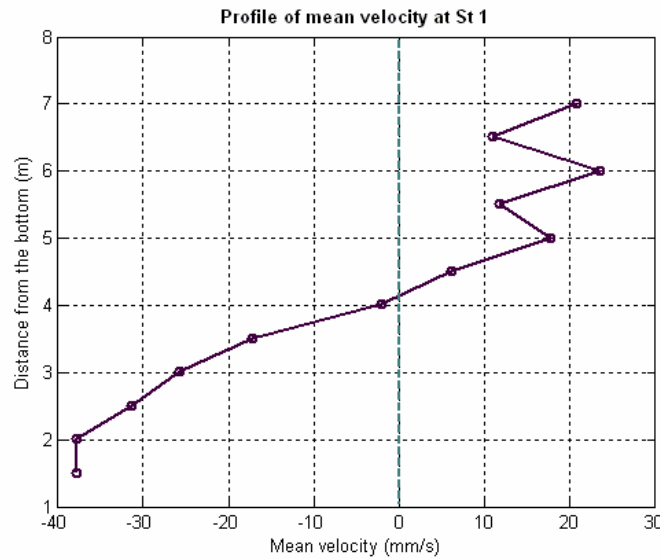


Fig. 6. Profile of the mean velocity for 14-min record length.

Bin	Mean flow (mm/s)	Accuracy (error of mean flow) (mm/s)
1	-37.81	4.86
2	-37.84	4.92
3	-31.40	4.18
4	-25.73	4.60
5	-17.17	4.26
6	-2.05	4.60
7	6.18	4.90
8	17.89	4.82
9	11.90	5.10
10	23.55	4.76
11	11.12	5.12
12	20.84	4.60

Table 4. Results for mean flow and its accuracy based on MNSE.

Values of the mean flow have been compared to the mean density current measured over the sill and plotted in Figure 1 (right). Average values obtained with ACDP in 14-minute periods of time in the bottom layer are ~ 4 cm/s and they are closer to the expected values of the mean flow obtained from current meters in this period of the year. The mean currents obtained from the ADCP are in agreement with measured density currents and an average time of 14 minutes seems to be an appropriate record length to achieve mean flow using ADCP with errors below 0.5 cm/s.

SUMMARY AND CONCLUSIONS

To determine the mean flow and its characteristics in aquatic systems with slow currents, the techniques to obtain accurate measurements depend on the instrument selection and the nature of the flow. Bottom-mounted ADCP obtains the true instantaneous velocity time series if currents are slow. Accuracy depends on the instrument specifications but it is important to know the general features of the flow at the measurement site and choose the appropriate parameters and settings from the ADCP. To get accurate values of mean profiles statistical analysis should be carried out.

The results presented in the previous sections show that mean flow can be estimated accurately by choosing the adequate operational and post-processing methods. For this it is proposed to study the stability of the statistics of the first and second moments of the instantaneous velocity using either a running test or a reverse arrangement test to confirm that the averaging of data are not affected by unsteady processes. Furthermore, a study of the variation of the normalized mean square error can be used to optimize the averaging period, keeping the error in the mean flow below a small percentage of the ensemble variance, and allowing the best resolution of the variation of the flow in time.

More precisely, a velocity profile of the mean flow calculated using a 14-minute record length is presented together with the error estimate. Velocities were found to be about 4 cm/s near the bottom and decreasing below the bias values (0.5 cm/s) at bin 6 (4 metres above the bottom). At the surface layer a mean current with a north component of around 2 cm/s, describing the expected general circulation of the lake. The accuracy obtained from the statistical analysis of the data does not exceed a value of 0.5 cm/s.

REFERENCES

- Beck T., Housh T., Weir J., Cramer J., Vardaxis V., Johnson G., Coburn J., Malek M., Mielke M. (2006) An examination of the Runs Test, Reverse Arrangements Test, and modified Reverse Arrangements Test for assessing surface EMG signal stationarity, *Jou. Neu. Met.* **156** 242-248.
- Bendat JS, Piersol AG. (1986) Random data: analysis and measurement procedures. 2n ed. New York John Wiley & Sons.
- Casamitjana X., Colomer J., Roget E and Serra T, Physical Limnology in Lake Banyoles, *Lim.* **25** (1-2), 181-188.
- Emery W., Thomson R. E. (2001) Data Analysis Methods in Physical Oceanography, Elsevier, 319-343.
- Gonzalez-Castro J., Oberg K., Duncker J., Effect of temporal resolution on the accuracy of ADCP measurements, in Proceedings of the German Hydrographic Society, Hydrographentag, Bremerhaven, Germany, 2000.
- Lu Y., Lueck R., (1999) Using a Broadband ADCP in a Tidal Channel, Part I: Mean flow and shear. *Jou. Atm. Oce. Tech.* **16** 1556-1567.
- Muste M., Yu K., Pratt T., Abraham D. (2003) Practical aspects of ADCP data use for quantification of mean river flow characteristics; Part II: fixed-vessel measurements. *Flow Meas. Instr.* **15**, 17-28.
- RD Instruments (1996), Acoustic Doppler Current Profiler- Principles of Operation; A Practical Primer , RD Instruments , San Diego CA.
- RD Instruments (1999) General River Profiling, Application Note.
- Roget E., Colomer J., Casamitjana X., Llebot J.E. (1993) Bottom currents induced by baroclinic forcing in Lake Banyoles (Spain) *Aqu. Sci.* **55** (3) 207-227.
- Siegel S., Castellan Jr. (1998) Nonparametric statistics for the behavioural sciences. 2nd ed. New York: McGraw-Hill 58-72.
- Tennekes U., Lumley J.L. (1997) A first course in turbulence, MIT Press, Cambridge, MA.

ADCP velocity profiles analysis in the Castellammare gulf

C. Nasello^{1*}, G. Ciraolo¹, G. La Loggia¹

¹ Department of Hydraulic Engineering and Environmental Applications
University of Palermo – Viale delle Scienze- 90128 Palermo, Italy

*Corresponding author, e-mail carmelo.nasello@unipa.it

ABSTRACT

Velocity profiles have been collected in three points within the Castellammare gulf at around 1500 m far from the coastline. This area is characterized by the presence of an aquaculture farm that positioned 5 floating cages in this zone. The impact of this activity on the environment strictly depends on the currents and water exchange. The general aim of this research is the characterization of the circulation characteristics of this area. The analysis of the free surface oscillations shows the typical behaviour of tide forcing, with high minima and maxima during the night, due to the higher moon attraction during these hours compared with the morning hours. A prevalent current direction from South-West to North-East has been recorded at each depth. This direction is almost parallel to the coastline. This behaviour is probably determined by morphology of the area and the general circulation of the Castellammare gulf.

KEYWORDS

Acoustic Doppler Profile; Coastal measures; gulf current; Sicily; velocity profiles.

INTRODUCTION AND STUDY AREA

The numerical modelling of the hydrodynamics in coastal areas requires a sound knowledge of the in-situ dynamical behaviour of the simulated variables (velocities, water elevations, etc). These measurements are essential in calibration and validation procedures (Cioffi et al., 2005) and they are also important to understand the physical system. In the past our research group carried out a number of field surveys aimed to understand the hydrodynamics of coastal water bodies (Nasello and Ciraolo, 2004; Nasello et al., 2005, 2006) and to plan possible actions to prevent the loss of the local species. Moreover, numerical models have been set up in order to reproduce the water levels and average velocities as function of the external tidal forces and of the coastal area physical parameters.

This paper illustrates results of field measurements carried out in a coastal Gulf, called Golfo di Castellammare, in the north-west part of Sicily (Italy), at around 1500 m far from the coastline. The area is seasonally influenced by continental inputs and, which originate from nearby rivers. This area is characterised by the presence of an aquaculture farm that positioned 5 floating cages in this zone. The impact of this activity on the environment strictly depends on the currents and water exchange.

METHODS

Velocity profiles have been collected in three points within the Castellammare gulf at around 1500 m far from the coastline (depths 28-38 m). This area is characterised by the presence of

an aquaculture farm that positioned 5 floating cages in this zone. The impact of this activity on the environment strictly depends on the currents and water exchange. The general aim of this research is the characterization of the circulation characteristics of this area. The data collected will be used to calibrate and to validate numerical mathematical models of circulation in coastal areas.

The distances between the ADCP systems range from 525 to 980 m (Fig. 1). The ADCP instruments have been positioned by scuba divers on concrete blocks. All the ADCP were up-looking systems.



Figure 1. a) The location of the study area (Castellammare gulf), b) locations of the 3 ADCP.

The instruments characteristics are reported in tab. 1. An average velocity profile every 20 min. has been recorded: each velocity is the averaged value of 50-273 measured values.

Table 1. ADCP measurement systems characteristics.

	Aquadop Nortek	Aquadop Nortek	ADP SonTek	ADP SonTek	Workhorse Monitor RDI
Water depth (m)	27.7	27.7	37.9	37.9	33.5
Number of profiles	3593	728	4169	4408	1873
Time of first profile	07/05/2008 12.00	26/06/2008 11.20	07/05/2008 12.20	30/07/2008 12.00	08/08/2008 8.55
Time of last profile	26/06/2008 09.40	06/07/2008 13.40	04/07/2008 11.00	29/09/2008 17.00	03/09/2008 8.55
Profile interval (s)	1200	1200	1200	1200	1200
Number of cells	14	27	10	38	35
Cell size (m)	2	1	4	1	1
Average interval (s)	90	120	120	120	--
Pings per ensemble	--	--	273	273	50

FREE SURFACE OSCILLATIONS (TIDE)

The first dataset we analysed is the free surface oscillations. The free surface oscillates according with the tide forcing, with high minima and maxima during the night, due to the higher moon attraction during these hours compared with the morning hours (fig. 2a). Of course these oscillations are higher during the full moon or new moon periods (fig. 2b). Fig. 2a shows recorded levels, recorded every 20 min, and the same signal filtered using a 1st order Butterwoorth digital filter with 4 hours cut off period.

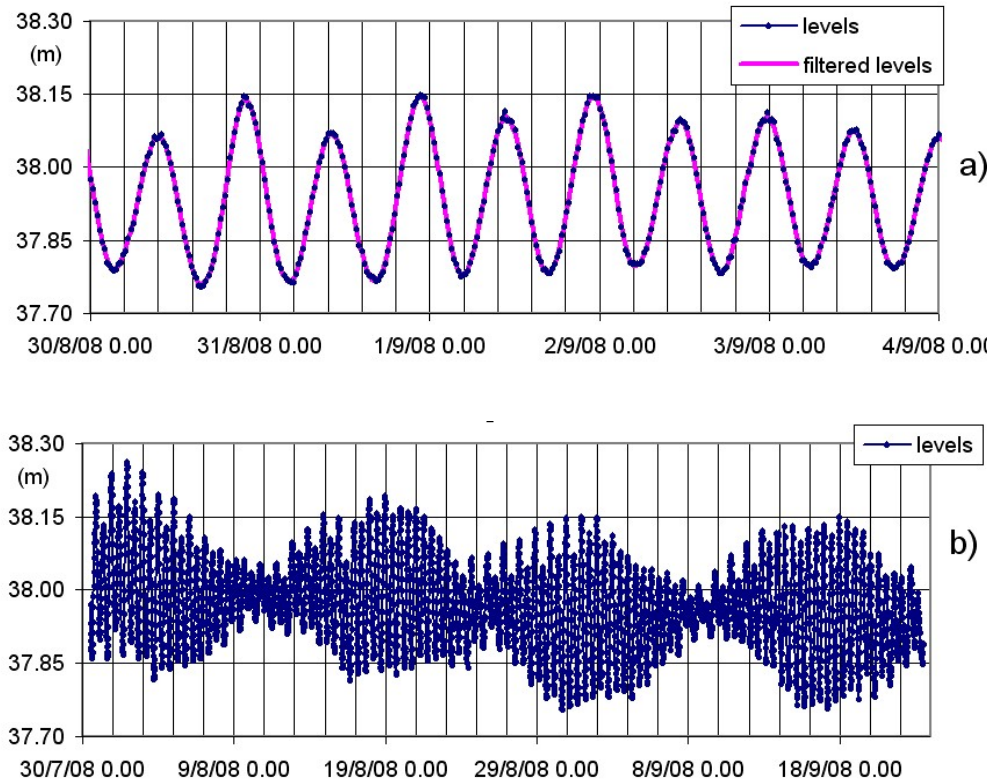


Figure 2. Tide levels recorded by ADP SonTek (38 cells); a) night and morning effect, b) full and new moon effect.

Power spectra of the filtered signal, both for the SonTek and the NorTek ADCP, shows the typical tide peaks (periods 21.5 and 12 hours) (fig. 3a, b).

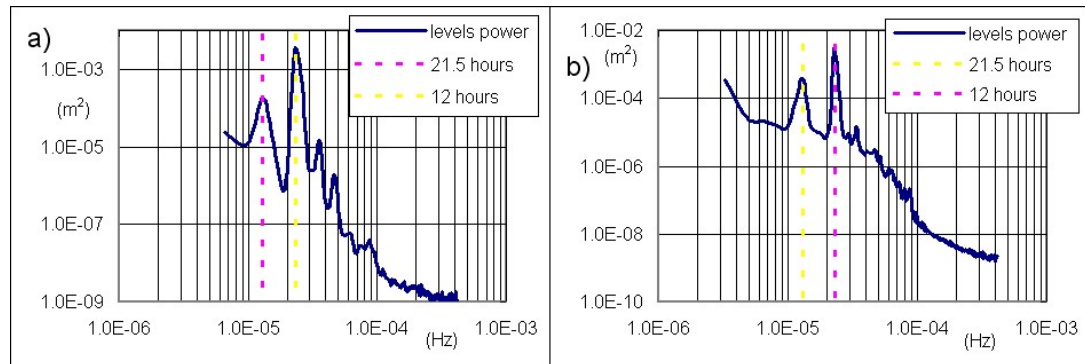


Figure 3. Tide spectra of the signal recorded by a) ADP SonTek (38 cells), b) Aquadop NorTek (14 cells).

VELOCITY MEASUREMENTS

To estimate the validity of velocity measures we considered that there are two sources of interference: the reflection of the acoustic pulse from the boundary, and the side lobe interference. We used the profile of return signal strength to determine the last good cell where the measurements can be considered accurate (SonTek, 2000, 2009). The profile of signal strength decays with distance from the transducers, with a large spike corresponding to the reflection of the surface (fig. 4). For this reason the measurements in the last two cells, near the surface, have been discarded.

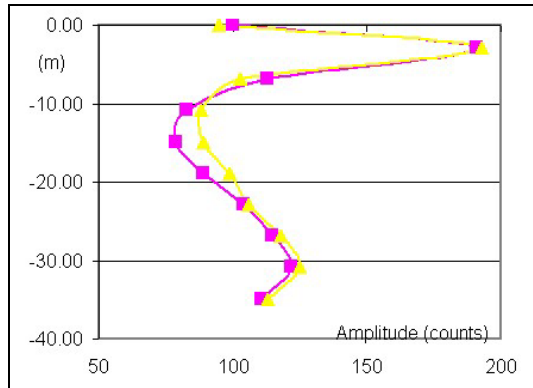


Figure 4. Spikes of profile of amplitude signal near surface (ADP SonTek - 10 cells).

As example we report the velocities recorded in East and North axes system for two days in correspondence of some particular depth h from the surface. On the recorded data we superimposed the original signal with a 1st order Butterwoorth filter (4 hours cut-off) (fig. 5).

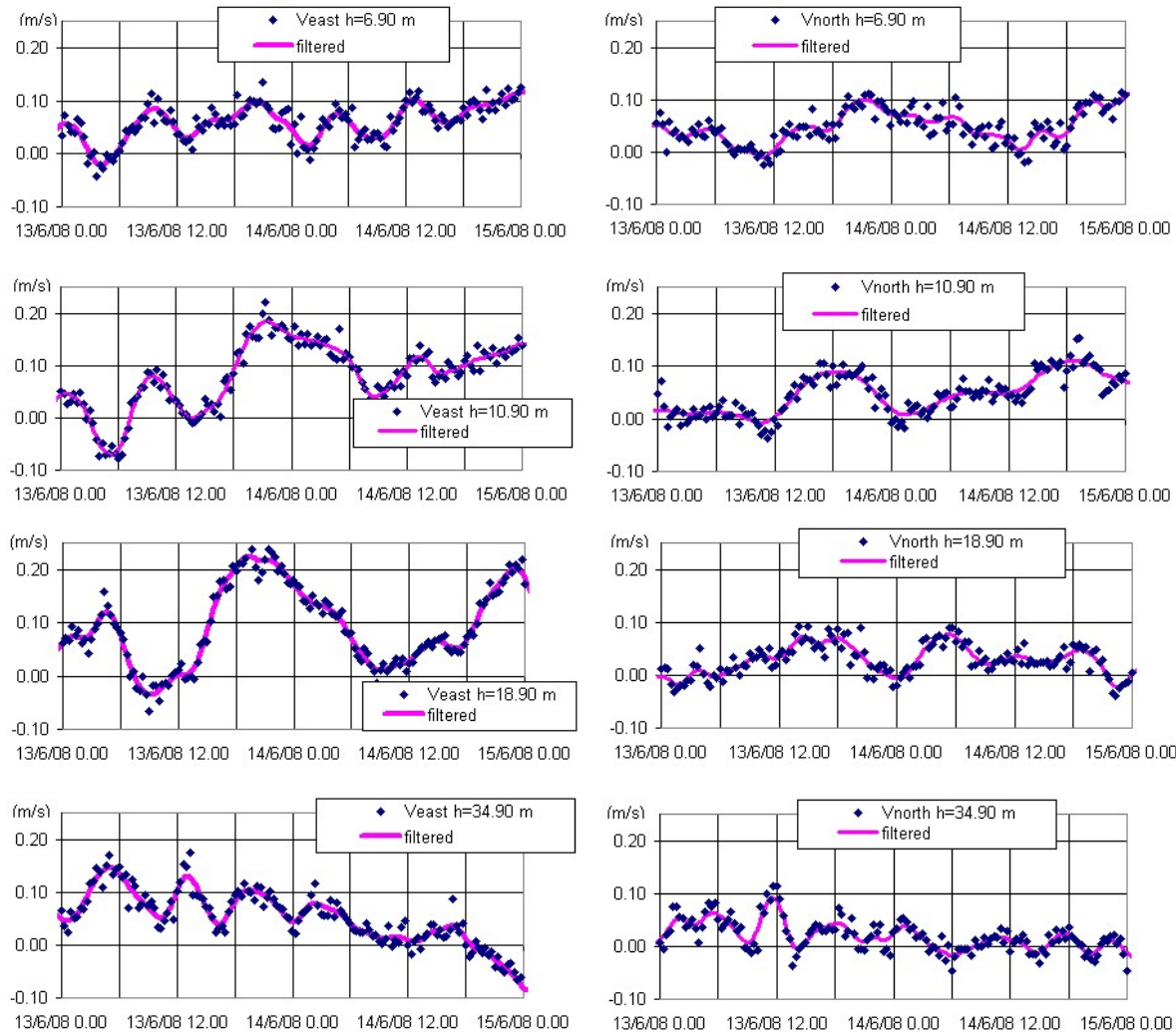


Figure 5. Veast and Vnorth velocities recorded by ADP SonTek (10 cells) at the depth h from the surface.

Analysing these signals it is possible to observe:

1. velocities show a cyclic behaviour due to the tide influence;
2. during these two days the two velocity component, V_{east} and V_{north} , are mostly positive. A prevalent current towards north-east directions seems to characterise this area.

The evidence of this prevailing current superimposed to the tidal cycle, can be argued from the vector representation of the filtered velocities (fig. 6). The two instruments (Aquadop Nortek and ADP SonTek) positioned at different depths h from the surface, show for three consecutive days the same direction of the velocity vectors.

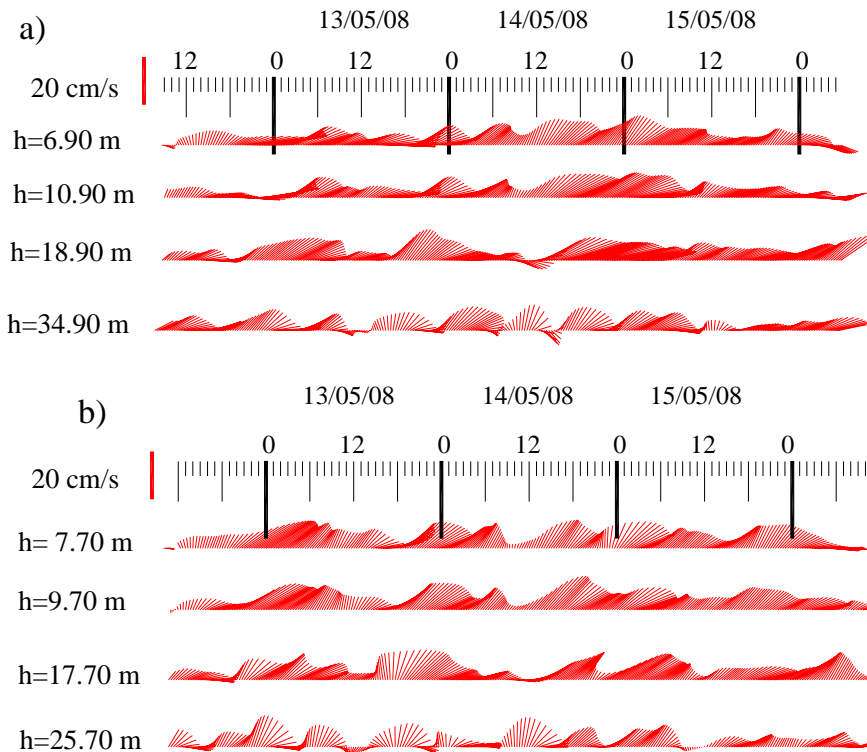


Figure 6. Prevailing current directed towards North-East direction. a) ADP SonTek 10 cells, b) Aquadop Nortek.

A different behaviour can be found during the 6th and the 7th of July. The two instruments recorded velocities in South-West direction (fig. 7).

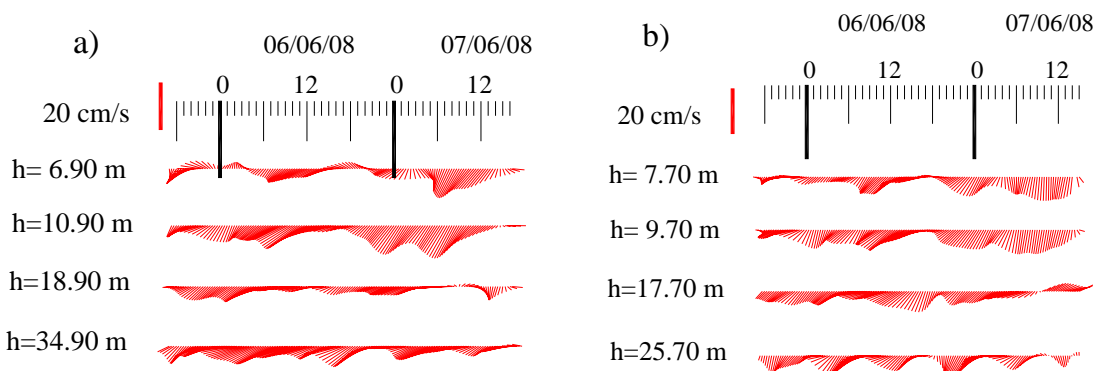


Figure 7. Prevailing current directed towards South-West- a) ADP SonTek 10 cells, b) Aquadop Nortek.

The analysis of the Figg. 6 and 7 highlights the presence of a persistent current from South-West to North-East direction that can invert in the opposite direction. The tide affects this current with accelerations or decelerations.

The presence of the tide effect on the velocities components can be argued also by the power spectra analysis of the (filtered) data (fig. 8). A peak at 22 hours period can be noted.

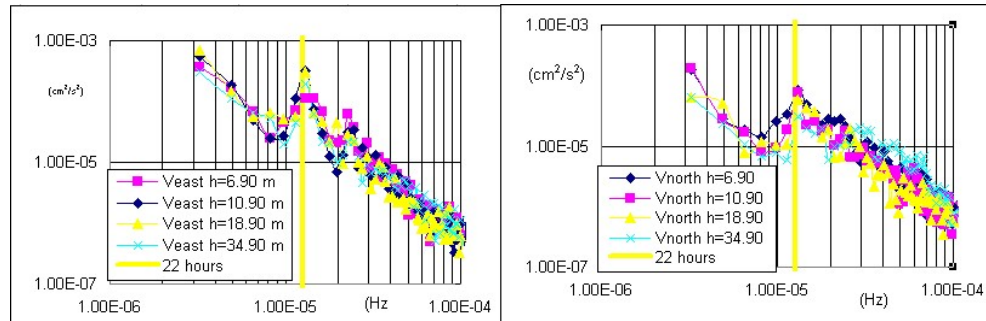


Figure 8. Power spectra of velocities components (ADP SonTek 10 cells).

A frequency analysis of the velocity directions has been also performed. The directions values have been subdivided in 24 sectors and the frequency of occurrence for each sector has been calculated (Fig. 9).

The prevailing direction South-West to North-East is present at each depth. This direction is almost parallel to the coastline. In particular the three instruments recorded dominant current in North-East direction (Fig. 9).

This behaviour is probably determined by the morphology of the area and the general circulation of the Castellammare gulf. The local circulation is strongly related to larger scale marine circulation.

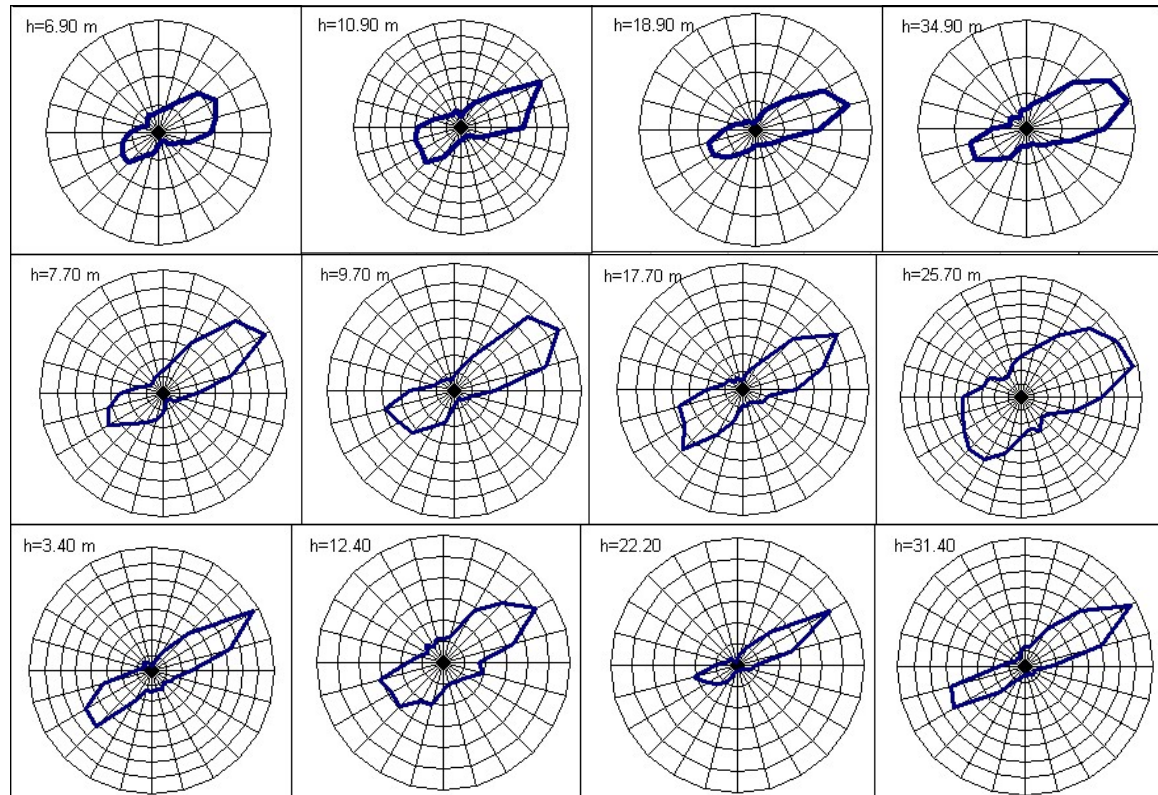


Figure 9. Frequency analysis of the velocity directions. a) ADP SonTek (10 cells), b) Aquadop Nortek (14 cells), c) ADP RDI.

CONCLUSIONS

The preliminary analysis of the collected data showed:

1. currents are parallel to the coastline of the study area;
2. the dominant direction is from South-East to North-West;
3. in some case an inversion occurs;
4. the tide influences the velocity field, accelerating and decelerating the above mentioned currents.

REFERENCES

- Nasello C. and Ciraolo G. (2004), Misure idrodinamiche nello Stagnone di Marsala, Proceedings of the XXIX Convegno di Idraulica e Costruzioni Idrauliche, September 2004. Vol. 1, pp. 699-706, Trento.
- Nasello C., Ciraolo G. and La Loggia G. (2005), Hydrodynamic Measurements in a Shallow Lagoon, 9th European Workshop on Physical Processes in Natural Waters, September 2005. pp. 125-134, Lancaster.
- Nasello C., Ciraolo G and La Loggia G. (2006), Misure di velocità e livelli nello Stagnone di Marsala. Proceedings of the XXX Convegno di Idraulica e Costruzioni Idrauliche, September 2006, CD-ROM, Roma.
- SonTek/YSI (2000). ADP: Acoustic Doppler Profiler Technical Documentation, September.,
- SonTek/YSI (2009). Acoustic Doppler Profiler Application Notes: ADP Versatility in San Felipe, Mexico Deployment. <http://www.sontek.com/apps/profiler/adp-sf/adp-sf.htm>, visited 20 March 2009.
- Cioffi F., Gallerano F. and Napoli E. (2005), Three-dimensional numerical simulation of wind-driven flows in closed channels and basins. *Journal of Hydraulic Research* **43**(3), 2005.

Investigating marine shallow waters dynamics to explore the role of turbidity on ecological responses

S. Di Marca^{1*}, M. Lo Martire¹, C. Nasello², G. Ciraolo², and G. Sarà¹

¹ Dipartimento di Ecologia, Università di Palermo, Viale delle Scienze, Ed. 16 – 90128 Palermo, Italy

² Dipartimento di Ingegneria Idraulica ed Applicazioni Ambientali, Università di Palermo, Viale delle Scienze, Ed. 8 – 90128 Palermo, Italy

*Corresponding author, e-mail s.dimarca@gmail.com

ABSTRACT

The ecological tangible effect of the complex interaction between sediments and water column in shallow waters is represented by turbidity which is a common feature of most aquatic ecosystems: it varies both temporally and spatially. Turbidity can cover large areas and persist for long periods or it can be very localized and temporary. Among many factors able to generate turbidity, wind generated wave action and water mass movements due to tides seem important in causing resuspension of sediments. Although there is much research spent in last decades on this topic and many models to explain the complexity of the wind-water-sediment interaction, some interactive aspects are highly site specific and then still poorly understood. On the other hand, this interaction involves many physical, chemical and trophic aspects like water flow velocity, turbulence, boundary layer thickness, environmental stresses and, in turn, resuspension, transport, and deposition of particulate matter, mechanical limits to size, larval dispersion, food availability.

KEYWORDS

Biological-physical interaction, ecological responses, hydrodynamics, resuspension, shallow water, turbulent kinetic energy, turbidity.

INTRODUCTION

In shallow waters, seagrass beds may exert strong effects on hydrodynamics extracting fluid momentum due to roughness of vegetation and enhancing turbulence levels at the canopy-water interface. This process creates two dynamically different environments: the first, called vegetated layer (i.e., below the canopy) which is characterized by low flow velocity, a vertical gradient and turbulence (Gambi *et al.*, 1990) and the second over the interface which is characterized by greater velocity and higher degrees of turbulence (Ciraolo *et al.*, 2004; Nezu and Sanjou, 2008). Under these conditions, turbulence is not only generated at the canopy-water interface but also by wind-induced-shear-stress at the surface. Thus, turbulence controls resuspension intensity and the residence time of suspended matter in the water column whose presence substantially affects biological and ecological responses of aquatic organisms. Hydrodynamic variables as flow and shear velocities, turbulence kinetic energy (TKE) depict the behaviour of the non-vegetated layer often characterised by a boundary layer (i.e. that layer with a logarithmic velocity profile expressed by a modified von Karman Prandtl law)

according to Hendriks *et al.* (2005): $u(z) = \frac{u_*}{\kappa} \ln\left(\frac{z-d}{z_v}\right)$ (1)

where $u(z)$ is the velocity at height above bottom, u^* is the shear velocity, κ is the von Karman constant (~ 0.41), d is the displacement height (i.e. the height above bottom where the log velocity profile goes virtually to zero) and z_v is the vegetation roughness (Klopstra *et al.*, 1997). Although there is much research spent in last decades on these topics and many models have been formulated to explain the complexity of the wind-water-sediment interaction, some interactive aspects are too highly site-specific and then still poorly understood. On the other hand, this interaction involves many physical, chemical and trophic aspects like water flow velocity, turbulence, boundary layer thickness, environmental stresses and, in turn, resuspension, transport, and deposition of particulate matter, mechanical limits to size, larval dispersion and food availability for secondary consumers. In the present paper, the effect of vegetation coverage on water column behaviour was studied with a long-continuous experiment in a Mediterranean shallow area (the Stagnone di Marsala, Western Sicily) with the main aim of exploring the relative importance of resuspension throughout the water column in comparison of a lateral advective transport.

MATERIALS AND METHODS

The study area

The study was carried out in a semi-enclosed marine system, the Marsala lagoon (western Sicily, the Mediterranean Sea; Figure 1). The basin is shallow ($\sim 1.5\text{m}$) and the seagrass are particularly luxuriant in the basin, especially in the southern part where they are able to affect currents and silting. Water exchanges with the open sea are ensured by currents (a mean speed between $\sim 5\text{ cm s}^{-1}$ and $\sim 3\text{ cm s}^{-1}$, respectively in the Southern in the Northern areas). Geographical and environmental details are extensively reported in Pusceddu *et al.* (1997, 1999) and Sarà (2006).

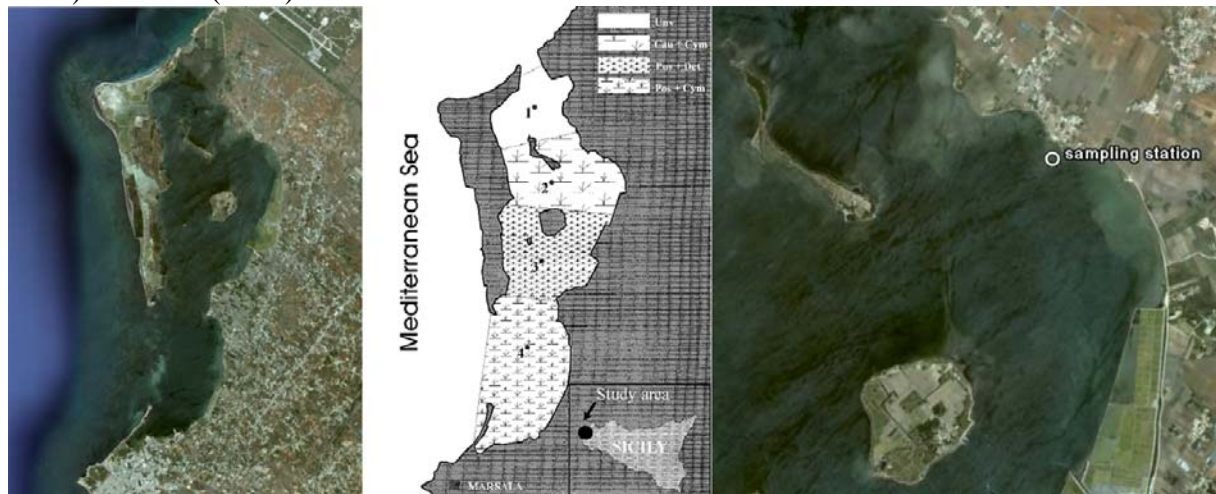


Figure 1 From the left side: Marsala lagoon (image from Google Earth); a schematic image that illustrate the spatial distribution of different algal and vascular plant coverage types (1. Unv = unvegetated; 2. Cau + Cym = *Caulerpa prolifera* + *Cymodocea nodosa*; 3. Pos + Det = *Posidonia oceanica* + detritus of *Posidonia*; 4. Pos + Cym = *Posidonia oceanica* + *Cymodocea nodosa*) (image from Pusceddu *et al.*, 1999), the study area and the sampling station (image from Google Earth).

Field measurements

The experiment was carried out between the 14 and 19 March 2007 for 5-continuous days in the north-eastern area of the Stagnone di Marsala characterised by 70% bottom coverage of seagrasses *Cymodocea nodosa* and *Ruppia maritima*. The sampling station was located at 100 m from the east coast ($37^{\circ}52'55.14''$ N, $12^{\circ}28'40.71''$ E) and had a depth of $\sim 0.9\text{ m}$ with a tidal amplitude of 0.25 m. The experiment consisted in collecting data (see Tab. 1 for details)

on wind speed and direction, water velocity at two different heights of the water column to understand the contextual response as turbidity and chlorophyll-a under conditions of seagrass coverage and flow regime driven by tides and wind events.

Instruments	Variables	Frequency	Positioning
<i>Meteorological station</i> Oregon Scientific WMR928X	Wind velocity (m s^{-1}) Wind direction ($^{\circ}$ from North magnetic)	1 data per minute	$\sim 2 \text{ m}$ above sea surface
<i>Multiprobe</i> YSI 6600	Turbidity (NTU)	1 data per minute	Sensor at 30 cm above bottom
<i>Acoustic doppler velocimeter</i> (ADV) Nortek	East ($x - \text{axis}$), North ($y - \text{axis}$) and Up ($z - \text{axis}$) component of flow velocity, respectively u , v , w (cm s^{-1})	8 data per second (8 Hz)	Sampling volume at 40 cm above bottom
<i>Electromagnetic current</i> <i>meter (ECM)</i> Valeport 808 EM	Magnitude of flow velocity in x - y plane (cm s^{-1}) Flow direction ($^{\circ}$ from North magnetic)	3 data per minute (0.05 Hz)	Sampling volume at 20 cm above bottom

Table 1

We used the linear wave theory and the empirical equations according to Carper and Bachmann (1984) and Demers *et al.* (1987) under the hypothesis that local resuspension was related to wind induced waves. In the linear wave theory the wavelength of a deepwater wave is related to its period by the well-known equation: $L = \frac{gT^2}{2\pi}$ (2)

where L is the wavelength, T is the wave period and g is the gravitational acceleration. In shallow waters like small lakes and lagoons, the wave period is related to wind velocity and effective fetch by the following equation (U.S. Army Coastal Engineering Research Center,

$$1977): \frac{gT}{2\pi W} = 1.20 \tanh \left[0.077 \left(\frac{gF}{W^2} \right)^{0.25} \right] \quad (3)$$

where W is the wind velocity and F is the effective fetch.

Data processing

From the whole dataset we obtained and calculated: **Flow velocity: F (cm s^{-1})** where F_1 i.e. F at 20 cm above bottom, is given from dataset of ECM; F_2 i.e. F at 40 cm above bottom, from datasets of ADV, calculated according the following equation: $F_2 = \sqrt{u^2 + v^2}$ (4)

Flow direction: α ($^{\circ}$) where α_1 i.e. α at 20 cm above bottom, is given from dataset of ECM; α_2 i.e. α at 40 cm above bottom, from dataset of ADV, calculated according the following equation: $\alpha_2 = \arccos \left(\frac{v_2}{F_2} \right)$ (5)

Turbulent kinetic energy: TKE ($\text{cm}^2 \text{s}^{-2}$): From dataset of ADV only, calculated according the following equation (Pope *et al.* 2006): $TKE = \frac{1}{2} (\overline{u'^2} + \overline{v'^2} + \overline{w'^2})$ (6)

Shear velocity [TKE]: u_* (cm s^{-1}). From dataset of ADV only, calculated according the following equation (Pope *et al.* 2006): $u_* = \sqrt{\frac{1}{2} C (\overline{u'^2} + \overline{v'^2} + \overline{w'^2})}$ where $C = 0.2$ (7)

Shear velocity [cov]: u_* (cm s^{-1}). From dataset of ADV only, calculated according the following equation modified after (Boudreau and Jørgensen, 2001): $u_* = \sqrt[4]{(u'w')^2 + (v'w')^2}$ (8)

Shear velocity [log]: u_* (cm s^{-1}). From dataset of ECM and ADV, when $F_2 > F_1$ and $|\alpha_1 - \alpha_2| < 30^\circ$ hypothesizing a log profile. Is given a value with linear regression according the following equation: $u_* = \frac{\kappa(F_2 - F_1)}{\ln\left(\frac{z_2}{z_1}\right)}$ (9)

Displacement height + roughness height: $d + z_v$ (cm). At the same condition above mentioned, is given a value of the sum $d + z_v$ according the following equation:

$$d + z_v = \exp\left[\ln z_2 - \left(\frac{F_2 \ln \frac{z_2}{z_1}}{F_2 - F_1}\right)\right] \quad (10)$$

It is well-known that z_v is negligible in comparison with d and for that the values obtained represent roughly 0.6 times the height of the inflection vegetation (Denny, 1986).

RESULTS AND DISCUSSION

Analysis of the velocity profile

Data coming from two different current meters allow us to deduce that the water column, during the big semidiurnal tidal transitional phase, had a flow field described the logarithmic layer following the wall law. In figures 2-5, we report some features of water column behaviour.

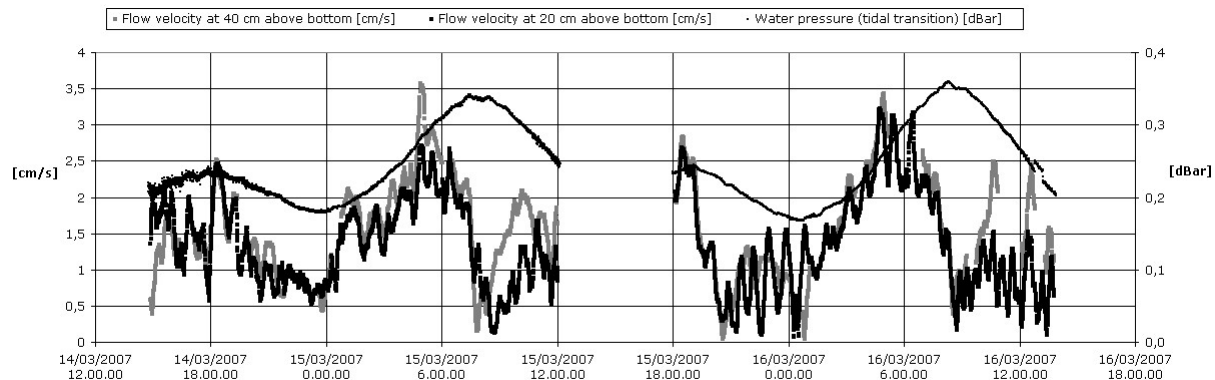


Figure 2 – Measured velocities and pressures

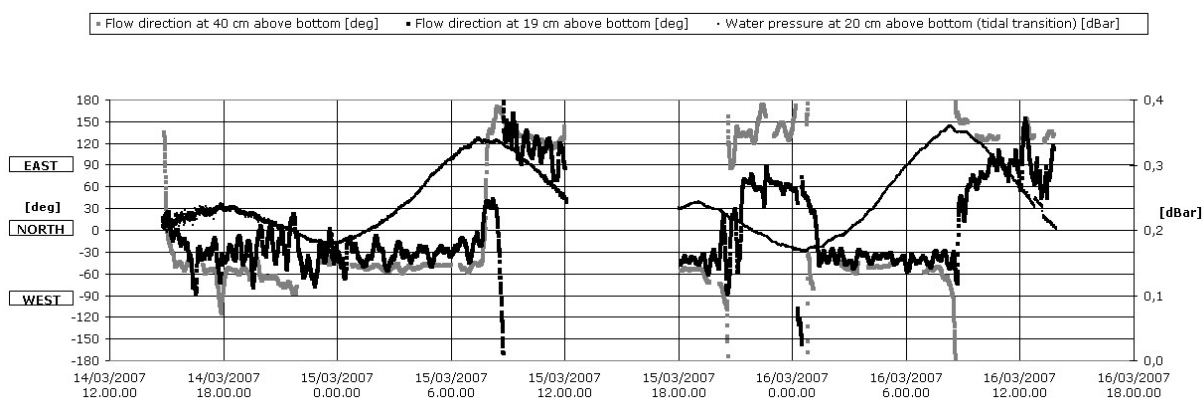


Figure 3– Measured flow directions and pressures

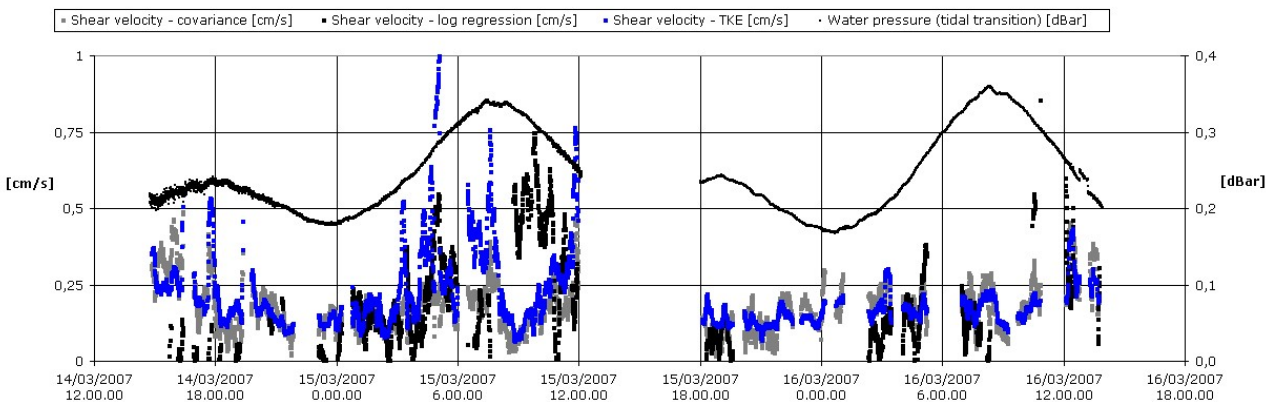


Figure 4– Shear velocities and pressures

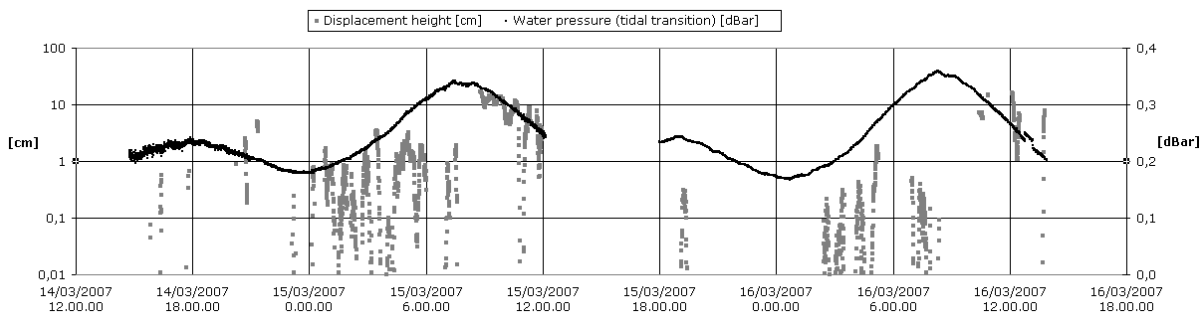


Figure 5– Displacement height and pressures

Analysis of interactions

Flow field was tidally driven (Figure 6), the wind and the turbulent kinetic energy (TKE) were in phase (Figure 7) while the CERC expected wave impact on the bottom (shadowed areas) and TKE were significantly correlated (Figure 8). These results suggested that, in terms of kinetic energy, the water column response to the wind action was substantially immediate (i.e., a few minutes). Nevertheless, the increase of water turbidity (and the concentrations of total suspended matter) and chlorophyll-a (as a proxy of food availability for consumers) (Figure 9) in the water column raised significant peaks with 8-hours shifts from the peaks in kinetic energy.

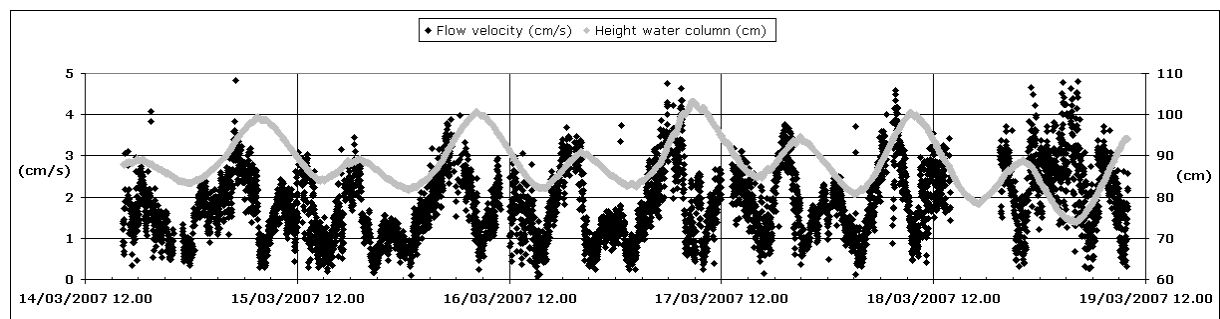


Figure 6 – Flow velocities and water level oscillations (tidally driven)

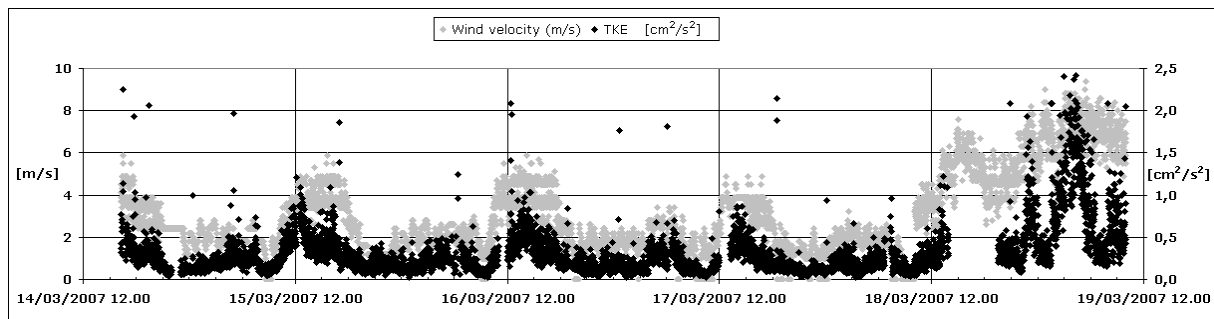


Figure 7 - Wind and the turbulent kinetic energy (TKE)

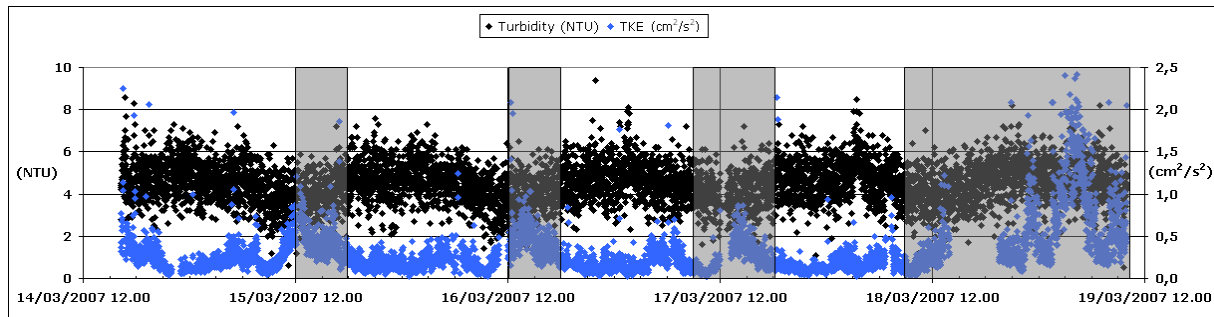


Figure 8 – Turbidity and turbulent kinetic energy (TKE)

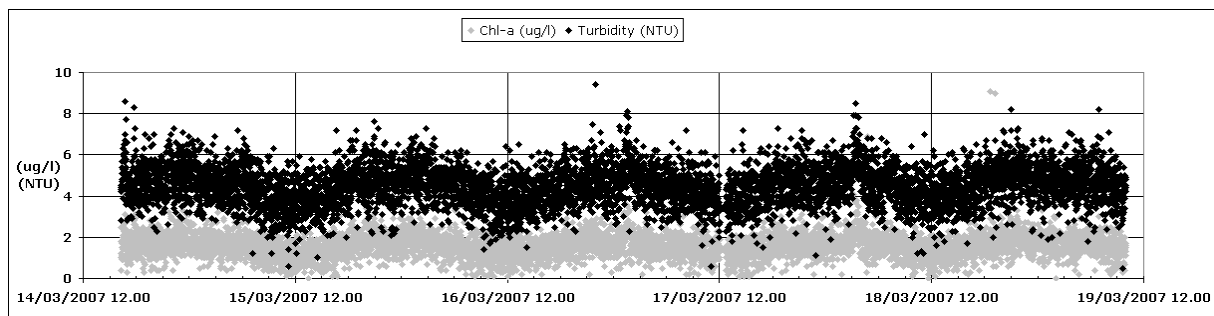


Figure 9 – Turbidity and Chl-a concentrations behaviour

The above figures indicates that vegetation play an important role as it influenced flow fields and sedimentary resuspension. Such a fact was pointed out by differences between observed and expected CERC patterns. Present results suggested that, through the turbulent motion, winds triggers effects on small scale (in the order of some meters) consisting in daily combined occurrence of wind events followed by turbidity peaks while. On larger scale (e.g., basin), winds induced a sort of inertial conveyor belt at surface after some hours of the starting of wind blowing. Thus, present preliminary data seems to confirm that the presence of the seagrass beds significantly attenuated wind-induced wave stress and such a fact should have important repercussions on ecological behaviour of pelagic species like resident fish and their main preys like zooplankton.

REFERENCES

- Boudreau B.P. and Jørgensen B.B. (2001). The benthic boundary layer. Transport processes and biogeochemistry. Oxford University Press.
- Carper G.L. and Bachmann R.W. (1984). Wind resuspension of sediment in a prairie lake. Can. J. Fish. Aquat. Sci., 41: 1763-1767
- Ciraolo G., Ferreri G. and La Loggia G. (2004). Flow resistance of *Posidonia oceanica* in shallow water. J. Hydraul. Res. 44 (2): 189-202

- Demers S., Therriault J., Bourget E. and Bah A. (1987). Resuspension in the shallow sublittoral zone of a microtidal estuarine environment: Wind influence. *Limnol. Oceanogr.*, 32 (2): 327-339
- Denny M., (1986). Biology and the mechanics of the wave-swept environment. Princeton University Press.
- Gambi M.C., Nowell A.R.M. and Jumars P.A. (1990). Flume observation on flow dynamics in *Zostera marina* (eelgrass) beds. *Mar. Ecol. Prog. Ser.*, 61: 159-169
- Hendriks I.E., van Duren L.A. and Herman P.M.J. (2006). Turbulence levels in a flume compared to the field: Implication for larval settlement studies. *J. Sea Res.*, 55: 15-29
- Jonsson P.R., van Duren L.A., Amielh M., Asmus R., Aspden R.J., Daunys D., Friedrichs M., Friend P.L., Olivier F., Pope N., Precht E., Sauriau P. and Schaaff E. (2006). Making water flow: a comparison of the hydrodynamic characteristics of 12 different benthic biological flumes. *Aquat. Ecol.*, 40: 409-438
- Klopstra D., Barneveld H.J., van Noortwijk J.M. and van Velzen E.H. (1997). Analytical model for hydraulic roughness of submerged vegetation. Proceedings of the 27th IAHR Congress in San Francisco, USA, 775-780
- Nezu I. and Sanjou M. (2008). Turbulence structure and coherent motion in vegetated canopy open-channel flows. *J. Hydro-env. Res.*, 2: 62-90
- Pope N.D., Widdows J. and Brinsley M.D. (2006). Estimation of bed shear stress using the turbulent kinetic energy approach – A comparison of annular flume and field data. *Cont. Shelf. Res.*, 26: 959-970
- Pusceddu A., Sarà G., Mazzola A. and Fabiano M. (1997). Relationships between suspended and sediment organic matter in a semi-enclosed marine system: the Stagnone di Marsala sound (western Sicily). *Water, Air Soil Pollution*, 99: 343-352
- Pusceddu A., Sarà G., Armeni M., Fabiano M., and Mazzola A. (1999). Seasonal and spatial changes in the sediment organic matter of a semi-enclosed marine system (W-Mediterranean Sea). *Hydrobiol.*, 397: 59-70
- Sarà G. (2006). Hydrodynamic effects on the origin and quality of organic matter for bivalves: an integrated isotopic, biochemical and transplant study. *Mar. Ecol. Prog. Ser.* 328: 65-73
- U.S. Army Coastal Engineering Research Center. (1977). Shore protection manual. Vol. I. U.S.- Army Coastal Engineering Research Center, Fort Belvoir, VA.
- Widdows J., Brinsley M.D., Salkeld P.N. and Lucas C.H. (2000). Influence of biota on spatial and temporal variation in sediment erodability and material flux on a tidal flat (Westerschelde, The Netherlands). *Mar. Ecol. Prog. Ser.* 194: 23-37

Turbidity analysis in Sicilian coastal zones by means of remote sensing images and spectroradiometric measurements

M. Tulone¹, A. Maltese^{1*}, G. Ciraolo¹ and G. La Loggia¹

¹ Dept. of Hydraulic Engineering and Environmental Applications, Università di Palermo (IT), Viale delle Scienze –Ed. 8, Palermo, 90128, Italy, IT

*Corresponding author, e-mail maltese@idra.unipa.it

ABSTRACT

Water turbidity has a wide range of variability both spatially and temporally. Rivers transport sediments to the river mouth following a seasonal behaviour and occasionally during flood events (Doxaran *et al.*, 2006; Pribble *et al.*, 2001). Once in the sea, sediments are spatially driven by currents, and re-suspended by waves from the bottom, changing water turbidity in the tidal and sub-tidal zones (Cloern *et al.*, 1989; Uncles *et al.*, 2002; Wolanski & Spagnol, 2003). Moreover human activities such as transport and dredging occasionally and locally influence turbidity magnitude and distribution (Schoellhamer, 1996).

In recent years the pollution of the maritime environment suggests that only operational monitoring activities can improve the preservation of this vulnerable and valuable ecosystem. Furthermore, these practices can aid the understanding of the anthropic impact on the maritime ecosystem. Within this framework, monitoring the spatial-temporal distribution of coastal water quality parameters plays a fundamental role. To this aim remote sensing techniques represent a suitable tool for water quality assessment, and for continuous monitoring of the Sicilian coastal waters. A chain of automatic processes has been developed in order to assess the Nephelometric Turbidity (NT). An algorithm has been calibrated using *in situ* data, obtained by intensive field campaigns undertaken in the three Sicilian gulfs (Castellammare, Augusta and Gela gulfs) during three periods in 2008 (at the beginning of July, August and September for each gulf).

KEYWORDS

Nephelometric turbidity; spectral reflectance; MODIS images.

INTRODUCTION

Turbidity is a measurement of the water transparency reduction due to suspended solids, organic matter particles and algal cells. It plays a key role in valuating the quality of sea coastal water, since it influences the light penetration, planktonic and benthonic algae productivity (Cloern, 1987; Cole & Cloern, 1987; Fisher *et al.*, 1999; Pennock & Sharp, 1994) and the growth of submerged vegetation and coral barrier (Anthony *et al.*, 2004, Moore *et al.*, 1997). Furthermore turbidity variability aids to understand the distribution of Total Suspended Solids (TSSs) and consequently coastal erosion as well as pollutant and chemical transport processes (Heyes *et al.*, 2004).

Optical instruments, for measurements of *in situ* turbidity, spread in the last decade; these are based on the interaction between ray light and substances within the water. Due to this interaction the light transfers energy to the substances, moreover it is refracted since the latter are characterized by a different refraction index from that of the water within which they are suspended.

Often conventional methods do not allow the characterization of turbidity dynamic due to spatial and temporal restrictions (*Chen et al, in press*). Remote sensors onboard of satellite platforms could be an valuable tool to retrieve repeated and synoptic maps of the surface water turbidity. Limits of the tool include the availability of simultaneous images characterized by high temporal and spatial resolution (*Doxaran et al., 2002; Miller et al., 2005; Ruddick et al., 2003; Stumpf & Pennock, 1989*).

Several authors successfully used Landsat TM (*Curran and Novo, 1988; Harrington et al., 1989; Reddy and Srinivasulu, 1994*).

Empirical relationships have been retrieved both for lakes and coastal waters, one commonly applied for a sea coastal water has been given by *Chen et al.* (2007), that has been calibrated using *in situ* data (43 samples) acquired in Tampa Bay (Florida) between May 2003 and April 2006 and MODIS images. Turbidity had obviously much lower values than in the lake case, ranging between 0.9 and 8.0 NTU.

Study aim

Aim of this study is to analyze temporal and spatial distribution of both turbidity and spectral reflectance, as well as to asses their statistical significance. Then the calibration of a nephelometric turbidity algorithm for a Mediterranean sea coastal water will be carried out.

We chose not to use NASA high level products such as Ocean Colour, LP DAAC (Land Processes Distributed Active Archive Center) etc., since their calibration is not adequate to fit the local field measurements.

The calibration process uses a dataset acquired in three Sicilian gulfs (Castellammare, Gela and Augusta) characterized by different morphology and bottom type (shallow, medium and deep waters).

Study area

The study area includes three main Sicilian gulfs (Castellammare, Augusta and Gela gulfs) that given their peculiar characteristics have been studied for many years. Data sampling has been carried out in three periods: at the beginning of July, August and September 2008.

Since the average diffuse attenuation coefficient K_d of the red wavelength is approximately $\sim 0.18 \text{ m}^{-1}$ the bottom influences the water leaving radiance up to a coast distance of 750 m at least. Therefore the remote sensing retrieved turbidity wouldn't be accurate within this area. MODIS Terra/Aqua images having 1 km spatial resolution have been processed only on no-land pixels; while samples were acquired between 1.5 km up to 5 km from the coastline.

The Castellammare gulf is the deeper inlet of the Sicilian coast, having a length ~ 60 km and a wire ~ 30 km. Moreover two intensive aquaculture farms produce tuna fish off the coast of Castellammare del Golfo town and sea bass and sea bream off the coast of Trappeto.

The Gela gulf has a coastline extending for about 75 km with a wire > 65 km. The water is prevalently shallow with a sandy bottom and the coast is characterized by several seaports and industrial activities. The latter include one of the bigger petrochemical refinery of the Mediterranean area.

Also the Augusta gulf has a coastline characterized by intensive chemical, petrochemical activities and several torrents flowing into the gulf. It extends for about 30 km with a wire > 15 km. Differently to the other gulfs, the Augusta gulf is mainly occupied by port structure (the Rada of Augusta).

The site choice was based on the NT variability, as can be preliminary analyzed on the remote sensing images calibrated using the *Chen et al.* (2007) empirical relationship.

Two zones having high anthropic pollution risk have been selected (Gela and Augusta gulfs), while the latter (Castellammare gulf) should be characterized by lower pollution. Sampling points were positioned along two transects having a distance of ~ 3.50 Km (Figure 1). Each

transect is almost orthogonal to the coastline and includes 3-4 sampling points. Within Castellammare gulf (Figure 1, top left panel), a further sampling point has been chosen between the two transects in order to assess peculiar characteristics of a fish factory (point C4).

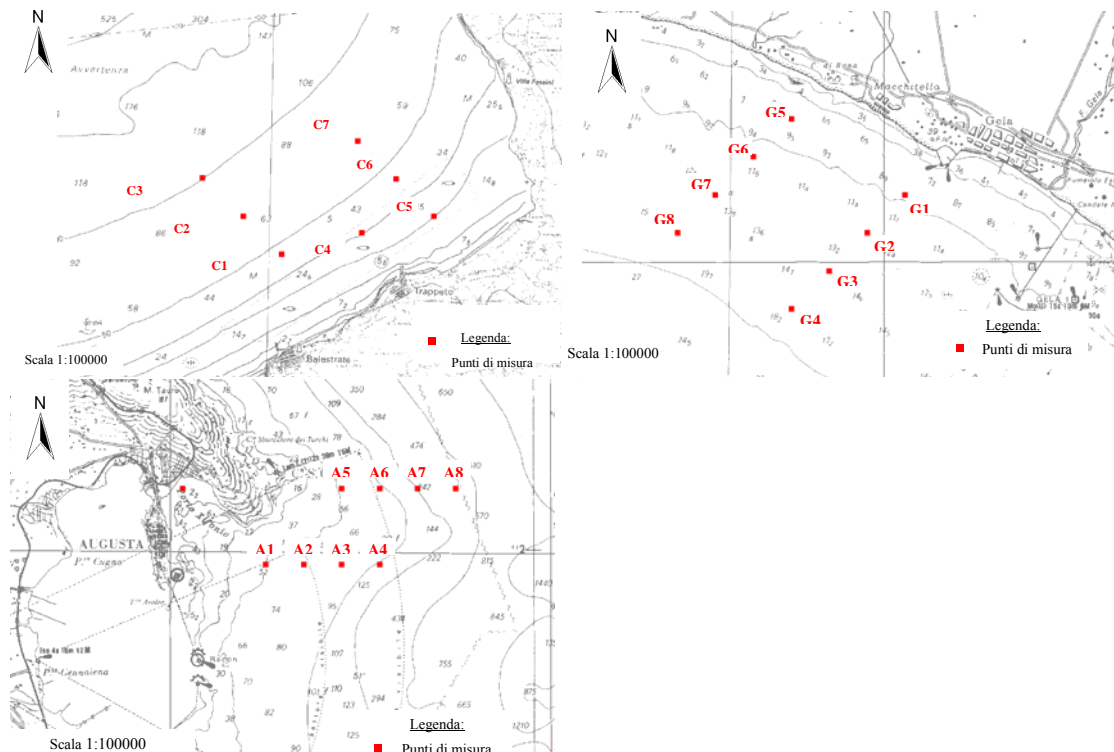


Figure 1. Sampling points geo-location within Castellammare (top left panel, from C1 to C7), Gela (top right panel, from G1 to G8) and Augusta (lower left panel, from A1 to A8) gulfs, over-imposed on Nautical maps.

MATERIAL

The dataset therefore includes *in situ* data of three campaigns carried out in the first week of July, August and September respectively; each day between 8.00 and 13.00 local time. Field data were positioned in UTM WGS84 using an EGNOS-enabled Magellan Meridian Platinum GPS device.

Spectroradiometric measurements

Underwater spectral irradiances and in-air upwelling spectral radiances were acquired using an Analytical Spectral Devices FieldSpec® HandHeld spectroradiometer operating between 325 and 1075 nm with a spectral resolution of 1.5 nm. A 10 meter long fiber optic cable, fitted with an underwater cosine diffuser probe, was used to acquire underwater irradiances at 11 depths from just below the water's surface, up to 5.5 meters.

Nephelometric turbidity measurements

Turbidimetry enables to assess a liquid turbidity by means of the absorption and reflection properties of the incident radiation at specific wavelengths.

A water turbidity increases, strongly affects the water warming due to the heat absorption of surface particles. The warming process determines a decreasing of dissolved oxygen concentration. Furthermore light is the most important element for photosynthetic processes

and a light intensity reduction affects the aquatic plants life and, then, a further dissolved oxygen reduction.

Turbidity is generally measured in Nephelometric Turbidity Units (NTUs) as specified by United States Environmental Protection Agency. The unit of measurement has been standardized on the formazin polymer compound, developed to match the gravimetric mass of Kaoline clay, so that a $1 \text{ NTU} \approx 1 \text{ mg l}^{-1}$ (of Kaoline within the water).

Remote sensed images

The MODIS (MODerate-resolution Imaging Spectroradiometer) spectroradiometer has 36 spectral bands: 21 between 0.4 and 3.0 μm , and the remaining 15 between 3.0 and 14.5 μm . It is characterized by a 2300 km footprint and a spatial resolution of 250 m for the first two bands, 500 m for the next 5 bands and 1 km for the remaining 29 bands, with a temporal resolution varying between 1 and 2 days. We chose not to use NASA high level products such as Ocean Colour, LP DAAC (Land Processes Distributed Active Archive Center) etc., since their calibration is not adequate to fit the local field measurements. The images have been automatically georeferenced using the Geographic Lookup Table (GLT) obtained from the latitude longitude dataset of the MOD03 product. The programming routines have been developed using the IDL programming language, allowing the simultaneous elaboration of the whole time series of images. MODIS level MOD02 - L1B images have been used within this research.

METHODS

NTU modelling

An empirical relationship, tested and calibrated on Tampa bay in Florida, can be applied in order to retrieve the surface turbidity from MODIS images (Chen, 2007). The relationship uses the remote sensing reflectance R_{rs} [sr^{-1}] of the red band (centred on 645 nm), calculated by rationing reflected radiance and downwelling irradiance. $R_{rs}(645)$ within the estuarine area of Tampa bay have shown values ranging between 0.001 and 0.008 sr^{-1} corresponding to *in situ* nephelometric turbidity (NT) ranging between 0.9 and 8.0 NTU (nephelometric turbidity unit). Empirical evidence ($n=43$) suggested a power relationship to better fit *in situ* data (1):

$$NT = a \cdot R_{rs}(645)^b \quad (1)$$

where the calibration coefficients $a=1203.9$ and $b=1.087$ are characterized by a determination coefficient $r^2=0.73$.

The equation (1) are valid for an estuarine area; since the aim of this research is to calibrate an empirical relationship useful to retrieve the NT for the Sicilian coastal zone, the multiplicative coefficient a and the exponent b need to be corrected using *in situ* data. Within our research, the reflectance R [-] has been calculated by rationing downwelling and upwelling radiances.

RESULTS

Water spectroradiometric properties

All the data were positioned in UTM Zone 33N WGS84 using an EGNOS-enabled Magellan Meridian Platinum GPS unit.

Spectral radiances were acquired using an Analytical Spectral Devices FieldSpec®HandHeld spectroradiometer operating between 325 and 1075 nm with a 1 nm nominal spectral resolution. The spectroradiometric measurements were carried out using a 25 degree optic lens and the distance from the target was approximately a metre. To calculate the spectral reflectance signatures of the coastal water, spectral radiances of the surface and of a white

reference panel are necessary. Reflectances were referenced to a calibrated white Labsphere Spectralon reference panel. Spectral reflectance measurements have been carried along two transects in each gulf for each sampling period.

The Castellammare gulf spectral characteristics

Spectral reflectance of July 2008 reach maxima at ≈ 450 nm, ranging between $\sim 2.5\%$ and $\sim 4.0\%$ with lower values characterizing the CA4 sampling point. The August 2008 spectral reflectance has maxima (≈ 450 nm) higher than those of July, ranging between $\sim 3.5\%$ and $\sim 7.0\%$. Lower values have been found within the Ittica Trappeto fish factory (CA4) as in July.

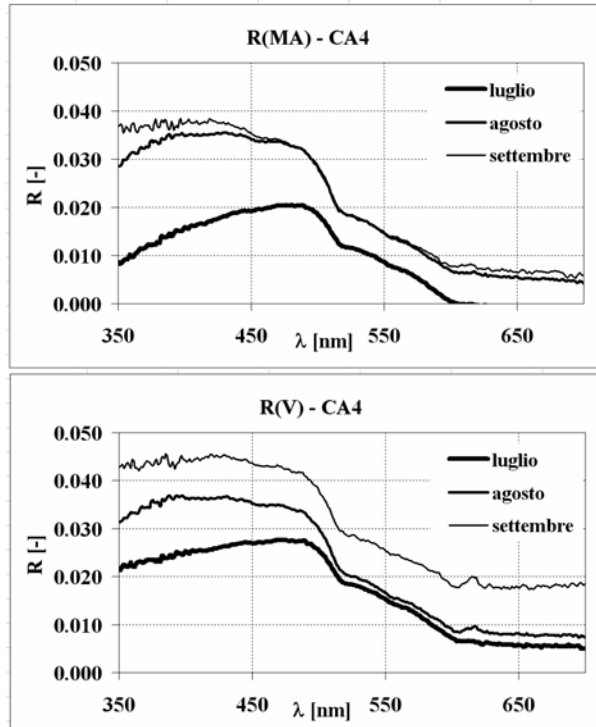


Figure 2. Spectral reflectance within the Castellammare gulf in July, August and September 2008.

The Gela gulf spectral characteristics

Spectral signatures in August are characterized by maxima (at ≈ 470 nm) similar to those of July. Values ranges between $\sim 3.0\%$ and $\sim 4.0\%$ with lower values characterizing the south-east transect close to the coastline. Spectral signatures of the north-west transect show anomalous values at ≈ 350 nm and in the near infrared. Spectral signatures in September show maxima (at ≈ 470 nm) similar to those acquired in the previous months. Values ranges between $\sim 3.0\%$ and $\sim 5.0\%$ with the lower values characterizing the off shore sampling points.

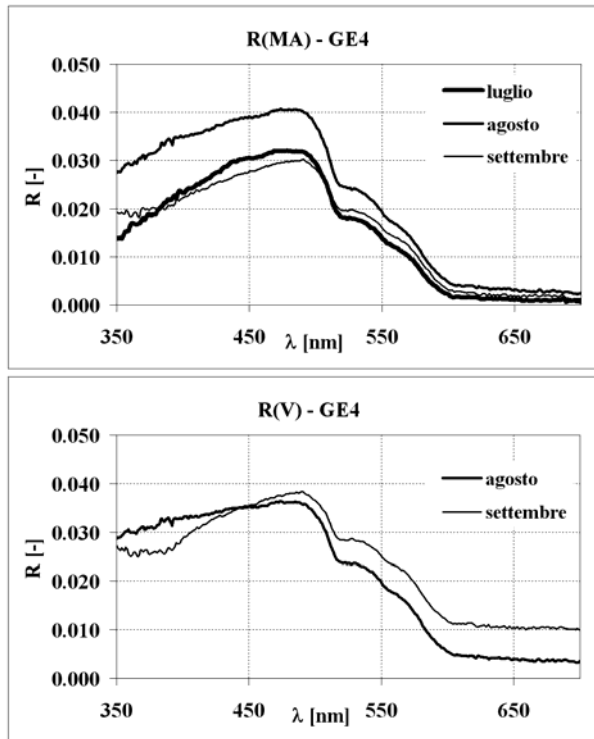


Figure 3. Spectral reflectance within the Gela gulf in July, August and September 2008.

The Augusta gulf spectral characteristics

Spectral signatures of July have maxima lower, on the average, than reflectances measured in Gela. Those values range between ~2.5% and ~3.5% with lower values characterizing sampling points closed to the coastline (A1 and A5, figure 4 left and right panel respectively). The second peak (at 550 nm) is less evident than that of Gela, like in Castellammare. The August spectral reflectances range between ~2.5% and ~4.0%, while the September signatures are lower than those of August (~3.0% - ~4.5%).

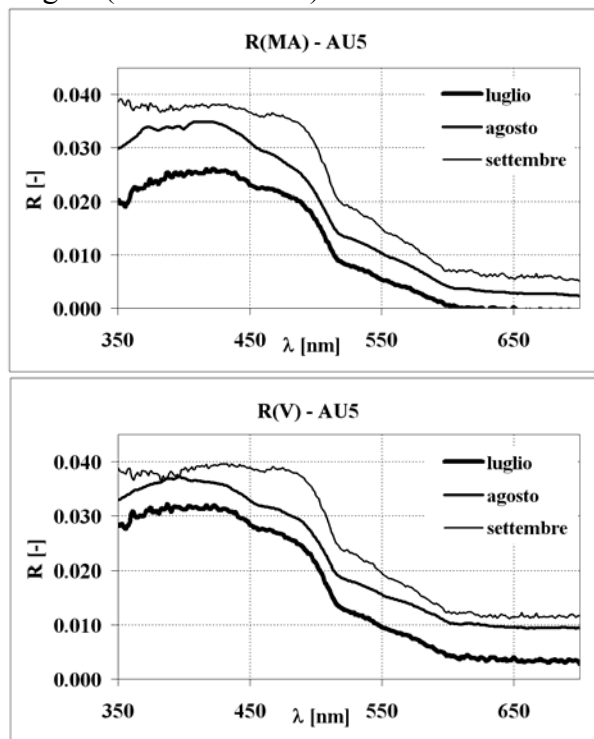


Figure 4. Spectral reflectance within the Gela gulf in July, August and September 2008.

Nephelometric properties

Nephelometric turbidity [NTU] shows maximum values during the first sampling period, where also the range of variability is higher: the minimum has been measured in Augusta (1.85 NTU) while the maximum has been measured in Gela (5.72 NTU). The NT decreases on the average in August, reaching minimum values in September with an absolute minimum measured both in Gela and Castellammare (1.27 NTU). Statistical values of the NT dataset are reported in Table 1.

Table 1. Nephelometric Turbidity average value (μ), standard deviation (σ), minimum (min) and maximum (max) and samples number (N), in the three Gulf of Sicily (Castellammare, Augusta and Gela gulfs) during three periods in 2008 (at the beginning of July, August and September).

	Castellammare					Gela					Augusta				
	N [-]	μ [NTU]	σ [NTU]	Min [NTU]	Max [NTU]	N [-]	μ [NTU]	σ [NTU]	Min [NTU]	Max [NTU]	N [-]	μ [NTU]	σ [NTU]	Min [NTU]	Max [NTU]
Jul	42	2.76	0.42	2.02	3.91	48	2.67	0.52	2.03	5.72	48	2.46	0.33	1.85	3.38
Aug	42	2.60	0.25	2.09	3.11	48	2.26	0.37	1.22	3.24	48	2.04	0.26	1.38	2.55
Sep	42	2.12	0.30	1.27	2.91	48	1.92	0.33	1.27	2.78	48	1.93	0.17	1.64	2.28

Algorithm calibration

Since the analysis shows that data acquired in different gulfs can be grouped together (23 samples), while they should left sub-divided depending on the month of acquisition (3 datasets), three datasets of calibration coefficients were obtained. The time series data of the three pairs of value (a pair of measured data and estimated values for each site) have been plotted on a Cartesian diagram to find a linear relationship by means the least square method. The correlation between the time series over different zones has been analyzed by means of the Pearson (r) coefficient, an appropriate statistical descriptor for continuous observations. Once retrieved the calibration coefficients, statistic calculation has been performed in order to verify their statistical significance.

Nevertheless, a strong correlation could be not statistically significant. The significance of the estimation has been assessed by means of probability distribution analysis of r for $P = 0.01$ (high significance level) and $P = 0.05$ (good significance level). The comparison between the r value retrieved from the experimental data with the one retrieved from the probability distribution (r^P were the subscript P denotes the significance level) has been carried out for fixed degrees of freedom: $GL = n-2$ (number of observation pairs minus the numbers of involved variables). In the present case $GL=21$ and $r^{0.01} = 0.526$ and $r^{0.05} = 0.413$.

Furthermore, the significance of the linear equation slope has been assessed through the T-Student test, aimed to verify if the statistical observed value t , given by the ratio between the slope and its standard error, is greater than the critical value t^P for chosen significance level P and for given degrees of freedom and two tales T-Student distribution. In the present $t^{0.01} = 2.831$ and $t^{0.05} = 2.079$. A comparison between the calibration coefficients retrieved from field spectroradiometric and NT data and those given by Chen et al. (2007) are reported in Table 2. The coefficient a does not change during the period of acquisitions, while the coefficient b reaches the maximum value in August and nevertheless, it is always higher then that found in literature.

Table 2. Reflectance to NTU calibration coefficient from in situ data (July, August and September) and given by Chen et al. (2007).

Calibration coefficients	July	August	September	Literature
<i>A</i>	1203.9	1203.9	1203.9	1203.9
<i>B</i>	1.112	1.399	1.290	1.087

Turbidity temporal and spatial distribution

The data analysis has been carried out on the average values of the above mentioned Gulfs as well as for the whole coastal area. The average NT ranges temporally between 3.8 and 6.4 NTU, and spatially between 0 and 10 NTU.

Average values reach the maximum in August (6.4 NTU), while NT in July and September is, on the average, 2.6 NTU lower. Castellammare, Gela and Augusta gulfs reach maximum values in August (8.7, 8.5 and 7.5 NTU respectively), while July is characterized by the minimum values (8.7, 1.5 and 2.1 NTU respectively). September NT is lower than August NT and higher than July NT except than in Castellammare gulf, (3.3, 5.3 e 5.7 NTU respectively).

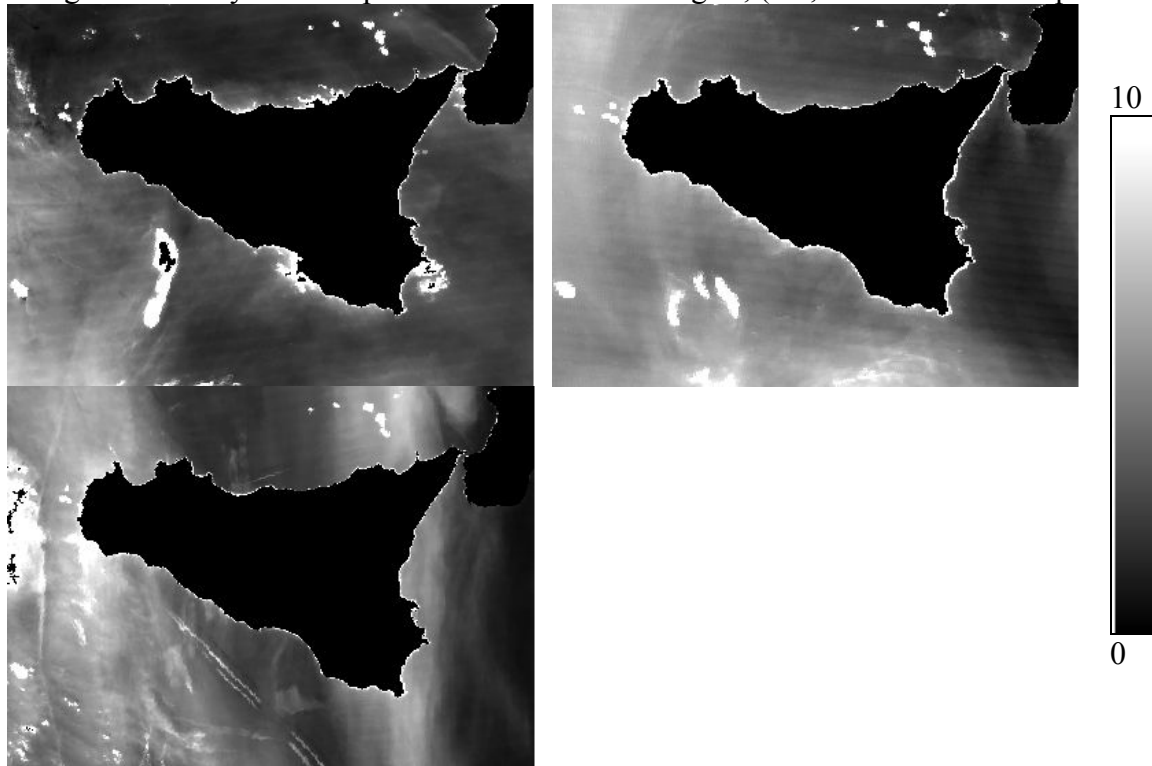


Figure 5. Nephelometric turbidity [NTU] in July 2008 (top left panel), August 2008 (top right panel) and September 2008 (lower left panel).

CONCLUSIONS

Field measurements, carried out during spring and summer period, have been taken into account to improve the local calibration of a nephelometric turbidity model using remote sensed images. Model setup for the Mediterranean coastal zone retrieve water quality maps matching field data better than NASA high level products, since the latter typically are *in situ* dependent or at best calibrated at global scale. As a consequence their use produces inaccurate water quality maps especially for the coastal marine zones.

Pre-calibration statistical analyses show that field data should be spatially grouped and temporally divided. Calibration shows that *a* is temporally constant (1203.9), differently from

the coefficient b increasing from July to August (1.112 to 1.399) and then decreasing in the last month (down to 1.290), always showing values higher than that found in literature (1.087). It is interesting to note that coastal sea waters show a reflectance peak between 450 and 470 nm with a second peak at 550 nm not always evident.

Turbidity temporal and spatial distribution are characterized by an average NT ranging temporally between 3.8 and 6.4 NTU, and spatially between 0 and 10 NTU.

The increased accuracy of the water quality maps represents important data to setup models for pollution assessment, and to implement products able to localise anomalies and trends of the water turbidity at regional scale.

ACKNOWLEDGEMENT

This research was partially funded by the ARPA (*Agenzia Regionale per la Protezione dell'Ambiente*) of the Sicilian Regional Government within the “*Monitoraggio della qualità delle acque marino-costiere siciliane con l'ausilio di tecniche di telerilevamento*” Project (Monitoring sea-coastal waters in Sicily using remote sensing techniques). Authors thank Dr. G. Sarà, of the Department of Ecology of the University of Palermo, for helping them in the field data interpretation, and Eng. A. Scordo and Dr. A. Vitagliano for field data acquisition.

REFERENCES

- Anthony, K. R. N., Ridd, P. V., Orpin, A. R., Larcombe, P., & Lough, J. (2004). Temporal variation of light availability in coastal benthic habitats: Effects of clouds, turbidity, and tides. *Limnology and Oceanography*, 49(6), 2201-2211.
- Chen, Z., Hu, C., Muller-Karger, F., & Luther, M. (in press). Physical forcing of short bio-optical variability in Tampa Bay: Observations from a coastal tower. *Limnology and Oceanography*.
- Chen Z., Hu C., Muller-Karger F. (2006). Monitoring turbidity in Tampa Bay using MODIS/Aqua 250-m imagery. *Remote Sensing of Environment*, 109 (2007), 207-220.
- Chen Z., Muller-Karger F., Hu C. (2007). Remote sensing of water clarity in Tampa Bay. *Remote Sensing of Environment*, 109 (2007), 249-259.
- Cloern J. E. (1987). Turbidity as a control on phytoplankton biomass and productivity in estuaries. *Continental Shelf Research*, 7(11), 1367-1381.
- Cloern, J. E., Powell, T. M., & Huzzey, L. M. (1989). Spatial and temporal variability in South San Francisco Bay. II. Temporal changes in salinity, suspended sediments, and phytoplankton biomass and productivity over tidal time scales. *Estuarine, Coastal and Shelf Science*, 28, 599-613.
- Cole, B. E., & Cloern, J. E. (1987). An empirical model for estimating phytoplankton productivity in estuaries. *Marine Ecology- Progress Series*, 36, 299-305.
- Curran, P. J., and Novo, E. M. L. M. (1988). The relationship between suspended sediment concentration and remotely sensed spectral radiance: a review. *Journal of Coastal Research*, 4, 351-368.
- Doxaran, D., Castaing, P., & Lavender, S. J. (2006). Monitoring the maximum turbidity zone and detecting fine-scale turbidity features in the Gironde estuary using high spatial resolution satellite sensor (SPOT HRV, Landsat ETM+) data. *International Journal of Remote Sensing*, 27, 2303-2321.
- Doxaran, D., Froidefond, J. M., Lavender, S., & Castaing, P. (2002). Spectral signature of highly turbid waters. Application with SPOT data to quantify suspended particulate matter concentrations. *Remote Sensing of Environment*, 81, 149-161.
- Fisher, T. R., Gustafson, A. B., Sellner, K., Lacouture, R., Haas, L. W., Wetzel, R. L., et al. (1999). Spatial and temporal variation of resource limitation in Chesapeake Bay. *Marine Biology*, 133(4), 763-778.
- Harrington, J. A. Jr., Schiebe, F. R., and Morrison, F. E. (1989). Monitoring lake recovery using Landsat MSS (International Association of Hydrological Sciences Publication) No. 182, 143-150.
- Heyes A., Miller C., Mason R. P. (2004). Mercury and methylmercury in Hudson River sediment: Impact of tidal resuspension on partitioning and methylation. *Marine Chemistry*, 90(1-4), 75-89.
- Miller, R. L., McKee, B. A., & D'SA, E. (2005). Monitoring bottom sediment resuspension and suspended sediments in shallow coastal waters. In R. L. Miller (Ed.), *Remote sensing of coastal aquatic environments*, 259-276.

- Moore, K. A., Wetzel, R. L., & Orth, R. J. (1997). Seasonal pulses of turbidity and their relations to eelgrass (*Zostera marina* L.) survival in an estuary. *Journal of Experimental Marine Biology and Ecology*, 215(1), 115-134.
- Pennock, J. R., & Sharp, J. H. (1994). Temporal alternation between lightlimitation and nutrient-limitation of phytoplankton production in coastalplain estuary. *Marine Ecology-Progress Series*, 111(3), 275-288.
- Reddy, M. A., and Srinivasulu, S. (1994). Comparison of IRS-IB LISS-IIA pixel array sizes for estimating suspended solids concentration in Hussain Sagar lake, Hyderabad, India-a statistical approach. *International Journal of Remote Sensing*, 15, 3693-3706.
- Ruddick, K., Park, Y., & Nechad, B. (2003). MERIS imagery of Belgian coastal waters: Mapping of suspended particulate matter and chlorophyll-a. *MERIS user workshop*, 10–13th of November. Frascati: ESA, pp. SP-549.
- Schoellhamer, D. H. (1996). Anthropogenic sediment resuspension mechanisms in a shallow microtidal estuary. *Estuarine, Coastal and Shelf Science*, 43(5), 533-548.
- Stumpf, R. P., & Pennock, J. R. (1989). Calibration of a general optical equatio for remote sensing of suspended sediments in a moderately turbid estuary. *Journal Geophysical Research*, 94(C10), 14363-14371.
- Uncles, R. J., Stephens, J. A., & Smith, R. E. (2002). The dependence of estuarine turbidity on tidal intrusion length, tidal range and residence time. *Continental Shelf Research*, 22, 1835-1856.
- Wolanski, E., & Spagnol, S. (2003). Dynamics of the turbidity maximum in King Sound, tropical Western Australia. *Estuarine, Coastal and Shelf Science*, 56, 877-890.